Development and Investigation of Electrochemical Properties of High-Voltage Spinel-based Cathode Materials and Recycling Methodology for Li-ion Batteries

by

Shivamurthy B P
10CC20J26019

A thesis submitted to the
Academy of Scientific & Innovative Research
for the award of the degree of

DOCTOR OF PHILOSOPHY

in

SCIENCE

Under the supervision of
Dr. Nayaka G P

CSIR-National Chemical Laboratory, Pune

Academy of Scientific and Innovative Research
AcSIR Headquarters, CSIR-HRDC campus
Sector 19, Kamla Nehru Nagar,
Ghaziabad, U.P. – 201 002, India

December, 2024

Certificate

This is to certify that the work incorporated in this Ph.D. thesis entitled, "*Development and Investigation of Electrochemical Properties of High-Voltage Spinel-based Cathode Materials and Recycling Methodology for Li-ion Batteries*", submitted by *Shivamurthy B P* to the Academy of Scientific and Innovative Research (AcSIR) in fulfillment of the requirements for the award of the Degree of *Doctor of Philosophy in Science*, embodies original research work carried-out by the student. We, further certify that this work has not been submitted to any other University or Institution in part or full for the award of any degree or diploma. Research material(s) obtained from other source(s) and used in this research work has/have been duly acknowledged in the thesis. Image(s), illustration(s), figure(s), table(s) etc., used in the thesis from other source(s), have also been duly cited and acknowledged.

(Signature of Student)

Shivamurthy B P

Date: 23-12-2024

(Signature of Supervisor)

Dr. G P Nayaka

Date: 23-12-2024

STATEMENTS OF ACADEMIC INTEGRITY

I Shivamurthy B P, a Ph.D. student of the Academy of Scientific and Innovative Research (AcSIR) with Registration No. 10CC20J26019, hereby undertake that, the thesis entitled *"Development and Investigation of Electrochemical Properties of High-Voltage Spinel-based Cathode Materials and Recycling Methodology for Li-ion Batteries"* has been prepared by me and that the document reports original work carried out by me and is free of any plagiarism in compliance with the UGC Regulations on *"Promotion of Academic Integrity and Prevention of Plagiarism in Higher Educational Institutions (2018)"* and the CSIR Guidelines for "*Ethics in Research and in Governance (2020)*".

Signature of the Student

Date : 23-12-2024

Place: Pune

It is hereby certified that the work done by the student, under my/our supervision, is plagiarism-free in accordance with the UGC Regulations on *"Promotion of Academic Integrity and Prevention of Plagiarism in Higher Educational Institutions (2018)"* and the CSIR Guidelines for "*Ethics in Research and in Governance (2020)*".

Signature of the Supervisor

Name : Dr. Nayaka G P

Date : 23-12-2024

Place : Pune

Acknowledgments

With immense gratitude and a heart full of appreciation, I thank all those who have supported and guided me throughout this incredible journey. This thesis is a culmination of the collective efforts, encouragement, and unwavering belief of many individuals who have been my companions in this academic pursuit.

First and foremost, I express my profound gratitude to my research supervisor, ***Dr. G. P. Nayaka****, for his exceptional mentorship, constant encouragement, and insightful guidance. His unwavering support and deep knowledge have been the cornerstone of my academic growth, and I will forever be grateful for his patience and belief in my potential.*

I am sincerely thankful to ***Dr. Manjusha V. Shelke*** *for providing crucial facilities that significantly contributed to the success of my research. Her guidance and collaboration have been invaluable.*

I deeply thank the former Director, Dr. Ashwini Kumar Nangia, the present Director, Dr. Ashish Lele, and the former deputy director, Dr. C S Gopinath, for their visionary leadership and for fostering an inspiring and enabling research environment.

I extend my heartfelt thanks to CSIR for providing financial support through the research fellowship, which allowed me to focus on my research and achieve my academic goals.
I am also grateful to the former Heads of the Department, Dr. P. A. Joy, Dr. B. L. V. Prasad, and Dr. Ajith Kumar T. G., as well as the present Head of the Department, Dr. Rajesh G. Gonnade, for their constant support and for creating a vibrant and nurturing academic culture.

I deeply appreciate the invaluable guidance and support of my Doctoral Advisory Committee members, ***Dr. R. Nandinidevi, Dr. J. Nithyanandhan, and Dr. Shatabdi P. Mukherjee****. Their constructive feedback and encouraging words have greatly enhanced the quality of my work and helped me navigate challenges effectively.*

I want to thank the neighbor scientists, Dr. Kirandeep Singh, and collaborators, Dr. Vrushali Jadhav and Dr. Kushal Bhatte, for contributing to my scientific footsteps at NCL.
My senior friends, Dr. Thripuranthaka M., Dr. Apurva Patrike, and Dr. Mahan S., for your constant encouragement and insightful discussions. Also, thank you, Dr. Vikash Chaturvedi, Dr.

Shibin T., and Dr. Kranti Salgaonkar, for your unwavering support throughout my journey. Their camaraderie and advice have inspired and strengthened me, and I deeply cherish our bond.

I would also like to thank my wonderful labmates, and I am especially grateful to my research companion, Purnima Rawat, for the constant helping hand. Also, Abhishek, Vaibhav Patil, and Ramachandra Birajdar, for their unwavering support, collaborative spirit, and shared moments of laughter and learning. Their companionship has made the laboratory a delightful place to work and given me cherished memories that I will carry forward.

I also express heartfelt gratitude to my extended lab members Kundan Wasnik, Meenakshi Powar, Anoushka Das, Vinay Mirzapure, Rajkiran, Priyanshi, Shweta, Amrutha and Rajesh Bhat for their help and support throughout my PhD journey.

I take time to convey my gratitude to the project intern students who worked with me, Saujanya Mondal, Sakshi Kale, Shivani Angadi, Ambika Unnikrishnan, Hamza Yasir, Vijay Kumar G Reddy, Ashlin J Varghese for their help during my PhD.

I want to thank all my friends who made my life at CSIR-NCL more cheerful. Dinesh Singh, Mayur P Sangole, Manoj K Patil, Asma Biradar, Pritam Chakraborty, Barnika Chakraborty, Basava Prabhu, Akash Mhase, Mayur Baravkar, Umasharan Sahu, Darren S Christi, M Vijay Kumar.

I am indebted to the Central Analytical Facility, the technicians Mr. Deo Srinivas (XPS), Mr. Chetan, Mr. Tushar, Mr. Nitin Dabke, Mr. Anirudh, and Mrs. Shruthi for their consistent and timely support for the analysis.

I would like to express my deepest gratitude to my beloved wife, Mamatha B C, for her unwavering support, boundless patience, and unconditional love. Her belief in me and constant encouragement have been my greatest strength throughout this journey.

Finally, I am deeply thankful to my parents, brothers and sisters, friends, and colleagues, whose love, encouragement, and unyielding support have been my greatest strength. They have been my anchor during challenging times and my cheerleaders in moments of triumph.

To all those who have been a part of my journey, thank you for your kindness, guidance, and belief in me. This thesis is a testament to your unwavering support, and I will always hold your contributions close to my heart.

Shivamurthy B P

Table of Contents

Table of Contents ……...i

List of Figures ……...ix

List of Tables ……....x

List of Abbreviations ……..…… xvii

Chapter 1 1

Introduction..... 1

1.1 Energy storage and conversion: Rechargeable Batteries 2

1.2 Elementary concept of rechargeable battery..... 3

1.3 Rechargeable batteries and their origin..... 4

1.4 Overview of Li-ion batteries..... 5

1.5 Role of Li-ion batteries in the energy transition 6

1.6 Key components of Li-ion batteries..... 6

1.6.1 Cathode Materials: 7

1.6.2 Anode Materials:..... 7

1.6.3 Electrolytes: 7

1.6.4 Separators:..... 8

1.7 Cathode: A crucial component in Li-ion batteries..... 8

1.8 $LiMn_2O_4$ cathode material: Evolution, Advantages and Challenges 10

1.9 Fundamentals of $LiMn_2O_4$ and its derivative cathode materials. 11

1.10 Research problem statement 13

1.10.1.1 Issues of LMO spinel cathode materials:..... 13

1.10.1.2 Jahn–Teller (J-T) effect of manganese ions:..... 13

1.10.1.3 The dissolution of manganese ions:..... 14

1.10.1.4 Oxygen evolution..... 15

1.10.1.5 Interfacial stability 15

1.11 Degradation mechanism of spinel cathode materials..... 15

1.12 Stabilization strategies of high voltage spinel cathode materials 17

1.12.1 Elemental doping/substitution 18

1.12.2 Surface strengthening by coating..... 18

1.12.3 Morphology and particle size control 19
1.12.4 Design of stable cathode-electrolytes interface (CEI) 20
1.12.5 Crystal plane engineering 20
1.13 Current research directions and challenges 21
1.14 Rationale of selection of host and dopant elements 22
1.15 Recycling methodology for end-of-life Li-ion batteries 22
1.16 State-of-the-art recycling methods 24
1.16.1 Pyrometallurgical recycling of Li-ion batteries 25
1.16.1.1 Steps involved in pyrometallurgical methods 25
1.16.1.2 Advantages 26
1.16.1.3 Limitations 26
1.16.2 Hydrometallurgical recycling of Li-ion batteries 26
1.16.2.1 Steps involved in the hydrometallurgical process 27
1.16.2.2 Advantages 27
1.16.2.3 Limitations 28
1.16.2.4 Emerging techniques 28
1.17 Thesis objective 28
1.17.1 Multi-cation doping: 28
1.17.2 Surface coating: 29
1.17.3 Regeneration of cathode material from spent Li-ion batteries: 29
1.17.4 Regeneration and repurposing of anode material from spent Li-ion batteries: 29
1.17.5 Recovery and reuse of polymeric separator from spent Li-ion batteries: 29
1.18 Scope of the thesis: 30
1.18.1 High-energy and high-voltage cathodes 30
1.18.2 Regeneration of electrode materials of spent Li-ion batteries 31
1.19 Research impact 31
1.20 References 32
Chapter 2A 38
Formation of secondary phase domain by multi-cation substitution for the superior electrochemical performance of spinel cathodes for high-voltage Li-ion batteries 38

2A.1 Introduction 40
2A.2 Methods and materials 42
2A.2.1 Preparation of $LiMn_{2-x-y-z}Ni_xFe_yAl_zO_4$ (x=0.8-0.5, y=0.1-0.25, z=0.1-0.25) 42
2A.2.2 Material characterization methods 43
2A.2.3 Fabrication of electrodes and electrochemical measurement methods 43
2A.3 Result and discussion 44
2A.3.1 Structural characterization 44
2A.3.1.1 X-ray diffraction study 44
2A.3.1.2 Raman spectroscopic analysis 49
2A.3.1.3 XPS analysis 50
2A.3.1.4 X-ray fluorescence spectroscopic analysis 53
2A.3.1.5 Electron microscopic analysis 54
2A.3.2 Electrochemical characterization 61
2A.3.2.1 Cyclic voltammetry analysis 61
2A.3.2.2 Electrochemical impedance spectroscopy (EIS) 62
2A.3.2.3 Galvanostatic charge-discharge analysis 64
2A.4 Effect of cation-disordered rocksalt structure in the spinel structure 66
2A.5 XRD analysis of electrodes after electrochemical test 67
2A.6 Full cell fabrication and electrochemical analysis 68
2A.6.1 Cyclic voltammetry study 68
2A.6.2 Galvanostatic charge-discharge study 69
2A.7 Conclusions 70
2A.8 References 72
Chapter 2B 78
Influence of crystal plane orientation in enhancing the electrochemical performance of trication substituted cathode for Li-ion batteries 78
2B.1 Introduction 80
2B.2 Materials and methods 82 2
2B.2.1 Preparation of $LiMn_{2-x-y-z}Ni_xFe_yAl_zO_4$ (x= 0.4-0.5, y & z = 0.05-0.1): 82
2B.2.2 Materials characterization: 83

2B.2.3 Electrochemical characterization: 84
2B.3 Results and discussion 84
2B.3.1 Structural characterization 84
2B.3.1.1 X-ray diffraction study 84
2B.3.1.2 Raman spectroscopic analysis 89
2B.3.1.3 BET surface area analysis 90
2B.3.1.4 XPS analysis 91
2B.3.1.5 Electron microscopic analysis 97
2B.3.2 Electrochemical Performance Analysis 101
2B.3.2.1 Cyclic voltammetry study 101
2B.3.2.2 Electrochemical impedance spectroscopic analysis 103
2B.3.2.3 Galvanostatic charge-discharge study 104
2B.4 Impact of plane orientation on the electrochemical performance 107
2B.5 Post-electrochemical test analysis of electrodes 109
2B.6 Conclusions 111
2B.7 References 113
Chapter 3A 120
Impact of surface modification with Nickel ferrite in reducing the Mn dissolution to enhance the cycle stability of $LiMn_2O_4$ cathode material for Li-ion batteries 120
3A.1 Introduction 122
3A.2 Materials and Methods 124
3A.2.1 Synthesis of α–MnO_2 124
3A.2.2 Preparation of $LiMn_2O_4$ 124
3A.2.3 Surface modification of $LiMn_2O_4$ with $NiFe_2O_4$ 125
3A.2.4 Material characterization 125
3A.2.5 Electrochemical characterization 126
3A.3 Results and Discussion 127
3A.3.1 Structural characterization 127
3A.3.1.1 X-ray diffraction study 127

3A.3.1.3 Atomic force microscopic analysis 133
3A.3.1.4 Electron microscopy study 135
3A.3.1.5 X-ray photoelectron spectroscopy study 139
3A.3.2 Electrochemical analysis 141
3A.3.2.1 Cyclic voltammetry analysis 141
3A.3.2.2 Electrochemical impedance spectroscopy study 142
3A.3.2.3 Galvanostatic charge-discharge studies 144
3A.4 Conclusions 145
3A.5 References 146
Chapter 3B 149
Electrochemical performance enhancement of $LiMn_2O_4$ cathode materials for Li-ion batteries through nickel aluminate surface modification 149
3B.1 Introduction 151
3B.2 Methods and materials 152
3B.2.1 Synthesis of α–MnO_2 152
3B.2.2 Preparation of $LiMn_2O_4$ 153
3B.2.3 Surface modification of $LiMn_2O_4$ with Nickel aluminum oxide 153
3B.2.4 Structural characterization 154
3B.2.5 Electrochemical characterization 155
3B.3 Result and Discussion 155
3B.3.1 Material characterization 155
3B.3.1.1 X-ray diffraction (XRD) studies 155
3B.3.1.2 Raman spectroscopic analysis 160
3B.3.1.3 Electron microscopy studies 162
3B.3.1.4 X-ray photoelectron spectroscopic study 166
3B.3.2 Electrochemical analysis 168
3B.3.2.1 Cyclic voltammetry study 168
3B.3.2.2 Galvanostatic charge-discharge study 172
3B.4 Conclusions 174

Chapter 4 179

Restoration of degraded spinel structure from spent Li-ion battery cathodes towards reclaiming for second life 179

4.1 Introduction 181
4.2 Materials and Methods 184
4.2.1 Recovery of cathode material from spent batteries: 184
4.2.2 Re-lithiation of recovered cathode material 184
4.3 Results and Discussion 186
4.3.1 Structural and Elemental Characterization 186
4.3.1.1 ICP-OES and XRF analysis 186
4.3.1.2 X-ray diffraction studies 187
4.3.1.3 Raman spectroscopic analysis 190
4.3.1.4 Electron microscopic studies 191
4.3.1.5 XPS studies 195
4.3.2 Electrochemical Characterization 197
4.3.2.1 Cyclic voltammetry and Electrochemical impedance spectroscopy study 197
4.3.2.2 Galvanostatic charge-discharge study 200
4.4 Conclusions 203
4.5 References 205

Chapter 5 207

Performance analysis of regenerated rGO-electrodes from spent Li-ion battery anodes for secondary energy device applications 207

5.1 Introduction: 209
5.2 Methods and Materials 211
5.2.1 Materials and reagents. 211
5.2.2 Synthesis of graphene oxide from graphite of spent LIBs anode. 211
5.2.3 Reduction of GO using ascorbic acid. 212
5.2.4 Material characterization 212
5.3 Results and Discussion 213
5.3.1 Structural studies 213

5.3.1.1 X-ray diffraction study 213
5.3.1.2 XPS studies 218
5.3.1.3 BET surface area analysis 219
5.3.2 Electrochemical studies 220
5.3.2.1 Cyclic Voltammetry Analysis 220
5.3.2.2 Galvanostatic charge-discharge study 222
5.4 Residual secondary acidic waste treatment and re-use 223
5.5 Conclusions 224
5.6 References 225
Chapter 6 228
Regeneration and reuse of polymeric separators from waste Li-ion batteries for second-life applications 228
6.1 Introduction 230
6.2 Methods and materials 231
6.2.1 Separation of separator material 231
6.2.2 Physical characterization 232
6.2.3 Electrochemical examination 232
6.3 Results and discussion 233
6.3.1 Physical and structural properties analysis 233
6.3.1.1 X-ray diffraction study 233
6.3.1.2 Stress and strain analysis 234
6.3.1.3 Scanning electron microscopic analysis 235
6.3.1.4 BET surface area analysis 236
6.3.1.5 X-ray photoelectron spectroscopic study 237
6.3.2 Electrochemical performance analysis 239
6.3.2.1 Cyclic voltammetry study 239
6.3.2.2 Electrochemical impedance spectroscopy 240
6.3.2.3 Galvanostatic charge-discharge study 241
6.4 Conclusions 243
6.5 References 244

Chapter 7 245

Summary of the Thesis 245

7.1 Summary 246

7.2 Future Perspectives 248

Chapter 1

Introduction

1.1 Energy storage and conversion: Rechargeable Batteries

The global energy landscape is undergoing a profound transformation driven by the need for sustainable energy sources, efficient storage solutions, and enhanced conversion technologies. As nations strive to reduce carbon emissions and mitigate climate change, energy conversion and storage systems have become crucial in harnessing renewable energy, ensuring grid stability, and powering the modern economy.[1,2] At the heart of this revolution, batteries serve as a linchpin technology in storing energy from renewable sources and powering an extensive array of applications, from consumer electronics to electric vehicles (EVs) and grid-scale energy systems.[3] Energy conversion refers to transforming energy from one form to another, such as converting solar energy into electricity using photovoltaic cells or converting chemical energy into electrical energy through batteries. However, renewable energy sources like solar and wind are sporadic and do not provide a constant electricity supply. The fluctuating of this energy supply creates an increasing need for storage solutions capable of capturing surplus power during peak production periods and distributing it when demand arises.[4] Integrating sustainable energy sources into global power grids has accelerated the demand for energy storage technologies. Bloomberg New Economy Forum (BNEF) projects a substantial increase in global energy storage capacity, with predictions indicating that worldwide cumulative storage will surpass 1,095 GW by 2040, primarily due to advancements in battery technology.[5]

Effectively implementing storage technologies, especially batteries, is crucial in maintaining grid stability, harmonizing energy production and consumption, and facilitating the broad integration of renewable energy sources. Currently, the global energy storage landscape is characterized by the prevalence of lithium-ion batteries (LIBs), accompanied by growing efforts in research and innovation focused on alternative technologies. These emerging options include

solid-state batteries, flow batteries, and sodium-ion batteries. As of 2023, LIBs account for over 90 % of the global battery storage industry due to their substantial energy storage capacity, extended lifespan, and swiftly decreasing prices.[6] This dominance is particularly evident in the electric vehicle market and residential energy storage systems. In 2023, the worldwide capacity of grid-scale battery energy storage systems (BESS) has attained roughly 15 GW capacity. Forecasts indicate that this capacity will surpass 100 GW by 2030.[5] This growth is driven mainly by the rapid expansion of renewable energy installations, particularly in regions like North America, Europe, and Asia-Pacific. Countries like China and the U.S. are leading the deployment of large-scale battery storage systems, with significant investments in infrastructure and technology.

1.2 Elementary concept of rechargeable battery

A battery converts chemical energy into electrical energy through an electrochemical redox reaction. The growing demand for mobile electronic devices, such as smartphones and laptops, has increased the need for enhanced energy sources. Despite using state-of-the-art batteries in most modern electronic products, their performance still falls short of expectations. Moreover, incorporating heavy metals in numerous contemporary battery designs poses environmental hazards. As public awareness of these issues grows, the demand for eco-friendly battery components also grows.

Battery technology has evolved significantly over time. The field progressed through various innovations, starting with Volta's copper/zinc battery in 1800. These include Plante's lead-acid battery (1859) and Leclanche's zinc/manganese-oxide design (1866). Further advancements saw the introduction of zinc-air batteries in 1878 and Jungner's Ni-Cd cells in 1899. The mid-20th century brought about Yao & Kummer's sodium-sulfur batteries (1966) and lithium primary cells

in the 1960s. Modern battery technology is represented by Ni-MH batteries, developed in the early 1980s, and Li-ion secondary cells, which emerged in the early 1990s.[7]

Batteries are divided into two main types: primary and secondary. Primary batteries are intended for one-time use, as their electrode reactions are irreversible. These batteries must be disposed of after they are depleted. On the other hand, secondary batteries have reversible electrode reactions, enabling them to be recharged and utilized repeatedly.

1.3 Rechargeable batteries and their origin

Rechargeable batteries have transformed the energy storage landscape, catalyzing significant technological advancements across numerous fields, including consumer electronics, electric vehicles (EVs), and large-scale renewable energy systems. According to John B Goodenough, developing lithium-ion rechargeable batteries has been crucial for advancing mobile and widespread electronic devices. He stated that these portable and omnipresent technologies would not have been feasible without the invention of rechargeable batteries.[8] LIBs have become the preferred choice among the various battery technologies available due to their superior characteristics. These include their high energy density, extended cycle life, and minimal self-discharge rate.[9] The benefits of LIBs have positioned them as a crucial component in the worldwide shift toward eco-friendly energy alternatives to reduce carbon emissions in transportation and incorporate renewable sources into their power grids.

Important terminology of batteries

Capacity (Ah): The quantity of electrical charge involved in the electrochemical process.

Specific capacity (Ah/kg): The amount of charge per unit of volume

Volumetric capacity (Ah/l): Capacity per volume unit

Energy (J or Wh): Quantity of electrical work done is V x I x t

Specific energy (Wh/kg): Energy per mass unit

Energy density (Wh/l): Energy per volume unit

Power (W): Rate at which the energy is available = V x I

Where V is voltage, I is current, t is time.

Charge or discharge rate (C/h): It is also termed as C rate, where h is the time in hours required to complete one charge or discharge.

1.4 Overview of Li-ion batteries

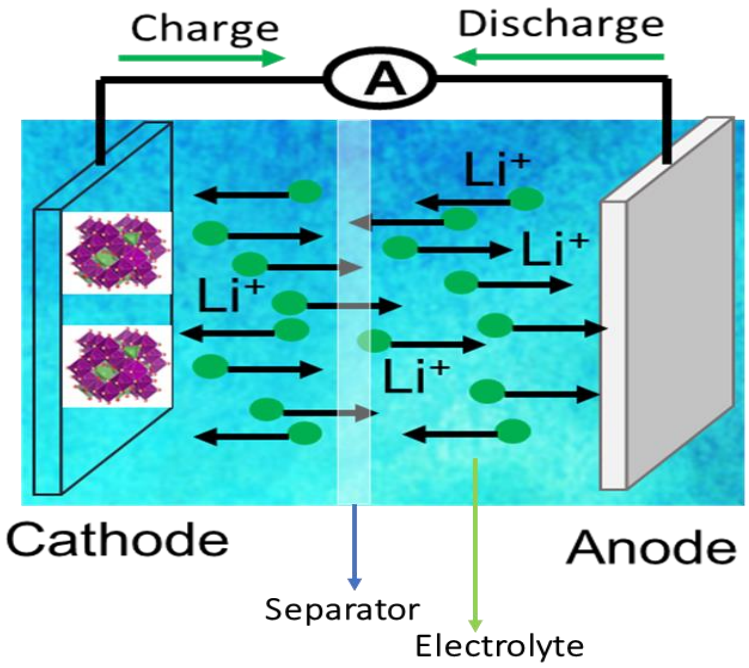

Figure 1.1. Schematic representation of Li-ion battery

Lithium-ion batteries (LIBs) were developed in the 1980s, with their commercial introduction by Sony Corporation in the 1990s. These batteries, featuring a $LiCoO_2$ cathode, were initially utilized in mobile phone technology. Later, extensive research and development on Li-ion energy storage technology was conducted globally to meet the escalating demand for consumer electronics.[10,11] The field of rechargeable batteries has witnessed considerable growth owing to

their extensive use in electric vehicles, renewable energy storage, space exploration, and defense technologies.[12] Advanced rechargeable batteries primarily rely on Li-ion technology, which requires compliance with various voltage, capacity, and power criteria based on the application. However, cathode materials mainly limit several technological obstacles to LIB development, such as their structural stability and low energy density.[13–15] A significant impediment to Li-ion battery technology is the short lifespan or accelerated degradation of materials following multiple charge-discharge cycles.[12]

1.5 Role of Li-ion batteries in the energy transition

In transitioning to a low-carbon economy, Li-ion batteries play a crucial role in electrifying transportation and facilitating the widespread adoption of renewable energy technologies. Their superior energy density and longevity make them suitable for electric vehicles and grid-scale energy storage systems, vital for reducing greenhouse gas emissions.[16] Nevertheless, the surging demand for Li-ion batteries has sparked concerns about the sustainability and availability of essential raw materials, including lithium, cobalt, and nickel.[17] To address these challenges, researchers are intensifying their efforts in various areas, such as developing battery recycling techniques, exploring alternative materials, and enhancing resource efficiency throughout the entire battery lifecycle.[16]

1.6 Key components of Li-ion batteries

Li-ion battery performance, longevity, and safety depend on the materials used in their essential components: the cathode, anode, electrolyte, and separator. Each component must be optimized to maximize energy output, durability, and operational safety.

1.6.1 Cathode Materials:

The choice of cathode material significantly affects the battery's energy density and thermal stability. Common cathode materials include $LiCoO_2$, $LiNi_xMn_yCo_zO_2$ (NMC), $LiMn_2O_4$, and $LiFePO_4$. Among all the cathodes, $LiMn_2O_4$, particularly its multi-cation doped form, attracts interest for its high voltage applications, cost-effectiveness, rapid charging capabilities, and eco-friendly nature. Nevertheless, it encounters challenges such as diminishing capacity resulting from Jahn-Teller distortion.[18]

1.6.2 Anode Materials:

Graphite remains the most widely used anode material, providing stable cycling with a low voltage profile. However, alternatives like silicon and lithium titanium oxide (LTO) offer significantly higher capacities, though they introduce new challenges, such as mechanical instability due to volumetric expansion during cycling.[10]

1.6.3 Electrolytes:

The electrolyte enables the movement of Li^+ ions between electrodes; despite their widespread use, liquid electrolytes pose safety risks due to their flammability and tend to deteriorate over time, which shortens battery lifespan. To address these issues, researchers have suggested using solid electrolytes to enhance safety and extend the longevity of future Li-ion battery designs.[19] The most commonly used electrolytes are based on lithium salts in organic solvents. Some examples are Lithium Salts such as $LiPF_6$, LiTFSI, LiFSI, and $LiBF_4$/$LiClO_4$, dissolved in Organic Solvents. Carbonates such as Ethylene Carbonate (EC), DMC/DEC, and some emerging electrolytes like fluorinated ethers for high-voltage applications. Solid-state electrolytes such as Inorganic Sulfides ($Li_{10}GeP_2S_{12}$), oxides (LLZO), and Polymeric PEO-based for solid-state systems.

1.6.4 Separators:

The separator maintains electrical separation and prevents the short circuit. Generally used separators are polyolefin-based separators such as polyethylene/polypropylene (PE/PP), which are cost-effective with good mechanical and thermal properties. PE/PP composite combines the advantages of both materials: ceramic-coated separators enhance thermal stability and prevent shrinkage, and nonwoven for high porosity and wettability, suitable for high-performance batteries.

1.7 Cathode: A crucial component in Li-ion batteries

A battery's essential components are the cathode, anode, and electrolyte. The active material in the positive electrode largely determines battery efficiency. Researchers have documented various cathode materials since their introduction in LIBs. During the 1980s, layered $LiCoO_2$ cathode materials have been widely used in portable electronic devices.[20] Nevertheless, the energy density of these batteries is insufficient for specific applications, such as electric vehicles (EVs) and stationary energy storage systems, due to their constrained practical capacity, which reaches only 160 mAh g^{-1}. As a result, advancing LIB cathode materials is crucial for enhancing the energy density of next-generation LIBs. This development focuses on identifying novel cathode materials that offer increased capacity or higher operating voltage.[14,21,22] Research interest in cathode materials has broadened beyond $LiCoO_2$ to encompass various other cathode chemistries. The layered compounds of $LiMO_2$ (where M represents Ni, Co, Mn, or other elements), spinel LiM_2O_4 (with M being Ni, Mn, or others), and Olivine $LiFePO_4$ are the other cathodes. The lithium-rich layered oxide xLi_2MnO_3 and low lithium oxides $(1-x)LiMO_2$ (where M denoting Ni, Co, Mn, or alternative elements) has sparked interest owing to its exceptionally high capacity, which surpasses 250 mAh g^{-1}.[23,24] The enhanced energy density of these cathodes

can be attributed to their higher operational voltage or increased discharge capacity. For example, cathode materials like $LiMn_2O_4$ and $LiNi_{0.5}Mn_{1.5}O_4$, which function at elevated voltages, exhibit a voltage plateau reaching as high as 4.7 V compared to Li/Li^+.[25] Additionally, Ni-rich layered $LiMO_2$ (M = Ni, Co, Mn, etc.) cathodes can achieve a discharge capacity of around 200 mAh g^{-1}.[22] Evaluating the effectiveness of cathode materials involves multiple aspects, including their ability to handle different charge rates, eco-friendliness, energy and power densities, durability over time, safety features, and economic viability. However, it is essential to note that all existing cathode materials face challenges in maintaining structural integrity, preserving capacity over time, and preventing potential thermal instability issues.

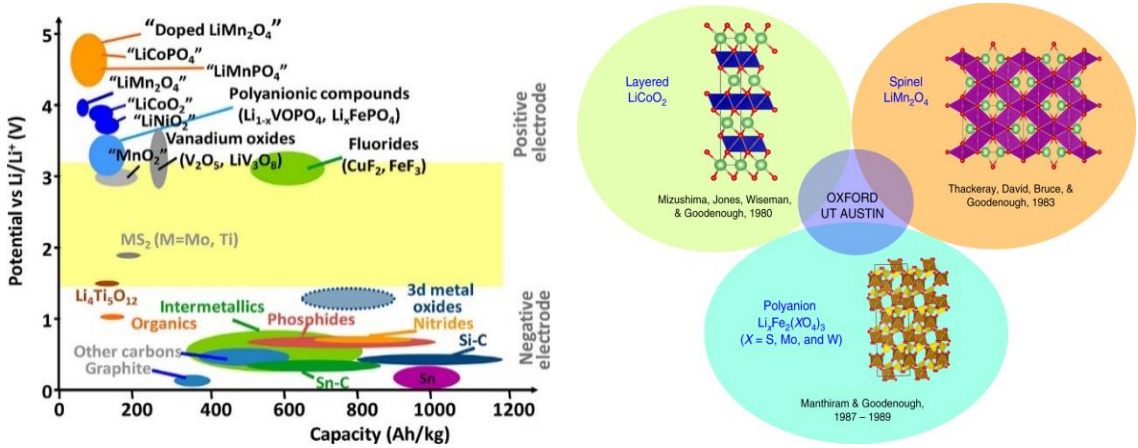

Figure 1.2. **(a)** Capacity v/s Voltage of electrode materials for LIBs (reproduced from ref. [26]), **(b)** Crystal structures of primary cathode materials (reproduced from ref. [10]).

The key performance indicators for LIB cathode materials should be assessed based on their energy and power densities, long-term durability, safety features, and economic viability.[27,28] Achieving high energy density requires both elevated voltage and substantial capacity. Therefore, cathode materials must exhibit high specific and volumetric capacities and operate within the electrolyte's electrochemical stability range at higher voltages.[29] Power density is another crucial criterion evaluated through metrics such as rate and faster charging capabilities, focusing on

diminishing cell resistance. Batteries must exhibit extended cycle stability and durability: a stable electrode material only can provide a stable interface between the electrode and electrolyte. Safety is a crucial requirement for successful cathode materials. The depreciation of heat generation from exothermic reactions and oxygen evolution from cathode materials must be considered at the cell material level. The cost of cathode materials should be economically viable.[27]

1.8 $LiMn_2O_4$ cathode material: Evolution, Advantages and Challenges

The search for inexpensive cathode materials with abundant metals led to the discovery of $LiMn_2O_4$. Hunter et. al. first reported the AB_2O_4 type of material in 1981.[30] This report claims that it converts spinel $LiMn_2O_4$ into a new form of manganese dioxide, called λ-MnO_2, through chemical de-lithiation in aqueous acidic solutions.[30] Following early investigations into the electrochemical lithiation of Fe_3O_4 spinel,[31] Thackeray and colleagues reported the electrochemical lithiation.[32] and de-lithiation[33] of $LiMn_2O_4$ spinel in 1983[32] and 1984,[33] respectively. These findings have significantly accelerated the research interest in this class of cathode materials owing to their excellent thermal stability. The main reasons for the reduced capacity of the $LiMn_2O_4$ cathode material are the **i)** disproportionation of Mn^{3+} ions into Mn^{4+} and Mn^{2+}, **ii)** Jahn–Teller distortion, and **iii)** Mn ion dissolution from the cathode.

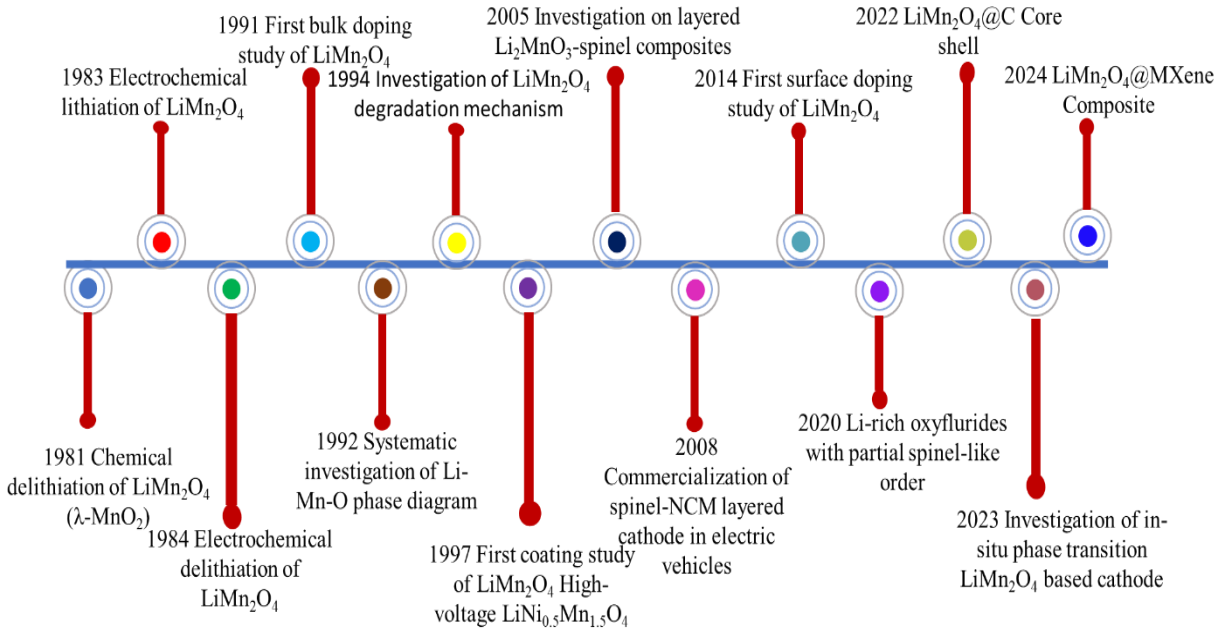

Figure 1.3. Historical timeline of the development of $LiMn_2O_4$ cathode material.

1.9 Fundamentals of $LiMn_2O_4$ and its derivative cathode materials.

Due to its excellent structural integrity during charge and discharge cycles, lithium manganate ($LiMn_2O_4$) becomes a potential cathode material for high-voltage LIBs. $LiMn_2O_4$ features a cubic spinel structure belonging to the oxide class AB_2O_4 under the space group Fd-3m. Its spinel structure allows for three-dimensional intercalation, thus enhancing its performance. In this spinel structure, the A-site Li cations occupied $1/8^{th}$ of the tetrahedral sites at 8a; at the B-site, Mn cations occupied half of the octahedral sites at 16d, and oxygen (O) anions formed a face-centered cubic (FCC) lattice at the 32e Wyckoff position. Its spinel structure allows for three-dimensional intercalation, thus enhancing its performance. The remaining half portion of the octahedral cation sites within the structure constitutes vacancies at the 16c positions. It is conjectured that these vacant 16c sites function as pathways for lithium migration bridged by two neighboring lithium ions located at the 8a site.[34,35]

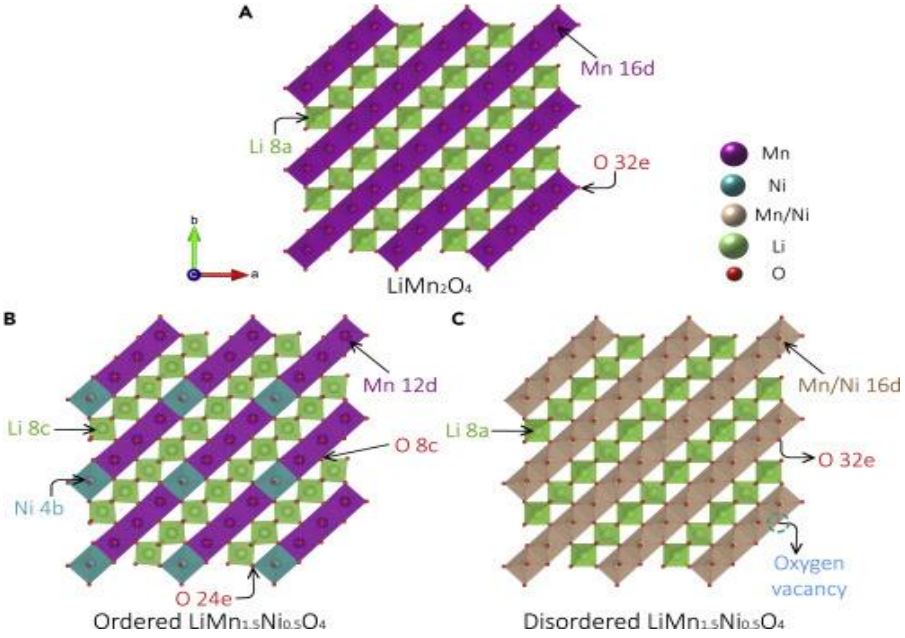

Figure 1.4(a-c). Schematic illustrations of the crystal structures of LMO-based cathode materials. (from ref [36])

$LiMn_2O_4$ has a theoretical capacity of 148 $mAhg^{-1}$ with a stable operating voltage from 3.0 to 4.3 V and a specific energy density of 490 $Whkg^{-1}$. The average valence state of Mn in $LiMn_2O_4$ is +3.5, which plays a crucial role in the J–T effect since half of the existing Mn ions are in the +3 state as Mn^{3+} ($t_{2g}^3e_g^1$).

The 3-dimensional B_2O_4 lattice was constructed through the edge-sharing of MnO_6 octahedra (as depicted in **Figure 1.5a**), establishing a robust network favorable for the three-dimensional diffusion of Li^+ ions. This diffusion occurs through vacant octahedral sites at 16c **(Figure 1.5b).**[37] Every 16c site is encircled by six 16d sites, creating a cation ring in a plane perpendicular to the lithium diffusion channel. This configuration serves as a structural unit known as a "gate site," facilitating the passage of lithium ions during migration, as illustrated in **Figure 1.5c**.[38]. Three-dimensional diffusion pathways can emerge inside the structure as each face of an 8a site is linked with a 16c site. The LiO_4 tetrahedra at the 8a sites share corners with MnO_6 octahedra positioned at 16d and faces with unoccupied octahedra positioned at 16c. Consequently,

Li-ions' movement from the tetrahedral 8a sites to the octahedral 16c sites returns to the 8a sites. Therefore, it is plausible to infer that despite its relatively lower theoretical capacity of approximately 148 mAh g^{-1}, LMO still exhibits high power-delivery capabilities.

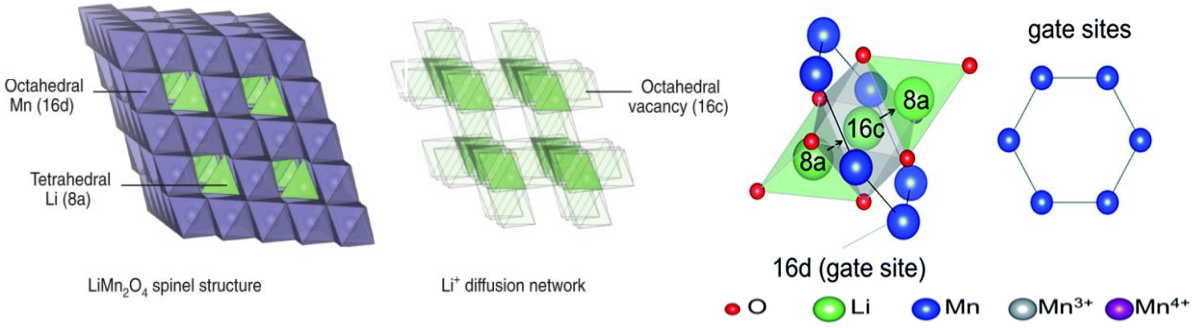

Figure 1.5 **(a)** 3D spinel structure of $LiMn_2O_4$ and **(b)** faster Li^+ diffusion network (adapted from ref.[39]) **(c)** Schematic picture of the Li diffusion channel from a tetrahedral 8a site to the adjacent 8a site through an octahedral 16c vacancy surrounded by 6 Mn ions in octahedral 16d gate sites. (adapted from ref.[38])

1.10 Research problem statement

1.10.1.1 Issues of LMO spinel cathode materials:

Spinel $LiMn_2O_4$ cathode materials have several advantages. However, their poor cycle life and discharge performance at a high current rate are less than ideal, particularly at elevated temperatures where a significant reduction of the discharge capacity occurs, limiting their large-scale application. These issues arise because of the following reasons:

1.10.1.2 Jahn–Teller (J-T) effect of manganese ions:

The J–T effect was first proposed by H.A. Jahn and E. Teller in 1937.[40] This is caused by the asymmetric occupation of electrons in degenerate orbitals, distorting the molecule's geometric configuration by reducing its symmetry and energy. Mn ions in the crystal structure consist of Mn^{3+} and Mn^{4+}, with Mn^{3+} being a high-spin, high-magnetic-moment Jahn-Teller ion.[41] During

discharge, as lithium ions continuously intercalate, the valence state of manganese decreases, converting Mn^{4+} to Mn^{3+}. This transition alters the crystal structure from cubic to low-symmetry tetragonal, impeding lithium-ion diffusion and electron conduction.[42]

Degradation in the Capacity of a battery typically occurs during two-phase reactions at cathodes, where the generation of Li-rich and Li-poor regions within the electrode material persuades unwanted stress between the particles, movement of the phase boundary, and pulverization of the particles. The surface instability of LMO and LNMO cathode materials also results in rapid capacity decay, often involving parasitic dissolution of transition metals, particularly Mn, into the electrolyte during cycling. Mn^{4+} is partially reduced to Mn^{3+} in LMO and LNMO cathode materials because of the oxygen loss during high-temperature sintering to maintain charge neutrality. However, Mn^{3+} undergoes disproportionation in the reaction $2Mn^{3+} \rightarrow Mn^{4+} + Mn^{2+}$, producing soluble Mn^{2+} in organic electrolytes.

1.10.1.3 The dissolution of manganese ions:

As discharge progresses, Mn^{3+} increases, leading to a disproportionation reaction on the material's surface, where Mn^{3+} is converted to Mn^{4+} and Mn^{2+}. The resulting Mn^{2+} dissolved in the electrolyte caused a loss of Mn ions. Additionally, the reaction between the lithium salt $LiPF_6$ in the electrolyte and trace water produces HF and other acidic substances, as shown in the following equations:

$$\boldsymbol{LiPF_6 + H_2O \rightarrow POF_3 + 2HF + LIF} \qquad \boldsymbol{---(1)}$$

$$\boldsymbol{4H^+ + 2LiMn_2O_4 \rightarrow 3\lambda MnO_2 + Mn^+ + 2Li^+ + 2H_2O} \qquad \boldsymbol{---(2)}$$

This dissolution of Mn^{2+} ions led to the destruction of the cathode material surface, accelerating the production of Mn^{2+} even further.[43] The use of non-electrochemically active

substances, which are formed due to these chemical changes, hinders the movement of Li^+ ions and significantly decreases the discharge capacity of spinel $LiMn_2O_4$.

1.10.1.4 Oxygen evolution:

Oxygen evolution is another major issue in cathode materials, especially under high-voltage conditions, as LMO-based cathode materials can operate at high-voltage ranges. Oxygen atoms can efficiently be released from the crystal lattices of Mn-based cathode materials, leading to structural deterioration, especially under external stress such as thermal runaway and collisions.[44] The oxygen species released will attack the electrolyte solvents and harm the cathode–electrolyte interphase (CEI) structures, accelerating the constructive environment for the irreversible redox reactions of the cathode materials.[45,46] The released oxygen can either form O_2 gas or oxidize the electrolyte to produce CO_2, causing battery swelling and eventual failure.[47]

1.10.1.5 Interfacial stability:

Instability at the solid electrode and liquid electrolyte interphase, led by the decomposition of organic electrolytes during operation at high voltage ranges, causes severe capacity decay in LIB cells.

1.11 Degradation mechanism of spinel cathode materials

$LiMn_2O_4$ and its derivative cathode materials have many superior qualities, including high voltage and energy. Despite its inherent advantages, the significant capacity fading limits its commercial applications. Mn's average electronic valence state in $LiMn_2O_4$ is +3.5, which is crucial for the J–T effect because half of the Mn ions are Mn^{3+} ($t_{2g}^3e_g^1$). One of the main reasons for this drawback is the presence of high-spin Mn^{3+} ions in $LiMn_2O_4$, which occupy an asymmetric state in the orbitals ($t_{2g}^3e_g^1$), which makes the Mn^{3+} cations more unstable.

The unstable Mn^{3+} in the system is stabilized by the deformation of MnO_6 octahedra, which extends the two axial Mn–O bonds and forces to contract the four equatorial Mn–O bonds.[48] The classification of the three-dimensional orbitals in Mn^{3}+ indicates that they can be divided into two degenerate orbitals, the e_g (d_{x2-y2} and d_z^2), and three degenerate t_{2g} orbitals (d_{xy}, d_{xz}, and d_{yz}). Due to their stable electronic configurations, Mn^{2+} and Mn^{4+} remain uninfluenced by the J-T effect. All the existing electrons of Mn^{3+} cation in a spin state occupy t_{2g} levels, resulting in a stable low-spin electronic state.[36] Nevertheless, the Jahn-Teller (J-T) effect can rapidly occur in the presence of a high-spin state Mn^{3+} cation due to the unsymmetrical distribution of electrons in the e_g orbitals (e_g^1). As the high-spin Mn^{3+} cation ($t_{2g}^3e_g^1$) of the cathode has only one electron in the e_g orbital (e_g^1) **(Figure 5b)**, the asymmetric distribution of electrons in the d_{x2-y2} and d_z^2 states could cause the varied levels of electronic shielding-effect over the Mn originated from diverse orientations. Additionally, the Oxygen anions shift further along the Z axis away from the Mn cation due to enhanced electrostatic repulsion. This repulsion occurs between the electrons in the dz^2 orbital of Mn^{3+} and the non-bonding electrons in the p orbital of the Oxygen anions that are coordinated with Mn cations[48] (**Figure 5a**). Such repulsive interaction transforms the phase from cubic spinel into the tetragonal. The Mn^{3+} cation in the center becomes unstable because of the irreconcilability between the complete d orbitals and the O_h symmetry of the octahedral structure. The symmetry of the MnO_6 octahedron structure gets abridged from Oh to D_{4h} to stabilize the Mn^{3+} ions, which would result in the formation of distorted crystal structures with two extended axial bonds of Mn-O and four constricted equatorial bonds of Mn-O. The decrease in symmetry of the structure subsidizes the stabilizing of the Mn^{3+} cation, which causes a diminished effect on the capability of the LMO cathode.[49] The cation/anion ratio (c/a) of MnO_6 changes by 16% owing to J-T deformation, which results in a 6.5% increase in the volume of the unit cell of the crystal structure.

Due to extensive Jahn-Teller distortion of high-spin Mn^{3+} ions of $LiMn_2O_4$, it experiences a phase transition from cubic spinel to orthorhombic. This significant change in the cell volume causes substantial damage to the particles in the structure and crushing, which causes the irreversible phase conversion and generation of microcracks in the particles. Further, it continues to increase the suspension of Mn ions into electrolytes, causing constant irreversible phase transformation, ultimately decreasing the capacity of $LiMn_2O_4$ (**Figure 5c**). Furthermore, the J-T distortion gets severe when the average electronic state arrives below +3.5V, triggering the additional decay in the capacity of $LiMn_2O_4$ at around 3V.

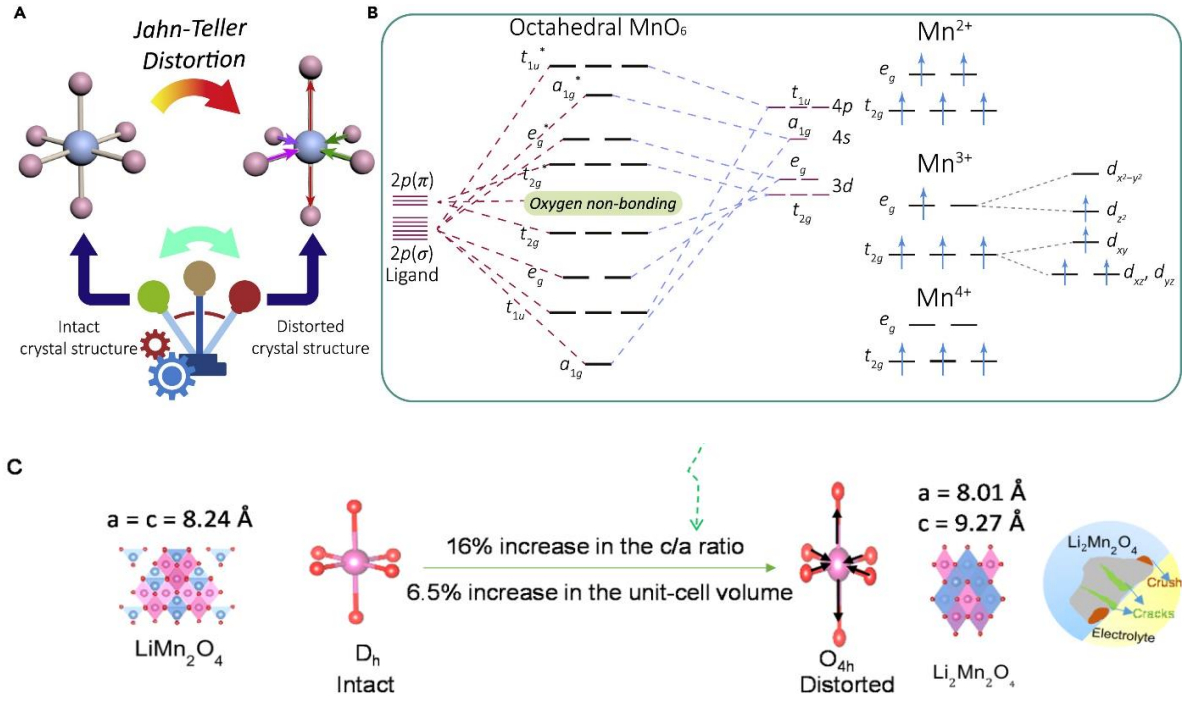

Figure 5. (a) Illustration of Jahn-Teller distortion, (b) schematic representation of electronic states of Mn ions (Reproduced from ref. [36]), (c) illustrating phase transition due to cell volume change. (Reproduced from ref. [48])

1.12 Stabilization strategies of high voltage spinel cathode materials

The high-voltage LMO-based cathode materials have several advantages owing to their high energy density, high capacity, and high voltage characteristics. The high-voltage LMO-based

cathode materials have several advantages, including their ability to stabilize and maintain performance even under extreme conditions, such as phase transitions and microcracks caused by mechanical stress. Furthermore, the movement of Mn ions can be regulated to prevent structural changes and irreversible phase transitions, which can also reduce capacity. Therefore, it is crucial to develop stabilization strategies to ensure long-term performance and reliability of high-voltage LMO-based cathode materials. Research and development on improving LMO cathode materials will primarily focus on the following strategy.

1.12.1 Elemental doping/substitution

Doping is widely accepted as an efficient method to advance the electrochemical properties of cathode materials. Doping is usually achieved with metal cations and nonmetal anions. Doping ions can alter LMO's structure, crystalline parameters, and composition, thus improving its cycling stability. The doping of different elements across the periodic table was investigated to enhance the performance of LMO cathode materials such as main group elements, transition metals, and rare earth elements, which could be doped alone or in combination with multiple elements have been investigated.

1.12.2 Surface strengthening by coating

In a battery, the breakdown of electrolytes can enhance the dissolution of Mn^{3+} by speeding up the disproportionation reaction. To mitigate this issue, Modifying the surface of LMO materials has become a common practice to enhance the stability of the electrode-electrolyte interface, minimize unwanted reactions with the electrolyte, and mitigate the leaching of transition metals. Protecting the material from the influence of the electrolyte is crucial for overcoming the Mn dissolution. The application of a surface coating effectively prevents Mn dissolution by creating a barrier between the electrolyte and the cathode material, inhibiting direct contact.

1.12.3 Morphology and particle size control

In addition to elemental doping and surface modification strategies, the morphology of the particles plays a crucial decisive role in the electrochemical properties of electrode materials to a large extent.[50] An alternative method aims to minimize surface and interfacial interactions, which can be accomplished by covering the surface and adjusting the precise morphology. This surface coating prevents direct contact between LMO and the electrolyte, suppressing the corrosion reaction. For instance, various metal oxides and Li^+ conductor materials have been proven to enhance the resistance of LMO against HF attack from electrolytes as a coating layer.[51] Improving interfacial stability through specific morphological control can also reduce cross-reactions and transition metal dissolution at the electrode/electrolyte interface. The surface plane lattice orientations primarily determine the strength of this interface based on the arrangement of the atoms.[52,53] Particle size is another crucial factor that affects interfacial stability. Researchers have proposed both nanostructured and large-size LMO materials. Nanoscale LMO has been widely demonstrated to increase the power output of LIBs owing to the shorter Li^+ diffusion pathways resulting from the reduced particle size.[170] Nanostructured materials have gained more attention than traditional bulk LMO materials on the microscale because they exhibit enhanced performance as high-rate cathodes for rechargeable lithium-ion batteries.[54] These materials' small size and nanostructure enable increased electrode-electrolyte contact areas, rapid ionic diffusion, and efficient electronic transport, resulting in superior performance.[27] Various nanostructures, such as nanowires,[55] nanorods,[56] hollow spheres,[57] ordered mesoporous structures,[58] and thin films,[59,60] have been fabricated to enhance the power density of LMO cathode materials. These nanostructured materials can achieve high current densities in lithium-ion batteries.

1.12.4 Design of stable cathode-electrolytes interface (CEI)

The formation of the CEI layer is caused by the decomposition of the electrolyte, which generates both inorganic salts, such as Li_2CO_3 and LiF, and organic compounds, like poly(ethylene carbonate).[61,62] This layer serves as an electrical insulator while still allowing for the movement of lithium ions. However, forming the CEI layer leads to an irreversible loss of lithium and capacity during the initial cycles, negatively affecting battery performance. The oxidation of electrolytes on the cathode surface necessitates continuous electron transfer.[63] To prevent further oxidation, an electrically insulating layer is necessary. Although CEI formation is a side reaction linked to the electrolyte, thick and heterogeneous CEI layers can also contribute to cathode material degradation. Uneven coverage of the cathode can result in the leaching of transition metals from the structure. At the same time, a thick CEI accelerates the surface phase change due to uneven lithium diffusion rates on the surface. Lastly, a dense and non-uniform CEI affects the local delithiation and lithiation levels after prolonged cycling, leading to intragranular cracks.[61]

1.12.5 Crystal plane engineering

The truncated structure exhibits improved and stable electrochemical performance, particularly in the (111) plane, which has been truncated into an octahedron with a combination of other planes (100) and (110) at partial proportions.[64,65] The durability of the solid electrolyte interface (SEI) layer is dependent on how the SEI layer and the density of the Mn crystal structure influence the dissolution of Mn.[52] Computations indicate that the (111) surface of $LiMn_2O_4$ exhibits the highest stability during charging and discharging cycles. This surface configuration leads to minimal Mn dissolution, attributed to the most compact arrangement of Mn atoms and limited interaction with the electrolyte.[66,67] Moreover, the SEI layer that formed on the (111) facet exhibited a thinner and more uniform structure compared to those on the (100) or (110) facets,

which improved cycling stability. Nevertheless, the (100) and (110) surfaces of LiMn2O4 demonstrated superior Li^+ diffusion kinetics in comparison to the (111) surface, enabling enhanced high-rate performance.[68,69] Specifically, the (110) surface orientation, which aligns with the Li^+ diffusion pathway, facilitates the movement of Li^+ ions, thus enhancing overall performance.[70] Nevertheless, the (110) surface is susceptible to Mn^{3+} dissolution. Controlling the facet effectively mitigated Mn^{3+} disproportionation and inhibited the dissolution of Mn^{3+}.[53] Thus, Suppressing the development of (110) planes shows potential for reducing Mn dissolution.[71] Furthermore, a superior technique for modifying the structure and fine-tuning the (111) facet was established to enhance both stability and rate performance concurrently. Techniques such as controlled crystal growth, chemical template methods, controlled calcination, and ball milling with optimized parameters have been used to control the facets of $LiMn_2O_4$.

1.13 Current research directions and challenges

Despite widespread adoption, Li-ion batteries face several technical and material challenges that limit their performance and sustainability. Key issues include safety risks from thermal runaway, limited availability of essential materials, and capacity fade during prolonged cycling. In particular, the Jahn-Teller distortion in manganese-based cathodes, such as $LiMn_2O_4$, continues to hamper their long-term stability and capacity retention.[18] Addressing these challenges requires innovation in material design, including multi-cation doping in cathodes, the development of high-capacity anodes, and advancements in electrolyte chemistry.[10]

This thesis investigates these advancements, particularly focusing on enhancing cathode material's performance to improve the efficiency and durability of lithium-ion batteries. Additionally, it addresses the crucial role of recycling/regeneration technologies of spent batteries, contributing to the sustainable growth of Li-ion battery technologies.[16]

1.14 Rationale of selection of host and dopant elements

The advantages of high-voltage LMO-based cathode materials are numerous, stemming from their exceptional energy density, capacity, and voltage properties. These materials demonstrate remarkable resilience and functionality, even when exposed to challenging circumstances such as phase transitions and microcracks caused by mechanical stress. Furthermore, it is possible to regulate the movement of Mn ions, thereby preventing structural changes and irreversible phase transitions that could potentially diminish the capacity. As a result, it is crucial to develop effective stabilization methods to guarantee the long-term robustness and dependability of high-voltage LMO-based cathode materials. Most structural issues of LMO cathode materials arise due to the dissolution, disproportionation, and Jahn-Teller distortion of Mn ions in the LMO cathode material. The stabilization of Mn ions to utilize most advantages of the LMO cathode is essential. Hence, the Mn site is chosen as the host to improve the cathode performance of the LMO cathode material. Here, different approaches have been made to mitigate the issues and improve the performance of cathode materials. For that purpose, the Ni, Fe, and Al elements were used as dopants and building blocks for surface modification because Ni, Fe, and Al-doped materials have improved the performance among the most reported substituent elements. Ni doping enhances the capacity and energy density,[72–75] Fe doping enhances electronic conductivity and Li^+ ion diffusion kinetics,[73,74,76] and Al doping enhances the structural stability and electrochemical performance.[72,77–79]

1.15 Recycling methodology for end-of-life Li-ion batteries

The growing popularity of LIBs poses considerable challenges regarding the substantial electronic waste they produce when they reach the end of their useful life, which has implications for both economic and environmental aspects. The hazardous components found in depleted LIBs,

such as electrolytes and metals, have the potential to pollute groundwater, and burning these batteries releases harmful gases like COx, which are detrimental to the environment. As a result, it is essential to establish a circular recycling process for LIB components that are used to ensure sustainable waste management. This strategy also helps address supply chain vulnerabilities related to raw materials between nations, reduces price fluctuations, and provides more significant economic advantages.[80–84] LIBs are designated as a highly combustible hazard in all waste battery guidelines, necessitating careful handling. The risk of self-ignition is present due to the flammable electrolytes ignited by minor electrical discharges in exposed battery components. Consequently, rigorous safety protocols must be implemented throughout recycling to prevent short-circuits and electrolyte leakage. In 2014, the Japan Portable Rechargeable Battery Recycling Centre (JBRC) developed a protocol for transporting waste LIBs. This protocol mandates the insulation of all exposed conductive areas, including connecting wires, electrode terminals, metal components, and damaged electrode fragments, using tape. The entire set of batteries should then be bundled to create a uniformly protected package before shipping. These properly taped battery sets are placed in robust, heat-resistant containers clearly labeled with warning signs. Finally, they will be transported cautiously to recycling facilities, minimizing excessive vibration during transit.[85,86]

The most common metals in LIBs cathodes are cobalt, nickel, lithium, aluminum, copper, and manganese. When inadequately disposed of, such metals may contaminate the environment and accumulate in the human body. Once absorbed by the body, these metals can cause various health problems. Cobalt and nickel are known to be carcinogens and mutagens. LIBs contain toxic and flammable compounds as solvents. A circular economy of spent LIBs may lead to the reduction of raw material consumption, prevention of environmental pollution, and recovery of high-value metals. The circular economy is an alternative economic model to the linear economy; the latter is

based on raw material extraction, manufacture, use, and disposal of products at the end of their life cycle. Geissdoerfer (2017) defined a circular economy as "a regenerative system in which the input and waste of resources, the emission, and energy leakage are minimized by decelerating, closing and narrowing the material and energy circuits. This can be achieved through long-term design, maintenance, repair, reuse, remanufacturing, reconditioning and recycling".[87] The second part of the thesis addresses the issues of spent LIBs disposal strategies and develops the recycling methodology for utilizing valuable resources from the spent LIBs.

1.16 State-of-the-art recycling methods

Figure 1.6. Schematic overview of the major recycling methods for Li-ion batteries.

Recycling LIBs is vital in conserving resources and safeguarding the environment. The primary methods for LIB recycling can be classified into three main categories: pyrometallurgical, hydrometallurgical, and direct recycling techniques. These approaches represent the fundamental strategies employed in the recycling process of LIBs. Recycling LIBs is vital in conserving resources and safeguarding the environment. Metal recovery through high-temperature smelting is the focus of pyrometallurgical techniques, whereas hydrometallurgical approaches employ

chemical leaching to extract valuable substances. In contrast, direct recycling methods seek to maintain the original structure of battery components, enabling their incorporation into new batteries. Each approach has its own benefits and drawbacks, with ongoing studies aimed at enhancing efficiency and minimizing environmental consequences.

1.16.1 Pyrometallurgical recycling of Li-ion batteries

Pyrometallurgical recycling is among the most established and industrialized methods for recycling Li-ion batteries (LIBs). This approach employs high-temperature techniques to extract valuable metals such as cobalt, nickel, and copper. Although effective for certain materials, this method faces energy efficiency and lithium recovery challenges. The pyrometallurgical process is particularly successful in extracting cobalt and nickel from LIBs. However, its high energy requirements and limited success in recovering lithium necessitate improvements and integration with other recycling methods to enhance its environmental and economic viability.

1.16.1.1 Steps involved in pyrometallurgical methods

i. **Pre-treatment**: Recycling batteries involves discharging and subjecting them to mechanical treatment to extract casings and electrolytes. The resulting material, either shredded or crushed, is called a “black mass”.

ii. **High-temperature treatment**: The black mass undergoes smelting in a furnace heated to between 1200 °C and 1500 °C. This process incinerates and eliminates organic elements such as binders and electrolytes.

iii. **Metal recovery**: The extraction process produces a metallic mixture containing cobalt, nickel, and copper. In contrast, lithium and manganese are generally found in the slag component, which might necessitate further processing techniques to recover these elements.

iv. **Refinement**: The metal alloy undergoes further refining to separate individual metals.

1.16.1.2 Advantages

i. **Scalability**: The method is well-suited for large-scale operations.

ii. **Ease of processing**: Handles mixed battery chemistries without extensive sorting.

iii. **Effective cobalt and nickel recovery**: Ensures efficient recovery of high-value metals.

1.16.1.3 Limitations

i. **Energy Consumption**: High temperatures lead to significant energy costs.

ii. **Environmental impact**: Carbon dioxide (CO_2) and harmful emissions are produced during smelting, contributing to greenhouse gas levels. To control these pollutants, efficient systems for treating exhaust gases are necessary.

iii. **Lithium and Manganese loss**: These components are usually confined within slag without additional processing steps and cannot be efficiently extracted.

iv. **Economic viability**: The profitability of this operation depends on elevated prices for cobalt and nickel, as these metals constitute the main source of revenue.

1.16.2 Hydrometallurgical recycling of Li-ion batteries

Hydrometallurgical recycling uses chemical processes to extract metals from spent lithium-ion batteries (LIBs). This method employs water-based chemical processes, including leaching, selective separation, and precipitation techniques, to extract valuable metals such as lithium, cobalt, nickel, and manganese. The versatility and efficiency of hydrometallurgical recycling have established it as a favored method for recovering metals from lithium-ion batteries (LIBs). Its high recovery rates and flexibility in handling various chemical compositions contribute to its widespread adoption, especially when combined with eco-friendly chemistry advancements and integrated processing methods. However, significant challenges remain in managing chemical

waste and reducing operational costs, which must be addressed for the broader implementation of this recycling technique.

1.16.2.1 Steps involved in the hydrometallurgical process

i. **Pre-treatment**: Batteries are discharged to neutralize any residual energy. The dismantling of casings is removed, and the cells are shredded to obtain black mass (a mixture of cathode and anode materials).

ii. **Leaching**: The black mass is treated with acidic or alkaline solutions (e.g., **H_2SO_4**, **HCl**, or organic acids like citric acid). A reducing agent (e.g., **H_2O_2**) is often added to enhance metal dissolution. Metals are dissolved into the leachate; **Li^+**, **Co^{2+}**, **Ni^{2+}**, and **Mn^{2+}** ions are extracted into the solution.

iii. **Metal recovery**: Multiple methods can be employed for the metal recovery, such as

Precipitation: Selective chemicals are added to precipitate lithium and cobalt as carbonates or hydroxides. **Solvent extraction**: Specific extractants (e.g., Cyanex 272) are used to isolate cobalt, nickel, or manganese selectively. **Electrowinning**: In some cases, metals like cobalt and nickel are recovered via electroplating.

iv. **Final refinement:** Purified metals are processed into compounds like **Li_2CO_3** (for lithium) or metal sulfates, which can be directly reused in battery manufacturing.

1.16.2.2 Advantages

i. **High Recovery efficiency**: Achieves > 90 % recovery rates for metals like lithium, cobalt, nickel, and manganese.

ii. **Selective recovery**: Chemical processes allow precise separation of target elements, ensuring high-purity products.

iii. **Scalability**: Adaptable to various LIB chemistries, including NMC, LFP, and LCO.

iv. **Lower environmental impact**: Generates fewer greenhouse gases than pyrometallurgical processes.

1.16.2.3 Limitations

i. **Chemical waste management**: Large volumes of acidic and neutralizing agents require proper handling to avoid environmental contamination.

ii. **Energy and cost**: Though less energy-intensive than pyrometallurgy, hydrometallurgy involves significant operational costs for reagents and chemical recovery.

iii. **Complexity**: Requires preprocessing of LIBs (shredding and separation) and precise control over process parameters.

1.16.2.4 Emerging techniques

i. **Electrochemical recycling**: Selective recovery of metals like lithium using electrochemical processes from spent batteries or leachates.

ii. **Biological recycling**: Using microorganisms or bioleaching agents to recover metals from LIBs.

iii. **Mechanical recycling**: Physical methods such as crushing, sieving, and separation to recover individual components before chemical treatment.

1.17 Thesis objective

This thesis aims to develop advanced high-energy and high-voltage $LiMn_2O_4$-based cathode materials by employing elemental doping and surface coating techniques to enhance their electrochemical performance, structural stability, and cycle life. The research will focus on the following key aspects:

1.17.1 Multi-cation doping:

Investigate the effects of Ni, Fe, and Al dopants on the $LiMn_2O_4$ crystal structure to reduce Jahn-Teller distortion, improve structural stability under high-voltage cycling, and enhance capacity retention. The goal is to determine the optimal concentrations and combinations of these

dopants that maximize energy density while maintaining the structural integrity of the cathode over extended cycling periods.

1.17.2 Surface coating:

Develop and refine surface coating techniques using metal oxides such as $NiFe_2O_4$ and $NiAl_2O_4$. These coatings will form protective layers to minimize electrolyte decomposition and structural degradation. The research will optimize the coating thickness, composition, and uniformity to improve electrochemical stability and enhance the compatibility at the electrode-electrolyte interface during high-voltage operation.

1.17.3 Regeneration of cathode material from spent Li-ion batteries:

Develop a practical methodology for recycling and regenerating spent lithium-ion batteries cathodes by lithiation. The lithiated cathode material would be recovered from Li-ion batteries used for the second-life application. This objective aims to establish a sustainable approach to reducing the environmental impact of battery waste while enhancing the economic viability of lithium-ion battery production through material recovery and reuse.

1.17.4 Regeneration and repurposing of anode material from spent Li-ion batteries:

To recover the anode material from used Li-ion batteries and functionalize the recovered anode material graphite into reduced graphene oxide for secondary electrochemical applications. Repurposing resources recovered from used batteries uplifts the sustainable utilization of environmental resources more judiciously and promotes the circular economy.

1.17.5 Recovery and reuse of polymeric separator from spent Li-ion batteries:

After the recovery of cathode and anode materials, the polymeric separator is still left as waste, which does not fulfill the aim of the recycling of the waste batteries in the point of environmental health concerns as it can be a threat to the environment due to its properties.

Therefore, the separator should also find repurposing reasons and applications to support better environmental health. The ultimate aim is to produce an improved and optimized $LiMn_2O_4$-based cathode material with superior energy density, enhanced stability, and extended cycling performance, contributing to advancing next-generation high-energy and high-voltage lithium-ion battery technology. Furthermore, to develop sustainable remediation such as recycling and regenerating electrode materials from used LIBs.

1.18 Scope of the thesis:

The thesis mainly focused on the high energy and high voltage $LiMn_2O_4$-based cathode for lithium-ion batteries and the regeneration of electrode materials from the used Li-ion batteries. The thesis is highly relevant, both academically and industrially.

The significant factors limit the practical applications, apparently fading capacity during prolonged cycling, especially at higher temperatures (>50 °C); the structural instability occurs due to the well-known phenomena Jahn-Teller distortion of Mn ions in inorganic oxides. The widely accepted reason and mechanism for the degradation of LMO cathode materials is the dissolution of manganese ions into the electrolyte solution, which usually occurs in the initial few cycles. The manganese dissolution originates from the disproportionation reactions of Mn^{3+} ions into Mn^{2+} and Mn^{4+} ions, which lead to the formation of manganese oxide (MnO_2) over the surface of the particles and allows Mn^{2+} ions to dissolve into the electrolyte. The breakdown of the significance of the thesis is as follows;

1.18.1 High-energy and high-voltage cathodes

Commercial Significance: $LiMn_2O_4$ is an economical and eco-friendly substitute for cobalt-based cathodes. Enhancing its durability by incorporating multiple cations (Ni, Fe, Al) and applying surface layers ($NiFe_2O_4$, $NiAl_2O_4$) directly tackle issues related to its cycling durability

and capacity reduction. The study aimed to counteract Jahn-Teller distortion, potentially resulting in extended battery life, which makes it attractive for application in electric vehicles and energy storage systems.

Innovative approaches to stabilization could pave the way for researchers to create materials with enhanced performance in the future. Applying cutting-edge surface coatings using substances such as $NiFe_2O_4$ and $NiAl_2O_4$ represents a groundbreaking technique that may provide valuable insights into enhancing interfacial chemistry.

1.18.2 Regeneration of electrode materials of spent Li-ion batteries

Recovering and reusing materials from discarded batteries is essential for minimizing reliance on extracting raw materials through mining, particularly for critical elements such as lithium and cobalt.

Commercial significance: Ecological Advantages: Minimizes electronic waste and lowers the carbon impact associated with battery production. Financial Opportunities: Offers cost-effective methods for recovering and reusing crucial elements, appealing to manufacturers looking to cut down on material costs.

1.19 Research impact

Integrating recycling processes with the development of cathode materials presents a circular approach to battery production. The findings outlined in the dissertation may garner attention from companies focused on developing sustainable battery solutions.

1.20 References

(1) Hassan, Q.; Viktor, P.; J. Al-Musawi, T.; Mahmood Ali, B.; Algburi, S.; Alzoubi, H. M.; Khudhair Al-Jiboory, A.; Zuhair Sameen, A.; Salman, H. M.; Jaszczur, M. The Renewable Energy Role in the Global Energy Transformations. *Renew. Energy Focus* **2024**, *48*, 100545. https://doi.org/10.1016/j.ref.2024.100545.

(2) Gielen, D.; Boshell, F.; Saygin, D.; Bazilian, M. D.; Wagner, N.; Gorini, R. The Role of Renewable Energy in the Global Energy Transformation. *Energy Strategy Rev.* **2019**, *24*, 38–50. https://doi.org/10.1016/j.esr.2019.01.006.

(3) Michaelides, E. E.; Nguyen, V. N. D.; Michaelides, D. N. The Effect of Electric Vehicle Energy Storage on the Transition to Renewable Energy. *Green Energy Intell. Transp.* **2023**, *2* (1), 100042. https://doi.org/10.1016/j.geits.2022.100042.

(4) Fekete, B. M.; Bacskó, M.; Zhang, J.; Chen, M. Storage Requirements to Mitigate Intermittent Renewable Energy Sources: Analysis for the US Northeast. *Front. Environ. Sci.* **2023**, *11*. https://doi.org/10.3389/fenvs.2023.1076830.

(5) *Global Energy Storage Market to Grow 15-Fold by 2030*. BloombergNEF. https://about.bnef.com/blog/global-energy-storage-market-to-grow-15-fold-by-2030/ (accessed 2024-09-29).

(6) Manthiram, A. An Outlook on Lithium Ion Battery Technology. *ACS Cent. Sci.* **2017**, *3* (10), 1063–1069. https://doi.org/10.1021/acscentsci.7b00288.

(7) *Linden's Handbook of Batteries*, 4th ed.; Reddy, T. B., Linden, D., Eds.; McGraw-Hill: New York, 2011.

(8) Goodenough, J. B. How We Made the Li-Ion Rechargeable Battery. *Nat. Electron.* **2018**, *1* (3), 204–204. https://doi.org/10.1038/s41928-018-0048-6.

(9) Tarascon, J.-M.; Armand, M. Issues and Challenges Facing Rechargeable Lithium Batteries. *Nature* **2001**, *414* (6861), 359–367. https://doi.org/10.1038/35104644.

(10) Manthiram, A. A Reflection on Lithium-Ion Battery Cathode Chemistry. *Nat. Commun.* **2020**, *11* (1), 1550. https://doi.org/10.1038/s41467-020-15355-0.

(11) Yu, X.; Yu, W. A.; Manthiram, A. Advances and Prospects of High-Voltage Spinel Cathodes for Lithium-Based Batteries. *Small Methods* **2021**, *5* (5), 2001196. https://doi.org/10.1002/smtd.202001196.

(12) Bhandari, A.; Bhattacharya, J. Review—Manganese Dissolution from Spinel Cathode: Few Unanswered Questions. *J. Electrochem. Soc.* **2017**, *164* (2), A106–A127. https://doi.org/10.1149/2.0101614jes.

(13) Yin, S.; Deng, W.; Chen, J.; Gao, X.; Zou, G.; Hou, H.; Ji, X. Fundamental and Solutions of Microcrack in Ni-Rich Layered Oxide Cathode Materials of Lithium-Ion Batteries. *Nano Energy* **2021**, *83*, 105854. https://doi.org/10.1016/j.nanoen.2021.105854.

(14) Li, W.; Erickson, E. M.; Manthiram, A. High-Nickel Layered Oxide Cathodes for Lithium-Based Automotive Batteries. *Nat. Energy* **2020**, *5* (1), 26–34. https://doi.org/10.1038/s41560-019-0513-0.

(15) Li, M.; Lu, J.; Chen, Z.; Amine, K. 30 Years of Lithium-Ion Batteries. *Adv. Mater.* **2018**, *30* (33), 1800561. https://doi.org/10.1002/adma.201800561.

(16) Gaines, L. The Future of Automotive Lithium-Ion Battery Recycling: Charting a Sustainable Course. *Sustain. Mater. Technol.* **2014**, *1–2*, 2–7. https://doi.org/10.1016/j.susmat.2014.10.001.

(17) Goodenough, J. B.; Kim, Y. Challenges for Rechargeable Li Batteries. *Chem. Mater.* **2010**, *22* (3), 587–603. https://doi.org/10.1021/cm901452z.
(18) Thackeray, M. M.; Kock, A. de; Rossouw, M. H.; Liles, D.; Bittihn, R.; Hoge, D. Spinel Electrodes from the Li-Mn-O System for Rechargeable Lithium Battery Applications. *J. Electrochem. Soc.* **1992**, *139* (2), 363. https://doi.org/10.1149/1.2069222.
(19) Xu, K. Nonaqueous Liquid Electrolytes for Lithium-Based Rechargeable Batteries. *Chem. Rev.* **2004**, *104* (10), 4303–4418. https://doi.org/10.1021/cr030203g.
(20) Mizushima, K.; Jones, P. C.; Wiseman, P. J.; Goodenough, J. B. LixCoO2 (0<x<-1): A New Cathode Material for Batteries of High Energy Density. *Mater. Res. Bull.* **1980**, *15* (6), 783–789. https://doi.org/10.1016/0025-5408(80)90012-4.
(21) Hu, M.; Pang, X.; Zhou, Z. Recent Progress in High-Voltage Lithium Ion Batteries. *J. Power Sources* **2013**, *237*, 229–242. https://doi.org/10.1016/j.jpowsour.2013.03.024.
(22) Liu, W.; Oh, P.; Liu, X.; Lee, M.; Cho, W.; Chae, S.; Kim, Y.; Cho, J. Nickel-Rich Layered Lithium Transition-Metal Oxide for High-Energy Lithium-Ion Batteries. *Angew. Chem. Int. Ed.* **2015**, *54* (15), 4440–4457. https://doi.org/10.1002/anie.201409262.
(23) Chen, Z.; Zhang, W.; Yang, Z. A Review on Cathode Materials for Advanced Lithium Ion Batteries: Microstructure Designs and Performance Regulations. *Nanotechnology* **2020**, *31* (1), 012001. https://doi.org/10.1088/1361-6528/ab4447.
(24) Yang, J.; Yang, P.; Wang, H. Enhancing the Storage Performance and Thermal Stability of Ni-Rich Layered Cathodes by Introducing Li2MnO3. *Energies* **2024**, *17* (4), 810. https://doi.org/10.3390/en17040810.
(25) Li, S.; Ma, G.; Guo, B.; Yang, Z.; Fan, X.; Chen, Z.; Zhang, W. Kinetically Controlled Synthesis of $LiNi_{0.5}Mn_{1.5}O_4$ Micro- and Nanostructured Hollow Spheres as High-Rate Cathode Materials for Lithium Ion Batteries. *Ind. Eng. Chem. Res.* **2016**, *55* (35), 9352–9361. https://doi.org/10.1021/acs.iecr.6b02463.
(26) Palacin, M. R. Battery Materials Design Essentials. *Acc. Mater. Res.* **2021**, *2* (5), 319–326. https://doi.org/10.1021/accountsmr.1c00026.
(27) Dou, S. Review and Prospects of Mn-Based Spinel Compounds as Cathode Materials for Lithium-Ion Batteries. *Ionics* **2015**, *21* (11), 3001–3030. https://doi.org/10.1007/s11581-015-1545-5.
(28) Cheng, F.; Liang, J.; Tao, Z.; Chen, J. Functional Materials for Rechargeable Batteries. *Adv. Mater.* **2011**, *23* (15), 1695–1715. https://doi.org/10.1002/adma.201003587.
(29) Kim, T.; Park, J.; Chang, S. K.; Choi, S.; Ryu, J. H.; Song, H. The Current Move of Lithium Ion Batteries Towards the Next Phase. *Adv. Energy Mater.* **2012**, *2* (7), 860–872. https://doi.org/10.1002/aenm.201200028.
(30) Hunter, J. C. Preparation of a New Crystal Form of Manganese Dioxide: λ-MnO2. *J. Solid State Chem.* **1981**, *39* (2), 142–147. https://doi.org/10.1016/0022-4596(81)90323-6.
(31) Thackeray, M. M.; David, W. I. F.; Goodenough, J. B. Structural Characterization of the Lithiated Iron Oxides LixFe3O4 and LixFe2O3 (0<x<2). *Mater. Res. Bull.* **1982**, *17* (6), 785–793. https://doi.org/10.1016/0025-5408(82)90029-0.
(32) Thackeray, M. M.; David, W. I. F.; Bruce, P. G.; Goodenough, J. B. Lithium Insertion into Manganese Spinels. *Mater. Res. Bull.* **1983**, *18* (4), 461–472. https://doi.org/10.1016/0025-5408(83)90138-1.
(33) Thackeray, M. M.; Johnson, P. J.; De Picciotto, L. A.; Bruce, P. G.; Goodenough, J. B. Electrochemical Extraction of Lithium from LiMn2O4. *Mater. Res. Bull.* **1984**, *19* (2), 179–187. https://doi.org/10.1016/0025-5408(84)90088-6.

(34) Tateishi, K.; Du Boulay, D.; Ishizawa, N. The Effect of Mixed Mn Valences on Li Migration in LiMn2O4 Spinel: A Molecular Dynamics Study. *Appl. Phys. Lett.* **2004**, *84* (4), 529–531. https://doi.org/10.1063/1.1644320.

(35) Xu, B.; Meng, S. Factors Affecting Li Mobility in Spinel LiMn2O4—A First-Principles Study by GGA and GGA+U Methods. *J. Power Sources* **2010**, *195* (15), 4971–4976. https://doi.org/10.1016/j.jpowsour.2010.02.060.

(36) Liu, S.; Wang, B.; Zhang, X.; Zhao, S.; Zhang, Z.; Yu, H. Reviving the Lithium-Manganese-Based Layered Oxide Cathodes for Lithium-Ion Batteries. *Matter* **2021**, *4* (5), 1511–1527. https://doi.org/10.1016/j.matt.2021.02.023.

(37) Huang, Y.; Dong, Y.; Li, S.; Lee, J.; Wang, C.; Zhu, Z.; Xue, W.; Li, Y.; Li, J. Lithium Manganese Spinel Cathodes for Lithium-Ion Batteries. *Adv. Energy Mater.* **2021**, *11* (2), 2000997. https://doi.org/10.1002/aenm.202000997.

(38) Xiao, W.; Xin, C.; Li, S.; Jie, J.; Gu, Y.; Zheng, J.; Pan, F. Insight into Fast Li Diffusion in Li-Excess Spinel Lithium Manganese Oxide. *J. Mater. Chem. A* **2018**, *6* (21), 9893–9898. https://doi.org/10.1039/C8TA01428K.

(39) House, R. A.; Bruce, P. G. Lightning Fast Conduction. *Nat. Energy* **2020**, *5* (3), 191–192. https://doi.org/10.1038/s41560-020-0583-z.

(40) Stability of Polyatomic Molecules in Degenerate Electronic States - I—Orbital Degeneracy. *Proc. R. Soc. Lond. Ser. - Math. Phys. Sci.* **1937**, *161* (905), 220–235. https://doi.org/10.1098/rspa.1937.0142.

(41) Chung, K. Y.; Lee, H. S.; Yoon, W.-S.; McBreen, J.; Yang, X.-Q. Studies of LiMn[Sub 2]O[Sub 4] Capacity Fading at Elevated Temperature Using In Situ Synchrotron X-Ray Diffraction. *J. Electrochem. Soc.* **2006**, *153* (4), A774. https://doi.org/10.1149/1.2172565.

(42) Ragavendran, K.; Xia, H.; Mandal, P.; Arof, A. K. Jahn–Teller Effect in $LiMn_2O_4$: Influence on Charge Ordering, Magnetoresistance and Battery Performance. *Phys. Chem. Chem. Phys.* **2017**, *19* (3), 2073–2077. https://doi.org/10.1039/C6CP07289E.

(43) Zheng, H.; Sun, Q.; Liu, G.; Song, X.; Battaglia, V. S. Correlation between Dissolution Behavior and Electrochemical Cycling Performance for LiNi1/3Co1/3Mn1/3O2-Based Cells. *J. Power Sources* **2012**, *207*, 134–140. https://doi.org/10.1016/j.jpowsour.2012.01.122.

(44) Sharifi-Asl, S.; Lu, J.; Amine, K.; Shahbazian-Yassar, R. Oxygen Release Degradation in Li-Ion Battery Cathode Materials: Mechanisms and Mitigating Approaches. *Adv. Energy Mater.* **2019**, *9* (22), 1900551. https://doi.org/10.1002/aenm.201900551.

(45) Zuo, W.; Luo, M.; Liu, X.; Wu, J.; Liu, H.; Li, J.; Winter, M.; Fu, R.; Yang, W.; Yang, Y. Li-Rich Cathodes for Rechargeable Li-Based Batteries: Reaction Mechanisms and Advanced Characterization Techniques. *Energy Environ. Sci.* **2020**, *13* (12), 4450–4497. https://doi.org/10.1039/D0EE01694B.

(46) Hu, E.; Yu, X.; Lin, R.; Bi, X.; Lu, J.; Bak, S.; Nam, K.-W.; Xin, H. L.; Jaye, C.; Fischer, D. A.; Amine, K.; Yang, X.-Q. Evolution of Redox Couples in Li- and Mn-Rich Cathode Materials and Mitigation of Voltage Fade by Reducing Oxygen Release. *Nat. Energy* **2018**, *3* (8), 690–698. https://doi.org/10.1038/s41560-018-0207-z.

(47) Zhang, X.; Liu, S.; Wang, B.; Wang, G.; Du, H.; Wang, X.; Zhang, H.; Zhao, S.; Wang, L.; Yu, H. Mn-Based Cathode Materials for Rechargeable Batteries. *Sci. China Chem.* **2024**, *67* (1), 87–105. https://doi.org/10.1007/s11426-023-1706-8.

(48) Hou, X.; Liu, X.; Wang, H.; Zhang, X.; Zhou, J.; Wang, M. Specific Countermeasures to Intrinsic Capacity Decline Issues and Future Direction of LiMn2O4 Cathode. *Energy Storage Mater.* **2023**, *57*, 577–606. https://doi.org/10.1016/j.ensm.2023.02.015.

(49) Ohzuku, T.; Kato, J.; Sawai, K.; Hirai, T. Electrochemistry of Manganese Dioxide in Lithium Nonaqueous Cells: IV . Jahn-Teller Deformation of In. *J. Electrochem. Soc.* **1991**, *138* (9), 2556–2560. https://doi.org/10.1149/1.2086016.

(50) Xiao, L.; Guo, Y.; Qu, D.; Deng, B.; Liu, H.; Tang, D. Influence of Particle Sizes and Morphologies on the Electrochemical Performances of Spinel LiMn2O4 Cathode Materials. *J. Power Sources* **2013**, *225*, 286–292. https://doi.org/10.1016/j.jpowsour.2012.10.070.

(51) Yang, X.; Yang, T.; Liang, S.; Wu, X.; Zhang, H. Modification of LiNi 0.5 Mn 1.5 O 4 High Potential Cathode from the Inner Lattice to the Outer Surface with Cr 3+ -Doping and Li + -Conductor Coating. *J Mater Chem A* **2014**, *2* (27), 10359–10364. https://doi.org/10.1039/C4TA00974F.

(52) Hirayama, M.; Ido, H.; Kim, K.; Cho, W.; Tamura, K.; Mizuki, J.; Kanno, R. Dynamic Structural Changes at $LiMn_2O_4$ /Electrolyte Interface during Lithium Battery Reaction. *J. Am. Chem. Soc.* **2010**, *132* (43), 15268–15276. https://doi.org/10.1021/ja105389t.

(53) Liu, H.; Wang, J.; Zhang, X.; Zhou, D.; Qi, X.; Qiu, B.; Fang, J.; Kloepsch, R.; Schumacher, G.; Liu, Z.; Li, J. Morphological Evolution of High-Voltage Spinel LiNi0.5Mn1.5O4 Cathode Materials for Lithium-Ion Batteries: The Critical Effects of Surface Orientations and Particle Size. *ACS Appl. Mater. Interfaces* **2016**, *8* (7), 4661–4675. https://doi.org/10.1021/acsami.5b11389.

(54) Deng, Y.; Zhou, Y.; Shi, Z.; Zhou, X.; Quan, X.; Chen, G. Porous LiMn2O4 Microspheres as Durable High Power Cathode Materials for Lithium Ion Batteries. *J. Mater. Chem. A* **2013**, *1* (28), 8170. https://doi.org/10.1039/c3ta11563a.

(55) Lee, H.-W.; Muralidharan, P.; Ruffo, R.; Mari, C. M.; Cui, Y.; Kim, D. K. Ultrathin Spinel $LiMn_2O_4$ Nanowires as High Power Cathode Materials for Li-Ion Batteries. *Nano Lett.* **2010**, *10* (10), 3852–3856. https://doi.org/10.1021/nl101047f.

(56) Luo, J.-Y.; Xiong, H.-M.; Xia, Y.-Y. $LiMn_2O_4$ Nanorods, Nanothorn Microspheres, and Hollow Nanospheres as Enhanced Cathode Materials of Lithium Ion Battery. *J. Phys. Chem. C* **2008**, *112* (31), 12051–12057. https://doi.org/10.1021/jp800915f.

(57) Luo, J.; Cheng, L.; Xia, Y. LiMn2O4 Hollow Nanosphere Electrode Material with Excellent Cycling Reversibility and Rate Capability. *Electrochem. Commun.* **2007**, *9* (6), 1404–1409. https://doi.org/10.1016/j.elecom.2007.01.058.

(58) Wang, Y.; Shao, X.; Xu, H.; Xie, M.; Deng, S.; Wang, H.; Liu, J.; Yan, H. Facile Synthesis of Porous LiMn2O4 Spheres as Cathode Materials for High-Power Lithium Ion Batteries. *J. Power Sources* **2013**, *226*, 140–148. https://doi.org/10.1016/j.jpowsour.2012.10.077.

(59) Lovett, A. J.; Daramalla, V.; Sayed, F. N.; Nayak, D.; De h-Óra, M.; Grey, C. P.; Dutton, S. E.; MacManus-Driscoll, J. L. Low Temperature Epitaxial $LiMn_2O_4$ Cathodes Enabled by $NiCo_2O_4$ Current Collector for High-Performance Microbatteries. *ACS Energy Lett.* **2023**, *8* (8), 3437–3442. https://doi.org/10.1021/acsenergylett.3c01094.

(60) Erinmwingbovo, C.; Siller, V.; Nuñez, M.; Trócoli, R.; Brogioli, D.; Tarancón, A.; Morata, A.; La Mantia, F. Effect of Film Thickness on the Kinetics of Lithium Insertion in $LiMn_2O_4$ Films Made by Multilayer Pulsed Laser Deposition for Thin-Film All-Solid-State Battery Cathode Materials**. *ChemElectroChem* **2023**, *10* (4), e202200759. https://doi.org/10.1002/celc.202200759.

(61) Xiao, B.; Sun, X. Surface and Subsurface Reactions of Lithium Transition Metal Oxide Cathode Materials: An Overview of the Fundamental Origins and Remedying Approaches. *Adv. Energy Mater.* **2018**, *8* (29), 1802057. https://doi.org/10.1002/aenm.201802057.

(62) Winter, M.; Wiemhöfer, H.; Kostecki, R.; Chen, X. SEI and Interphases at Electrodes. *Batter. Supercaps* **2020**, *3* (3), 212–213. https://doi.org/10.1002/batt.201900148.

(63) Goodenough, J. B.; Kim, Y. Challenges for Rechargeable Batteries. *J. Power Sources* **2011**, *196* (16), 6688–6694. https://doi.org/10.1016/j.jpowsour.2010.11.074.

(64) Shivamurthy, B. P.; Thripuranthaka, M.; Shelke, M. V.; Nayaka, G. P. Influence of the Crystal Plane Orientation in Enhancing the Electrochemical Performance of a Trication-Substituted Cathode for Li-Ion Batteries. *Energy Fuels* **2024**, *38* (5), 4653–4665. https://doi.org/10.1021/acs.energyfuels.3c03794.

(65) Wu, Y.; Cao, C.; Zhang, J.; Wang, L.; Ma, X.; Xu, X. Hierarchical LiMn 2 O 4 Hollow Cubes with Exposed 111 Planes as High-Power Cathodes for Lithium-Ion Batteries. *ACS Appl. Mater. Interfaces* **2016**, *8* (30), 19567–19572. https://doi.org/10.1021/acsami.6b06820.

(66) Zhu, J.; Liu, Q.; Xiang, M.; Guo, J.; Bai, H.; Liu, X.; Su, C.; Bai, W. Facile Synthesis of Truncated Octahedron LiNi0.10Mn1.90O4 for High-Performance Li-Ion Batteries. *Ceram. Int.* **2020**, *46* (10). https://doi.org/10.1016/j.ceramint.2020.02.250.

(67) Kim, J.-S.; Kim, K.; Cho, W.; Shin, W. H.; Kanno, R.; Choi, J. W. A Truncated Manganese Spinel Cathode for Excellent Power and Lifetime in Lithium-Ion Batteries. *Nano Lett.* **2012**, *12* (12), 6358–6365. https://doi.org/10.1021/nl303619s.

(68) Liu, R.-R.; Deng, X.; Liu, X.-R.; Yan, H.-J.; Cao, A.-M.; Wang, D. Facet Dependent SEI Formation on the LiNi $_{0.5}$ Mn $_{1.5}$ O $_{4}$ Cathode Identified by in Situ Single Particle Atomic Force Microscopy. *Chem Commun* **2014**, *50* (99), 15756–15759. https://doi.org/10.1039/C4CC07290A.

(69) Xu, W.; Zheng, Y.; Lin, L.; Lei, W.; Wang, Z.; Song, H.; Cheng, Y.; Qi, R.; Peng, H.; Lin, H.; Yang, Z.; Huang, R. Atomic Insights into Surface Orientations and Oxygen Vacancies in the LiMn2O4 Cathode for Lithium Storage. *J. Alloys Compd.* **2021**, *870*, 159387. https://doi.org/10.1016/j.jallcom.2021.159387.

(70) Huang, S.; Wu, H.; Chen, P.; Guo, Y.; Nie, B.; Chen, B.; Liu, H.; Zhang, Y. Facile pH-Mediated Synthesis of Morphology-Tunable MnCO3 and Their Transformation to Truncated Octahedral Spinel LiMn2O4 Cathode Materials for Superior Lithium Storage. *J. Mater. Chem. A* **2015**, *3* (7), 3633–3640. https://doi.org/10.1039/c4ta06522k.

(71) Kong, F.; Zhang, G.; Wu, D.; Sun, F.; Tao, S.; Chu, S.; Qian, B.; Chu, W.; Song, L. Insight into the Cation Migration and Surface Structural Evolution of Spinel LiNi0.5Mn1.5O4 Cathode Material for Lithium-Ion Batteries. *Chem. Eng. J.* **2023**, *451*, 138708. https://doi.org/10.1016/j.cej.2022.138708.

(72) Wang, S.; Xiang, M.; Lu, Y.; Guo, J.; Su, C.; Bai, H.; Liu, X. Facile Solid-State Combustion Synthesis of Al–Ni Dual-Doped LiMn2O4 Cathode Materials. *J. Mater. Sci. Mater. Electron.* **2020**, *31* (8), 6036–6044. https://doi.org/10.1007/s10854-020-03155-7.

(73) Sharma, P.; Das, C.; Indris, S.; Bergfeldt, T.; Mereacre, L.; Knapp, M.; Geckle, U.; Ehrenberg, H.; Darma, M. S. D. Synthesis and Characterization of a Multication Doped Mn Spinel, LiNi 0.3 Cu 0.1 Fe 0.2 Mn 1.4 O 4 , as 5 V Positive Electrode Material. *ACS Omega* **2020**, *5* (36), 22861–22873. https://doi.org/10.1021/acsomega.0c02174.

(74) Zhong, G. B.; Wang, Y. Y.; Yu, Y. Q.; Chen, C. H. Electrochemical Investigations of the LiNi0.45M0.10Mn1.45O4 (M=Fe, Co, Cr) 5V Cathode Materials for Lithium Ion Batteries. *J. Power Sources* **2012**, *205*, 385–393. https://doi.org/10.1016/j.jpowsour.2011.12.037.

(75) Liu, H.; Li, M.; Xiang, M.; Guo, J.; Bai, H.; Bai, W.; Liu, X. Effects of Crystal Structure and Plane Orientation on Lithium and Nickel Co-Doped Spinel Lithium Manganese Oxide for Long Cycle Life Lithium-Ion Batteries. *J. Colloid Interface Sci.* **2021**, *585*. https://doi.org/10.1016/j.jcis.2020.10.052.

(76) Liu, J.; Manthiram, A. Understanding the Improved Electrochemical Performances of Fe-Substituted 5 V Spinel Cathode LiMn1.5Ni0.5O4. *J. Phys. Chem. C* **2009**, *113* (33), 15073–15079. https://doi.org/10.1021/jp904276t.

(77) Chen, M.; Wu, R.; Ju, S.; Zhang, X.; Xue, F.; Xing, W. Improved Performance of Al-Doped LiMn2O4 Ion-Sieves for Li+ Adsorption. *Microporous Mesoporous Mater.* **2018**, *261*, 29–34. https://doi.org/10.1016/j.micromeso.2017.10.058.

(78) Peng, C.; Huang, J.; Guo, Y.; Li, Q.; Bai, H.; He, Y.; Su, C.; Guo, J. Electrochemical Performance of Spinel LiAlxMn2-xO4 Prepared Rapidly by Glucose-Assisted Solid-State Combustion Synthesis. *Vacuum* **2015**, *120* (PA). https://doi.org/10.1016/j.vacuum.2015.07.001.

(79) Xu, W.; Zheng, Y.; Cheng, Y.; Qi, R.; Peng, H.; Lin, H.; Huang, R. Understanding the Effect of Al Doping on the Electrochemical Performance Improvement of the LiMn 2 O 4 Cathode Material. *ACS Appl. Mater. Interfaces* **2021**, *13* (38), 45446–45454. https://doi.org/10.1021/acsami.1c11315.

(80) Li, Y.; Lv, W.; Huang, H.; Yan, W.; Li, X.; Ning, P.; Cao, H.; Sun, Z. Recycling of Spent Lithium-Ion Batteries in View of Green Chemistry. *Green Chem.* **2021**, *23* (17), 6139–6171. https://doi.org/10.1039/D1GC01639C.

(81) Jiang, Y.; Chen, X.; Yan, S.; Ou, Y.; Zhou, T. Mechanochemistry-Induced Recycling of Spent Lithium-Ion Batteries for Synergistic Treatment of Mixed Cathode Powders. *Green Chem.* **2022**, *24* (15), 5987–5997. https://doi.org/10.1039/D2GC01929A.

(82) Zhang, X.; Li, L.; Fan, E.; Xue, Q.; Bian, Y.; Wu, F.; Chen, R. Toward Sustainable and Systematic Recycling of Spent Rechargeable Batteries. *Chem. Soc. Rev.* **2018**, *47* (19), 7239–7302. https://doi.org/10.1039/C8CS00297E.

(83) Mao, J.; Ye, C.; Zhang, S.; Xie, F.; Zeng, R.; Davey, K.; Guo, Z.; Qiao, S. Toward Practical Lithium-Ion Battery Recycling: Adding Value, Tackling Circularity and Recycling-Oriented Design. *Energy Environ. Sci.* **2022**, *15* (7), 2732–2752. https://doi.org/10.1039/D2EE00162D.

(84) Hou, J.; Ma, X.; Fu, J.; Vanaphuti, P.; Yao, Z.; Liu, Y.; Yang, Z.; Wang, Y. A Green Closed-Loop Process for Selective Recycling of Lithium from Spent Lithium-Ion Batteries. *Green Chem.* **2022**, *24* (18), 7049–7060. https://doi.org/10.1039/D2GC01811J.

(85) Morita, Y.; Saito, Y.; Yoshioka, T.; Shiratori, T. Estimation of Recoverable Resources Used in Lithium-Ion Batteries from Portable Electronic Devices in Japan. *Resour. Conserv. Recycl.* **2021**, *175*, 105884. https://doi.org/10.1016/j.resconrec.2021.105884.

(86) Bhar, M.; Ghosh, S.; Krishnamurthy, S.; Kaliprasad, Y.; Martha, S. K. A Review on Spent Lithium-Ion Battery Recycling: From Collection to Black Mass Recovery. *RSC Sustain.* **2023**, *1* (5), 1150–1167. https://doi.org/10.1039/D3SU00086A.

(87) Geissdoerfer, M.; Savaget, P.; Bocken, N. M. P.; Hultink, E. J. The Circular Economy – A New Sustainability Paradigm? *J. Clean. Prod.* **2017**, *143*, 757–768. https://doi.org/10.1016/j.jclepro.2016.12.048.

Chapter 2 A

Formation of secondary phase domain by multi-cation substitution for the superior electrochemical performance of spinel cathodes for high-voltage Li-ion batteries

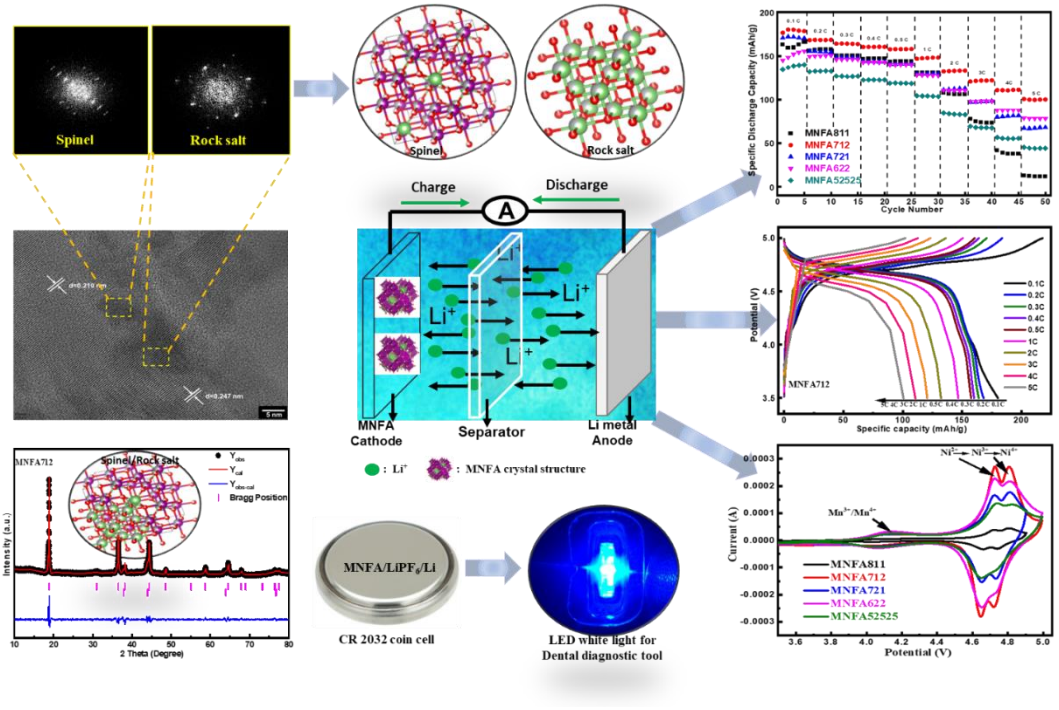

Highlights

- Disorder-structured spinel oxides are opening frontiers for high-capacity/high-voltage cathodes to meet the challenges of independence on cobalt-containing cathodes toward cheap and sustainable energy storage sources in Li-ion batteries (LIBs).
- In the present work, a series of Co-free materials: $LiMn_{2-x-y-z}Ni_xFe_yAl_zO_4$ (x = 0.8−0.5, y = 0.1−0.25, and z= 0.1−0.25) with spinel/rock salt disordered structures are reported.
- The research in the chapter addresses the influence of the secondary phase on the electrochemical activity and the reduction of the Mn^{3+} ratio to alleviate the Mn dissolution issue for bettered stability.
- Cyclic voltammetry studies have shown that the material can be a potential candidate for 5 V applications.

- The results of this chapter published as **BP Shivamurthy**, M Thripuranthaka, MV Shelke, **GP Nayaka***, Formation of the Secondary Phase Domain by Multi-Cation Substitution for the Superior Electrochemical Performance of Spinel Cathodes for High-Voltage Li-Ion Batteries, **ACS Applied Energy Materials** 5 (12), 15345-15355, 2022.
- The research work of this chapter is filed and published for patent as **BP Shivamurthy, GP Nayaka,** COBALT FREE $LiMn_{2-x-y-z}Ni_XFe_YAl_ZO_4$ SPINEL AS CATHODE MATERIAL FOR Li-ION BATTERIES WO Patent **WO2023095155A1.**

2A.1 Introduction

The large-scale consumption of fossil fuels worldwide deteriorates the environment daily and causes ecological imbalance. Developing robust energy storage systems to hoard renewable energy and electrification of transport systems is necessary to reduce the dependence on fossil fuels.[1,2] Hybrid electric vehicles (HEVs) and electric vehicles (EVs) are considered sound alternative transport systems. Therefore, it is essential to develop high-performing, environmentally safe, and economically feasible energy storage devices for the electrification of the transport system.[3,4] Li-ion batteries (LIBs) are the first choice among secondary batteries because of their high energy density, low memory effect, longer cyclability, and safety features.[3] The cathode material is a crucial part of the energy storage cells. Three cathode chemistries, layered, spinel, and olivine-type materials, have occupied the space.[5] In cathode chemistries, Co plays a vital role; there is an urgent need to develop Co-free cathode material owing to its scarcity, environmental compatibility, and significant fluctuation in their prices.[6–8] In current years, the price of Co has varied expansively from $ 30000 to $90000 per metric ton as EVs have developed rapidly around the globe; the global development of LIBs production size is projected to rush from ≈290 GWh to ≈1700 GWh by 2028.[9] This global dependence on Co might affect rivalry for raw materials and subsequent conflicts, encouraging scientists to look for Co-free energy storage technology.[10]

$LiMn_2O_4$ (LMO) spinel cathode is economically and environmentally friendly among the existing cathode materials. It has attracted many researchers since Thackeray et al.'s first report of lithiation and de-lithiation in 1983, 1984.[11–13] Mn-based cathode materials are the cost-effective alternative for automotive applications owing to their high energy density and high voltage.[14] In recent years, $LiMn_{1.5}Ni_{0.5}O_4$ has been the focus of many researchers[15] because of its high capacity, less environmental impact, low production cost, and high operating voltage of 4.7 V.[16] However, the practical capacity of materials with spinel framework is less. It faces a capacity fading issue

over the cycles, which pulls back this material in effective commercialization. This capacity fading over the cycling is mainly caused by two factors: (i) disproportionation reaction and (ii) Jahn-Teller distortion. The cycling performance of these spinel materials was affected by an irreversible phase transition in crystal structure over the cycling[17,18] and oxygen loss. Another main issue with this spinel material is the dissolution of Mn ion into the electrolyte, leading to passive layer deposition on the anode surface. This layer on the anode deteriorates the solid electrolyte interface (SEI) layer, leading to capacity decay.[19,20]

Researchers have made several approaches to improve cyclability by suppressing the problems associated with LMO cathodes. They are mainly doping with transition metal ions,[21–25] surface coating with conductive compound and inert materials [26–28]. Among them, doping with transition metal ions efficiently improved or enhanced the system's structural stability and electrochemical properties. In this direction, many metal ions have been used as dopants viz., Ti,[21] Sc,[22] Cr,[24] Ni,[23] Fe,[25] Co,[23,29] Cu,[25,30] Zn,[31] Al,[30] etc. Ni, Fe, and Al-doped materials showed improved performance among the most reported substituent elements. Ni doping enhances the capacity and energy density,[25,32–34] Fe doping enhances electronic conductivity and Li^+ ion diffusion kinetics,[25,33,35] and Al doping enhances the structural stability and electrochemical performance.[32,36–38] To utilize the maximum contribution of Ni to achieve more capacity than well-known $LiMn_{1.5}Ni_{0.5}O_4$ spinel cathode material, we have increased the Ni proportion with the support of other substituents, Al and Fe.

Herein, we developed multi-cation-doped high-energy LMO cathodes. The effect of partial substitution of redox-active Ni^{+3} and redox-inactive Al^{3+}, Fe^{3+}, and metal ions for Mn^{3+} in $LiMn_2O_4$ has been studied. The structural, morphological, and electrochemical characterization of a series of materials **$LiMn_{2-x-y-z}Ni_xFe_yAl_zO_4$ (x=0.8-0.5, y=0.1-0.25, z=0.1-0.25)** is reported in this work.

An accelerating discussion regarding this series of materials is termed MNFA811, MNFA712, MNFA721, MNFA622, and MNFA52525. The structural and morphological characterization shows the effective formation of a disordered spinel at 750 °C. The electrochemical studies showed excellent behavior towards high specific capacity and longer cyclability. As of our knowledge, this combination of elements, such as dopants forming disordered spinel structures for better performance, has not been reported elsewhere.

2A.2 Methods and materials

2A.2.1 Preparation of $LiMn_{2-x-y-z}Ni_xFe_yAl_zO_4$ (x=0.8-0.5, y=0.1-0.25, z=0.1-0.25)

Multi-cation doped $LiMn_2O_4$ spinel material is successfully synthesized by a simple sol-gel method. Stoichiometric amounts of Lithium acetate dihydrate ($CH_3COOLi \cdot 2H_2O$) (Thomas Baker 99%) (5 % excess taken to recompense the loss of Li at high temperature during calcination), Manganese (II) acetate tetrahydrate $(CH_3COO)_2Mn\ 4H_2O$) (Sigma Aldrich >99%), Nickel (II) acetate tetrahydrate $(CH_3COO)_2Ni\ 4H_2O$) (Sigma Aldrich >98%), Iron oxalate dihydrate ($FeC_2O_4\ 2H_2O$) (Sigma Aldrich >99%), and Aluminum nitrate nonahydrate ($Al(NO_3)_3\ 9H_2O$) (Sigma Aldrich >98%) were taken in a solution of 1:4 citric acid monohydrate ($C_6H_8O_7\ H_2O$) (Sigma Aldrich >99%). The dissolved solution was kept for stirring and heating at 60 °C to get the viscous gel. The viscous gel obtained was dried in a hot air oven at 100 °C for 2 h and then ground for a few minutes. The obtained precursor was heat-treated at 400 °C for 4 h to get the intermediate compound. The powder was further ground and calcined at 750 °C for 10 h in air and cooled to room temperature, then ground into a fine powder of $LiMn_{2-x-y-z}Ni_xFe_yAl_zO_4$ (x=0.8-0.5, y=0.1-0.25, z=0.1-0.25).

2A.2.2 Material characterization methods

Crystalline structure analysis of prepared material was accomplished by X-ray diffraction with Cu-Kα radiation (k = 1.54 Å) (Panalytical Xpert Pro). The microscopic images were obtained by Field emission scanning electron microscope (FEI-NOVA NANOSEM 450). Compositional analysis was done by energy dispersive spectroscopy (EDS), crystalline nanostructures were observed by HR-Transmission electron microscope (JEOL JEM F-200), and elemental mapping by STEM-HAADF. X-ray photoelectron spectroscopy (XPS) was performed using Thermo Scientific Model K-alpha XPS instrument with monochromatic Al-Kα as the X-ray source. Raman spectra were acquired in the spectral region 100-1200 cm^{-1} using the HORIBA-J-Y Lab RAM HR 800 Raman spectrometer instrument with NIR He-Ne laser (wavelength 632.88 nm). The elemental quantification was done by using X-ray fluorescence spectrometry by employing the Panalytical $Epsilon3^{XLE}$, Energy dispersive X-ray fluorescence spectrometer (EDXRF) with Rh50 tube anode and Ag100 filter.

2A.2.3 Fabrication of electrodes and electrochemical measurement methods

The electrical and electrochemical studies were performed by assembling CR-2032-coin cells in an argon-filled glovebox with oxygen and H_2O levels of ≤ 0.1 ppm. The as-prepared cathode active powder (80 wt%), super C-65 (10 wt%), and polyvinylidene fluoride (10 wt%) were mixed with a few drops of *N*-methyl pyrrolidone solvent to obtain a homogeneous slurry. This slurry was then coated on carbon-coated Al-foil by doctor blade method, dried at 80 ºC in a vacuum oven, and cut into circular discs of 14 mm. Li-foil was used and considered as both a reference and negative electrode. Celgard®2325 was used as a separator, and 1M $LiPF_6$ in ethylene carbonate-dimethyl carbonate-ethyl methyl carbonate (EC/DMC/EMC 1:1:1) solution was used as electrolyte.

Cyclic voltammetry (CV) studies have been carried out at a scan rate of 0.1 mVs^{-1} between voltage windows of 3.50 V–4.99 V vs. Li. Electrochemical impedance spectroscopy (EIS) was studied at a frequency range from 1 MHz to 100 mHz with an amplitude of 50 mV in a Metrohm-Auotolab multi-channel electrochemical workstation (Multiautolab M204.). Galvanostatic charge-discharge studies were conducted with a voltage window of 3.5 V to 5 V at different current densities using a Neware battery testing system (BTS4000).

2A.3 Result and discussion

2A.3.1 Structural characterization

2A.3.1.1 X-ray diffraction study

Figure 2a.1(a). shows the XRD patterns of the $LiMn_{2-x-y-z}Ni_xFe_yAl_zO_4$ powders; the obtained peak patterns are well-matched with standard JCPDS No. 00-035-0782. The obtained diffraction pattern describes the prominent peaks related to the cubic spinel phase with space group $Fd\bar{3}m$. The pattern also showed the presence of minor peaks related to the secondary phase in the material with space group $Fm\bar{3}m$ (JCPDS No. 01-075-0543). This secondary phase is due to the loss of oxygen during the calcination at higher temperatures,[25] leading the spinel material to decompose and form another phase, $Li_xNi_{1-x}O$.[39–44]

To obtain more information about the mixed-phase formed here, we have done Rietveld refinement with Fullprof software, as shown in **Fig 2a.2(a-e)**. The lattice parameters of the materials obtained after Rietveld refinement are given in **Table 2a.1**. The refinement studies confirmed that the materials synthesized are mixed-phase, i.e., cubic spinel and cubic rocksalt structures. More details on structural parameters from Rietveld refinement are given in **Tables 2a.2 and 2a.3.** Here, the Ni content played a significant role in forming the secondary phase, i.e., $Li_xNi_{1-x}O$. The crystal structure parameters reveal that the secondary phase fractions reduce as the

Ni content reduces and the material forms a pure spinel structure (MNFA52525). The structural illustration of all materials demonstrates the presence of a secondary phase in all the materials except MNFA52525, as shown in **Figure 2a.3.** The structural illustration of MNFA811, MNFA712, MNFA721, and MNFA622 looks the same as there is not much difference in cell volume as well in the oxygen centers. The oxygen deficiency is different in all the materials, and the phase quantification is also different.

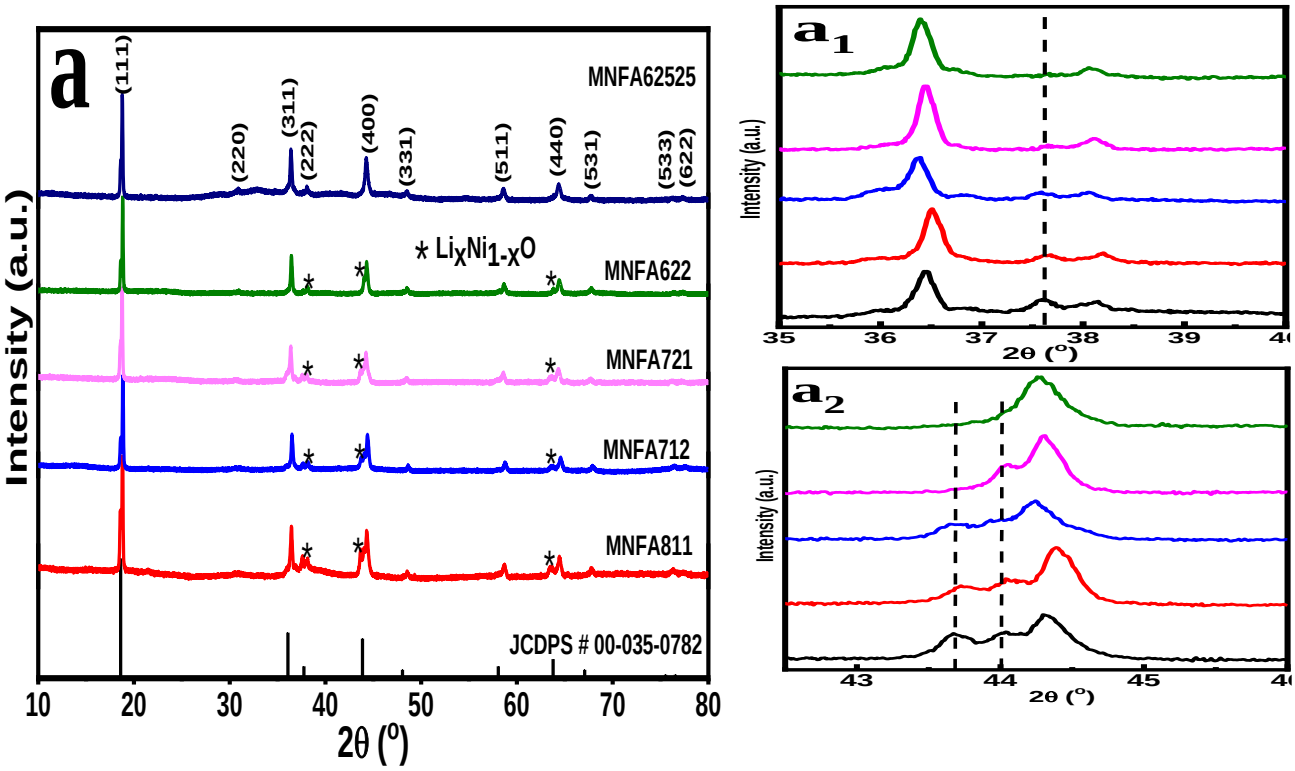

Figure.2a.1. **(a)**, XRD pattern and **(b-f)**. Rietveld refinement results of $LiMn_{2-x-y-z}Ni_xFe_yAl_zO_4$. **(a1-a2)** magnified parts of **(a)**.

The structural stability of our synthesized materials was also predicted by evaluating the ratio of the relative integrated intensities of 311 and 400 reflections related to the degree of tetragonal distortion (M_2O_4) in spinel materials.[45] This I_{311}/I_{400} peaks ratio lies between 0.96-1.10 for all the multi-cation doped materials (i.e., 1.05 for (MNFA811), 1.0 for (MNFA712), 1.08 for

(MNFA721), 1.09 for (MNFA622), 1.09 for (MNFA52525)), confirming that the synthesized materials are stable enough for electrochemical applications.[46,47]

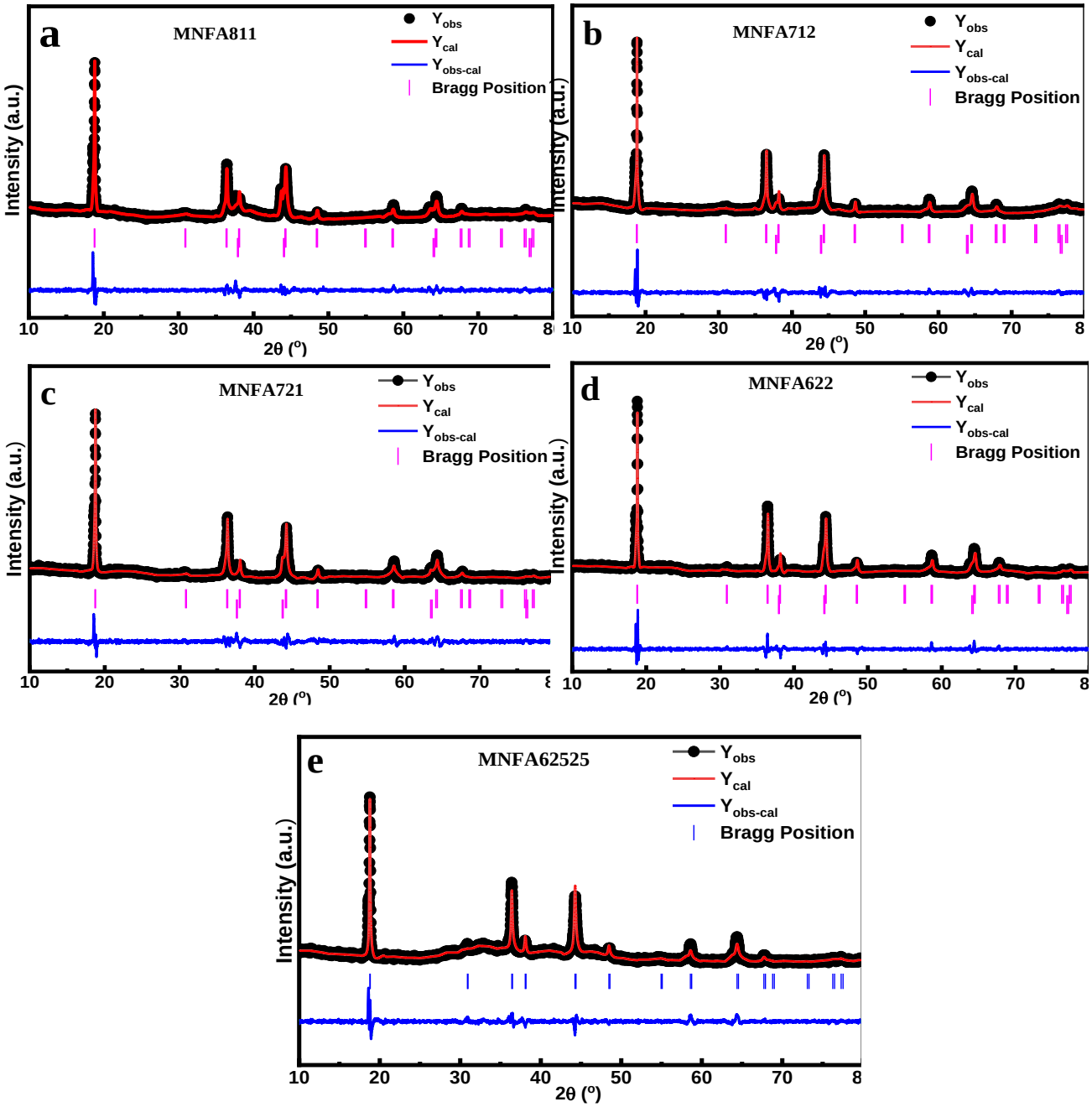

Figure 2a.2, (a-e) Rietveld refinement plots of X-ray diffraction data of $LiMn_{2-x-y-z}Ni_xFe_yAl_zO_4$ (x=0.8-0.5, y=0.1-0.25, z=0.1-0.25) materials.

Sample	Space group	Lattice constant (Å)	Cell volume	R_{bragg}	R_F^2	$\chi 2$	Phase Fraction (%)
$LiMnNi_{0.8}Fe_{0.1}Al_{0.1}O_4$ **MNFA811**	$Fd\bar{3}m$ $Fm\bar{3}m$	8.18 4.14	548.41 70.99	5.32 2.63	3.36 1.64	2.95	85.32 14.68
$LiMnNi_{0.7}Fe_{0.1}Al_{0.2}O_4$ **MNFA712**	$Fd\bar{3}m$ $Fm\bar{3}m$	8.17 4.13	546.25 70.68	6.79 2.34	4.49 3.48	3.75	69.48 30.52
$LiMnNi_{0.7}Fe_{0.2}Al_{0.1}O_4$ **MNFA721**	$Fd\bar{3}m$ $Fm\bar{3}m$	8.20 4.14	552.34 71.11	5.33 7.82	3.11 6.16	2.56	70.29 29.71
$LiMnNi_{0.6}Fe_{0.2}Al_{0.2}O_4$ **MNFA622**	$Fd\bar{3}m$ $Fm\bar{3}m$	8.18 4.11	548.96 69.48	9.02 3.29	7.12 3.15	3.24	76.98 23.02
$LiMnNi_{0.5}Fe_{0.25}Al_{0.25}O_4$ **MNFA52525**	$Fd\bar{3}m$	8.17	546.82	8.33	8.74	2.46	100

Table 2a.1. Lattice parameters of $LiMn_{2-x-y-z}Ni_xFe_yAl_zO_4$ (x = 0.8-0.5, y & z = 0.1-0.25)

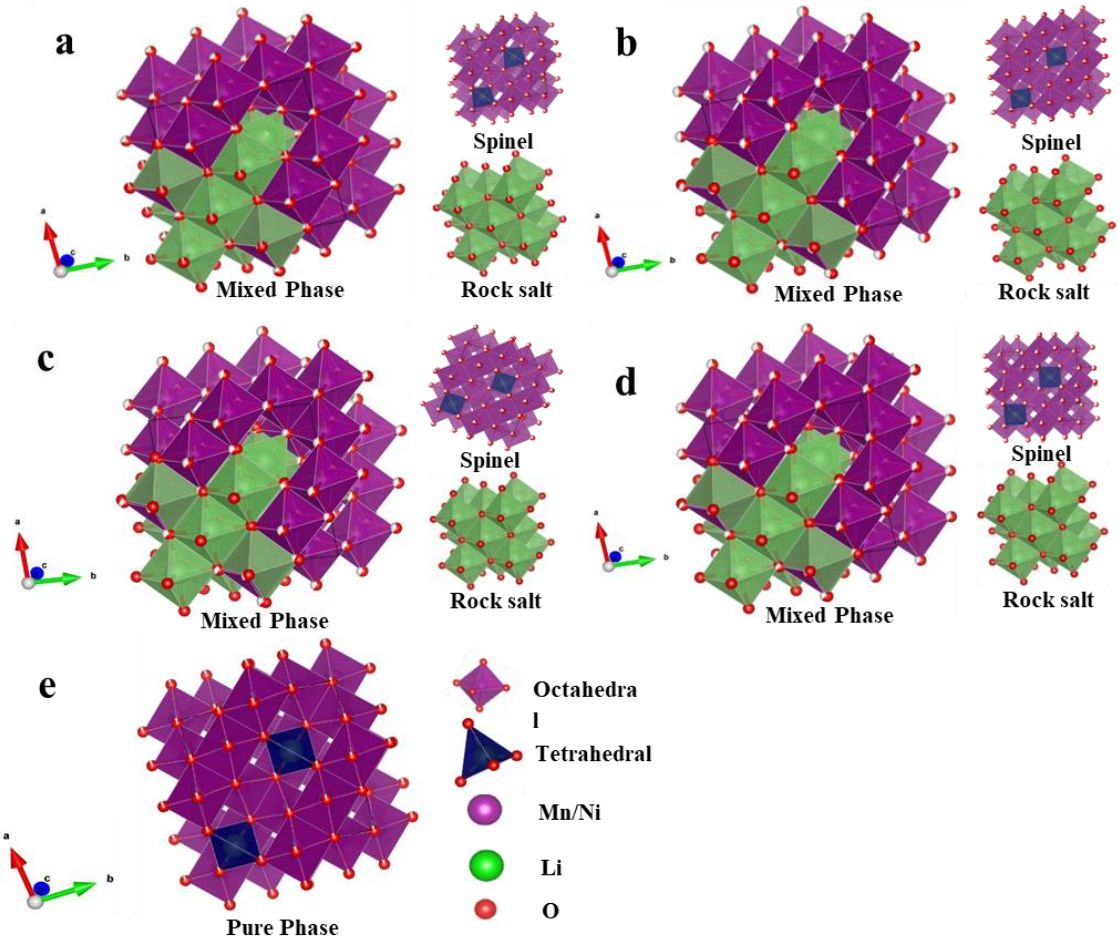

Figure 2a.3. Structural illustration of. **(a)** MNFA811, **(b)** MNFA712, **(c)** MNFA721, **(d)** MNFA622 and, **(e)** MNFA52525.

Sample	Atom	Wyckoff Position	x	y	z	Occupancy	B_{iso}	Cell Volume $(Å)^3$
$LiMnNi_{0.8}Fe_{0.1}Al_{0.1}O_4$	Li	8a	1/8	1/8	1/8	0.493	0.533	
(MNFA811)	Mn	16d	1/2	1/2	1/2	0.528	1.777	
	Ni	16d	1/2	1/2	1/2	0.470	1.777	548.416
(Fd-3m)	Fe	16d	1/2	1/2	1/2	0.019	1.777	
	Al	16d	1/2	1/2	1/2	0.132	1.777	
	O	32e	0.271	0.271	0.271	1.436	1.338	
$LiMnNi_{0.7}Fe_{0.1}Al_{0.2}O_4$	Li	8a	1/8	1/8	1/8	0.545	0.540	
(MNFA712)	Mn	16d	1/2	1/2	1/2	0.694	0.606	
	Ni	16d	1/2	1/2	1/2	0.591	0.606	546.25
(Fd-3m)	Fe	16d	1/2	1/2	1/2	0.106	0.606	
	Al	16d	1/2	1/2	1/2	0.223	0.606	
	O	32e	0.258	0.258	0.258	1.639	0.755	
$LiMnNi_{0.7}Fe_{0.2}Al_{0.1}O_4$	Li	8a	1/8	1/8	1/8	0.496	0.021	
(MNFA721)	Mn	16d	1/2	1/2	1/2	0.625	0.021	
	Ni	16d	1/2	1/2	1/2	0.590	0.021	552.34
(Fd-3m)	Fe	16d	1/2	1/2	1/2	0.415	0.021	
	Al	16d	1/2	1/2	1/2	0.132	0.021	
	O	32e	0.263	0.263	0.263	1.379	0.021	
$LiMnNi_{0.6}Fe_{0.2}Al_{0.2}O_4$	Li	8a	1/8	1/8	1/8	0.532	0.598	
(MNFA622)	Mn	16d	1/2	1/2	1/2	0.525	2.720	
	Ni	16d	1/2	1/2	1/2	0.495	2.720	548.96
(Fd-3m)	Fe	16d	1/2	1/2	1/2	0.2021	2.720	
	Al	16d	1/2	1/2	1/2	0.212	2.720	
	O	32e	0.275	0.275	0.275	1.288	1.921	
$LiMnNi_{0.5}Fe_{0.25}Al_{0.25}O_4$	Li	8a	1/8	1/8	1/8	0.902	1.180	
(MNFA52525)	Mn	16d	1/2	1/2	1/2	0.409	1.187	
	Ni	16d	1/2	1/2	1/2	0.386	1.187	546.82
(Fd-3m)	Fe	16d	1/2	1/2	1/2	0.066	1.187	
	Al	16d	1/2	1/2	1/2	0.052	1.187	
	O	32e	0.273	0.273	0.273	1.182	2.402	

Table 2a.2. Structural parameters obtained from the cubic spinel structure's Rietveld refinement X-ray diffraction data.

Sample	Atom	Wyckoff Position	x	y	z	Occupancy	B_{iso}	Cell Volume $(Å)^3$
$LiMnNi_{0.8}Fe_{0.1}Al_{0.1}O_4$	Li	4a	0.00	0.00	0.00	0.122	0.0792	
(MNFA811)	Ni1	4a	0.00	0.00	0.00	0.315	0.0792	
(Fm-3m)	Ni2	4a	0.00	0.00	0.00	0.191	0.0792	70.99
	O	4b	0.50	0.50	0.50	0.401	1.0582	
$LiMnNi_{0.7}Fe_{0.1}Al_{0.2}O_4$	Li	4a	0.00	0.00	0.00	0.0412	1.241	
(MNFA712)	Ni1	4a	0.00	0.00	0.00	0.0560	1.241	
(Fm-3m)	Ni2	4a	0.00	0.00	0.00	0.0300	1.241	70.08
	O	4b	0.50	0.50	0.50	0.280	1.864	
$LiMnNi_{0.7}Fe_{0.2}Al_{0.1}O_4$	Li	4a	0.00	0.00	0.00	0.293	0.499	
(MNFA721)	Ni1	4a	0.00	0.00	0.00	0.388	0.499	71.11
	Ni2	4a	0.00	0.00	0.00	0.299	0.499	
(Fm-3m)	O	4b	0.50	0.50	0.50	0.993	0.714	
$LiMnNi_{0.6}Fe_{0.2}Al_{0.2}O_4$	Li	4a	0.00	0.00	0.00	0.153	0.924	
(MNFA622)	Ni1	4a	0.00	0.00	0.00	0.244	0.924	69.48
	Ni2	4a	0.00	0.00	0.00	0.153	0.924	
(Fm-3m)	O	4b	0.50	0.50	0.50	1.172	1.883	

Table 2a.3. Crystallographic data of rocksalt structure

2A.3.1.2 Raman spectroscopic analysis

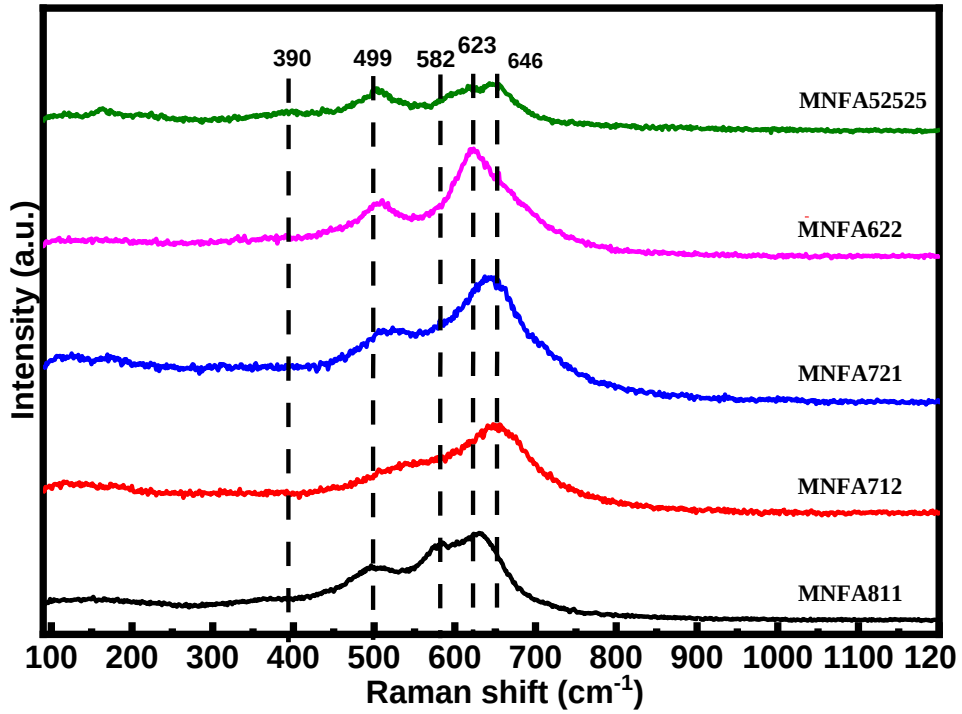

Figure 2a.4. Raman spectra of $LiMn_{2-x-y-z}Ni_xFe_yAl_zO_4$ (x=0.8-0.5, y=0.1-0.25, z=0.1-0.25).

The Raman spectra of $LiMn_{2-x-y-z}Ni_xFe_yAl_zO_4$, as shown in **Figure 2a.4**, the broad peak observed at 646 cm^{-1} corresponds to Mn-O stretching vibrations of the MnO_6 octahedral group, with A1g symmetry in the Oh^7 spectroscopic space group. A low-intensity peak at 615 cm^{-1} corresponds to F2g(1) symmetry.[48] This low-intensity band relates to the spinel structure's average oxidation state of Mn.[49] The peak observed at 499 cm^{-1} corresponds to Ni-O stretching vibration of NiO_6 octahedral groups, with the F2g(2) symmetry,[50,51] which confirms the successful incorporation of Ni into the octahedral sites of Mn in the spinel.[49] The peak at 390 cm^{-1} corresponds to the Li-O stretching vibration of the LiO_4 tetrahedral group.[52] Here, the peaks observed are slightly shifted compared to the literature due to the dopant's concentration and nature.

2A.3.1.3 XPS analysis

Figure 2a.5 (a-e) shows the XPS survey and expected elemental composition of MNFA811, MNFA712, MNFA721, MNFA622, and MNFA52525. The XPS analysis was performed for all the materials to understand their elemental composition and valence states. XPSPEAK41 software is used to deconvolute the XPS spectra with a Shirley baseline and Lorentzian−Gaussian fitting. The deconvoluted spectra of Mn2p consist of $Mn2p_{1/2}$ and $Mn2p_{3/2}$ core levels are shown in **Figure 2a.5 (a_1-e_1).** The deconvoluted peak $Mn2p_{3/2}$ core, shows Mn^{4+} and Mn^{3+} state with binding energies 642.66eV, 643.89eV, 643.17eV, 643.6eV, 646.44eV and 641.89eV, 642.56eV, 642.29eV, 642.58eV, 642.14eV respectively, for MNFA811, MNFA712, MNFA721, MNFA622, MNFA52525. The deconvoluted peak $Mn2p_{1/2}$ core shows only the Mn^{4+} state for all the materials in the series with binding energies 653.98eV, 654.78eV, 654.56eV, 654.71eV, and 654.45eV for MNFA811, MNFA712, MNFA721, MNFA622, and MNFA52525 respectively. These values are close to the reported values of Dang *et. al.,* Peng *et. al.,* and Xu *et al.,*[53–55], which clarifies the reason for the appearance of a tiny peak for Mn^{3+}/Mn^{4+} redox behavior

at the ~4V range in the cyclic voltammograms, which is evident for the minimal existence of Mn^{3+} in the material. The peak height and area of Mn^{4+} ions more than Mn^{3+} ions in the deconvoluted $Mn2p_{3/2}$ spectrum of all the materials, which gives a clear representation of substituent elements, Ni, Fe, and Al significantly reduced the Mn^{3+} ratio in all materials. The reduced Mn^{3+} content ensures structural stability to minimize the Jahn-Teller distortion and dissolution of Mn^{3+} ions in the electrolyte, driving better electrochemical performance.[25]

The deconvoluted spectra of Ni2p consist of $Ni2p_{3/2}$ and $Ni2p_{1/2}$ core levels situated at around 854-855 eV and 871-872 eV, respectively, for all the materials shown in **Figure 2a.5 (a_2-e_2).** The deconvoluted peak $Ni2p_{3/2}$ core, shows $Ni2^{+}$ and Ni^{3+} state with binding energies 854.12eV, 854.8eV, 854.68eV, 855.13eV, 854.45eV and 855.13eV, 855.92eV, 855.83eV, 856.04eV, 855.59eV respectively for MNFA811, MNFA712, MNFA721, MNFA622, MNFA52525. These values are in close agreement with the reported values.[55–57] The oxidation states of these can be correlated with redox behavior seen in cyclic voltammetry and galvanostatic charge/discharge profiles as the Mn and Ni are redox elements present in the cathode active materials, and the existence of redox inactive Fe^{3+} and Al^{3+} are acting as electrochemical stabilizers so that the charge/discharge behavior resembles the well-known cathode material $LiMn_{1.5}Ni_{0.5}O_4$. Deconvoluted spectra of the other substituent elements Fe and Al are given in **Figure 2a.6.** The Fe and Al binding energies confirm that all the substituents were appropriately doped to the Mn^{3+}site, forming a well-aligned stable structure.

The Li ions +1, Mn ions +3/+4, Ni ions +2/+3, Al ions +3, and Fe ions +3 are expected to carry the respective charges. The charge neutrality balancing for the synthesis considers the charges mentioned above and keeps the -2 state for oxygen atoms. The charge balance is calculated by

considering the materials' expected molecular formula. The secondary phase material formed is predicted with Ni ions carrying +2 majorly and Li ions with +1 charge.

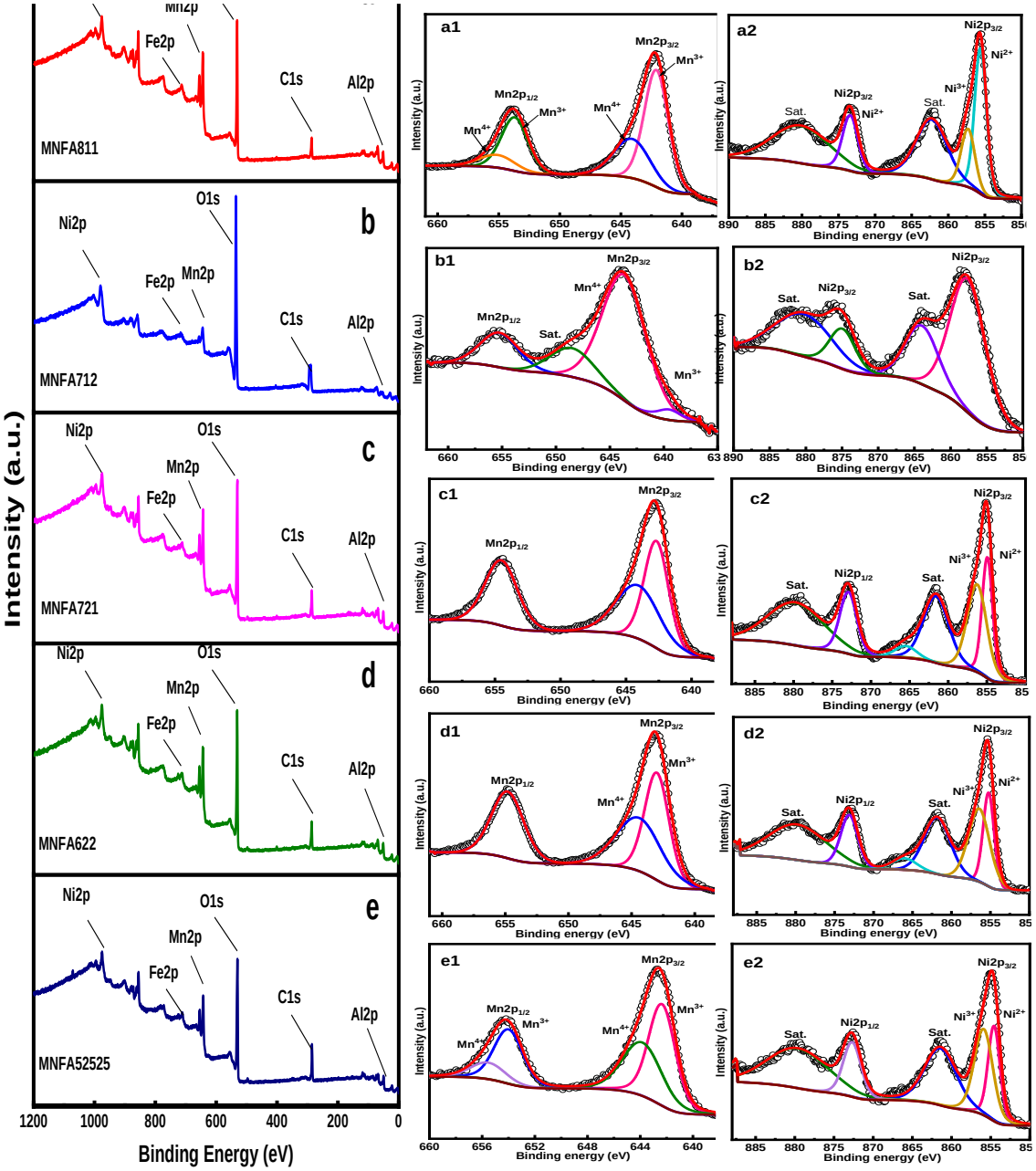

Figure 2a.5. XPS surveys of **(a)** MNFA811, **(b)** MNFA712, **(c)** MNFA721, **(d)** MNFA622 and **(e)** MNFA52525. High-resolution XPS of **(a_1-e_1)** Mn2p and **(a_2-e_2)** Ni2p for all samples.

The deconvoluted spectra of Al2p and Fe2p of MNFA811, MNFA712, MNFA 721, MNFA622, and MNFA52525 given above can show a slight shift in the peak positions due to variation in the ratio of composition of different substituents across the materials.

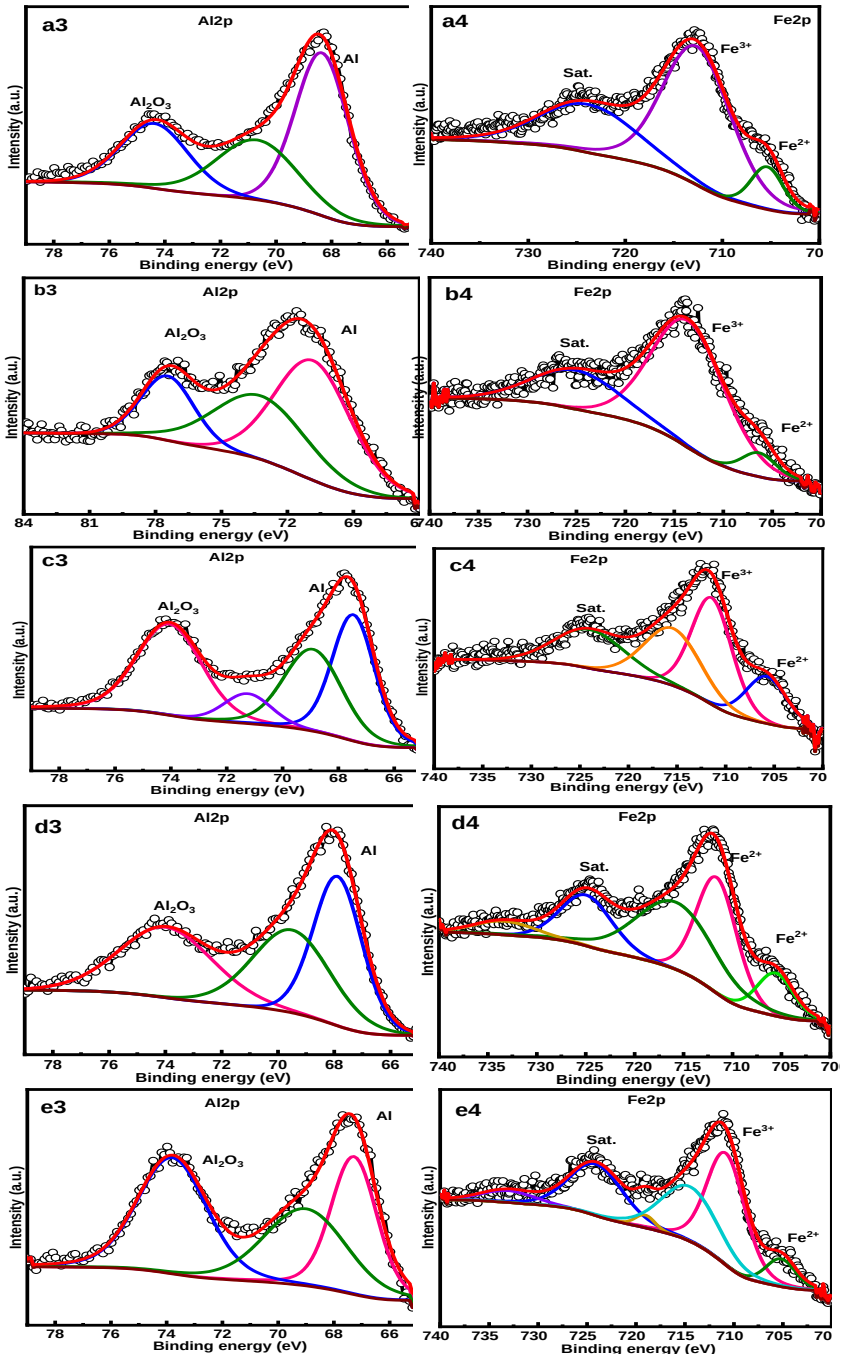

Figure 2a.6 Deconvoluted XPS peaks of Al2p and Fe2p core levels of (a)MNFA811, (b) MNFA712, (c) MNFA721, (d) MNFA622 and, (e) MNFA52525. High-resolution XPS of (a3-e3) Al2p and (a4-e4) Fe2p for all samples.

2A.3.1.4 X-ray fluorescence spectroscopic analysis

X-ray fluorescence spectrometric studies were carried out to determine the samples' elemental composition. The mole percentage of metal ions present in the active materials (except

Li as XRF cannot detect Li) is given in **Table 2a.4**. The outlook of this composition ratio of cations shows that the composition of Al is comparatively less because Al is the lighter element as compared to other heavier elements such as Mn, Ni, and Fe present in our materials. Because the XRF spectrometry is relatively less sensitive to lighter elements. The overall ratio of the metals matching the composition varied in all the materials.

Mn		Ni		Fe		Al	
Theoretical	**Experimental**	**Theoretical**	**Experimental**	**Theoretical**	**Experimental**	**Theoretical**	**Experimental**
49.98	54.8	42.72	37.8	5.08	5.5	2.45	1.7
51.34	53.4	38.39	36.6	5.21	5.3	5.04	4.5
49.99	51.2	37.39	36.3	10.16	10.5	2.45	1.7
51.48	51.3	33.01	32.8	10.46	10.3	5.05	5.4
52.33	53.9	27.95	27.5	13.29	13.8	6.42	4.6

Table 2a.4 Molar percentage composition of metal ions obtained from XRF spectrometry.

2A.3.1.5 Electron microscopic analysis

The morphology of multi-cation doped disorder structured spinel materials was studied by scanning electron and transmission electron microscopy. **Figure 2a.7a** shows the FE-SEM image of MNFA712. The particles obtained are agglomerated with good crystallinity and polydisperse in nature. The particles' grain size is in the range of ~100-600 nm, with an average particle size of ~236 nm for the selected FE-SEM image. The agglomeration of particles might be due to using citric acid as a complexing agent during the synthesis via the sol-gel method.[58]**Figure 2a.7b** shows the HR-TEM image of MNFA712, wherein the lattice fringes are marked with the *d* spacing of 0.210 nm, 0.240 nm, and 0.247 nm at different areas, which correspond to crystal planes of (222) (311) and (400), respectively. The inset of **Figure 2a.7b** shows the Fast Fourier Transform (FFT) images for selected areas marked with rectangles that depict the presence of both spinel and rock

salt phase structures.[59] The corresponding SAED pattern is shown in **Figure 2a.7c,** confirming the mixed-phase presence in the synthesized materials.[60] Furthermore, the material composition has been evaluated by STEM-HAADF elemental mapping, shown in **Figure 2a.7(d-i)**. The mapping results reveal the proper infusion of all the dopants into the crystal structure.

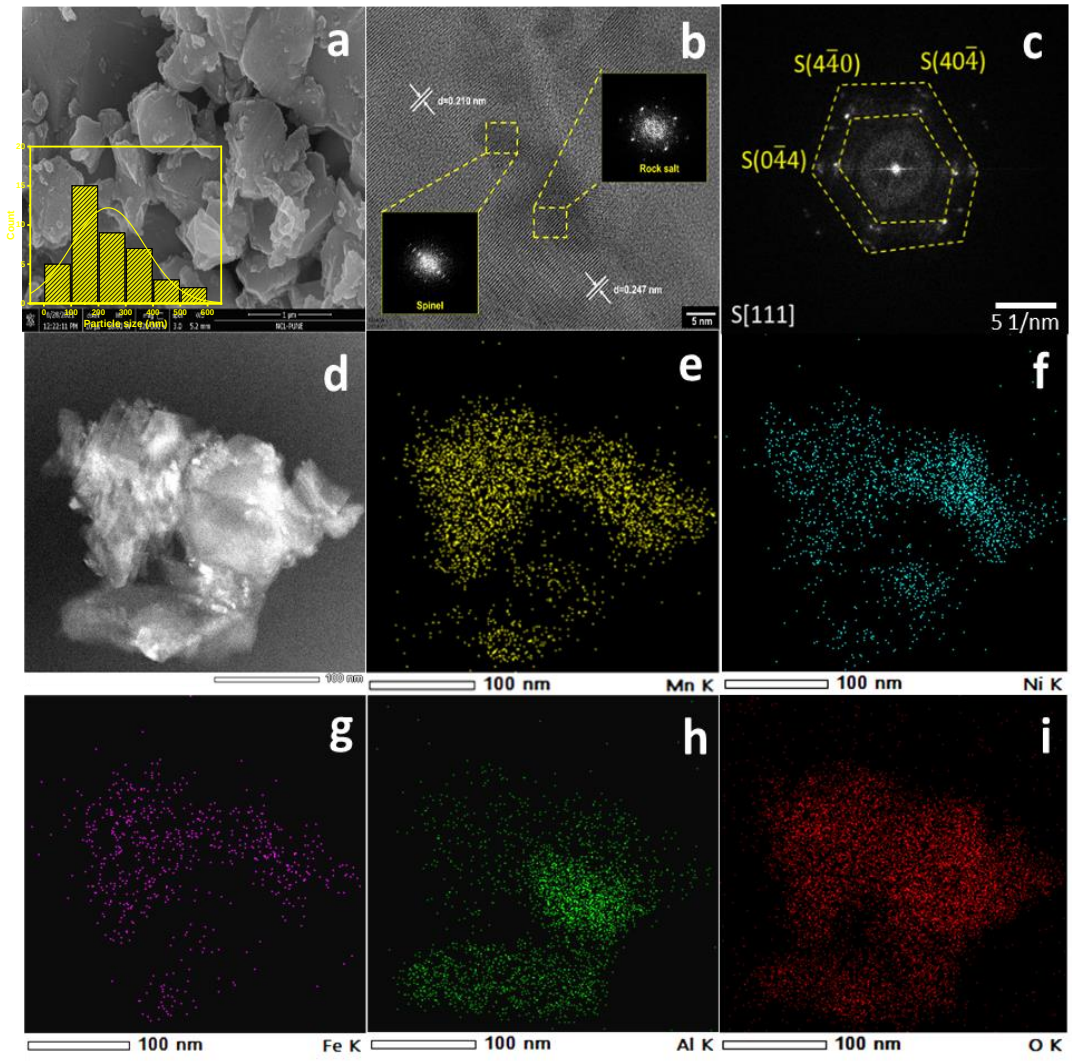

Figure 2a.7 (a) FE-SEM image, (b) HR-TEM image, (c) SAED pattern, **(d)** STEM-HAADF image and EDS elemental mapping of **((e)** Mn, **(f)** Ni, **(g)** Fe, **(h)** Al and, **(i)** O**)** MNFA712 particles. The inset of Figure 2a.7(a) is a histogram of particle size distribution.

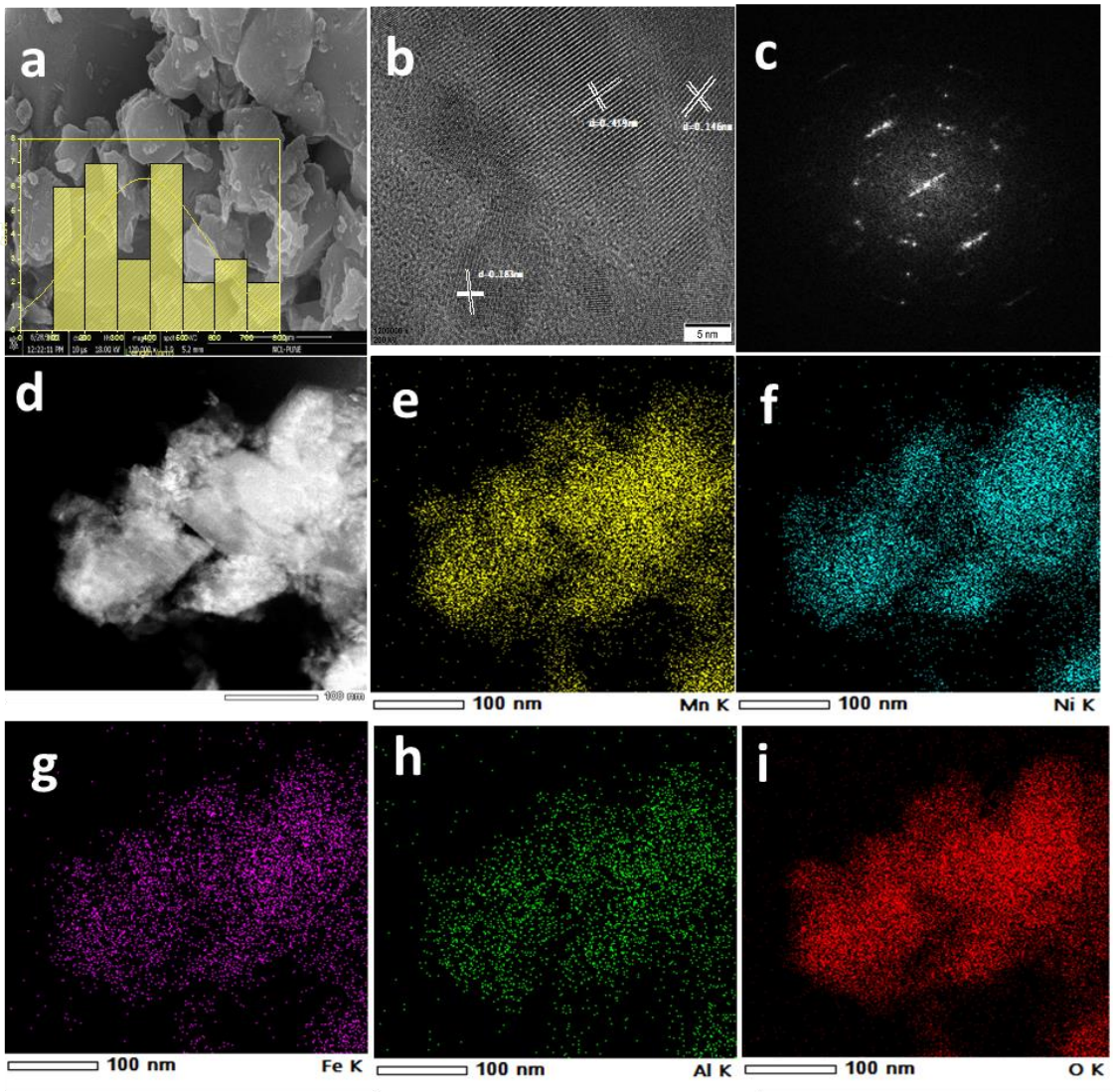

Figure 2a.8. **(a)** FE-SEM image **(b)** HR-TEM image, **(c)** SAED pattern **(d)** STEM-HAADF image and EDS elemental mapping of (**(e)** Mn, **(f)** Ni, **(g)** Fe, **(h)** Al and, **(i)** O) of MNFA811. The inset of Figure 2a.8(a) is a histogram of particle size distribution.

Figure 2a.8a shows the FE-SEM image of MNFA811. The particles obtained are agglomerated with good crystallinity and polydisperse in nature. The particles' grain size is in the range of ~100-800 nm, with an average particle size of ~390 nm for the selected FE-SEM image. **Figure 2a.8b** shows the HR-TEM image of MNFA811, wherein the lattice fringes are marked with the *d* spacing of 0.419 nm, 0.246 nm, and 0.183 nm at different areas, which correspond to

crystal planes of (111) (311) and (400), respectively. The corresponding SAED pattern is shown in **Figure 2a.8c,** confirming the mixed-phase presence in the synthesized materials. Furthermore, the material composition has been evaluated by STEM-HAADF elemental mapping, shown in **Figure 2a.8(d-i)**. The mapping results reveal the successful proper infusion of all the dopants into the host structure.

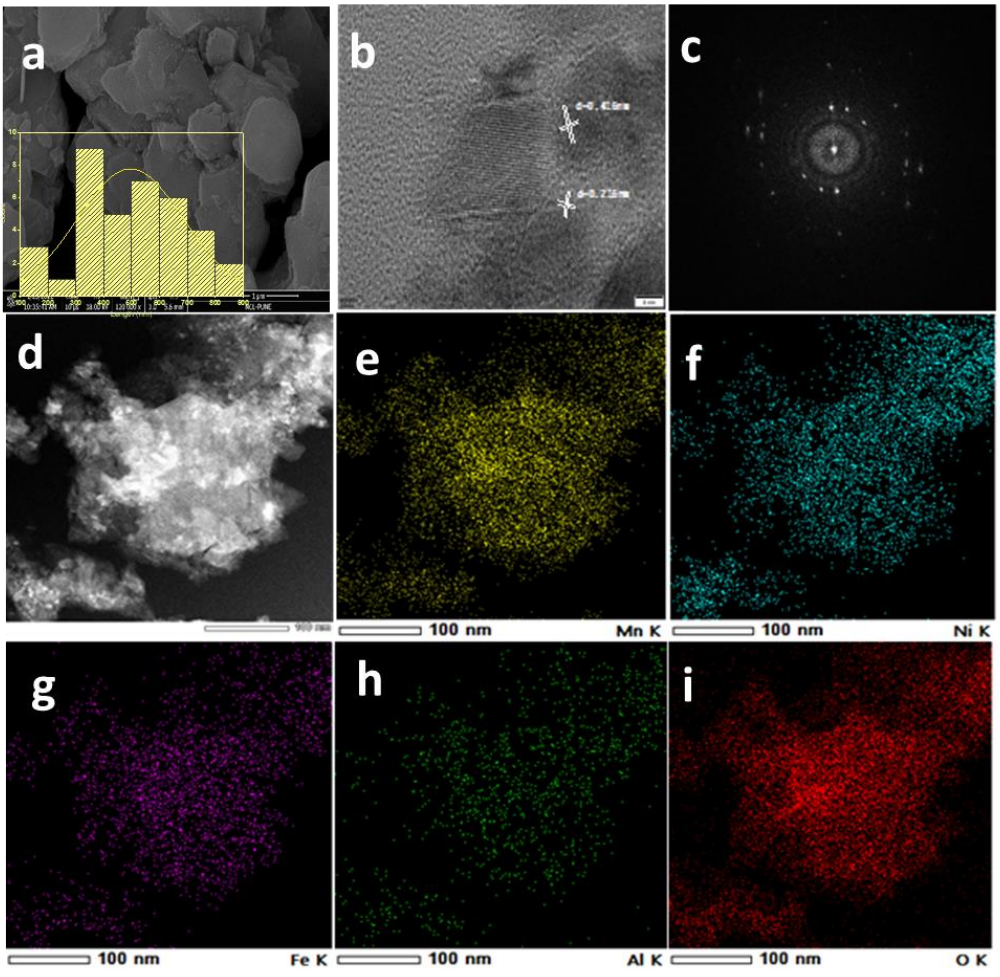

Figure 2a.9. **(a)** FE-SEM image **(b)** HR-TEM image, **(c)** SAED pattern **(d)** STEM-HAADF image and EDS elemental mapping of (**(e)** Mn, **(f)** Ni, **(g)** Fe, **(h)** Al and, **(i)** O) of MNFA721. The inset of Figure 2a.9a is a histogram of particle size distribution.

Figure 2a.9a shows the FE-SEM image of MNFA721. The particles obtained are agglomerated with good crystallinity and polydisperse in nature. The particles' grain size is in the

range of ~100-800 nm, with an average particle size of ~460 nm for the selected FE-SEM image. **Figure 2a.9b** shows the HR-TEM image of MNFA721, wherein the lattice fringes are marked with the *d* spacing of 0.42 nm and 0.216 nm at different areas, corresponding to crystal planes of (111) and (311), respectively. The corresponding SAED pattern is shown in **Figure 2a.9c,** confirming the mixed-phase presence in the synthesized materials. Furthermore, the material composition has been evaluated by STEM-HAADF elemental mapping, shown in **Figure 2a.9(d-i)**. The mapping results reveal the successful proper infusion of all the dopants into the host structure.

The FE-SEM image of MNFA622 is displayed in **Figure 2a.10a.** The resulting particles exhibit agglomeration, good crystallinity, and polydispersity. The grain size of these particles ranges from approximately 100 to 800 nm, with an average size of about 460 nm in the selected FE-SEM image. **Figure 2a.10b** presents the HR-TEM image of MNFA622, highlighting lattice fringes with d spacings of 0.426 nm and 0.218 nm in different areas, which correspond to the (111) and (311) crystal planes, respectively. The accompanying SAED pattern, shown in **Figure 2a.10c,** verifies the presence of mixed phases in the synthesized materials. The material's composition was also analyzed using STEM-HAADF elemental mapping, as illustrated in **Figure 2a.10(d-i).** The mapping results demonstrate the effective incorporation of all dopants into the host structure. The uniform distribution of elements throughout the sample further confirms the successful synthesis of the desired multi-component material. This homogeneous elemental distribution is crucial for achieving the intended properties and performance of the synthesized material. Moreover, the combination of SAED and STEM-HAADF techniques comprehensively characterize the material's structural and compositional features, enabling a deeper understanding of its intrinsic properties.

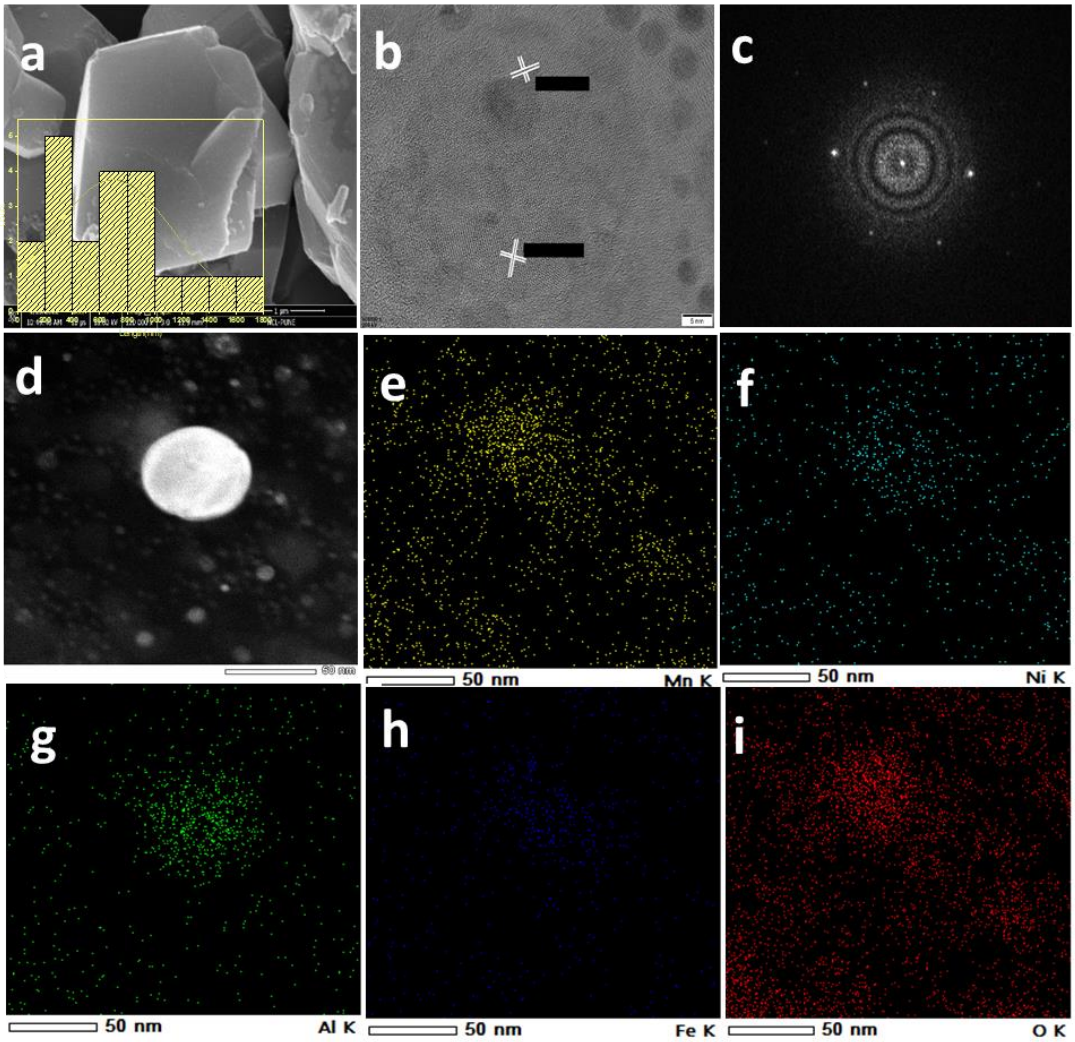

Figure 2a.10. (a) FE-SEM image **(b)** HR-TEM image, **(c)** SAED pattern **(d)** STEM-HAADF image and EDS elemental mapping of (**(e)** Mn, **(f)** Ni, **(g)** Fe, **(h)** Al and, **(i)** O) of MNFA622. The inset of Figure 2a.10(a) is a histogram of particle size distribution.

The FE-SEM image of MNFA622 is displayed in **Figure 2a.11a.** The resulting particles exhibit agglomeration, good crystallinity, and polydispersity. The grain size of these particles ranges from approximately 100 to 800 nm, with an average size of about 650 nm in the selected FE-SEM image. The HR-TEM image of MNFA5225, displayed in **Figure 2a.11b,** reveals lattice fringes with d spacings of 0.417 nm, 0.180 nm, and 0.357 nm in distinct regions, corresponding to the (111) and (400) crystal planes, respectively. **Figure 2a.11c** showcases the accompanying SAED pattern, which confirms the existence of multiple phases in the produced materials.

Moreover, **Figure 2a.11(d-i)** presents the elemental mapping conducted using STEM-HAADF, which was employed to examine the material's composition. The mapping results indicate that all dopants were effectively incorporated into the host structure. The uniform distribution of elements throughout the sample further confirms the successful synthesis of the intended multi-component material. This homogeneous elemental dispersion is crucial for achieving the desired properties and effectiveness of the synthesized material. Furthermore, the combined application of SAED and STEM-HAADF techniques provides a comprehensive analysis of the material's structural and compositional characteristics, enabling a deeper understanding of its intrinsic properties.

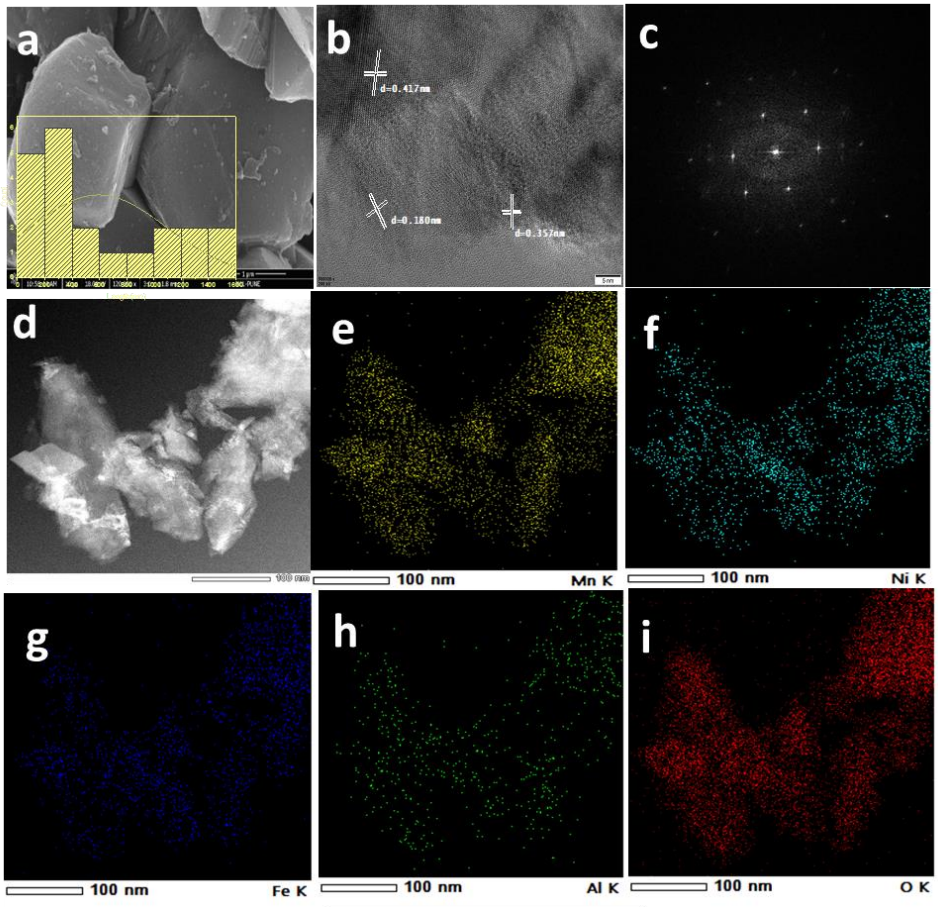

Figure 2a.11. (a) FE-SEM image (b) HR-TEM image, (c) SAED pattern (d) STEM-HAADF image and EDS elemental mapping of ((e) Mn, (f) Ni, (g) Fe, (h) Al and, (i) O) of MNFA52525. The inset of Figure 2a.11(a) is a histogram of particle size distribution.

2A.3.2 Electrochemical characterization

2A.3.2.1 Cyclic voltammetry analysis

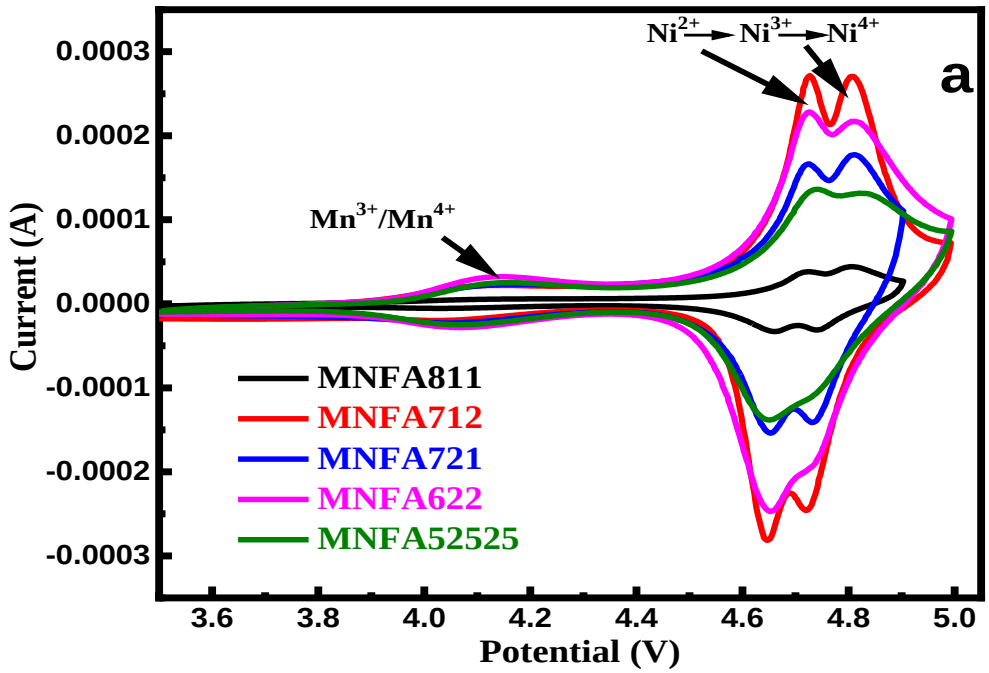

Figure 2a.12. Cyclic voltammograms at a scan rate of 0.1 mVs^{-1} MNFA811, MNFA712, MNFA721, MNFA622, and MNFA52525.

Cyclic voltammetry (CV) studies were carried out to know the redox behaviors of synthesized materials. **Figure 2a.12** shows cyclic voltammograms of fabricated 2032-coin cells with MNFA811, MNFA712, MNFA721, MNFA622, and MNFA52525 as cathode materials at room temperature with a scan rate of 0·1 mV s^{-1}. It is clear from the CV curves that the peak positions of all materials are the same. Still, the intensity of the peaks varies, which specifies that the lithiation/de-lithiation process is not the same for all materials.[61] As shown in **Figure 2a.12,** three pairs of redox peaks are observed at ~ 4.08/4.03 V, ~ 4.72/4.63 V, and ~ 4.81/4.73 V, indicating three-step intercalation/deintercalation of Li^+ during oxidation/reduction reaction. The first weak redox peak observed at 4.08/4.03 V corresponds to the Mn^{4+}/ Mn^{3+} redox couple. This

feeble peak is due to most Mn being in the Mn^{4+} state, indicating the minimized content of Mn^{3+}in the material,[31] which minimizes the John-Teller distortion. The second and third highly intense redox peaks observed at 4.72/4.63 V and 4.81/4.73 V, respectively, correspond to Ni^{2+}/Ni^{4+}, which indicates the predominant electrochemical activity of Ni in the active material. These redox peaks of lithiation/de-lithiation at higher voltage indicate that more driving force is necessary to urge the Li-ions from the cathode to the anode.

No peak is observed in the CV for Fe because Fe is redox inactive and acts as an electrochemical stabilizer.[62] Also, no peak was observed for Al because Al is a redox inactive dopant in this material, and therefore, it does not influence CV behavior. However, the presence of Al in the structure helps stabilize rather than improve the discharge capacity.[32,37,38,63]

2A.3.2.2 Electrochemical impedance spectroscopy (EIS)

Electrochemical impedance spectroscopy (EIS) studies were performed with two electrode systems for the fresh cells to know the interface resistance and kinetics of the Li^+ insertion/exertion mechanism. The obtained data has fitted with the equivalent circuit, which is provided in the inset of **Figure 2a.13**, where R1 represents the ohmic resistance arrives from the electrochemical system (Rs), R2 represents the resistance of solid electrolyte interface (R_{SEI}), R3 represents charge-transfer resistance (R_{ct}), CPE represents constant phase element (Q), and the W is the Warburg diffusion impedance (W). The fitted results of the equivalent circuit for all materials are given in **Table 2a.5**. All materials' Nyquist plots **(Figure 2a.13)** The high-frequency region exhibits a flattened arc. In contrast, the low-frequency region displays a linear pattern. The compressed arc in the high-frequency area results from combining two semicircles, representing the resistance of the solid electrolyte interface (R_{SEI}) and the charge-transfer resistance (R_{ct}). This indicates the process of lithium-ion insertion at the electrode-electrolyte boundary. The linear segment observed in the

low-frequency region signifies the interface resistance. In the low-frequency region, the inclined line represents Warburg impedance (W), while the vertical straight line indicates enhanced Li+ ion movement through the electrolyte toward the anode. These values of these circuit elements help to understand the kinetics of surface film formation between electrode-electrolyte, charge transfer, and Li-ion diffusion mechanisms.

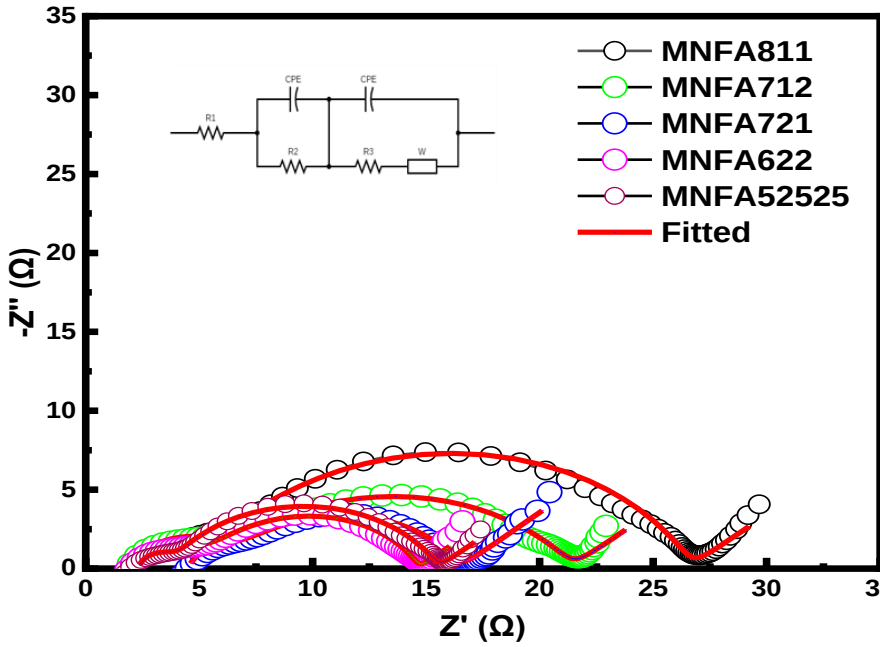

Figure 2a.13. Nyquist plots of MNFA811, MNFA712, MNFA721, MNFA622, and MNFA52525.

Material	**R1 (Ω)** R_s	**R2 (Ω)** R_{SEI}	**R3 (Ω)** R_{ct}	**Chi-squared**
MNFA811	1.7640	4.5927	20.2161	0.5360
MNFA712	1.9597	3.9529	15.2912	0.2879
MNFA721	4.5203	1.9434	9.98781	1.3802
MNFA622	1.8858	3.5832	9.15935	0.4385
MNFA52525	2.3364	1.3813	11.7527	0.3652

Table 2a.5. The EIS fitted data of MNFA811, MNFA712, MNFA721, MNFA622, and MNFA52525

2A.3.2.3 Galvanostatic charge-discharge analysis

Figure 2a.14a displays the performance of all materials at different current densities, spanning from 0.1 C to 5 C, within a voltage window of 3.5 V to 5.0 V. This figure demonstrates that as the applied current density increases, the specific discharge capacities of all materials progressively decline. The observed decrease in rate performance for all materials at higher current rates may be attributed to the reformation of the layer on the electrode surface and the phase transition of active material during cycling. These phenomena potentially impede the unrestricted movement of Li^+ ions.[64]

Galvanostatic charge-discharge experiments were conducted at a steady current density of 1C for 1000 cycles, with voltage limits set between 3.5 and 5V, as shown in **Figure 2a.14b**. It is observed that the initial discharge capacities are 123.1 $mAhg^{-1}$ (MNFA811), 148.7 $mAhg^{-1}$ (MNFA712), 131.2 $mAhg^{-1}$ (MNFA721), 126.4 $mAhg^{-1}$ (MNFA622), 101.2 $mAhg^{-1}$ (MNFA52525) while at the end of 1000 cycles, the discharge capacities were decreased to 104.5 $mAhg^{-1}$ (MNFA811), 118.3 $mAhg^{-1}$ (MNFA712), 108.7 $mAhg^{-1}$ (MNFA721), 112.4 $mAhg^{-1}$ (MNFA622), 81.5 $mAhg^{-1}$ (MNFA52525) with almost 100 % coulombic efficiency. All the materials showed a very good capacity retention of 82.4.9 % (MNFA811), 79.5 % (MNFA712), 82.8 % (MNFA721), 88.9 % (MNFA622), 80.5 % (MNFA52525) over 1000 cycles. Compared to all other materials, MNFA712 showed much better electrochemical performance with high capacity and stability. The presence of redox-inactive Fe^{3+} and Al^{3+} helps to improve stability, and it has been proved that the stability of all the materials is excellent. In MNFA622, the capacity retention of the material is about 88.9 %, which is more than all the materials and is due to the increased concentration of Al3+ and Fe^{3+}. This proves that Al^{3+} and Fe^{3+} play a critical role in the stability of the material. MNFA52525 has the least capacity among all materials due to decreasing Ni content and

increasing Fe and Al content. This indicates that the increase in substitution of Fe and Al atoms to a certain level improves the capacity of materials. Excess doping leads to capacity decay. Peng Li et. al.'s report has shown that doping Al^{3+} to a specific limit can reduce the capacity and increase the stability,[30] and the reports of C. Peng et al. and Xu et al. have shown capacity decay if the Al^{3+} ratio increases.[37,38] The same behavior is observed in our materials.

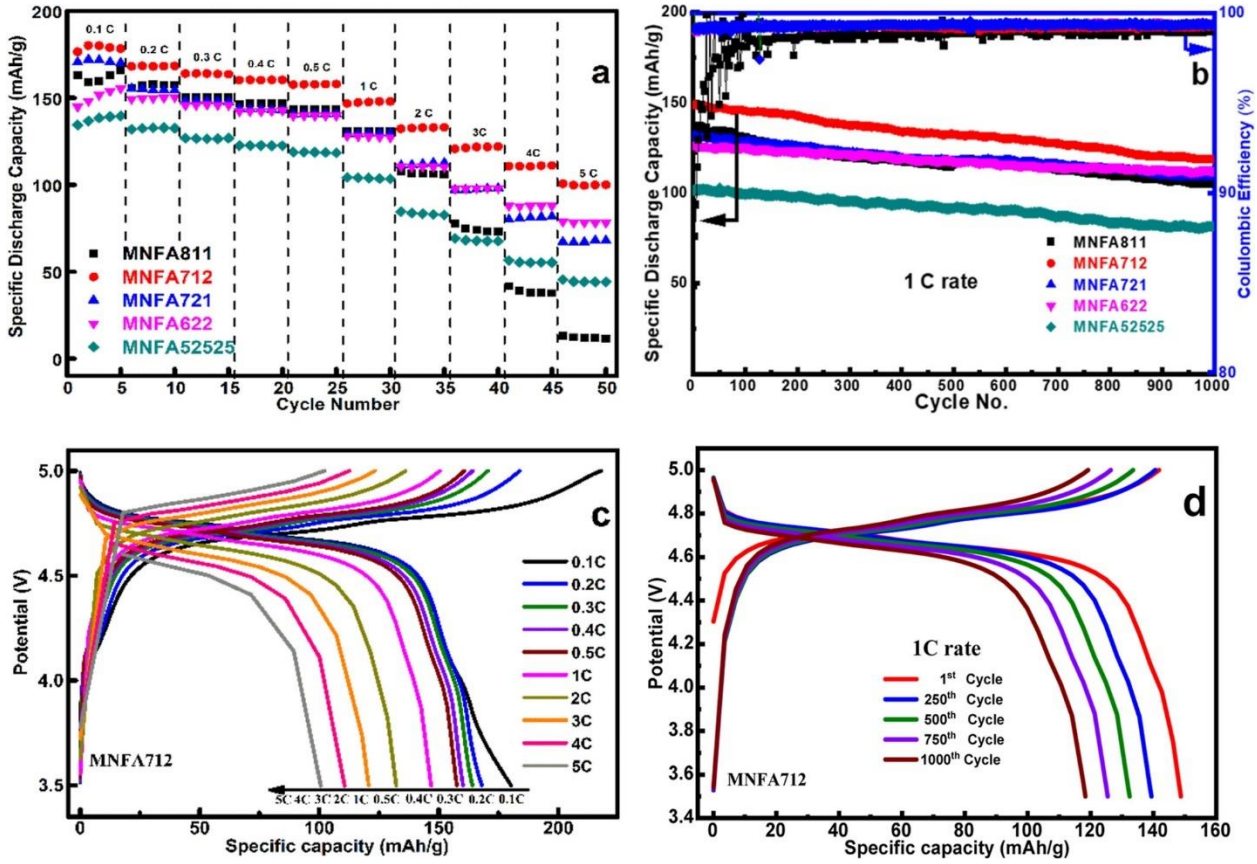

Figure 2a.14. **(a)** Rate capability at different C rate, **(b)** Cyclability plot at 1C rate, **(c)** Specific capacity ($mAhg^{-1}$) v/s Potential (V) at different C rate, **(d)** Specific capacity ($mAhg^{-1}$) v/s Potential (V) plot at 1C rate.

Figure 2a.14c shows the specific capacity v/s Voltage curves of MNFA712 cycled at different current densities, illustrating capacity degradation at higher currents. In **Figure 2a.14d**, the capacity retention of MNFA712 is exhibited by specific capacity v/s voltage curves of different galvanostatic charge-discharge cycles at different intervals at a 1C rate. Initially, it showed 148.7

$mAhg^{-1}$ with coulombic efficiency of 98.8 % at 1C rate. At the same time, at the end of 1000 continuous galvanostatic charge-discharge cycles, the specific capacity decreased to 118.3 mAg^{-1} with a coulombic efficiency of 99.2 %, implying that capacity retention of MNFA712 is 79.5 %. This behavior of MNFA712, well supported by various characterizations, can strongly imply that this material can be used for 5V applications in Li-ion batteries.

It has been proved from the literature that disordered spinel-type cathode materials have shown a significant improvement in capacity over pure spinel material. The existence of the secondary phase in spinel will enhance the energy density of the cathode materials.[7,65–67] According to the study of Patoux *et al.,* the ordered spinel material has a rapid capacity of fading at higher C rates than disordered spinel material.[68] This has been proved in our case also, the disordered samples have shown better electrochemical performance than the ordered phase.

2A.4 Effect of cation-disordered rocksalt structure in the spinel structure

Structural characterizations like XRD, TEM, and Raman studies confirm the co-substitution of multiple cations, which can contribute to the formation of cation-disordered rocksalt structure in the bulk spinel structure. To reduce the JT-distortion process, triple cations like Ni, Fe, and Al were co-substituted into half of the Mn ions in the spinel structure. Ni is the predominant substituent, the leading candidate while forming the cation-disordered rocksalt phase (i.e., LixNi1-xO) due to the oxygen loss in spinel structure at high temperature during the calcination. As a consequence of this second phase, the larger ionic radius of Ni^{2+} (0.72Å) in the rocksalt phase as compared to Mn^{3+} (0.65Å) could expand the Li^{+} ion diffusion channels,[69] while Fe^{3+} and Al^{3+} ions possibly accommodate in the stacks elicited due to the co-substitution of Ni ions. The synergistic effects of multi-cation substitution are attributed to the formation of the rocksalt phase, which leads to attaining superior capacity at different C-rates. The rocksalt structure is favorable for capacity

enhancement due to its minimal isotopic changes during charge-discharge cycling. The proper ratio of the rocksalt phase can improve the capacity by expanding the Li^+ ion diffusion channels and rapid Li^+ ion insertion and extraction. Still, the excess quantity of the rocksalt phase can lead to high capacity and degradation.[65,68] In our case, MNFA712 has shown more capacity and stability than all other materials, and the proper amount of rocksalt phase can achieve superior capacity. Thus, the spinel cathode with appropriate rocksalt proportions results in outstanding reversible cycling performance and rate capability.

2A.5 XRD analysis of electrodes after electrochemical test

Cathodes before and after cycling were subjected to XRD analysis to examine the structural changes of the MNFA series. The XRD of all the electrodes before cell fabrication was recorded and given in **Figure. 2a.15a**, and the XRD of the electrodes after cycling was given in **Figure 2a.15b**. Here, it can be observed that the diffraction peaks are still characteristic for all the samples except for the Al peaks (at 2 theta values 65 and 80 degrees) resulting from the Al current collector signifying the stable crystalline structure for all the samples.

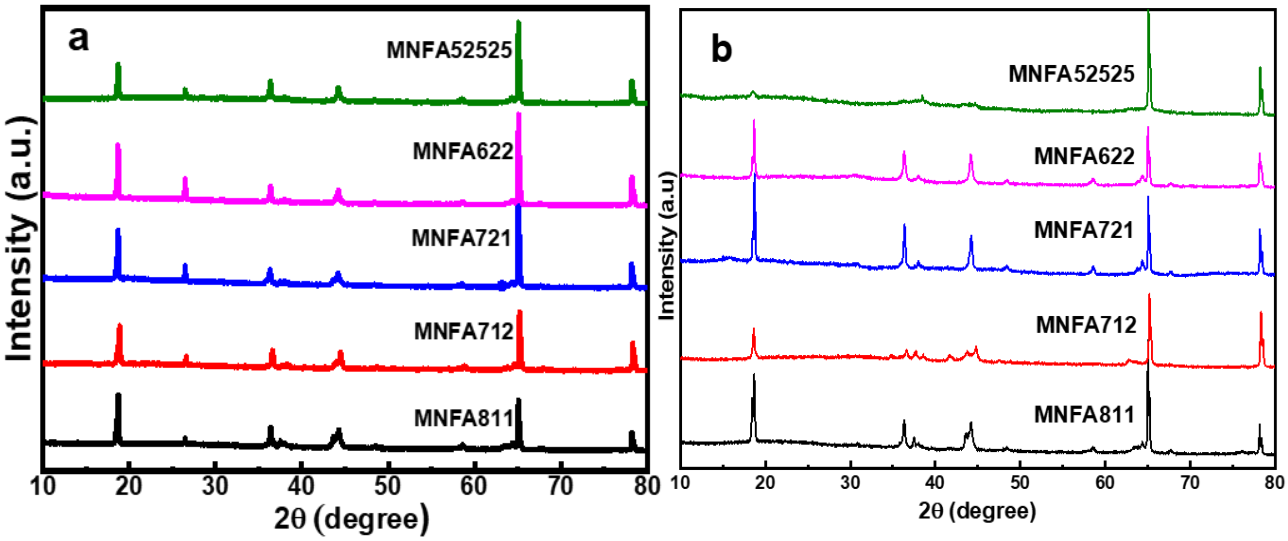

Figure 2a.15 Post-test XRD analysis of the electrodes **(a)** after coating on Al foil and **(b)** after cycling.

2A.6 Full cell fabrication and electrochemical analysis

Although half-coin cells are straightforward to fabricate and deliver reproducible results, they might not accurately portray the behavior of a material in a complete lithium-ion cell (referred to as a "full cell"). This absurdity is primarily attributed to the abundance of lithium in half cells, which can potentially conceal issues linked to side reactions that consume the available lithium supply. As a result, a half cell utilizing a particular positive electrode material may exhibit promising outcomes, while a full cell employing the same material could demonstrate poor performance. Moreover, half-cell experiments cannot demonstrate the interplay between positive and negative electrodes in a complete lithium-ion cell. These constraints make it difficult to accurately predict the behavior of a full cell based on half-cell studies alone.[70,71] Establishing a reliable approach for constructing accurate and consistent full coin cells would be valuable in anticipating the efficacy of emerging electrode materials for lithium-ion batteries. However, scientific literature lacks a substantial discussion on applying full Li-ion coin cells, and robust protocols for manufacturing precise cells remain undeveloped.

$LiMnNi_{0.7}Fe_{0.1}Al_{0.2}O_4$ // Graphite entire cell is prepared by using $LiMnNi_{0.7}Fe_{0.1}Al_{0.2}O_4$ as cathode, Graphite as an anode, conductive carbon C-65 as conducting agent, and PVDF as a binder. The active material, conductive agent, and binder are in a 90:5:5 ratio. The 1M $LiPF_6$ in EC: DMC: EMC (1:1:1 volume ratio) electrolyte was used for the cell fabrication. The N:P ratio of cathode and anodes is 1.5 after capacity balance.[70]

2A.6.1 Cyclic voltammetry study

Cyclic Voltammetry was used to measure the electrochemical performances of these coin cells. CV measurement was carried out on sample MNFA712 with graphite in the form of full cells assembled into coin cells. It was carried out to determine the electrochemical performance of the

MNFA712 and graphite anode. **Figures 2a.16a and 2a.16b** are data curves from CV measurement in the form of curves that show the relation between voltage (V) and the scan rate 100 mV as input voltage (V) and current (mA) as output. The redox curves in the case of full cells were not intensely visible as they appeared in half-cell formats, which is due to the properties, such as areal mass loading, thickness, and density of all electrode coatings, as the ratio of electrode and electrolyte usage in full cells is higher than half cells. It is quite complicated to control and maintain the N: P ratio. However, the number of redox pairs remained the same as in half cells but slightly shifted towards the lower potential region.

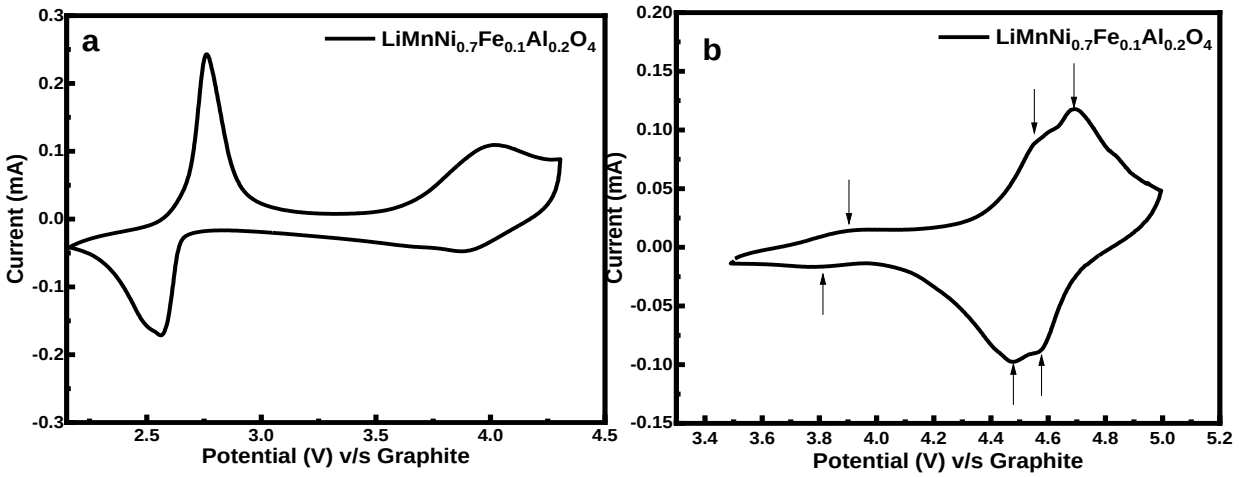

Figure 2a.16. **(a, b)** Cyclic voltammograms of full cells with MNFA712 cathode material and graphite anode at different voltage windows.

2A.6.2 Galvanostatic charge-discharge study

The galvanostatic charge-discharge (GCD) method was employed to assess the effectiveness of electrode materials. This technique involves subjecting the material or device to a steady current during the charging and discharging processes while recording the voltage changes over time. The

rate capability curves of GCD analysis are given in Figure 11a, and potential (V) against specific capacity in Figure 11b for a better understanding.

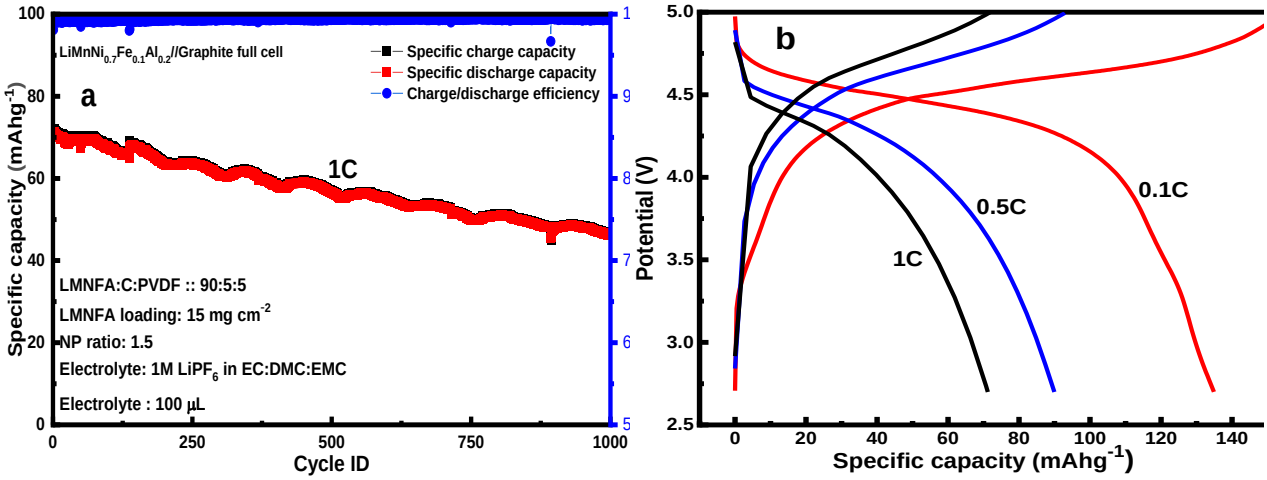

Figure 2a.17. Galvanostatic charge-discharge (a) cycle stability, (b) potential v/s specific capacity curves of MNFA712 material.

The full cell has demonstrated a specific capacity of 70.69 $mAhg^{-1}$ at 1C and a capacity retention of 65.2% after 1000 cycles of charge/discharge with a specific capacity of 46.1 $mAhg^{-1}$. The energy density in 1st cycle at 1C rate is 279 $WhKg^{-1}$. It is observed that the full cells show lower specific capacity as compared to the half cells of the same electrode active material, which is due to the limited availability of lithium inventory in full cells that it is partly consumed by the graphite anode surface irreversibly during the formation SEI layer.

2A.7 Conclusions

This study equipped a Ni, Fe, and Al co-doped $LiMn_2O_4$ cathode material to improve rate performance and cyclability. $LiMn_{2-x-y-z}Ni_xFe_yAl_zO_4$ (x=0.8-0.5, y=0.1-0.25, z=0.1-0.25) with disordered structure has been studied successfully, synthesized via simple sol-gel method followed by calcination at 750 $^{\circ}C$. XRD and TEM confirm the formation of mixed /disordered spinel. The multiple metal cation doping stabilizes the structure by reducing the Jahn-Teller effect. XPS results

suggest that all the substituents were appropriately doped to the Mn^{3+}site, which forms a well-aligned stable structure. Electrochemical studies of MNFA712 with disordered spinel/rocksalt structure have shown the possibility of efficient cathode material for the next generations of Li-ion batteries for 5V applications.

2A.8 References

(1) Scrosati, B.; Garche, J. Lithium Batteries: Status, Prospects and Future. *Journal of Power Sources*. 2010, pp 2419–2430. https://doi.org/10.1016/j.jpowsour.2009.11.048.

(2) Nitta, N.; Wu, F.; Lee, J. T.; Yushin, G. Li-Ion Battery Materials: Present and Future. *Mater. Today* **2015**, *18* (5), 252–264. https://doi.org/10.1016/j.mattod.2014.10.040.

(3) Manthiram, A. An Outlook on Lithium Ion Battery Technology. *ACS Cent. Sci.* **2017**, *3* (10), 1063–1069. https://doi.org/10.1021/acscentsci.7b00288.

(4) Kim, T.; Song, W.; Son, D.-Y.; Ono, L. K.; Qi, Y. Lithium-Ion Batteries: Outlook on Present, Future, and Hybridized Technologies. *J. Mater. Chem. A* **2019**, *7* (7), 2942–2964. https://doi.org/10.1039/C8TA10513H.

(5) Mohamed, N.; Allam, N. K. Recent Advances in the Design of Cathode Materials for Li-Ion Batteries. *RSC Adv.* **2020**, *10* (37), 21662–21685. https://doi.org/10.1039/D0RA03314F.

(6) Li, W.; Cho, Y.-G.; Yao, W.; Li, Y.; Cronk, A.; Shimizu, R.; Schroeder, M. A.; Fu, Y.; Zou, F.; Battaglia, V.; Manthiram, A.; Zhang, M.; Meng, Y. S. Enabling High Areal Capacity for Co-Free High Voltage Spinel Materials in next-Generation Li-Ion Batteries. *J. Power Sources* **2020**, *473*, 228579. https://doi.org/10.1016/j.jpowsour.2020.228579.

(7) Muralidharan, N.; Self, E. C.; Dixit, M.; Du, Z.; Essehli, R.; Amin, R.; Nanda, J.; Belharouak, I.; Muralidharan, N.; Dixit, M.; Du, Z.; Essehli, R.; Amin, R.; Belharouak, I.; Self, E. C.; Nanda, J. Next-Generation Cobalt-Free Cathodes-A Prospective Solution to the Battery Industry's Cobalt Problem Broadly Highlights the Enormous Promise of "Zero-Cobalt" Li-Ion Batteries to Enable Sustainable Production of EVs in the Coming Decades. **2022**. https://doi.org/10.1002/aenm.202103050.

(8) Zhang, J.; Wang, P. F.; Bai, P.; Wan, H.; Liu, S.; Hou, S.; Pu, X.; Xia, J.; Zhang, W.; Wang, Z.; Nan, B.; Zhang, X.; Xu, J.; Wang, C. Interfacial Design for a 4.6 V High-Voltage Single-Crystalline LiCoO2 Cathode. *Adv. Mater.* **2022**, *34* (8). https://doi.org/10.1002/adma.202108353.

(9) Gourley, S. W. D.; Or, T.; Chen, Z. Breaking Free from Cobalt Reliance in Lithium-Ion Batteries. *iScience*. 2020. https://doi.org/10.1016/j.isci.2020.101505.

(10) Overland, I. The Geopolitics of Renewable Energy: Debunking Four Emerging Myths. *Energy Research and Social Science*. 2019. https://doi.org/10.1016/j.erss.2018.10.018.

(11) Thackeray, M. M.; David, W. I. F.; Bruce, P. G.; Goodenough, J. B. Lithium Insertion into Manganese Spinels. *Mater. Res. Bull.* **1983**, *18* (4). https://doi.org/10.1016/0025-5408(83)90138-1.

(12) Thackeray, M. M.; Johnson, P. J.; de Picciotto, L. A.; Bruce, P. G.; Goodenough, J. B. Electrochemical Extraction of Lithium from LiMn2O4. *Mater. Res. Bull.* **1984**, *19* (2), 179–187. https://doi.org/10.1016/0025-5408(84)90088-6.

(13) Huang, Y.; Dong, Y.; Li, S.; Lee, J.; Wang, C.; Zhu, Z.; Xue, W.; Li, Y.; Li, J. Lithium Manganese Spinel Cathodes for Lithium-Ion Batteries. *Adv. Energy Mater.* **2021**, *11* (2), 2000997. https://doi.org/10.1002/aenm.202000997.

(14) Hosono, E.; Kudo, T.; Honma, I.; Matsuda, H.; Zhou, H. Synthesis of Single Crystalline Spinel LiMn 2 O 4 Nanowires for a Lithium Ion Battery with High Power Density. *Nano Lett.* **2009**, *9* (3), 1045–1051. https://doi.org/10.1021/nl803394v.

(15) Xu, G.; Pang, C.; Chen, B.; Ma, J.; Wang, X.; Chai, J.; Wang, Q.; An, W.; Zhou, X.; Cui, G.; Chen, L. Prescribing Functional Additives for Treating the Poor Performances of High-

Voltage (5 V-Class) LiNi 0.5 Mn 1.5 O 4 /MCMB Li-Ion Batteries. *Adv. Energy Mater.* **2018**, *8* (9), 1701398. https://doi.org/10.1002/aenm.201701398.

(16) Nitta, N.; Wu, F.; Lee, J. T.; Yushin, G. Li-Ion Battery Materials: Present and Future. *Mater. Today* **2015**, *18* (5), 252–264. https://doi.org/10.1016/j.mattod.2014.10.040.

(17) Xie, Y.; Jin, Y.; Xiang, L. Tuning the Nanoarea Interfacial Properties for the Improved Performance of Li-Rich Polycrystalline Li-Mn-O Spinel. *ACS Appl. Mater. Interfaces* **2019**, *11* (16), 14796–14802. https://doi.org/10.1021/acsami.9b01651.

(18) Liao, B.; Li, H.; Wang, X.; Xu, M.; Xing, L.; Liao, Y.; Liu, X.; Li, W. Significantly Improved Cyclability of Lithium Manganese Oxide, Simultaneously Inhibiting Electrochemical and Thermal Decomposition of the Electrolyte by the Use of an Additive. *RSC Adv* **2017**, *7* (74), 46594–46603. https://doi.org/10.1039/C7RA07870F.

(19) Diederichsen, K. M.; McShane, E. J.; McCloskey, B. D. Promising Routes to a High Li + Transference Number Electrolyte for Lithium Ion Batteries. *ACS Energy Lett.* **2017**, *2* (11), 2563–2575. https://doi.org/10.1021/acsenergylett.7b00792.

(20) Xu, J. Critical Review on Cathode–Electrolyte Interphase Toward High-Voltage Cathodes for Li-Ion Batteries. *Nano-Micro Lett.* **2022**, *14* (1), 166. https://doi.org/10.1007/s40820-022-00917-2.

(21) Xue, J. Enhanced Electrochemical Properties of Titanium Doped Lithium Manganese Oxide with Nanorod-like Morphology. *Int. J. Electrochem. Sci.* **2020**, *15* (9), 8732–8742. https://doi.org/10.20964/2020.09.61.

(22) Bhuvaneswari, S.; Varadaraju, U. V.; Gopalan, R.; Prakash, R. Structural Stability and Superior Electrochemical Performance of Sc-Doped LiMn 2 O 4 Spinel as Cathode for Lithium Ion Batteries. *Electrochimica Acta* **2019**, *301*, 342–351. https://doi.org/10.1016/j.electacta.2019.01.174.

(23) Li, W.; Deng, H.; Jiang, J. Improved Electrochemical Performance of LiMn 2 O 4 via Ni and Co Gradient Doping. *Sci. Adv. Mater.* **2018**, *10* (12), 1823–1829. https://doi.org/10.1166/sam.2018.3425.

(24) Iqbal, A.; Iqbal, Y.; Khan, A. M.; Ahmed, S. Effect of Bication (Cu-Cr) Substitution on the Structure and Electrochemical Performance of LiMn2O4 Spinel Cathodes at Low and High Current Rates. *J. Saudi Chem. Soc.* **2018**, *22* (4), 449–458. https://doi.org/10.1016/J.JSCS.2017.07.011.

(25) Sharma, P.; Das, C.; Indris, S.; Bergfeldt, T.; Mereacre, L.; Knapp, M.; Geckle, U.; Ehrenberg, H.; Darma, M. S. D. Synthesis and Characterization of a Multication Doped Mn Spinel, LiNi 0.3 Cu 0.1 Fe 0.2 Mn 1.4 O 4 , as 5 V Positive Electrode Material. *ACS Omega* **2020**, *5* (36), 22861–22873. https://doi.org/10.1021/acsomega.0c02174.

(26) Wang, C. M.; Jin, F. M.; Shi, T.; Chen, L. The Effect of LaMnO3 with High Electronic Conductivity on the High Rate Charge-Discharge Performance of LiMn2O4. *J. Electroanal. Chem.* **2016**, *775*, 306–310. https://doi.org/10.1016/J.JELECHEM.2016.05.025.

(27) Park, K.; Park, J.-H.; Hong, S.-G.; Yoon, J.; Park, S.; Kim, J.-H.; Yoon, D.; Kim, H.; Son, Y.-H.; Park, J.-H.; Kwon, S. Induced AlF3 Segregation for the Generation of Reciprocal Al2O3 and LiF Coating Layer on Self-Generated LiMn2O4 Surface of over-Lithiated Oxide Based Li-Ion Battery. *Electrochimica Acta* **2016**, *222*, 830–837. https://doi.org/10.1016/j.electacta.2016.11.044.

(28) Zhang, Z.-J.; Chou, S.-L.; Gu, Q.-F.; Liu, H.-K.; Li, H.-J.; Ozawa, K.; Wang, J.-Z. Enhancing the High Rate Capability and Cycling Stability of LiMn 2 O 4 by Coating of Solid-State

Electrolyte LiNbO 3. *ACS Appl. Mater. Interfaces* **2014**, *6* (24), 22155–22165. https://doi.org/10.1021/am5056504.

(29) Yi, Z. Rheological Phase Reaction Synthesis of Co-Doped LiMn2O4 Octahedral Particles. *J. Mater. Sci. Mater. Electron.* **2016**, *27* (10), 10347–10352. https://doi.org/10.1007/s10854-016-5120-2.

(30) Li, S.; Wei, Y.; Wang, P.; Feng, Y.; Liang, W.; Ding, H.; Cui, X. Synergism of Cu and Al Co-Doping on Improvements of Structural Integrity and Electrochemical Performance for LiNi0.5Mn1.5O4. *J. Alloys Compd.* **2020**, *820*, 153140. https://doi.org/10.1016/j.jallcom.2019.153140.

(31) Piao, J.-Y.; Duan, S.-Y.; Lin, X.-J.; Tao, X.-S.; Xu, Y.-S.; Cao, A.-M.; Wan, L.-J. Surface Zn Doped LiMn 2 O 4 for an Improved High Temperature Performance. *Chem. Commun.* **2018**, *54* (42), 5326–5329. https://doi.org/10.1039/C8CC01878B.

(32) Wang, S.; Xiang, M.; Lu, Y.; Guo, J.; Su, C.; Bai, H.; Liu, X. Facile Solid-State Combustion Synthesis of Al–Ni Dual-Doped LiMn2O4 Cathode Materials. *J. Mater. Sci. Mater. Electron.* **2020**, *31* (8), 6036–6044. https://doi.org/10.1007/s10854-020-03155-7.

(33) Zhong, G. B.; Wang, Y. Y.; Yu, Y. Q.; Chen, C. H. Electrochemical Investigations of the LiNi0.45M0.10Mn1.45O4 (M=Fe, Co, Cr) 5V Cathode Materials for Lithium Ion Batteries. *J. Power Sources* **2012**, *205*, 385–393. https://doi.org/10.1016/j.jpowsour.2011.12.037.

(34) Liu, H.; Li, M.; Xiang, M.; Guo, J.; Bai, H.; Bai, W.; Liu, X. Effects of Crystal Structure and Plane Orientation on Lithium and Nickel Co-Doped Spinel Lithium Manganese Oxide for Long Cycle Life Lithium-Ion Batteries. *J. Colloid Interface Sci.* **2021**, *585*. https://doi.org/10.1016/j.jcis.2020.10.052.

(35) Liu, J.; Manthiram, A. Understanding the Improved Electrochemical Performances of Fe-Substituted 5 V Spinel Cathode LiMn1.5Ni0.5O4. *J. Phys. Chem. C* **2009**, *113* (33), 15073–15079. https://doi.org/10.1021/jp904276t.

(36) Chen, M.; Wu, R.; Ju, S.; Zhang, X.; Xue, F.; Xing, W. Improved Performance of Al-Doped LiMn2O4 Ion-Sieves for Li+ Adsorption. *Microporous Mesoporous Mater.* **2018**, *261*, 29–34. https://doi.org/10.1016/j.micromeso.2017.10.058.

(37) Peng, C.; Huang, J.; Guo, Y.; Li, Q.; Bai, H.; He, Y.; Su, C.; Guo, J. Electrochemical Performance of Spinel LiAlxMn2-xO4 Prepared Rapidly by Glucose-Assisted Solid-State Combustion Synthesis. *Vacuum* **2015**, *120* (PA). https://doi.org/10.1016/j.vacuum.2015.07.001.

(38) Xu, W.; Zheng, Y.; Cheng, Y.; Qi, R.; Peng, H.; Lin, H.; Huang, R. Understanding the Effect of Al Doping on the Electrochemical Performance Improvement of the LiMn 2 O 4 Cathode Material. *ACS Appl. Mater. Interfaces* **2021**, *13* (38), 45446–45454. https://doi.org/10.1021/acsami.1c11315.

(39) Amdouni, N.; Zaghib, K.; Gendron, F.; Mauger, A.; Julien, C. M. Structure and Insertion Properties of Disordered and Ordered LiNi0.5Mn1.5O4 Spinels Prepared by Wet Chemistry. *Ionics* **2006**, *12* (2), 117–126. https://doi.org/10.1007/s11581-006-0021-7.

(40) Kim, D.; Shiiba, H.; Zettsu, N.; Yamada, T.; Kimijima, T.; Sánchez-Santolino, G.; Ishikawa, R.; Ikuhara, Y.; Teshima, K. Full Picture Discovery for Mixed-Fluorine Anion Effects on High-Voltage Spinel Lithium Nickel Manganese Oxide Cathodes. *NPG Asia Mater.* **2017**, *9* (7), e398–e398. https://doi.org/10.1038/am.2017.90.

(41) Wang, L.; Li, H.; Huang, X.; Baudrin, E. A Comparative Study of Fd-3m and P4332 "LiNi0.5Mn1.5O4." *Solid State Ion.* **2011**, *193* (1), 32–38. https://doi.org/10.1016/j.ssi.2011.04.007.

(42) Idemoto, Y.; Narai, H.; Koura, N. Crystal Structure and Cathode Performance Dependence on Oxygen Content of LiMn1.5Ni0.5O4 as a Cathode Material for Secondary Lithium Batteries. *J. Power Sources* **2003**, *119–121*, 125–129. https://doi.org/10.1016/S0378-7753(03)00140-X.

(43) Xue, Y.; Wang, Z.; Zheng, L.; Yu, F.; Liu, B.; Zhang, Y.; Ke, K. Investigation on Preparation and Performance of Spinel LiNi0.5Mn1.5O4 with Different Microstructures for Lithium-Ion Batteries. *Sci. Rep.* **2015**, *5* (1), 13299. https://doi.org/10.1038/srep13299.

(44) Bianchini, M.; Fauth, F.; Suard, E.; Leriche, J.-B.; Masquelier, C.; Croguennec, L. Spinel Materials for Li-Ion Batteries: New Insights Obtained by Operando Neutron and Synchrotron X-Ray Diffraction. *Acta Crystallogr. Sect. B Struct. Sci. Cryst. Eng. Mater.* **2015**, *71* (6), 688–701. https://doi.org/10.1107/S2052520615017199.

(45) Liu, J.; Li, G.; Yu, Y.; Bai, H.; Shao, M.; Guo, J.; Su, C.; Liu, X.; Bai, W. Synthesis and Electrochemical Performance Evaluations of Polyhedra Spinel LiAlxMn2-xO4 (X≦0.20) Cathode Materials Prepared by a Solution Combustion Technique. *J. Alloys Compd.* **2017**, *728*. https://doi.org/10.1016/j.jallcom.2017.09.098.

(46) Zhao, H.; Li, F.; Liu, X.; Cheng, C.; Zhang, Z.; Wu, Y.; Xiong, W.; Chen, B. Effects of Equimolar Mg (II) and Si (IV) Co-Doping on the Electrochemical Properties of Spinel LiMn2-2xMgxSixO4 Prepared by Citric Acid Assisted Sol-Gel Method. *Electrochimica Acta* **2015**, *151*. https://doi.org/10.1016/j.electacta.2014.11.095.

(47) Feng, X. Y.; Shen, C.; Xiang, H. F.; Liu, H. K.; Wu, Y. C.; Chen, C. H. High Rate Capability of 5 V LiNi0.5Mn1.5O4 Cathode Material Synthesized via a Microwave Assist Method. *J. Alloys Compd.* **2017**, *695*, 227–232. https://doi.org/10.1016/J.JALLCOM.2016.10.186.

(48) Samarasingha, P. B.; Andersen, N. H.; Sørby, M. H.; Kumar, S.; Nilsen, O.; Fjellvåg, H. Neutron Diffraction and Raman Analysis of LiMn1.5Ni0.5O4 Spinel Type Oxides for Use as Lithium Ion Battery Cathode and Their Capacity Enhancements. *Solid State Ion.* **2016**, *284*, 28–36. https://doi.org/10.1016/j.ssi.2015.11.018.

(49) Nageswara Rao, B.; Narsimulu, D.; Srinadhu, E. S.; Satyanarayana, N. Structural, Electrical, and Dielectric Properties of Nickel-Doped Spinel LiMn 2 O 4 Nanorods. *Ionics* **2019**, *25* (3), 981–990. https://doi.org/10.1007/s11581-018-2697-x.

(50) Bhatia, A.; Dridi Zrelli, Y.; Pereira-Ramos, J. P.; Baddour-Hadjean, R. Detailed Redox Mechanism and Self-Discharge Diagnostic of 4.9 V LiMn1.5Ni0.5O4spinel Cathode Revealed by Raman Spectroscopy. *J. Mater. Chem. A* **2021**, *9* (23), 13496–13505. https://doi.org/10.1039/d1ta00989c.

(51) Boulet-Roblin, L.; Villevieille, C.; Borel, P.; Tessier, C.; Novák, P.; Ben Yahia, M. Versatile Approach Combining Theoretical and Experimental Aspects of Raman Spectroscopy to Investigate Battery Materials: The Case of the LiNi0.5Mn1.5O4 Spinel. *J. Phys. Chem. C* **2016**, *120* (30), 16377–16382. https://doi.org/10.1021/acs.jpcc.6b04155.

(52) Vijayan, S.; Kirubasankar, B.; Pazhamalai, P.; Solarajan, A. K.; Angaiah, S. Electrospun Nd3+-Doped LiMn2O4 Nanofibers as High-Performance Cathode Material for Li-Ion Capacitors. *ChemElectroChem* **2017**, *4* (8), 2059–2067. https://doi.org/10.1002/celc.201700161.

(53) Dang, R.; Qu, Y.; Ma, Z.; Yu, L.; Duan, L.; Lü, W. The Effect of Elemental Doping on Nickel-Rich NCM Cathode Materials of Lithium Ion Batteries. *J. Phys. Chem. C* **2022**, *126* (1), 151–159. https://doi.org/10.1021/acs.jpcc.1c09691.

(54) Peng, Z.; Mu, K.; Cao, Y.; Xu, L.; Du, K.; Hu, G. Enhanced Electrochemical Performance of Layered Li-Rich Cathode Materials for Lithium Ion Batteries via Aluminum and Boron Dual-Doping. *Ceram. Int.* **2019**, *45* (4). https://doi.org/10.1016/j.ceramint.2018.11.087.

(55) Xu, W.; Zheng, Y.; Cheng, Y.; Qi, R.; Peng, H.; Lin, H.; Huang, R. Understanding the Effect of Al Doping on the Electrochemical Performance Improvement of the LiMn2O4Cathode Material. *ACS Appl. Mater. Interfaces* **2021**, *13* (38). https://doi.org/10.1021/acsami.1c11315.

(56) Abebe, E. B.; Yang, C.-C.; Wu, S.-H.; Chien, W.-C.; Li, Y.-J. J. Effect of Li Excess on Electrochemical Performance of Ni-Rich LiNi 0.9 Co 0.05 Mn 0.05 O 2 Cathode Materials for Li-Ion Batteries . *ACS Appl. Energy Mater.* **2021**, *4* (12). https://doi.org/10.1021/acsaem.1c03004.

(57) Meng, Y.; Wang, M.; Zhu, Z.; Jiang, T.; Liu, Z.; Chen, N.; Shen, C.; Peng, Q.; Chen, W. Multifunctional Nickel-Cobalt Phosphates for High-Performance Hydrogen Gas Batteries and Self-Powered Water Splitting. *ACS Appl. Energy Mater.* **2021**, *4* (11). https://doi.org/10.1021/acsaem.1c02582.

(58) Seyedahmadian, M.; Houshyarazar, S.; Amirshaghaghi, A. Synthesis and Characterization of Nanosized of Spinel LiMn 2O4 via Sol-Gel and Freeze Drying Methods. *Bull. Korean Chem. Soc.* **2013**, *34* (2). https://doi.org/10.5012/bkcs.2013.34.2.657.

(59) Nguyen, T. X.; Patra, J.; Chang, J. K.; Ting, J. M. High Entropy Spinel Oxide Nanoparticles for Superior Lithiation-Delithiation Performance. *J. Mater. Chem. A* **2020**, *8* (36). https://doi.org/10.1039/d0ta04844e.

(60) Zhang, H.; Karki, K.; Huang, Y.; Whittingham, M. S.; Stach, E. A.; Zhou, G. Atomic Insight into the Layered/Spinel Phase Transformation in Charged LiNi0.80Co0.15Al0.05O2 Cathode Particles. *J. Phys. Chem. C* **2017**, *121* (3). https://doi.org/10.1021/acs.jpcc.6b10220.

(61) Jerliu, B.; Hüger, E.; Dörrer, L.; Seidlhofer, B. K.; Steitz, R.; Horisberger, M.; Schmidt, H. Lithium Insertion into Silicon Electrodes Studied by Cyclic Voltammetry and: Operando Neutron Reflectometry. *Phys. Chem. Chem. Phys.* **2018**, *20* (36). https://doi.org/10.1039/c8cp03540g.

(62) Callegari, D.; Coduri, M.; Fracchia, M.; Ghigna, P.; Braglia, L.; Anselmi-Tamburini, U.; quartarone, eliana. Lithium Intercalation Mechanisms and Critical Role of Multi-Doping in LiFexMn2-x-yTiyO4 as High-Capacity Cathode Material for Lithium-Ion Batteries. *J. Mater. Chem. C* **2022**. https://doi.org/10.1039/D2TC00573E.

(63) Cai, Z.; Ma, Y.; Huang, X.; Yan, X.; Yu, Z.; Zhang, S.; Song, G.; Xu, Y.; Wen, C.; Yang, W. High Electrochemical Stability Al-Doped Spinel LiMn2O4 Cathode Material for Li-Ion Batteries. *J. Energy Storage* **2020**, *27*. https://doi.org/10.1016/j.est.2019.101036.

(64) Edge, J. S.; O'Kane, S.; Prosser, R.; Kirkaldy, N. D.; Patel, A. N.; Hales, A.; Ghosh, A.; Ai, W.; Chen, J.; Yang, J.; Li, S.; Pang, M. C.; Bravo Diaz, L.; Tomaszewska, A.; Marzook, M. W.; Radhakrishnan, K. N.; Wang, H.; Patel, Y.; Wu, B.; Offer, G. J. Lithium Ion Battery Degradation: What You Need to Know. *Physical Chemistry Chemical Physics*. 2021. https://doi.org/10.1039/d1cp00359c.

(65) Kwon, D. H.; Lee, J.; Artrith, N.; Kim, H.; Wu, L.; Lun, Z.; Tian, Y.; Zhu, Y.; Ceder, G. The Impact of Surface Structure Transformations on the Performance of Li-Excess Cation-Disordered Rocksalt Cathodes. *Cell Rep. Phys. Sci.* **2020**, *1* (9). https://doi.org/10.1016/j.xcrp.2020.100187.

(66) Lee, J.; Kitchaev, D. A.; Kwon, D. H.; Lee, C. W.; Papp, J. K.; Liu, Y. S.; Lun, Z.; Clément, R. J.; Shi, T.; McCloskey, B. D.; Guo, J.; Balasubramanian, M.; Ceder, G. Reversible

Mn2+/Mn4+ Double Redox in Lithium-Excess Cathode Materials. *Nature* **2018**, *556* (7700). https://doi.org/10.1038/s41586-018-0015-4.

(67) Freire, M.; Kosova, N. V.; Jordy, C.; Chateigner, D.; Lebedev, O. I.; Maignan, A.; Pralong, V. A New Active Li-Mn-O Compound for High Energy Density Li-Ion Batteries. *Nat. Mater.* **2016**, *15* (2). https://doi.org/10.1038/nmat4479.

(68) Patoux, S.; Daniel, L.; Bourbon, C.; Lignier, H.; Pagano, C.; Le Cras, F.; Jouanneau, S.; Martinet, S. High Voltage Spinel Oxides for Li-Ion Batteries: From the Material Research to the Application. *J. Power Sources* **2009**, *189* (1), 344–352. https://doi.org/10.1016/J.JPOWSOUR.2008.08.043.

(69) Xu, L.; Chen, S.; Li, N.; Li, Y.; Fang, Y.; Wei, C.; Chen, L.; Cao, D.; Lu, Y.; Wang, M.; Bao, L.; Su, Y. Formation of Rocksalt Domains by Dual Substitution to Boost Electrochemical Capability of Co-Free Li-Rich Layered Cathodes. *ACS Appl. Energy Mater.* **2022**. https://doi.org/10.1021/acsaem.2c01620.

(70) Murray, V.; Hall, D. S.; Dahn, J. R. A Guide to Full Coin Cell Making for Academic Researchers. *J. Electrochem. Soc.* **2019**, *166* (2), A329–A333. https://doi.org/10.1149/2.1171902jes.

(71) Björklund, E.; Brandell, D.; Hahlin, M.; Edström, K.; Younesi, R. How the Negative Electrode Influences Interfacial and Electrochemical Properties of $LiNi_{1/3}Co_{1/3}Mn_{1/3}O_2$ Cathodes in Li-Ion Batteries. *J. Electrochem. Soc.* **2017**, *164* (13), A3054–A3059. https://doi.org/10.1149/2.0711713jes.

Chapter 2B

Influence of crystal plane orientation in enhancing the electrochemical performance of tri-cation substituted cathode for Liion batteries

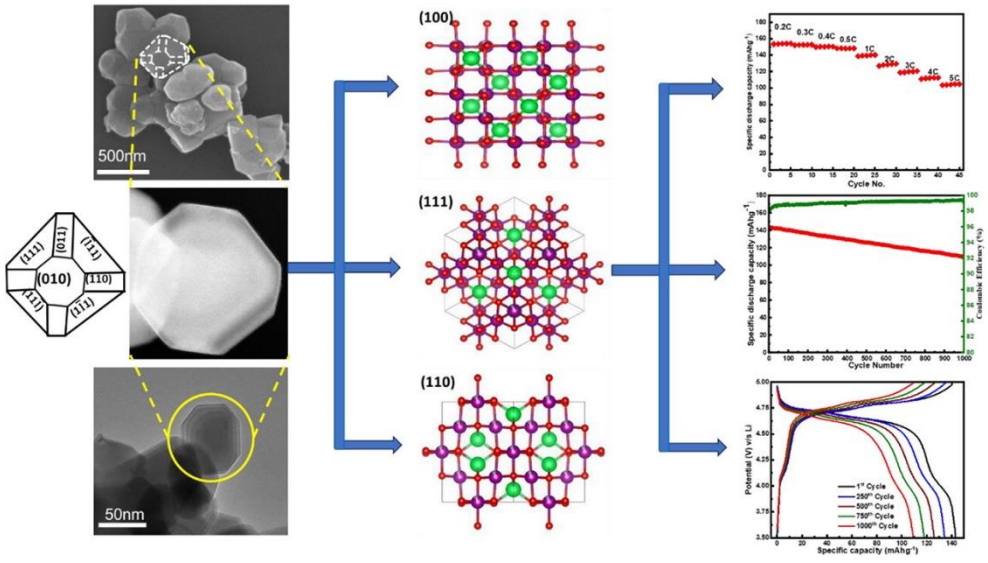

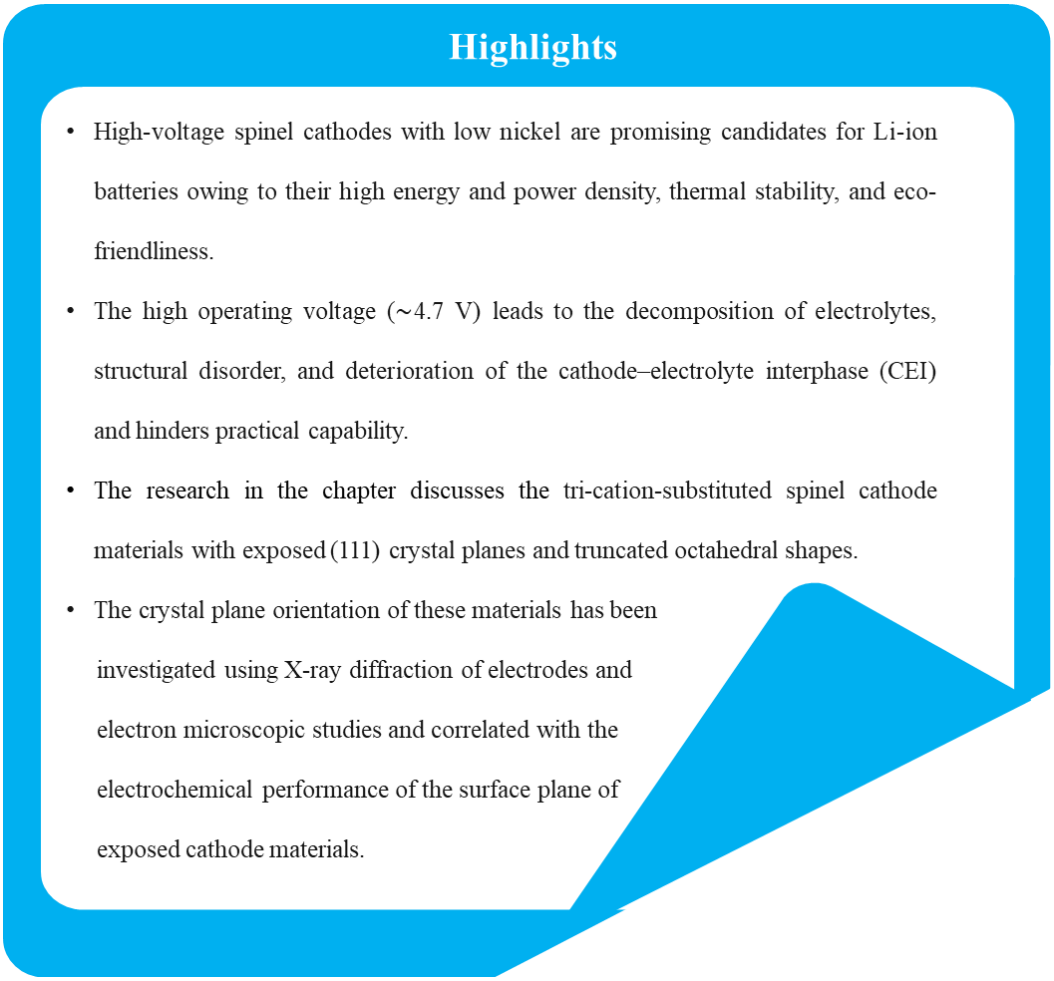

- The results of this chapter published as **BP Shivamurthy**, M Thripuranthaka, MV Shelke, **GP Nayaka*,** Influence of crystal plane orientation in enhancing the electrochemical performance of tri-cation substituted cathode for Li-ion batteries, **Energy Fuels**, 2024, 38, 5, 4653–4665.

2B.1 Introduction

Cathode materials play a vital role in determining the energy density of Li-ion batteries (LIB). The eagerness towards the invention and development of high-energy cathode materials comprises low-cost and earth-abundant elements that could reduce the production cost of batteries. Besides, the availability of high-voltage cathode materials with increased energy density is a concern for successful commercialization. The $LiMn_2O_4$ cathode materials belong to the spinel type of cathode materials, which are the priority choice for high-voltage applications as they can exhibit exceptional thermal stability. But simultaneously, it suffers from Mn dissolution issues in electrolytes. This forced the researchers to modify this spinel cathode material to reduce Mn dissolution. As a result, $LiMn_{1.5}Ni_{0.5}O_4$ spinel (LMNO) cathode materials emerged as promising candidates because of their high operational voltage of ~4.7 V and ability to provide high energy density and power density with longer cycling performance.[1] However, the real-time applications of spinel-based cathode materials are hindered by several drawbacks, such as (i) structural instability arising from Mn^{3+} ions. These Mn^{3+} ions have a $3d^4$ configuration, which undergoes a rapid disproportionation reaction to form Mn^{4+} and Mn^{2+} ions. This disproportionation reaction of Mn^{3+} ions tends to dissolve in the electrolyte solutions, shortening the battery's cycle life.[2] (ii) low interfacial stability between the electrode and electrolyte hinders the real-time application of the materials.[3]

The LMNO-based cathodes are the choice for high-voltage LIB applications; generally, this class of cathode materials has been reported with *P4332* and *Fd*3

$\bar{}$*m* space groups. The *P4332* space group is associated when the low-temperature synthesis conditions are employed, and the $Fd\bar{3}m$ space group is associated when the high-temperature synthesis conditions are employed.[4] This $Fd\bar{3}m$ space group is also accompanied by rock salt impurity, which we have reported previously.[5]

In our case, the synthetic temperature is higher; therefore, the phase of the material belongs to the $Fd\bar{3}m$ space group through a cubic close-packed structure capable of intercalating one Li^+ ion into an anode per unit formula. The oxygen atoms form the cubic close-packing, and the corresponding oxygen octahedra are associated with common edges. Li- and Mn- ions occupy 8a tetrahedral and 16d octahedral sites, respectively.[6] A three-dimensional network is present in the structure, which allows the Li-ions to diffuse easily; this makes spinel materials more suitable for their use in giant power batteries. Nevertheless, spinel-based materials still face several problems. Their cycling stability and high-rate discharge capacity are insufficient, particularly at elevated temperatures, which pull back this material for large-scale applications. The said problems are due to the dissolution of Mn ions into the electrolyte and the Jahn-Teller (J-T) distortion of Mn ions, which hinders the practical applicability of this material. To overcome the issues linked with these spinel materials, researchers have tried different approaches, viz., doping with stable cations (Ni,[7–9] Zn,[10] Cu,[7] Fe,[7] Co,[11] Al[8,12], etc.) anions (F^-,[13] Cl^-[14,] etc.), and surface modifications with metal oxides (Al_2O_3,[15] AlF_3,[16] ZnO,[17] ZrO2,[18], etc.). To uplift the capacity of this spinel cathode material, Mn^{3+} ions have been replaced by Ni ions.[7] To achieve electrochemical stability and extended cycle life of the cathode materials during charge/discharge processes, LMO cathodes have been substituted by Fe^{3+} and Al^{3+} ions into Mn^{3+} sites.[7,12] Therefore, combining all these metal ions in LMO cathodes will enhance the electrochemical performance by reducing the J-T effect and Mn^{3+} ions dissolutions. The influence of Fe^{3+} and Al^{3+} in the material is discussed in our previously published work, in which we reported dual-phase material.[5] Therefore, our prime focus in the present work was to achieve pure phase material by substituting tri-cations, and we have succeeded in synthesizing pure phase material. Further, the dissolution issue of Mn ions can also be resolved by tailored exposure of planes,[19] particularly (111) plane which is truncated into octahedron with

partial proportions of other planes (100) and (110).[20,21] Herein, (111) plane, the atomic arrangement will be denser, and this will help to form SEI layers, which help to suppress Mn dissolution in the electrolyte.[22]. The other planes (100) and (110) arrangements will be less dense, and this will help in the close interaction of Mn ions with the electrolyte, which helps in fast diffusion channels for Li-ions.[20,21,20,23] Hence, this truncated structure demonstrates a stable and enhanced electrochemical performance. Nevertheless, it is challenging to develop materials with truncated octahedral geometry; it requires harsh synthetic conditions and template-based methods. But in this case, we succeeded in synthesizing material with truncated octahedral geometry with an exposed (111) plane via a sol-gel approach.

In the present work, we report the continued work of our previously published material with the same metal composition to achieve single-phased material. Here, we have synthesized pure/single-phased $LiMn_{2-x-y-z}Ni_xFe_yAl_zO_4$ (x= 0.4-0.5, y & z = 0.05-0.1) cathode materials with substitution of multi-cations; Ni, Al, and Fe, into the crystal.

2B.2 Materials and methods

2B.2.1 Preparation of $LiMn_{2-x-y-z}Ni_xFe_yAl_zO_4$ (x= 0.4-0.5, y & z = 0.05-0.1):

$LiMn_{2-x-y-z}Ni_xFe_yAl_zO_4$ (x= 0.4-0.5, y & z = 0.05-0.1) cathode materials were synthesized using the sol-gel method. The stoichiometric amount of Manganese (II) acetate tetrahydrate ($Mn(CH_3COO)_2 \cdot 4H_2O$) (Sigma Aldrich >99%), Nickel (II) acetate tetrahydrate ($Ni(CH_3COO)_2 \cdot 4H_2O$) (Sigma Aldrich >98%), Iron oxalate dihydrate ($FeC_2O_4 \cdot 2H_2O$) (Sigma Aldrich >99%), Aluminium nitrate nonahydrate ($Al(NO_3)_3 \cdot 9H_2O$) (Sigma Aldrich >98%) and Lithium acetate dihydrate ($CH_3COOLi \cdot 2H_2O$) (Thomas Baker 99%) (5 % excess) were dissolved in appropriate quantity of de-mineralized water and these solutions were mixed with Citric acid monohydrate ($C_6H_8O_7 \cdot H_2O$) (Sigma-Aldrich >99%) (1:1 ratio). The mixed solution was kept for stirring at 80

°C to get homogeneous and viscous gel, which was further dried and ground to collect the precursor powder. The powder was then heat treated at 400 °C for 4 hours with a temperature ramp rate of 5 °C/min to reach 400 °C Then, the obtained powder was ground and further calcined for 800 °C for 10 h with a ramp rate of 3 °C/min to reach 800 °C. After the heating process, it was allowed to cool down naturally, and finally, the calcined material was ground into fine powder and collected.

2B.2.2 Materials characterization:

The crystal structure of the prepared materials was studied using X-ray diffraction (XRD) (Panalytical Xpert Pro) with Cu as an X-ray source at 40kV and 30mA with Ni as kβ filter. The obtained XRD patterns were refined using the Rietveld Refinement technique with the help of Fullprof suite software. The input parameters were gathered from the PDF number 00-035-0782. Raman spectra of the samples were recorded between the spectral region 100–1200 cm^{-1} using a HORIBA-J-Y Lab RAM HR 800 Raman spectrometer instrument with a NIR He–Ne laser (wavelength 632.88 nm). The Brunauer–Emmett–Teller (BET) surface area of the materials was measured by the nitrogen gas adsorption-desorption method on a Quantachrome Quadrasorb surface area measurement and pore size analyzer instrument. The surface structure and morphology of the materials were studied by using Field emission scanning electron microscope (FE-SEM) (FEI-NOVA NANOSEM 450) and high-resolution transmission electron microscope (HR-TEM) (JEOL JEM F-200) coupled with energy dispersive spectrometer (EDS). X-ray photoelectron spectroscopy (XPS) studied the valence states of the elements, which was performed using the Thermo Scientific Model K-alpha XPS instrument with monochromatic Al-Kα as the X-ray source. For ease of discussion, the series of materials is termed LMNFA1

($LiMn_{1.4}Ni_{0.4}Fe_{0.1}Al_{0.1}O_4$), LMNFA2 ($LiMn_{1.3}Ni_{0.5}Fe_{0.1}Al_{0.1}O_4$), LMNFA3 ($LiMn_{1.5}Ni_{0.4}Fe_{0.05}Al_{0.05}O_4$).

2B.2.3 Electrochemical characterization:

The as-prepared cathode materials were studied for electrochemical behavior by fabricating 2032-type coin cells. The positive electrodes are comprised of 80 weight % of the active cathode material, 10% of polyvinylidene difluoride (PVDF) as the binder, and 10% of Super C-60 carbon black as the conducting material. All these materials were mixed well by adding N-methyl pyrrolidone as the solvent to form a uniform slurry. The as-prepared slurry was cast onto a carbon-coated aluminium foil by doctor blade method and dried at 100 ^{0}C for 12 hrs under vacuum. The foil was subjected to calendering and punched into 14 mm circular discs. These circular cathode discs were used to fabricate the 2032 type coin cells; Li metal disc is used as an anode, Celgard-2325 as the separator, and 1M $LiPF_6$ in 1:1:1 volume ratio of EC/DMC/EMC solvents as the electrolyte. The fabrication of coin cells was carried out in an argon-filled glove box at $\leq$ 0.1 ppm of O_2 and H_2O levels. These fabricated coin cells were used to perform cyclic voltammetry (voltage window 3.5 V - 4.9 V at scan rate 0.1 mV s^{-1}) and electrochemical impedance analysis (EIS) using the Metrohm electrochemical work station (Multiautolab M204). The galvanostatic charge/discharge studies were performed using the Neware battery testing system (CT-4008).

2B.3 Results and discussion

2B.3.1 Structural characterization

2B.3.1.1 X-ray diffraction study

A set of cathode materials $LiMn_{2-x-y-z}Ni_xFe_yAl_zO_4$ (x= 0.4-0.5, y & z = 0.05-0.1) were prepared by sol-gel method and are characterized by X-ray diffraction (**Figure 2b.1a**) to know the structural details. XRD patterns show that all planes indexed the pure phase formation of $LiMn_{2-x-y-}$

$_zNi_xFe_yAl_zO_4$ (x= 0.4-0.5, y & z = 0.05-0.1) spinel structure without any dopant-related impurities. The obtained XRD patterns are well matched with standard PDF number 00-035-0782. Rietveld refinement studies were performed using Fullprof software, shown in **Figure 2b.1(b−d)** to attain more information about the plane's orientation, lattice parameter, and occupancy**.** The diffraction patterns of all three materials are indexed to a cubic spinel structure with $Fd\bar{3}m$ space group and good crystallinity. In the cubic spinel structure, Li^+ ions occupy 8a sites, and there are chances of entering the other cation into the 8a site when we dope multiple cations. The stability factor for spinel-type materials could be analyzed by the intensity ratio of diffraction peaks (400) and (311). The tetrahedral site occupancy of cations was further confirmed by calculating the integrated intensity ratios of (400) and (311) planes. The obtained intensity ratio values are lower than the reported value for $LiMn_2O_4$.[6,23], indicating that cation occupancy is higher in tetrahedral 8a Li lattice sites. To understand the influence of variable dopant composition on lattice parameters, the lattice parameter 'a' of the materials is calculated for XRD results using the d-spacing value of the (400) plane and is given in **Table 2b.1** (obtained from X-ray diffraction raw data) and in **Table 2b.2** (obtained from Rietveld refinement of X-ray diffraction data), which are in close agreement with each other for the spinel phase, other refined parameters are given in **Table 2b.3** The average crystallite size of the synthesized materials is calculated using a Scherer relation by considering prominent (111) peaks. The extent of the surface orientation of the LMNFA cathode materials is determined by calculating the intensity ratio of the planes (111) and (400) (**Table 2b.1**). From the table, it can be observed that the intensity ratio value of the (111)/(400) plane for LMNFA2 material is slightly more than that of LMNFA1 and LMNFA3, which is due to the dominance of the (111) plane in the crystal structure.[24] It also shows the dominant facets of the (111) plane corresponding to the truncated type.[9] The Mn^{3+}(0.64 Å) ions in $LiMn_2O_4$ are substituted by

Fe^{3+}(0.65 Å) ions, resulting in a low-angle shift according to Bragg's law. Variations in the Fe concentration in all the materials influence (111) plane dominance in the crystal surface which could affect the growth of a truncated octahedral shape.[24]

Sample	Intensity ratio		Lattice constant (Å)	Crystallite size (nm)
	(111)/(400)	(111)/(440)	$\frac{1}{d_{hkl}^2} = \frac{1}{a^2}(h^2 + k^2 + l^2)]$	
LMNFA1	2.58	4.82	8.168	39.73
LMNFA2	2.62	4.96	8.162	43.46
LMNFA3	2.51	4.56	8.170	38.29

Table 2b.1 Crystal parameters calculated from X-ray diffraction data

Material	Space group	Lattice constant (Å)	Cell volume	Rp	Rwp	R_{bragg}	R_F^2	$\chi 2$
LMNFA1	$Fd\bar{3}m$	8.169	545.27	3.55	3.48	3.55	3.4	2.1
LMNFA2	$Fd\bar{3}m$	8.168	545.12	3.06	4.19	5.08	6.1	3.1
LMNFA3	$Fd\bar{3}m$	8.186	548.55	2.61	3.37	2.77	2.6	1.6

Table 2b.2. Rietveld refinement results of LMNFA1, LMNFA2 and LMNFA3 materials

The {100} and {110} planes, whose orientations are associated with Li diffusion channels, are most susceptible to Mn dissolution, whereas the {111} facets, on which Mn atoms are utmost compactly packed, have the lowest surface energy and exhibit better stability.[25] The exposure of the dominant (111) plane forms the crystals with the lowest surface energy state than the (100) and (110) planes.[26] The dominant (111) planes are packed with dense atomic arrangements that are prone to stable SEI layers which suppress the Mn dissolution into the electrolyte. Meanwhile, the (100) and (110) planes are less densely packed with Mn ions could mitigate Mn dissolution and provide faster Li^+ diffusion channels to achieve superior performance.[27,28] This confirms that the dominant (111) plane influences the electrochemical capabilities of the materials.[27] The

corresponding crystal structures (generated from VESTA software using a CIF file)[29] of the atomic arrangement and Li^+ diffusion channels along the planes (111), (100), and (110) are shown in **Figure 2b.2**.

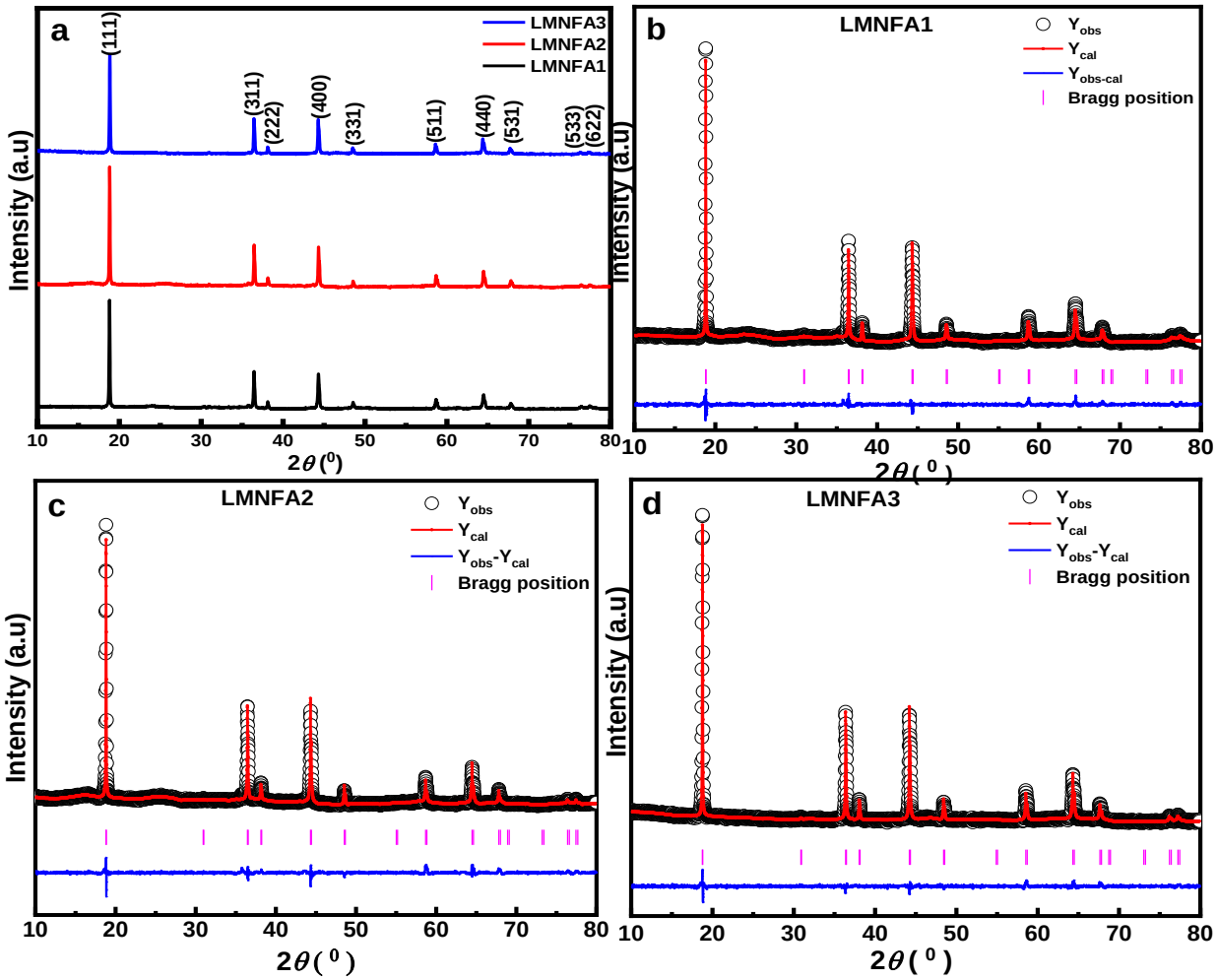

Figure 2b.1 **(a)** X-ray diffraction patterns of $LiMn_{2-x-y-z}Ni_xFe_yAl_zO_4$ (x= 0.4-0.5, y & z = 0.05-0.1), Rietveld refinement plots of **(b)** LMNFA1 **(c)** LMNFA2 **(d)** LMNFA3.

Material	a (Å)	Atom	Wyckoff Position	x	y	z	Occupancy	B_{iso}	Cell Volume $(Å)^3$
LMNFA1	8.169	Li	8a	0.125	0.125	0.125	0.1649	1.000	545.27
		Mn	16d	0.500	0.500	0.500	0.1161	1.000	
		Ni	16d	0.500	0.500	0.500	0.0327	1.000	
		Fe	16d	0.500	0.500	0.500	0.0087	1.000	
		Al	16d	0.500	0.500	0.500	0.0103	1.000	
		O	32e	0.2619	0.2619	0.2619	0.5105	1.000	
LMNFA2	8.168	Li	8a	0.125	0.125	0.125	0.1394	1.000	545.12
		Mn	16d	0.500	0.500	0.500	0.1100	1.000	
		Ni	16d	0.500	0.500	0.500	0.0410	1.000	
		Fe	16d	0.500	0.500	0.500	0.0083	1.000	
		Al	16d	0.500	0.500	0.500	0.0088	1.000	
		O	32e	0.2563	0.2563	0.2563	0.5818	1.000	
LMNFA3	8.186	Li	8a	0.125	0.125	0.125	0.1183	1.000	552.34
		Mn	16d	0.500	0.500	0.500	0.1127	1.000	
		Ni	16d	0.500	0.500	0.500	0.0409	1.000	
		Fe	16d	0.500	0.500	0.500	0.0047	1.000	
		Al	16d	0.500	0.500	0.500	0.0074	1.000	
		O	32e	0.2582	0.2582	0.2582	0.5253	1.000	

Table 2b.3 Crystal Structure parameters obtained from Rietveld refinement

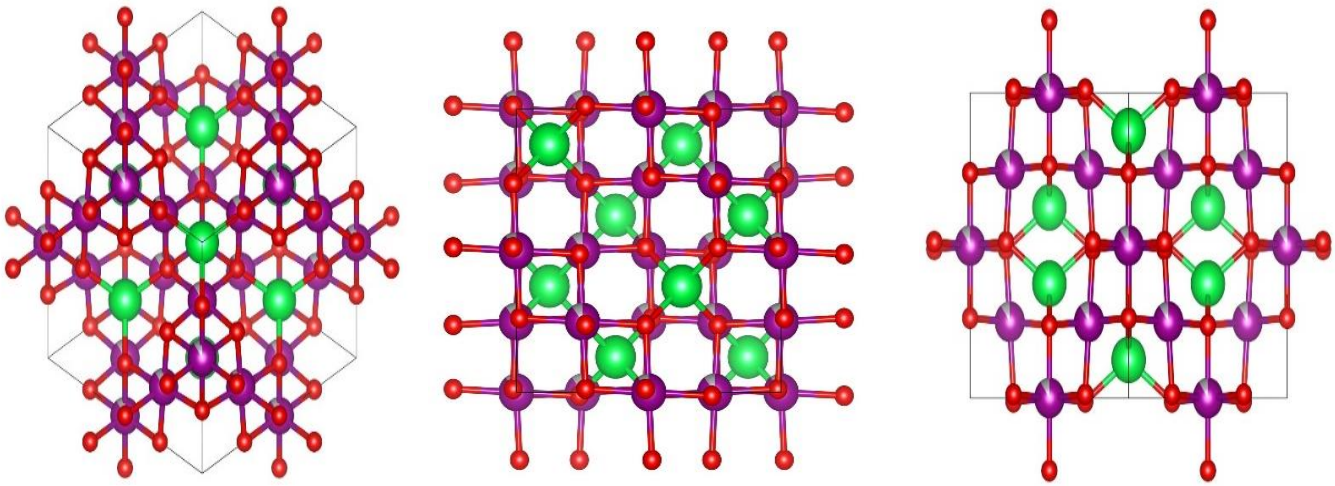

Figure 2b.2. Crystal structures of LMNFA1 are represented along the planes (111), (100), and (110).

3.3.1.2 Raman spectroscopic analysis

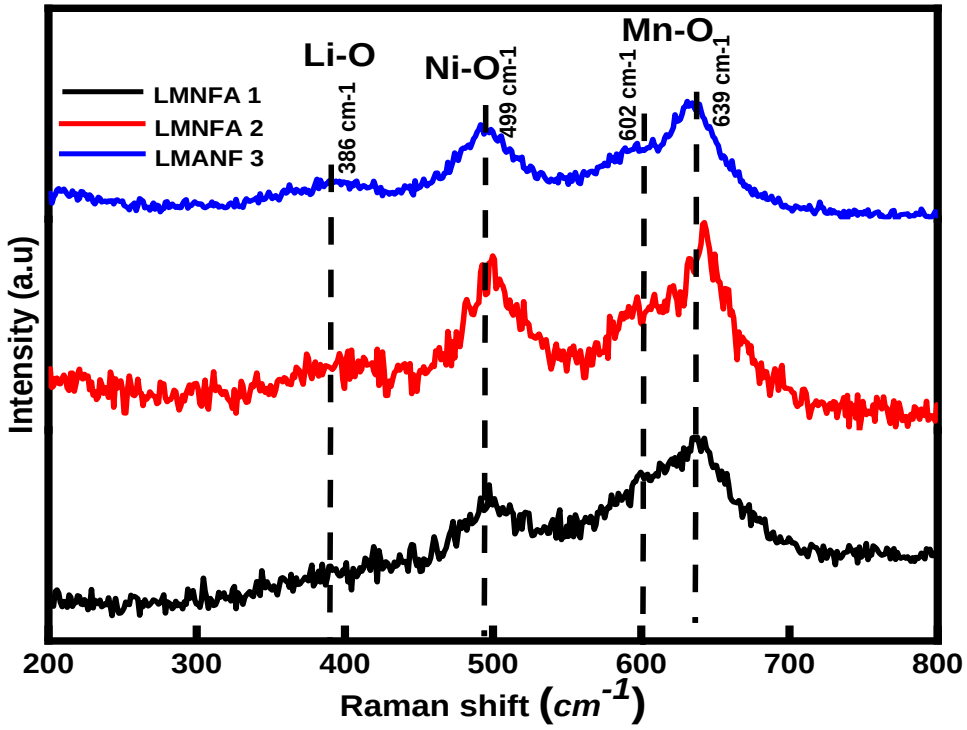

Figure 2b.3 Raman spectra of LMNFA cathode materials.

The Raman spectra of the synthesized LMNFA cathode materials are shown in **Figure 2b.3**; the broad peak observed at 639 cm^{-1} indicates the presence of Mn-O stretching vibrations of the MnO_6 octahedral geometry through the A1g symmetry in Oh^7 spectroscopic space group. The blue shift observed in the A1g symmetry level for the material LMNFA2 with an increased Ni ratio could cause a change in bond lengths. A1g mode comprises the mixed information of Mn-O and Ni-O bonds in [Mn(Ni)O_6] octahedrons, as it is quite complex to resolve the Mn^{4+}-O, Mn^{3+}-O and Ni-O bands.[30] Slight excess Ni content contributed to an increase in intensity and caused a slight shift in the main phonon mode at 623 cm^{-1}, which was attributed to the change in electronic states of Mn by Ni substitution. As the material LMNFA has a slightly higher concentration of Ni, the Mn(Ni)-O bond in the doped material is responsible for the blue shift, demonstrating the cathode material's structural stability.[31] A feeble peak observed at 602 cm^{-1} indicates the existence

of F2g(I) symmetry, which corresponds to the Mn average electronic state in the spinel-structured cathode materials.[32,33] The peak at 499 cm^{-1} indicates the presence of Ni-O stretching vibration of NiO_6 octahedral geometry through F2g(II) symmetry[34,35]. This confirms the doping of Ni into the octahedral Mn sites in the spinel structure, which helps achieve structural stability of the active material during electrochemical studies.[33] The low intense peak observed at 386 cm^{-1} indicates the Li-O stretching vibration of the LiO_4 tetrahedral geometry.[36] The Raman results' analysis confirms the successful incorporation of metal ions into their constituent sites.

2B.3.1.3 BET surface area analysis

BET-specific surface area measurements of the synthesized LMNFA series cathode materials were conducted to examine their impact on electrochemical performance. **Figure 2b.4(a-c)** shows the BET adsorption-desorption curves of LMNFA1, LMNFA2, and LMNFA3 cathode materials. As per the literature, a higher specific surface area of the material leads to extending the contact region between the electrode and electrolyte. As a result, Mn ions in cathode materials could suffer from the dissolution in electrolytic solution.[37] Therefore, materials with lower specific surface areas will help in extended cycle life and have better rate capability. This has been proved in our material, as the LMNFA2 (12.88 m^2/g) cathode material has a less specific surface area as compared to LMNFA1(21.37 m^2/g) and LMNFA3 (20.81 m^2/g) materials. The LMNFA2 has shown better capacity and stability. The report by Ryu J et al. [31] has shown that the larger surface area of the cathode materials would lead to more interfacial contact between the electrode and electrolyte, which could demonstrate a higher discharge capacity, but simultaneously, which undergoes a large extent of metal ion dissolution results in the reduced cycle life.[38,39] In correlation with our synthesized cathode materials, LMNFA1 and LMNFA3 have shown higher discharge capacities but lower cycle stability as compared to the LMNFA2 cathode material.

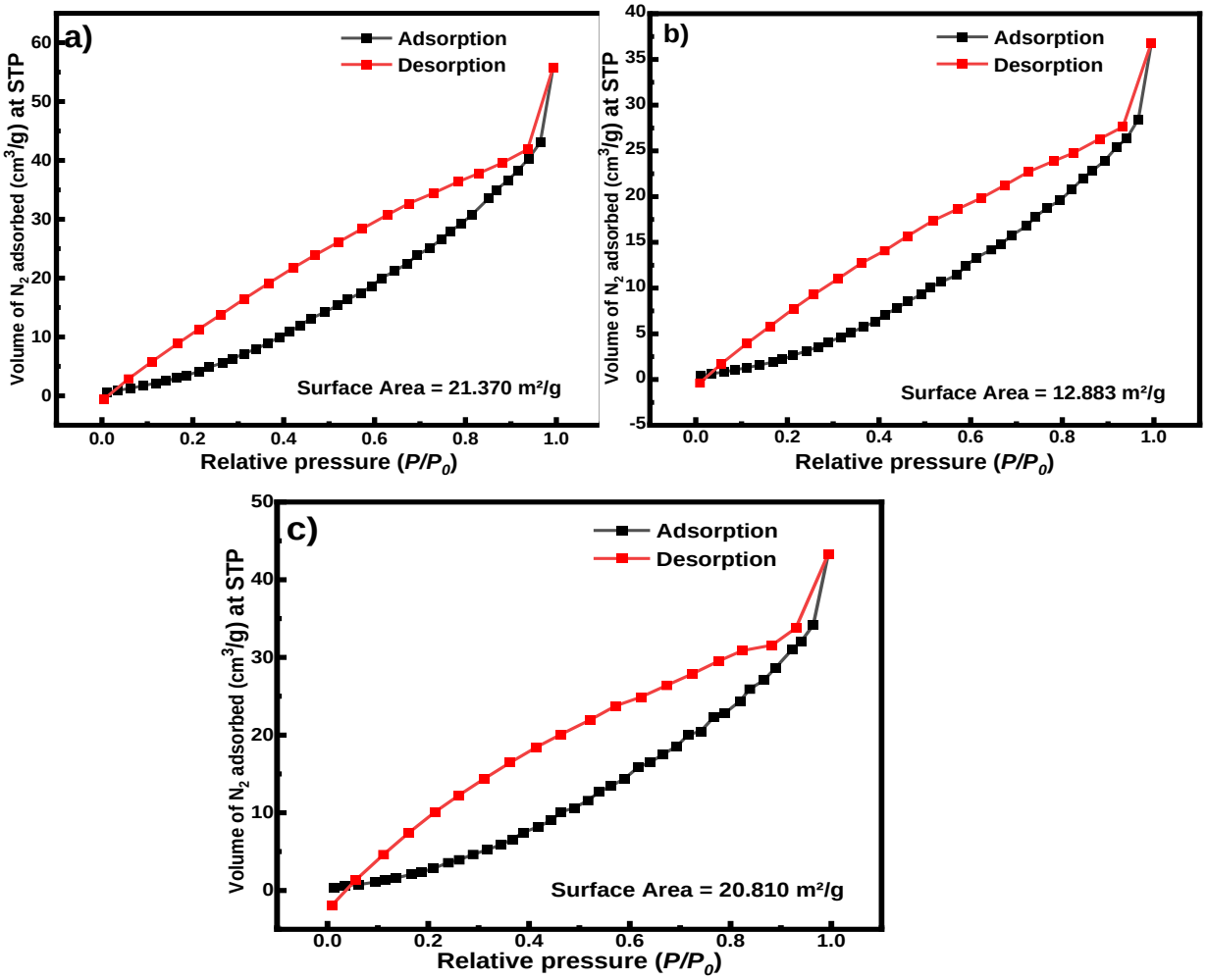

Figure 2b.4 BET adsorption-desorption curves of **(a)** LMNFA1, **(b)** LMNFA2, and **(c)** LMNFA3 cathode materials, respectively.

2B.3.1.4 XPS analysis

The electronic valence states and elemental composition of the synthesized cathode materials were characterized by XPS. The peak signals observed for Li 1s, Mn 2p, Ni 2p, Fe 2p, and Al2p confirm the well-matched composition as expected. The deconvoluted spectra of Li1s core levels of all the materials are shown in **Figure 2b.5(a-c).** The binding energy of prominent peak Li1s core levels is 49.92 eV (LMNFA1), 49.93 eV(LMNFA2), 49.96 eV (LMNFA3), confirms the chemical and electronic state.[40]

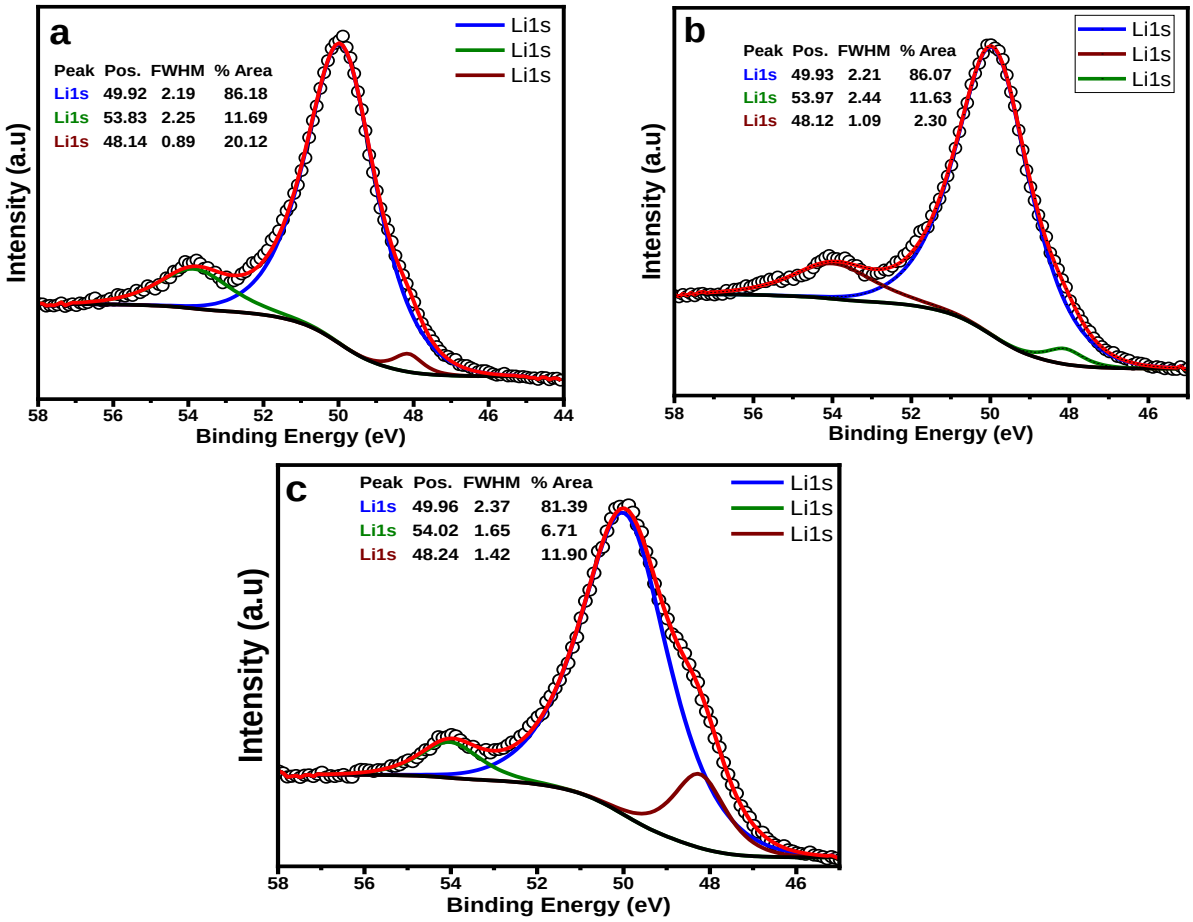

Figure 2b.5. Deconvoluted XPS spectra of Li1s of **(a)** LMNFA1 **(b)** LMNFA2 **(c)** LMNFA3.

The deconvoluted spectra of Mn2p levels in **Figure 2b.6(a, c, e)** core level exhibit two components, $Mn2p_{3/2}$ and $Mn2p_{1/2}$, due to spin-orbit coupling.[12,41] The binding energies of $Mn2p_{3/2}$ and $Mn2p_{1/2}$ core levels are 642.2 eV (LMNFA1), 642.3 (LMNFA2), 642.2 (LMNFA3) and 654.0 eV (LMNFA1), 654.2(LMNFA2), 654.0 eV (LMNFA3) respectively. The obtained binding energy values for Mn^{4+} and Mn^{3+} in Mn2p cores levels are in close agreement with the values as reported by Nesbitt et al.[42]. The binding energy values provided the information of Mn^{4+} and Mn^{3+} states, which gives evidence of the existence of both the states, which supplements the Raman results. The deconvoluted spectra of Ni2p levels in **Figure 2b.6(b, d, f)** core level also have two

components $Ni2p_{3/2}$ and $Ni2p_{1/2}$ due to spin-orbit coupling. The binding energies of $Ni2p_{3/2}$ and $Ni2p_{1/2}$ core levels are 854.7 eV (LMNFA1), 854.8 (LMNFA2), 854.6 (LMNFA3) and 872.2 eV (LMNFA1), 872.2 (LMNFA2), 872.0 eV (LMNFA3) respectively. These electronic states of Ni are complemented with the Raman signals for Ni-O in NiO_6 and $[Mn(Ni)O_6]$ octahedrons. The deconvoluted peaks of Fe2p core levels exhibit two components $Fe2p_{3/2}$ and $Fe2p_{1/2}$ are displayed in **Figure 2b.7(a, c, e).** The binding energies of $Fe2p_{3/2}$ and $Fe2p_{1/2}$ core levels are 711.46 eV (LMNFA1) 711.16 eV (LMNFA2) 715.54 eV (LMNFA3) and 724.42 eV (LMNFA1) 724.02 eV (LMNFA2), 724.40 eV (LMNFA3) respectively, which confirms the successful substitution of Fe^{3+} ion into the lattice.[43,44] The deconvoluted peaks of Al2p levels are also given in **Figure 2b.7(b, d, f)** along with the resolved peak area proportion. The binding energies of $Al2p_{1/2}$ and $Al2p_{3/2}$ core levels are 73.47 eV (LMNFA1), 70.34 eV(LMNFA2), 68.55 eV (LMNFA3) and 68.07 eV (LMNFA1), 68.01 eV (LMNFA2), 67.49 eV(LMNFA3) respectively, which confirms the incorporation of Al^{3+} into the lattice.[12,45]

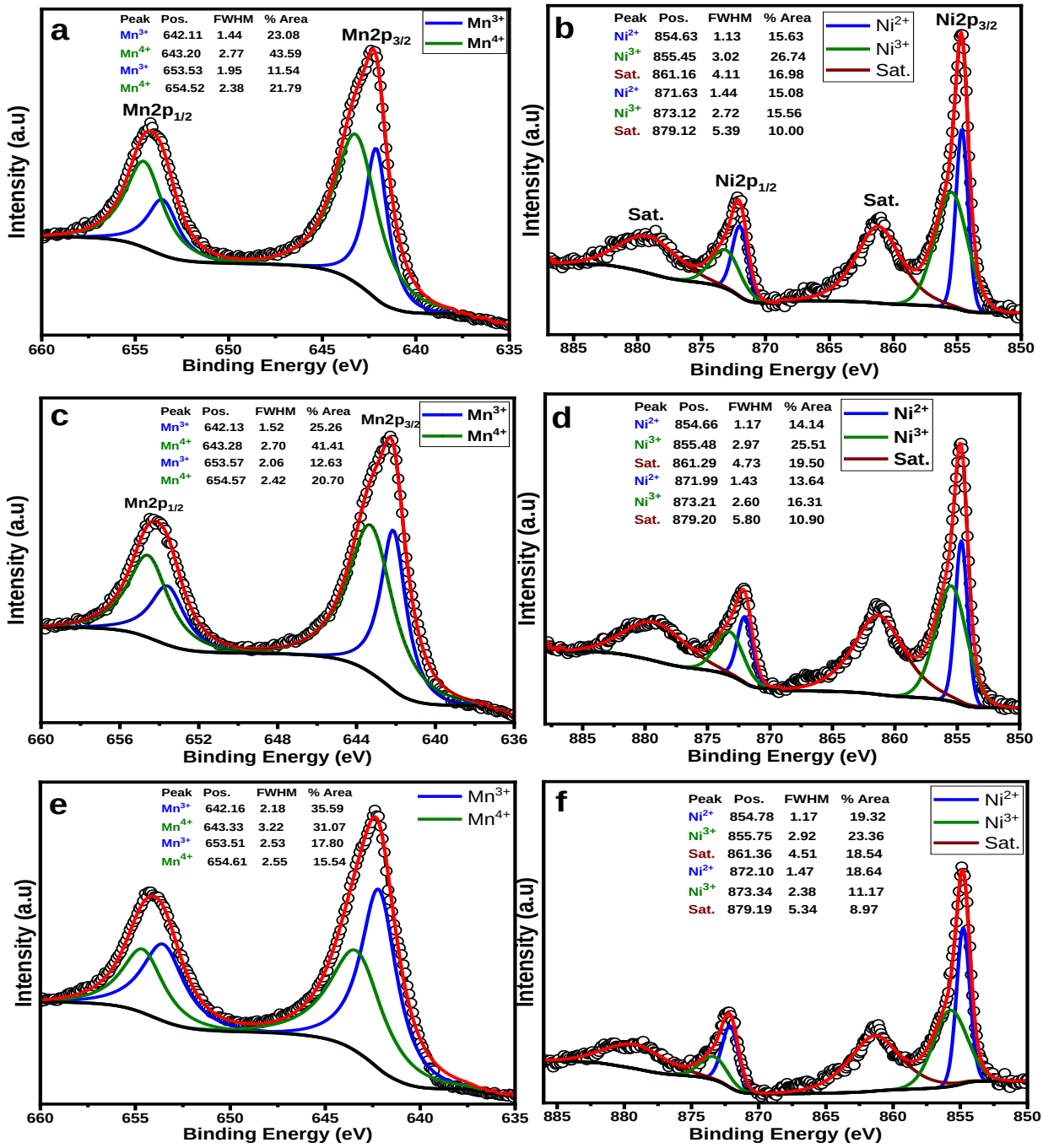

Figure 2b.6. Deconvoluted XPS spectra of Mn2p of **(a)** LMNFA1, **(c)** LMNFA2, **(e)** LMNFA3 and Ni2p of **(b)** LMNFA1, **(d)** LMNFA2, **(f)** LMNFA3 respective**.**

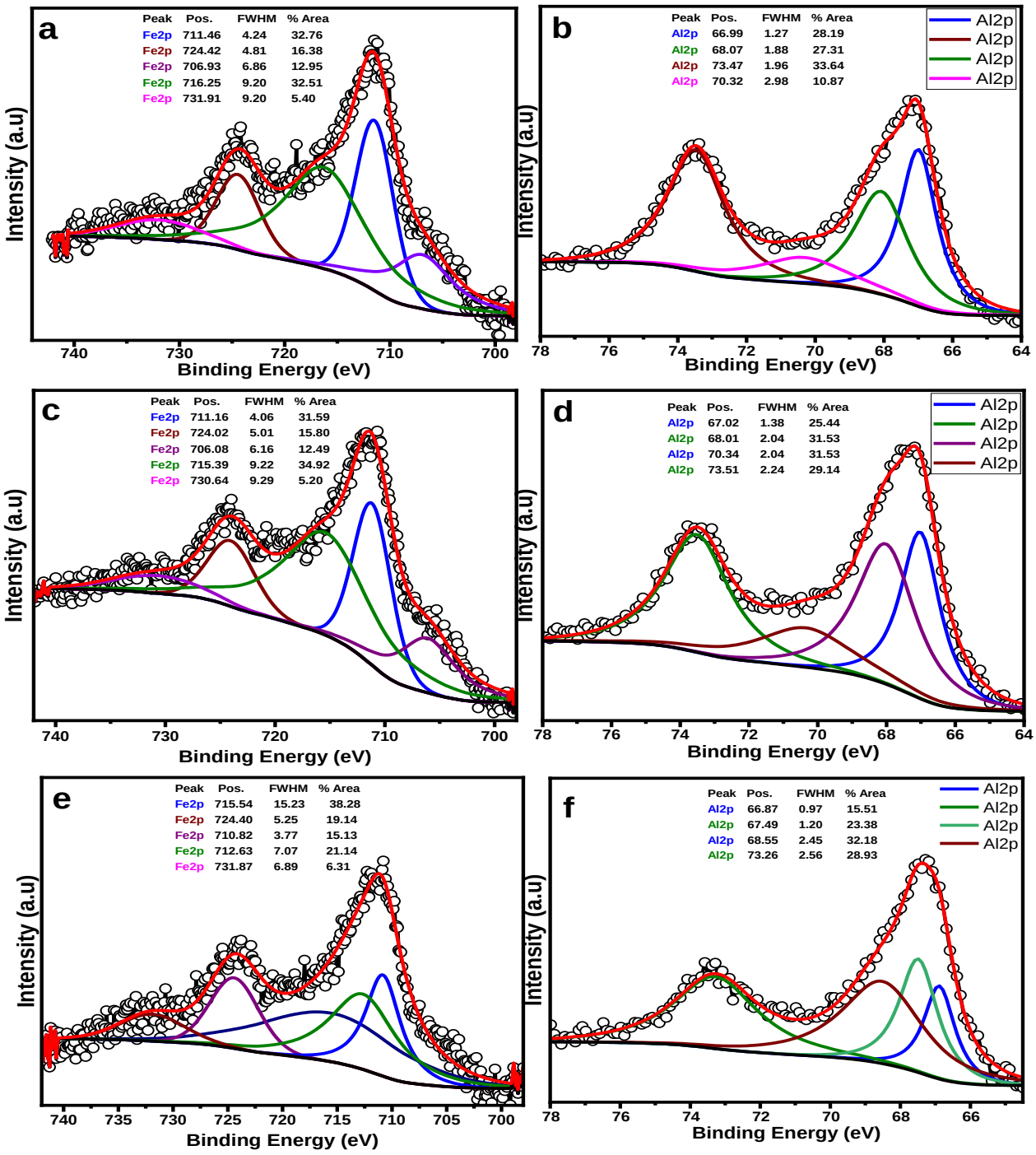

Figure 2b.7. Deconvoluted XPS spectra of Fe2p p of **(a)** LMNFA1, **(b)** LMNFA2, **(c)** LMNFA3 and Al2 of **(a)** LMNFA1, **(b)** LMNFA2, **(c)** LMNFA3 respectively.

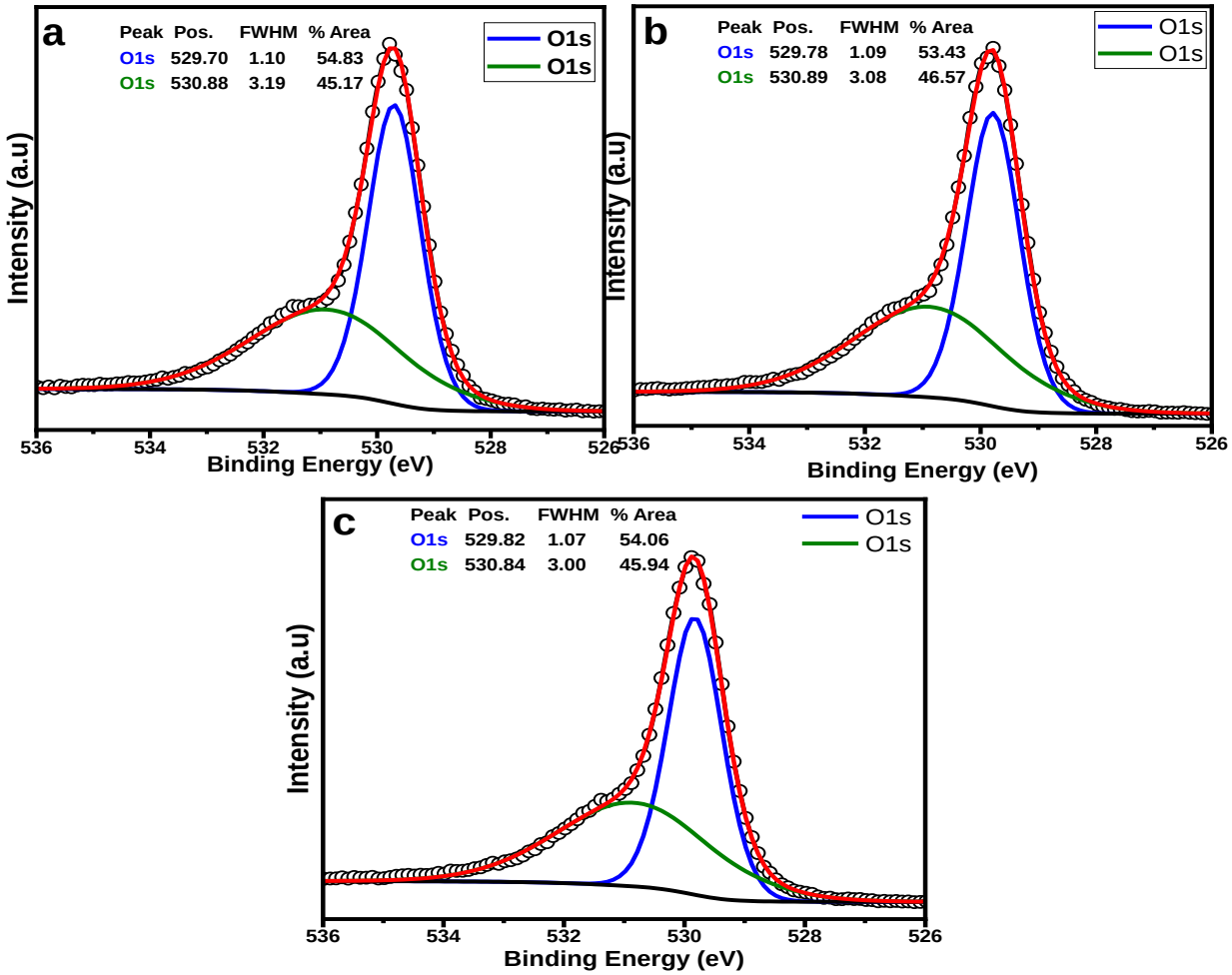

Figure 2b.8. Deconvoluted XPS spectra of Mn2p and Ni2p of **(a)** LMNFA1 **(b)** LMNFA2 **(c)** LMNFA3.

The deconvoluted peaks of O1s core level are observed at 529.7 eV, (LMNFA1) 529.78 eV, (LMNFA2) and 529.82 eV (LMNFA1) are displayed in **Figure 2b.8(a-c)** The obtained binding energies indicate an M-O (M = Mn, Ni) relation with FWHM values of ~1.1, indicating the oxide lattice structure. Peak fitting of all the elemental core levels is performed using CasaXPS software (Peak fitted parameters are given in the respective plots).

2B.3.1.5 Electron microscopic analysis

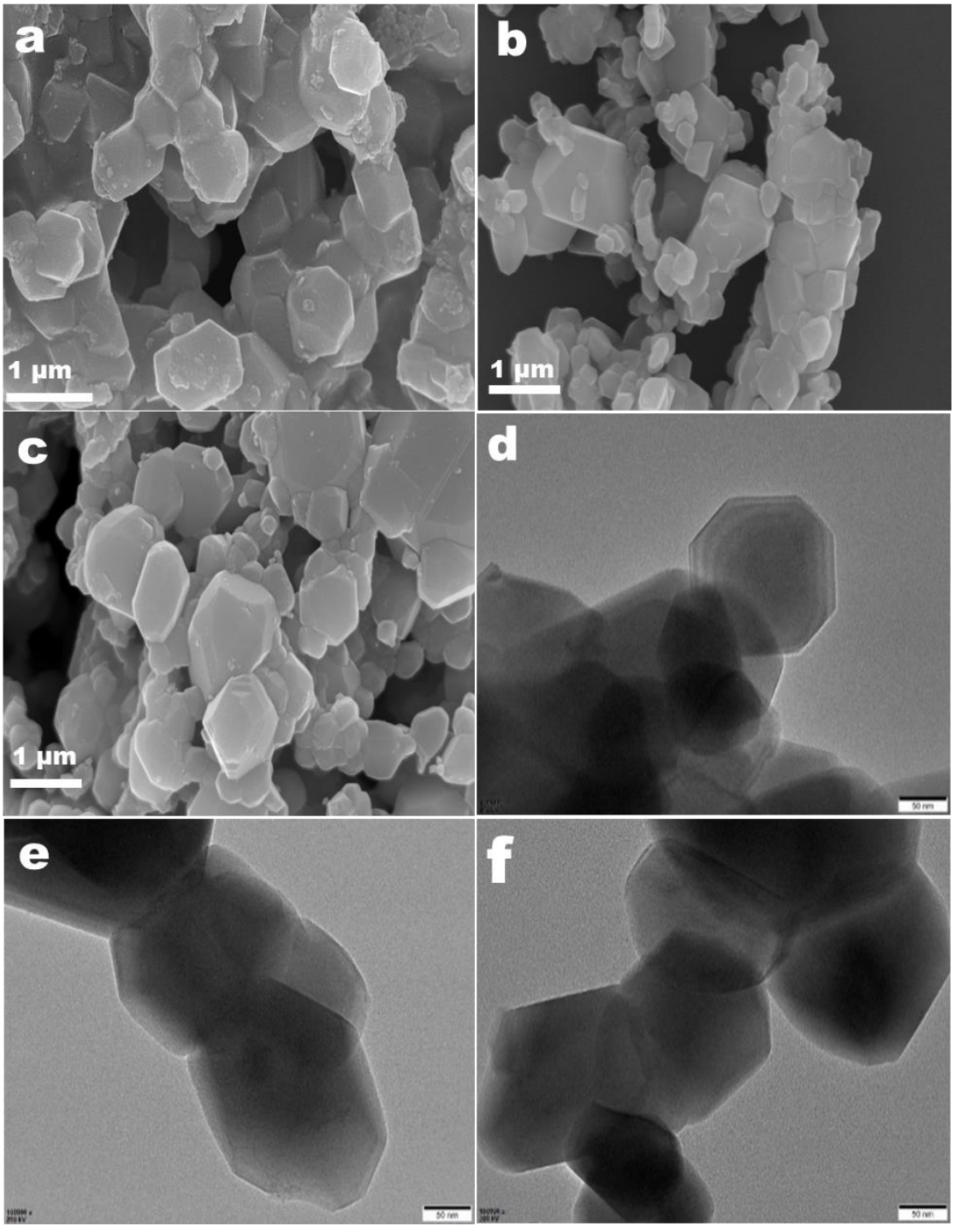

Figure 2b.9. FE-SEM images of **(a)** LMNFA1 **(b)** LMNFA2 **(c)** LMNFA3, TEM images of **(d)** LMNFA1 **(e)** LMNFA2 **(f)** LMNFA3.

Scanning electron microscopy (SEM) and transmission electron microscopy (TEM) studies were performed to know the structural morphology of the synthesized materials. **Figure 2b.9(a-c)** shows FESEM images that visualize the truncated octahedral shape of the particles. From the SEM images, it is understood that the extent of morphological orientation is not the same in all three materials and are slightly different from one another. This difference in morphology gives an idea about the influence of crystal plane orientation on the electrochemical performance of the materials. The TEM images given in **Figure 2b.9(d-f)** confirm the truncated octahedral-shaped particles, which visualize the soft edges of octahedral morphology. The truncated octahedral shapes are formed more effectively in the case of LMNFA2 as compared to the other two materials. Also, the average particle size of truncated octahedral-shaped LMNFA2 is smaller than LMNFA1 and LMNFA3, as per histogram results, shown in **Figure. 2b.10 (a-c).**

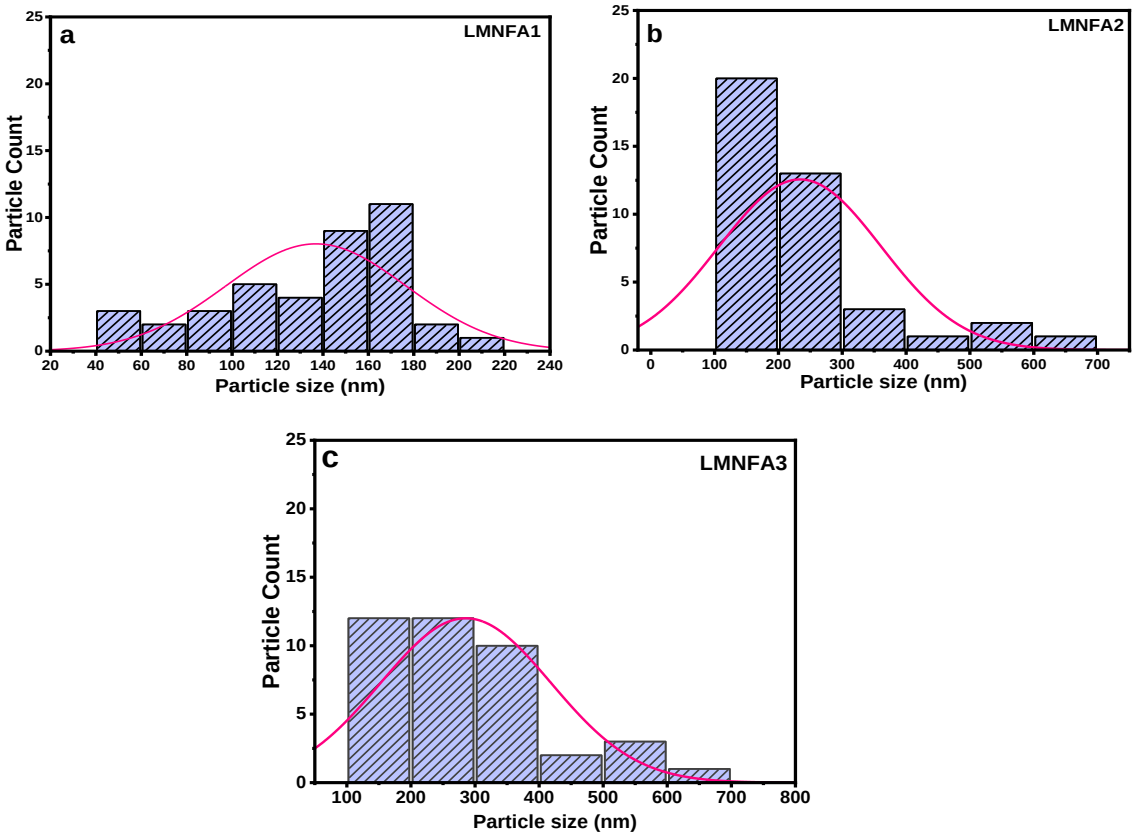

Figure 2b.10, Particle size distribution histograms of materials **(a)** LMNFA1, **(b)** LMNFA2, and **(c)** LMNFA3.

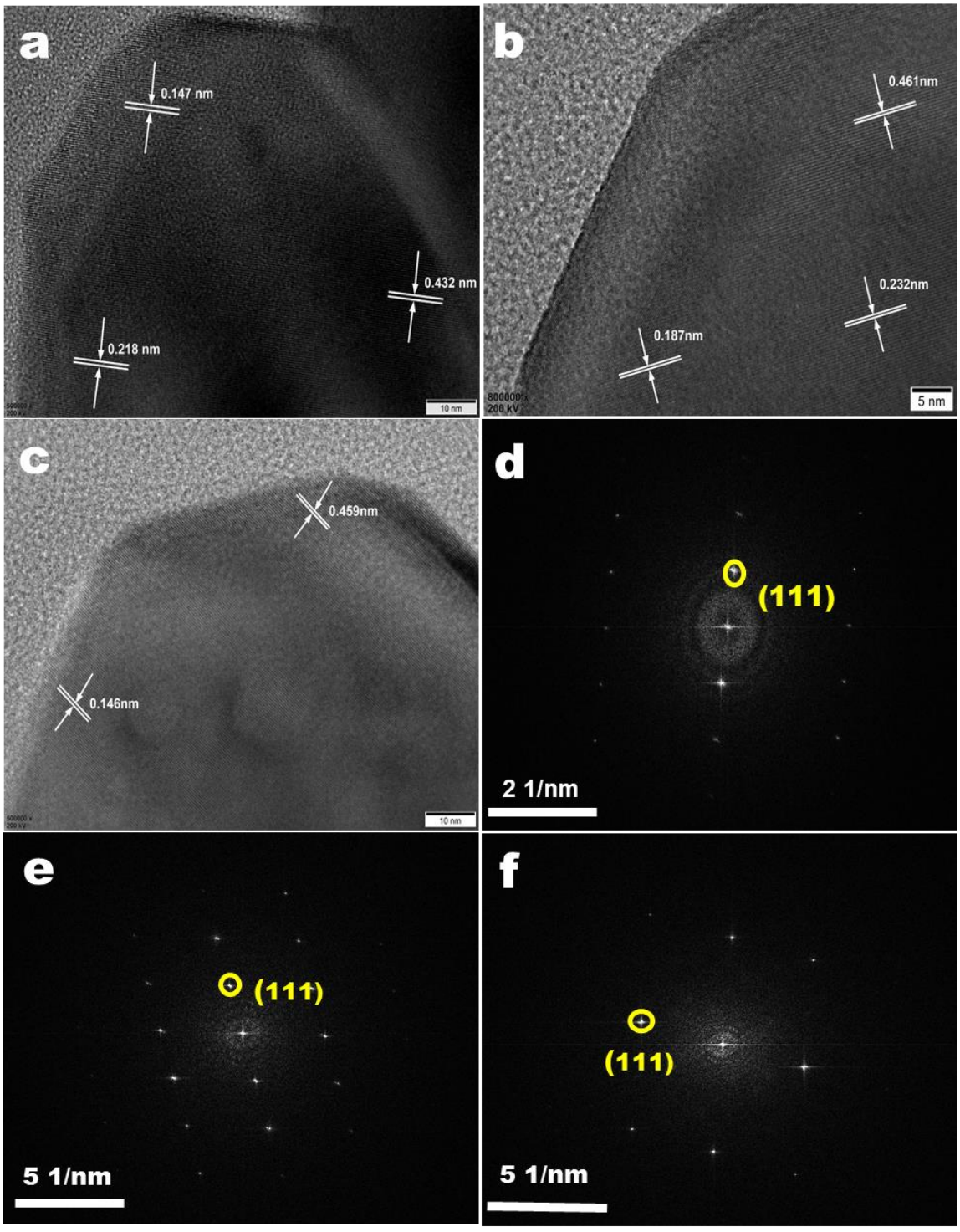

Figure 2b.11. HR-TEM image of **(a)** LMNFA1 **(b)** LMNFA2 **(c)** LMNFA3 indexed with lattice spacing values and SAED patterns of **(d)** LMNFA1, **(e)** LMNFA2 and **(f)** LMNFA3 with (111) plane indexed.

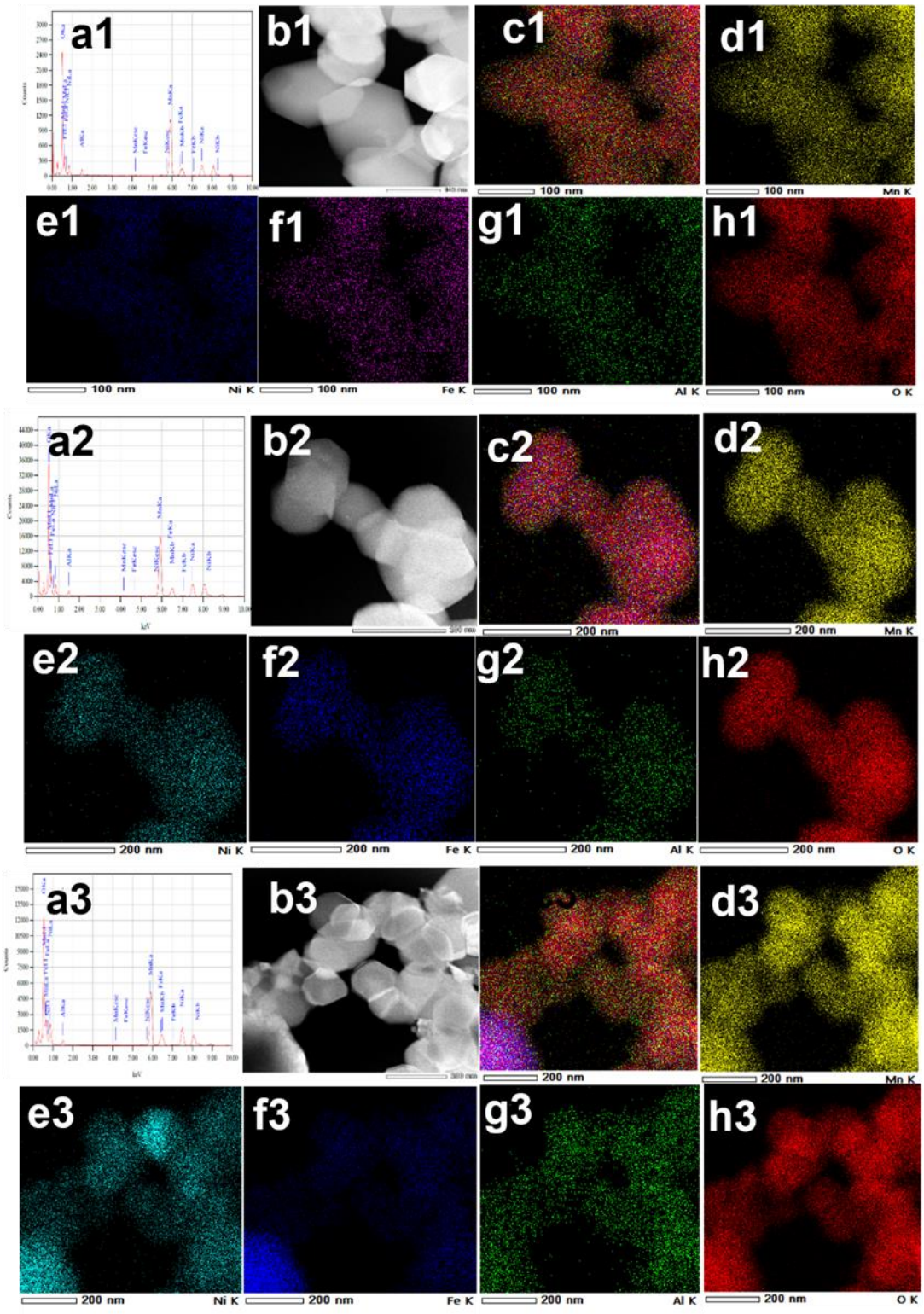

Figure 2b.12, STEM, EDS elemental mapping images of LMNFA1, LMNFA2 & LMNFA3 materials **(a1-a3))** elemental mapping overlay of Mn, Ni, Fe, Al and O, **(b1-b3**) STEM-HAADF image **(c1-c3)** Elemental quantitative map of image **(d1-d3), (e1-e3), (f1-f3), (g1-g3)** and **(h1-h3)** elemental mapping of Mn, Ni, Fe, Al and O respectively.

Figure 2b.11(a-c) shows the HRTEM images of LMNFA1, LMNFA2, and LMNFA3 samples where one edge portion of the truncated octahedron structure has magnified to view the lattice fringes, which were used to calculate the d-spacing values. The lattice-spacing values for the (111) planes of all three materials identified in HRTEM images and compared are around ~0.471 nm. The d-spacing values obtained are related to (111) crystal planes from the X-ray diffraction are depicted in the respective images. The obtained d-spacing values are well-matched with the interplanar spacing values obtained from X-ray diffraction data. F**igure 2b.11(d-f)** shows the SAED pattern which shows the well-defined diffraction spots which are marked to corresponding planes (111), (311) and (022).[9] The distribution of all the elements in the synthesized materials is confirmed by STEM-EDS elemental mapping, which confirms the incorporation of all the elements into the cathode structure, the results for all the materials are provided in **Figure. 2b.12(a1-h3).**

2B.3.2 Electrochemical Performance Analysis

2B.3.2.1 Cyclic voltammetry study

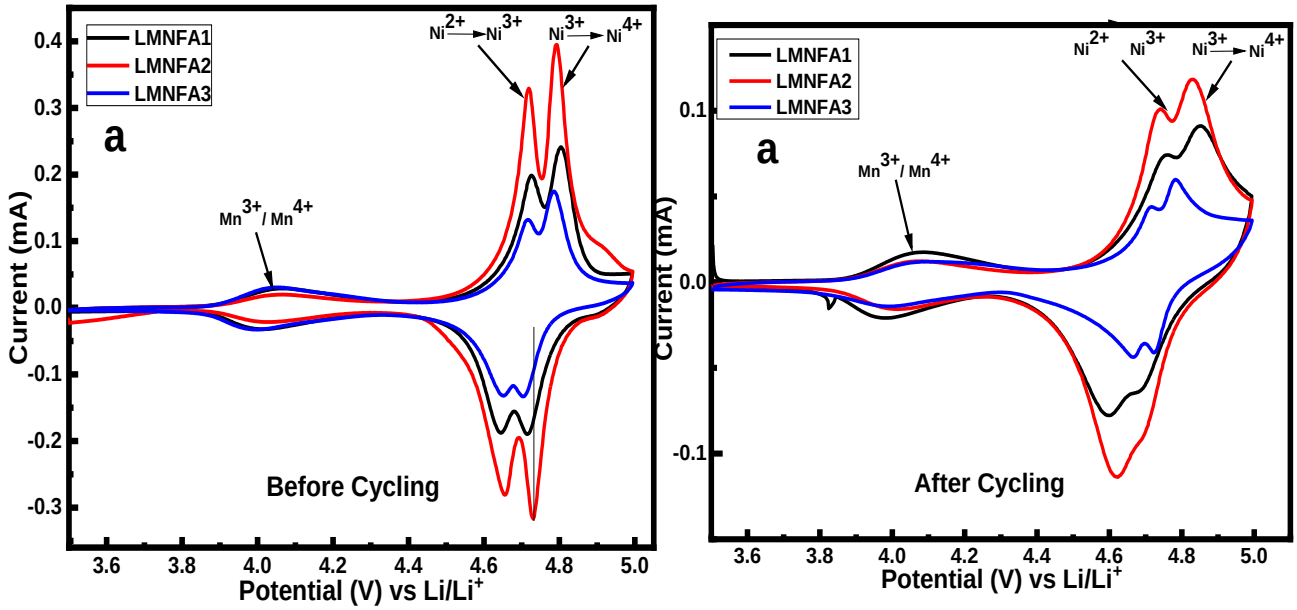

Figure 2b.13. Cyclic voltammetry **(a)** before and **(b)** after cycling.

To evaluate the electrochemical performance of the electrodes prepared from the tri-cation substituted LMO active materials, coin cells were fabricated. These fabricated coin cells were subjected to cyclic voltammetry **Figure 2b.13(a-b)** to understand the redox behaviour at a voltage window of 3.5 V to 4.9 V v/s Li. All three materials have shown three pairs of well-defined anodic and cathodic characteristic peaks, which indicates a three-step lithiation and de-lithiation process. Here the dopants Fe and Al are redox inactive,[8,46] and are not involved in charge compensation in the redox reactions. Mn and Ni ions are responsible for redox reactions.

As shown in **Figure 2b.13(a-b),** the characteristic weak redox peaks for Mn^{3+}/Mn^{4+} are observed at ~4.06 V/4.01 V (before cycling, **Figure 2b.13a)** and ~4.08 V/3.98 V (after cycling, **Figure 2b.13b**) which indicates the minimized content of Mn^{3+} in the cathode active material. This minimized content of Mn^{3+} in spinel improves the stability of the material by reducing the John−Teller effect and results in better electrochemical performance.[7] The second pair of redox peaks observed at ~ 4.71 V/4.65 V, 4.79 V/4.72 V (before cycling, **Figure 2b.13a**) and 4.74 V/ 4.61 V, 4.83V / 4.68 V (after cycling, **Figure 2b.13b**) correspond to the redox behavior of Ni^{2+}/Ni^{3+}, Ni^{3+}/Ni^{4+} respectively. From the CV curves, we can observe the peak current is not the same for all the materials even though the scan rate is maintained the same. The peak current is varied concerning cathode materials, which is influenced by the varied concentration of the redox active species in the cathode active materials.[47,47] The material LMNFA2 showed an increased peak current and sharp redox peaks; these behaviors might be due to the faster diffusion of Li^+ ions. As discussed above in the XRD section, the dominant (111) plane influences the electrochemical capabilities of the materials as it is densely packed with Mn ions, which mitigates the dissolution of Mn and provides faster Li^+ diffusion channels. These observed redox peaks are dominating the overall redox behavior of the materials, which influences the high voltage

operational capabilities of the cathode active materials. In CV, Fe and Al have not shown any redox activity as these two are redox inactive but act as an electrochemical stabilizer to improve stability.[12,46]

2B.3.2.2 Electrochemical impedance spectroscopic analysis

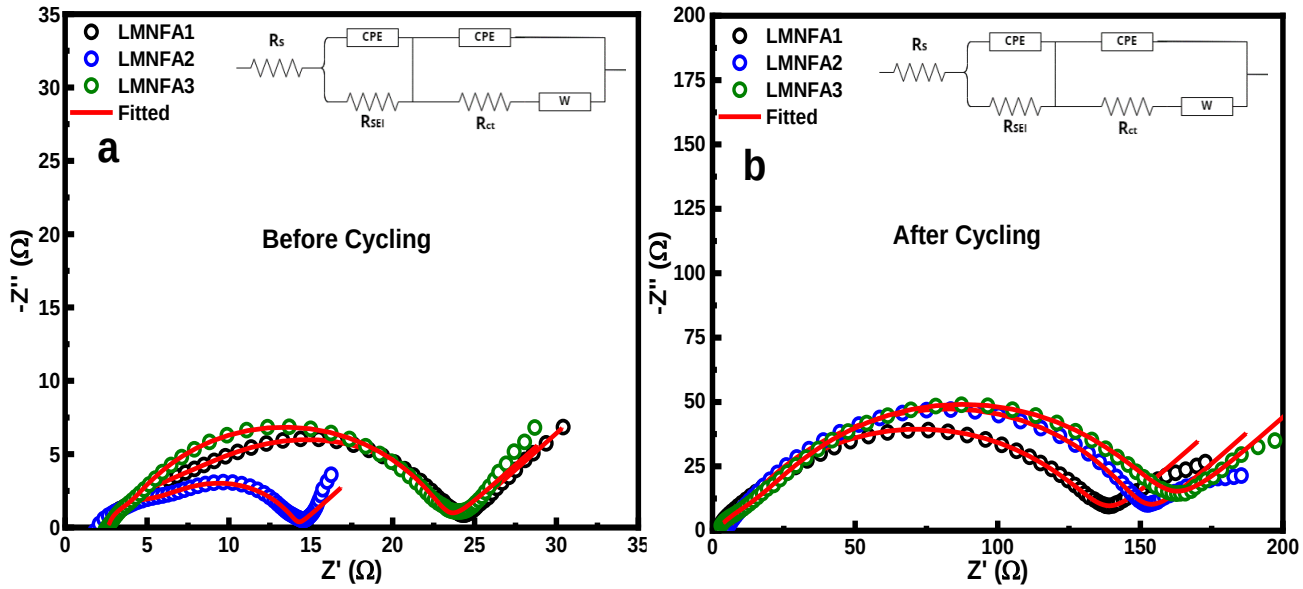

Figure 2b.14 Nyquist plots **(a)** before and **(b)** after cycling.

The Li^+ ion diffusion kinetics studies were performed through electrochemical impedance spectroscopy, and the Nyquist plots for all the sets of materials before and after galvanostatic charge/discharge (GCD) studies are given in **Figure 2b.14(a-b)**. The inset of the **figure. 2b.14(a-b)** shows the equivalent circuit used to fit the data, where **CPE** denotes constant phase element, R_s denotes Ohmic resistance, R_{SEI} denotes resistance of the SEI, R_{ct} denotes charge transfer resistance, and ***W*** denotes Warburg diffusion impedance. In **Figure 2b.14a**. all materials showed a semicircle in the high-frequency region due to charge transfer resistance (R_{ct}) and SEI resistance (R_{SEI}), this semicircle in the high-frequency region indicates the Li^+ ions insertion into the electrode/electrolyte interface. Also, we can observe a straight line in the low-frequency region

indicates the interface resistance, and it corresponds to Warburg impedance (*W*). **Figure 2b.14b**. shows the Nyquist plots for the same materials but after cycling which exhibits a large difference in the impedance. After 1000 repeated charge/discharge cycles the resistance of the materials is increased which leads to the capacity fade. The fitted values of the equivalent circuit are given in **Table 2b.4**.

Material / Parameter	LMNFA1		LMNFA2		LMNFA3	
	Before Cycling	After Cycling	Before Cycling	After Cycling	Before Cycling	After Cycling
R_s (Ω)	2.443	1.379	1.138	1.209	2.617	1.230
R_{SEI} (Ω)	5.585	8.889	3.800	17.430	1.255	17.987
R_{ct} (Ω)	15.576	126.142	9.280	132.009	19.46	138.577
χ^2	0.301	0.417	0.624	0.528	0.492	0.225

Table 2b.4. Resistance values were obtained from the EIS fitting data.

2B.3.2.3 Galvanostatic charge-discharge study

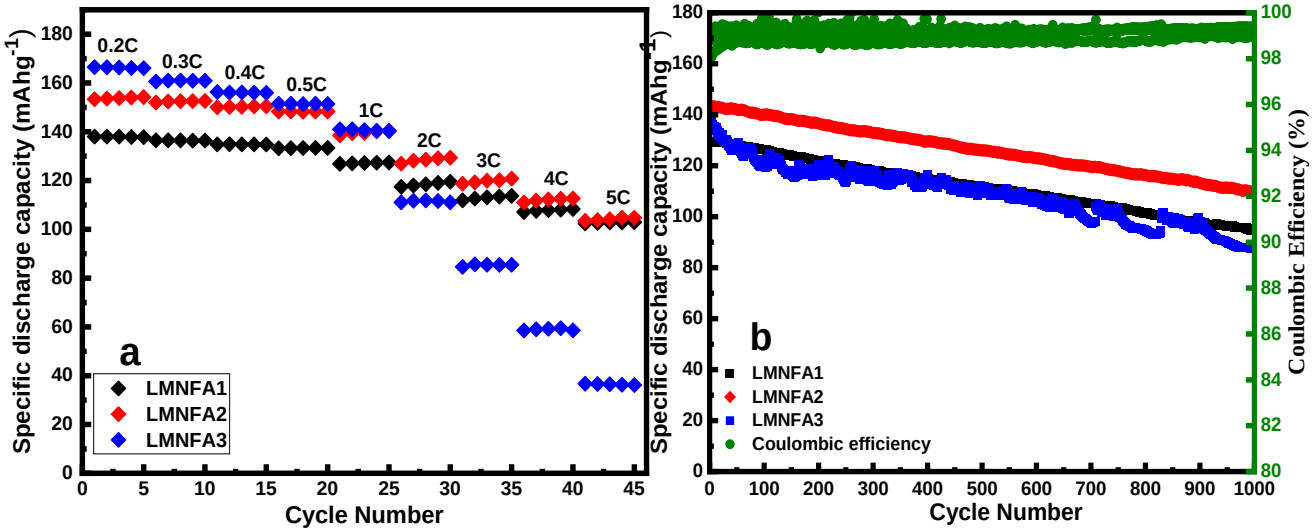

Figure. 2b.15. (a) Rate capability **(b)** Cycle stability **(at 1C) of LMFA1, 2, 3 materials**.

Figure. 2b.15a depicts the rate capabilities of LMNFA1, LMNFA2, and LMNFA3 electrodes at 0.2 to 5 current densities (C rate) with a 3.5 V to 5.0 V voltage window. Here, the performance of

LMNFA2 at different current densities is better than that of **LMNFA1** and **LMNFA3** materials. The three substituents for Mn in LMO are Ni^{3+}, Al^{3+}, and Fe^{3+} which contributed differently to the performance of the cathode materials. This variation is due to the largely exposed facet of the plane (111) in the truncated octahedral crystals.[25] Correspondingly, the replacement of Ni^{3+} ions for the Mn^{3+} ions is responsible for the increase in the specific capacity of the material. Al^{3+} and Fe^{3+} ions substitution could enhance the conductivity and stability of the cathode material during the prolonged cycling process as they are not redox active in the potential window. The Ni composition plays an important role in the capacity enhancement at higher currents, Al and Fe composition act as stabilizers. **Figure. 2b.15b**, shows a specific discharge capacity *v/s* voltage curve at 1C current density between 3.5 and 5 V over 1000 cycles. It can be observed that LMNFA2 has shown better specific discharge capacity and stable cyclability than the other two materials. This is due to a slightly higher ratio of Ni in the LMNFA2 compared to LMNFA1 and LMNFA3. The materials **LMNFA1, LMNFA2,** and **LMNFA3** show initial specific capacities of 129.01 $mAhg^{-1}$, 143.18 $mAhg^{-1}$, 140.22 $mAhg^{-1}$ respectively. At the end of 1000 continuous charge/discharge cycles, the gradual decrease in capacity is observed up to 94.86 $mAhg^{-1}$, 109.29 $mAhg^{-1}$, 87.59 $mAhg^{-1}$ with a capacity retention of 73.52%, 76.33% and 62.47% respectively. The capacity retention of **LMNFA2** is more than **LMNFA1,** and **LMNFA3,** due to the more Ni concentration and the lesser capacity retention of **LMNFA1 and LMNFA3** due to lesser proportions of Ni, Fe and Al. Here Ni acts as a capacity enhancer, and Fe and Al act as electrochemical stabilizers. As well, the other reason might be the crystal plane orientation of the truncated octahedral geometry, the XRD result values (**Table 2**) supported the statement. The galvanostatic charge/discharge profiles are shown graphically in **Figure. 2b.16(a-c**) to visualize the decrease in specific discharge capacities of the electrodes.

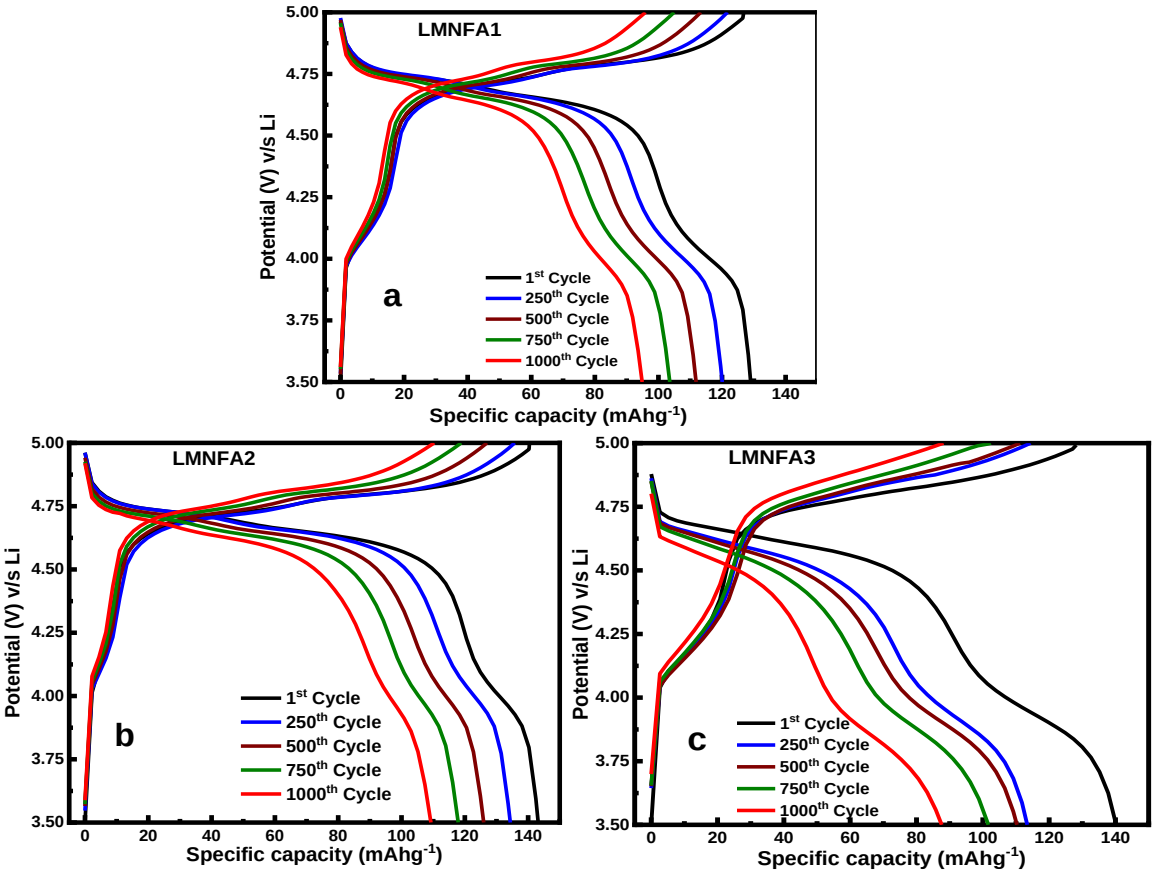

Figure 2b.16 (a-c) Specific capacity v/s Potential (V) curves of **LMNFA1, LMNFA2** and **LMNFA3.**

The initial discharge capacities of **LMNFA1, LMNFA2** and **LMNFA3** are 129.01 $mAhg^{-1}$, 143.18 $mAhg^{-1}$, 140.22 $mAhg^{-1}$ at a 1C rate, while at the end of 1000 continuous galvanostatic charge−discharge cycles, the specific capacity has decreased to 94.86 $mAhg^{-1}$, 109.29 $mAhg^{-1}$, 87.59 $mAhg^{-1}$ with a Coulombic efficiency of 98 %, 99 % and 99 % respectively. The slightly higher discharge capacities than the charge capacities can be seen in **Figure 2b.16(a-c**) because the cells tested for the rate capability continued to charge-discharge at 1C for cyclability analysis. This might be because irregular amounts of Li^+ ions are transported during charge-discharge due to structural interferences caused by the sudden change in the current density from 5C rate to 1C rate, which might result in a smaller number of Li^+ ions intercalated during the charging process

than the discharge process, and also possibly more Li^+ ions are released during slower discharge process at 1C than 5C. The above results are compared with the published results of spinel cathode material LiMn1.5Ni0.5O4 with similar morphological features.[48–50] Which enlightens the present cathode materials with the appropriate ratio of cation substitution, which could improve the cell performance.

2B.4 Impact of plane orientation on the electrochemical performance

The cation migration conforming surface chemical evolution always impact the electrochemical performance, especially when it is operated within the broader range of voltage window. The kind of uncontrolled reactions can occur through unexpected reactions resulting from the complicated cation migration phenomena by the structural instability over the electrochemical cycling process, which implies their cyclic performance. Reports of Liu et al.,[48] have shown that the material with fully exposed (111) planes has not performed better. But, the materials, along with truncated geometry and more exposed (111) planes, less exposed (100) and (110) planes, have shown better performance. This is due to (100) and (110) planes being well aligned to wider Li^+ ion diffusion channels, which favor stable interfacial contact establishment between the cathode and electrolyte.[48,51] This type of plane exposure will help control the side reactions such as dissolution of active material, decomposition, passivation of the binder, and conductive carbon.[52] The prevention of such unwanted side reactions makes the crystal structure stable and avoids structural evolution, which causes deterioration of the cathode structure. The Ni and Fe substituted LMO spinel cathode material with exposed (111) plane with truncated octahedral geometry has shown enhancement in cycling stability and rate capability. The exposed (111) plane in LMNFA cathode materials provides channels for Li^+ ions and lowers the dissolution of Mn ions with extra stable surface orientation than other crystal facets of the cathode.[27,28] The highest

specific discharge capacity and better capacity retention delivered by the LMNFA2 cathode demonstrates that the exposed (111) plane orientation in the crystal structure is more stable and could meritoriously reduce the dissolution of Mn ions. This more stable and exposed plane will delay the structure rearrangements during cycling and lead to better capacity retention.[53] In the crystal structure, the dominant (111) plane surfaces were densely packed with Mn ions and were less exposed to the dissolution as compared to the (100) and (110) plane surfaces which are less densely packed with Mn ions.[7] These less densely packed Mn ions are more liable to interact with electrolytes and accelerate the Mn dissolution. Here the minimised Mn dissolution leads to the superior cycle life and enhanced discharge capacity with the support of Ni, Fe, and Al as dopants.[20] From the literature, there are some theoretical studies which suggest that the majority of Mn ions will be at the surface in a trivalent state.[45,46] These trivalent Mn ions will disproportionate into tetravalent and divalent Mn ions and the tetravalent Mn ions will be retained in a solid state whereas the divalent Mn ions will be dissolved into an electrolyte solution which leads to degradation of cathode.[54] Reports of Sun et al. showed that the DFT-based calculations on dissolution energies of surface orientations of Mn at (100), (110), and (111) planes are 13.8 eV, 8.6 eV and 5.3 eV respectively. The plane (111) surface has shown maximum positive dissolution energy which has more competence to avoid Mn dissolution as compared to the other two plane surfaces (100) and (110), and is more susceptible to Mn dissolution which leads to capacity loss and reduced cycle life.[55] Our materials also showed the same behaviour and correlate with the experimental studies, the material with more exposed (111) plane surface has shown superior performance. As discussed earlier in the XRD studies, LMNFA2 cathode material has a crystal structure with extensively exposed (111) plane and has shown superior capacity as well as retention as compared to LMNFA1 and LMNFA3. Although the LMNFA3 material showed higher

discharge capacity initially, later it decayed faster than the other two materials over continuous cycling. This might be due to the substituent concentration effects as it has higher Mn content in the structure. The LMNFA2 shown to become an efficient cathode material for extended electrochemical applications in Li-ion batteries.

2B.5 Post-electrochemical test analysis of electrodes

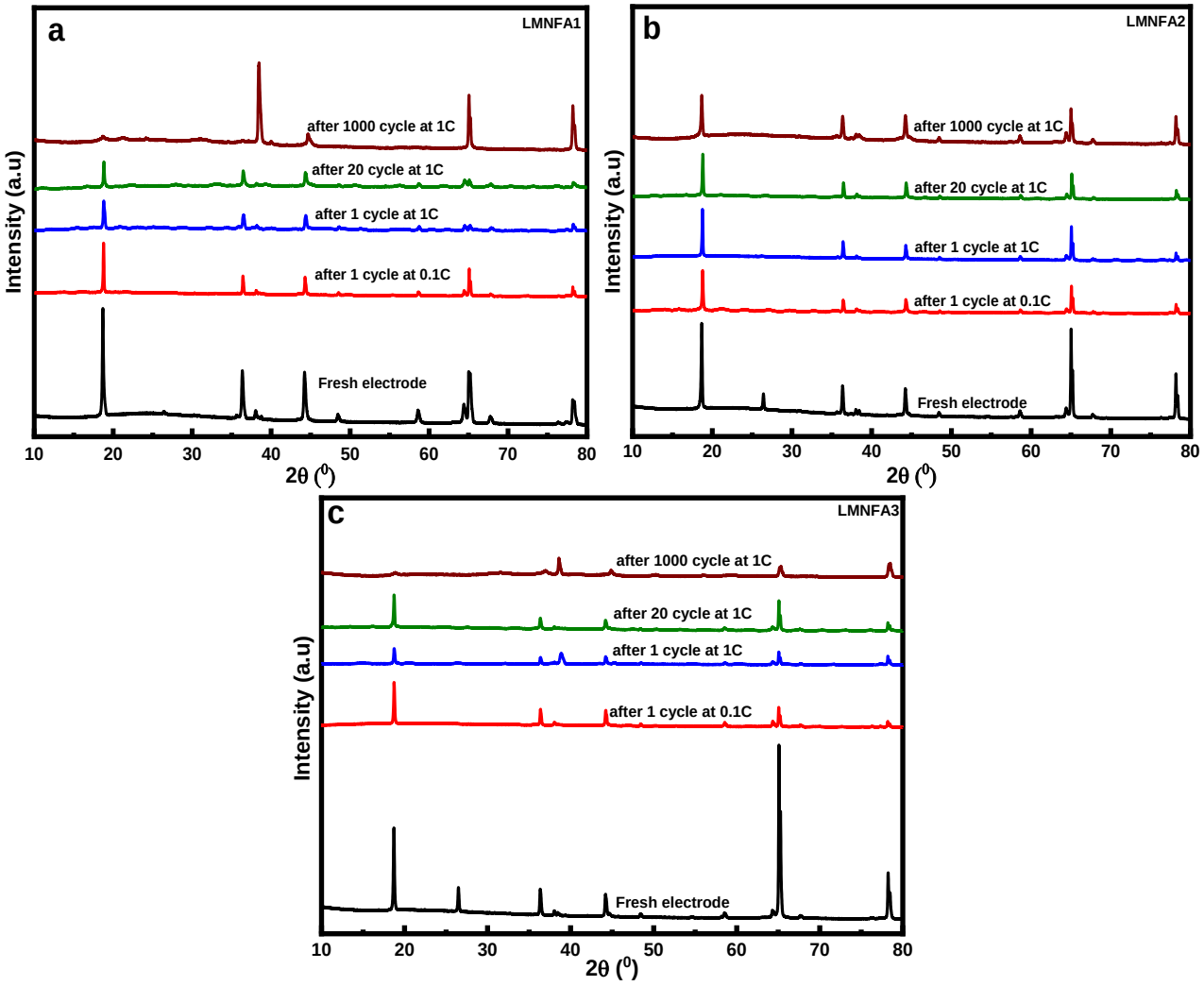

Figure 2b.17. X-ray diffraction patterns of the electrodes at different GCD cycle intervals of **(a)** LMNFA1 (**b**) LMNFA2 and (**c**) LMNFA1.

Generally, the oxide-based cathode materials exhibit structural changes during the charge-discharge cycles. We have attempted to track the changes by conducting the X-diffraction studies

for the electrodes at different cycled conditions at current densities of 0.1C for the activation cycle and at 1C for prolonged cycles. XRD and FESEM studies were conducted to determine the structural and morphology changes of active material-coated electrodes before and after electrochemical studies. **Figure 2b.17(a-c)**, shows the XRD results of the fresh and used electrodes. Initially, at 0.1C rate, there is no large difference between the diffraction patterns from the fresh electrodes and the electrode after one cycle at a low current density of 0.1C rate. Later, slight changes in diffraction patterns can be observed in the peak intensity at 2θ ~18.5 which corresponds to the (111) plane and finally, the results clearly show that after 1000 continuous charge-discharge cycles there is not much change in the peak position of LMNFA2 material as compared to XRD results of fresh electrodes. This indicates that there is not much structural change in the cathode even after 1000 cycles. But in the other two materials, LMNFA1 and LMNFA3, the peak positions are not maintained as compared to fresh electrodes due to material degradation over the repeated cycling. The material LMNFA2 with a more exposed (111) plane has shown better electrochemical performance. This indicates that the crystal orientation of the material plays a major role in the enhancement of the electrochemical performance of the material. The FESEM images of the electrode surface before and after electrochemical studies are given in **Figure 2b.18,** which shows that the fresh electrodes **(Figure 2b.18a-c)** do not show any kind of cracks on the surface whereas used electrodes (**Figure 2b.18d-f)** have developed cracks and holes which provide an idea about the cause for the electrochemical performance degradation. The extent of cracks is not the same in all the cases. As mentioned above, in X-ray diffraction studies, the materials with more exposed (111) plane are less prone to electrode degradation, which can be visualized with the given images.

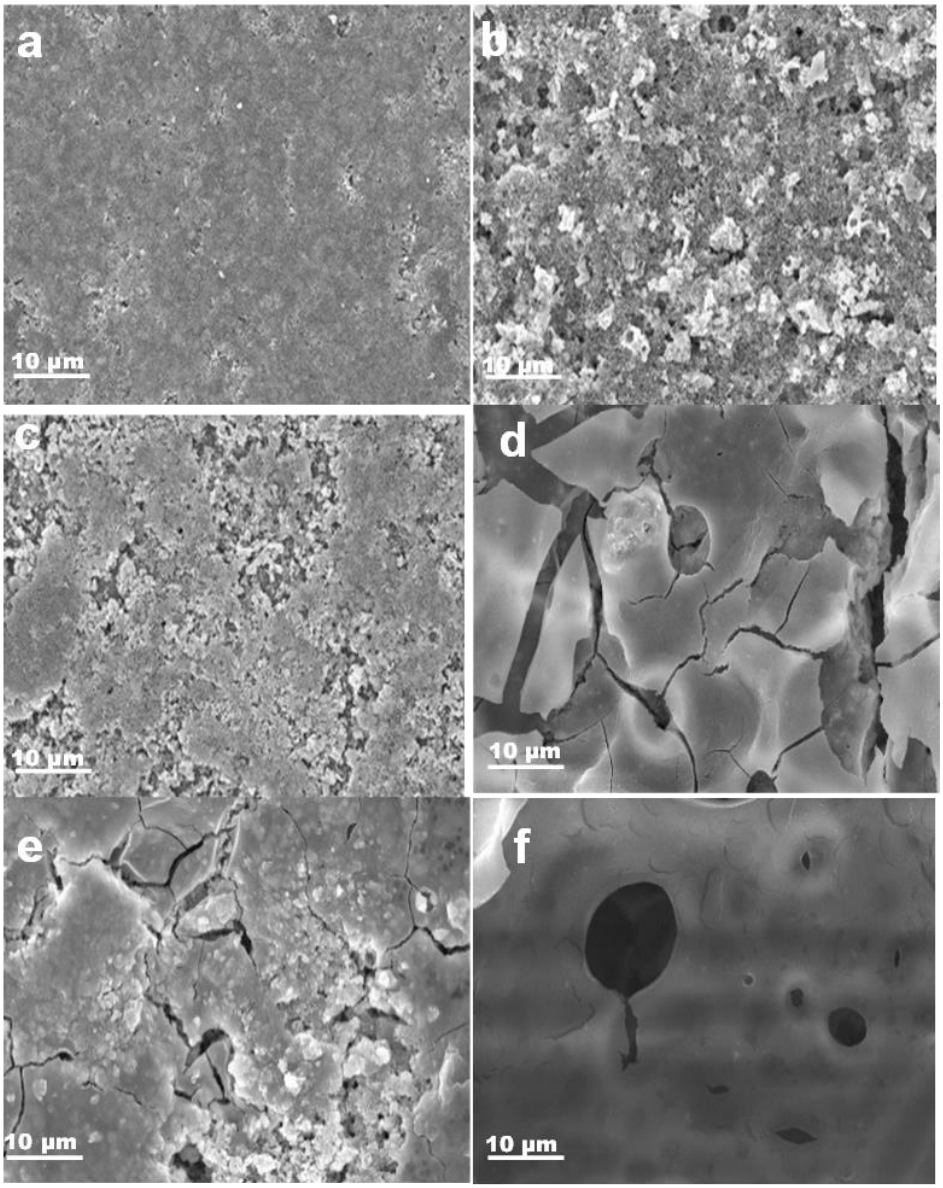

Figure 2b.18. FESEM images of the electrodes (**a)** LMNFA1 (**b**) LMNFA2 and (**c**) LMNFA1 before and (**d)** LMNFA1 (**e**) LMNFA2 and (**f**) LMNFA3 after electrochemical testing.

2B.6 Conclusions

To conclude, a group of LMO spinel cathode materials with tri-cation substitution was produced using a straightforward sol-gel technique. These materials exhibited a truncated octahedral shape. X-ray diffraction and Rietveld refinement results show that the spinel materials

are formed with a pure phase $Fd\bar{3}m$ space group. When combined in optimal proportions, the LMNFA cathode materials with tri-cation substitution demonstrate a well-defined crystalline structure. This structure features strategically oriented (111) planes, which help reduce Mn dissolution, alongside (110) plane orientations that facilitate Li^+ movement. The advantageous arrangement of crystal planes in the tri-substituted cathode material results in enhanced rate capability, extended cycle life, and high specific capacity. Notably, the modified spinel cathode material LMNFA2 maintained 81.47% of its capacity after an extensive 1000 cycles, delivering a specific capacity of 105.11 $mAhg^{-1}$ with approximately 99% coulombic efficiency at 1C. These findings underscore the crucial role of crystal plane orientation in minimizing the dissolution of transition metals into the electrolyte, enhancing the cathode material's performance. This innovative approach to cathode material design, combining specific elements and crystal structure manipulation, shows significant promise for developing spinel cathode materials with high energy density, superior rate capability, and long-term cycling stability.

2B.7 References

(1) Zhu, Z.; Zhang, D.; Yan, H.; Li, W.; Qilu. Precise Preparation of High Performance Spherical Hierarchical $LiNi_{0.5}Mn_{1.5}O_4$ for 5 V Lithium Ion Secondary Batteries. *J. Mater. Chem. A* **2013**, *1* (18), 5492. https://doi.org/10.1039/c3ta10980a.

(2) Talyosef, Y.; Markovsky, B.; Salitra, G.; Aurbach, D.; Kim, H.-J.; Choi, S. The Study of $LiNi_{0.5}Mn_{1.5}O_4$ 5-V Cathodes for Li-Ion Batteries. *J. Power Sources* **2005**, *146* (1–2), 664–669. https://doi.org/10.1016/j.jpowsour.2005.03.064.

(3) Mereacre, V.; Stüble, P.; Ghamlouche, A.; Binder, J. R. Enhancing the Stability of $LiNi_{0.5}Mn_{1.5}O_4$ by Coating with Linbo3 Solid-State Electrolyte: Novel Chemically Activated Coating Process versus Sol-Gel Method. *Nanomaterials* **2021**, *11* (2), 1–13. https://doi.org/10.3390/nano11020548.

(4) Wang, L.; Li, H.; Huang, X.; Baudrin, E. A Comparative Study of Fd-3m and P4332 "$LiNi_{0.5}Mn_{1.5}O_4$." *Solid State Ionics* **2011**, *193* (1), 32–38. https://doi.org/10.1016/j.ssi.2011.04.007.

(5) Shivamurthy, B. P.; Thripuranthaka, M.; Shelke, M. V.; Nayaka, G. P. Formation of the Secondary Phase Domain by Multi-Cation Substitution for the Superior Electrochemical Performance of Spinel Cathodes for High-Voltage Li-Ion Batteries. *ACS Appl. Energy Mater.* **2022**, *5* (12), 15345–15355. https://doi.org/10.1021/acsaem.2c02667.

(6) Taddesse, P.; Tsona, C.; Murali, N.; Babu, K. V. Effect of Ni and Fe Substitution on the Thermal, Structural, Vibrational Spectroscopic and Electrochemical Properties of $LiMn_2O_4$ Cathode Material. *Sci. African* **2021**, *14*, *e00975*. https://doi.org/10.1016/j.sciaf.2021.e00975.

(7) Sharma, P.; Das, C.; Indris, S.; Bergfeldt, T.; Mereacre, L.; Knapp, M.; Geckle, U.; Ehrenberg, H.; Darma, M. S. D. Synthesis and Characterization of a Multication Doped Mn Spinel, $LiNi_{0.3}Cu_{0.1}Fe_{0.2}Mn_{1.4}O_4$, as 5 V Positive Electrode Material. *ACS Omega* **2020**, *5* (36), 22861–22873. https://doi.org/10.1021/acsomega.0c02174.

(8) Wang, S.; Xiang, M.; Lu, Y.; Guo, J.; Su, C.; Bai, H.; Liu, X. Facile Solid-State Combustion Synthesis of Al–Ni Dual-Doped $LiMn_2O_4$ Cathode Materials. *J. Mater. Sci. Mater. Electron.* **2020**, *31* (8), 6036–6044. https://doi.org/10.1007/s10854-020-03155-7.

(9) Liu, H.; Li, M.; Xiang, M.; Guo, J.; Bai, H.; Bai, W.; Liu, X. Effects of Crystal Structure and Plane Orientation on Lithium and Nickel Co-Doped Spinel Lithium Manganese Oxide

for Long Cycle Life Lithium-Ion Batteries. *J. Colloid Interface Sci.* **2021**, *585*. https://doi.org/10.1016/j.jcis.2020.10.052.

(10) Piao, J.-Y.; Duan, S.-Y.; Lin, X.-J.; Tao, X.-S.; Xu, Y.-S.; Cao, A.-M.; Wan, L.-J. Surface Zn Doped $LiMn_2O_4$ for an Improved High Temperature Performance. *Chem. Commun.* **2018**, *54* (42), 5326–5329. https://doi.org/10.1039/C8CC01878B.

(11) Garhi, G.; Aklalouch, M.; Favotto, C.; Mansori, M.; Saadoune, I. Coprecipitation Synthesis of Co-Doped $LiMn_{1.5}Ni_{0.5}O_4$ Material as 5 V Cathode of Li-Ion Batteries with Huge Rate Capability for High Power Applications. *J. Electroanal. Chem.* **2020**, *873*, 114413. https://doi.org/10.1016/J.JELECHEM.2020.114413.

(12) Xu, W.; Zheng, Y.; Cheng, Y.; Qi, R.; Peng, H.; Lin, H.; Huang, R. Understanding the Effect of Al Doping on the Electrochemical Performance Improvement of the $LiMn_2O_4$Cathode Material. *ACS Appl. Mater. Interfaces* **2021**, *13* (38), 45446–45454. https://doi.org/10.1021/acsami.1c11315.

(13) Bao, S. J.; Liang, Y. Y.; Zhou, W. J.; He, B. L.; Li, H. L. Enhancement of the Electrochemical Properties of $LiMn_2O_4$ through Al^{3+} and F- Co-Substitution. *J. Colloid Interface Sci.* **2005**, *291* (2), 433–437. https://doi.org/10.1016/j.jcis.2005.05.013.

(14) Han, D.-W.; Ryu, W.-H.; Kim, W.-K.; Eom, J.-Y.; Kwon, H.-S. Effects of Li and Cl Codoping on the Electrochemical Performance and Structural Stability of $LiMn_2O_4$ Cathode Materials for Hybrid Electric Vehicle Applications. *J. Phys. Chem. C* **2013**, *117* (10), 4913–4919. https://doi.org/10.1021/jp310011m.

(15) Liu, H.; Yang, F.; Guo, J.; Xiang, M.; Bai, H.; Wang, R.; Su, C. Facile Combustion Synthesis of Amorphous Al_2O_3-Coated $LiMn_2O_4$ cathode Materials for High-Performance Li-Ion Batteries. *New J. Chem.* **2021**, *45* (23), 10534–10540. https://doi.org/10.1039/d1nj01052b.

(16) Shapira, A.; Tiurin, O.; Solomatin, N.; Auinat, M.; Meitav, A.; Ein-Eli, Y. Robust AlF3 Atomic Layer Deposition Protective Coating on $LiMn_{1.5}Ni_{0.5}O_4$ Particles: An Advanced Li-Ion Battery Cathode Material Powder. *ACS Appl. Energy Mater.* **2018**, *1* (12), 6809–6823. https://doi.org/10.1021/acsaem.8b01048.

(17) Li, Q. L.; Xu, W. Q.; Bai, H. L.; Guo, J. M.; Su, C. W. ZnO-Coated $LiMn_2O_4$ Cathode Material for Lithium-Ion Batteries Synthesized by a Combustion Method. *Ionics (Kiel).* **2016**, *22* (8), 1343–1351. https://doi.org/10.1007/s11581-016-1655-8.

(18) Zhao, J.; Wang, Y. Atomic Layer Deposition of Epitaxial ZrO_2 Coating on $LiMn_2O_4$ Nanoparticles for High-Rate Lithium Ion Batteries at Elevated Temperature. *Nano Energy* **2013**, *2* (5), 882–889. https://doi.org/10.1016/j.nanoen.2013.03.005.

(19) Fu, S.; Zhang, Y.; Bian, Y.; Xu, J.; Wang, L.; Liang, G. Effect of Fe^{3+} and/or PO_4^{3-} Doping on the Electrochemical Performance of $LiNi_{0.5}Mn_{1.5}O_4$ Cathode Material for Li-Ion Batteries. *Ind. Eng. Chem. Res.* **2023**, *62* (2), 1016–1028. https://doi.org/10.1021/acs.iecr.2c04037.

(20) Kim, J. S.; Kim, K.; Cho, W.; Shin, W. H.; Kanno, R.; Choi, J. W. A Truncated Manganese Spinel Cathode for Excellent Power and Lifetime in Lithium-Ion Batteries. *Nano Lett.* **2012**, *12* (12), 6358–6365. https://doi.org/10.1021/nl303619s.

(21) Jiang, C.; Tang, Z.; Wang, S.; Zhang, Z. A Truncated Octahedral Spinel $LiMn_2O_4$ as High-Performance Cathode Material for Ultrafast and Long-Life Lithium-Ion Batteries. *J. Power Sources* **2017**, *357*, 144–148. https://doi.org/10.1016/j.jpowsour.2017.04.079.

(22) Karunawan, J.; Suryadi, P. N.; Mahfudh, L.; Santosa, S. P.; Sumboja, A.; Iskandar, F. Truncated Octahedral Shape of Spinel $LiNi_{0.5}Mn_{1.5}O_4$ via a Solid-State Method for Li-Ion Batteries. *Energy and Fuels* **2023**, *37* (1), 754–762. https://doi.org/10.1021/acs.energyfuels.2c03507.

(23) Hashem, A. M.; Abbas, S. M.; Hou, X.; Eid, A. E.; Abdel-Ghany, A. E. Facile One Step Synthesis Method of Spinel $LiMn_2O_4$ Cathode Material for Lithium Batteries. *Heliyon* **2019**, *5* (7), e02027. https://doi.org/10.1016/j.heliyon.2019.e02027.

(24) Lee, S.-N.; Park, D.; Kim, J.; Moon, S.-H.; Jang, J.-S.; Kim, S.-B.; Shin, J.-H.; Park, Y.; Park, K.-W. Enhanced Cycling Performance of Fe-doped $LiMn_2O_4$ Truncated Octahedral Cathodes for Li-Ion Batteries. *ChemElectroChem* **2022**, *9* (11), e202200385. https://doi.org/10.1002/celc.202200385.

(25) Huang, S.; Wu, H.; Chen, P.; Guo, Y.; Nie, B.; Chen, B.; Liu, H.; Zhang, Y. Facile PH-Mediated Synthesis of Morphology-Tunable $MnCO_3$ and Their Transformation to Truncated Octahedral Spinel $LiMn_2O_4$ Cathode Materials for Superior Lithium Storage. *J. Mater. Chem. A* **2015**, *3* (7), 3633–3640. https://doi.org/10.1039/c4ta06522k.

(26) Hendriks, R.; Cunha, D. M.; Singh, D. P.; Huijben, M. Enhanced Lithium Transport by Control of Crystal Orientation in Spinel $LiMn_2O_4$ Thin Film Cathodes. *ACS Appl. Energy Mater.* **2018**, *1* (12), 7046–7051. https://doi.org/10.1021/acsaem.8b01477.

(27) Yang, C.; Deng, Y.; Gao, M.; Yang, X.; Qin, X.; Chen, G. High-Rate and Long-Life Performance of a Truncated Spinel Cathode Material with off-Stoichiometric Composition at Elevated Temperature. *Electrochim. Acta* **2017**, *225*, 198–206. https://doi.org/10.1016/j.electacta.2016.12.096.

(28) Luo, X.; Xiang, M.; Li, Y.; Guo, J.; Liu, X.; Bai, H.; Bai, W.; Su, C. Surface-Orientation for Boosting the High-Rate and Cyclability of Spinel $LiNi_{0.02}Mn_{1.98}O_4$ Cathode Material. *Vacuum* **2020**, *179*, 109505. https://doi.org/10.1016/j.vacuum.2020.109505.

(29) Momma, K.; Izumi, F. VESTA 3 for Three-Dimensional Visualization of Crystal, Volumetric and Morphology Data. *J. Appl. Crystallogr.* **2011**, *44* (6), 1272–1276. https://doi.org/10.1107/S0021889811038970.

(30) Tabassam, L.; Nazir, T.; Manzoor, U.; Mehmood, S.; Hassan, M. U.; Bhatti, A. S. Raman Spectroscopy of Nominally Ni-Doped $LiMn_{2-x}Ni_xO_4$ ($0 \leq x \leq 0.20$). *Mater. Res. Express* **2019**, *6* (11), 115550. https://doi.org/10.1088/2053-1591/ab3970.

(31) Dos Santos Junior, G. A.; Fortunato, V. D. S.; Bastos, G. A. A.; Silva, G. G.; Ortega, P. F. R.; Lavall, R. L. High-Performance Lithium-Ion Hybrid Supercapacitors Based on Lithium Salt/Imidazolium Ionic Liquid Electrolytes and Ni-Doped $LiMn_2O_4$ Cathode Materials. *ACS Appl. Energy Mater.* **2020**, *3* (9), 9028–9039. https://doi.org/10.1021/acsaem.0c01435.

(32) Samarasingha, P. B.; Andersen, N. H.; Sørby, M. H.; Kumar, S.; Nilsen, O.; Fjellvåg, H. Neutron Diffraction and Raman Analysis of $LiMn_{1.5}Ni_{0.5}O_4$ Spinel Type Oxides for Use as Lithium Ion Battery Cathode and Their Capacity Enhancements. *Solid State Ionics* **2016**, *284*, 28–36. https://doi.org/10.1016/j.ssi.2015.11.018.

(33) Nageswara Rao, B.; Narsimulu, D.; Srinadhu, E. S.; Satyanarayana, N. Structural, Electrical, and Dielectric Properties of Nickel-Doped Spinel $LiMn_2O_4$ Nanorods. *Ionics (Kiel).* **2019**, *25* (3), 981–990. https://doi.org/10.1007/s11581-018-2697-x.

(34) Bhatia, A.; Dridi Zrelli, Y.; Pereira-Ramos, J. P.; Baddour-Hadjean, R. Detailed Redox Mechanism and Self-Discharge Diagnostic of 4.9 V $LiMn_{1.5}Ni_{0.5}O_4$ spinel Cathode Revealed by Raman Spectroscopy. *J. Mater. Chem. A* **2021**, *9* (23), 13496–13505. https://doi.org/10.1039/d1ta00989c.

(35) Boulet-Roblin, L.; Villevieille, C.; Borel, P.; Tessier, C.; Novák, P.; Ben Yahia, M. Versatile Approach Combining Theoretical and Experimental Aspects of Raman Spectroscopy to Investigate Battery Materials: The Case of the $LiNi_{0.5}Mn_{1.5}O_4$ Spinel. *J.*

Phys. Chem. C **2016**, *120* (30), 16377–16382. https://doi.org/10.1021/acs.jpcc.6b04155.

(36) Vijayan, S.; Kirubasankar, B.; Pazhamalai, P.; Solarajan, A. K.; Angaiah, S. Electrospun Nd^{3+}-Doped $LiMn_2O_4$ Nanofibers as High-Performance Cathode Material for Li-Ion Capacitors. *ChemElectroChem* **2017**, *4* (8), 2059–2067. https://doi.org/10.1002/celc.201700161.

(37) Bakierska, M.; Świętoslawski, M.; Gajewska, M.; Kowalczyk, A.; Piwowarska, Z.; Chmielarz, L.; Dziembaj, R.; Molenda, M. Enhancement of Electrochemical Performance of $LiMn_2O_4$ Spinel Cathode Material by Synergetic Substitution with Ni and S. *Materials (Basel).* **2016**, *9* (5), 366. https://doi.org/10.3390/ma9050366.

(38) Ryu, J. H.; Park, B. G.; Kim, S. B.; Park, Y. J. Effects of Surface Area on Electrochemical Performance of $Li[Ni_{0.2}Li_{0.2}Mn_{0.6}]O_2$ Cathode Material. *J. Appl. Electrochem.* **2009**, *39* (7), 1059–1066. https://doi.org/10.1007/s10800-008-9757-2.

(39) Wang, F. X.; Xiao, S. Y.; Gao, X. W.; Zhu, Y. S.; Zhang, H. P.; Wu, Y. P.; Holze, R. Nanoporous $LiMn_2O_4$ Spinel Prepared at Low Temperature as Cathode Material for Aqueous Supercapacitors. *J. Power Sources* **2013**, *242*, 560–565. https://doi.org/10.1016/j.jpowsour.2013.05.115.

(40) Zhao, H.; Li, D.; Wang, Y.; Li, F.; Wang, G.; Wu, T.; Wang, Z.; Li, Y.; Su, J. Sol-Gel Synthesis of Silicon-Doped Lithium Manganese Oxide with Enhanced Reversible Capacity and Cycling Stability. *Materials (Basel).* **2018**, *11* (8), 1455. https://doi.org/10.3390/ma11081455.

(41) Gieu, J. B.; Winkler, V.; Courrèges, C.; El Ouatani, L.; Tessier, C.; Martinez, H. New Insights into the Characterization of the Electrode/Electrolyte Interfaces within $LiMn_2O_4/Li_4Ti_5O_{12}$ Cells, by X-Ray Photoelectron Spectroscopy, Scanning Auger Microscopy and Time-of-Flight Secondary Ion Mass Spectrometry. *J. Mater. Chem. A* **2017**, *5* (29), 15315–15325. https://doi.org/10.1039/c7ta02529g.

(42) Nesbitt, H. W.; Banerjee, D. Interpretation of XPS Mn(2p) Spectra of Mn Oxyhydroxides and Constraints on the Mechanism of MnO_2 Precipitation. *Am. Mineral.* **1998**, *83* (3–4), 305–315. https://doi.org/10.2138/am-1998-3-414.

(43) Ji, Y.; Liu, H.; Guo, Y.; Guo, J.; Xiang, M.; Bai, W.; Liu, X.; Bai, H. Improved Capacity Retention and Ultralong Cycle Performance of Ni-Fe Co-Doped $LiMn_2O_4$ Cathode Material at High Current Densities. *Colloids and Surfaces A: Physicochemical and Engineering*

Aspects. September 2022, p 129259. https://doi.org/10.1016/j.colsurfa.2022.129259.

(44) Medvedeva, A.; Makhonina, E.; Pechen, L.; Politov, Y.; Rumyantsev, A.; Koshtyal, Y.; Goloveshkin, A.; Maslakov, K.; Eremenko, I. Effect of Al and Fe Doping on the Electrochemical Behavior of $Li_{1.2}Ni_{0.133}Mn_{0.534}Co_{0.133}O_2$ Li-Rich Cathode Material. *Materials (Basel).* **2022**, *15* (22), 8225. https://doi.org/10.3390/ma15228225.

(45) LI, F.; ZHANG, G.; ZHANG, Z.; YANG, J.; LIU, F.; JIA, M.; JIANG, L. Regeneration of Al-Doped $LiNi_{0.5}Co_{0.2}Mn_{0.3}O_2$ Cathode Material by Simulated Hydrometallurgy Leachate of Spent Lithium-Ion Batteries. *Trans. Nonferrous Met. Soc. China* **2022**, *32* (2), 593–603. https://doi.org/10.1016/S1003-6326(22)65818-7.

(46) Callegari, D.; Coduri, M.; Fracchia, M.; Ghigna, P.; Braglia, L.; Anselmi Tamburini, U.; Quartarone, E. Lithium Intercalation Mechanisms and Critical Role of Multi-Doping in $LiFe_xMn_{2-x-y}Ti_yO_4$ as High-Capacity Cathode Material for Lithium-Ion Batteries. *J. Mater. Chem. C* **2022**, *10* (23), 8994–9008. https://doi.org/10.1039/D2TC00573E.

(47) Kim, T.; Choi, W.; Shin, H. C.; Choi, J. Y.; Kim, J. M.; Park, M. S.; Yoon, W. S. Applications of Voltammetry in Lithium Ion Battery Research. *Journal of Electrochemical Science and Technology*. 2020, pp 14–25. https://doi.org/10.33961/jecst.2019.00619.

(48) Liu, H.; Wang, J.; Zhang, X.; Zhou, D.; Qi, X.; Qiu, B.; Fang, J.; Kloepsch, R.; Schumacher, G.; Liu, Z.; Li, J. Morphological Evolution of High-Voltage Spinel $LiNi_{0.5}Mn_{1.5}O_4$ Cathode Materials for Lithium-Ion Batteries: The Critical Effects of Surface Orientations and Particle Size. *ACS Appl. Mater. Interfaces* **2016**, *8* (7), 4661–4675. https://doi.org/10.1021/acsami.5b11389.

(49) Wang, P.; Li, H.; Wei, Y.; Zhao, D.; Mao, L.; Cui, X.; Zhang, H.; Zhou, X.; Li, S. Truncated Octahedral $LiNi_{0.5}Mn_{1.5}O_4$ with Excellent Electrochemical Properties for Lithium-Ion Batteries Prepared by a Graphite Assisted Calcination Method. *New J. Chem.* **2019**, *43* (38), 15396–15404. https://doi.org/10.1039/c9nj03174j.

(50) Nasrinpour, H.; Masoudpanah, S. M.; Soltanieh, M. Oxalate-Assisted Solvothermal Synthesis of Octahedral $LiMn_{1.5}Ni_{0.5}O_4$ Particles for Lithium-Ion Batteries. *J. Mater. Res. Technol.* **2021**, *13*, 61–69. https://doi.org/10.1016/j.jmrt.2021.04.033.

(51) Kong, F.; Zhang, G.; Wu, D.; Sun, F.; Tao, S.; Chu, S.; Qian, B.; Chu, W.; Song, L. Insight into the Cation Migration and Surface Structural Evolution of Spinel $LiNi_{0.5}Mn_{1.5}O_4$ Cathode Material for Lithium-Ion Batteries. *Chem. Eng. J.* **2023**, *451*, 138708.

https://doi.org/10.1016/j.cej.2022.138708.

(52) Kim, J.; Cha, H.; Lee, H.; Oh, P.; Cho, J. Surface and Interfacial Chemistry in the Nickel-Rich Cathode Materials. *Batteries and Supercaps*. 2020, pp 309–322. https://doi.org/10.1002/batt.201900131.

(53) Xu, C.; Li, J.; Feng, X.; Zhao, J.; Tang, C.; Ji, B.; Hu, J.; Cao, C.; Zhu, Y.; Butt, F. K. The Improved Performance of Spinel $LiMn_2O_4$ Cathode with Micro-Nanostructured Sphere-Interconnected-Tube Morphology and Surface Orientation at Extreme Conditions for Lithium-Ion Batteries. *Electrochim. Acta* **2020**, *358*, 136901. https://doi.org/10.1016/j.electacta.2020.136901.

(54) Manthiram, A. A Reflection on Lithium-Ion Battery Cathode Chemistry. *Nat. Commun.* **2020**, *11* (1), 1550. https://doi.org/10.1038/s41467-020-15355-0.

(55) Sun, W.; Li, Y.; Xie, K.; Luo, S.; Bai, G.; Tan, X.; Zheng, C. Constructing Hierarchical Urchin-like $LiNi_{0.5}Mn_{1.5}O_4$ Hollow Spheres with Exposed {111} Facets as Advanced Cathode Material for Lithium-Ion Batteries. *Nano Energy* **2018**, *54*, 175–183. https://doi.org/10.1016/j.nanoen.2018.10.006.

Chapter 3A

Impact of surface modification with Nickel ferrite in reducing the Mn dissolution to enhance the cycle stability of $LiMn_2O_4$ cathode material for Li-ion batteries.

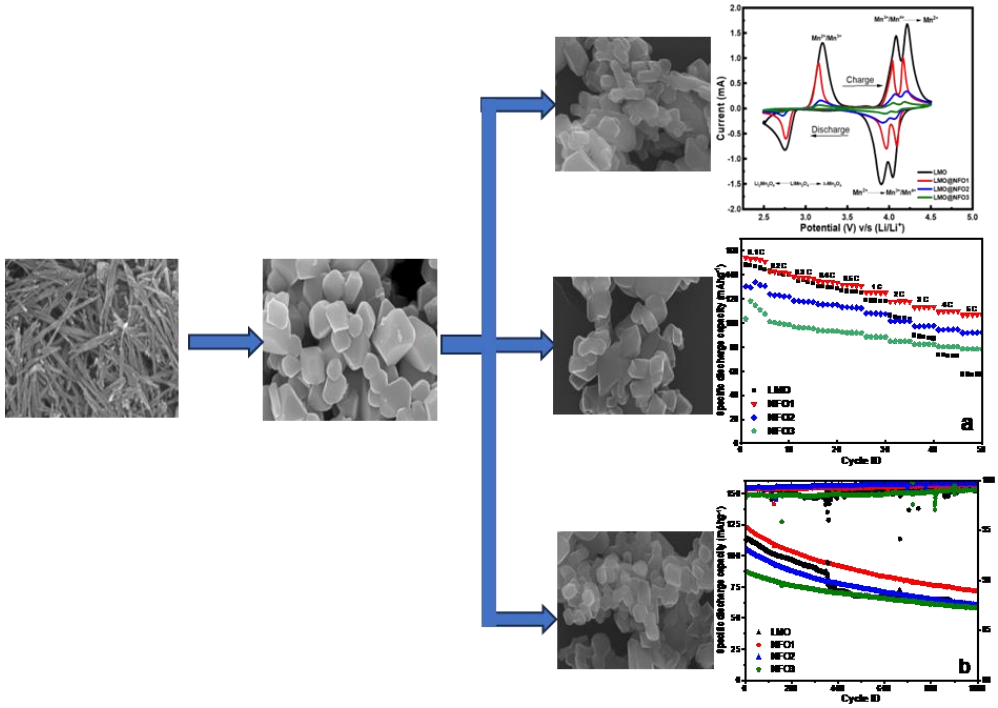

Highlights

- Spinel Li-manganate, $LiMn_2O_4$ (LMO) cathode materials are extensively applied for high-voltage Li-ion batteries (LIBs).
- Nevertheless, these materials suffer from critical issues such as poor cyclability, low-capacity retention, and rate capability due to Mn dissolution and structural distortion.
- Herein, we demonstrate the surface modification of LMO cathode material with thin layer deposition of $NiFe_2O_4$ (NFO) spinel oxide material to overcome the Mn dissolution and Jahn-Teller distortion.
- The surface of the LMO materials was deposited with a thin layer of NFO materials with 1%, 2%, and 3%.
- The surface-modified LMO cathode materials demonstrate enhanced cycle stability with better rate capability

- The results of this chapter will be published as **BP Shivamurthy**, MV Shelke, **GP Nayaka*,** Impact of surface modification with Nickel ferrite in reducing the Mn dissolution to enhanced cycle stability of $LiMn_2O_4$ cathode material for Li-ion batteries

3A.1 Introduction

The global climate crisis is a big concern for environmentalists and researchers today. The reduction of greenhouse gas emissions is crucial to reducing global warming. As the population increases, the usage of fossil fuels for energy requirements also increases. Energy generation from renewable sources and storage are essential to avoid using these fossil fuels for energy requirements. Therefore, developing sustainable and environmentally friendly battery chemistries is most important. Li-ion batteries stand tall as critical pillars in the fossil-fuel-free economy in storage systems, particularly for e-mobility.[1,2] Li-ion batteries (LIBs) are the prior choice for energy storage due to their high degree of technological maturity and practical performance characteristics such as high energy density, high volumetric and gravimetric energy density, energy efficiency, and long cycle life.[3] The performance of a LIB mainly depends on the electrode materials; in particular, the cathode plays a crucial role in deciding the capacity and energy density of the battery, as well as the cost. Even though the LIBs are commercialized successfully, there are still some drawbacks in cathode materials that make a way to explore better strategies to solve the issues generally state-of-the-art cathode materials face to achieve high performance.[2] However, as compared to the state-of-the-art cathode materials, layered $LiNi_{1-x-y}Co_xMn_yO_2$ (NCM) and poly anionic $LiFePO_4$, the spinel $LiMn_2O_4$ (LMO) and $LiMn_{1.5}Ni_{0.5}O_4$ (LMNO) cathode materials are facing critical issues despite of having, high-power density, high voltage applicability, low cost, high thermal stability and environmental friendliness.[4–6] Lithium manganese oxide ($LiMn_2O_4$) stands out among several cathode options as a highly promising material for electric vehicles (EVs). This class of cathode is so appealing due to its cost-effectiveness, widespread availability, environmental friendliness, and minimal safety risks, all essential attributes for the widespread adoption of EV batteries on a large scale.[7]

The major problem associated with this class of positive electrode materials for large-scale commercialization is the poor cyclability during continuous charge/discharge processes at elevated temperatures and high voltage conditions. This poor cyclability is due to the disastrous side reactions such as dissolution of Mn ions in electrolyte and structural instability due to the Jahn-teller distortion and disproportionation reactions of Mn^{3+} ions into Mn^{2+} and Mn^{4+} ions.[8,9] These Mn^{2+} ions undergo dissolution in the electrolyte and cause electrode/electrolyte interfacial instability, which degrades the cathode performance.[2] Hence, solving the issues of LMO-based cathode materials is crucial for large-scale commercial use. However, many researchers have attempted to solve these issues through cationic and anionic substitution to Mn ions,[10–13] surface modification through oxides,[14–16] core-shell structures[17], and fluorides.[18] Along with these techniques, the morphology-controlled approach, particle size-controlled approach, and controlled crystallographic plane orientation approaches have been made to solve the issues of LMO-type cathodes.[19] However, these issues have not been resolved entirely, and much research and development is still required to improve the performance of this class of cathode materials. To improve the performance of LMO cathode materials, researchers have tried elemental substitution into Mn sites and surface modification with stable materials as a protective layer. The surface of cathode materials is modified with inert materials against the acid phase formed in electrolytes, especially HF, coating of carbon,[17] graphite,[20] metal halides,[21] and metal oxides.[16,22] Among these surface modification approaches, metal oxide coating is an effective option for solving spinel cathode materials' structural and thermal issues.[22]

Our previously published paper studied LMO cathodes modified with tri-cation substitutions such as Ni, Fe, and Al.[23,24] A series of spinel cathode materials with mixed phases have been studied to determine the effect of mixed-phase on cathode performance[23], and in another study, a

set of spinel cathodes with exposed (111) planes have been studied. The exposed (111) planes effectively enhanced electrochemical performance with an optimized ratio.[19,20,24] Ni served as a capacity enhancer in both cases, and Fe and Al served as an electrochemical stabilizer, effectively improving the overall cathode performance. Based on our previous studies, considering the effective utilization of Ni and Fe elements to improve the electrochemical performance, Ni and Fe are employed for the surface modification of LMO materials with spinel nickel ferrite oxide $NiFe_2O_4$ (NFO).

We have synthesized the morphology-controlled truncated LMO materials using the shape-controlled α-MnO_2 nanostructures. The LMO material is surface-modified with NFO layers as a protective barrier. This barrier will help to overcome the Mn dissolution in electrolytes for improved electrochemical performance and longer cycle life.

3A.2 Materials and Methods

3A.2.1 Synthesis of α–MnO_2

α–MnO_2 nanorods were prepared from 5 g of Manganese acetate ($Mn(CH_3COO)_2 \cdot 4H_2O$) (Sigma Aldrich >99%) dissolved in 80 ml of deionized water by adding 4.7 g of ammonium persulfate with constant stirring for 2 hours. Then, the homogeneous solution with brown-colored particles was transferred into the Teflon inline stainless-steel autoclave for hydrothermal reaction. The autoclave reaction was done at 120 ^{0}C for 12 hours. After being cooled to room temperature normally, the solution was filtered, washed, and dried in a 100 ^{0}C vacuum oven for 10 hours. Finally, the dried **α–MnO_2** material was ground well into fine powder.

3A.2.2 Preparation of $LiMn_2O_4$

The truncated octahedral structures of $LiMn_2O_4$ were prepared by mixing the stoichiometric ratios of previously prepared Manganese dioxide (α – MnO_2) nanorods and lithium

hydroxide (LiOH) (Sigma Aldrich > 99%) into 60 ml of deionized water with constant stirring to get a homogeneous mixture. The slurry was evaporated at 80 ^{0}C to take off the excess water. The dried powders were heat treated at 750 ^{0}C for 12 hours with a temperature ramp rate of 3 ^{0}C/min. After cooling to room temperature normally, the powders are ground well and collected as $LiMn_2O_4$ material with a truncated octahedron geometrical shape.

3A.2.3 Surface modification of $LiMn_2O_4$ with $NiFe_2O_4$

The surface modification of as prepared $LiMn_2O_4$ cathode materials with nickel ferrite has been done by sol-gel method, the stoichiometric ratio of Nickel acetate ($Ni(CH_3COO)_2 \cdot 4H_2O$) (Sigma Aldrich >98%), and Iron nitrate ($Fe(NO_3)_3$ (Sigma Aldrich >98%)) of desired percentage composition was dissolved in 50 ml of DI water thoroughly, then citric acid was added into the solution, the molar ratio of metal ions and citric acid is maintained 1:2. The solution kept stirring at 50 ^{0}C for 2 hours. The calculated quantity of $LiMn_2O_4$ materials was added into the solution with constant stirring and heating until it formed a viscous gel. The viscous gel is dried at 100 ^{0}C for 12 hours in a vacuum oven. The dried material was ground into a fine powder and calcined at 750 ^{0}C for 8 hours with a temperature ramp rate of 5 ^{0}C/min. The calcined powder was then collected and subjected to Structural characterization to confirm the surface modification of LMO cathode material. The same experiments were repeated by varying the molar ratio of NFO precursors by 1%, 2%, and 3% by keeping the quantity of LMO constant. The surface-modified cathode materials are hereafter termed LMO@NFO1, LMO@NFO2, and LMO@NFO3 based on the percentage of the surface coating.

3A.2.4 Material characterization

The crystal structure of the synthesized materials was studied using X-ray diffraction (XRD) (Panalytical Xpert Pro) with Cu as an X-ray source at 40kV and 30mA with Ni as kβ filter.

The obtained XRD patterns were well refined using the Rietveld refinement technique using Fullprof suite software. The input parameters were gathered from the standard PDF numbers 44-0141, 00-035-0782, and 86-2667 for α-MnO_2, LMO, and NFO, respectively. The structural analysis was done using Raman measurements, and analysis was done using an IndiRam CTR confocal Raman microscope with a Nd:YAG diode laser DL-532 (wavelength 532 nm, maximum power 100 mW). The samples were measured with input power in between 0.1 mW to 0.5 mW. The surface structure and morphology of the materials were studied using Field Emission Scanning Electron Microscope (FE-SEM) (FEI-NOVA NANOSEM 450) and High-Resolution Transmission Electron Microscope (HR-TEM) (JEOL JEM F-200) coupled with energy dispersive spectrometer (EDS). The valence states of the elements are studied by employing X-ray photoelectron spectroscopy (XPS), which was performed using the Thermo Scientific Model K-alpha XPS instrument with monochromatic Al-Kα as the X-ray source. Topographical analysis was done using atomic force microscopy (AFM) using the Nano Observer System S-SPM-00001.

3A.2.5 Electrochemical characterization

The electrical and electrochemical behavior of surface-modified LMO cathode materials was studied by fabricating 2032-type coin cells. The positive electrodes were prepared with 80:10:10 weight % of the active cathode material, polyvinylidene difluoride (PVDF), and Super C-60 carbon black, respectively. All these materials were mixed well with an appropriate quantity of N-methyl pyrrolidone solvent to form a uniform slurry. Using the doctor blade method, the slurry was then coated onto a carbon-coated aluminum foil and dried at 100 ^{0}C for 12 hrs under a vacuum. The cathode-coated Al foil was subjected to calendaring and punched into 14 mm circular discs. The 2032 type coin cells were fabricated using circular discs as the cathode, Li metal disc as anode, Celgard-2325 as the separator, and 1M $LiPF_6$ (in 1:1:1 of EC/DMC/EMC) as the

electrolyte. The coin cells were fabricated in an argon-filled glove box at ≤ 0.1 ppm of O_2 and H_2O levels. Finally, the fabricated coin cells were tested for cyclic voltammetry and electrochemical impedance analysis (EIS) using the Metrohm electrochemical workstation (Multiautolab M204). The galvanostatic charge/discharge measurements were carried out with the Neware battery testing system (CT4008).

3A.3 Results and Discussion

3A.3.1 Structural characterization

3A.3.1.1 X-ray diffraction study

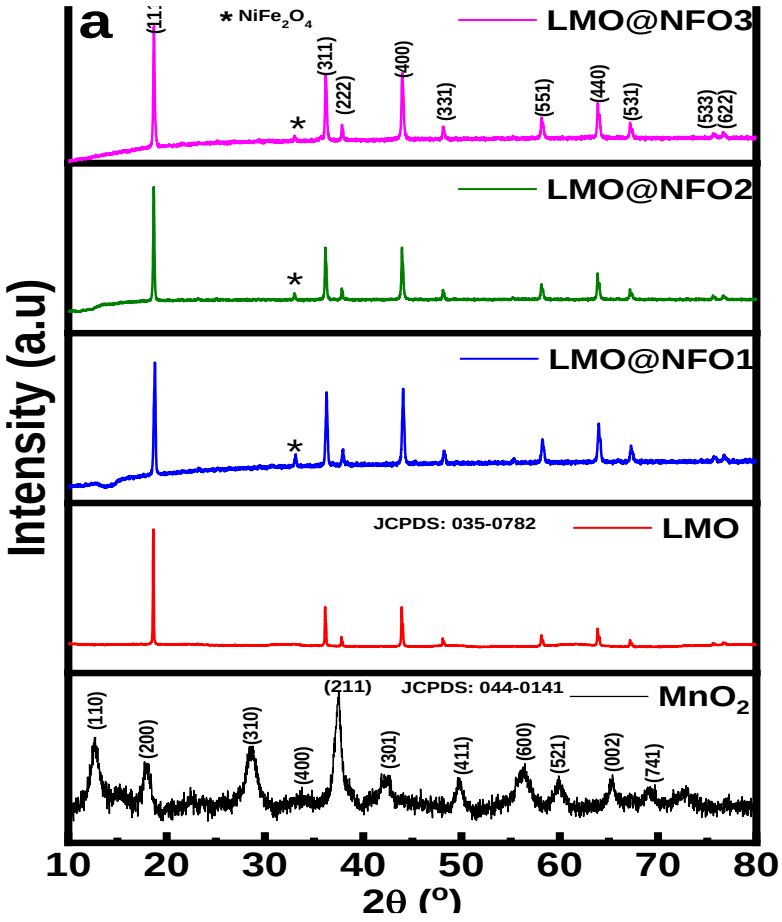

Figure 3a.1 XRD patterns of α-MnO_2, LMO, LMO@NFO1, LMO@NFO2, LMO@NFO3.

Figure 3a.1 shows the X-ray diffraction patterns of the α-MnO_2 precursor nanostructures, LMO, LMO@NFO1, LMO@NFO2, and LMO@NFO3. All the diffraction peaks of α-MnO_2 are attributed to the pure tetragonal crystal structure with the space group I4/m, and the pattern is well matched with the standard JCPDS number 44-0141. The obtained lattice constant values of α-MnO_2 are a=b=9.7847 and c= 2.8630 and are well matched with the literature reports.[25,26] The diffraction peaks of LMO, LMO@NFO1, LMO@NFO2, and LMO@NFO3 materials were attributed to the non-stoichiometric cubic spinel structure with the space group Fd-3m, and the patterns were well matched with standard JCPDS number 035-0782. The synthesized LMO materials formed octahedral structures with exposed (111) planes. These structures are the same as our previous reports, in which we studied the influence of the exposed (111) plane with compactly packed Mn ions and less densely packed (100) and (110) planes.[24] Herein, in this study, the surface of the LMO spinel is modified by coating with the $NiFe_2O_4$ spinel by varying the coating percentage. The patterns were well matched with standard JCPDS number 86-2667.[27] In **Figure 3a.1**, a small peak can be observed at around 33° and 55° in surface-modified cathode materials due to the formation of an NFO layer over the surface of the particles of LMO material. These minor peaks of the NFO surface of cathode materials are indexed as (311) and (422) planes.[27]

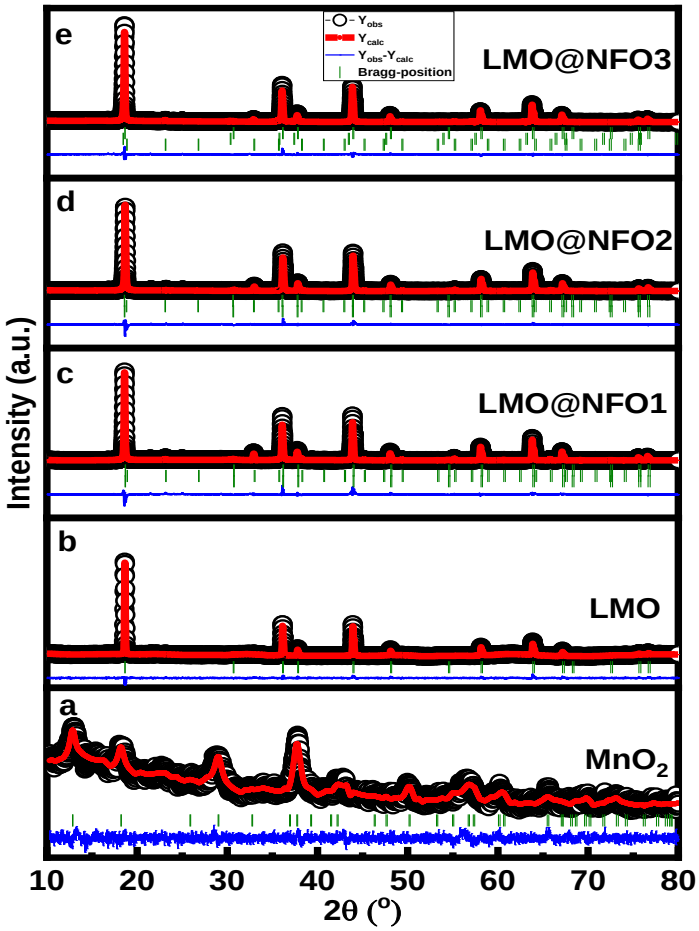

Figure 3a.2, Rietveld refinement results of **(a)** α-MnO_2, **(b)** LMO, **(c)** LMO@NFO1, **(d)** LMO@NFO2, **(e)** LMO@NFO3.

Further, to get detailed information about the crystal structures, Rietveld refinement studies **(Figure 3a.2 (a-e))** were performed with the Fd-3m space group as a reference, and the lattice parameters obtained are given in **Table 3a.1.** The α - MnO_2 and LMO materials were well fitted with a single phase, while LMO@NFO1, LMO@NFO2, and LMO@NFO3 materials were fitted with three phases belonging to $LiMn_2O_4$, $NiFe_2O_4$ with space group Fd-3m and Mn_2O_3 with space groups Ia-3 exhibit the cubic crystal structures. This second phase is due to low fractions of NFO present over the particle surface LMO. The third phase is of Mn_2O_3 material, formed due to the dissolution of some traces of Mn ions into the aqueous solution during the sol-gel coating of NFO

material over the surface of LMO, which is very low in quantity, along with the cathode active material in sedimentary form. The crystallographic data for this phase is matched with ICDD reference number 00-041-1442 for Mn_2O_3 material.

Sample	Space group	Average R_{wp}	Phase fraction (%)	Lattice constant (Å)	Cell volume	$\chi 2$
α - MnO_2	$Fd\bar{3}m$	9.79	100	a, b = 9.73 c=2.84	269.93	0.84
LMO ($LiMn_2O_4$)	$Fd\bar{3}m$	6.02	100	8.238	559.18	1.44
LMO@NFO1	$Fd\bar{3}m$		89.45	8.242	560.75	
($LiMn_2O_4$ Mn_2O_3 $NiFe_2O_4$)	$Ia\bar{3}$	15.0	7.08	9.409	833.22	6.4
	$Fd\bar{3}m$		3.47	8.243	560.259	
LMO@NFO2	$Fd\bar{3}m$		91.9	8.242	560.063	
($LiMn_2O_4$ Mn_2O_3 $NiFe_2O_4$)	$Ia\bar{3}$	9.3	5.4	9.409	833.216	6.7
	$Fd\bar{3}m$		3.7	8.328	577.699	
LMO@NFO3	$Fd\bar{3}m$	8.6	93.5		559.741	
($LiMn_2O_4$ Mn_2O_3 $NiFe_2O_4$)	$Ia\bar{3}$		2.1	9.401	832.608	6.5
	$Fd\bar{3}m$		4.4		559.344	

Table 3a.1. Rietveld refinement results of XRD data of the α – MnO_2, LMO, LMO@NFO1, LMO@NFO2, and LMO@NFO3 materials.

3A.3.1.2 Raman spectroscopic analysis

Raman spectroscopy has been used extensively in the past few decades to study the $LiMn_2O_4$ material.[28–30] The structural studies of the LMO, LMO@NFO1, LMO@NFO2, and LMO@NFO3 materials are done by measuring in the wavelength range of 100 to 1200 cm^{-1}

Figure 3a.3 shows the Raman spectra of LMO, LMO@NFO1, LMO@NFO2, and LMO@NFO3 materials. All the peak positions of Raman bands are well matched with the recent report of $LiMn_2O_4$ with a slight shift.[31] This slight shift in the positions is due to introducing a thin layer of another oxide material over the surface of the LMO material. Five Raman active modes were predicted to be shown by $LiMn_2O_4$, such as one A_{1g}, one E_g, and three F_{2g}. In our case, the A_{1g} band corresponds to the vibration modes of Mn-O bonds of the MnO_6 octahedrons.[28] which appears at around 623 to 654 cm^{-1} for the set of cathode active materials. This Mn-O band appeared for LMO at ~654 cm^{-1}, for LMO@NFO1 appeared at ~633 cm^{-1}, for LMO@NFO2 appeared at ~640 cm^{-1}, for LMO@NFO3 appeared at ~621 cm^{-1}. The A_{1g} band of surface-coated materials shifted slightly towards the red band, as the surface thickness varies.

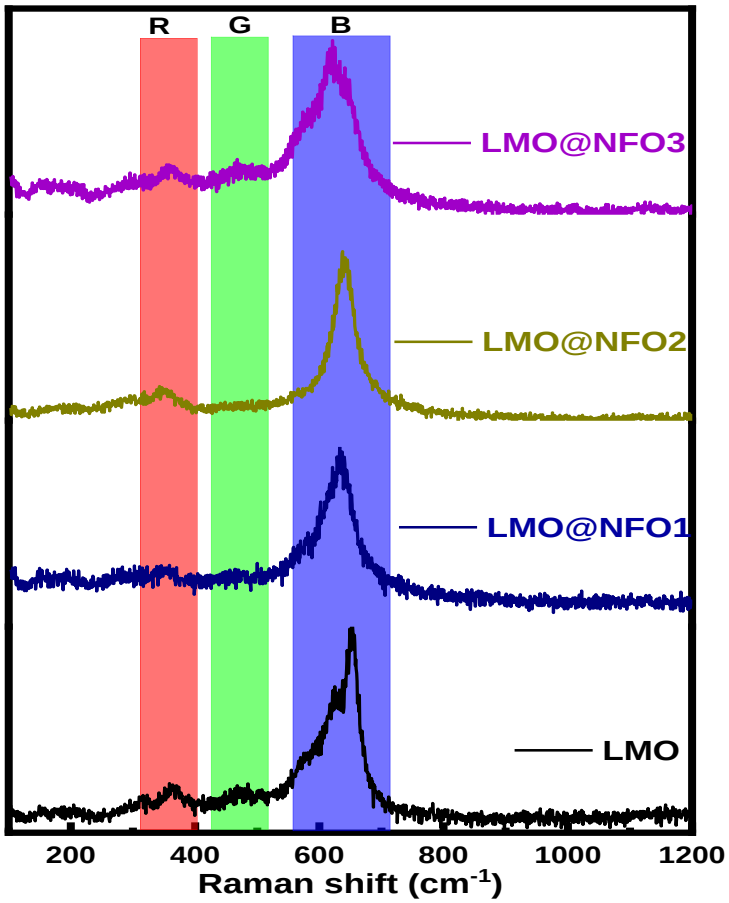

Figure 3a.3. Raman spectra of LMO, LMO@NFO1, LMO@NFO2, and LMO@NFO3 materials with designated R, G, and B bands.

The E_g band corresponds to the weak vibration modes of oxygen and appears at around 403 to 412 cm^{-1}, corresponding to the deformation mode of M-O-M bonds due to surface modification.[31] Two F_{2g}(II) and F_{2g}(III) bands among three F_{2g} modes correspond to the high-frequency scattering bands, which arise largely due to the vibrations of oxygen atoms and slightly due to the manganese atoms. These bands appear as weak shoulders at about ~575 to 632 cm^{-1} for our cathode active materials. The other low-intense scattering band, F_{2g}(I), appeared at about ~380 cm^{-1}, corresponding to the vibration of Li-O bonds corresponding to the mentioned red band in the spectra which is related to the LiO_4 tetrahedral group.[32,33]

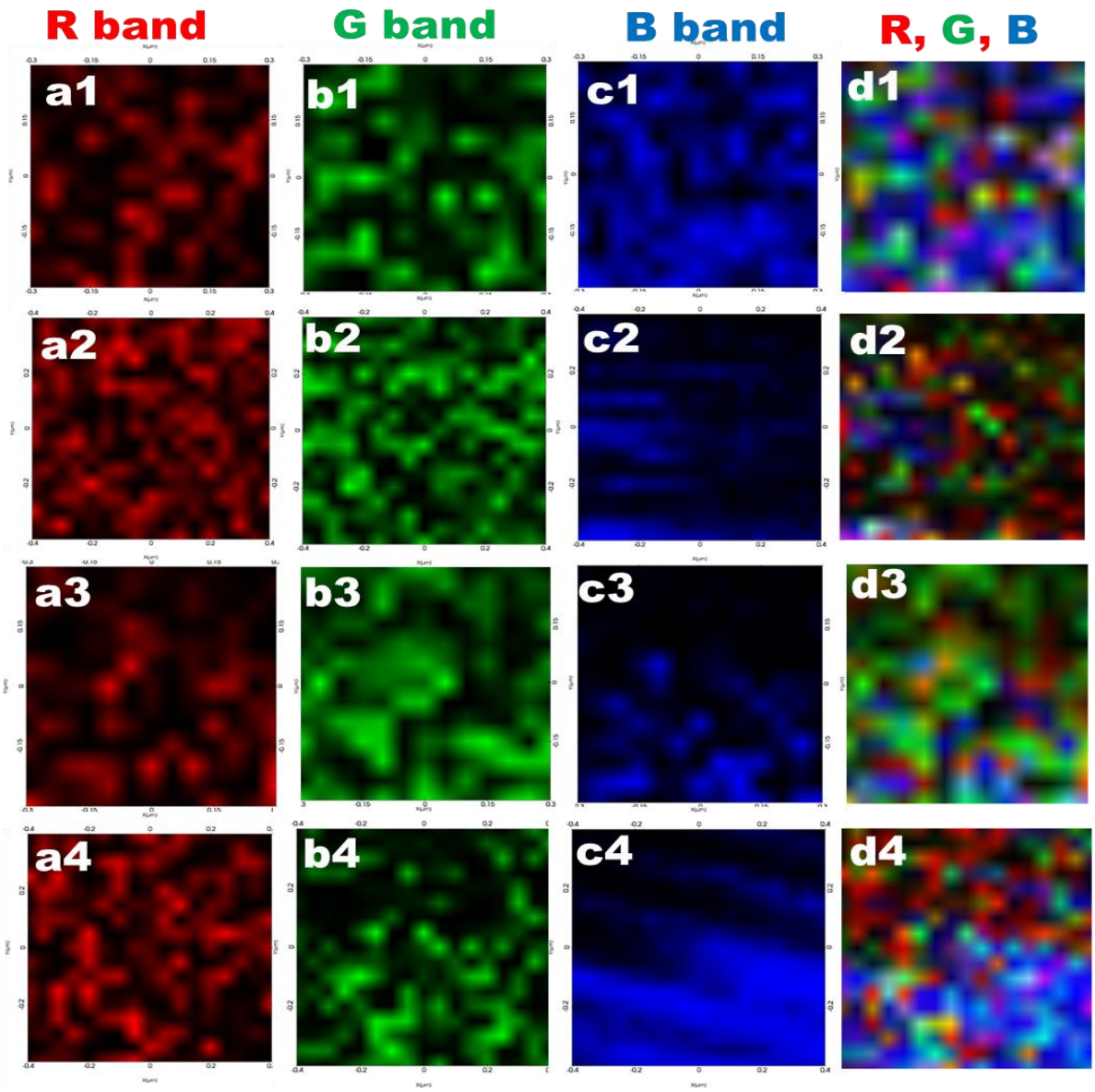

Figure 3a.4. Raman mapping images of R, G, B bands and R, G, B bands overlay of LMO **(a1-d1)**, LMO@NFO1**(a2-d2)**, LMO@NFO2**(a3-d3),** and LMO@NFO3**(a4-d4)** respectively.

The electrodes were mapped and measured at 3600 μm^2 with a 0.05 µm step. The laser power was maintained as low as 0.1 mW to 0.5 mW to avoid the destruction of the spinel structure at high laser power. The Raman spectral line in **Figure 3a.4** is marked with red, green, and blue bands to facilitate the mapping of spectral regions. Raman maps of the fresh electrodes **(Figure 3a.4)** show the homogeneous spectra over the entire measured area of each electrode. The grains

are visible in the red and green region mappings compared to the blue region mapping, indicating the LMO structure's Lithiation condition[31]. **Figure 3a.4 (d1-d4).** shows the overlay mapping of the red, green, and blue regions of the Raman spectra, confirming the homogeneous distribution of the Raman active phonons A_{1g}, E_g, and F_{2g}.

3A.3.1.3 Atomic force microscopic analysis

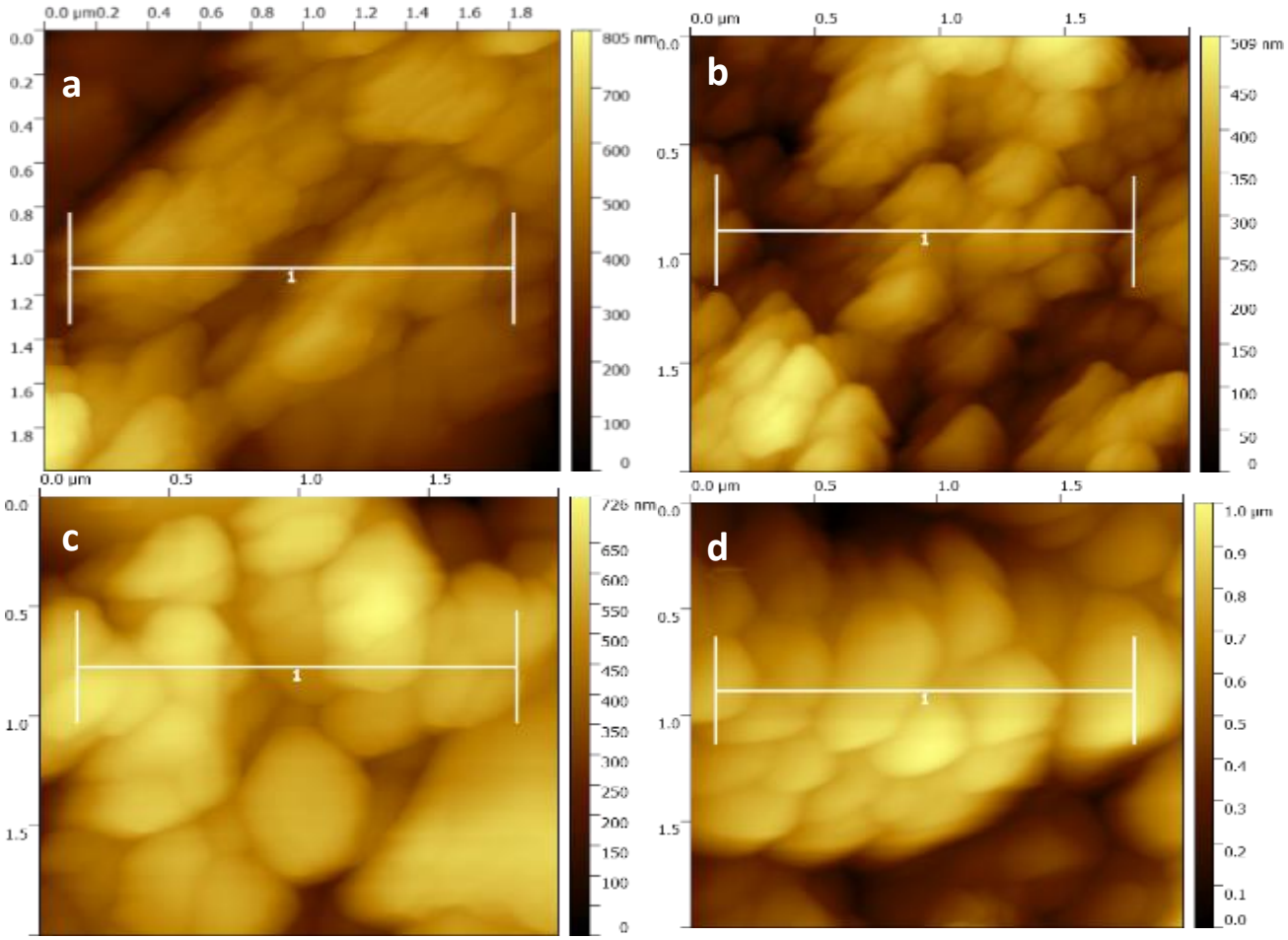

Figure 3a.5. AFM topographical images of the **(a)** LMO, **(b)** LMO@NFO1, **(c)** LMO@NFO2, **(d)** LMO@NFO3.

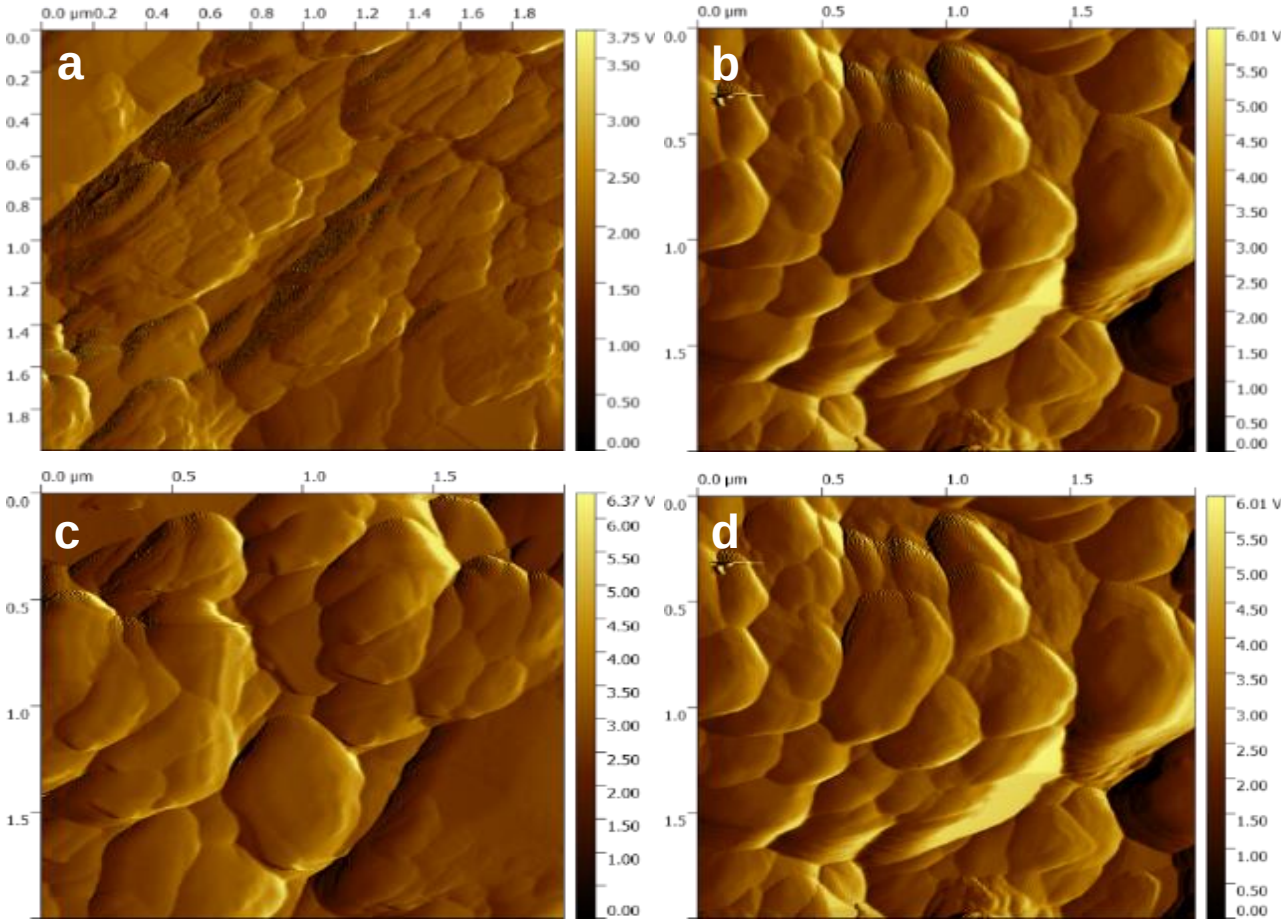

Figure 3a.6 AFM amplitude images of the **(a)** LMO, **(b)** LMO@NFO1, **(c)** LMO@NFO2, **(d)** LMO@NFO3.

Figure 3a.5 (a-d) shows the topographical images of the electrodes captured from AFM measurement, **Figure 3a.6 (a-d)** displays the amplitude images of the respective topographical images, and **Figure 3a.7 (a-d)** shows the average roughness graphs of the surface of the electrodes measured and analyzed from the AFM data. The average roughness of the surface of the electrodes was calculated across the line drawn over the topographic images. The average roughness of the LMO cathode was 2.16 nm, the NFO1 cathode was 1.8 nm, the NFO2 cathode was 2.1 nm, and 3.15 nm. The surface roughness of the electrodes can be correlated to the electrochemical performance of the electrodes. The cathode surface has the lowest roughness average and demonstrated superior rate capability and cycle stability performance. This indicates that the lower surface roughness of the electrodes leads to better electrochemical performance.

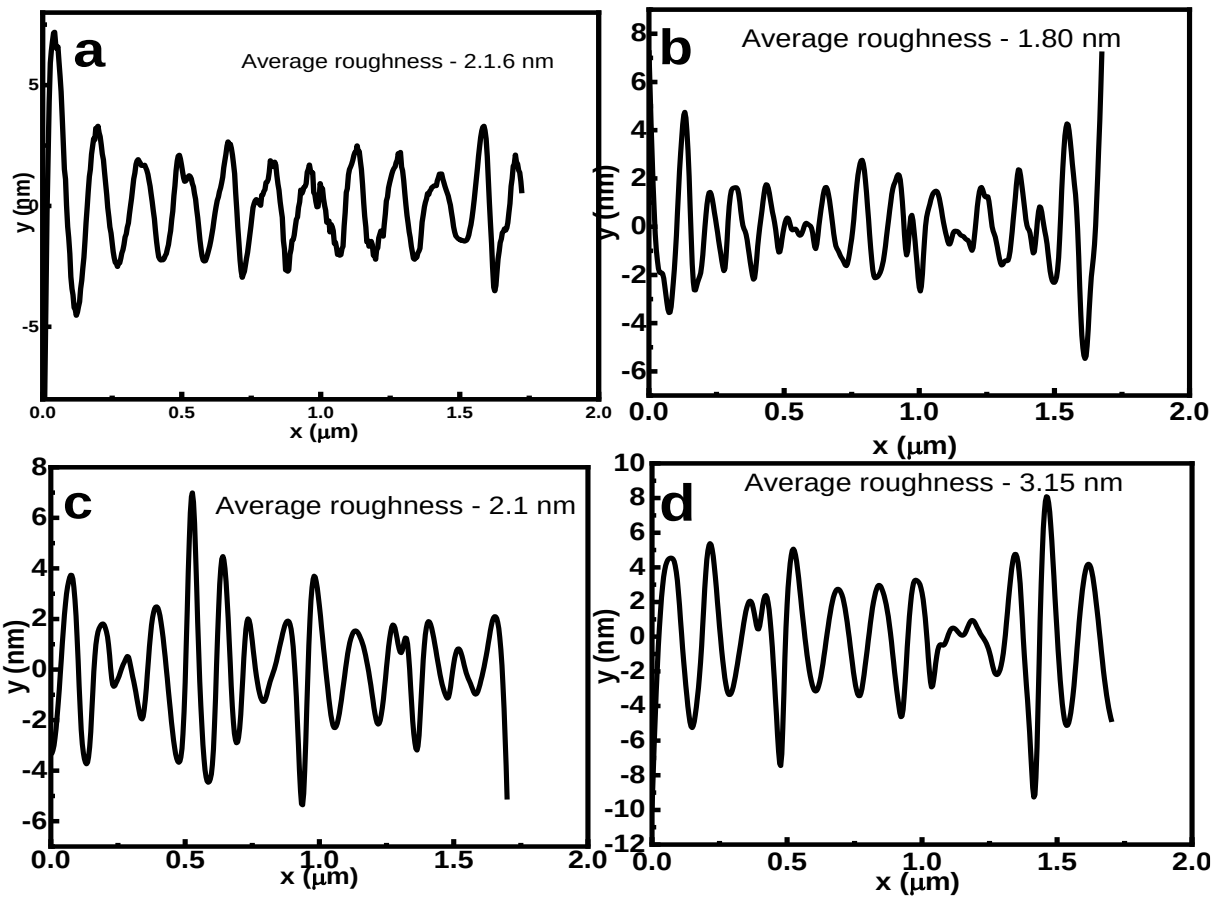

Figure 3a.7. AFM images derived average roughness plots of the **(a)** LMO, **(b)** LMO@NFO1, **(c)** LMO@NFO2, **(d1-)** LMO@NFO3.

3A.3.1.4 Electron microscopy study

Figure 3a.8 shows the FESEM **(Figure 3a.8(a-e)),** TEM **(Figure.3a.8 (a1-e1))** images and SAED (inset of **Fig.3a.8(a1-e1)** patterns of α-MnO_2, LMO, LMO@NFO1, LMO@NFO2, and LMO@NFO3 respectively. In Fig. 5a, we can see nanorods-shaped morphology for α-MnO_2 materials. These nanorods were used to synthesize LMO materials. During the calcination of synthesized LMO, the nanorods were smashed and formed truncated octahedral-type geometry **(Figure 3a.8b).** The octahedral-shaped LMO materials surface was modified with the coating NFO materials in varied proportions **(Figure 3a.8 (c-e)).**

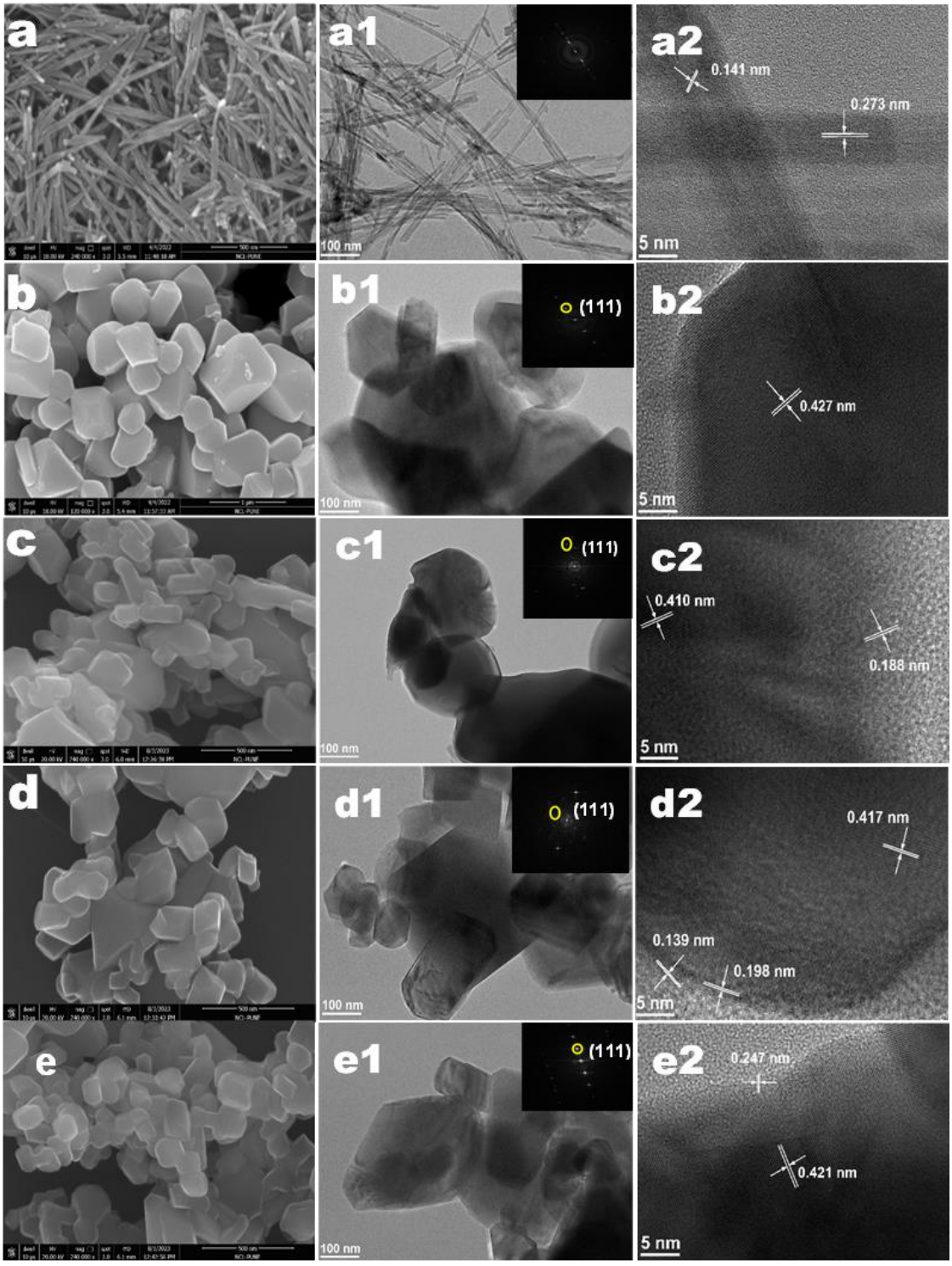

Figure 3a.8 (a-e) Field emission scanning electron microscopy images, **(a1-e1)** TEM images, SAED patterns (inset), and **(a2-e2)** HRTEM of α-MnO2, LMO, LMO@NFO1, LMO@NFO2, LMO@NFO3 respectively.

The surface orientation can be used to observe these surface modifications compared to the LMO materials. From the FESEM images, it can be observed that there is no agglomeration of particles, which indicates that the NFO particles are accumulated thoroughly over the surface of LMO materials. **Figure 3a.8 (a1-e1)** shows the TEM images at lower magnification and the SAED patterns (inset), and **Figure 3a.8 (a2-e2)** shows HRTEM images with lattice fringes and lattice spacing values. The lattice spacing values of α – MnO_2 are labeled 0.273 nm and 0.141 nm, corresponding to the (011) and (002) planes, respectively. The lattice spacing values for LMO and LMO@NFO1, LMO@NFO2, and LMO@NFO3 materials are marked in the range 0.410 nm to 0.427 nm, corresponding to the (111) plane. At the particle edges of the LMO@NFO1, LMO@NFO2, and LMO@NFO3 materials, the lattice spacing values are 0.188 nm, 0.139 nm, 0.198 nm, and 0.247 nm correspond to the planes (331), (531), (400), and (311) respectively.

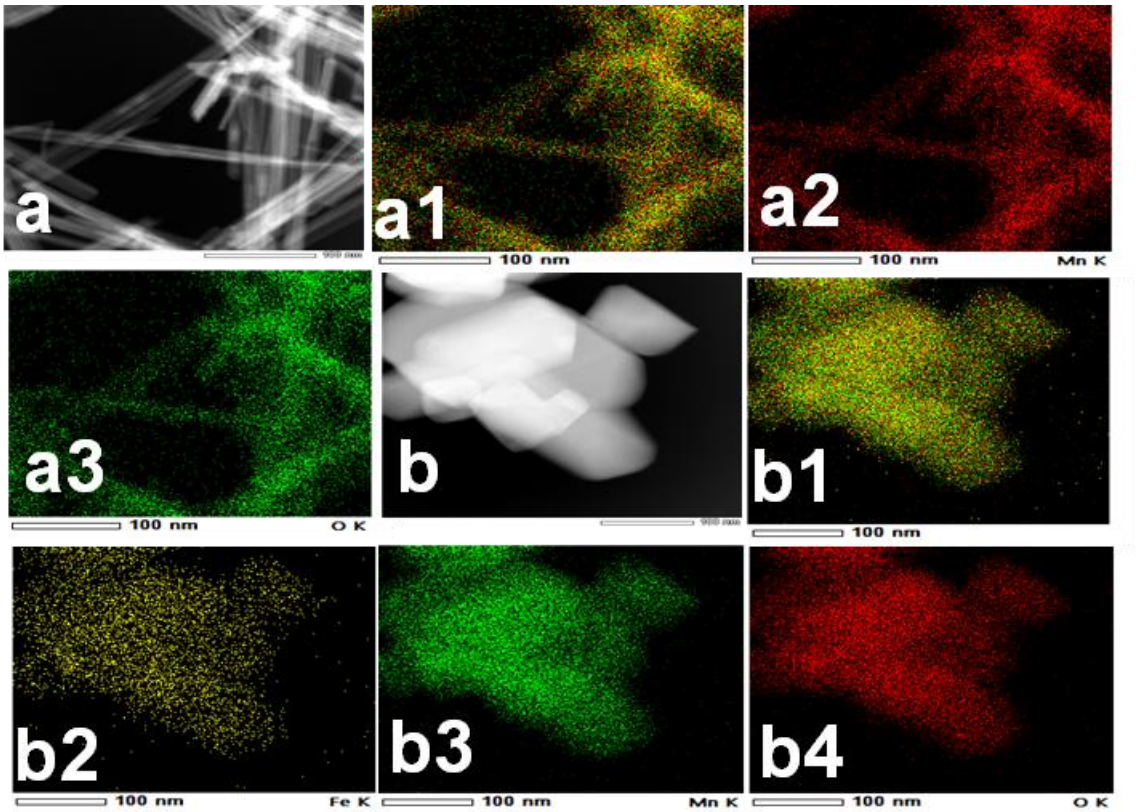

Figure 3a.9 STEM elemental mapping of (a-a3) α-MnO_2 and (b-b3) LMO respectively.

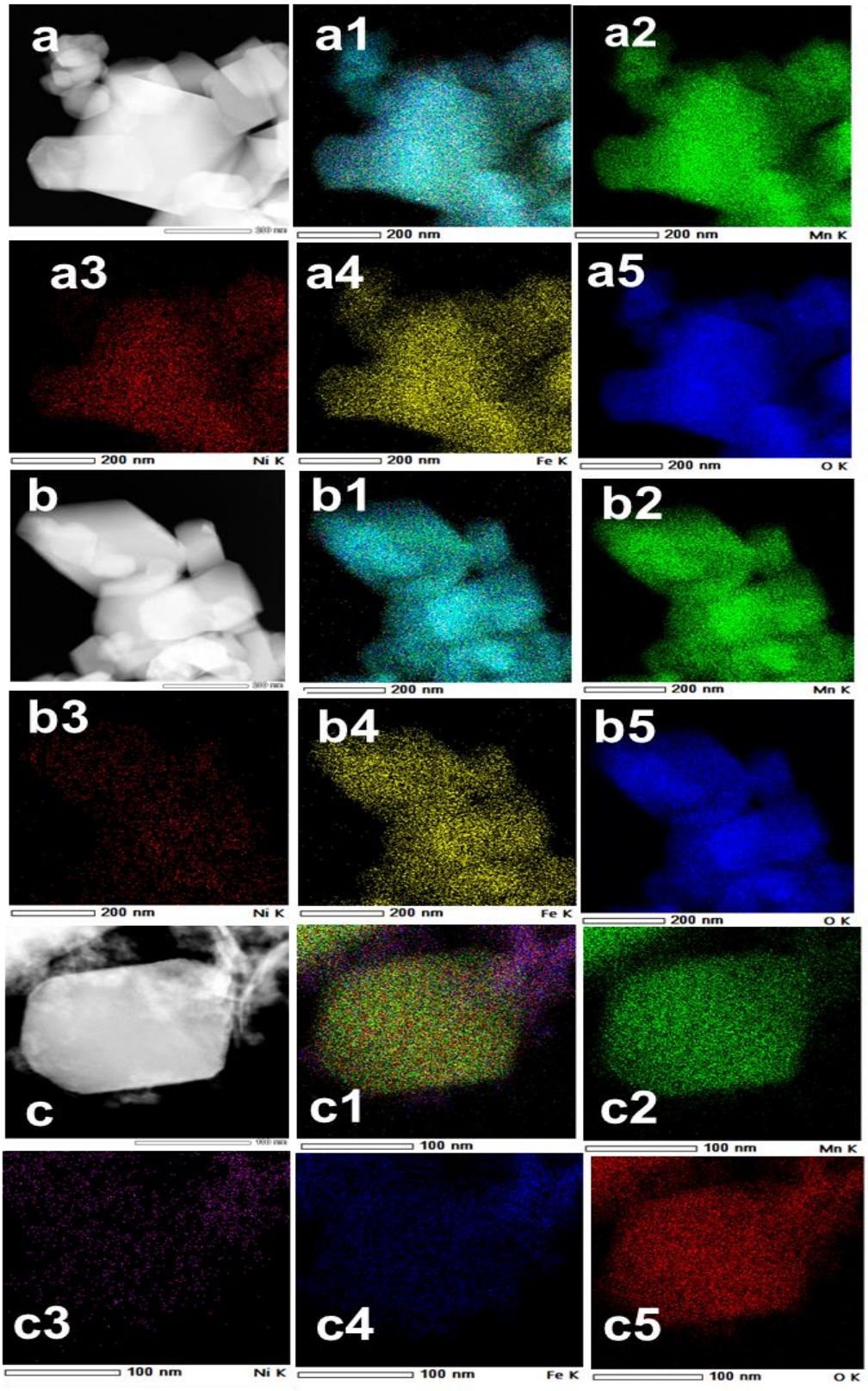

Figure 3a.10 STEM elemental mapping of α-MnO2, LMO, LMO@NFO1, LMO@NFO2, LMO@NFO3 respectively.

Figures 3a.9 and **3a.10 show** the STEM elemental mapping of the surface-modified cathode materials such as LMO@NFO1, LMO@NFO2, and LMO@NFO3 to understand the distribution of elements of core material and the elements of the surface-coated materials. It can be observed that all the elements are distributed throughout the particle structures of all three materials, which is in support of the successful coating of NFO materials over the surface of the LMO material.

3A.3.1.5 X-ray photoelectron spectroscopy study

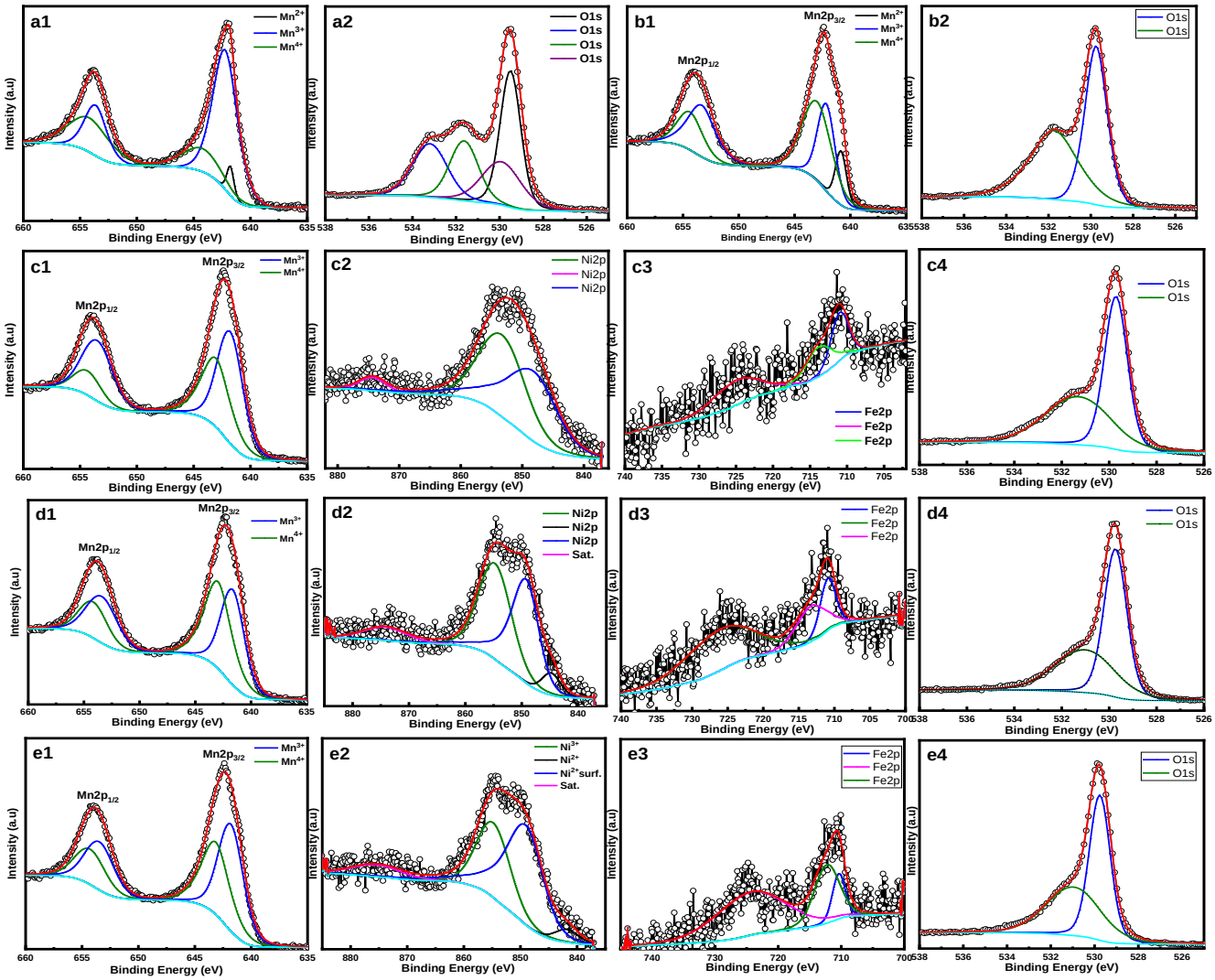

Figure 3a.11. Deconvoluted XPS spectra of (a1) Mn2p **(a2)** O1s of α-MnO_2, **(b1)** Mn2p, **(b2)** O1s of LMO, **(c1)** Mn2p, **(c2)** Ni2p, **(c3)** Fe2p, **(c4)** O1s of LMO@NFO1, **(d1)** Mn2p, **(d2)** Ni2p, **(d3)** Fe2p, **(d4)** O1s of LMO@NFO2, and **(e1)** Mn2p, **(e2)** Ni2p, **(e3)** Fe2p, **(e4)** O1s of LMO@NFO3.

XPS studies characterized the elemental valence electronic states, and deconvolution and peak fitting of all the elemental core levels were done using CasaXPS software. **Figure 3a.11** shows the XPS peak signals of α-MnO_2, LMO, LMO@NFO1, LMO@NFO2, and LMO@NFO3. The deconvoluted spectra of Mn2p in **Figure 3a.11(a1-e1)** core level exhibit two components, $Mn2p_{3/2}$ and $Mn2p_{1/2}$, due to spin-orbit coupling. The binding energies of $Mn2p_{3/2}$ and $Mn2p_{1/2}$ core levels are 641.9 eV (α-MnO_2), 642.3 eV (LMO), 642.3 eV (LMO@NFO1), 642.2 (LMO@NFO2), 642.3 (LMO@NFO3) and 653.8 eV (α-MnO_2), 653.9 eV (LMO), 653.9 eV (LMO@NFO1), 653.8 eV (LMO@NFO2), 653.9 eV (LMO@NFO3) respectively. The obtained binding energy values for Mn^{4+} and Mn^{3+} in Mn2p core levels are in close agreement with previous reports.[32,33] Due to spin-orbit coupling, the deconvoluted spectra of Ni2p in (**Figure 3a.11 (c2-e2))** core level demonstrate two components, $Ni2p_{3/2}$ and $Ni2p_{1/2}$. The binding energies of $Ni2p_{3/2}$ and $Ni2p_{1/2}$ core levels are not well separated. This is due to the quantity of Ni being deficient in which NFO material coated as a thin layer over the LMO material surface; the binding energy signal values are slightly deviated as compared to the element Ni, is due to the incorporation of iron and surface absorbed β-$Ni(OH)_2$.[34] The obtained binding energy values for the $Ni2p_{3/2}$ core levels are 852.2 eV (LMO@NFO1), 853.1 (LMO@NFO2), and 852.7 (LMO@NFO3). The deconvoluted spectra of Fe2p core levels exhibit two components, $Fe2p_{3/2}$ and $Fe2p_{1/2}$ are displayed in **Figure 3a.11(c3-e3).** The binding energies of $Fe2p_{3/2}$ core levels are 711.46 eV (LMO@NFO1), 711.16 eV (LMO@NFO2), 715.54 eV (LMO@NFO3), and $Fe2p_{1/2}$ core levels are 724.42 eV (LMO@NFO1), 724.02 eV (LMO@NFO2), 724.40 eV (LMO@NFO3). **Figure 3a.11(a2, b2, c4-e4)** depicts the deconvoluted spectra of O1s core levels observed at 529.5 eV (MNO), 529.7 eV (LMO), 529.7 eV (LMO@NFO1), 529.7 (LMO@NFO2), 529.8

(LMO@NFO3). The obtained binding energies indicate an M-O (M = Mn, Ni, Fe) relation with FWHM values of ~1.1, which indicates the characteristic values for the oxide lattice structure.

3A.3.2 Electrochemical analysis

3A.3.2.1 Cyclic voltammetry analysis

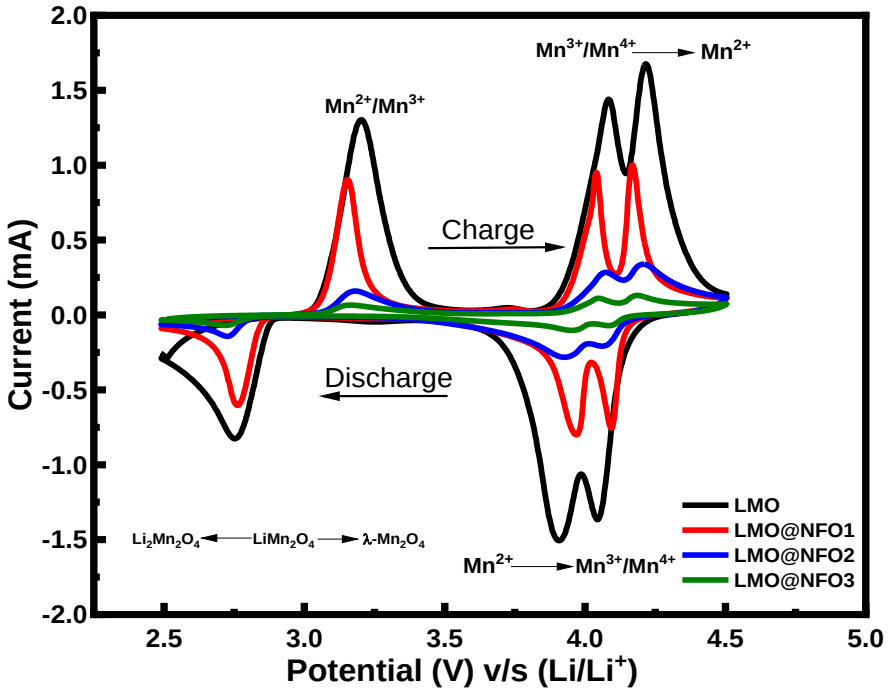

Figure 3a.12 **(a)** Cyclic voltammograms and **(b)** Nyquist plots of LMO, LMO@NFO1, LMO@NFO2, LMO@NFO3.

The electrochemical redox behavior and ion transport properties of the cathode-active materials were evaluated by cyclic voltammetry and electrochemical impedance spectroscopy. **Figure 3a.12a.** The cyclic voltammograms of LMO and surface-modified LMO materials were carried out between 2.5 and 4.5V conditions. The prominent peak at around 4.0-4.2V in all the materials corresponds to the redox couples Mn^{3+}/Mn^{4+}. The charging peaks appeared at 4.08V and 4.21 V with a peak separation potential of ~110 mV. The discharge peaks are at 3.9V and 4.05V, with a peak separation potential of 150 mV. The other charge peak appeared at ~3.2 V, and its redox pair peak appeared on the discharge curve at 2.75 V; the redox pair corresponds to the Li^+ extraction

of the cathode and insertion into the cathode active material. It is observed that the intensity of the redox peaks in cyclic voltammograms is decreased with the increased thickness of the surface coating layer. The kinetics of the ion transfer upon Li^+ extraction and insertion of the cathode materials have been evaluated by using electrochemical impedance spectroscopy.

3A.3.2.2 Electrochemical impedance spectroscopy study

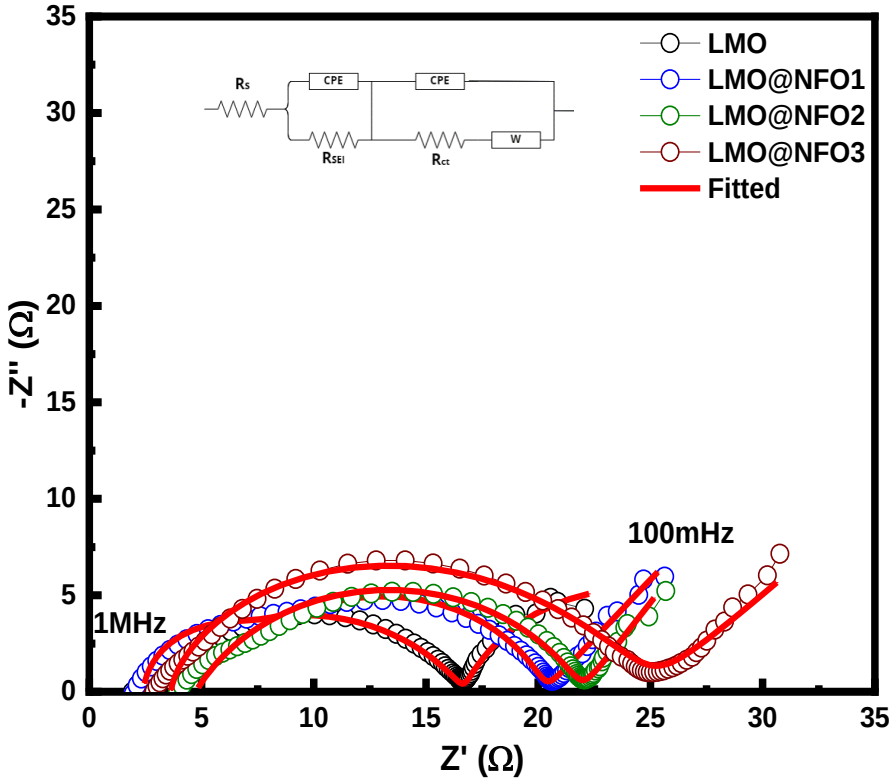

Figure 3a.12 Nyquist plots of LMO, LMO@NFO1, LMO@NFO2, LMO@NFO3.

EIS studies were performed to know the kinetics of the Li^+ insertion/exertion mechanism. F**igure 3a.12b.** shows the Nyquist plots of all the cathode materials, and the inset is the equivalent circuit used to fit the obtained experimental data. The circuit has three resistance elements R_s is the system resistance, R_{SEI} is the solid-electrolyte interface resistance, R_{ct} is the charge transfer resistance, the constant phase element is given as CPE, and W is the Warburg impedance. From

the Nyquist plots, it can be observed that the surface-modified LMO materials show more charge transfer resistance than pristine LMO. The equivalent circuit fitting values are given in **Table 3a.2**. All the materials show an overlapping semicircle in the higher frequency region associated with the SEI resistance (R_{SEI}) and charge transfer resistance (Rct), which indicates the insertion of Li ions into the electrode/electrolyte interface. With careful observation of the plots, two relatively small and large semicircles were observed at the higher and mid-frequency regions, respectively. This small semicircle at a higher frequency is due to the cathode-electrode resistance (R_{SEI}). The larger semicircle at the mid-frequency region corresponds to the charge transfer resistance (Rct). Among all the cathode materials, the LMO has shown the least charge transfer resistance, which indicates the enhanced electronic conductivity in LMO as it is barely exposed to the electrolyte in the cell. On the other hand, the surface-modified cathode materials have shown more charge transfer resistance than the pristine LMO material. As the surface coating percentage increases, the charge transfer resistance also increases due to the surface layer acting as a barrier, which results in lower specific capacities in charge-discharge studies. A straight line at the low-frequency region indicates the interface resistance and faster Li^+ ions diffusion through the electrolyte to the anode.

Material / **Parameter**	**LMO**	**LMO@NFO1**	**LMO@NFO2**	**LMO@NFO3**
R_s (Ω)	1.9	2.04	3.99	2.98
R_{SEI} (Ω)	1.75	4.12	3.94	2.27
R_{ct} (Ω)	13.01	12.46	14.17	19.85
χ^2	0.35	0.43	0.48	0.56

Table 3a.2. Resistance values were obtained from the EIS fitting data

3A.3.2.3 Galvanostatic charge-discharge studies

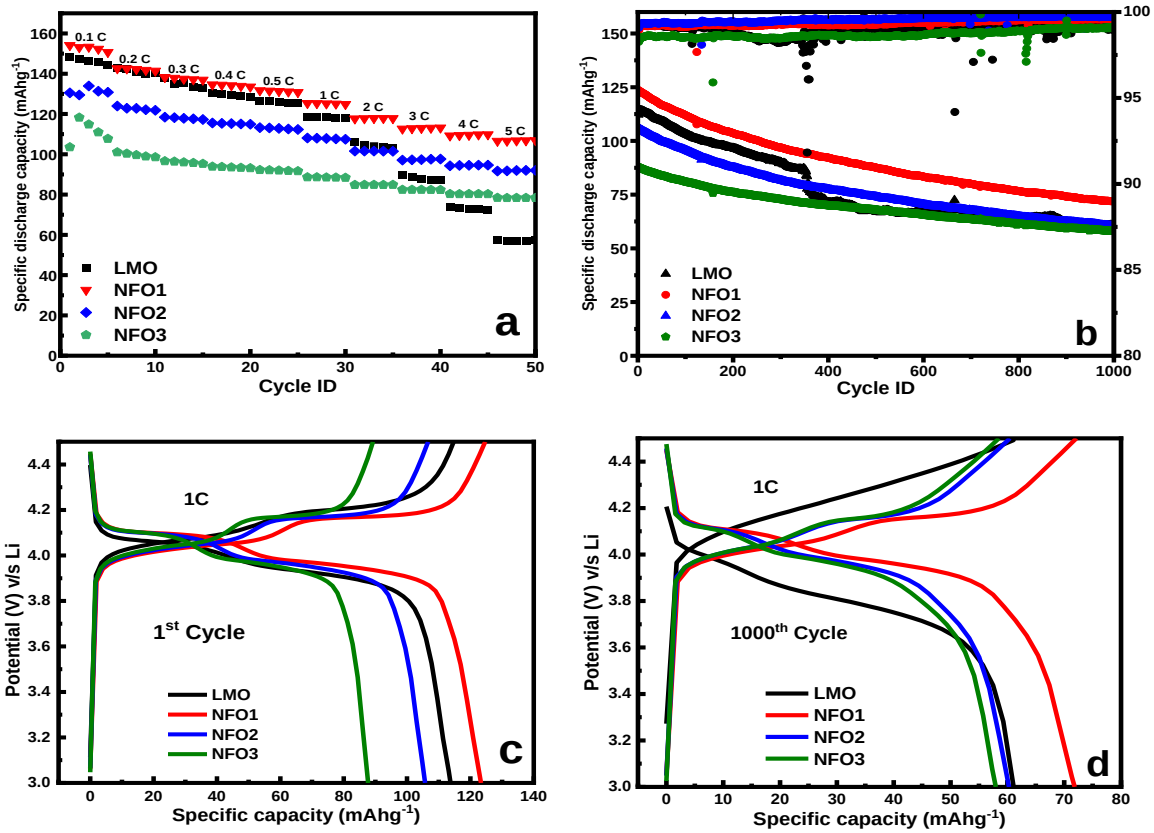

Figure 3a.13 **(a)** rate capability and **(b)** cycle stability **(c-d)** potential v/s specific capacity plots (1st cycle and 1000th cycle) of LMO, LMO@NFO1, LMO@NFO2, LMO@NFO3.

Figure 3a.13 (a) shows the rate capability test of the cathode materials at different current densities. The specific discharge capacities at lower current densities are higher than those at higher current densities due to the loss of Li^+ ions. This loss of Li^+ ions might be due to undesired side reactions at higher current rates, which restrict the flawless reversible lithiation and de-lithiation process. **Figure 3a.13b** shows the cycle stability of the cathode materials at 1C rate for continuous 1000 cycles. The initial specific discharge capacities of the cathode materials are 118.7 $mAhg^{-1}$, 125.3 $mAhg^{-1}$, 108.1 $mAhg^{-1}$, and 88.66 $mAhg^{-1}$ for LMO, NFO1, NFO2, and NFO3 respectively. After the continuous 1000 cycles, the cathode materials exhibited the specific discharge capacities 61.1 $mAhg^{-1}$, 71.8 $mAhg^{-1}$, 60.3 $mAhg^{-1}$, and 57.9 $mAhg^{-1}$ with capacity

retention of 51.5%, 57.3%, 55.8%, and 65.3%, respectively. It can be observed that, at the 1C rate, the specific discharge capacities of the cathode materials decrease as the surface coating percentage increases. The pristine LMO material has shown a little less specific discharge capacity than that of LMO@NFO1. The specific discharge capacities of LMO@NFO2 and LMO@NFO3 followed the decreased trend as the surface coating layer increased. Compared to the LMO cathode, LMO@NFO1, LMO@NFO2, and LMO@NFO3 showed long cycling stability, which implies that the surface coating of NFO acts as a protecting layer on LMO and this protecting layer helps in suppressing the Mn dissolution. It also confirms that the thick surface layer also leads to capacity loss but possesses more stability with high-capacity retention.

3A.4 Conclusions

In this work, the $LiMn_2O_4$ (LMO) cathode material has been modified with a surface coating of $NiFe_2O_4$ (NFO) using the sol-gel method. The coating layer composition ratio is varied, and electrochemical studies are being done to understand the effect of surface modification on the performance of the cathode material. Firstly, the MnO_2 nanostructures were prepared using the hydrothermal method. Later, the prepared MnO_2 was used as an Mn precursor for the synthesis of LMO by the sol-gel method. The prepared LMO materials are surface coated with the NFO material at different ratios of 1% to 3% to study the effect of surface layer thickness on electrochemical performance. The cathode materials LMO, LMO@NFO1, LMO@NFO2, and LMO@NFO3 have shown the initial specific discharge capacities, 118.7 $mAhg^{-1}$, 125.3 $mAhg^{-1}$, 108.1 $mAhg^{-1}$, and 88.66 $mAhg^{-1}$ respectively. These cathode active materials exhibited decreased specific discharge capacities 61.1 $mAhg^{-1}$, 71.8 $mAhg^{-1}$, 60.3 $mAhg^{-1}$, and 57.9 $mAhg^{-1}$ with capacity retention of 51.5%, 57.3%, 55.8%, and 65.3%, respectively at 1 C rate after 1000 continuous galvanostatic charge/discharge cycles.

3A.5 References

(1) Chen, H.; Sun, C. Recent Advances in Lithium-Rich Manganese-Based Cathodes for High Energy Density Lithium-Ion Batteries. *Chemical Communications* **2023**, *59* (59). https://doi.org/10.1039/d3cc02195e.

(2) Manthiram, A. A Reflection on Lithium-Ion Battery Cathode Chemistry. *Nature Communications* **2020**, *11* (1), 1550. https://doi.org/10.1038/s41467-020-15355-0.

(3) Mohamed, N.; Allam, N. K. Recent Advances in the Design of Cathode Materials for Li-Ion Batteries. *RSC Advances* **2020**, *10* (37), 21662–21685. https://doi.org/10.1039/D0RA03314F.

(4) Kim, J.; Cha, H.; Lee, H.; Oh, P.; Cho, J. Surface and Interfacial Chemistry in the Nickel-Rich Cathode Materials. *Batteries and Supercaps*. 2020, pp 309–322. https://doi.org/10.1002/batt.201900131.

(5) Muralidharan, N.; Self, E. C.; Dixit, M.; Du, Z.; Essehli, R.; Amin, R.; Nanda, J.; Belharouak, I.; Muralidharan, N.; Dixit, M.; Du, Z.; Essehli, R.; Amin, R.; Belharouak, I.; Self, E. C.; Nanda, J. Next-Generation Cobalt-Free Cathodes-A Prospective Solution to the Battery Industry's Cobalt Problem Broadly Highlights the Enormous Promise of "Zero-Cobalt" Li-Ion Batteries to Enable Sustainable Production of EVs in the Coming Decades. **2022**. https://doi.org/10.1002/aenm.202103050.

(6) Li, W.; Deng, H.; Jiang, J. Improved Electrochemical Performance of LiMn 2 O 4 via Ni and Co Gradient Doping. *Science of Advanced Materials* **2018**, *10* (12), 1823–1829. https://doi.org/10.1166/sam.2018.3425.

(7) Lee, M. J.; Lee, S.; Oh, P.; Kim, Y.; Cho, J. High Performance LiMn2O4 Cathode Materials Grown with Epitaxial Layered Nanostructure for Li-Ion Batteries. *Nano Letters* **2014**, *14* (2). https://doi.org/10.1021/nl404430e.

(8) Sturge, M. D. The Jahn-Teller Effect in Solids. *Solid State Physics - Advances in Research and Applications* **1968**, *20* (C). https://doi.org/10.1016/S0081-1947(08)60218-0.

(9) Wang, S.; Liu, H.; Xiang, M.; Guo, J.; Bai, W.; Bai, H.; Liu, X.; Su, C. Improved Electrochemical Properties and Kinetics of an LiMn2O4-Based Cathode Co-Modified: Via Cu Doping with Truncated Octahedron Morphology. *New Journal of Chemistry* **2020**, *44* (25). https://doi.org/10.1039/d0nj01290d.

(10) Lee, S.-N.; Park, D.; Kim, J.; Moon, S.-H.; Jang, J.-S.; Kim, S.-B.; Shin, J.-H.; Park, Y.; Park, K.-W. Enhanced Cycling Performance of Fe-doped LiMn 2 O 4 Truncated Octahedral Cathodes for Li-Ion Batteries. *ChemElectroChem* **2022**, *9* (11), e202200385. https://doi.org/10.1002/celc.202200385.

(11) Sharma, P.; Das, C.; Indris, S.; Bergfeldt, T.; Mereacre, L.; Knapp, M.; Geckle, U.; Ehrenberg, H.; Darma, M. S. D. Synthesis and Characterization of a Multication Doped Mn Spinel, LiNi 0.3 Cu 0.1 Fe 0.2 Mn 1.4 O 4 , as 5 V Positive Electrode Material. *ACS Omega* **2020**, *5* (36), 22861–22873. https://doi.org/10.1021/acsomega.0c02174.

(12) Sha, O.; Tang, Z.; Wang, S.; Yuan, W.; Qiao, Z.; Xu, Q.; Ma, L. The Multi-Substituted LiNi0.475Al0.01Cr0.04Mn1.475O3.95F0.05 Cathode Material with Excellent Rate Capability and Cycle Life. *Electrochimica Acta* **2012**, *77*, 250–255. https://doi.org/10.1016/j.electacta.2012.05.096.

(13) Ji, H.; Wu, J.; Cai, Z.; Liu, J.; Kwon, D. H.; Kim, H.; Urban, A.; Papp, J. K.; Foley, E.; Tian, Y.; Balasubramanian, M.; Kim, H.; Clément, R. J.; McCloskey, B. D.; Yang, W.; Ceder, G.

Ultrahigh Power and Energy Density in Partially Ordered Lithium-Ion Cathode Materials. *Nature Energy* **2020**, *5* (3), 213–221. https://doi.org/10.1038/s41560-020-0573-1.

(14) Li, Q. L.; Xu, W. Q.; Bai, H. L.; Guo, J. M.; Su, C. W. ZnO-Coated LiMn2O4 Cathode Material for Lithium-Ion Batteries Synthesized by a Combustion Method. *Ionics* **2016**, *22* (8), 1343–1351. https://doi.org/10.1007/s11581-016-1655-8.

(15) Liu, H.; Yang, F.; Guo, J.; Xiang, M.; Bai, H.; Wang, R.; Su, C. Facile Combustion Synthesis of Amorphous Al2O3-Coated LiMn2O4cathode Materials for High-Performance Li-Ion Batteries. *New Journal of Chemistry* **2021**, *45* (23), 10534–10540. https://doi.org/10.1039/d1nj01052b.

(16) Lai, F.; Zhang, X.; Wu, Q.; Zhang, J.; Li, Q.; Huang, Y.; Liao, Z.; Wang, H. Effect of Surface Modification with Spinel NiFe2O4 on Enhanced Cyclic Stability of LiMn2O4 Cathode Material in Lithium Ion Batteries. *ACS Sustainable Chemistry and Engineering* **2018**, *6* (1). https://doi.org/10.1021/acssuschemeng.7b02876.

(17) Tomon, C.; Sarawutanukul, S.; Phattharasupakun, N.; Duangdangchote, S.; Chomkhuntod, P.; Joraleechanchai, N.; Bunyanidhi, P.; Sawangphruk, M. Core-Shell Structure of LiMn2O4 Cathode Material Reduces Phase Transition and Mn Dissolution in Li-Ion Batteries. *Communications Chemistry* **2022**, *5* (1). https://doi.org/10.1038/s42004-022-00670-y.

(18) Huang, Y.; Dong, Y.; Li, S.; Lee, J.; Wang, C.; Zhu, Z.; Xue, W.; Li, Y.; Li, J. Lithium Manganese Spinel Cathodes for Lithium-Ion Batteries. *Advanced Energy Materials* **2021**, *11* (2), 2000997. https://doi.org/10.1002/aenm.202000997.

(19) Luo, X.; Xiang, M.; Li, Y.; Guo, J.; Liu, X.; Bai, H.; Bai, W.; Su, C. Surface-Orientation for Boosting the High-Rate and Cyclability of Spinel LiNi0.02Mn1.98O4 Cathode Material. *Vacuum* **2020**, *179*, 109505. https://doi.org/10.1016/j.vacuum.2020.109505.

(20) Wang, P.; Li, H.; Wei, Y.; Zhao, D.; Mao, L.; Cui, X.; Zhang, H.; Zhou, X.; Li, S. Truncated Octahedral LiNi0.5Mn1.5O4 with Excellent Electrochemical Properties for Lithium-Ion Batteries Prepared by a Graphite Assisted Calcination Method. *New Journal of Chemistry* **2019**, *43* (38), 15396–15404. https://doi.org/10.1039/c9nj03174j.

(21) Tron, A.; Park, Y. D.; Mun, J. AlF3-Coated LiMn2O4 as Cathode Material for Aqueous Rechargeable Lithium Battery with Improved Cycling Stability. *Journal of Power Sources* **2016**, *325*. https://doi.org/10.1016/j.jpowsour.2016.06.049.

(22) Paparoni, F.; Mijit, E.; Darjazi, H.; Nobili, F.; Zitolo, A.; Di Cicco, A.; Parmar, R.; Gunnella, R.; Rezvani, S. J. Oxide Coating Role on the Bulk Structural Stability of Active LiMn2O4 Cathodes. *Journal of Physical Chemistry C* **2023**, *127* (18). https://doi.org/10.1021/acs.jpcc.3c00342.

(23) Shivamurthy, B. P.; Thripuranthaka, M.; Shelke, M. V.; Nayaka, G. P. Formation of the Secondary Phase Domain by Multi-Cation Substitution for the Superior Electrochemical Performance of Spinel Cathodes for High-Voltage Li-Ion Batteries. *ACS Applied Energy Materials* **2022**, *5* (12), 15345–15355. https://doi.org/10.1021/acsaem.2c02667.

(24) Shivamurthy, B. P.; Thripuranthaka, M.; Shelke, M. V.; Nayaka, G. P. Influence of the Crystal Plane Orientation in Enhancing the Electrochemical Performance of a Trication-Substituted Cathode for Li-Ion Batteries. *Energy and Fuels* **2024**, *38* (5). https://doi.org/10.1021/acs.energyfuels.3c03794.

(25) Wan, X.; Yang, S.; Cai, Z.; He, Q.; Ye, Y.; Xia, Y.; Li, G.; Liu, J. Facile Synthesis of MnO2 Nanoflowers/N-Doped Reduced Graphene Oxide Composite and Its Application for Simultaneous Determination of Dopamine and Uric Acid. *Nanomaterials* **2019**, *9* (6). https://doi.org/10.3390/nano9060847.

(26) Huang, X.; Cui, W.; Yu, J.; Lu, S.; Liao, X. Preparation of Mesoporous MnO2 Catalysts with Different Morphologies for Catalytic Ozonation of Organic Compounds. *Catalysis Letters* **2022**, *152* (5). https://doi.org/10.1007/s10562-021-03745-y.

(27) Jia, C.; Zhang, Y.; Kong, Q.; Wang, Q.; Chen, G.; Guam, H. T.; Dong, C. Soft-Template Synthesis of Mesoporous NiFe2O4 for Highly Sensitive Acetone Detection. *Journal of Materials Science: Materials in Electronics* **2020**, *31* (8). https://doi.org/10.1007/s10854-020-03151-x.

(28) Slautin, B.; Alikin, D.; Rosato, D.; Pelegov, D.; Shur, V.; Kholkin, A. Local Study of Lithiation and Degradation Paths in Limn2o4 Battery Cathodes: Confocal Raman Microscopy Approach. *Batteries* **2018**, *4* (2). https://doi.org/10.3390/batteries4020021.

(29) Ramana, C. V.; Massot, M.; Julien, C. M. XPS and Raman Spectroscopic Characterization of LiMn2O 4 Spinels. In *Surface and Interface Analysis*; 2005; Vol. 37. https://doi.org/10.1002/sia.2022.

(30) Anzue, N.; Itoh, T.; Mohamedi, M.; Umeda, M.; Uchida, I. In Situ Raman Spectroscopic Study of Thin-Film Li1-xMn2O4 Electrodes. *Solid State Ionics* **2003**, *156* (3–4). https://doi.org/10.1016/S0167-2738(02)00693-8.

(31) Buchberger, D. A.; Hamankiewicz, B.; Michalska, M.; Głaszczka, A.; Czerwinski, A. Ex Situ Raman Mapping of LiMn2O4 Electrodes Cycled in Lithium-Ion Batteries. *ACS Omega* **2024**. https://doi.org/10.1021/acsomega.4c01480.

(32) Marchini, F.; Rubi, D.; Del Pozo, M.; Williams, F. J.; Calvo, E. J. Surface Chemistry and Lithium-Ion Exchange in LiMn2O4 for the Electrochemical Selective Extraction of LiCl from Natural Salt Lake Brines. *Journal of Physical Chemistry C* **2016**, *120* (29). https://doi.org/10.1021/acs.jpcc.5b11722.

(33) Tang, C. Y.; Leung, K.; Haasch, R. T.; Dillon, S. J. LiMn2O4 Surface Chemistry Evolution during Cycling Revealed by in Situ Auger Electron Spectroscopy and X-Ray Photoelectron Spectroscopy. *ACS Applied Materials and Interfaces* **2017**, *9* (39). https://doi.org/10.1021/acsami.7b10442.

(34) Ganesan, P.; Sivanantham, A.; Shanmugam, S. Inexpensive Electrochemical Synthesis of Nickel Iron Sulphides on Nickel Foam: Super Active and Ultra-Durable Electrocatalysts for Alkaline Electrolyte Membrane Water Electrolysis. *Journal of Materials Chemistry A* **2016**, *4* (42). https://doi.org/10.1039/c6ta04499a.

Chapter 3B

Electrochemical performance enhancement of $LiMn_2O_4$ cathode materials for Li-ion batteries through nickel aluminate surface modification

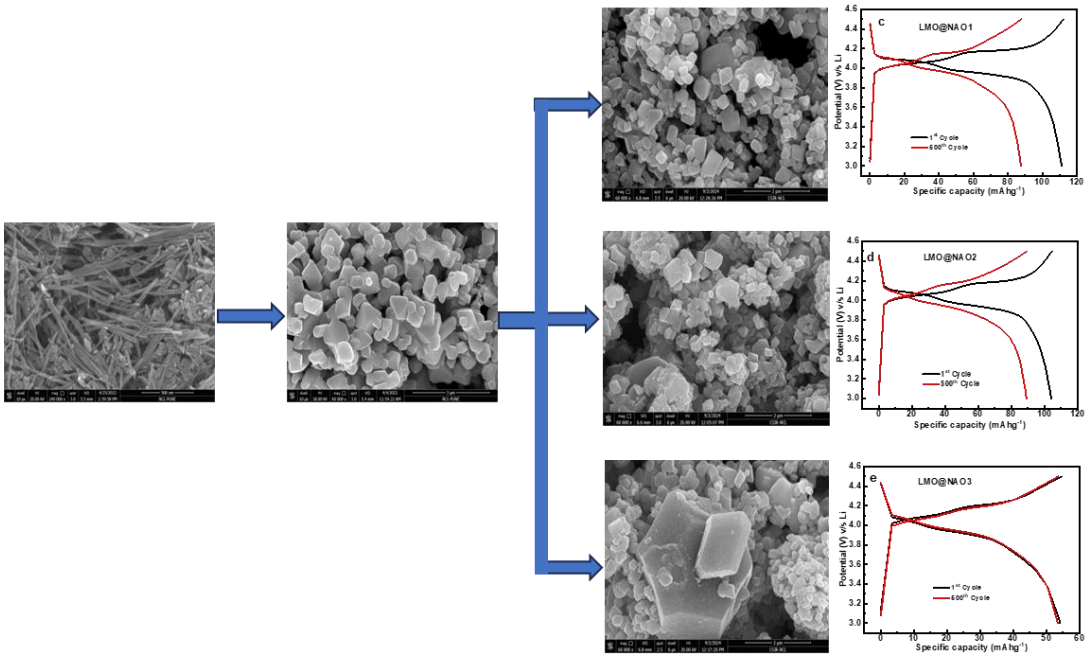

Highlights

- This study showcases modifying the LMO cathode material's surface by applying a thin $Ni_xAl_yO_z$ (NAO) spinel oxide material layer.
- This approach addresses the issues of Mn dissolution and Jahn-Teller distortion.
- Our research involves preparing shape-controlled LMO cathode materials with a truncated octahedron structure featuring preferential crystal plane orientation that facilitates faster Li-ion diffusion.
- A thin layer coating of NAO materials, ranging from 1% to 3%, was applied to the exterior of the LMO materials.
- These surface-modified LMO cathode materials exhibited improved cycling stability and enhanced rate performance within the 3.0 – 4.5 V voltage range.
- Investigate the influence of coating on electrochemical performance.

- The results of this chapter will be published as **BP Shivamurthy**, MV Shelke, **GP Nayaka*,** Electrochemical performance enhancement of $LiMn_2O_4$ cathode materials for Li-ion batteries through nickel aluminate surface modification.

3B.1 Introduction

The main obstacle impeding widespread commercial use of these positive electrode materials is their limited longevity during continuous charge-discharge cycles, especially at elevated temperatures and voltages. This shortened lifespan results from harmful side reactions, including manganese ion dissolution into the electrolyte, structural instability induced by Jahn-Teller distortion,[1] and decomposition of Mn^{3+} ions into Mn^{2+} and Mn^{4+} ions.[2] The resulting Mn^{2+} ions dissolve into the electrolyte, undermining the stability of the electrode-electrolyte interface and subsequently degrading cathode performance.[3–5] Addressing the challenges of LMO-based cathode materials is essential for their extensive commercial application. Researchers have explored numerous strategies to overcome these issues, such as replacing Mn ions with alternative cations[6–8] and anions,[9,10] applying oxide coatings,[11,12] designing core-shell structures[13,14], electrolyte coatings[15] and employing fluorides.[16,17] Additionally, scientists have investigated methods to modify morphology, adjust particle size, and alter the orientation of crystallographic planes in LMO-type cathodes.[17–19] Despite these efforts, the existing problems have not been fully resolved, highlighting the necessity for ongoing research and development to enhance the performance of these cathode materials.[20] Researchers have employed various strategies to enhance the efficiency of LMO cathode materials. These include substituting elements into Mn sites[21] and applying a protective layer of stable materials to modify the surface.[22] The cathode materials' surface is coated with inert substances to shield against acidic components in electrolytes, particularly HF. Such coatings may contain carbon,[22] graphite[23], metal halides,[9] or metal oxides.[24] Among these surface modification techniques, applying metal oxide coatings has proven effective for addressing both structural and thermal challenges associated with spinel cathode materials.[11,12]

Our earlier research examined LMO cathodes modified with tri-cation substitutions, including Ni, Fe, and Al.[8] We investigated a range of spinel cathode materials with mixed phases to assess the impact of phase mixing on cathode performance. Additionally, we explored a group of spinel cathodes featuring exposed (111) planes.[17] These exposed planes significantly enhanced electrochemical performance when optimally proportioned. Ni acted as a capacity booster in both studies, while Fe and Al functioned as electrochemical stabilizers, collectively improving overall cathode performance. Building on these findings and considering the effective use of Ni and Al elements in enhancing electrochemical performance, we now employ Ni and Al for surface modification of LMO materials using nickel aluminum oxide $Ni_xAl_yO_z$ (NAO). As of our knowledge, the combination of nickel and aluminum oxide has not been explored in the past literature; hereby, we shed light on the study of the influence of nickel aluminum oxide coating over lithium manganese oxide spinel to enhance the electrochemical stability of Li-ion batteries.

The LMO materials preparation steps were carried out according to the methods discussed in Chapter 3A. Using shape-controlled α-MnO_2 nanostructures, we have prepared morphology-controlled truncated LMO materials. The LMO material's surface is coated with NAO layers, acting as a protective shield. This shield prevents Mn dissolution in electrolytes, resulting in enhanced electrochemical performance and extended cycle life.

3B.2 Methods and materials

3B.2.1 Synthesis of α–MnO_2

The synthesis of α–MnO2 nanorods involved dissolving 5 g of Manganese acetate ($Mn(CH_3COO)_2 \cdot 4H_2O$) (Sigma Aldrich >99%) in 80 ml of deionized water. To this solution, 4.7 g of ammonium persulfate was added, and the mixture was continuously stirred for 2 hours. The resulting homogeneous solution, containing brown-colored particles, was then transferred to a

Teflon inline stainless-steel autoclave for hydrothermal treatment. The autoclave reaction proceeded at 120 °C for 12 hours. After the reaction, the solution was allowed to cool to room temperature naturally. Subsequently, the product was filtered, washed, and dried in a vacuum oven at 100 °C for 10 hours. The final step involved thoroughly grinding the dried α–MnO2 material into a fine powder.

3B.2.2 Preparation of $LiMn_2O_4$

$LiMn_2O_4$ with truncated octahedral morphology was synthesized by combining precise amounts of pre-made Manganese dioxide ($\alpha - MnO_2$) nanorods and lithium hydroxide (LiOH) (Sigma Aldrich > 99%) in 60 ml of deionized water. The mixture was continuously stirred to achieve uniformity. Excess water was removed by evaporating the slurry at 80 °C. The resulting dry powder underwent heat treatment at 750 °C for 12 hours, with the temperature increasing rate 3 °C/min. After naturally cooling to room temperature, the powder was thoroughly ground. The final product was collected as $LiMn_2O_4$ material exhibiting a truncated octahedron geometric shape.

3B.2.3 Surface modification of $LiMn_2O_4$ with Nickel aluminum oxide

Using the sol-gel technique, the as-prepared $LiMn_2O_4$ cathode materials undertook surface modification with nickel aluminate. The process involved dissolving a stoichiometric ratio of Nickel acetate ($Ni(CH_3COO)_2 \cdot 4H_2O$) (Sigma Aldrich >98%) and Aluminum nitrate ($Al(NO_3)_3 \cdot 9H_2O$) (Sigma Aldrich >98%)) of the desired percentage composition in 50 ml of deionized water. Citric acid was added to the solution, maintaining a 1:2 molar ratio between metal ions and citric acid. The resulting mixture was stirred at 50 °C for a duration of 2 hours. A specified quantity of $LiMn_2O_4$ materials was added to the solution while continuously stirring and heating until a thick gel was produced. The gel was then dried in a vacuum oven at 100 °C for 12 hours. Following this,

the dried material was ground into a fine powder and calcined at 750 °C for 8 hours, with the temperature rising at 5 C/min rate. After calcination, the powder was collected and subjected to structural characterization to validate the surface modification of the LMO cathode material. This process was repeated, adjusting the NAO precursor molar ratios to 1%, 2%, and 3% while keeping the LMO quantity unchanged. Based on their coating percentages, the resulting surface-modified cathode materials were designated as LMO@NAO1, LMO@NAO2, and LMO@NAO3.

3B.2.4 Structural characterization

X-ray diffraction (XRD) analysis was employed to examine the crystal structure of the synthesized materials. The XRD measurements were conducted using a Panalytical Xpert Pro instrument, utilizing Cu as the X-ray source. The obtained XRD patterns were successfully refined using the Rietveld refinement technique implemented in the Fullprof suite software. The starting parameters were obtained from standard PDF numbers 44-0141 for α-MnO2, 00-035-0782 for LMO, and 23-10278 for NAO. Raman spectroscopy was employed for the structural examination, utilizing an IndiRam CTR500 confocal Raman microscope equipped with a Nd: YAG diode laser DL-532 (532 nm wavelength). The materials' surface structure and morphology were examined using advanced microscopy techniques. A Field Emission Scanning Electron Microscope (FE-SEM), specifically the FEI-NOVA NANOSEM 450 model, was employed. Additionally, a High-Resolution Transmission Electron Microscope (HR-TEM), namely the JEOL JEM F-200, equipped with an energy dispersive spectrometer (EDS), was utilized for further analysis. X-ray photoelectron spectroscopy (XPS) is utilized to examine the valence states of the elements. This analysis uses the Thermo Scientific Model K-alpha XPS device, which employs monochromatic Al-Kα as its X-ray source. The XPS peaks are deconvoluted by considering the reference for binding energy taken as C1s at 284.8 eV by using CasaXPS software.

3B.2.5 Electrochemical characterization

To examine the electrochemical characteristics of surface-modified LMO cathode materials, researchers assembled 2032-type coin cells. The positive electrodes were fabricated using 80% active cathode material, 10% polyvinylidene difluoride (PVDF), and 10% Super C-60 carbon black by weight. The components were thoroughly combined with adequate N-methyl pyrrolidone solvent to create a homogeneous mixture. This mixture was then applied to a carbon-coated aluminum sheet using the doctor blade technique and dried in a vacuum at 100 ℃ for 12 hours. Following this, the aluminum foil with the cathode coating underwent calendaring and was cut into circular shapes measuring 14 mm in diameter. For the assembly of 2032-type coin cells, circular discs of coated aluminum foil were employed as cathodes, while Li metal discs served as anodes. Celgard-2325 was utilized as the separator, and the electrolyte comprised 1M $LiPF_6$ in a 1:1:1 ratio of EC/DMC/EMC. The cell fabrication process was carried out in a glove box filled with argon, where O_2 and H_2O levels were maintained at around 0.1 ppm. The assembled coin cells were utilized for the electrochemical characterization using various techniques. Cyclic voltammetry and electrochemical impedance spectroscopy (EIS) were conducted using a Metrohm electrochemical workstation (Multiautolab M204). For galvanostatic charge/discharge measurements, a Neware battery testing system (CT4008) was employed.

3B.3 Result and Discussion

3B.3.1 Material characterization

3B.3.1.1 X-ray diffraction (XRD) studies

The X-ray diffraction patterns proved in **Figure 3b.1** for all materials confirmed the respective crystal structures. The materials possess high crystallinity with cubic phase. The characteristic diffraction peaks of the three surface-coated materials have no significant changes compared with

the diffraction, which indicates that the thin layer coating of $Ni_xAl_yO_z$ does not induce the structural changes in $LiMn_2O_4$ much. Still, small diffraction peaks at 22, 34, and 54° indicate the successful formation of a thin layer over the surface of the LMO particles.[24] The XRD patterns of LMO and surface-modified LMO materials are indexed to cubic phase with Fd-3m space group; in the crystal structure, the atoms such as Li, Mn, and O are residing at 8a tetrahedral sites, 16d octahedral sites, and 32e Wyckoff sites respectively.

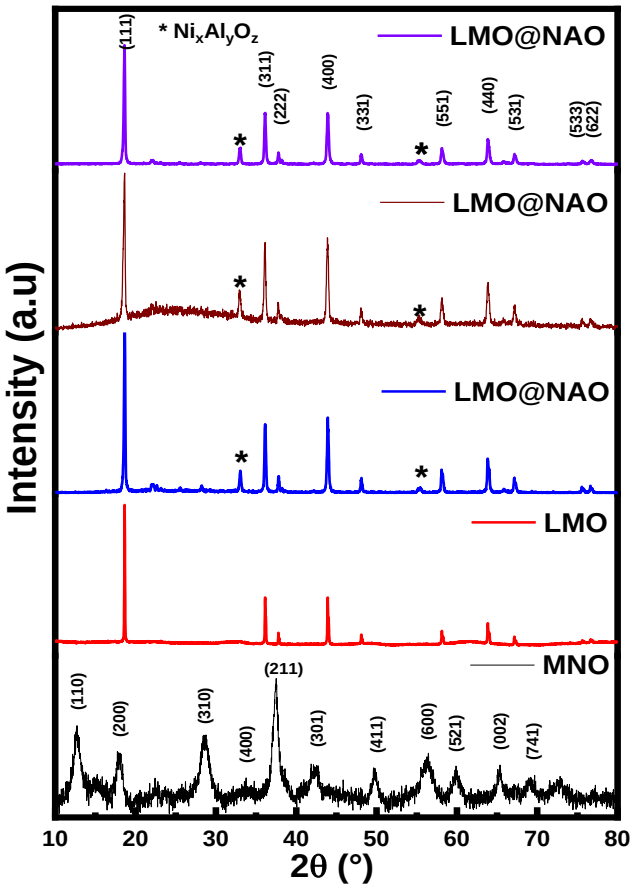

Figure 3b.1 X-ray diffraction patterns of XRD data of α-MnO_2, LMO, LMO@NFO1, LMO@NFO2, and LMO@NFO3 materials.

All the diffraction peaks of α-MnO_2 are attributed to the pure tetragonal crystal structure with the space group I4/m, and the pattern is well matched with the standard JCPDS number 44-0141. The obtained lattice constant values of α-MnO_2 are a=b=9.7847 and c= 2.8630 and are well matched with the literature reports.[25,26] The diffraction peaks of LMO, LMO@NAO1,

LMO@NAO2, and LMO@NAO3 materials were attributed to the non-stoichiometric cubic spinel structure with the space group Fd-3m, and the patterns were well-matched with standard JCPDS number 035-0782. Some peaks also matched with X-ray diffraction patterns and were well matched with crystallographic open database code number 2310278, which belongs to the nickel aluminum oxide material $Al_{4.6}Ni_{1.4}O_6$ material reported by JM Cowley.[27] The synthesized NAO-coated LMO materials formed octahedral structures with exposed (111) planes. These structures are similar to our previous reports, in which we studied the influence of the exposed (111) plane with compactly packed Mn ions and less densely packed (100) and (110) planes.[17] Herein, in this study, the surface of the LMO spinel is modified by coating with the orthorhombic NAO structure by varying the coating percentage. The patterns matched the pdf file number 23-10278.[28] In **Figure 3b.1**. A small peak can be observed at around 33^0 and 55^0 in surface-modified cathode materials due to the formation of an NAO layer over the surface of the particles of LMO material. These minor peaks at 2θ ~33° and 2θ ~55° of the NAO surface of cathode materials are indexed as (220) and (420) planes.[28] Further, to get detailed information about the crystal structures, Rietveld refinement has been performed with the X-diffraction data using Fullprof suite software to obtain detailed information about the crystal structures. Figure 2b and Table 1 presents the refinement patterns and data. The residual data of the refinement is given in supplementary information.[13] Rietveld refinement studies plotted in **Figure 3b.2** were performed with the Fd-3m space group as a reference for the LMO cubic spinel structure and the pbmm space group as a reference for the NAO orthorhombic structure and the lattice parameters obtained are given in **Table 3b.1**.

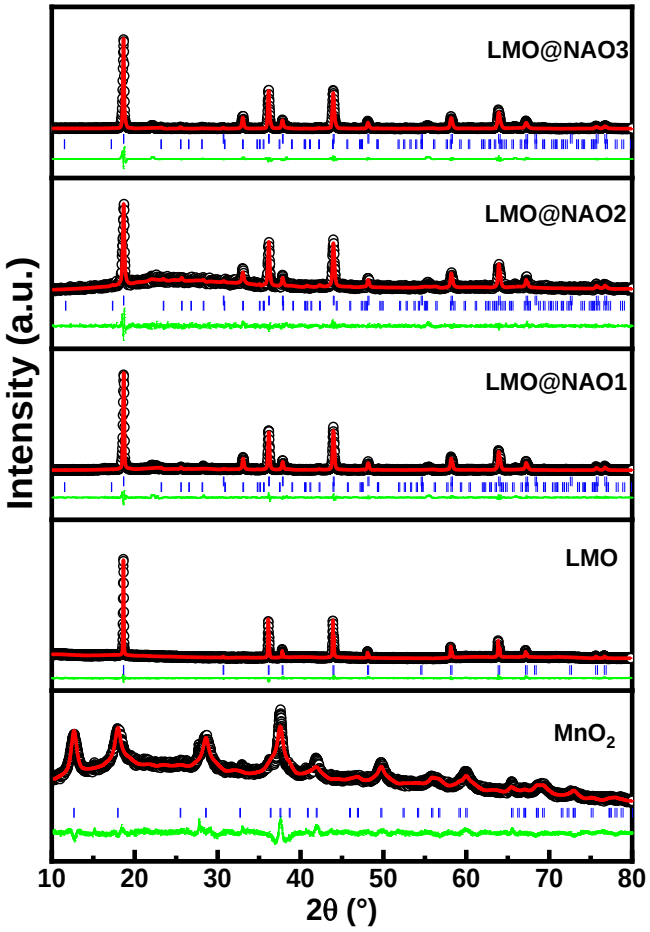

Figure 3b.2 Rietveld refinement profile plots of XRD data of α-MnO_2, LMO, LMO@NFO1, LMO@NFO2, and LMO@NFO3 materials.

The α - MnO_2 and LMO materials were well fitted with a single phase, while LMO@NAO1, LMO@NAO2, and LMO@NAO3 materials were fitted with a dual phase. This dual phase is due to low fractions of NAO present over the particle surface LMO. **Tables 3b.2 and 3b.3** display the atomic displacement parameters for the refined structures of LMO and NAO materials, where it is observed that some of the fractional coordinates are negative. The negative fractional coordinates can result in the negative Wyckoff positions as well. Generally, a negative Wyckoff position / negative fractional coordinates can result from applying symmetry operations to the atomic positions.[29] The crystal structures often exhibit symmetry operations, such as rotations, reflections, or translations. The consequences of these negative coordinates or Wyckoff

positions may lead to the atomic displacement from its ideal lattice position, which affects the bonding and coordination environment of the atom, or it influences the stability of the crystal structure. Here in our case the thin layer of nickel aluminum oxide coating over the surface of the LMO particles has influenced the structural stability and improved the stability which made the surface modified cathode materials act stable during electrochemical applications.

Sample	**Space group**	**Lattice constant (Å)**	**Cell volume**	**R_f**	**$\chi 2$**	**Phase fraction (%)**
α - MnO_2	$Fd\bar{3}m$	a, b = 9.87 c=2.84	277.93	16.1	2.84	100
LMO	$Fd\bar{3}m$	a=b=c=8.234	559.18		1.44	100
LMO@NFO1	$Fd\bar{3}m$	a=b=c=8.234	558.29	3.6	1.9	97.05
	pbmm	a=7.66 b=6.96 c=2.89	154.5	25.4		2.95
LMO@NFO2	$Fd\bar{3}m$	a=b=c=8.233	558.25	4.9	1.3	97.17
	pbmm	a=7.58 b=6.93 c=2.90	152.58	22.2		2.83
LMO@NFO3	$Fd\bar{3}m$	a=b=c=8.234	558.39	4.57	2.6	97.75
	pbmm	a=7.67 b=6.97 c=2.89	155.10	24.9		2.25

Table 3b.1. Rietveld refinement results of XRD data of the α – MnO_2, LMO, LMO@NAO1, LMO@NAO2, and LMO@NAO3 materials.

$LiMn_2O_4$, Space group: Fd-3m, a=b=c=8.23, α=β=γ=90, Crystal System: Cubic					
Atom	X	Y	Z	Biso	Occ.
Li	0.125	0.125	0.125	0.16745	0.28271
Mn	0.500	0.500	0.500	0.05669	0.51423
O	0.26085	0.26085	0.26085	0.07230	1.02011

Table 3b.2. Atomic displacement parameters for LMO material phase.

$Al_{4.6}Ni_{1.4}O_6$, Space group: Pbmm, a=7.66, b=6.96, c=2.89, α=β=γ=90, Crystal System: Orthorhombic					
Atom	X	Y	Z	Biso	Occ.
Ni1	0.11771	0.25000	0.50000	1.000	0.25925
Al1	0.92005	0.58935	0.50000	1.000	0.50829
O1	0.56473	0.25000	0.00000	1.000	1.01982
Ni2	0.11771	0.25000	0.50000	1.000	0.25925
Al2	-0.39328	0.50429	0.00000	1.000	0.69592
O2	0.76289	0.10835	0.50000	1.000	1.00332
Ni3	0.89411	2.11265	0.50000	1.000	0.10346
Al3	0.35421	0.25000	0.00000	1.000	0.36697

Table 3b.3. Atomic displacement parameters for NAO material phase.

3B.3.1.2 Raman spectroscopic analysis

The Raman spectra of LMO, LMO@NAO1, LMO@NAO2, and LMO@NAO3 samples are displayed in **Figure 3b.3.** The observed Raman band peak positions align closely with those reported recently for LiMn2O4, exhibiting only minor deviations.[30] The minor alteration in the positions can be attributed to applying a thin coating of other oxide substances of nickel and aluminum on the LMO material's surface. $LiMn_2O_4$ was anticipated to exhibit five Raman-active modes, including one A_{1g}, one E_g, and three F_{2g}. In this study, the A_{1g} band, associated with the vibration modes of Mn-O bonds within the MnO_6 octahedrons,[31] was observed in the range of 623

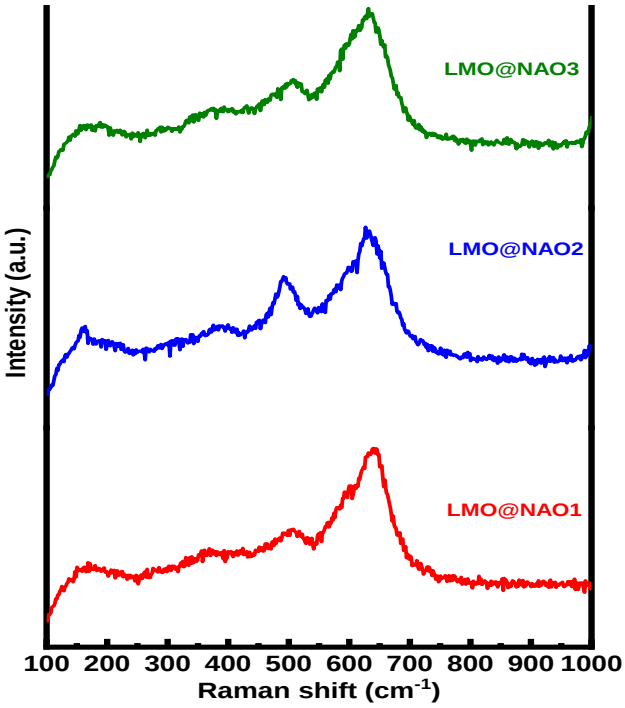

Figure 3b.3. Raman spectra of the α – MnO_2, LMO, LMO@NAO1, LMO@NAO2, and LMO@NAO3 materials.

The Mn-O band was observed at different wavenumbers for various samples: approximately 654 cm^{-1} for LMO, 633 cm^{-1} for LMO@NAO1, 640 cm^{-1} for LMO@NAO2, and 621 cm^{-1} for LMO@NAO3. The Eg band, which is associated with the weak oxygen vibration modes, typically appears between 403 and 412 cm^{-1}. This band corresponds to the M-O-M bond deformation mode, which is influenced by surface modifications.[30] The A1g band, the most intense peak in the Raman spectrum of spinel structures, is attributed to the symmetric stretching vibration of oxygen atoms along Mn-O bonds. It usually appears as a sharp, prominent peak in the range of 620-650 cm^{-1}, providing valuable information about the local structure and symmetry of the MnO_6 octahedra in the spinel lattice. Among the three F_{2g} modes, two bands - F_{2g}(II) and F_{2g}(III) - correspond to high-frequency scattering. These primarily result from oxygen atom vibrations, with a minor contribution from manganese atoms. In our cathode active materials, these bands manifest

as subtle shoulders in the range of approximately 575 to 632 cm^{-1}. On the other hand, the F2g(I) mode is associated with low-frequency scattering and primarily involves the vibration of lithium atoms. The low-intense scattering band, F_{2g}(I), appeared at about ~380 cm^{-1}, corresponding to the vibration of Li-O bonds corresponding to the mentioned red band in the spectra related to the LiO_4 tetrahedral group.[32,33] This low-intensity scattering band provides valuable information about the lithium environment within the cathode material structure. The presence and characteristics of these Raman-active modes offer insights into the structural integrity and local bonding arrangements of the LMO and LMO@NAO samples, allowing for a comprehensive analysis of the coating effects on the underlying $LiMn_2O_4$ structure.

3B.3.1.3 Electron microscopy studies

Figure 3b.4 shows the FESEM (Figure 3b.4(a-d)), TEM (Figure 3b.4(e-h)) images, of LMO, LMO@NFO1, LMO@NFO2, and LMO@NFO3 respectively. In Fig. 5a, we can see nanorods-shaped morphology for α-MnO_2 materials. The LMO particles formed semi-truncated octahedral-type geometry, which can be seen in **(Figure 3b.3a)** with sharp edges. The magnified image of the particular particle is given in the inset of **Figure 3b.3a.** The surface of the octahedral-shaped LMO materials was modified with the coating of NAO materials in varied proportions **(Figure 3b.3(b-d)).** The modified blunt surface can be used to observe these surface modifications compared to the LMO materials. The FESEM images show that the particles have the least agglomeration, indicating that the NAO particles accumulate thoroughly over the surface of LMO materials. The uniform distribution of NAO particles on the LMO surface suggests improved electrochemical performance. This modification likely enhances the material's conductivity and

stability during cycling. Further transmission electron microscopy (TEM) analysis could provide more detailed insights into the interface between LMO and NAO particles.

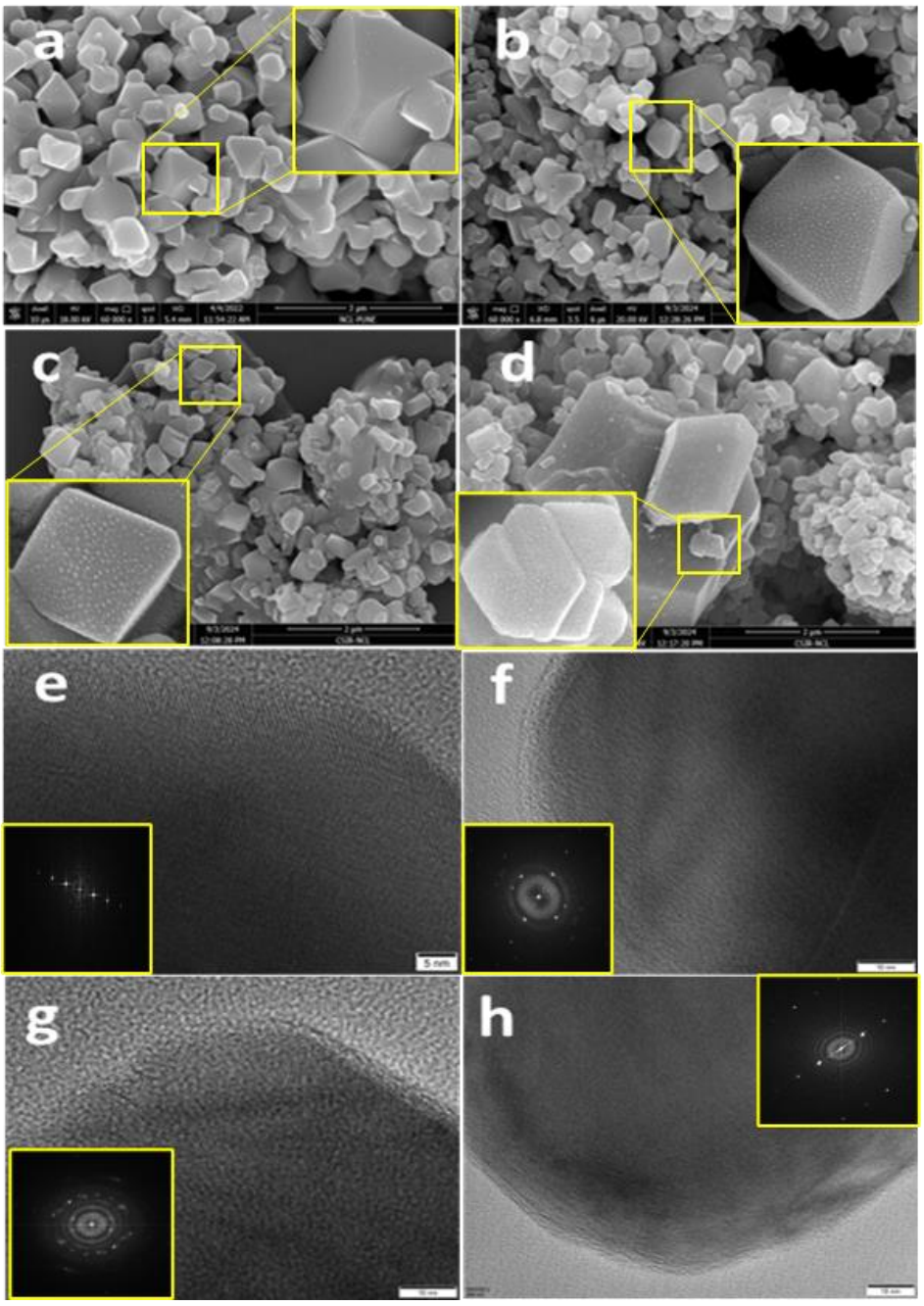

Figure 3b.4. FESEM images of **(a)** LMO, (b) LMO@NAO1, **(c)** LMO@NAO2, and **(d)** LMO@NAO3, HRTEM images of **(e)** LMO, (f) LMO@NAO1, **(g)** LMO@NAO2, and **(h)** LMO@NAO3.

Figure 3b.4(e-h) shows the TEM images at lower magnification and the SAED patterns (inset); the TEM images confirm the surface changes of the NAO-coated materials compared to the LMO material. It can be observed that there is no complexity on the surface of LMO materials. In contrast, the surface of NAO-coated materials shows roughness, which could be confirmed by observing the SAED patterns provided as an inset of the respective TEM images.

Figure 3b.5(a-d) shows HRTEM images with lattice fringes and spacing values. The lattice spacing values for LMO and LMO@NAO1, LMO@NAO2, and LMO@NAO3 materials and the inset of all images show the inverse FFT image of the marked region for the better understanding of lattice spacing values of the particular region, which are marked in the range 4.4 to 4.495 Å, corresponding to the (111) plane which is the prominent plane of cubic spinel structure of the LMO and 2.57 Å related to the (311) plane of spinel cubic LMO structure. At the particle edges of the LMO@NAO1, LMO@NAO2, and LMO@NAO3 materials, the lattice spacing values are 1.63 Å, 2.68 Å, and 2.27 Å, corresponding to the planes (231), (311), and (021) respectively which belongs to the orthorhombic structured phase of NAO materials deposited as thin layer over the surface of the LMO material. This dual-phase nature confirms the successful surface coating of nickel aluminum oxide coating over lithium manganese oxide material.

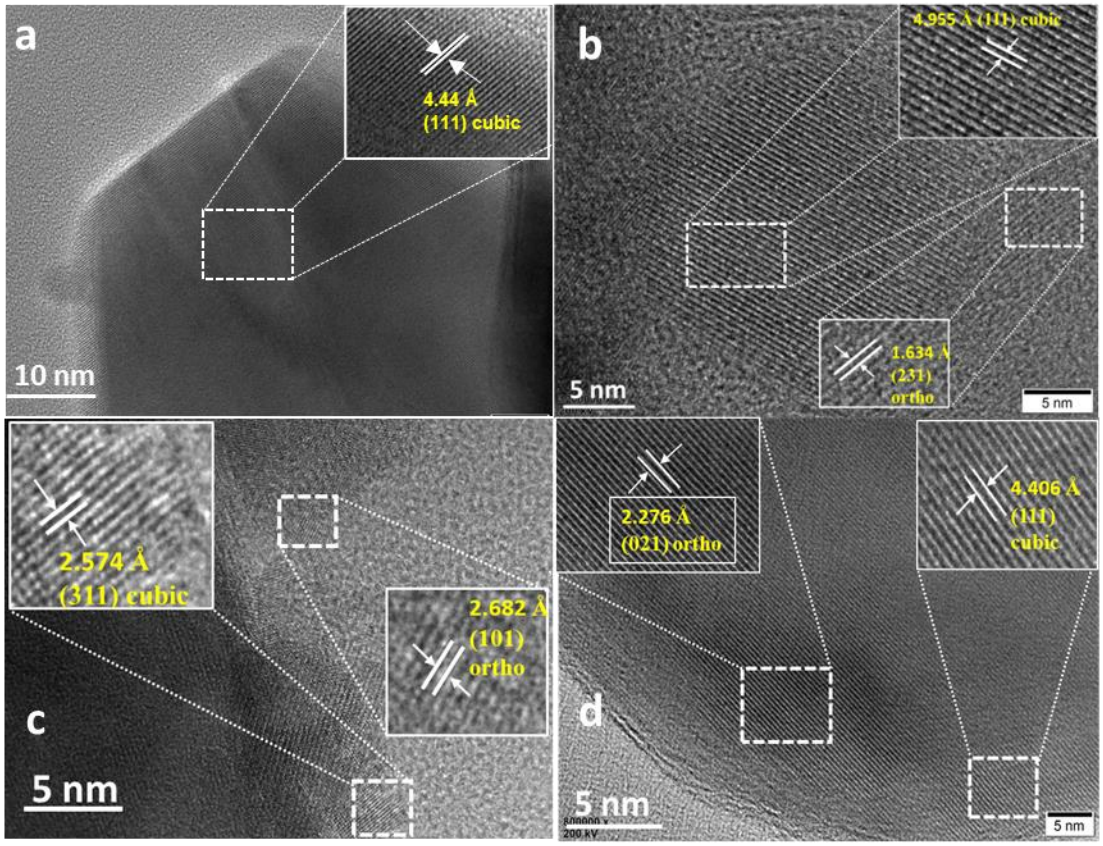

Figure 3b.5. HRTEM images of (a) LMO, (b) LMO@NAO1, (c) LMO@NAO2, and (d) LMO@NAO3, which are indexed with the lattice spacing values corresponding to the respective crystal structures (the inset of each image is an FFT image of the marked area).

Furthermore, the material composition has been evaluated by STEM-HAADF elemental mapping, as shown in **Figure 3b.6.** The mapping results reveal the proper infusion of all the dopants into the crystal structure. The mapping results confirm the presence of Mn, Ni, Al, and O in the synthesized material. The distribution of all these elements appears uniform throughout the sample, indicating successful incorporation into the crystal lattice. This homogeneous distribution is crucial for achieving electrochemical properties and material performance. Further analysis of the elemental mapping data could provide insights into any potential clustering or segregation of dopants, which may impact the overall functionality of the synthesized compound.

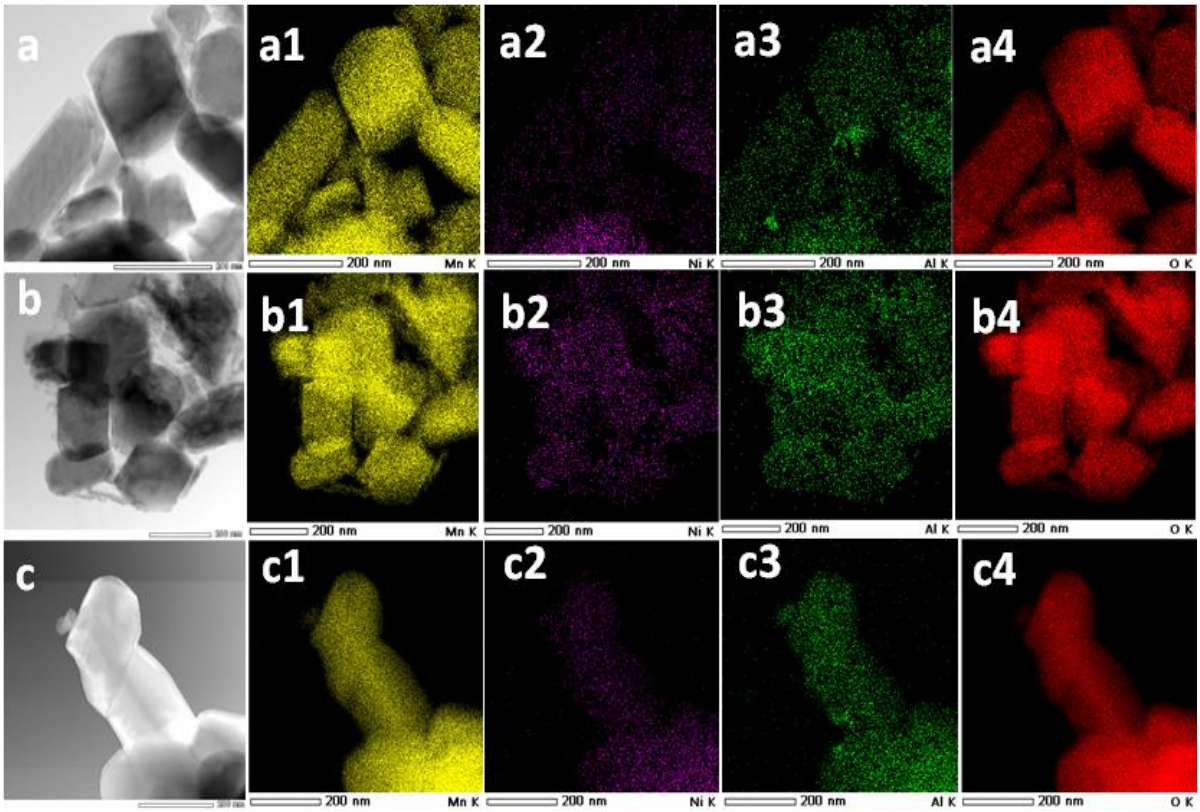

Figure 3b.6. STEM EDS elemental mapping of all the elements of **(a)** STEM image, **(a1)** Mn, **(a2)** Ni, **(a3)** Al, **(a4)** O of LMO@NAO1, **(b)** STEM image, **(b1)** Mn, **(b2)** Ni, **(b3)** Al, **(b4)** O of LMO@NAO2, and **(c)** STEM image, **(c1)** Mn, **(c2)** Ni, **(c3)** Al, **(c4)** O of LMO@NAO3 materials.

3B.3.1.4 X-ray photoelectron spectroscopic study

XPS analysis was conducted to investigate the electronic state of elemental valence, with all elemental core levels deconvoluted and peak-fitted using CasaXPS software. **Figure 3b.7** presents the XPS peak signals for LMO@NAO1, LMO@NAO2, and LMO@NAO3. The deconvoluted spectra of the Mn2p core level, as illustrated in **Figure 3b.7(a1-c1)**, exhibit two components: $Mn2p_{3/2}$ and $Mn2p_{1/2}$. These components arise from spin-orbit coupling, a phenomenon that is particularly evident in heavy elements where relativistic effects are more prominent. This interaction causes atomic energy levels to split, resulting in the observation of fine structure in spectroscopic data. The binding energies for $Mn2p_{3/2}$ are 642.3 eV (LMO@NAO1), 642.2 (LMO@NAO2), and 642.3 (LMO@NAO3). For $Mn2p_{1/2}$, the binding energies are 653.8

eV (α-MnO2), 653.9 eV (LMO), 653.9 eV (LMO@NFO1), 653.8 eV (LMO@NFO2), and 653.9 eV (LMO@NFO3). These observed binding energy values for Mn^{4+} and Mn^{3+} in Mn2p core levels align closely with previously reported findings.[32,33]

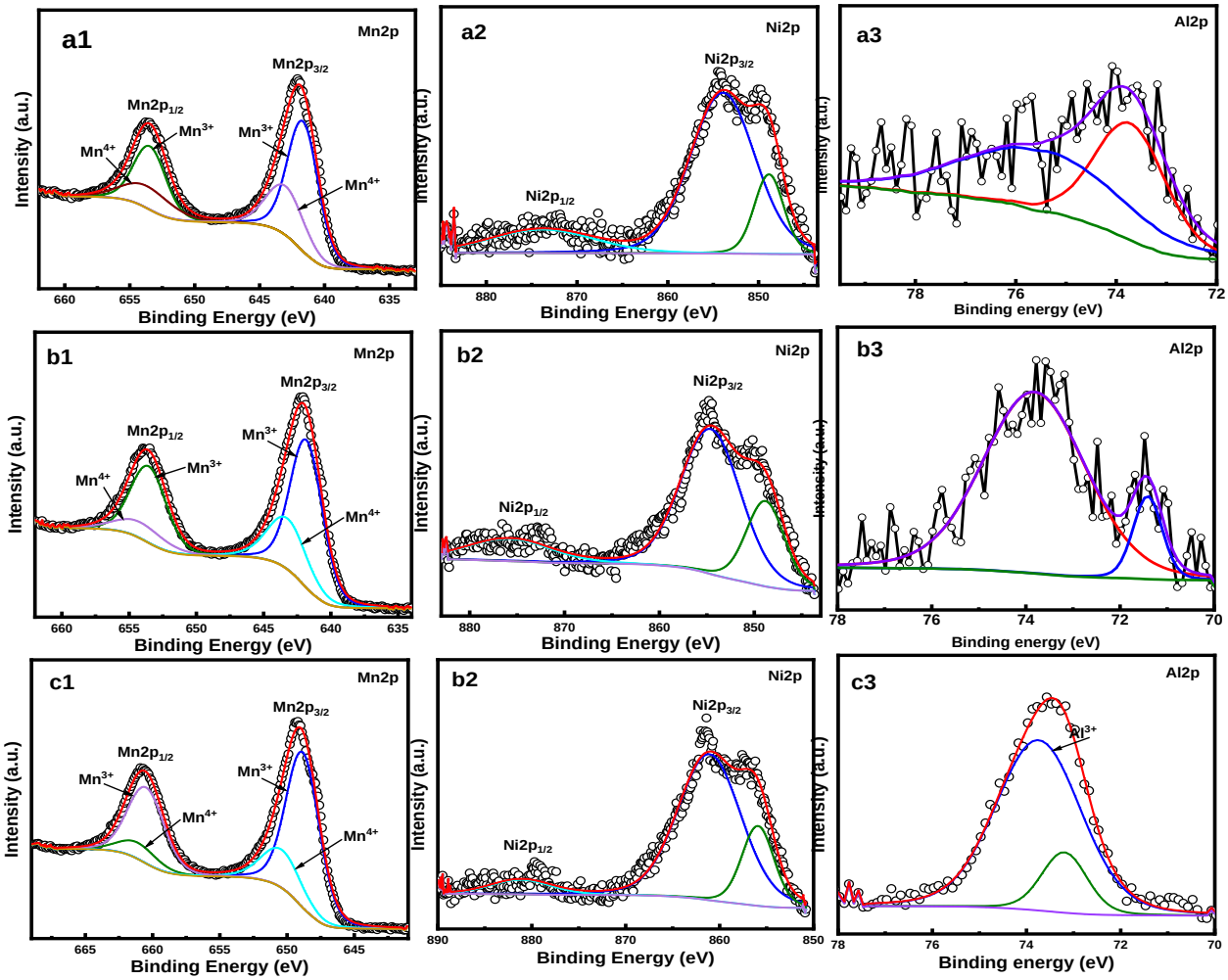

Figure 3b.7 Deconvoluted XPS spectra of **(a1-a3)** Mn2, Ni2p, and Al2p core levels of LMO@NAO1, **(b1-b3)** Mn2, Ni2p, and Al2p core levels of LMO@NAO2, and **(c1-c3)** Mn2, Ni2p, and Al2p core levels of LMO@NAO3.

The deconvoluted spectra of Ni2p in **Figure 3b.7(a2-c2)** core level exhibit two components, $Ni2p_{3/2}$ and $Ni2p_{1/2}$, as a result of spin-orbit coupling. These core levels of $Ni2p_{3/2}$ and $Ni2p_{1/2}$ have binding energies that are not distinctly separated. This lack of clear separation

can be attributed to the limited quantity of Ni in the NAO material, which is applied as a thin coating on the LMO material surface. The binding energy signal values show slight deviations compared to elemental Ni, which is caused by the incorporation of aluminum and surface-absorbed β-Ni(OH)2.[34] The obtained binding energy values for the $Ni2p_{3/2}$ core levels are 852.2 eV (LMO@NAO1), 853.1 (LMO@NAO2), and 852.7 (LMO@NAO3). The deconvoluted spectra of Al2p core levels are shown in **Figure 3b.7(a1-a3).** The signals for Al2p levels are quite lesser as its composition is low in the materials and also a lighter element in comparison with Mn and Ni, which would result in the weaker separation of peaks even after deconvolution.

3B.3.2 Electrochemical analysis

3B.3.2.1 Cyclic voltammetry study

Cyclic voltammetry was employed to assess the electrochemical oxidation-reduction characteristics and ionic conduction properties of the materials active in the cathode. The cyclic voltammograms revealed distinct oxidation and reduction peaks, indicating the reversible nature of the redox reactions occurring within the cathode materials. The peak separation and current density provided insights into the kinetics of electron transfer and the overall electrochemical performance of the materials. Further analysis of the voltammetric data allowed for the determination of diffusion coefficients, which shed light on the ion mobility and transport mechanisms within the cathode structure. **Figure (3b.8a)** shows the cyclic voltammograms of surface-modified LMO materials carried out between 2.5 and 5V conditions. A notable peak occurs around 4.0-4.2V in all the materials, corresponding to the Mn^{3+}/Mn^{4+} redox couples. Charging peaks are observed at 4.07V and 4.21V, with a peak separation potential of approximately 130 mV. Discharge peaks appear at 3.9V and 4.06V, exhibiting a peak separation potential of 150 mV. An additional charge peak is evident at roughly 3.2V, with its redox pair peak

manifesting on the discharge curves at around 2.66 to 2.69V range; this redox pair is associated with Li^+ extraction from and insertion into the cathode active material.

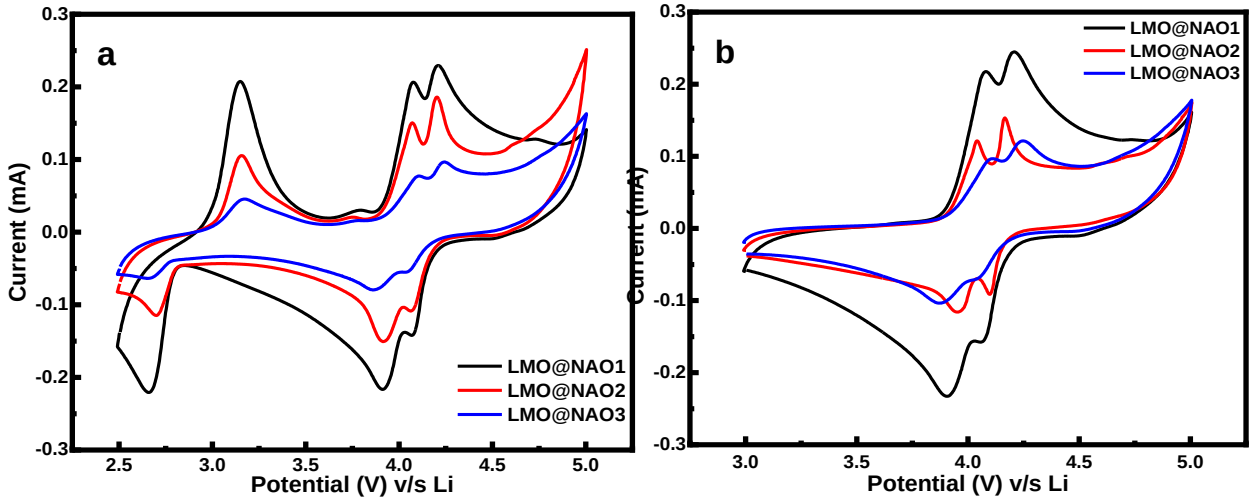

Figure 3b.8. Cyclic voltammograms **(a)** before cycling **(b)** after cycling of LMO@NAO1, LMO@NAO2, and LMO@NAO3 materials. Nyquist plots of **(c)** before cycling and **(d)** after cycling of LMO@NAO1, LMO@NAO2, and LMO@NAO3 materials.

Analysis of the cyclic voltammograms indicates that the intensity of redox peaks diminishes as the thickness of the surface coating layer grows. This observation implies that thicker coatings hinder the transfer of electrons between the electrode surface in the solution and the redox-active species. The observed reduction in peak intensity may result from high resistance or restricted diffusion of electroactive species through the coating material. Additional studies exploring the correlation between coating thickness and electrochemical performance could yield valuable insights for enhancing electrode design across various applications. **Figure 3b.8b** displays the cyclic voltammograms of the surface-modified LMO materials between 3.0 to 5 V window after 500 continuous cycles of charge discharge, revealing that there is not much change in the redox behavior of materials after 500 cycles of charge discharge.

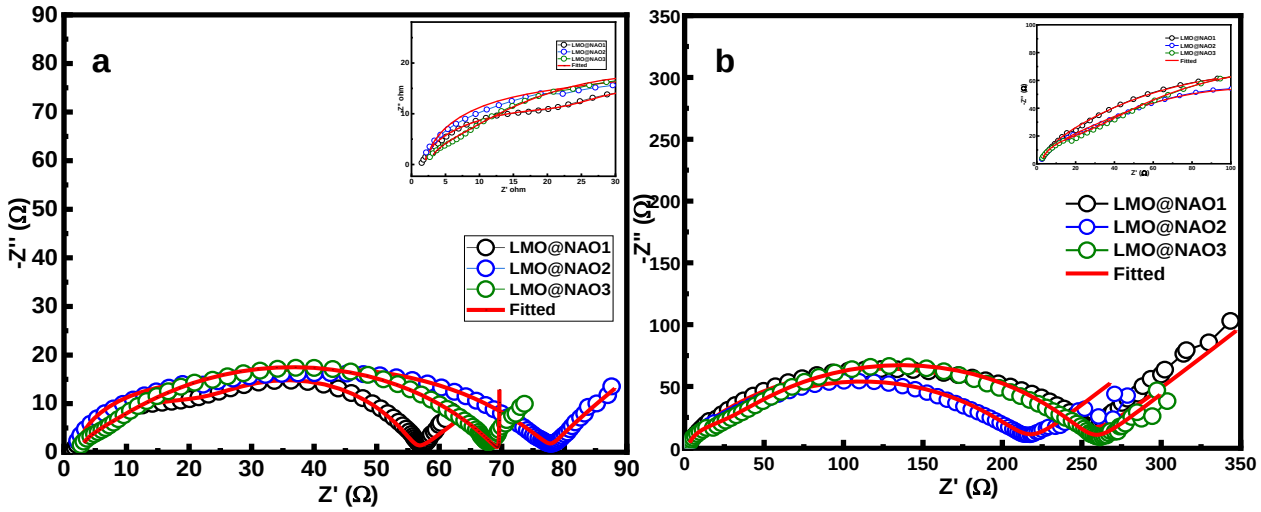

Figure 3b.9 Nyquist plots of **(a)** before cycling **(b)** after cycling of LMO@NAO1, LMO@NAO2, and LMO@NAO3 materials.

Electrochemical impedance spectroscopy has been employed to examine the kinetics of Li^+ extraction and insertion within cathode materials. EIS experiments were performed to elucidate the underlying mechanisms of Li^+ movement during insertion and extraction. The Nyquist plots obtained from these EIS measurements revealed characteristic semicircles and sloped lines, providing valuable insights into the electrode-electrolyte interface and diffusion processes. Analysis of the equivalent circuit models derived from the EIS data allowed for determining charge transfer resistance and diffusion coefficients. These parameters vary significantly with the state of charge and cycling history of the cathode material, highlighting the complex nature of Li^+ transport in these systems.

The Nyquist plots for all cathode materials are displayed in **Figure 3b.9a**, with the inset depicting the equivalent circuit used to fit the experimental data. This circuit comprises three resistance components: R_s (system/electrolyte resistance), R_{SEI} (solid-electrolyte interface resistance), Rct (charge transfer resistance), and (R_{diff}.) diffusion resistance, which usually occurs at low-frequency regions due to the capacitive effects.[35] Additionally, it includes a constant phase

element (CPE) and Warburg impedance (W). Analysis of the Nyquist plots reveals that LMO materials with modified surfaces exhibit higher charge transfer resistance than unmodified LMO. The materials exhibit a common feature in their Nyquist plots: an overlapping semicircle in the high-frequency region. This semicircle is associated with two resistances: the SEI resistance (R_{SEI}) and the charge transfer resistance (R_{ct}). The R_{SEI} can be observed in the magnified inset figure, which shows a detailed view of the Nyquist plots. The Rct indicates lithium-ion insertion at the interface between the electrode and electrolyte. Upon close examination of the plots, two semicircles of different sizes were identified: a smaller one in the higher frequency range and a larger one in the mid-frequency area. The smaller semicircle, observed at higher frequencies, represents the cathode-electrode resistance (R_{SEI}). In contrast, the larger semicircle in the mid-frequency region indicates the charge transfer resistance (Rct). Among the cathode materials evaluated, LMO@NAO1 demonstrates the smallest charge transfer resistance, indicating enhanced electronic conductivity due to minimal electrolyte exposure within the cell. Conversely, surface-modified cathode materials show higher charge transfer resistance than unmodified LMO. The charge transfer resistance increases proportionally with the surface coating percentage, as the surface layer impedes conductivity, reducing specific capacities during charge-discharge studies. In the low-frequency region, a linear trend signifies the interface resistance and swifter diffusion of Li^+ ions through the electrolyte towards the anode, though smaller diffusion resistance was also observed. In the case of Nyquist plots of cycled cells shown in **Figure 3b.9b**, it is observed that the charge transfer resistance (Rct) is higher than that of the fresh cells. The charge transfer resistance (R_{ct}) is directly related to the kinetics of electrochemical reactions of the cell, which is the major part of the total resistance of the cell, which is termed cell resistance. The charge transfer resistance greatly contributes to the overall impedance. The reasons for the increased R_{ct} in Li-ion

cells are either aging of the cells or increased Li plating;[36] the aged cells attain less reversibility, which leads to the increase of impedance from cycle to cycle, and another reason is more Li plating could block pathways for Li^+ interaction.[37] This accumulation of irreversible changes and Li plating can significantly impact the overall performance and lifespan of the battery. As the number of charge-discharge cycles increases, the battery's capacity and efficiency gradually decline.

3B.3.2.2 Galvanostatic charge-discharge study

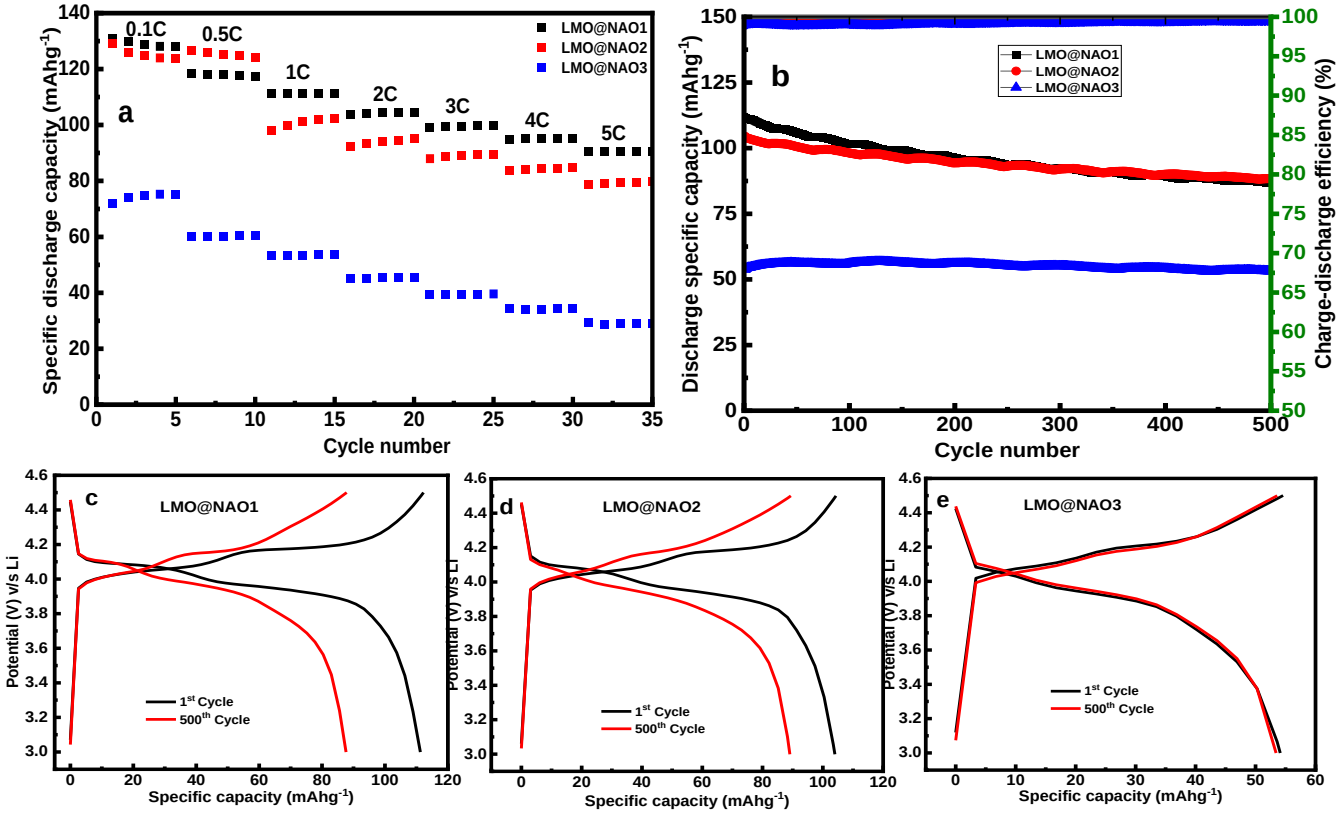

Figure 3b.10. Galvanostatic charge-discharge plots of **(a)** rate capability, **(b)** cycle stability and **(c-e)** potential v/s specific capacity curves of LMO@NAO1, LMO@NAO2, and LMO@NAO3 respectively.

Galvanostatic charge-discharge tests were conducted for the cells prepared with LMO@NAO materials to understand the rate capabilities and cycling stabilities. The rate capability test results for the cathode materials at various current densities are depicted in **Figure**

3b.10(a). Higher specific discharge capacities are observed at lower current densities than higher ones, which can be attributed to the depletion of Li^+ ions. This reduction in Li^+ ions may result from unwanted side reactions at increased current rates, impeding the smooth reversible lithiation and de-lithiation process. Developing a solid electrolyte interphase (SEI) layer on the electrode's surface can worsen this problem by depleting Li^+ ions and enhancing internal resistance. When current rates are higher, the movement of Li^+ ions within the electrode material may become a restricting factor, resulting in incomplete use of the active material. These combined effects contribute to the reduction of capacity and decreased cycling stability, emphasizing the importance of developing advanced electrode designs and electrolyte compositions to address these issues in high-rate battery applications. **Figure 3b.10(b)** shows the cycle stability of the cathode materials at 1C rate for continuous 500 cycles. The LMO@NAO cathode materials exhibited superior long-term cycling performance with enhanced cycle stability after 500 cycles. In contrast, the pristine LMO cathode exhibits a significant capacity fade, retaining only 56.88 % of its initial discharge capacity of 118.17 $mAhg^{-1}$ at 1C after the same number of cycles. This enhanced cycle stability of the LMO@NAO cathode materials can be attributed to the protective nickel aluminum oxide (NAO) coating, which effectively mitigates electrode degradation and electrolyte decomposition during prolonged cycling. On the other hand, the initial specific discharge capacities of the cathode materials are 111.49 $mAhg^{-1}$, 104.5 $mAhg^{-1}$, and 53.74 $mAhg^{-1}$ for NAO1, NAO2, and NAO3, respectively. After the continuous 500 cycles, the cathode materials exhibited the specific discharge capacities 86.64 $mAhg^{-1}$, 88.41 $mAhg^{-1}$, and 53.1 $mAhg^{-1}$with capacity retention of 77.7%, 84.6%, and 98.8%, respectively. GCD analysis reveals that as the surface coating percentage increases, the specific discharge capacities of the cathode materials at the 1C rate decrease. The uncoated LMO material exhibits a better initial specific discharge capacity than

LMO@NAO1. LMO@NAO2 and LMO@NAO3 continue this downward trend as the surface coating layer thickens. However, LMO@NAO1, LMO@NAO2, and LMO@NAO3 demonstrate improved cycling stability compared to the LMO cathode, suggesting that the NAO surface coating serves as a protective barrier on LMO, helping to inhibit Mn dissolution. This observation also indicates that while a thicker surface layer may result in some capacity loss, it provides enhanced stability with higher capacity retention. The specific capacity versus voltage curves for materials cycled at 1C current densities during the first cycle and 500^{th} of each cathode material are displayed in **Figure 3b.10c** of LMO@NAO1**, Figure 3b.10d** of LMO2NAO2, and **Figure 3b.10e** of LMO@NAO3. The image showcases the reduction in capacity following prolonged cycling for 500 cycles. **Figures 3b.10(c-d)** display the capacity decline of the materials through voltage-specific capacity curves at 500-cycle intervals during galvanostatic charge-discharge cycles at a 1C rate. The findings strongly indicate that materials with surface coatings exhibit more stable performance over extended cycling periods.

3B.4 Conclusions

This study focused on modifying the $LiMn_2O_4$ (LMO) cathode material by applying a $Ni_xAl_yO_z$ (NAO) surface coating through the sol-gel technique. We have investigated the impact of this surface modification on the cathode material's performance by varying the coating layer composition ratio and conducting electrochemical analyses. Initially, MnO_2 nanostructures were synthesized using a hydrothermal approach. Subsequently, these MnO_2 structures served as the manganese source for LMO production via the sol-gel technique. To investigate the impact of surface layer thickness on electrochemical performance, the synthesized LMO materials were coated with NAO at varying concentrations ranging from 1% to 3%. The initial specific discharge capacities of cathode materials LMO@NAO1, LMO@NAO2, and LMO@NAO3 were measured

at 111.49 $mAhg^{-1}$, 104.5 $mAhg^{-1}$, and 53.74 $mAhg^{-1}$, respectively. After 500 consecutive galvanostatic charge/discharge cycles at a 1 C rate, these cathode active materials demonstrated reduced specific discharge capacities of 86.64 $mAhg^{-1}$, 88.41 $mAhg^{-1}$, and 53.1 $mAhg^{-1}$, corresponding to capacity retention rates of 77.7%, 84.6%, and 98.8%, respectively.

3B.5 References

(1) Yamada, A.; Tanaka, M.; Tanaka, K.; Sekai, K. Jahn–Teller Instability in Spinel Li–Mn–O. *Journal of Power Sources* **1999**, *81–82*, 73–78. https://doi.org/10.1016/S0378-7753(99)00106-8.

(2) Wu, J.; Yang, J.; Leong, Z. Y.; Zhang, F.; Deng, H.; Ouyang, G. F.; Yu, J. A Method to Inhibit Disproportionation of Mn^{3+} for Low-Cost Mn–Fe All-Flow Battery. *ACS Appl. Energy Mater.* **2022**, *5* (12), 14646–14651. https://doi.org/10.1021/acsaem.2c03075.

(3) Manthiram, A. A Reflection on Lithium-Ion Battery Cathode Chemistry. *Nat Commun* **2020**, *11* (1), 1550. https://doi.org/10.1038/s41467-020-15355-0.

(4) Jaber-Ansari, L.; Puntambekar, K. P.; Kim, S.; Aykol, M.; Luo, L.; Wu, J.; Myers, B. D.; Iddir, H.; Russell, J. T.; Saldaña, S. J.; Kumar, R.; Thackeray, M. M.; Curtiss, L. A.; Dravid, V. P.; Wolverton, C.; Hersam, M. C. Suppressing Manganese Dissolution from Lithium Manganese Oxide Spinel Cathodes with Single-Layer Graphene. *Advanced Energy Materials* **2015**, *5* (17), 1500646. https://doi.org/10.1002/aenm.201500646.

(5) Jang, D. H.; Shin, Y. J.; Oh, S. M. Dissolution of Spinel Oxides and Capacity Losses in 4 V Li / Li x Mn2 O 4 Cells. *J. Electrochem. Soc.* **1996**, *143* (7), 2204–2211. https://doi.org/10.1149/1.1836981.

(6) Iqbal, A.; Iqbal, Y.; Khan, A. M.; Ahmed, S. Effect of Bication (Cu-Cr) Substitution on the Structure and Electrochemical Performance of LiMn2O4 Spinel Cathodes at Low and High Current Rates. *Journal of Saudi Chemical Society* **2018**, *22* (4), 449–458. https://doi.org/10.1016/J.JSCS.2017.07.011.

(7) Garhi, G.; Aklalouch, M.; Favotto, C.; Mansori, M.; Saadoune, I. Coprecipitation Synthesis of Co-Doped LiMn1.5Ni0.5O4 Material as 5 V Cathode of Li-Ion Batteries with Huge Rate Capability for High Power Applications. *Journal of Electroanalytical Chemistry* **2020**, *873*, 114413. https://doi.org/10.1016/J.JELECHEM.2020.114413.

(8) Shivamurthy, B. P.; Thripuranthaka, M.; Shelke, M. V.; Nayaka, G. P. Formation of the Secondary Phase Domain by Multi-Cation Substitution for the Superior Electrochemical Performance of Spinel Cathodes for High-Voltage Li-Ion Batteries. *ACS Appl. Energy Mater.* **2022**, *5* (12), 15345–15355. https://doi.org/10.1021/acsaem.2c02667.

(9) Kim, D.; Shiiba, H.; Zettsu, N.; Yamada, T.; Kimijima, T.; Sánchez-Santolino, G.; Ishikawa, R.; Ikuhara, Y.; Teshima, K. Full Picture Discovery for Mixed-Fluorine Anion Effects on High-Voltage Spinel Lithium Nickel Manganese Oxide Cathodes. *NPG Asia Materials* **2017**, *9* (7), e398–e398. https://doi.org/10.1038/am.2017.90.

(10) Han, D.-W.; Ryu, W.-H.; Kim, W.-K.; Eom, J.-Y.; Kwon, H.-S. Effects of Li and Cl Codoping on the Electrochemical Performance and Structural Stability of LiMn 2 O 4 Cathode Materials for Hybrid Electric Vehicle Applications. *The Journal of Physical Chemistry C* **2013**, *117* (10), 4913–4919. https://doi.org/10.1021/jp310011m.

(11) De Taeye, L. L.; Vereecken, P. M. Chemo-Mechanical Effect of Chlorine Modified TiO_2 Coatings on LMO. *J. Mater. Chem. A* **2022**, *10* (45), 24398–24409. https://doi.org/10.1039/D2TA06009D.

(12) Mereacre, V.; Stüble, P.; Ghamlouche, A.; Binder, J. R. Enhancing the Stability of Lini0.5mn1.5o4 by Coating with Linbo3 Solid-State Electrolyte: Novel Chemically Activated Coating Process versus Sol-Gel Method. *Nanomaterials* **2021**, *11* (2), 1–13. https://doi.org/10.3390/nano11020548.

(13) Tomon, C.; Sarawutanukul, S.; Phattharasupakun, N.; Duangdangchote, S.; Chomkhuntod, P.; Joraleechanchai, N.; Bunyanidhi, P.; Sawangphruk, M. Core-Shell Structure of LiMn2O4 Cathode Material Reduces Phase Transition and Mn Dissolution in Li-Ion Batteries. *Commun Chem* **2022**, *5* (1), 54. https://doi.org/10.1038/s42004-022-00670-y.

(14) Guo, J.; Cai, Y.; Zhang, S.; Chen, S.; Zhang, F. Core-Shell Structured o-LiMnO2@Li2CO3 Nanosheet Array Cathode for High-Performance, Wide-Temperature-Tolerance Lithium-Ion Batteries. *ACS Applied Materials and Interfaces* **2016**, *8* (25). https://doi.org/10.1021/acsami.6b04616.

(15) Bi, Z.; Zhao, N.; Ma, L.; Shi, C.; Fu, Z.; Xu, F.; Guo, X. Surface Coating of $LiMn_2O_4$ Cathodes with Garnet Electrolytes for Improving Cycling Stability of Solid Lithium Batteries. *J. Mater. Chem. A* **2020**, *8* (8), 4252–4256. https://doi.org/10.1039/C9TA11203K.

(16) Mu, C.-L.; Huang, M.; Zhu, H.-L.; Qi, Y.-X.; Wang, Y.-X.; Li, T.; Bai, Y.-J. Promoting the Electrochemical Performance of Commercial LiMn2O4 by Hydrothermal Modification with Poly (Vinylidene Fluoride). *Materials Today Sustainability* **2022**, *18*, 100128. https://doi.org/10.1016/j.mtsust.2022.100128.

(17) Shivamurthy, B. P.; Thripuranthaka, M.; Shelke, M. V.; Nayaka, G. P. Influence of the Crystal Plane Orientation in Enhancing the Electrochemical Performance of a Trication-Substituted Cathode for Li-Ion Batteries. *Energy and Fuels* **2024**, *38* (5). https://doi.org/10.1021/acs.energyfuels.3c03794.

(18) Wu, Y.; Cao, C.; Zhang, J.; Wang, L.; Ma, X.; Xu, X. Hierarchical LiMn 2 O 4 Hollow Cubes with Exposed 111 Planes as High-Power Cathodes for Lithium-Ion Batteries. *ACS Applied Materials & Interfaces* **2016**, *8* (30), 19567–19572. https://doi.org/10.1021/acsami.6b06820.

(19) Liu, H.; Li, M.; Xiang, M.; Guo, J.; Bai, H.; Bai, W.; Liu, X. Effects of Crystal Structure and Plane Orientation on Lithium and Nickel Co-Doped Spinel Lithium Manganese Oxide for Long Cycle Life Lithium-Ion Batteries. *Journal of Colloid and Interface Science* **2021**, *585*, 729–739. https://doi.org/10.1016/j.jcis.2020.10.052.

(20) Jung, S.; Gwon, H.; Hong, J.; Park, K.; Seo, D.; Kim, H.; Hyun, J.; Yang, W.; Kang, K. Understanding the Degradation Mechanisms of $LiNi_{0.5}Co_{0.2}Mn_{0.3}O_2$ Cathode Material in Lithium Ion Batteries. *Advanced Energy Materials* **2014**, *4* (1), 1300787. https://doi.org/10.1002/aenm.201300787.

(21) Han, C. G.; Zhu, C.; Saito, G.; Akiyama, T. Improved Electrochemical Properties of LiMn2O4 with the Bi and La Co-Doping for Lithium-Ion Batteries. *RSC Advances* **2015**, *5* (89), 73315–73322. https://doi.org/10.1039/c5ra13005k.

(22) Chudzik, K.; Świ\c etosławski, M.; Bakierska, M.; Kubicka, M.; Gajewska, M.; Molenda, M. Surface Modification and Carbon Coating Effect on a High-Performance K and S Doped LiMn2O4. *Applied Surface Science* **2020**, *531*, 147138. https://doi.org/10.1016/j.apsusc.2020.147138.

(23) Wang, J.; Zhang, Q.; Li, X.; Wang, Z.; Guo, H.; Xu, D.; Zhang, K. Sputtering Graphite Coating to Improve the Elevated-Temperature Cycling Ability of the LiMn2O4 Electrode. *Physical Chemistry Chemical Physics* **2014**, *16* (30). https://doi.org/10.1039/c4cp01069h.

(24) Luo, G.; Li, X.; Chen, L.; Zhang, Y.; Gu, J.; Chao, Y.; Zhu, W.; Liu, Z.; Xu, C. Island-like CeO2 Decorated LiMn2O4: Surface Modification Enhancing Electrochemical Lithium Extraction and Cycle Performance. *Chemical Engineering Journal* **2023**, *455*, 140928. https://doi.org/10.1016/j.cej.2022.140928.

(25) Wan, X.; Yang, S.; Cai, Z.; He, Q.; Ye, Y.; Xia, Y.; Li, G.; Liu, J. Facile Synthesis of MnO2 Nanoflowers/N-Doped Reduced Graphene Oxide Composite and Its Application for

Simultaneous Determination of Dopamine and Uric Acid. *Nanomaterials* **2019**, *9* (6). https://doi.org/10.3390/nano9060847.

(26) Huang, X.; Cui, W.; Yu, J.; Lu, S.; Liao, X. Preparation of Mesoporous MnO2 Catalysts with Different Morphologies for Catalytic Ozonation of Organic Compounds. *Catalysis Letters* **2022**, *152* (5). https://doi.org/10.1007/s10562-021-03745-y.

(27) Cowley, J. M. Structure Analysis of Single Crystals by Electron Diffraction. III. Modification of Alumina. *Acta Cryst* **1953**, *6* (11), 846–853. https://doi.org/10.1107/S0365110X53002489.

(28) Jia, C.; Zhang, Y.; Kong, Q.; Wang, Q.; Chen, G.; Guam, H. T.; Dong, C. Soft-Template Synthesis of Mesoporous NiFe2O4 for Highly Sensitive Acetone Detection. *Journal of Materials Science: Materials in Electronics* **2020**, *31* (8). https://doi.org/10.1007/s10854-020-03151-x.

(29) Kennedy, B. J.; Howard, C. J.; Knight, K. S.; Zhang, Z.; Zhou, Q. Structures and Phase Transitions in the Ordered Double Perovskites $Ba_2 Bi^{III} Bi^{V} O_6$ and $Ba_2 Bi^{III} Sb^{V} O_6$. *Acta Crystallogr B Struct Sci* **2006**, *62* (4), 537–546. https://doi.org/10.1107/S0108768106018842.

(30) Buchberger, D. A.; Hamankiewicz, B.; Michalska, M.; Głaszczka, A.; Czerwinski, A. Ex Situ Raman Mapping of LiMn2O4 Electrodes Cycled in Lithium-Ion Batteries. *ACS Omega* **2024**. https://doi.org/10.1021/acsomega.4c01480.

(31) Slautin, B.; Alikin, D.; Rosato, D.; Pelegov, D.; Shur, V.; Kholkin, A. Local Study of Lithiation and Degradation Paths in LiMn2O4 Battery Cathodes: Confocal Raman Microscopy Approach. *Batteries* **2018**, *4* (2), 21. https://doi.org/10.3390/batteries4020021.

(32) Marchini, F.; Rubi, D.; Del Pozo, M.; Williams, F. J.; Calvo, E. J. Surface Chemistry and Lithium-Ion Exchange in LiMn2O4 for the Electrochemical Selective Extraction of LiCl from Natural Salt Lake Brines. *Journal of Physical Chemistry C* **2016**, *120* (29). https://doi.org/10.1021/acs.jpcc.5b11722.

(33) Tang, C. Y.; Leung, K.; Haasch, R. T.; Dillon, S. J. LiMn2O4 Surface Chemistry Evolution during Cycling Revealed by in Situ Auger Electron Spectroscopy and X-Ray Photoelectron Spectroscopy. *ACS Applied Materials and Interfaces* **2017**, *9* (39). https://doi.org/10.1021/acsami.7b10442.

(34) Ganesan, P.; Sivanantham, A.; Shanmugam, S. Inexpensive Electrochemical Synthesis of Nickel Iron Sulphides on Nickel Foam: Super Active and Ultra-Durable Electrocatalysts for Alkaline Electrolyte Membrane Water Electrolysis. *Journal of Materials Chemistry A* **2016**, *4* (42). https://doi.org/10.1039/c6ta04499a.

(35) Pérez, A.; Benavides, M.; Rozas, H.; Seria, S.; Orchard, M. Guidelines for the Characterization of the Internal Impedance of Lithium-Ion Batteries in PHM Algorithms. *International Journal of Prognostics and Health Management* **2018**, *9* (3). https://doi.org/10.36001/ijphm.2018.v9i3.2746.

(36) Brown, D. E.; McShane, E. J.; Konz, Z. M.; Knudsen, K. B.; McCloskey, B. D. Detecting Onset of Lithium Plating during Fast Charging of Li-Ion Batteries Using Operando Electrochemical Impedance Spectroscopy. *Cell Reports Physical Science* **2021**, *2* (10), 100589. https://doi.org/10.1016/j.xcrp.2021.100589.

(37) Zhang, S. S.; Xu, K.; Jow, T. R. Electrochemical Impedance Study on the Low Temperature of Li-Ion Batteries. *Electrochimica Acta* **2004**, *49* (7), 1057–1061. https://doi.org/10.1016/j.electacta.2003.10.016.

Chapter4
Restoration of degraded spinel structure from spent Li-ion battery cathodes towards re-claiming for second life

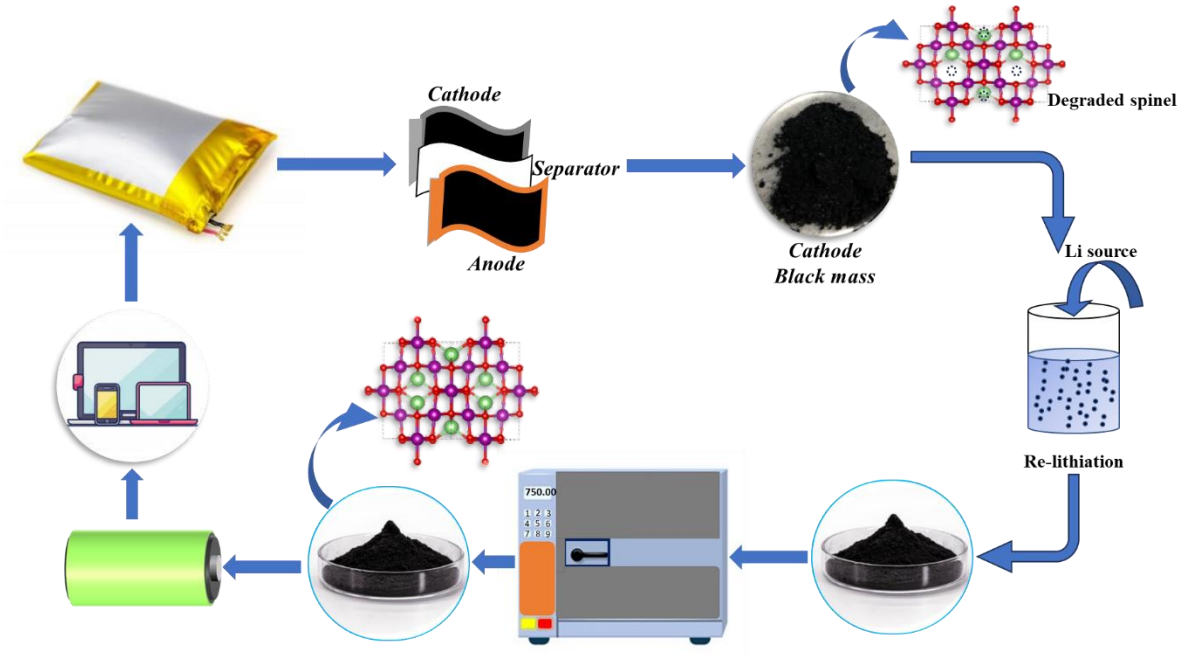

Highlights

- The direct regeneration of electrode materials from used Li-ion batteries has gained significant attention and is interesting due to its streamlined approach, lower energy consumption, and high cost-efficiency.
- Typically, the regeneration of depleted cathodes requires a source of lithium to address lithium loss. The precise management of Li^+ ion concentrations in the resulting lithium-rich solution can be employed directly to reintroduce lithium into depleted cathodes.
- This study involves the restoration of lost Li^+ ions in depleted Ni, Co dual substituted $LiMn_2O_4$ cathode through aqueous lithiation.
- The work involves a simple aqueous-based strategy to relitigate the diminished cathode material could provide a second life for the used cathode materials from the waste LIBs.

- The results of this chapter are published as **BP Shivamurthy**, Purnima Rawat, Manjusha V Shelke, Zhongren Zhou, **GP Nayaka*,** Restoration of degraded spinel structure from spent Li-ion battery cathodes towards Reclaiming for second life. ACS Sustainable Resour. Manage. 2025, XXXX, XXX, XXX-XXX, https://doi.org/10.1021/acssusresmgt.4c00533

4.1 Introduction

Lithium-ion batteries (LIBs) have been widely used in various electric and electronic devices such as smartphones, laptops, and electric automobiles due to their high energy density and extended lifespan.[1,2] Expediting the shift towards electric vehicles (EVs) is crucial for the automotive sector to reduce our reliance on fossil fuels and mitigate energy and environmental concerns.[3,4] However, the flourishing production of LIBs results in the inevitable generation of large quantities of spent batteries containing hazardous metal elements and flammable electrolytes, posing environmental risks and potential threats to human health.[5] By 2030, it's been estimated that the quantity of end-of-life (EoL) LIBs will hit 2 million metric tons.[6] The metals in spent LIBs, such as Li, Co, and Ni, hold Precious/ semi-precious status with considerable value and are recoverable. Developing efficient recycling methods to recover these valuable metals is essential in the present scenario, and better recycling strategies could relieve the mineral shortage issues. The existing methods for recycling EoL batteries encompass pyrometallurgical, hydrometallurgical, and direct regeneration.[7]

Typically, the pyrometallurgical approach involves high-temperature conditions for smelting and significant energy consumption to generate a metal alloy.[8,9] On the other hand, the hydrometallurgical method relies on strong acid or alkali reagents and entails multiple stages to acquire a high-purity precursor.[10,11] Furthermore, by considering the energy consumption and greenhouse gas emissions involved in the process, it is necessary to look into a feasible, easier method for the revival of cathode material. In this regard, the direct regeneration of the electrode materials is an effective approach focused on rejuvenating the composition and structure of deteriorated cathode material back to its initial form, thereby maximizing the sustainability of used LIBs.[12] To rejuvenate the cathode material to its original state, it is crucial to understand the failure

mechanism of the electrode materials, particularly concerning the restoration of cathode materials. Primarily, the predominant cause of capacity decay upon prolonged charge-discharge cycles is the loss of Li ions. This happens due to a substantial amount of active Li ions utilized from the cathode, particularly during the initial cycles, alongside electrolyte decomposition. This process could form a shielding passivation layer on the anode (solid electrolyte interphase, SEI) and the cathode (cathode electrolyte interphase, CEI).[3,13] It has to be considered that this interphase layer could protect the electrode material from additional corrosion; however, the instability of the SEI layer due to the substantial volume expansion in the anode, which accelerates the dendritic growth of Li on the electrode surface leads to the further irreversible loss of Li.[14] This could bring down the reversible capacity of the battery because of the significant loss of active Li ion within the cathode.[15]

The kinetics of charge transfer between Li^+ and cathode at the electrode-electrolyte interface significantly influences the stability and efficiency of the batteries.[16–18] A key factor hindering optimal Li^+ charge transfer kinetics is the generation of an unstable cathode-electrolyte interphase (CEI) layer during the charging and discharging cycles.[16] Typically, a CEI layer comprises various organic and inorganic substances resulting from the electrolyte and electrode breakdown. These components include LiF, Li_2CO_3, MnO_x, MnF_x, CoO_x, NiO, ROLi, and $ROCO_2Li$, where R represents an alkyl group.[16,19] These chemical substances can hinder the migration of Li^+ ions at the interface between the electrode and electrolyte.[19] Nevertheless, this process leads to the oxidative breakdown of the electrolyte, resulting in the production of gases and undesirable side products. In the highly delithiated state, the cathode surface's crystal structure becomes distorted, causing electrolyte oxidation and the formation of a non-uniform cathode-electrolyte interphase (CEI).[20] During charge-discharge cycles, mixing cations in cathode materials leads to irreversible

changes in crystal structure and the release of transition metal ions into the electrolytes. These liberated transition metal ions initiate undesired reactions at the interface with the electrolyte through catalytic and complexation mechanisms, leading to unstable cathode electrolyte interphase (CEI) growth.[21] The dynamic instability of the CEI fails to effectively shield against interfacial reactions and degradation, consequently resulting in significant performance deterioration.[22] For the regeneration of cathode material, it is crucial to eliminate the undesired Li-based compounds that form on the cathode materials surface due to unstable cathode-electrolyte interface (CEI). The oxidative leaching process must remove these compounds without impacting the cathode material's transition metals. Ammonium persulphate is an effective oxidizing agent that selectively leaches out Li and facilitates the removal of the unwanted layer on the cathode surface. The potential reaction mechanism of ammonium persulphate is presented in equation-1. The depleted Li ions are likewise replenished through chemical re-lithiation processes. Hence, to regenerate the recycled cathode materials from EoL LIBs, the re-lithiation of the cathode is essential to make it a potential candidate for their second life, which makes these batteries more sustainable.

$$LiMO_4 + xSO_2O_8^{2-} \rightarrow Li_{1-x}MO_2 + xSO_4^{2-} + xLi^+ \qquad \text{Eq. ---------- (1)}$$

In the present work, we report on the facile method of regenerating cathode materials from spent LIBs. The recovered cathode materials were investigated to estimate the loss of Li ions and their impact on the performance of the cathode material. The recovered material is identified as Ni, Co co-doped $LiMn_2O_4$-based cathode material, and detailed structural and compositional analyses were discussed in subsequent article sections. A simple lithiation strategy was employed to rejuvenate the cathode materials, and the varied concentrations of re-lithiation of cathode materials and their electrochemical performances were studied. The performance of the recovered cathode materials was significantly improved after the re-lithiation.

4.2 Materials and Methods

4.2.1 Recovery of cathode material from spent batteries:

The spent LIBs were collected from the electronics service centers in Pune. The spent batteries are subjected to chemical discharge to remove the residual potential in the cells. After chemical discharge, the cells dry sufficiently and are dismantled to separate the cell components such as cathode, anode, separator, and outer cell cases. The separated cathodes were cut into 5 x 5 cm^2 slices and immersed in DI water. Ammonium persulfate is added into the beaker containing cathode slices for the oxidative separation of cathode material from the Al current collector. The beaker containing cathode slices is subjected to ultrasonication for 10 minutes to remove the cathode material from the Al current collector completely. The Al current collector foils were separated, and the cathode materials were filtered off and dried at 80 ^{0}C for 12 hours. The recovered cathode material is divided into two portions; one is designated as RECAT, and the other is heated at 600 ^{0}C for 4 hours in the air, defined as RECAT6; heating is done to remove the possible impurities from the binder and conductive agents.

4.2.2 Re-lithiation of recovered cathode material

The re-lithiation of RECAT6 materials was carried out using the sol-gel method by introducing 5 %, 10 %, and 15 % of Li_2CO_3. The calculated quantity of Li_2CO_3 was dispersed in 50ml of deionized water and stirred to get the uniform dispersion mixture of partially dissolved Li_2CO_3/Water sol. Then, the requisite quantity of the heat-treated cathode material obtained from the previous step is added and kept for constant stirring for 1 hour. The excess water was evaporated at 80 ^{0}C completely to get Li_2CO_3 encapsulated cathode materials. Then, the cathode materials were calcinated at 750 ^{0}C for 10 hrs to get lithiated cathode materials. For ease of discussion, the lithiated materials were labeled as 5LiRECAT6, 10LiRECAT6, and 15LiRECAT6

based on the ratio of lithium source used. The schematic of the regeneration process is given in **Figure 4.1.**

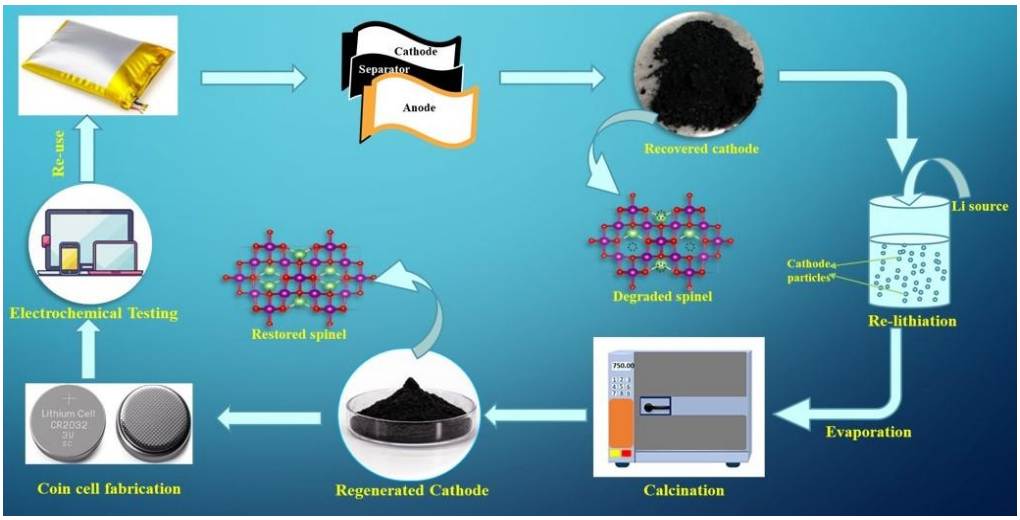

Figure 4.1. Schematic representation of regeneration of cathode materials.

4.1.1 Material Characterization

The crystal structure of the recovered and regenerated cathode materials was studied using powder X-ray diffraction (PXRD) (Rigaku Smartlab) with Cu as an X-ray source at 40kV and 30mA with Ni as kβ filter. The obtained XRD patterns were refined using the Rietveld refinement technique with the help of Fullprof suite software. The surface structure and morphology were analyzed by using Field emission scanning electron microscope (FE-SEM) (FEI-NOVA NANOSEM 450) and high-resolution transmission electron microscope (HR-TEM) (JEOL JEM F-200) coupled with energy dispersive spectrometer (EDS). The electronic states of the elements are studied using X-ray photoelectron spectroscopy (XPS), performed by the Thermo Scientific Model K-alpha XPS instrument with monochromatic Al-Kα as the X-ray source.

4.1.2 Electrochemical characterization

The electrochemical analyses of the recovered and regenerated cathode materials were conducted in 2032-type coin cells. Cell fabrication uses directly recovered, heat-treated, and

regenerated materials as cathodes. All these positive electrodes comprise 80:10:10 weight % of the active cathode material, polyvinylidene difluoride (PVDF) as the binder, and Super C-60 carbon black as the conducting material. All these materials were mixed well by adding an appropriate N-methyl pyrrolidone as the solvent to form a uniform slurry. The slurry was coated onto a conductive carbon-coated aluminum foil by doctor blade method and dried at 100 ^{0}C for 12 hrs under vacuum. The foil was subjected to calendaring and punched into 14 mm circular discs. These circular cathode discs were used to fabricate the 2032-type coin cells. A circular Li metal disc is used as an anode, Celgard-2325 as the separator, and 1M LiPF6 in a 1:1:1 volume ratio of EC/DMC/EMC solvents as the electrolyte. The coin cells were prepared in an argon-filled glove box at $\leq$ 0.1 ppm of O_2 and H_2O levels. The coin cells were tested by performing cyclic voltammetry and electrochemical impedance analysis (EIS) using the Metrohm electrochemical workstation (Multiautolab M204). The galvanostatic charge/discharge measurements were carried out with the Neware battery testing system (CT4008).

4.3 Results and Discussion

4.3.1 Structural and Elemental Characterization

4.3.1.1 ICP-OES and XRF analysis

The cathode material from the spent LIB was subjected to ICP-OES and XRF to determine the elemental composition of all the metals in the recovered cathode (RECAT) materials. The ICP-OES ((0.23 ppm Li), 4047 ppm Mn), (1.43ppm Ni) (054 ppm Co)), and XRF ((61.3% Mn), (24.7% Ni), and (11.3% Co)) results reveal that the recovered cathode material contains Mn metal predominantly followed by Ni and Co. Considering the ICP-OES and XRF results, the recovered cathode material can be identified as $LiMn_{1.5}Ni_{0.5}O_4$ cathode material with Co doping.

4.3.1.2 X-ray diffraction studies

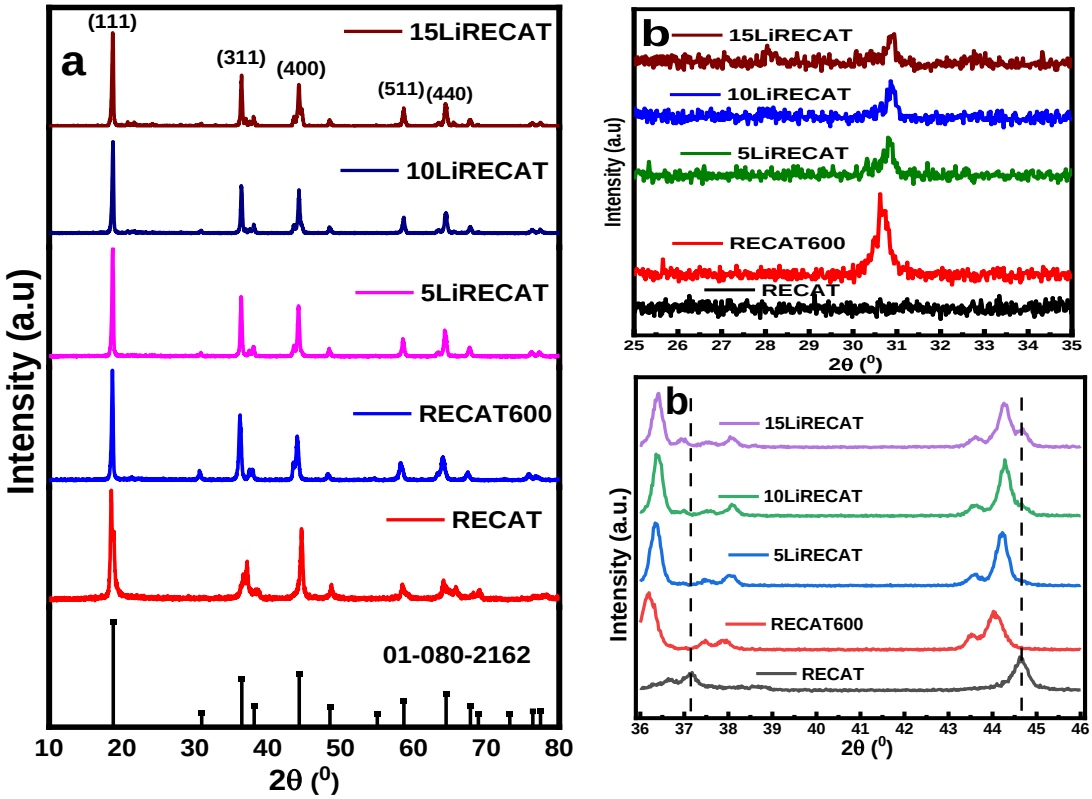

Figure 4.2. (a) X-ray diffraction patterns of RECAT, RECAT600, 5LiRECAT, 10LiRECAT, and 15LiRECAT materials, respectively, and **(b)** Magnified part of 2θ value range from 25 to 35 and 36 to 46 degrees of X-ray diffraction patterns of image (a).

The recovered and re-lithiated cathode materials are subjected to X-ray diffraction analysis to understand the crystallographic information of the cathode materials. The X-ray diffraction patterns are given in **Figure 4.2a,** which were well-matched with the diffraction peaks of PDF reference number 01-080-2162 of $LiMn_{1.5}Ni_{0.5}O_4$ (LMNO) material. The X-ray diffraction planes are indexed as per the reference PDF file. The X-ray diffraction patterns reveal that there was no peak observed at 2θ around 31 degrees for the recovered cathode material, but in the case of heat-treated material, a small peak appeared at 2θ around 31 degrees and remained after the lithiation of cathode materials (see **Figure 4.2b**). This indicates the reconstruction/reformation of the crystal lattice of the recovered cathode material by removing passive surface and inactive compounds

over the surface of the cathode material. The small diffraction peak is identified as the (220) plane in the x-ray diffraction pattern of the cathode material.

During prolonged charge-discharge cycles, the loss of Li ions occurs, and this loss of Li ions leads to the distortion or dilation of the cathode active material.[23] Wangda Li et al's,[24] report suggests that the collapse in the crystal lattice of the cathode material depends entirely on utilizing Li content irrespective of the transition metals; the loss of Li ions from cathode materials distorts the cathode structure. The irreversible structural changes happen due to cation mixing during the lithiation, and the de-lithiation mechanism of cathode active material could lead to Li loss, which leads to structural collapse due to the change in the oxidation states of the metals.[25] Further, the X-ray diffraction pattern analysis reveals that the diffraction peaks indexed as (311) and (400) are compared between the recovered and regenerated cathode materials. It is observed that the peaks are shifted towards lower 2θ, and also, it could be observed that the splits in the peaks are due to the expansion of the lattice parameters and crystal lattice. The contracted crystal lattice of the used cathode material regained its stable structure after heat treatment and re-lithiation. The literature report advocates that the contraction of crystal structure occurs due to de-lithiation.[25,26] The shift of diffraction peaks towards lower 2θ indicates increased lattice parameters and expanded volume.[26] The diffraction peaks shift towards higher 2θ indicates the contraction of the crystal lattice due to stress and non-stoichiometric phase reasons. In our case, the recovered cathode material showed a shift in the critical diffraction peaks toward higher 2θ due to the loss of Li after continuous charge-discharge cycles in their first life, causing the formation of non-stoichiometric phases that led to the contraction of the crystal lattice. After removing inactive compounds over the surface of the cathode active material upon heating, the cathode materials regained the crystal structure and caused expansion of the crystal lattice, which could be confirmed by identifying the

shift in the diffraction peaks towards lower 2θ due to the expansion of the crystal lattice. The shift in the 2θ values for the peaks indexed as (311) and (400) is shown in **Figure 4.2b**; in the exact figure, it can be observed that the appearance of small peaks upon an increase in the lithiation percentage, which indicates the formation of Li-rich phases. In the X-ray diffraction patterns, the peak labeled as (311) is considerably small; it might be due to structural changes during the charge-discharge mechanism of their first life. The change in the X-ray diffraction pattern is identified as the transformed material crystal structure, which was converted into a low Li manganese oxide, which also belongs to the cubic crystal with space group Fd-3m. This phase material possibly formed due to the reaction between the byproducts of the unstable CEI layer and the dissolved Mn ions in the electrolyte.

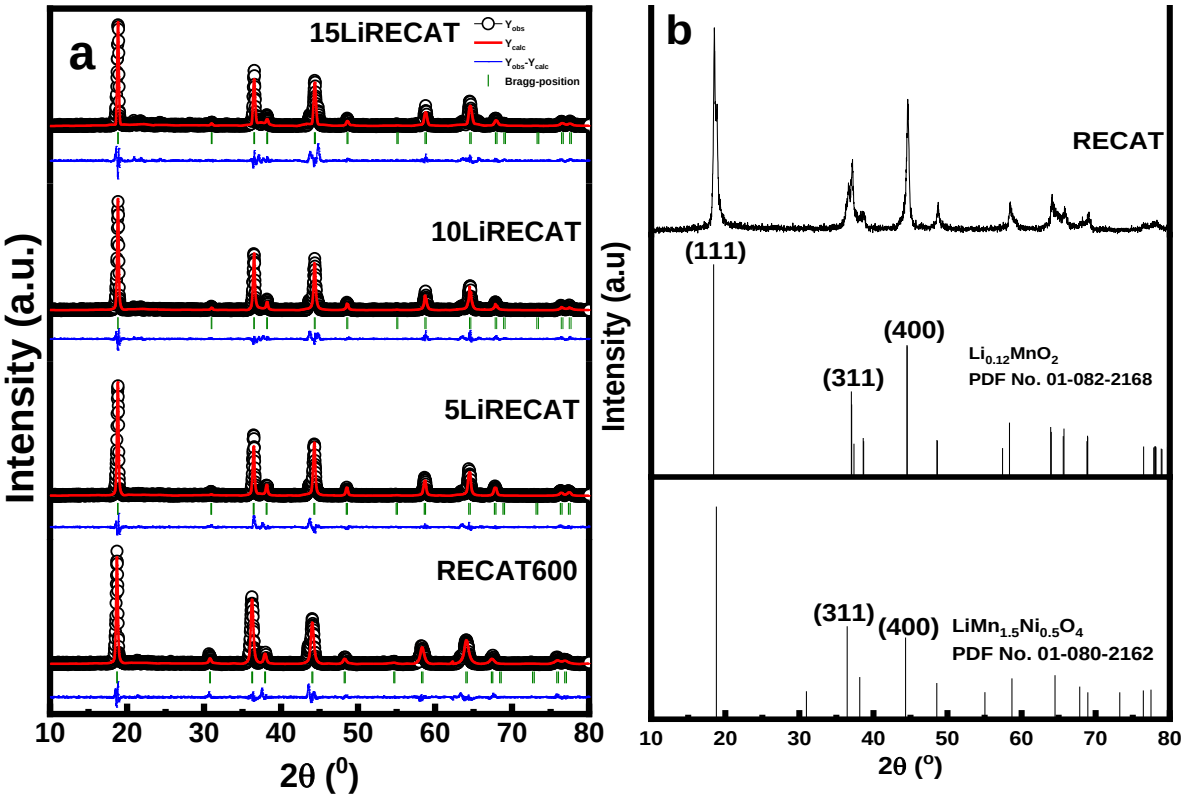

Figure 4.3. **(a)** Rietveld refinement plots of RECAT600, 5LiRECAT, 10LiRECAT, and 15LiRECAT materials, respectively. **(b)** comparison of the X-ray diffraction pattern of RECAT with corresponding reference datasets.

The comparison of the X-ray diffraction pattern of RECAT with corresponding reference datasets is given in **Figure 4.3(b)** of Supporting information. Several reports say the spinel phase favors faster Li-ion diffusion kinetics and better battery performance.[27,28] However, during long charge-discharge cycles and loss of Li ions, the cathode structure undergoes phase changes, which causes the failure of the battery. The (311) peaks of regenerated cathode materials eventually grew upon lithiation and re-constructed the spinel phase. Rietveld refinement studies for the x-ray diffraction patterns of the RECAT600, 5LiRECAT, 10LiRECAT, and 15LiRECAT were performed using Fullprof software and are shown in **Figure 4.3(a).** The diffraction patterns of all the materials are indexed to a cubic spinel structure with $Fd\bar{3}m$ space group.

4.3.1.3 Raman spectroscopic analysis

Figure 4.4. shows Raman spectra of the recovered, heat treated and regenerated cathode materials. It is observed that the vibrational peaks for the recovered and heat-treated cathodes are slightly broader compared to the lithiated cathode materials, which is due to the loss of long-range translational symmetry and reciprocal lattice/crystal lattice distortion[29], which correlates well with X-ray diffraction results. The broadening of the peaks in Raman spectra indicates the distorted entities[30] in the used cathode material, which is also slightly present even after heat treatment. The peak broadening is reduced in lithiated cathode materials, resulting in sharp peaks comparatively. The prominent peak appeared at around 627.3 cm^{-1} and 602.4 cm^{-1} for RECAT and RECAT600 materials. The redshift in RECAT and RECAT600 material spectra indicates the distorted structure of used cathode materials as the vibrational peak at this range is related to the Mn-O bonding of MnO_6 Oh symmetry. The blueshift in the spectra 607.4 cm^{-1} for 5LiRECAT, 614.6 cm^{-1} for 10LiRECAT, and 615.4 cm^{-1} for 15LiRECAT materials indicate the lithiation and formation of stable structure. The other peaks indicate the vibrational behavior of Ni-O bonding of NiO_6

octahedral groups at Raman shift around 498.2 cm^{-1}, 478.7 cm^{-1}, 485.7 cm^{-1}, 495.5 cm^{-1}, and 495.5 cm^{-1} for RECAT, RECAT600, 5LiRECAT, 10LiRECAT, and 15LiRECAT respectively. This also follows a similar trend as in the case of the Mn-O vibrational peak, as it shifts toward the left (redshift) initially and toward the right (blueshift) side of the spectra. The small broad peak in the range at around 390 cm^{-1} can be observed only in the case of lithiated material. Such a peak is significantly weak or not clearly observed for recovered and heat-treated cathode material and is related to Li-O stretching vibrations of LiO_4 tetrahedral groups.

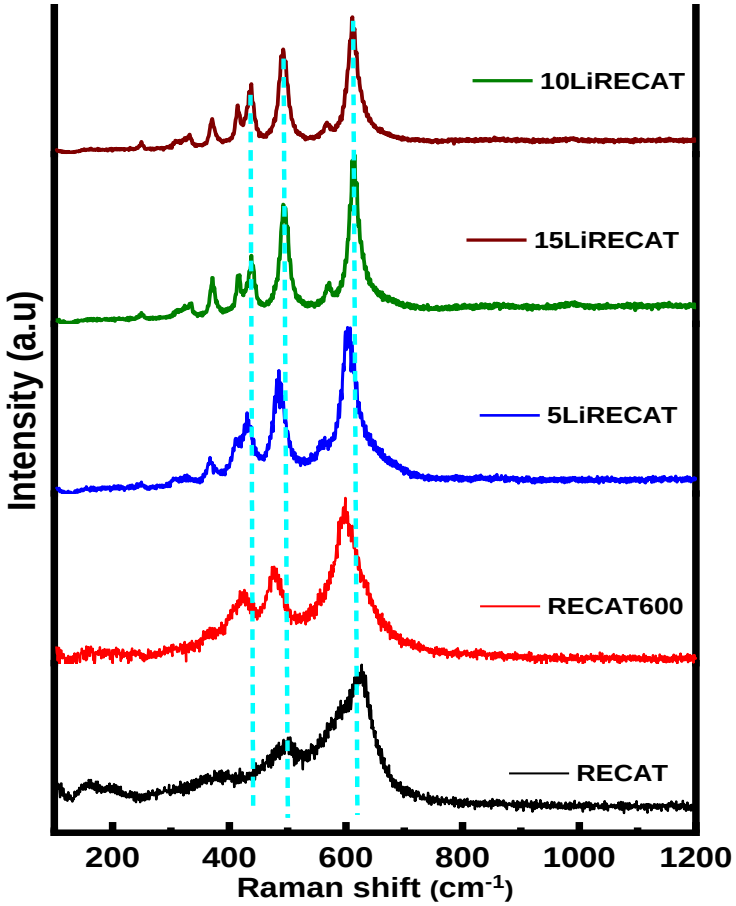

Figure 4.4. Raman spectra of RECAT, RECAT600, 5LiRECAT, 10LiRECAT, and 15LiCAT materials.

4.3.1.4 Electron microscopic studies

Field emission scanning electron microscopy (FESEM) images of RECAT, RECAT600, 5LiRECAT, 10LiRECAT, and 15LiRECAT materials were displayed in **Figure 4.5a-e**. Recovered

cathode material (**Figure 4.5a**) (before heating) shows the bulk structure, which has a mixture of metal oxide cathode material and carbon structure that can be seen as small fibrous structures over the surface of the cathode particles. The carbon content and the cathode material are present due to the use of carbon conductive agents during electrode fabrication. After heat treatment of the recovered cathode material, such carbonaceous structures were burned away, and the cubical morphology of the particles formed, which can be observed in **Figure 4.5b**. As seen in the Figure, the lithiated cathode materials also formed cubic structures with sharp edges**. 4.5c-e**.

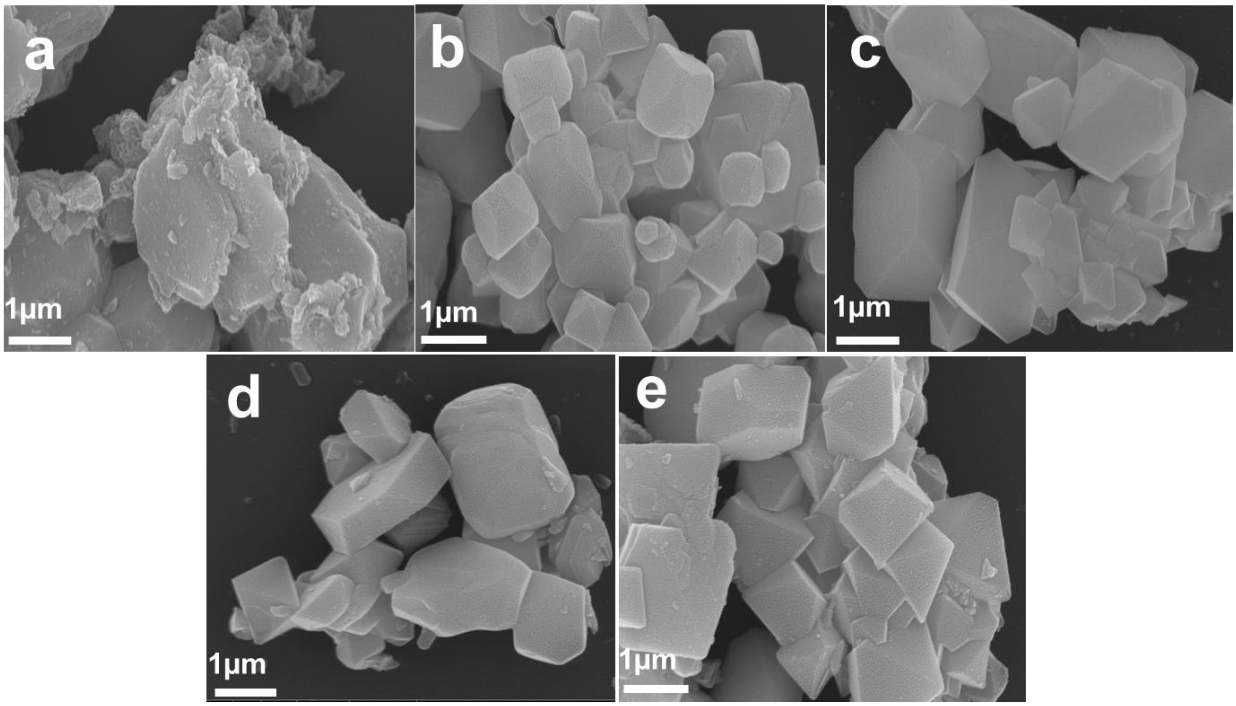

Figure 4.5. FESEM images of **(a)** RECAT, **(b)** RECAT600, **(c)** 5LiRECAT, **(d)** 10LiRECAT, and **(e)** 15LiCAT materials.

Figure. 4.6 (a-e) shows the high-resolution transmission electron microscopic (HR-TEM) images of the recovered and regenerated cathode materials. The inset figures are magnified areas of the particular region marked with the square with a white outline generated by Fast Fourier Transform (FFT) and inverse FFT given to ease of visualization of the lattice fringe widths. Inset

of **Figure. 4.6a** displays the composite behavior identified by measuring the lattice fringe widths from the HRTEM image, the fringe width of 0.45 nm, which is comparable to the d-spacing of the value of (111) plane of the X-ray diffraction pattern of the cathode material, the same image has shown the lattice fringe width of 0.23 nm which is related to the (100) plane of the X-ray diffraction of the pattern of carbonaceous material. **Figures. 4.6 (b-e)** shows the HRTEM images of the RECAT600, 5LiRECAT, 10LiRECAT, and 15LiRECAT materials, and the inset images show the lattice fringe widths of 0.42 nm, 0.41 nm, 0.43, and 0.47 nm respectively, all these values are analogous to the lattice spacing of the (111) plane of the LMNO based cathode materials.

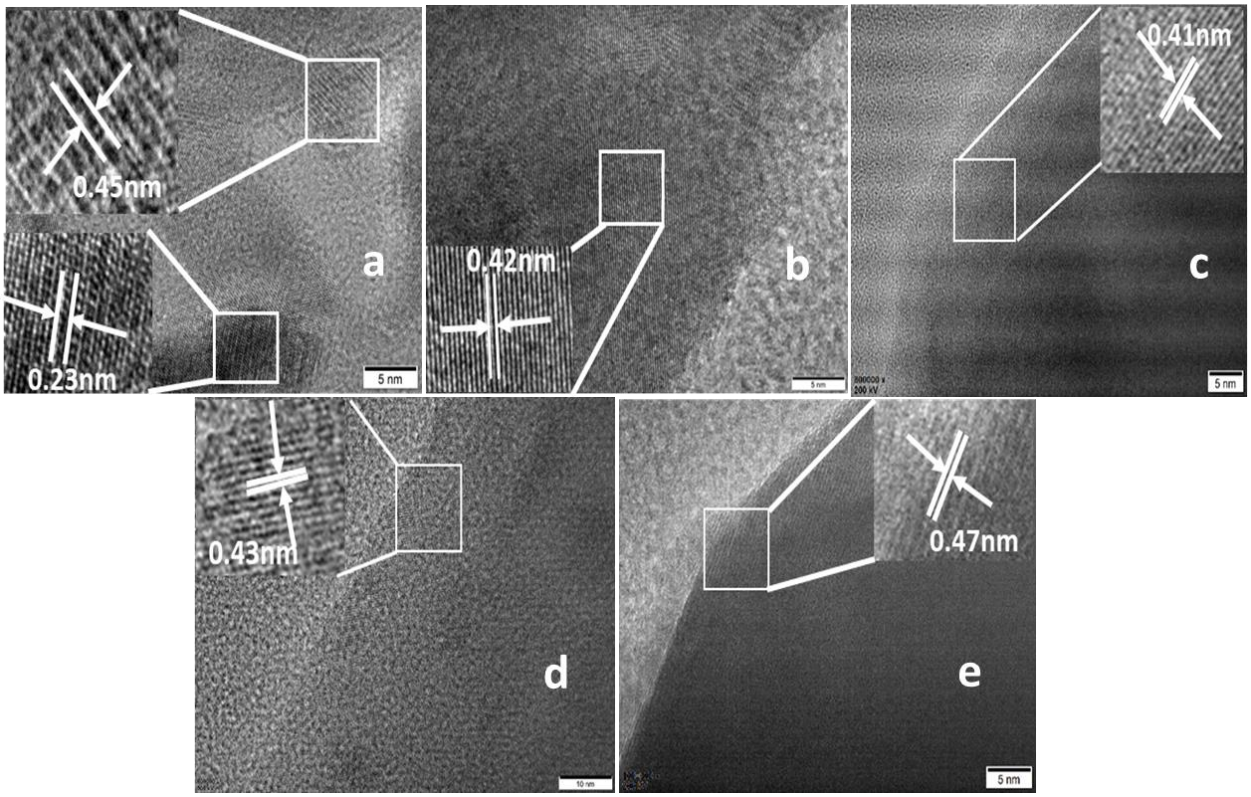

Figure 4.6. HR-TEM image of **(a)** RECAT, **(b)** RECAT600, **(c)** 5LiRECAT, **(d)** 10LiRECAT, and **(e)** 15LiCAT materials. (Inset images are the marked fast Fourier transform (FFT) region.

The STEM images and the EDS elemental mapping of the recovered and regenerated cathode materials are shown in **Figures 4.7 (a1-e1)** and **4.7 (a2-e2).**

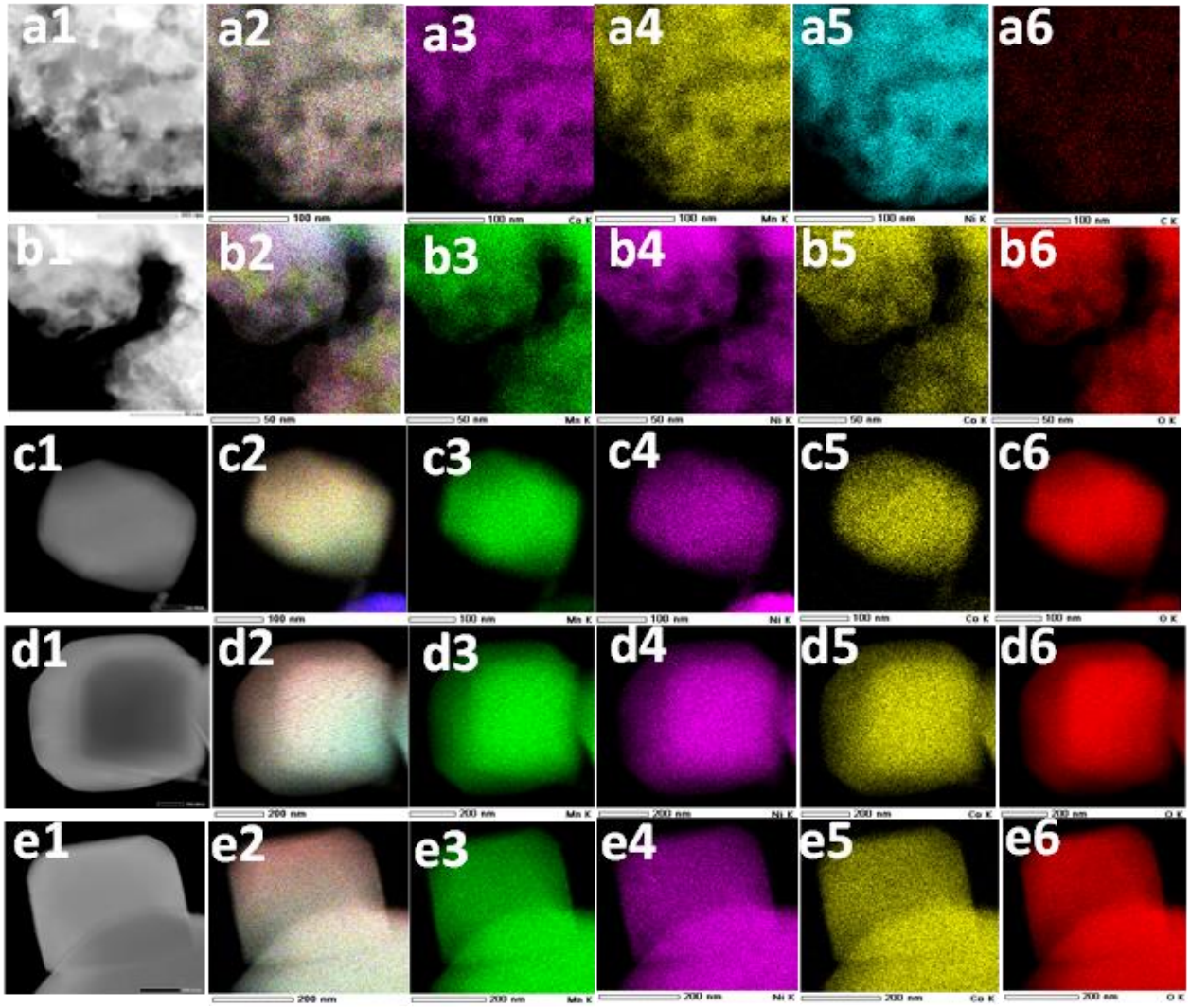

Figure 4.7. (a1-e1) Scanning Tunnelling Electron Microscopic (STEM) images, (a2-e2) EDS elemental mapping overlay of all the elements and remaining images **(a3-e6)** are of mapping of individual elements C, Mn, Ni, Co of **(a1-a6)** RECAT, Mn, Ni, Co, O **(b1-b6)** RECAT600, **(c1-c6)** 5LiRECAT, **(d1-d6)** 10LiRECAT, **(e1-e6)** 15LiCAT.

The STEM images and the elemental mapping of the respective area of the spread particles confirm the morphological changes from the recovered cathode and the regenerated cathode materials upon heating. The careful observation of the images in **Figure 4.7 (a1-e1)** could reveal the evolution of particle morphology changing from bulk structure to a particular cubical shape. The elemental mapping confirms the uniform distribution of all the elements throughout the

material structures. It can be observed that carbon content is present in the recovered cathode material RECAT. However, in the case of heated and lithiated materials, there is no carbon content, which appears and indicates the removal of carbon upon heating. The mapping results confirm the presence of all the elements Mn, Ni, Co, and O, distributed thoroughly in the cathode structures, which indicates the transition elements composition was not affected in the first life of the cathode materials in the used cells. As a result, the cathode material revived successfully after lithiation.

4.3.1.5 XPS studies

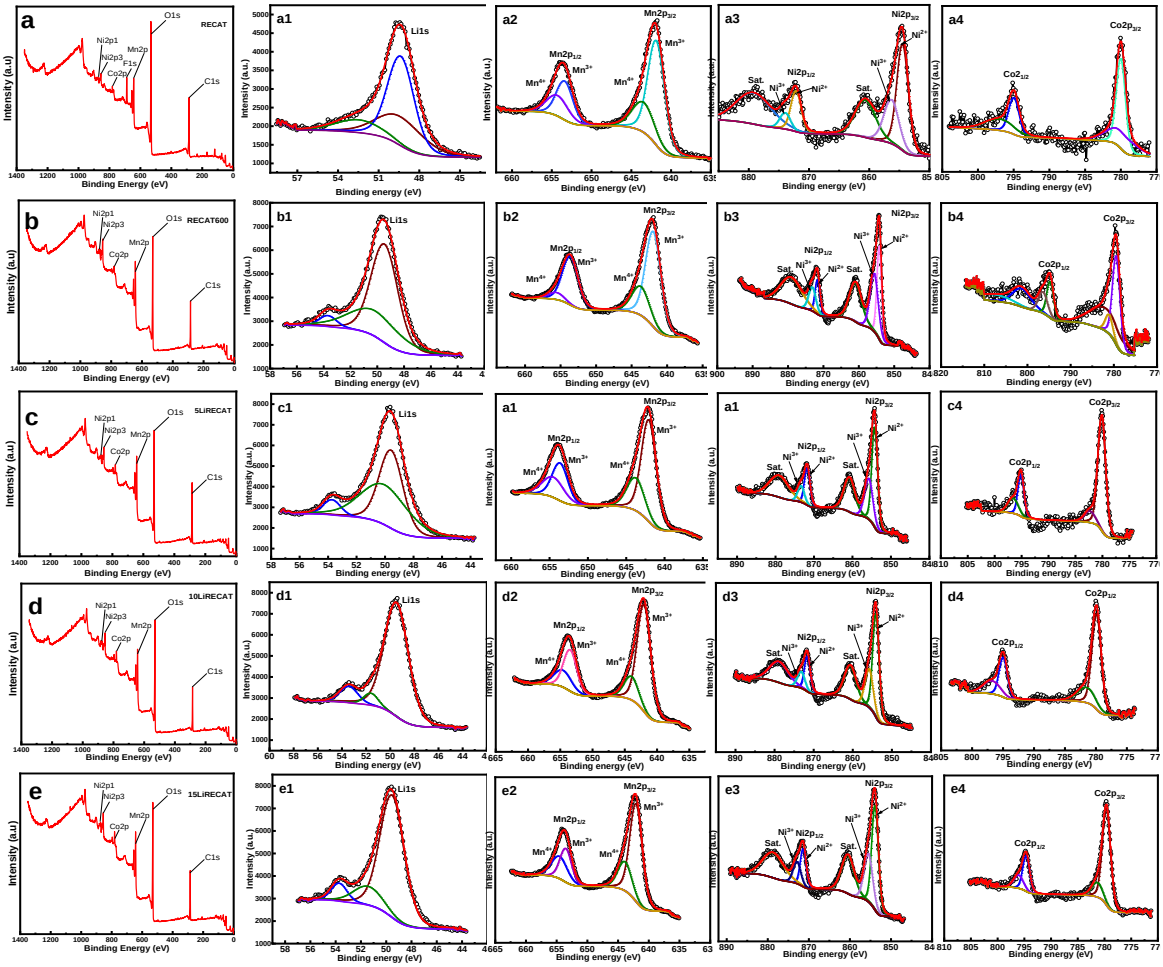

Figure 4.8. **(a-e)** XPS survey spectra, **(a1-a4)** Deconvoluted peaks of XPS core levels of Li1s, Mn2p, Ni2p, Co2p for RECAT, RECAT600 **(b1-b4)**, 5LiRECAT**(c1-c4)**, 10LiRECAT (d1-d4), 15LiRECAT (e1-e4).

The XPS analysis was employed to understand the valence states and elemental composition of the recovered, regenerated, and lithiated cathode materials. All the peaks were deconvoluted and resolved using CasaXPS software. **Figure 4.8** shows the XPS survey spectra **(Figure 4.8 (a-e))** and deconvoluted signals of Li1s, Mn2p, Ni2p, Co2p, and O1s core levels for the RECAT, RECAT600, 5LiRECAT, 10LiRECAT, and 15LiRECAT materials. The deconvoluted spectra of Li1s core level are shown in **Figure 4.8 (a1-e1)**; the prominent peak of Li1s core level has the binding energy 49.4 eV for the RECAT material confirms the chemical and electronic state and the binding energy values for the Li1s level for heat treated and lithiated materials are around 49.6 eV. However, the intensity of the prominent peak of Li1s core level for recovered material is lesser than that of other materials, such as heat-treated and lithiated cathode materials. RECAT material has F1s signals, which can be seen in survey spectra (**Figure 4.8 (a-e)**). The F1s signal is due to the formation of LiF over the surface of the used cathode material, which is also contributed by the PVDF binder or other carbon fluorides formed by the side reactions during the charge-discharge reactions. The F1s XPS signal has not been observed in the case of other electrode materials such as RECAT600, 5LiRECAT, 10LiRECAT, and 15LiRECATand this indicates that upon heat treatment and lithiation, thermal treatment vanishes the LiF and other unwanted impurities. The 15LiRECAT materials have shown more intensity for the Li1s core level, confirming the Li ions' loss in the used cathode material and the increased Li ions after re-lithiation. It can be concluded that the re-lithiation could revive the cathode structure effectively. The deconvoluted spectra for Mn2p core levels of RECAT, RECAT600, 5LiRECAT, 10LiRECAT, and 15LiRECAT materials were displayed in Figure. **4.8 (a2-e2)**, the Mn2p core level exhibit two components, Mn2p3/2 and Mn2p1/2, due to spin-orbit coupling.[31] Mn2p core levels are comprised of $Mn2p_{3/2}$ levels with binding energy 642.2 eV (RECAT), 642.3

(RECAT600), 642.2 (5LiRECAT), 642.2 (10LiRECAT) and 642.2 (5LiRECAT), and $Mn2p_{1/2}$ levels with binding energy 642.2 eV (RECAT), 642.3 (RECAT600), 642.2 (5LiRECAT), 642.2 (10LiRECAT) and 642.2 (5LiRECAT). The obtained values of binding energies for Mn2p core levels are in close agreement with the values for Mn^{3+} and Mn^{4+}, as reported by Nesbitt et al.[32] The spin-orbit coupling occurs in Ni2p core level as well, the deconvoluted spectra of the Ni2p core level also have two components, $Ni2p_{3/2}$ and $Ni2p_{1/2}$ **(Figure. 4.8 (a3-e3))**. Ni2p core levels are comprised of $Ni2p_{3/2}$ levels with binding energy 854.7 eV (RECAT), 854.8 (RECAT600), 854.6 (5LiRECAT), 854.6 (10LiRECAT) and 854.6 (15LiRECAT), and $Ni2p_{1/2}$ levels with binding energy 872.2 eV (RECAT), 872.2 (RECAT600), 872.0 eV (5LiRECAT), 872.0 eV (10LiRECAT), and 872.0 eV (15LiRECAT). The Co2p core level also has two sub-levels, $Co2p_{3/2}$ and $Co2p_{1/2}$ **(Figure. 4.8 (a4-e4))**; the deconvoluted spectra of the Co2p core have $Co2p_{3/2}$ levels at binding energy values 854.7 eV (RECAT), 854.8 (RECAT600), 854.6 (5LiRECAT), 854.6 (10LiRECAT) and 854.6 (15LiRECAT). $Co_2p_{1/2}$ levels with binding energy 872.2 eV (RECAT), 872.2 (RECAT600), 872.0 eV (5LiRECAT), 872.0 eV (10LiRECAT), and 872.0 eV (15LiRECAT).

4.3.2 Electrochemical Characterization

4.3.2.1 Cyclic voltammetry and Electrochemical impedance spectroscopy study

Cyclic voltammetry and electrochemical impedance spectroscopic studies were employed to assess the electrochemical redox characteristics and ionic transport capabilities of recovered (RECAT), heat treated (RECAT600), and regenerated (5LiRECAT, 10LiRECAT, and 15LiRECAT) cathode materials. **Figure. 4.9a** shows the cyclic voltammograms carried out in a potential window of 2.5V and 5V under the sweep rate 100 mVS^{-1} conditions. It can be observed that there are four pairs of reversible redox peaks at three different potential regions, which are

characteristic of different redox-active metals present in the cathode-active materials. The first pair of redox peaks appeared at around 2.6V/3.0V, a characteristic behavior of the transition of Mn^{2+}/Mn^{3+} states.[33] The other prominent redox peaks at around 4.0-4.2V in all the materials correspond to the redox couples Mn^{3+}/Mn^{4+}. The other charge peak appeared at ~3.2 V, and its redox pair peak appeared on the discharge curve at 2.75 V; the redox pair corresponds to the Li^+ extraction of the cathode and insertion into the cathode active material. The third and fourth redox peaks with predominant intensity were observed at higher potential ranges of 4.72/4.63 V and 4.81/4.73 V, respectively, corresponding to Ni^{2+}/Ni^{4+}, which indicates the electrochemical activity of Ni in the active material.[34]

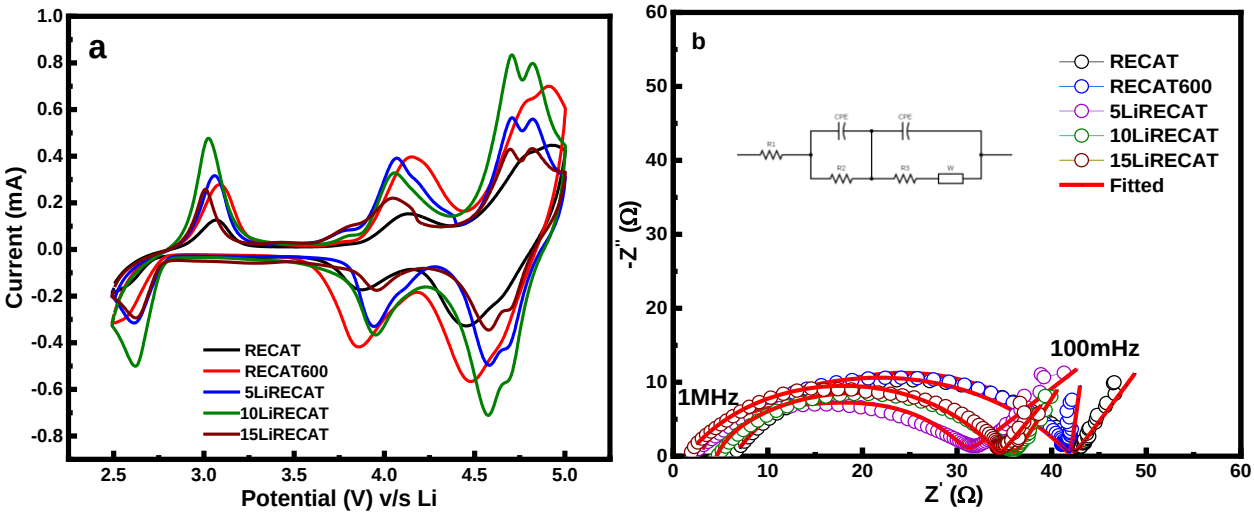

Figure 4.9. **(a)** Cyclic voltammograms and **(b)** Nyquist plots of RECAT, RECAT600, 5LiRECAT, 10LiRECAT, and 15LiRECAT materials.

These redox peaks of lithiation/de-lithiation at higher voltage indicate that more driving force is necessary to urge the Li-ions from the cathode to the anode. It is observed that after careful comparison and analysis of the redox peaks in the cyclic voltammograms of the recovered cathode material, heat-treated cathode, and lithiated cathode materials, the redox peaks of RECAT material

are less intense and much sharper as compared to the regenerated cathode materials which indicate the destitute nature of cathode structure to be an efficient cathode active material. The recovered cathode material has been subjected to re-processing steps such as heat treatment and re-lithiation, which has supported the regain of its cathode active capabilities and efficient performance.

Electrochemical impedance spectroscopy (EIS) was employed to investigate the kinetics of Li-ion insertion and exertion processes. The Nyquist plots for all cathode materials are displayed in **Figure. 4.9b**, with the inset showing the equivalent circuit to fit the experimental data. This circuit comprises several resistance components: R_s represents the system resistance, R_{SEI} denotes the solid-electrolyte interface resistance, and R_{ct} stands for the charge transfer resistance. Additionally, the circuit includes a constant phase element (CPE) and Warburg impedance (W). The equivalent circuit is depicted in the figure inset**. 4.9b** was used to fit the Nyquist plots. The fitting values for the equivalent circuit are given in **Table 4.1**. In the high-frequency region, all materials exhibit an overlapping semicircle, attributed to both the SEI resistance (R_{SEI}) and charge transfer resistance (R_{ct}), indicating the insertion of Li ions at the interface between the electrode and electrolyte. A more detailed examination reveals two distinct semicircles: a smaller one in the higher frequency range and a larger one in the mid-frequency range. The smaller semicircle at higher frequencies is associated with the cathode-electrode resistance (R_{SEI}), while the larger semicircle in the mid-frequency region corresponds to the charge transfer resistance (R_{ct}). The 5LiRECAT has shown the least charge transfer resistance among all the cathode materials. Conversely, the recycled cathode material has exhibited higher charge transfer resistance than other materials. This indicates that the recovered cathode materials are degraded during their initial use, losing their ability to efficiently transport electrochemically active ions, resulting in reduced specific capacities during charge-discharge tests. By re-lithiating the recovered cathode materials,

their capacity for rapid ion transfer, crucial in Li-ion batteries, has been restored. A linear segment in the low-frequency range signifies the interface resistance and enhanced diffusion of Li^+ ions from the electrolyte to the anode.

Material / Parameter	RECAT	RECAT600	5LiRECAT	10LiRECAT	15LiRECAT
R_s (Ω)	5.45	2.48	2.17	4.71	2.32
R_{SEI} (Ω)	3.65	3.82	4.86	3.51	3.43
R_{ct} (Ω)	32.53	35.52	24.59	27.86	28.91

Table 4.1. Resistance values were obtained from the EIS fitting data**.**

The Recovered cathode material has more resistance than the regenerated cathode materials. However, the RECAT600 has shown more charge transfer resistance than the RECAT electrode due to the lesser availability of Li^+ ions in the cathode material. The re-lithiated cathode materials have shown comparatively lower resistance values, which indicates the cathode materials are well restored to their Li insertion-de-insertion properties, which is essential for the faster Li+ ion diffusion kinetics, which is a critical requirement for a good cathode material.[35]

4.3.2.2 Galvanostatic charge-discharge study

Figure 4.10 displays the galvanostatic charge-discharge studies of the recovered, heat-treated, and regenerated cathode materials. Initially, the recovered cathode materials from the spent LIBs were used directly, after heating and lithiation, to fabricate fresh coin cells and electrochemically tested to understand the charge-discharge behavior and the efficiency of the spent cathode material. The rate capability tests were conducted in the range of current densities, starting from 20mA to 200mA. The recovered cathode material subjected to the heat treatment and lithiation was also tested similarly.

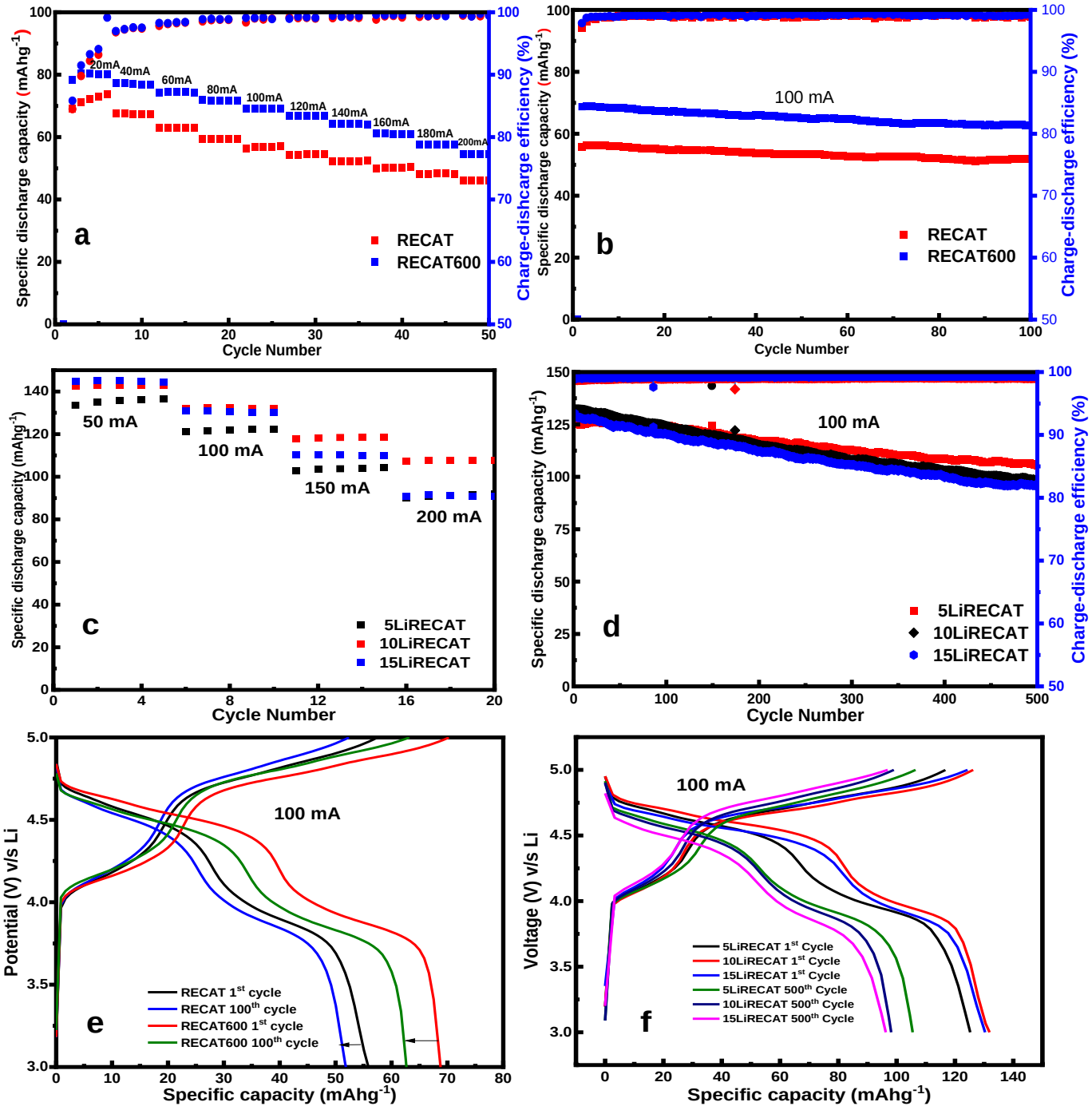

Figure 4.10. **(a)** rate capability, **(b)** cycle stability, (c) Potential v/s specific capacity curves of RECAT and RECAT600 cathode materials, (d) rate capability, (e) cycle stability, **(f)** Potential *v/s* specific capacity curves of 5LiRECAT, 10LiRECAT, and 15LiRECAT cathode materials.

As shown in **Figure 4.10 (a)**, the recovered cathode material (RECAT) has shown a low initial specific discharge capacity of 69.18 $mAhg^{-1}$ at 20mA current density. In contrast, the heat-treated cathode material (RECAT600) exhibited an initial specific discharge capacity of 78.37 $mAhg^{-1}$. The specific discharge capacity slightly increases after heat treatment because of the unwanted impurity surface over the spent cathode material is burnt off, which can enhance the activity of the cathode materials. In both recovered and heat-treated cathode materials, the charge-discharge efficiency is less at initial cycles, which is increased gradually; it might be due to the cathode surface slowly getting activated by forming a cathode-electrolyte interface (CEI).

The spent cathode materials have shown low discharge capacities due to the loss of Li^+ ions during their first life.[3,12,36] The spent cathode materials were rejuvenated by retrieving lost Li^+ ions from the cathode structures by re-lithiation with different ratios of lithium source. The re-lithiated spent cathode materials were also subjected to the electrochemical examination to understand the effect of re-lithiation on the performance of regenerated cathode materials. The heat-treated cathode materials were re-lithiated with 5% (5LiRECAT), 10% (10LiRECAT), and 15% (15LiRECAT) Li sources of the total cathode mass used for the re-lithiation.

The rejuvenated cathode materials were used as cathode materials for the fabrication of coin cells. The as-prepared coin cells are imperiled to the galvanostatic charge-discharge tests for a better understanding of their rate capability at different current densities, which is displayed in **Figure 4.10 (a, b)**, and long cycle stability tests at 100 mA current density, which is shown in **Figure 4.10 (c, d)**. The 5LiRECAT, 10LiRECAT, 15LiRECAT material has shown an initial specific discharge capacity of 125.2 $mAhg^{-1}$, 131.8 $mAhg^{-1}$, 130.3 $mAhg^{-1}$, and at the end of 500 cycles it shown 105.5 $mAhg^{-1}$,100.2 $mAhg^{-1}$, 96.2 $mAhg^{-1}$ with a capacity retention of 84.2%, 76.1% and 73.8% respectively. These charge-discharge results indicate that the lithiation could

revive the electrochemical activity of the used cathode materials by lithiation. Excessive lithiation causes a relatively lower capacity than controlled lithiation, which might be because excess lithiation may form non-favorable sedimentation over the surface of the cathode materials. The excess Li can re-order the cathode materials, which may cause structural instabilities, which lead to lower capacity retention. The 5% lithiated cathode materials have shown more capacity retention but lower discharge capacity compared to 10%and 15% lithiated cathode materials. The excess lithiated cathode materials have shown more discharge capacities as they behave as lithium-rich cathode active materials. The controlled lithiation could revive the activity of the cathode material. **Figure. 4.10 (c,d)** shows the specific capacity v/s voltage curves of recovered, heat-treated, and lithiated cathode materials cycled at 100 mA current density, illustrating capacity degradation at different cycles. Therefore, this study supplements the drastic improvement in the capacity of the material after lithiation. Also, the obtained capacity retention with long cycle stability of electrochemical studies displays the recovered cathode material's potential for the second life.

4.4 Conclusions

This study has demonstrated an effective method of regenerating cathode active materials from spent LIBs via aqueous chemical lithiation to directly regenerate the LMNO-based spinel class of cathode materials. The elements in the used cathode material Li, Mn, Ni, Co, and O are identified and evaluated in their crystal structure. The lithiation proportions are controlled by increasing the Li^+ concentration in the solution. The initial specific discharge capacity of the electrode made of the re-lithiation strategy could demonstrate 125.2 $mAhg^{-1}$, 131.8 $mAhg^{-1}$, and 130.3 $mAhg^{-1}$ at 100mA current density for 5LiRECAT, 10LiRECAT, and 15LiRECAT respectively. The electrode materials' specific discharge capacities reached 105.5 $mAhg^{-1}$, 100.2 $mAhg^{-1}$, and 96.2

$mAhg^{-1}$ after 500 continuous cycles for 5LiRECAT, 10LiRECAT, and 15LiRECAT respectively. Among these electrodes, the 5% lithiated cathode material (5LiRECAT) has shown capacity retention of 84.2%, more than other regenerated cathode material variants. Overall, the simple aqueous-based strategy to relitigate the diminished cathode material could provide a second life for the used cathode materials from the waste LIBs.

4.5 References

1 Y. Zhao, X. Yuan, L. Jiang, J. Wen, H. Wang, R. Guan, J. Zhang and G. Zeng, 2020, preprint, DOI: 10.1016/j.cej.2019.123089.

2 X. Zhang, L. Li, E. Fan, Q. Xue, Y. Bian, F. Wu and R. Chen, 2018, preprint, DOI: 10.1039/c8cs00297e.

3 B. Zhang, Y. Xu, D. S. Silvester, C. E. Banks, W. Deng, G. Zou, H. Hou and X. Ji, *J. Power Sources*, DOI:10.1016/j.jpowsour.2023.233728.

4 E. Fan, L. Li, Z. Wang, J. Lin, Y. Huang, Y. Yao, R. Chen and F. Wu, 2020, preprint, DOI: 10.1021/acs.chemrev.9b00535.

5 G. P. Nayaka, J. Manjanna, K. V. Pai, R. Vadavi, S. J. Keny and V. S. Tripathi, *Hydrometallurgy*, 2015, **151**, 73–77.

6 T. Wang, H. Luo, Y. Bai, I. Belharouak, K. Jayanthi, M. P. Paranthaman, B. T. Manard, E. T. H. Wang, F. Dogan, S. B. Son, B. J. Ingram, Q. Dai and S. Dai, *J. Power Sources*, DOI:10.1016/j.jpowsour.2023.233798.

7 Z. J. Baum, R. E. Bird, X. Yu and J. Ma, *ACS Energy Lett.*, DOI:10.1021/acsenergylett.1c02602.

8 B. Makuza, Q. Tian, X. Guo, K. Chattopadhyay and D. Yu, 2021, preprint, DOI: 10.1016/j.jpowsour.2021.229622.

9 L. Reinhart, D. Vrucak, R. Woeste, H. Lucas, E. Rombach, B. Friedrich and P. Letmathe, *J. Clean. Prod.*, DOI:10.1016/j.jclepro.2023.137834.

10 J. C. Y. Jung, P. C. Sui and J. Zhang, 2021, preprint, DOI: 10.1016/j.est.2020.102217.

11 Y. Yao, M. Zhu, Z. Zhao, B. Tong, Y. Fan and Z. Hua, 2018, preprint, DOI: 10.1021/acssuschemeng.8b03545.

12 G. Ji, J. Wang, Z. Liang, K. Jia, J. Ma, Z. Zhuang, G. Zhou and H. M. Cheng, *Nat. Commun.*, DOI:10.1038/s41467-023-36197-6.

13 R. Hausbrand, G. Cherkashinin, H. Ehrenberg, M. Gröting, K. Albe, C. Hess and W. Jaegermann, 2015, preprint, DOI: 10.1016/j.mseb.2014.11.014.

14 C. Pastor-Fernández, T. F. Yu, W. D. Widanage and J. Marco, 2019, preprint, DOI: 10.1016/j.rser.2019.03.060.

15 N. Mao, T. Zhang, Z. Wang and Q. Cai, *J. Power Sources*, DOI:10.1016/j.jpowsour.2021.230767.

16 T. Kim, L. K. Ono and Y. Qi, *J. Mater. Chem. A*, 2023, **11**, 221–231.

17 W. Li, A. Dolocan, P. Oh, H. Celio, S. Park, J. Cho and A. Manthiram, *Nat. Commun.*, 2017, **8**, 14589.

18 G. Cherkashinin, M. Motzko, N. Schulz, T. Späth and W. Jaegermann, *Chem. Mater.*, 2015, **27**, 2875–2887.

19 I. Takahashi, H. Kiuchi, A. Ohma, T. Fukunaga and E. Matsubara, *J. Phys. Chem. C*, 2020, **124**, 9243–9248.

20 J. Li and A. Manthiram, *Adv. Energy Mater.*, 2019, **9**, 1902731.

21 J. Zhang, P.-F. Wang, P. Bai, H. Wan, S. Liu, S. Hou, X. Pu, J. Xia, W. Zhang, Z. Wang, B. Nan, X. Zhang, J. Xu and C. Wang, *Adv. Mater. Deerfield Beach Fla*, 2022, **34**, e2108353.

22 Z. Zhang, C. Qin, K. Wang, X. Han, J. Li, M. Sui and P. Yan, *J. Energy Chem.*, 2023, **81**, 192–199.

23 J. C. Stallard, L. Wheatcroft, S. G. Booth, R. Boston, S. A. Corr, M. F. L. De Volder, B. J. Inkson and N. A. Fleck, *Joule*, 2022, **6**, 984–1007.

24 W. Li, H. Y. Asl, Q. Xie and A. Manthiram, *J. Am. Chem. Soc.*, 2019, **141**, 5097–5101.
25 J. P. Pender, G. Jha, D. H. Youn, J. M. Ziegler, I. Andoni, E. J. Choi, A. Heller, B. S. Dunn, P. S. Weiss, R. M. Penner and C. B. Mullins, *ACS Nano*, 2020, **14**, 1243–1295.
26 J. Zhu, K. Yoo, A. Denduluri, W. Hou, J. Guo and D. Kisailus, *J. Mater. Res.*, 2015, **30**, 286–294.
27 X. Zhu, A. Huang, I. Martens, N. Vostrov, Y. Sun, M. Richard, T. U. Schülli and L. Wang, *Adv. Mater.*, 2024, **36**, 2403482.
28 W. Zhu, H. Su, P. Bai, Z. Li, J. Zhang, J. Zhang, M. Li, Y. Chen and Y. Xu, *Chem. Eng. J.*, 2024, **480**, 148045.
29 G. Gouadec and P. Colomban, *Prog. Cryst. Growth Charact. Mater.*, 2007, **53**, 1–56.
30 Y. Gao and P. Yin, *Sci. Rep.*, 2017, **7**, 43602.
31 J. B. Gieu, V. Winkler, C. Courrèges, L. El Ouatani, C. Tessier and H. Martinez, *J. Mater. Chem. A*, 2017, **5**, 15315–15325.
32 H. W. Nesbitt and D. Banerjee, *Am. Mineral.*, 1998, **83**, 305–315.
33 L. L. De Taeye and P. M. Vereecken, *J. Mater. Chem. A*, 2022, **10**, 24398–24409.
34 Y. Bencherifi, B. Larhrib, A. Sayegh, G. Nikiforidis and M. Anouti, *J. Appl. Electrochem.*, 2021, **51**, 1651–1664.
35 M. Gaberšček, *Nat. Commun.*, 2021, **12**, 6513.
36 Y. Liu, B. Jiao, X. Guo, S. Li, X. Lou, F. Jiang, X. Weng, M. Cao, J. Chen, Q. Zhang, G. Wang, J. Di and P. Xu, *Energy Storage Mater.*, 2024, **72**, 103684.

Chapter5

Performance analysis of regenerated rGO-electrodes from spent Li-ion battery anodes for secondary energy device applications

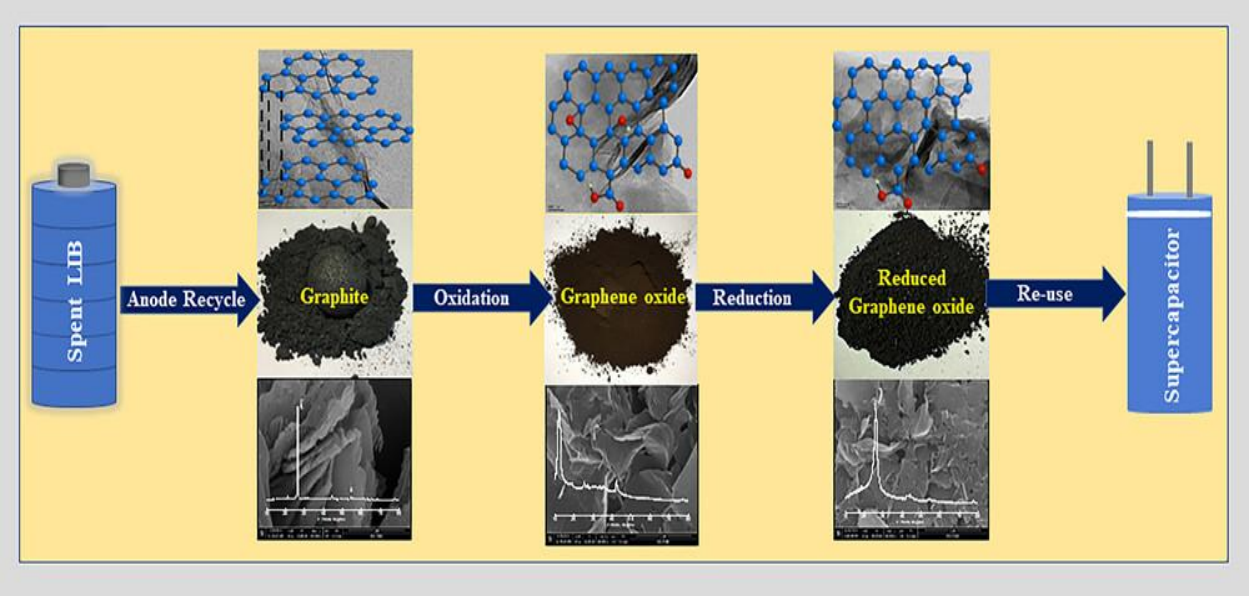

Highlights

- This study aims to recycle graphite from spent anode material
- Synthesize reduced graphene oxide (rGO) in an environmentally friendly approach. rGO was prepared from graphene oxide (GO) obtained from the spent graphite (G) electrode by the modified Hummer's method.
- The graphene oxide powder was reduced by ascorbic acid at 60 ^{0}C through a chemical reduction process using GO. The structural morphology of G, GO, and rGO were characterized by XRD, FE-SEM, HR-TEM Raman, and XPS.
- The spent graphite recovered and functionalized to prepare rGO.
- The prepared rGO are studied electrochemically for the supercapacitor application.
- The prepared materials from the recovered spent graphite showed prominent electrochemical performance.

- The results of this chapter published as **BP Shivamurthy**, **GP Nayaka***, G Santhosh Performance Analysis of Regenerated rGO Electrodes from Spent Li-ion Battery Anodes for Secondary Energy Device Applications, **Energy & Fuels**, 37 (4), 3188–3195, 2023.
- The portion of research work in this chapter is filed for patent as "Process for the production of agricultural fertilizers from acid waste left after modified Hummer's method process. Application No. **IN202411071629**.

5.1 Introduction:

Li-ion batteries are the key components for the energy sources in the present era owing to their unique, lightweight, long cycle life, high energy density, and small memory effect properties.[1] A study by Natarajan et al.,[2] has reported that the consumption of spent LIBs between 2017 and 2030 is estimated to be 11 million tons or more. If handled improperly, this large number of spent LIBs will cause major environmental issues. Because these spent LIBs contain heavy metals, hazardous gases, and flammable elements.[3] Therefore, disposal of these spent LIBs into a landfill is impossible, as contaminating soil and water will cause danger to the health and environment.[4] As a result, recycling these spent LIBs is the most favored way to conquer the problem connected with it.

We urgently need scalable, effective, environmentally friendly, and economical recycling methods to recover metals from spent LIBs. Most recycling technologies are not cost-effective and cannot recover the critical components. Throughout the recycling of these spent LIBs, more extra attentiveness has been given to cathode materials recycling than the anode materials. This may be due to transition metals in oxide materials as they participate in several applications.[5] LIB external metal cases and anodes were neglected while cathode materials were being recycled. The anode materials contain graphite in a larger percentage, which can also be recycled easily and used to synthesize graphene due to its excellent electrical properties, which have been used in various applications like supercapacitors, fuel cells, batteries, solar cells, and many more.[6–10]

Till today, many methods have been developed to synthesize reduced graphene oxide (rGO) viz., chemical vapor deposition,[11] thermal reduction,[12] arc discharge,[13] epitaxial growth,[14] and solution-based.[15] Among the mentioned methods, the solution-based method is the best to synthesize rGO in bulk at a low cost.[15] To synthesize rGO, Graphene oxide (GO) is reduced

chemically using various reducing agents like sodium borohydrate,[16] hydrazine monohydrate,[17] hydroquinone,[18] and alkali.[19] All these methods need expensive and ecologically hazardous chemicals in sophisticated environments. By keeping this in mind, we have used ascorbic acid in this study to reduce GO. Ascorbic acid is an environmentally friendly mild reducing agent with a non-toxic property and has also been used as a primary reductant in laboratories. It is naturally employed as a reducing agent in living things.[20,21]

In this study, GO was successfully prepared from graphite powder recovered from the spent LIB anode through the modified Hummer's method. The prepared GO was reduced by a reducing agent, ascorbic acid, at 60 ^{0}C for about 30 min. The flow chart for the complete process is depicted in **Figure. 1**. The as-synthesized samples were characterized by XRD, FTIR, UV Vis., XPS, Raman, BET surface area, FE-SEM, and HR-TEM. Electrochemical studies were conducted to know the cyclic voltammetry, Impedance, and charge-discharge behaviors. The present study proposes an easy waste-to-wealth approach for synthesizing rGO from spent LIBs.

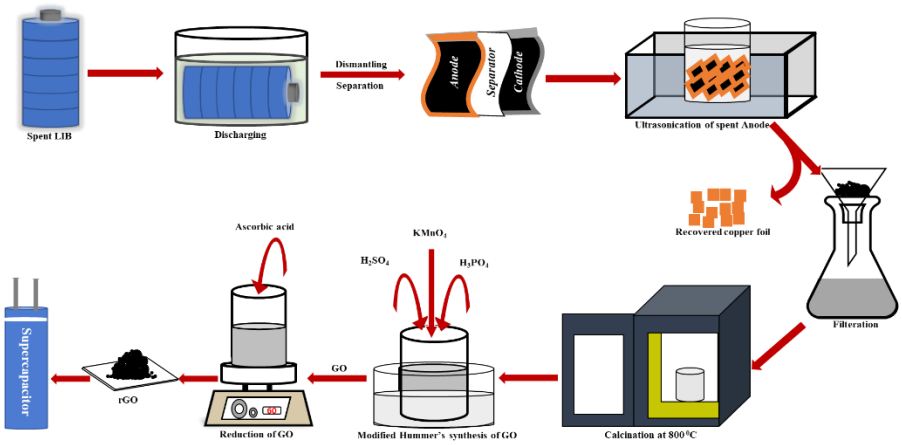

Figure 5.1 Flow chart for the complete recycling process

5.2 Methods and Materials

5.2.1 Materials and reagents.

The chemicals and reagents used in this study are of analytical grade. The graphite powder used here was taken from spent Li-ion polymer batteries (iPhone) and dismantled to obtain the anode material. To avoid explosion and hampering, the spent LIBs were discharged fully in a salt solution and dissembled to take apart the anode and cathode materials layered on coiled Al-foil and Cu-foil. The Cu-foil was uncoiled and cut into small pieces of 1×1 cm, then immersed in de-ionized water followed by sonication. After completely removing active anode material from Cu-foil, it was filtered and calcined at 800 ^{o}C for 2 h in an air atmosphere to burn out the binder and other organic materials.

5.2.2 Synthesis of graphene oxide from graphite of spent LIBs anode.

Graphene oxide was prepared through a modified Hummer's method using spent graphite powder recovered from spent LIBs.[22] 1:9 volume ratio of H_3PO_4 and H_2SO_4 taken in a beaker and stirred for 30 min in the ice bath. To this, 1 g of recovered graphite powder, followed by the addition of 6 g $KMnO_4$ slowly, and stirred for 30 min till the color of the mixture turns dark brown; then 100 mL of de-ionized water is added slowly, which leads to an exothermic reaction. Finally, to stop the $KMnO_4$ reaction, a mixture of H_2O_2 and de-ionized water is added. After keeping this mixture overnight, the supernatant liquid was separated from powder and neutralized to convert it into water-soluble nitrogen, phosphorus, and potassium plant fertilizer (also known as N, P, K fertilizer) to balance the soil pH level, and the separated powder sample was washed with a mixture of HCl and water 1:10 ratio. Finally, the obtained GO was dried in a hot air oven at 60 ^{0}C. This was ground in an agate mortar to be used in the next step.

5.2.3 Reduction of GO using ascorbic acid.

The obtained GO (0.5 g) was dispersed in a beaker containing 100 ml of de-ionized water. Then, 5 g of ascorbic acid was added to the beaker and kept on the hot plate with a stirrer at 60 ^{0}C for 1 h. Finally, the mixture was centrifuged, washed, and dried at 60 ^{0}C for 24 h to get rGO.

5.2.4 Material characterization

The recovered and synthesized powder samples were characterized by X-ray diffraction (XRD) with Cu-Kα radiation (k = 1.54 Å) (PANalytical X'pert Pro). The Raman spectra were obtained using the HORIBA-J-Y Lab RAM HR 800 Raman spectrometer instrument. Fourier transform infrared (FTIR) analyses were carried out from the samples prepared in potassium bromide pellets by using a PerkinElmer Spectrum Two spectrometer. XPS studies were done on Thermo Fisher Scientific Instrument (K-α^+) with monochromatic Al-Kα as X-ray source. The BET surface area and porosity of the material were assessed by the Quantasorb instrument. UV-Visible spectroscopic studies were performed using VARIAN (Cary 300) instrument by dispersing the samples in de-ionized water. Morphology of the samples was observed using Quanta 200 3D, field emission scanning electron microscope (FE-SEM), and Transmission electron microscope (JEOL JEM F-200)**.**

Cyclic voltammetry and charge-discharge (galvanostatic) analyses were carried out in three electrodes with a potentiostat–galvanostat (Metrohm Autolab M204) system (Ag/AgCl reference electrode, rGO modified electrode as working electrode, and platinum wire counter electrode). The working electrodes were prepared with active material (80 wt%), super P carbon black (15 wt%), and polyvinylidene fluoride (5 wt%). These were ground with a drop of *N*-methyl pyrrolidone solvent to form a slurry. This slurry was drop cast on to glassy carbon electrode as well coated on

Torey-carbon paper and dried at 60 ^{0}C for a few hours. 1 M H_2SO_4 solution was used as an electrolyte for this study.

5.3 Results and Discussion

5.3.1 Structural studies

5.3.1.1 X-ray diffraction study

The XRD is used to determine the transformation of graphite (G) to graphene oxide (GO) and GO to reduced graphene oxide (rGO). **Figure 5.2** depicts the XRD patterns of recovered G, GO, and rGO. The high-intensity diffraction peak for the recovered anode is observed at 26.4° and

54.5°, which correspond to (002) and (004) planes, respectively, which indicates the high crystallinity of graphite. Upon oxidation, a fresh diffraction peak appeared at 10°, corresponding to the (001) plane, and is a characteristic of carbon. The appearance of this peak confirms the successful formation of GO. Upon chemical reduction of GO with ascorbic acid, the diffraction peak at 10° was moved out, and a broad peak (002) appeared at 26°. This confirms the reduction

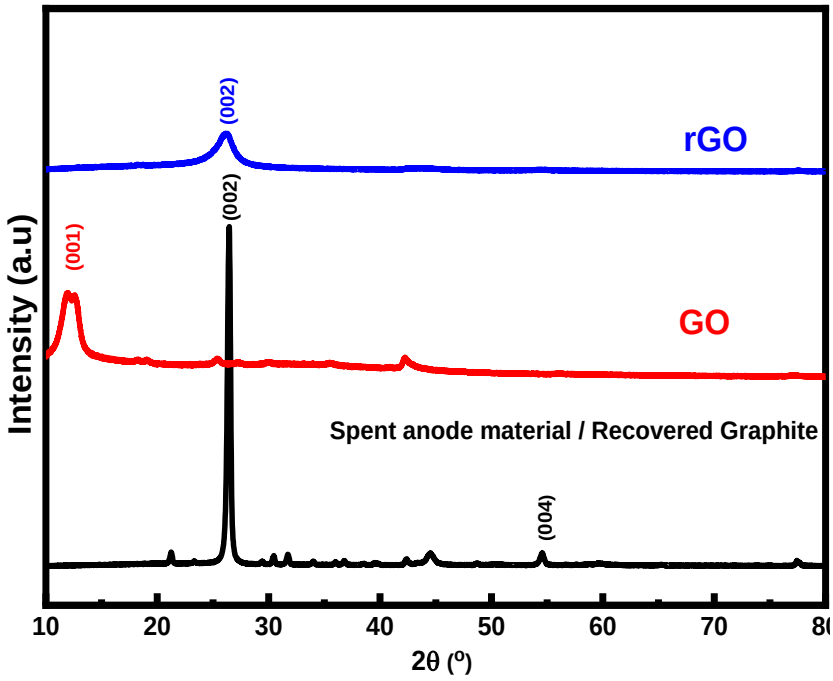

Figure 5.2. X-ray diffraction patterns of G, GO, and rGO.

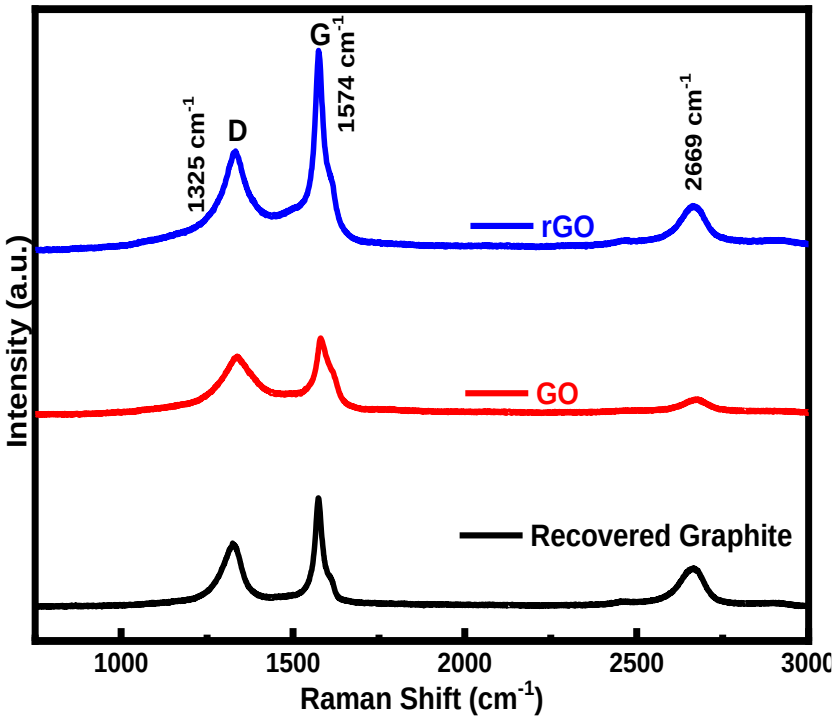

Figure 5.3. Raman spectra of G, GO and rGO.

Raman study is the most powerful technique for analyzing carbon-based materials' defects and structural changes. Along with this, allotropes of carbon can also be well-defined.[23] **Figure. 5.3**, depicts the Raman spectra of recovered G, GO, and rGO samples. The D band corresponds to the breathing mode of the k-point phonon of A1g symmetry, which is related to structural defects and disorders. The G band corresponds to the scattering of first-order E_{2g} phonons by sp^2 hybrid atoms.[10,24] G, GO, and rGO show a strong G band and weak D band at 1576 cm^{-1} and 1333 cm^{-1}, correspondingly, and a 2D band also appeared at 2669 $cm^{-1}$is due to the eradication of oxygenases groups and configuration of new conjugated carbon atoms.[24] After reducing GO by ascorbic acid, rGO showed a slight shift owing to the distortion of sp^2 nature and configuration of defects. G, GO, and rGO spectra showed a slight shift in D and G bands by 5-10 cm^{-1}, which agrees with the previous reports.[24,25]

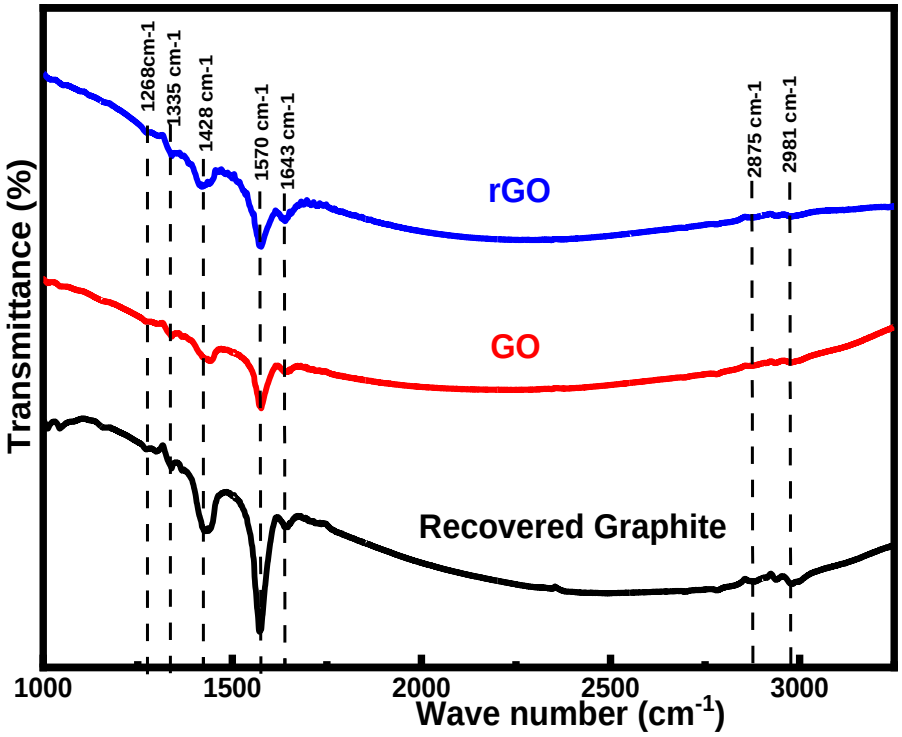

Figure 5.4. FTIR spectra of G, GO, and rGO.

To further know the conversion of G to GO and GO to rGO, an FTIR study was done and shown in **Figure 5.4** Graphite has shown a distinctive signal at 2981 cm^{-1} corresponds to symmetric and 2875 cm^{-1} corresponds to asymmetric C–H stretching vibrations, which exist in the hexagonal backbone structure of graphite. It has also shown a weak signal at 1643 cm^{-1} and a strong signal at 1570 cm^{-1} corresponds to the C=C stretching vibrations.[26] Other prominent peak signals at 1428 cm^{-1}, 1335 cm^{-1}, and 1268 cm^{-1} correspond to the O–H deformation, the C–O stretching vibration (epoxy), and the C–O stretching vibration (alkoxy), respectively. These stretching vibrations of G and GO, which have been weakened in the rGO's spectrum, this weakened stretching vibrations of epoxy, alkoxy, and carbonyl groups indicate the effective conversion of graphite to GO and reduction of GO to rGO.[27]

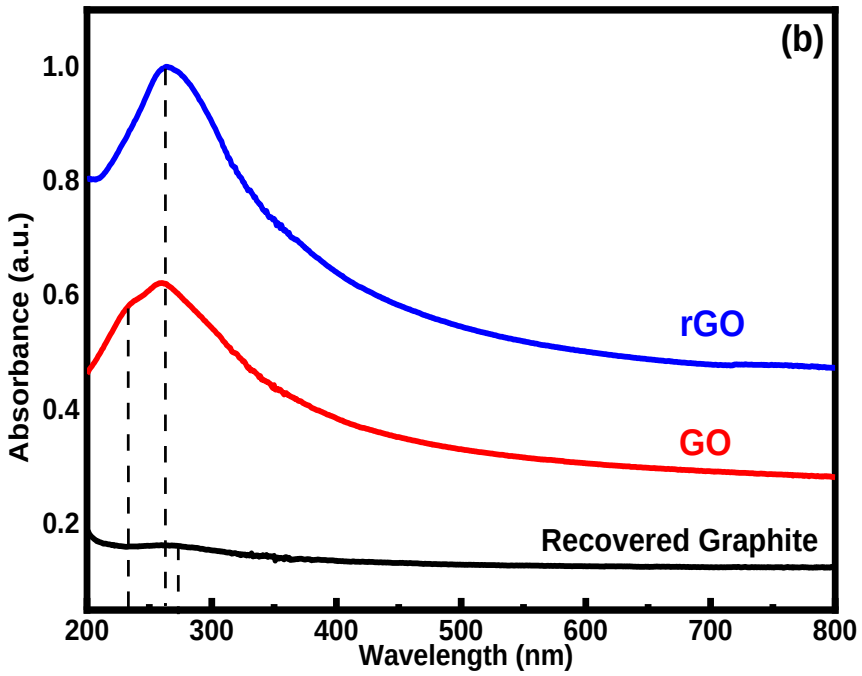

Figure 5.5. UV-Vis. spectra of G, GO, and rGO.

Figure 5.5 depicts the UV-Vis. Spectra of G, GO, and rGO. The absorption spectra were observed at 272 nm for G, 235 nm and 260 nm for GO, and 264 nm for rGO. GO shows two

absorption peaks are attributed to the π−π*(C−C) and n−π (C=O) transition. Here, the peak observed for GO is slightly red-shifted in rGO, which indicates the elimination of oxygen-containing functional groups. This result well matches with the literature reports.[9,10]

The structure and morphology of the obtained samples were observed by FE-SEM, TEM, and SAED patterns shown in Fig. 4. The obtained powder images of G, GO, and rGO are shown in **Figure 5.6 (a-c)**. The FE-SEM image **Figure 5.6 (d-f)** shows a flake-like G, GO, and rGO structure enclosing the distinct and interlinked three-dimensional sheets. The images show the existence of sharp edges, which are advantageous for field emission. **Figure 5.7(a-c)** shows the HR-TEM images, which indicate no agglomeration on the surface of the sheets, suggesting that we have successfully recovered graphite and synthesized pure rGO. The thickness of the sample is very thin, and folds can also be observed in some areas due to the overlapping of sheets. **Figure 5.7(d-e)** shows SAED G, GO, and rGO patterns, indicating no bright visible spots in the diffraction rings except G is due to oxidation/reduction.[23]

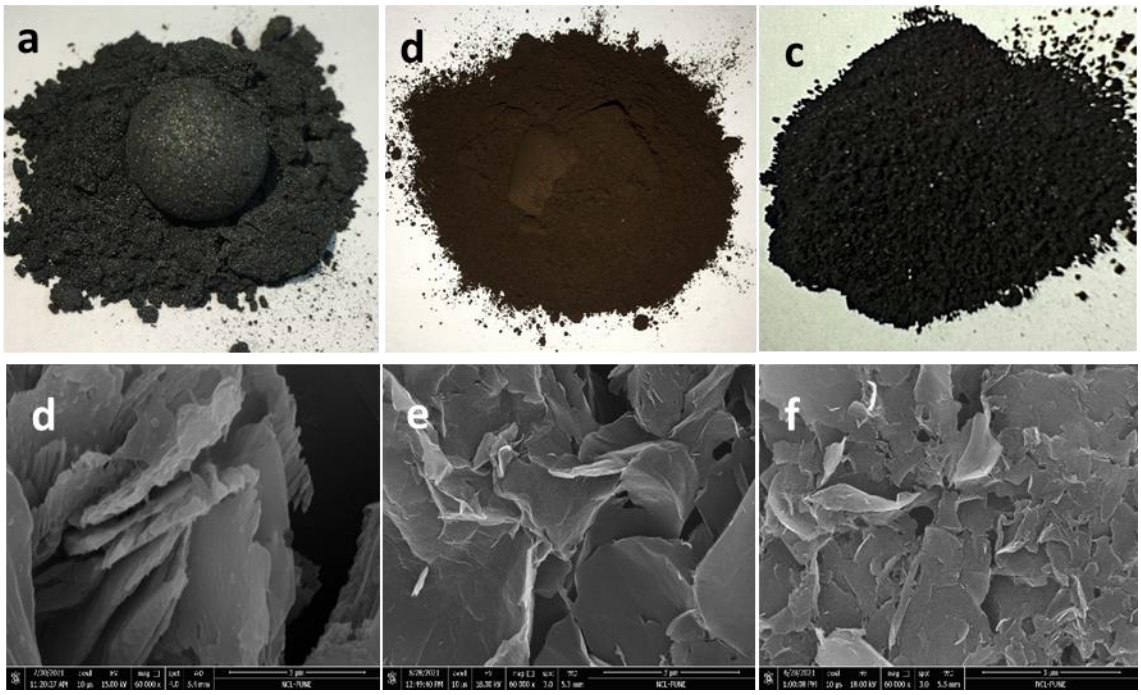

Figure 5.6. **(a-c)** Powder images **(d-f)** FE-SEM images of G, GO, and rGO, respectively.

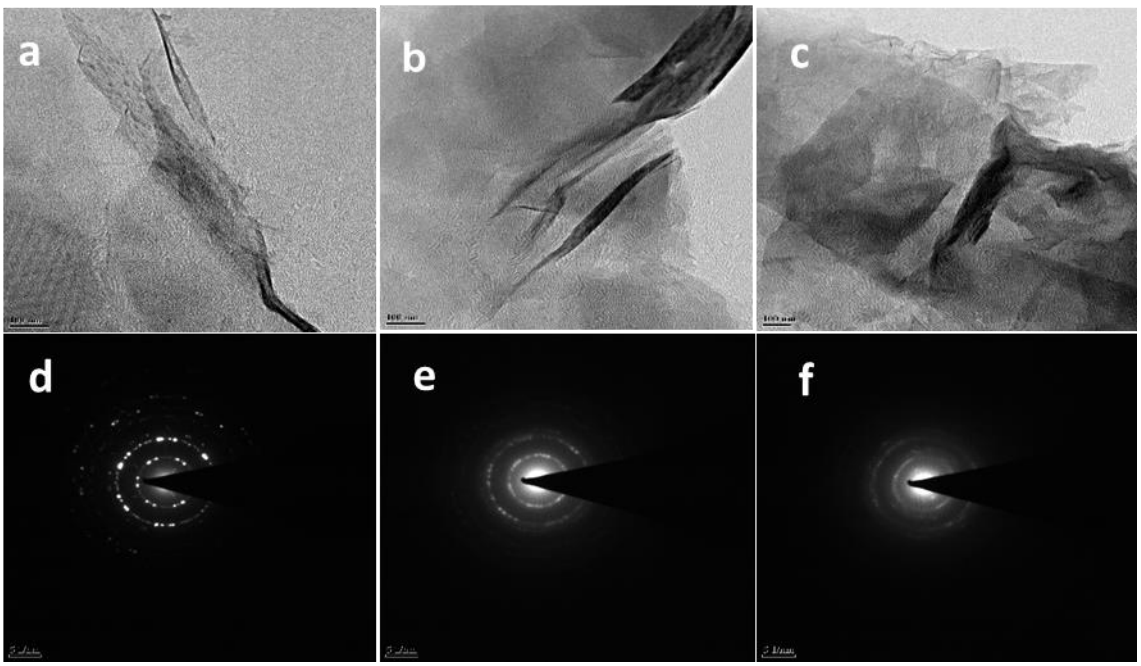

Figure 5.7. (a-c) HR-TEM images and (d-f) G, GO, and rGO SAED patterns, respectively.

5.3.1.2 XPS studies

An XPS analysis was carried out to study the reduction behavior of GO. **Figure 8** shows the C 1s spectra of recovered graphite, GO, and rGO. The C 1s spectra of recovered graphite show a prominent peak at ≈283.8 eV, which corresponds to C-C, and a small peak at ≈286 eV, which corresponds to C-OH. In GO, the C 1s spectrum consists of three peaks centered at 284.2 eV, 287.0 eV, and 289.0 eV, which corresponds to C=C/C-C (aromatic), O=C-OH (hydroxyl), and C=O (carbonyl) groups. The C=C/C-C and O=C-OH peaks indicate the oxidation of recovered graphite.[12] The peak intensities of oxygen-containing groups were lower after ascorbic acid reduction, indicating that the oxygen functional group is converted. This demonstrates that the carbon atom is partly transformed from sp^3 to sp^2 hybridization.[12] The C1s spectrum of rGO also

consists of three peaks centered at 284.4 eV, 286.5 eV, and 288.8 eV, corresponding to graphitic carbon.[28] C-OH (epoxy/hydroxyl), and C=O (carbonyl) groups, respectively.

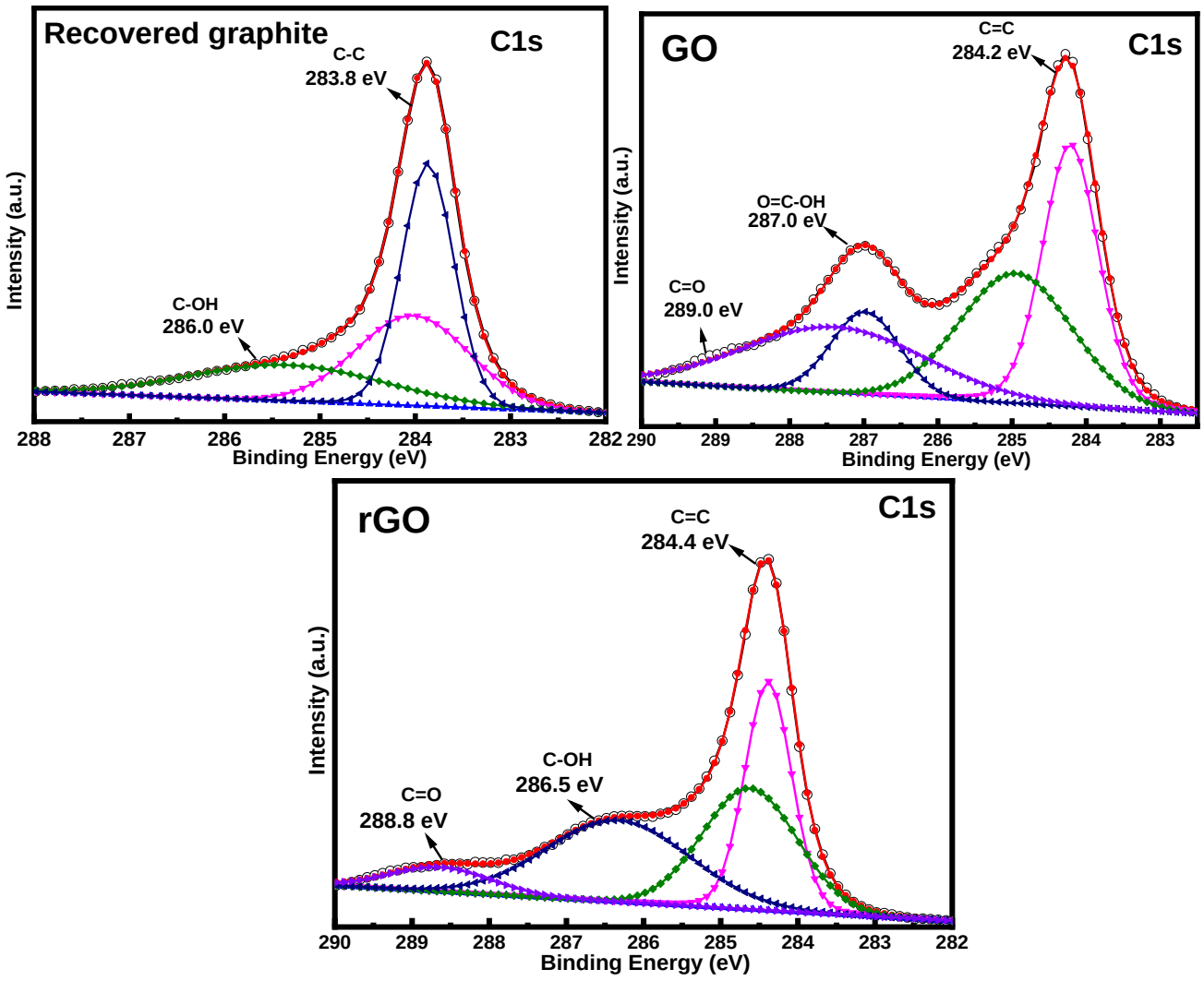

Figure 5.8. C1s XPS spectra of G, GO, and rGO.

5.3.1.3 BET surface area analysis

Figure 5.9 shows the N_2 adsorption-desorption isotherm and corresponding pore size distribution curves of rGO. BET isotherm follows type IV isotherms with a hysteresis loop indicating the presence of mesopores according to IUPAC classification,[29,30] Pore size distribution

has been assessed by assuming slit pore shapes through a hybrid nonlocal density functional theory (NLDFT) revealed pore diameter is in the range 2-17 nm confirming the mesoporous structure rGO.[24,31,32]

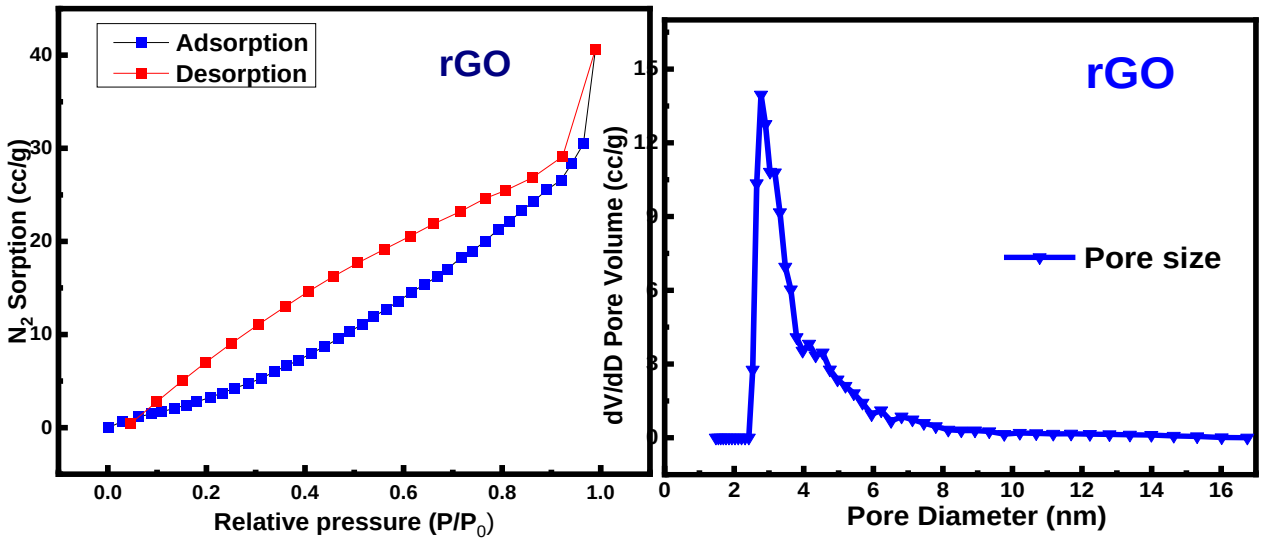

Figure 5.9. BET Surface area analysis of rGO.

5.3.2 Electrochemical studies

5.3.2.1 Cyclic Voltammetry Analysis

Cyclic voltammetry is employed to understand the redox behavior of the materials. **Figure 5.10a** and **Figure 5.10b** show the cyclic voltammogram (CV) profiles with glassy carbon electrode (GCE) and tore carbon electrode (TCE) with a scan rate of 0.25 mV/s within the voltage range of 0-1 V in 1.0 M H_2SO_4. The CV behavior of rGO coated on GCE and TCE is different from bare GCE and GO-coated GCE **(Figure 5.10a),** and bare TCE and GO-coated TCE **(Figure 5.10b)**. The CV behavior of rGO on GCE and TCE is almost rectangular in shape compared to GO-coated and bare electrodes, which indicates the reductive and resistive behavior of GO-coated and bare electrodes, respectively. The rectangular-shaped behavior is due to electrical double-layer capacitance (EDLC).[31] This behavior is more prominent in GO-coated TCE than in rGO-coated

GCE. The redox behavior of rGO was observed around 0.5 V/ 0.3 V (**Figure 5.10a**) and 0.5 V/ 0.25 V (**Figure 5.10b**). This behavior of rGO is due to carbon-oxygen (C-O) functionalities and EDLC.[24,28]

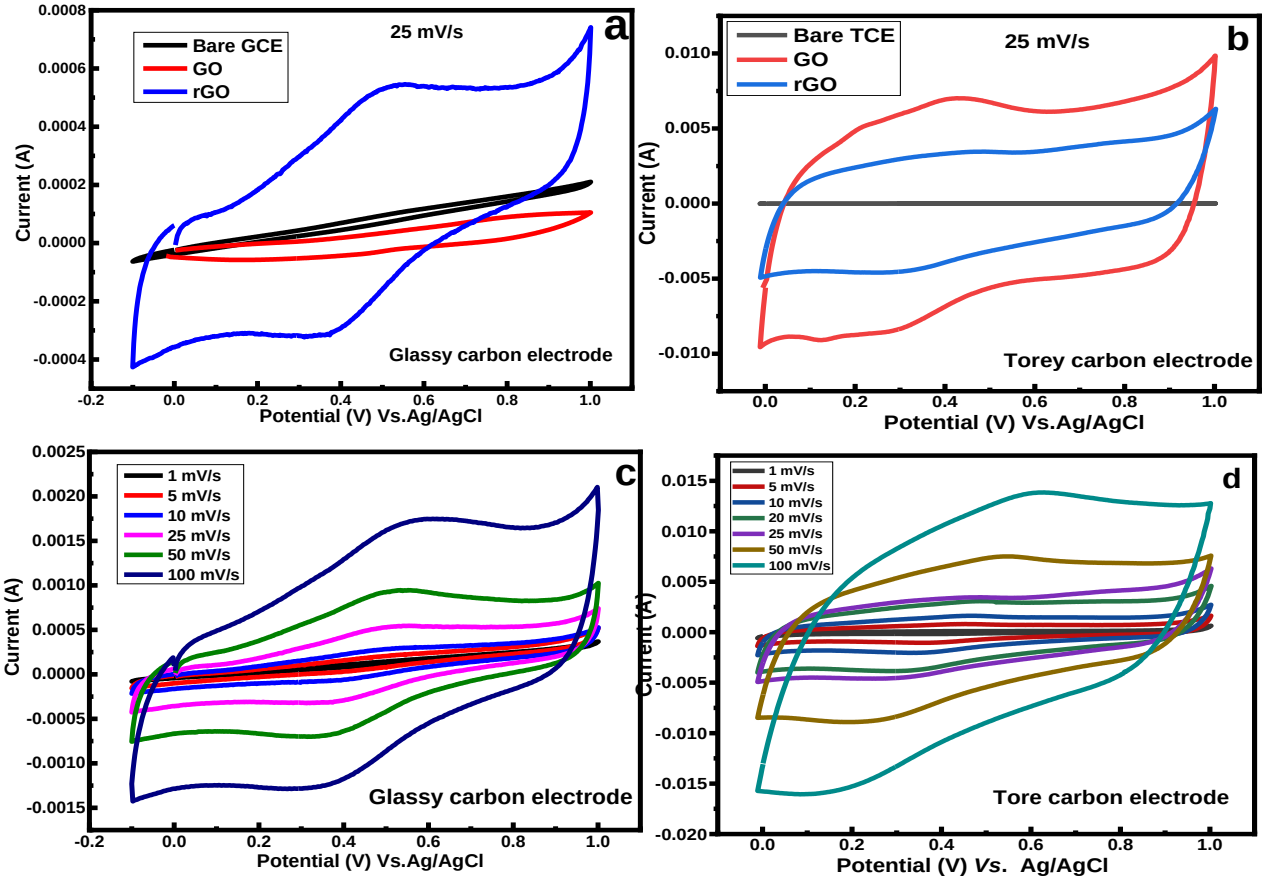

Figure 10. **(a)** Cyclic voltammogram of bare GCE, GO-coated GCE, and rGO-coated GCE, **(b)** bare TCE, GO-coated TCE, and RGO-coated TCE at 25 mV/s in 1.0 M H_2SO_4, **(c)** Cyclic voltammogram of rGO on GCE, **(d)** rGO on TCE at different scan rates.

The cyclic voltammetry of rGO at varied scan rates is shown in **Figure 5.10c and Figure 5.10d**. The shape and shift of redox peaks were observed in both cases of **Figures 5.10c and 5.10d** as the scan rate increased from 1 mV/s to 100 mV/s. This shift is due to ohmic resistance and polarization, resulting from irreversible kinetics in the redox process. The peak current increases as the scan rate increases and is evidence for better rate capability and electrochemical performances.

5.3.2.2 Galvanostatic charge-discharge study

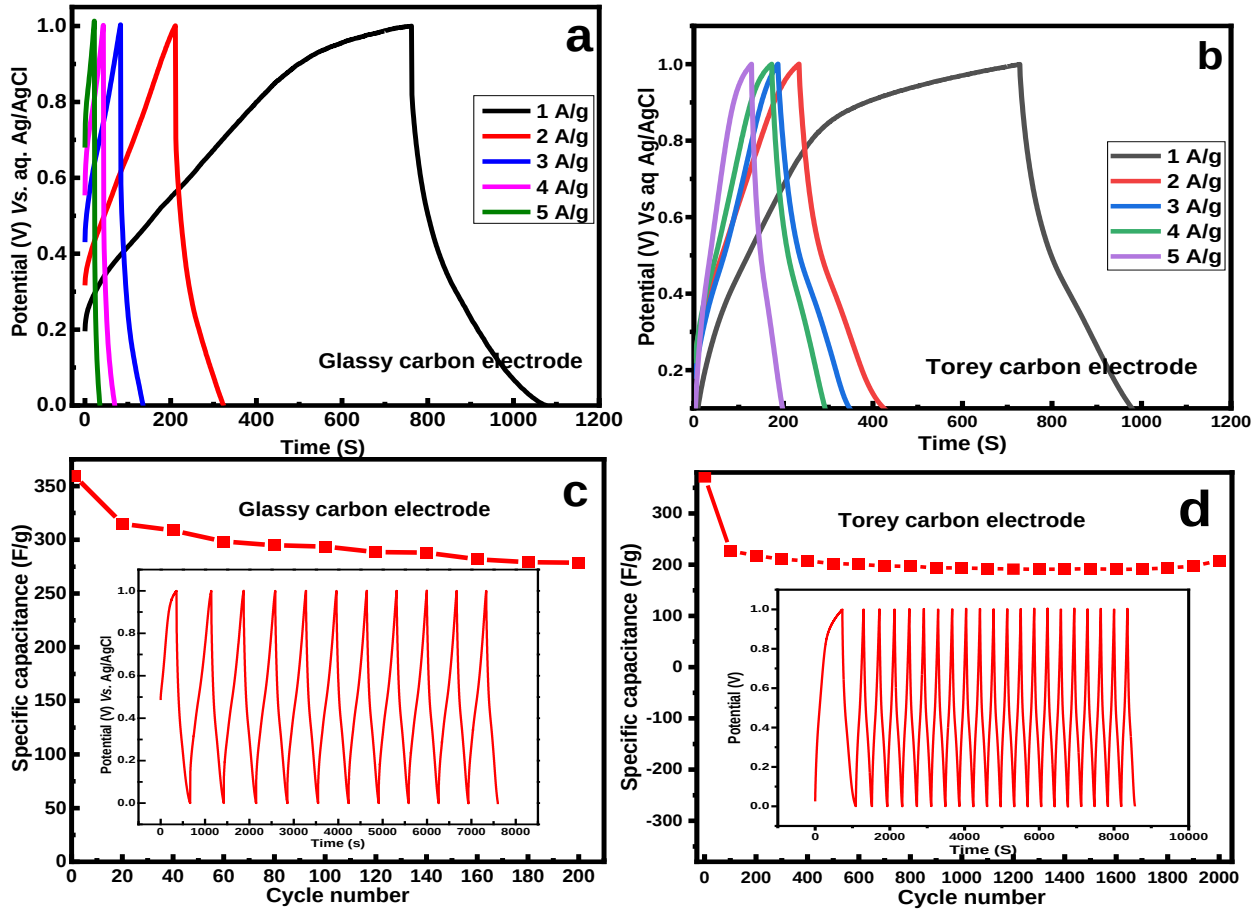

Figure 5.11. Galvanostatic charge-discharge (GCD) curves of **(a)** rGO/Glassy carbon electrode, (b) rGO/Torey carbon at different current densities, **(c**) Specific capacitance of rGO/Glassy carbon electrode, and **(d)** rGO/Torey carbon after different cycles at 1 A/g.

Figure 5.11a and Figure 5.11b show the galvanostatic charge-discharge curves recorded using rGO on GCD and TCE at varied current densities. From the figure, it is clear that rGO shows good reversible charge-discharge characteristics for supercapacitor applications. The specific capacitance of rGO on GCD is 359 F/g (1 A/g), 318 F/g (2 A/g), 268 F/g (3 A/g), 220 F/g (4 A/g), 158 F/g (5 A/g) (**Figure 5.11a**) and the specific capacitance of rGO on TCE is 371.47 F/g (1 A/g), 201.01 F/g (2 A/g), 211.90 F/g (3 A/g), 157.44 F/g (4 A/g), 104.78 F/g (5 A/g) (**Figure 5.11b**), is calculated using the below equation by taking the slope of the discharge curve.[26]

$$C_{sp} = \frac{Idt}{mdV}$$

Where C_{sp} is the specific capacitance of the electrode (F), I is the current (A) applied, it is the discharge time (s), m is the mass of active material on the electrode, and dV is the voltage difference of discharge curve (V). The specific capacitance of the rGO is decreased as the current density increases. This decrease in specific capacitance is due to lesser ionic diffusion into the surface of the electrode at higher currents. To know the stability of rGO, charge-discharge cycles were performed at a current density of 1 A/g.

Figure 5.11c and Figure 5.11d show the cycling performance of the rGo-coated GCE (200 cycles) and TCE (2000 cycles) between 0 and 1 V at a current density of 1 A/g. It can be seen that the initial discharge capacities were 359 F/g and 371.47 F/g for GCE and TCE, respectively. At the end of 200 cycles (for GCE) and 2000 cycles (for TCE), the discharge capacities were decreased to 278.5 F/g (77.5 % capacity retention) and 207.9 F/g (55.9 % capacity retention), for GCE and TCE, respectively. The inset in **Figure 5.11c and Figure 5.11d** shows the electrode's symmetric charge-discharge behavior which maintains good symmetry even after long cycles, which verifies its good electrochemical durability. More studies are needed to enhance capacity retention over many cycles.

5.4 Residual secondary acidic waste treatment and re-use

The acidic waste left out after the Hummer's method process contains H_2SO_4, $KMnO_4$ in major proportions, and H_3PO_4 in minor proportions. To treat this secondary acidic waste, we have neutralized it by adding an NH_4OH solution, which can be a useful plant fertilizer. Below are the possible reactions that can occur, which are given in equations (1), (2) & (3). The major by-products of these reactions are ammonium sulfate, ammonium phosphate, potassium sulfate, and a small amount of $MnSO_4$. It's well-known that nitrogen, phosphorus, and potassium-based

fertilizers (Known as N.P.K fertilizers) provide essential nutrients to plants,[33,34] so the byproducts obtained from the secondary acidic waste treatment are water-soluble compounds that can be used as a plant fertilizer.

$$2NH_4OH + H_2SO_4 \xrightarrow{yields} (NH_4)_2SO_4 + 2H_2O \quad \cdots \quad (1)$$

$$3NH_4OH + H_3PO_4 \xrightarrow{yields} (NH_4)_3PO_4 + 3H_2O \quad \cdots \quad (2)$$

$$2NH_4OH + 2KMnO_4 + 3H_2SO_4 \xrightarrow{yields} K_2SO_4 + 2MnSO_4 + 8H_2O + N_2\uparrow \quad \cdots (3)$$

The by-product obtained, which is a source of nitrogen, sulfur (Ref. eq. (1)), helps to balance the soil pH. Another by-product, which has been an effective fertilizer for years, is rich in nitrogen and phosphorous (Ref. eq. (2)). Further, one more by-product obtained is an excellent source of potash and sulfur (Ref. eq. (3)), which provides nutrition and is useful in protein synthesis in plants. Additionally, a small amount of $MnSO_4$ is another by-product that can also be used for foliar fertigation of plants, which is essential for plant growth.[35]

5.5 Conclusions

The successful recovery of graphite from the active anode material of spent LIBs using an eco-friendly approach is reported here. rGo was synthesized by reducing GO using ascorbic acid as a reductant. Structural characterizations confirmed the reduction of GO from recovered spent graphite. The FE-SEM analysis shows the flake-like structure. HR-TEM images indicate no agglomeration on the surface of the sheets, which suggests that we have successfully recovered graphite and synthesized pure rGO. Electrochemical studies of the rGO show its potential to operate in supercapacitor applications, with a specific capacitance of 207.9 F/g at the end of 2000 cycles at a current density of 1A/g. Thus, this is a simple and easy method to recover graphite from spent LIBs.

5.6 References

(1) Yang, L.; Yang, L.; Xu, G.; Feng, Q.; Li, Y.; Zhao, E.; Ma, J.; Fan, S.; Li, X. Separation and Recovery of Carbon Powder in Anodes from Spent Lithium-Ion Batteries to Synthesize Graphene. *Sci. Rep.* **2019**, *9* (1). https://doi.org/10.1038/s41598-019-46393-4.

(2) Natarajan, S.; Aravindan, V. Recycling Strategies for Spent Li-Ion Battery Mixed Cathodes. *ACS Energy Lett.* **2018**, *3* (9), 2101–2103. https://doi.org/10.1021/acsenergylett.8b01233.

(3) Zheng, X.; Zhu, Z.; Lin, X.; Zhang, Y.; He, Y.; Cao, H.; Sun, Z. A Mini-Review on Metal Recycling from Spent Lithium Ion Batteries. *Engineering* **2018**, *4* (3), 361–370. https://doi.org/10.1016/j.eng.2018.05.018.

(4) He, L.-P.; Sun, S.-Y.; Yu, J.-G. Performance of LiNi1/3Co1/3Mn1/3O2 Prepared from Spent Lithium-Ion Batteries by a Carbonate Co-Precipitation Method. *Ceram. Int.* **2018**, *44* (1), 351–357. https://doi.org/10.1016/j.ceramint.2017.09.180.

(5) Meshram, P.; Pandey, B. D.; Mankhand, T. R. Hydrometallurgical Processing of Spent Lithium Ion Batteries (LIBs) in the Presence of a Reducing Agent with Emphasis on Kinetics of Leaching. *Chem. Eng. J.* **2015**, *281*. https://doi.org/10.1016/j.cej.2015.06.071.

(6) Guo, P.; Song, H.; Chen, X. Electrochemical Performance of Graphene Nanosheets as Anode Material for Lithium-Ion Batteries. *Electrochem. commun.* **2009**, *11* (6). https://doi.org/10.1016/j.elecom.2009.04.036.

(7) Stoller, M. D.; Park, S.; Yanwu, Z.; An, J.; Ruoff, R. S. Graphene-Based Ultracapacitors. *Nano Lett.* **2008**, *8* (10). https://doi.org/10.1021/nl802558y.

(8) Yoo, E. J.; Okata, T.; Akita, T.; Kohyama, M.; Nakamura, J.; Honma, I. Enhanced Electrocatalytic Activity of Pt Subnanoclusters on Graphene Nanosheet Surface. *Nano Lett.* **2009**, *9* (6). https://doi.org/10.1021/nl900397t.

(9) Chen, J.; Yao, B.; Li, C.; Shi, G. An Improved Hummers Method for Eco-Friendly Synthesis of Graphene Oxide. *Carbon N. Y.* **2013**, *64*, 225–229. https://doi.org/10.1016/j.carbon.2013.07.055.

(10) Roy, I.; Sarkar, G.; Mondal, S.; Rana, D.; Bhattacharyya, A.; Saha, N. R.; Adhikari, A.; Khastgir, D.; Chattopadhyay, S.; Chattopadhyay, D. Synthesis and Characterization of Graphene from Waste Dry Cell Battery for Electronic Applications. *RSC Adv.* **2016**, *6* (13). https://doi.org/10.1039/c5ra21112c.

(11) Miller, J. R.; Outlaw, R. A.; Holloway, B. C. Graphene Double-Layer Capacitor with Ac Line-Filtering Performance. *Science (80-.).* **2010**, *329* (5999). https://doi.org/10.1126/science.1194372.

(12) Ramadoss, A.; Saravanakumar, B.; Kim, S. J. Thermally Reduced Graphene Oxide-Coated Fabrics for Flexible Supercapacitors and Self-Powered Systems. *Nano Energy* **2015**, *15*. https://doi.org/10.1016/j.nanoen.2015.05.009.

(13) Shen, B.; Ding, J.; Yan, X.; Feng, W.; Li, J.; Xue, Q. Influence of Different Buffer Gases

on Synthesis of Few-Layered Graphene by Arc Discharge Method. *Appl. Surf. Sci.* **2012**, *258* (10). https://doi.org/10.1016/j.apsusc.2012.01.019.

(14) Huang, Q.; Kim, J. J.; Ali, G.; Cho, S. O. Width-Tunable Graphene Nanoribbons on a SiC Substrate with a Controlled Step Height. *Adv. Mater.* **2013**, *25* (8). https://doi.org/10.1002/adma.201202746.

(15) Rajagopalan, B.; Chung, J. S. Reduced Chemically Modified Graphene Oxide for Supercapacitor Electrode. *Nanoscale Res. Lett.* **2014**, *9* (1). https://doi.org/10.1186/1556-276X-9-535.

(16) Shen, J.; Hu, Y.; Shi, M.; Lu, X.; Qin, C.; Li, C.; Ye, M. Fast and Facile Preparation of Graphene Oxide and Reduced Graphene Oxide Nanoplatelets. *Chem. Mater.* **2009**, *21* (15). https://doi.org/10.1021/cm901247t.

(17) Li, D.; Müller, M. B.; Gilje, S.; Kaner, R. B.; Wallace, G. G. Processable Aqueous Dispersions of Graphene Nanosheets. *Nat. Nanotechnol.* **2008**, *3* (2). https://doi.org/10.1038/nnano.2007.451.

(18) Guoxiu, W.; Juan, Y.; Jinsoo, P.; Xinglong, G.; Bei, W.; Hao, L.; Jane, Y. Facile Synthesis and Characterization of Graphene Nanosheets. *J. Phys. Chem. C* **2008**, *112* (22). https://doi.org/10.1021/jp710931h.

(19) Fan, X.; Peng, W.; Li, Y.; Li, X.; Wang, S.; Zhang, G.; Zhang, F. Deoxygenation of Exfoliated Graphite Oxide under Alkaline Conditions: A Green Route to Graphene Preparation. *Adv. Mater.* **2008**, *20* (23). https://doi.org/10.1002/adma.200801306.

(20) Nayaka, G. P.; Manjanna, J.; Pai, K. V.; Vadavi, R.; Keny, S. J.; Tripathi, V. S. Recovery of Valuable Metal Ions from the Spent Lithium-Ion Battery Using Aqueous Mixture of Mild Organic Acids as Alternative to Mineral Acids. *Hydrometallurgy* **2015**, *151*. https://doi.org/10.1016/j.hydromet.2014.11.006.

(21) Zhang, J.; Yang, H.; Shen, G.; Cheng, P.; Zhang, J.; Guo, S. Reduction of Graphene Oxide via L-Ascorbic Acid._Supporting Information. *Chem. Commun. (Camb).* **2010**, *2* (c).

(22) Marcano, D. C.; Kosynkin, D. V.; Berlin, J. M.; Sinitskii, A.; Sun, Z.; Slesarev, A.; Alemany, L. B.; Lu, W.; Tour, J. M. Improved Synthesis of Graphene Oxide. *ACS Nano* **2010**, *4* (8). https://doi.org/10.1021/nn1006368.

(23) Paranthaman, V.; Sundaramoorthy, K.; Chandra, B.; Muthu, S. P.; Alagarsamy, P.; Perumalsamy, R. Investigation on the Performance of Reduced Graphene Oxide as Counter Electrode in Dye Sensitized Solar Cell Applications. *Phys. Status Solidi Appl. Mater. Sci.* **2018**, *215* (18). https://doi.org/10.1002/pssa.201800298.

(24) Natarajan, S.; Rao Ede, S.; Bajaj, H. C.; Kundu, S. Environmental Benign Synthesis of Reduced Graphene Oxide (RGO) from Spent Lithium-Ion Batteries (LIBs) Graphite and Its Application in Supercapacitor. *Colloids Surfaces A Physicochem. Eng. Asp.* **2018**, *543*. https://doi.org/10.1016/j.colsurfa.2018.01.054.

(25) Zhang, W.; Liu, Z.; Xia, J.; Li, F.; He, W.; Li, G.; Huang, J. Preparing Graphene from

Anode Graphite of Spent Lithium-Ion Batteries. *Front. Environ. Sci. Eng.* **2017**, *11* (5). https://doi.org/10.1007/s11783-017-0993-8.

(26) Johra, F. T.; Jung, W.-G. Hydrothermally Reduced Graphene Oxide as a Supercapacitor. *Appl. Surf. Sci.* **2015**, *357*, 1911–1914. https://doi.org/10.1016/j.apsusc.2015.09.128.

(27) Thareja, S.; Kumar, A. One-Pot In Situ Synthesis of Mn3O4/N-RGO Nanohybrids for the Fabrication of High Cell Voltage Aqueous Symmetric Supercapacitors: An Analysis of Redox Activity of Mn3O4 toward Stabilizing the High Potential Window in Salt-in-Water and Water-in-Salt Electrolytes. *Energy & Fuels* **2022**, *36* (24), 15177–15187. https://doi.org/10.1021/acs.energyfuels.2c02803.

(28) Gardner, S. D.; Singamsetty, C. S. K.; Booth, G. L.; He, G.-R.; Pittman, C. U. Surface Characterization of Carbon Fibers Using Angle-Resolved XPS and ISS. *Carbon N. Y.* **1995**, *33* (5), 587–595. https://doi.org/10.1016/0008-6223(94)00144-O.

(29) Sawangphruk, M.; Srimuk, P.; Chiochan, P.; Krittayavathananon, A.; Luanwuthi, S.; Limtrakul, J. High-Performance Supercapacitor of Manganese Oxide/Reduced Graphene Oxide Nanocomposite Coated on Flexible Carbon Fiber Paper. *Carbon N. Y.* **2013**, *60*. https://doi.org/10.1016/j.carbon.2013.03.062.

(30) Alazmi, A.; El Tall, O.; Rasul, S.; Hedhili, M. N.; Patole, S. P.; Costa, P. M. F. J. A Process to Enhance the Specific Surface Area and Capacitance of Hydrothermally Reduced Graphene Oxide. *Nanoscale* **2016**, *8* (41). https://doi.org/10.1039/c6nr04426c.

(31) Vermisoglou, E. C.; Giannakopoulou, T.; Romanos, G.; Giannouri, M.; Boukos, N.; Lei, C.; Lekakou, C.; Trapalis, C. Effect of Hydrothermal Reaction Time and Alkaline Conditions on the Electrochemical Properties of Reduced Graphene Oxide. In *Applied Surface Science*; 2015; Vol. 358. https://doi.org/10.1016/j.apsusc.2015.08.127.

(32) Vadivel, S.; Tejangkura, W.; Sawangphruk, M. Graphite/Graphene Composites from the Recovered Spent Zn/Carbon Primary Cell for the High-Performance Anode of Lithium-Ion Batteries. *ACS Omega* **2020**, *5* (25). https://doi.org/10.1021/acsomega.0c01270.

(33) Guha, T.; Gopal, G.; Kundu, R.; Mukherjee, A. Nanocomposites for Delivering Agrochemicals: A Comprehensive Review. *Journal of Agricultural and Food Chemistry*. 2020. https://doi.org/10.1021/acs.jafc.9b06982.

(34) Gawali, J.; Dhamak, A.; Zade, S. Effect of Water Soluble Fertilizers through Fertigation on Soil Available N, P, K and Yield of Bt Cotton. *Int. J. Curr. Microbiol. Appl. Sci.* **2020**, *9* (11). https://doi.org/10.20546/ijcmas.2020.911.062.

(35) Guo, Y.; Zhang, M.; Liu, Z.; Zhao, C.; Lu, H.; Zheng, L.; Li, Y. C. Applying and Optimizing Water-Soluble, Slow-Release Nitrogen Fertilizers for Water-Saving Agriculture. *ACS Omega* **2020**, *5* (20). https://doi.org/10.1021/acsomega.0c00303.

Chapter 6
Regeneration and reuse of polymeric separators from waste Li-ion batteries for second-life applications

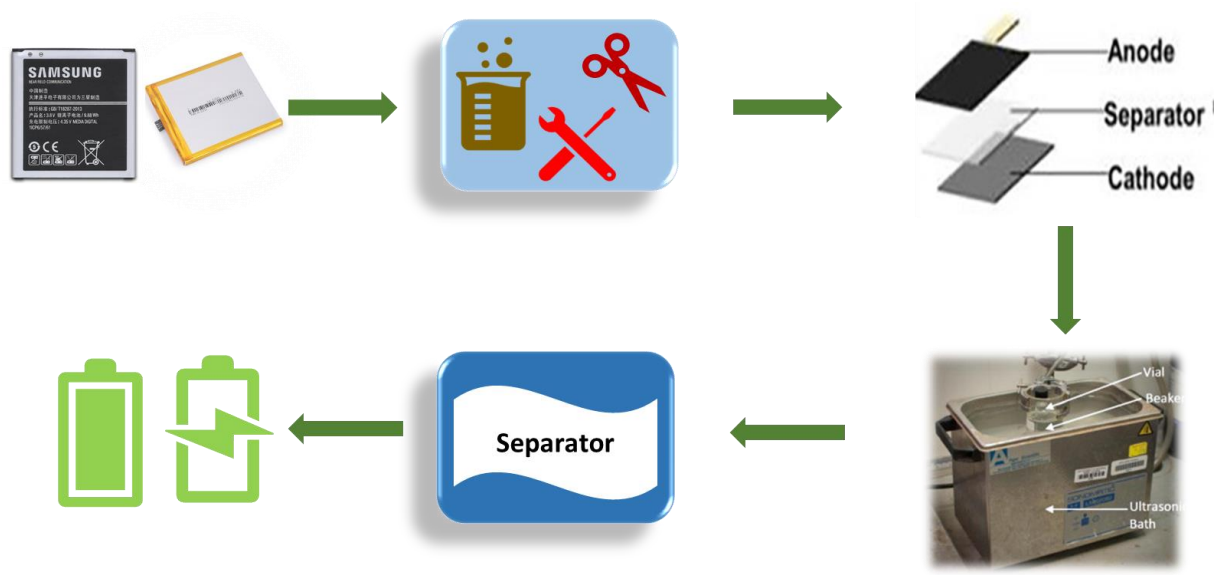

Highlights

- Current recycling methods primarily concentrate on extracting valuable metals from these batteries, but they contain considerable amounts of harmful polyolefins.
- This research introduces an innovative method that aligns with Green Chemistry's "3R" principles and circular economy by extracting and cleaning the separator from used LIBs and then reusing it without modifying the production of new batteries.
- We assessed the recovered separator's viability for reuse through various characterization methods, including X-ray diffraction studies, tensile strength, porosity analyses by the BET method, interfacial resistance, and electrochemical applicability in Li-ion cells.
- The findings of our study demonstrated that the reclaimed separator could be effectively utilized in a half-cell setup, with $LiFePO_4$ functioning as the cathode and Li metal as the anode.

- The results of this chapter will be published as **BP Shivamurthy**, Purnima Rawat, MV Shelke, **GP Nayaka*,** Regeneration and reuse of polymeric separators from waste Li-ion batteries for second-life applications.

6.1 Introduction

Lithium-ion batteries (LIBs) have become a flourishing technology with applications in diverse fields, such as domestic electronic devices and electric transportation. Over the last few decades, the LIB technology constantly upgraded to meet the energy storage standards per government policies to reduce carbon footprints. Such rigorous development has made this technology into a multi-billion-dollar market, expected to reach 139 billion dollars by the end of 2029.[1,2] This would increase the production and usage of LIBs in large numbers worldwide. Subsequently, the batteries retire at the end of their life, and it becomes a great challenge for the end user and the industries to dispose of them properly without any adverse environmental effects. The estimated generation of spent LIBs by 2030 is expected to reach more than five million metric tons.[3] This would generate tremendously spent LIBs, threatening environmental health as these LIBs contain toxic heavy metals and organic electrolytes. The direct landfills of such batteries or their components could contaminate the groundwater, which indirectly causes adverse effects on human health.[4] Therefore, effective and sustainable technologies are the present requirement for the disposal, recycling, and reuse of the components of spent LIBs to address this issue.

The commercial LIBs typically contain cathode (generally metal oxides coated on Al foil), anode (generally Graphite coated on Cu foil), commonly $LiPF_6$ dissolved in organic carbonates such as ethylene carbonate (EC), dimethylene carbonate (DMC), Ethylene methylene carbonate (EMC) and/or propylene carbonate (PC) as an electrolyte, typically porous polypropylene / Polyethylene films are used as separators. The commercial LIBs may be equipped with various polymeric separators based on polyolefin materials, such as porous polypropylene materials typically used. The commercial 18650 type of cylindrical LIB has a ~14% contribution from polyolefin separator materials in the total percentage of components of a cell, and it takes up ~24%

of the production cost of the battery. Usually, the separators used in LIBs are porous materials with ~30-50% porosity with ~0.03 to 0.1 μm pore diameters, which allows ion transfer and prevents the short circuit of the cells by maintaining the integrity of the cells. The state-of-the-art LIB recycling research mainly focuses on recycling cathode parts due to their high economic value, which are composed of valuable metals. Anode recycling is also not focussed as some research strategies could abolish them by burnout or leave them as they are after cathode recycling. However, compared with the electrode research, the recycling of polymer separators is relatively ignored, which can create antagonistic possessions on ecological well-being. Hence, recycling separators is a very important requirement before passing them into larger quantities of waste streams. Therefore, separator recovery and reuse are equally important as electrode recycling research.

The present work has studied the polymer separator from recovered and regenerated to reuse in Li-ion batteries for their second-life applications. The work has been enlightening the recovery of the polypropylene separator from the used LIBs, which were reused to prepare the new cells after proper washing. The study was done by fabricating the cells and characterizing them electrochemically compared to the commercially available fresh separator materials to understand better the used separators' capabilities.

6.2 Methods and materials

6.2.1 Separation of separator material

The waste LIBs are collected from the discarded laptops from the e-waste dumping yard facility of our institute, CSIR-National Chemical Laboratory. The collected spent batteries are subjected to a chemical discharge process in an alkaline solution for a few hours. After the complete discharge, the batteries were dismantled mechanically, and the electrode materials and

separators were parted carefully. The recovered electrode materials are subjected to suitable recycling processes, which have been reported conveniently. The separator is collected and washed with demineralized water using an ultrasonication process to clean the pores of the separator without electrode active contaminants.

6.2.2 Physical characterization

The commercially available and recovered separator samples were characterized by X-ray diffraction (XRD) with Cu-Kα radiation (k = 1.54 Å) (PANalyticalX'pert pro). The porous morphology was analyzed using a Field emission scanning electron microscope (FE-SEM). The material's tensile strength was examined using the Universal testing machine (UTM). The elemental oxidation states were studied using X-ray photoelectron spectroscopy (XPS), performed by the Thermo Scientific Model K-alpha XPS instrument with monochromatic Al-Kα as the X-ray source. The BET surface area porosity measurement and material analysis were assessed using a Quantasorb instrument.

6.2.3 Electrochemical examination

Cyclic voltammetry and electrochemical impedance spectroscopy (EIS) studies and analyses were conducted using the Metrohm Multi-Autolab electrochemical workstation. The galvanostatic charge-discharge (GCD) studies employ the Neware battery testing system. The electrochemical application feasibility of the separator materials is carried out by preparing 2032 type of coin cells in an Ar glove box with O_2 and H_2O levels < 0.1 ppm. The coin cells are fabricated using a working cathode prepared by coating commercial Lithium iron phosphate (LFP) material coated on Al foil by mixing with appropriate amounts of conductive carbon and PVDF as binder with the help of N-methyl pyrrolidinone as a dispersing agent, and the metallic Li disc used as an anode. The electrolyte used in the cell fabrication is 1M $LiPF_6$ in ethylene carbonate (EC),

ethylene methylene carbonate (EMC), and di-methylene carbonate (DMC) at a 1:1:1 ratio by volume.

6.3 Results and discussion

6.3.1 Physical and structural properties analysis

6.3.1.1 X-ray diffraction study

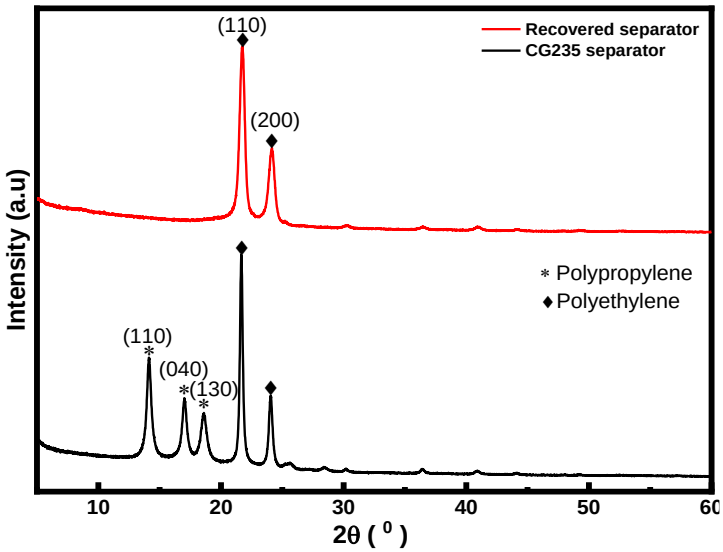

Figure 6.1 X-ray diffraction pattern of CG2325 and recovered separator.

Figure 6.1 illustrates the X-ray diffraction of the recovered separator from the spent Li-ion battery and the commercially available celgard2325 (CG2325) separator. X-ray diffraction peaks are matched with the ICDD pdf numbers 00-011-0834 and 00-061-1416, designated to polyethylene and polypropylene, respectively. The diffraction patterns match the previous report well.[5] The X-ray diffraction studies reveal that the recovered separator is a polyethylene-based monolayer separator. The CG2325 separator used for the comparative studies is a polyethylene and polypropylene-based tri-layer separator. The monolayer and tri-layer separators are differentiated with the X-ray diffraction data, and the diffraction peaks are labeled with respective hkl values.

6.3.1.2 Stress and strain analysis

The recovered separator was subjected to the determination of the tensile strength and tensile strain. The determined results are also compared to the commercial CG2325 separator. **Figure 6.2(a-b)** shows the Tensile stress v/s tensile strain plots. The fresh CG2325 separator can take up to a maximum of 180MPa, but the used separator could be able to take up to a maximum of 69 MPa stress, which is due to the reason that the used separator already undergone the 'n' number of ionic charges transfers rapidly through the porous polymeric membrane while using in LIBs might be caused the deterioration of porous membrane and caused the decrease in the mechanical properties of the separator. The plots also indicate the average tensile strain at the breakpoint of the CG 2325 separator is 97.82%, which is greater than that of the recovered separator; that is due to the reason that the CG2325 is a tri-layer separator comprised of both polyethylene and polypropylene materials embedded together. In contrast, the recovered separator is made of monolayer polyethylene materials, and these values support the XRD results of these separator materials.

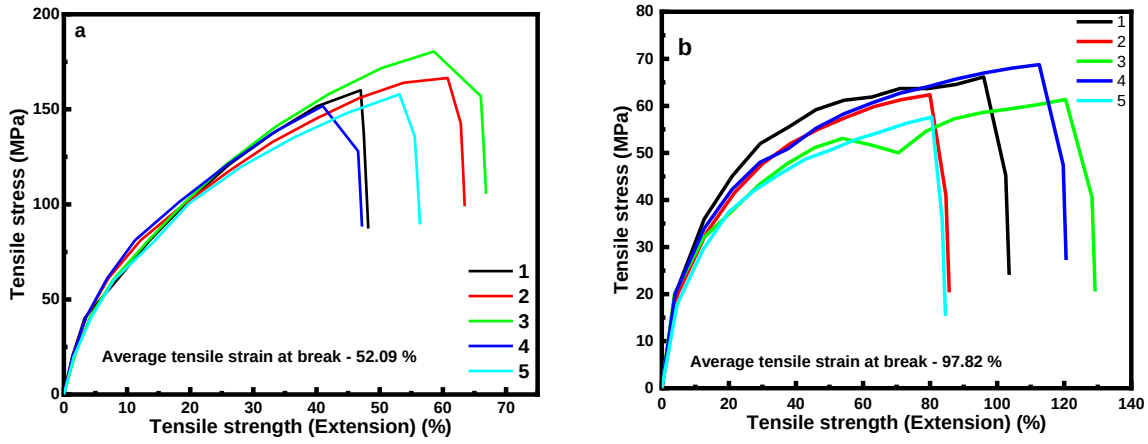

Figure 6.2. Tensile stress v/s Tensile strain of **(a)** CG2325 separator and **(b)** Recovered PE separator.

6.3.1.3 Scanning electron microscopic analysis

To visualize the morphology and porous structure of the recovered separator and CG2325 separator, for comparison, are subjected to the FESEM analysis. **Figure 6.3** displays the FESEM images of the separators; all these images show a strip type of porous structure, the image of CG2325 reveals the multiple layers and the recovered separator indicates the monolayer structure. The distribution of pores across the surface of the separator is uniform in both fresh and used separators.[6,7] Such a multi-layer nature of CG2325 contributes to bearing more stress than the monolayer separator. A slight difference can be seen between the recovered separator and the ultrasonically cleaned separator without a wash; some particles can be observed through the pores of the separator in the case of an unwashed separator that has been minimized in the washed separator. These particles could block the pores and slow the ion movement between the electrodes.

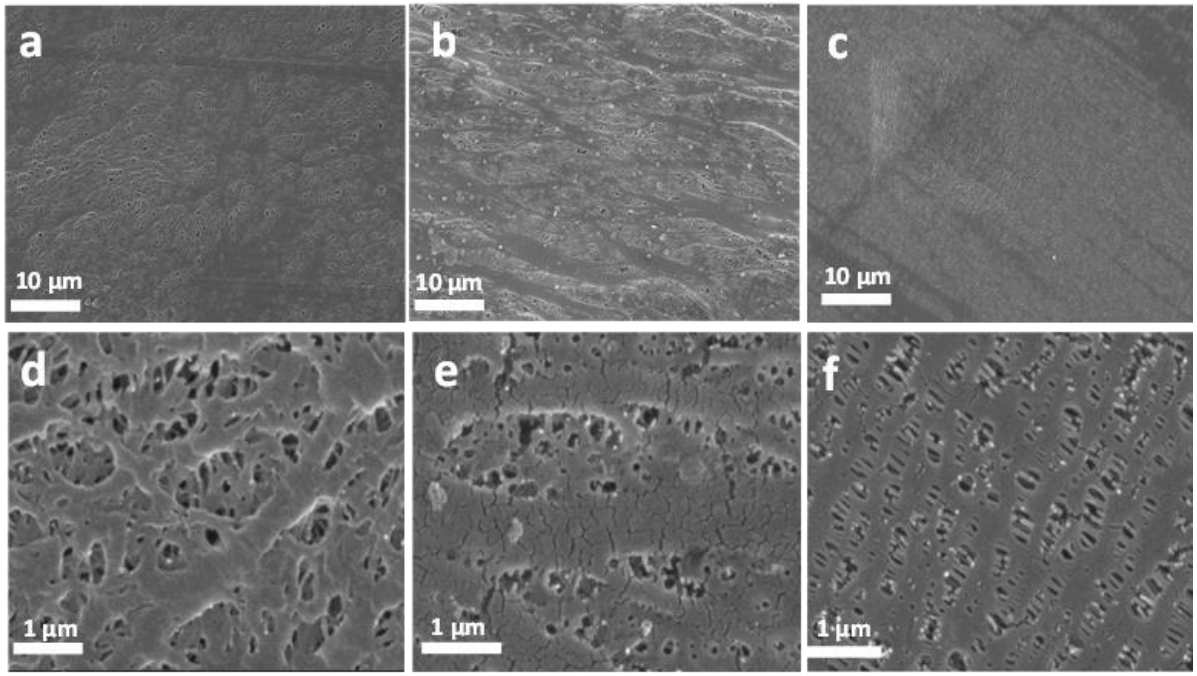

Figure 6.3. Low and high magnification FESEM images of (a & d) CG2325 separator, (b & e) Recovered separator, and (c & f) Recovered separator after ultrasonic cleaning.

6.3.1.4 BET surface area analysis

Figure. 6.5 shows the deconvoluted spectra of XPS core levels of the CG2325, recovered and washed separators; **Figure 6.5(a-a2)** displays the C1s and O1s core levels of the commercial CG2325 separator. **Figure 6.5(b-b4)** displays the recovered separator's C1s, O1s, Co2p, and Ni2p core levels from a spent Li-ion battery. The recovered separator has also shown Co2p and Ni2p levels, along with C1s and O1s. The reason for detecting the traces of Co2p and Ni2p levels is that the cathode active material was trapped in the separator's porous structure during the battery's active life.

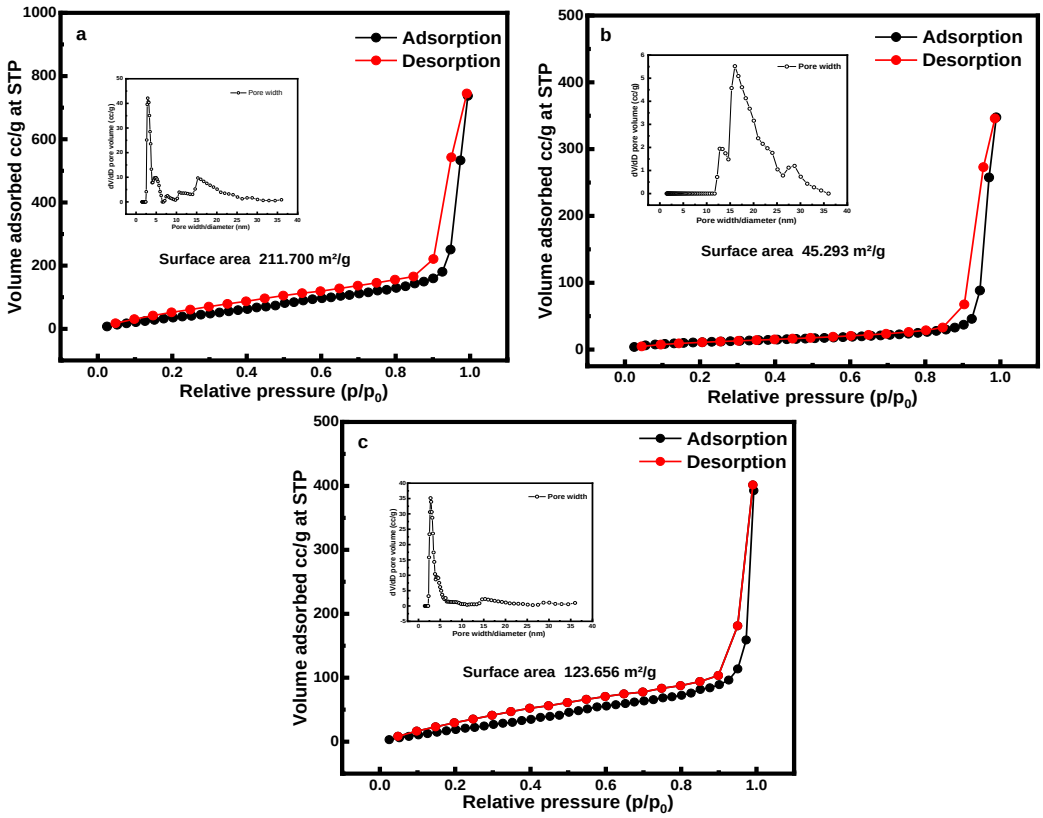

Figure 6.4 Nitrogen adsorption and desorption isotherms of (a) Celgard2325 (b) Recovered separator (c) Recovered separator after ultrasonic clean, corresponding pore width distribution curves (inset).

Figure 6.4 shows the N_2 adsorption-desorption curves of the CG2325 separator, recovered separator, and recovered separator after ultrasonic cleaning; the BET isotherms confirm the

mesoporous nature of the separator samples. The surface area of CG2325 is 211.7 m^2/g obtained from the adsorption-desorption measurement, the surface area of the recovered separator was 123.6 m^2/g, and the recovered separator after ultrasonic cleaning has shown the surface area 45.3 m^2/g. The washed separator's surface area was significantly reduced compared to the directly recovered separator sample, which might be due to the presence of active material traces from the spent battery over the surface of the separator contributed to the larger surface area. The pore size distribution of the samples has been measured and analyzed by assuming slit pore shapes through hybrid nonlocal density functional theory (NLDFT), revealing that the average pore diameter of CG2325 separator is 15.31 nm, the recovered separator has recorded the average pore width of 2.89 nm and the ultrasonically cleaned recovered separator has shown 16.01 nm. The average pore diameter of the recovered separator is significantly low; the reason for the least pore width might be the pores are blocked by the electrode active materials from the spent battery; the recovered separator has shown a significantly larger pore diameter than the recovered separator and also slightly larger than CG2325 separator, which is possible because of the recovered separator already exposed for the prolonged ion transportation during its first life in rechargeable battery which might expand the pore diameters which got cleared after the thorough ultrasonic cleaning of the recovered separator.

6.3.1.5 X-ray photoelectron spectroscopic study

Figure 6.5(c-c2), also displays the C1s and O1s core levels for the recovered and ultrasonically washed separator. It can be observed that no Co and Ni remain in the recovered separator after it has been washed ultrasonically. Assuming the presence of Mn in the recovered separator, it was also scanned for Mn2p levels. However, there were proofs for the existence of Mn ions that might be due to the unavailability of Mn ions in the particular cathode chemistry

which was used in battery or Mn ions got dissolved into electrolyte completely due to the disproportionation reaction of Mn ion[9] and well-known Jahn-teller distortion of Mn ions.[10]

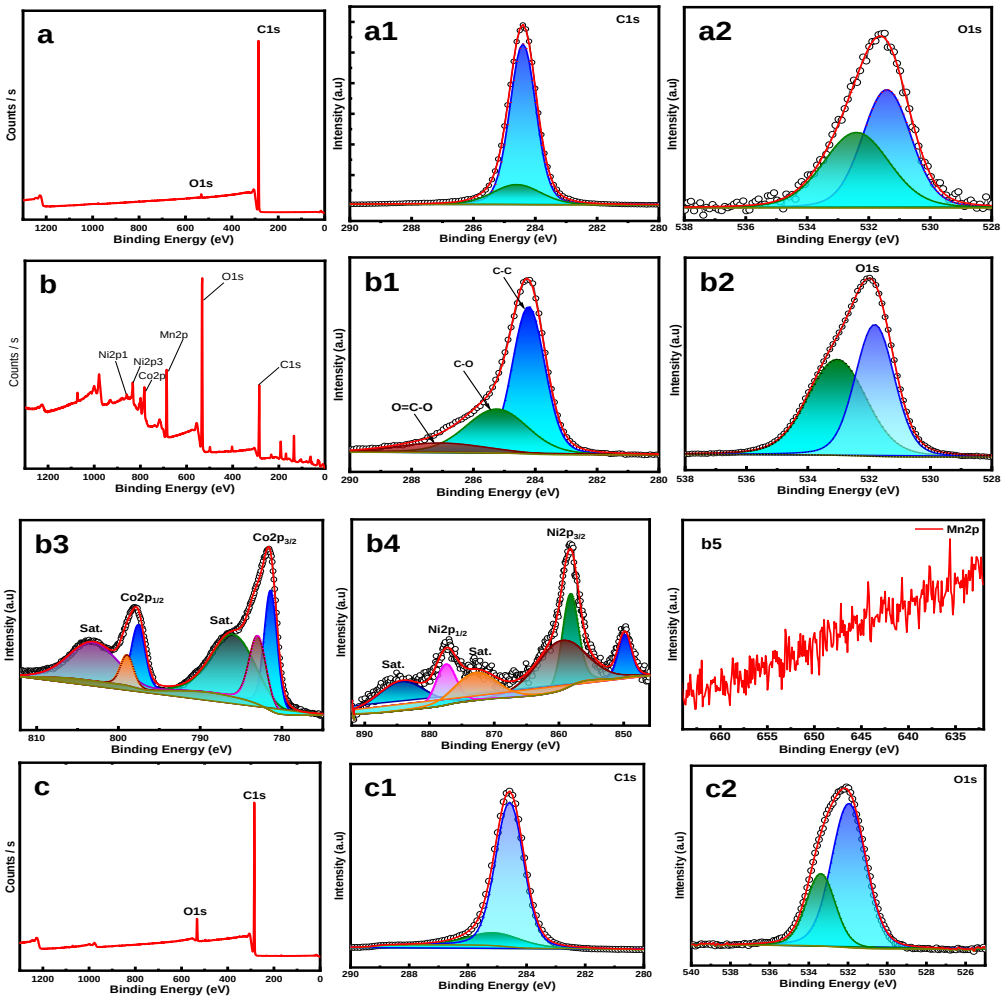

Figure 6.5. XPS survey spectra of **(a)** CG2325, **(b)** recovered separator, and **(c)** Washed separator, Deconvoluted XPS curves of **(a1)** C1s, **(a2)** O1s, CG2325 separator **(b1)** C1s **(b2)** O1s **(b3)** Co2p, and **(b4)** Ni2p **(b5)** Mn2p of the recovered separator, **(c1)** C1s and **(c2)** O1s of ultrasonically washed recovered separator.

The atomic percentages of the elements measured from the XPS studies have been given in **Table. 6.1,** to better understand the existence of transition element traces over the surface of the recovered separator.

Elemental core level	C1s	O1s	Co2p	Ni2p1	Ni2p3	Mn2p1	Mn2p3
Atomic percentage (%)	32.69	37.62	4.08	0.26	0.34	0.06	0.03

Table 6.1. The atomic percentage of the elemental core levels of the recovered separator was obtained from the XPS analysis.

6.3.2 Electrochemical performance analysis

To investigate the practicability of these recovered used separators for the application in LIBs, the recovered separator has been used to fabricate 2032-type coin cells in a half-cell configuration with Li metal. The cells were fabricated using a commercial CG2325 separator and commercial LFP as a cathode to understand better.

6.3.2.1 Cyclic voltammetry study

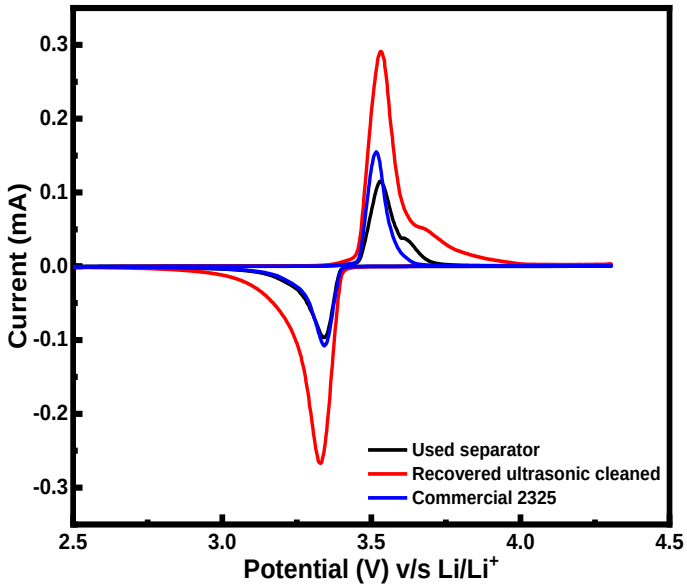

Figure 6.6. Cyclic voltammogram of commercial LFP cathode using recovered PE separator.

Figure 6.6 shows the cyclic voltammograms of the used separator recovered from the spent battery, the recovered separator cleaned ultrasonically, and the commercial CG2325 separator. The intensity of the redox behavior of the LFP cathode materials with different separator samples has

shown significant changes as the used separator has demonstrated very less intense redox peaks, whereas the used separator, after ultrasonic cleaning, demonstrated the higher peak current, which influences that the pores of the used separator were blocked which affected the smoother movement of ions that reduced the extent of redox activity of cathode the active material. The used separator was exposed more to the ion transfer; the porosity got blocked, and the cleaned separator provided a larger area of the pathway for the ion movement and caused more intense redox behavior. In **Figure 6.6** the cyclic voltammograms of the coin cells with CG2325 and recovered separators; comparatively, the redox curves of the cells with the ultrasonically washed separator recovered from spent LIB are more intense than those of the fresh separator, which might be due to the used separator already exposed to the 'n' number of ionic charge carriers and which has made wider channels for the ion transfer. The fresh separator has a more ordered porous structure, allowing the movement of ions that might be controlled.

6.3.2.2 Electrochemical impedance spectroscopy

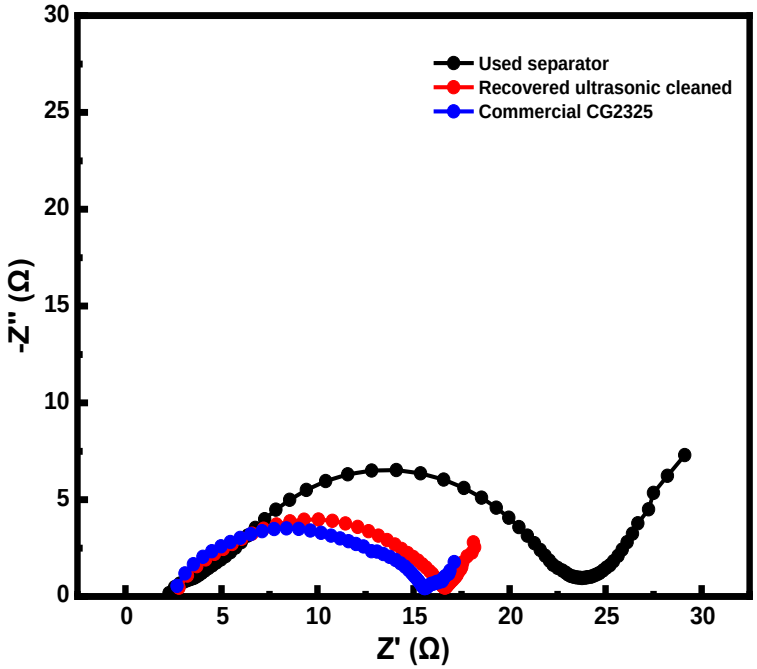

Figure 6.7. Nyquist plot of commercial LFP cathode using recovered PE separator.

Figure 6.7 displays the Nyquist plots of cells with the recovered separator and CG2325 separator. Overall, the cell with the recovered separator has more resistance than the cell with the fresh separator. Based on the Nyquist plots, it can be concluded that the cell with the recovered separator has faster Li^+ ion diffusion kinetics than the cell with the fresh separator.

6.3.2.3 Galvanostatic charge-discharge study

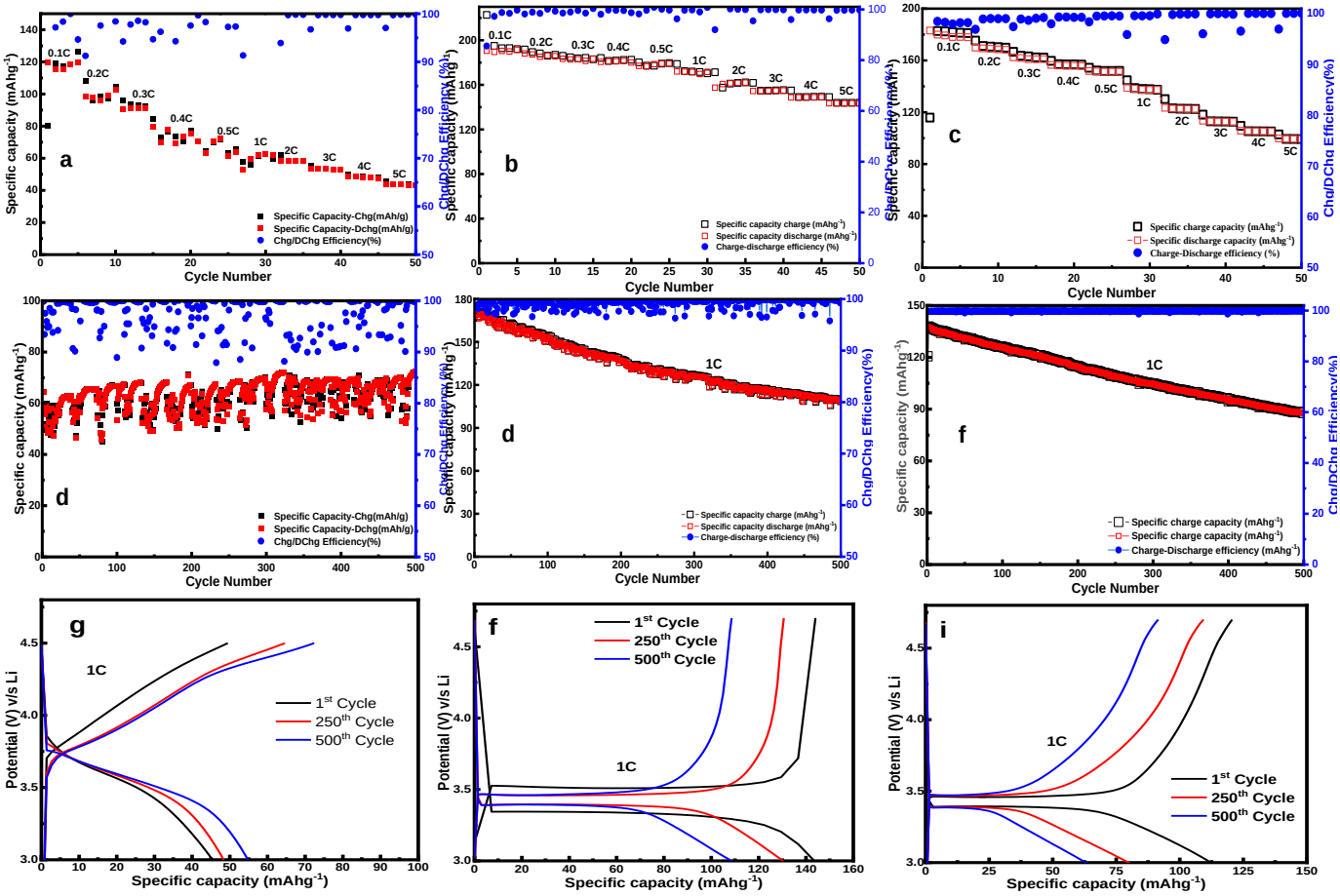

Figure 6.8. The rate capability of LFP cathode with **(a)** recovered separator, **(b)** recovered separator after ultrasonic cleaning and **(c)** commercial CG2325 separator. Cycle stability of LFP cathode with **(d)** recovered separator, **(e)** recovered separator after ultrasonic cleaning, **(f)** commercial CG2325 separator. Potential v/s Specific capacity plots of coin cells of LFP cathode with of LFP cathode with **(g)** recovered separator, **(h)** recovered separator after ultrasonic cleaning, **(i)** commercial CG2325 separator.

To evaluate the electrochemical capabilities of the recovered separator for practical application in LIBs, the cells fabricated with recovered separators are subjected to galvanostatic charge-discharge studies; there are three sets of cells prepared by using the recovered separator without any treatment, the recovered separator after ultrasonic clean, and the fresh CG2325 separator. **Figures 6.8(a-c)** display the rate capability of the recovered separator, ultrasonically cleaned recovered separator, and CG2325 separator. cycle stability plots without washing. **Figures 6.8(d-f)** show the cycle stability plots of the recovered separator, ultrasonically cleaned recovered separator, and CG2325 separator. **Figures 6.8(g-i)** show the cells' voltage v/s specific capacity curves of the recovered separator, ultrasonically cleaned recovered separator, and CG2325 separator, respectively. The cell prepared with the recovered separator without any treatment exhibited very poor performance with a lot of fluctuations with specific capacity values, which indicates the unstable performance of the used separator with underperformed values as the particular discharge capacity 119.6 $mAhg^{-1}$ at 0.1C rate, 64.4 $mAhg^{-1}$ at 1C rate, and the specific discharge has reached 72.3 $mAhg^{-1}$ at 1C rate after 500 cycles, which confirms the unstable performance of the used separator. In contrast, the cell with the ultrasonically washed separator has exhibited a significant improvement in capacity and electrochemical stability of the cells. The specific discharge capacity of the cell with an ultrasonically cleaned separator is 190.6 $mAhg^{-1}$ at a 0.1C rate. It showed an excellent rate capability of 143.5 mAhg-1 at a 5C rate, and the specific capacity of 170.8 $mAhg^{-1}$ at a 1C rate in the first cycle of the cycle stability revealed that the specific discharge capacity reached 108 $mAhg^{-1}$ at a 1C rate after 500 cycles with capacity retention of 63.2%. The specific discharge capacity of the cell with CG2325 separator has exhibited a specific discharge capacity of 183.03 $mAhg^{-1}$ at 0.1C and 137.7 $mAhg^{-1}$ at 1C at the first cycle which has reached 87.9 $mAhg^{-1}$ at 1C after 500^{th} cycle with capacity retention of 63.8%.

The specific discharge capacity of the cell with recovered separator washed ultrasonically is greater than the cell with CG2325 separator, which is due to the used porous structure already more exposed to ionic charge carriers and also aligned with Li-ion diffusion channels makes it exhibit better specific discharge capacity. The assessed values of pore diameters of the recovered and ultrasonically cleaned separator were also supportive of the increased specific capacity values for the cells with the ultrasonically cleaned separator.

6.4 Conclusions

This work has studied the re-usability of the separator recovered from the spent LIB for the second life application. The porous polymeric separator has been recovered from the spent LIB and evaluated the capabilities for reuse in Li-ion cells; it is suggested that based on the findings of the work, the recovered separator washed ultrasonically has met the requisite mechanical and electrochemical properties to a suitable separator for LIBs. The cells prepared with the recovered separator have exhibited decent electrochemical performance with good rate capability and cycle stability. Therefore, the findings of the work could encourage the recycling industry and energy storage researchers to reuse the separators recovered from the spent LIBs.

6.5 References

(1) Ma, X.; Chen, M.; Chen, B.; Meng, Z.; Wang, Y. High-Performance Graphite Recovered from Spent Lithium-Ion Batteries. *ACS Sustain. Chem. Eng.* **2019**, *7* (24), 19732–19738. https://doi.org/10.1021/acssuschemeng.9b05003.

(2) Baum, Z. J.; Bird, R. E.; Yu, X.; Ma, J. Lithium-Ion Battery Recycling─Overview of Techniques and Trends. *ACS Energy Lett.* **2022**, *7* (2). https://doi.org/10.1021/acsenergylett.1c02602.

(3) Lu, Y.; Peng, K.; Zhang, L. Sustainable Recycling of Electrode Materials in Spent Li-Ion Batteries through Direct Regeneration Processes. *ACS EST Eng.* **2022**, *2* (4), 586–605. https://doi.org/10.1021/acsestengg.1c00425.

(4) Nayaka, G. P.; Manjanna, J.; Pai, K. V.; Vadavi, R.; Keny, S. J.; Tripathi, V. S. Recovery of Valuable Metal Ions from the Spent Lithium-Ion Battery Using Aqueous Mixture of Mild Organic Acids as Alternative to Mineral Acids. *Hydrometallurgy* **2015**, *151*, 73–77. https://doi.org/10.1016/j.hydromet.2014.11.006.

(5) Love, C. T. Thermomechanical Analysis and Durability of Commercial Micro-Porous Polymer Li-Ion Battery Separators. *J. Power Sources* **2011**, *196* (5), 2905–2912. https://doi.org/10.1016/j.jpowsour.2010.10.083.

(6) Arora, P.; Zhang, Z. (John). Battery Separators. *Chem. Rev.* **2004**, *104* (10), 4419–4462. https://doi.org/10.1021/cr020738u.

(7) Natarajan, S.; Subramanyan, K.; Dhanalakshmi, R. B.; Stephan, A. M.; Aravindan, V. Regeneration of Polyolefin Separators from Spent Li-Ion Battery for Second Life. *Batter. Supercaps* **2020**, *3* (7), 581–586. https://doi.org/10.1002/batt.202000024.

(8) Raja, M.; Angulakshmi, N.; Thomas, S.; Kumar, T. P.; Stephan, A. M. Thin, Flexible and Thermally Stable Ceramic Membranes as Separator for Lithium-Ion Batteries. *J. Membr. Sci.* **2014**, *471*, 103–109. https://doi.org/10.1016/j.memsci.2014.07.058.

(9) Wu, J.; Yang, J.; Leong, Z. Y.; Zhang, F.; Deng, H.; Ouyang, G. F.; Yu, J. A Method to Inhibit Disproportionation of Mn^{3+} for Low-Cost Mn–Fe All-Flow Battery. *ACS Appl. Energy Mater.* **2022**, *5* (12), 14646–14651. https://doi.org/10.1021/acsaem.2c03075.

(10) Yamada, A.; Tanaka, M.; Tanaka, K.; Sekai, K. Jahn–Teller Instability in Spinel Li–Mn–O. *J. Power Sources* **1999**, *81–82*, 73–78. https://doi.org/10.1016/S0378-7753(99)00106-8.

Chapter 7

Summary of the Thesis

7.1 Summary

This thesis presents research to enhance $LiMn_2O_4$-based cathode materials for improved energy density and voltage performance. The study addressed key challenges, such as diminishing capacity and structural instability, primarily attributed to the Jahn-Teller effect in Mn^{3+} ions and the dissolution of Mn into the electrolyte. The researchers employed a two-pronged strategy involving elemental doping and surface modification techniques to overcome these issues.

The $LiMn_2O_4$ structure was stabilized, and its electrochemical performance was enhanced by incorporating elemental dopants. A thorough examination of the effects of multi-cation doping using Ni, Fe, and Al elements was conducted. Adding Ni improved the material's electronic conductivity, facilitating better charge transport. Fe doping enhanced structural stability by mitigating Mn dissolution, while Al doping provided increased thermal and structural robustness during high-voltage operation. A methodical optimization of dopant concentrations was performed to strike a balance between electrochemical stability, capacity retention, and rate capability. Comprehensive structural and electrochemical analyses were carried out to assess the impact of these dopants, revealing notable improvements in cycling stability and capacity retention, especially at elevated voltages.

To combat capacity loss and enhance material longevity, researchers employed a crucial strategy involving the application of protective coatings for surface modification. $LiMn_2O_4$ particles were coated with thin layers of $NiFe_2O_4$ and $NiAl_2O_4$. These protective layers served as physical barriers, shielding the active material from direct electrolyte contact, thereby substantially reducing Mn dissolution and unwanted surface reactions. Importantly, the coatings maintained ionic conductivity, preserving the material's electrochemical performance. To verify the uniformity and efficacy of these protective layers, researchers utilized sophisticated

characterization methods, including electron microscopy and spectroscopy. These techniques demonstrated the coatings' role in improving the cathode material's stability.

The combined approach of multi-cation doping and surface coating led to the successful development of cathode materials with improved cycling stability, higher capacity retention, and better performance at elevated temperatures and voltages. This work addresses the key limitations of LiMn2O4 and contributes to the broader objective of developing cost-effective, high-performance cathode materials for next-generation lithium-ion batteries.

The thesis also explores the process of recycling and revitalizing electrodes from used lithium-ion batteries, with an emphasis on eco-friendly retrieval and repurposing of cathode components. Given the increasing need for lithium-ion batteries and the ecological issues linked to their disposal, this study seeks to create effective techniques for reclaiming and restoring valuable materials for further use.

Battery recycling begins with disassembling spent batteries and extracting cathode materials using mechanical, chemical, and thermal methods. These materials are then treated to restore their electrochemical properties, which includes removing contaminants, reconstructing the cathode composition, and replenishing the depleted lithium content.

The study aimed to restore LMO-based cathode materials to a level of electrochemical performance similar to that of newly synthesized cathodes. By refining synthesis parameters and using specific reagents, researchers successfully revitalized the structural and electrochemical properties of the material. The restored cathode material exhibited outstanding cycling durability and capacity retention, rendering it appropriate for integration into new battery systems.

The recycling and repurposing of anode components and separators from exhausted lithium-ion batteries (LIBs) have been investigated for their potential in secondary applications. Cutting-edge analytical techniques were utilized to examine the reclaimed materials' crystalline structure, surface characteristics, and electrochemical behavior. These assessments confirmed the successful elimination of unwanted substances, restoration of the original crystal configuration, and improvement in electrochemical performance. The study also underscores the scalability and environmental sustainability of the recycling methodology. Researchers developed resource-efficient and cost-effective processes that adhere to circular economy concepts. This approach ensures that recycled materials comply with industry requirements while reducing the need for virgin resources and minimizing the ecological impact of LIB production.

This research contributes to the broader field of cathode material development by offering a comprehensive strategy for enhancing lithium-ion battery lifecycle performance and environmental sustainability.

7.2 Future Perspectives

The outlook for research on high-energy and high-voltage $LiMn_2O_4$-based cathode materials and Li-ion battery recycling is varied and encouraging. Continued refinement of doping techniques can boost structural integrity by minimizing Jahn-Teller distortion while enhancing conductivity and heat resistance. Innovative multi-cation doping combinations and their cooperative effects show promise for improving electrochemical efficiency. Advancements in surface coating, such as hybrid layers combining materials like $NiFe_2O_4$ and $NiAl_2O_4$ with polymers or fluorides, can offer improved surface durability and minimize unwanted reactions, making these materials more suitable for use with advanced electrolytes, including solid-state and wide electrochemical window liquid variants. Expanding the production of modified $LiMn_2O_4$

cathodes would involve optimizing synthesis methods to reduce expenses and energy use while ensuring environmentally friendly manufacturing processes. These developments can expedite the market adoption of these materials in sectors where cost-effectiveness and environmental sustainability are crucial.

This study has important ramifications for recycling practices and the circular economy. Investigations into recovering valuable components from used batteries could aid in developing closed-loop recycling systems, particularly when combined with the electrochemical lithium recovery techniques currently under examination. Integrating these systems makes it feasible to minimize environmental impact while maintaining a sustainable material supply. The enhanced cathodes could also be customized for high-power uses such as electric vehicles, drones, and mobile electronics, where thermal stability and rapid charging are essential. Moreover, the methods and findings from this research may apply to other battery types, including $NaMn_2O_4$ for sodium-ion batteries or even spinel-type materials for lithium-sulfur or lithium-air systems, thus contributing to progress in emerging energy storage technologies.

Furthermore, your study aligns with worldwide sustainability objectives and efforts to reduce carbon emissions. Creating more environmentally friendly synthesis and recycling methods can contribute to setting industry benchmarks, decreasing the carbon impact of battery manufacturing, and fostering sustainable energy storage solutions. In essence, the research has the potential to make significant strides in enhancing battery efficiency and durability while also supporting a broader vision of a sustainable and circular economy.

ABSTRACT

Name of the Student: Shivamurthy B P
Registration No.: 10CC20J26019
Faculty of Study: Chemical Sciences
Year of Submission: 2024
CSIR Lab: NCL, Pune
Name of the Supervisor: Dr. Nayaka G P

Title of the Thesis: Development and Investigation of Electrochemical Properties of High-Voltage Spinel-based Cathode Materials and Recycling Methodology for Li-ion Batteries

This thesis explores the development of high-voltage cathode materials for Li-ion batteries (LIBs) with improved specific capacity. One section synthesizes and characterizes LiMn2O4-based cathode materials modified with a Co-free cation doping approach and surface modification using Ni, Fe, and Al cations. Another section addresses the recovery and regeneration of electrode materials from end-of-life batteries. ***Chapter 1*** of this thesis provides an overview of the history and progress of LMO-based cathode materials, the challenges, and remedial approaches to overcome the issues. Also, an overview of the recycling and regeneration methodology of spent LIBs is provided. ***Chapter 2, Part A*** investigates the effect of doping of cations like Ni, Al, and Fe into the crystal structure to minimize the Mn^{3+} content to mitigate the issue of disproportionation reaction of Mn^{3+} ions and dissolution of Mn ions, which would enhance the electrochemical performance with increased energy density. The cathode materials $LiMn_{2-x-y-z}Ni_xFe_yAl_zO_4$ (x = 0.8-0.5, y & z = 0.1-0.25) are formed with dual phases in the crystal structure due to high Ni substitution. The materials were characterized and studied electrochemically to understand the influence of the secondary phase on the electrochemical performance. ***Chapter 2, Part B*** deals with the extended part of the previous chapter, where the materials possess a secondary phase that influences the electrochemical performance of the material. Therefore, to achieve phase purity in the cathode materials, synthesis conditions were optimized to prepare the materials $LiMn_{2-x-y-z}Ni_xFe_yAl_zO_4$ (x=0.4-0.5, y & z = 0.05-0.1). ***Chapter 3, Part A*** studies the influence of surface modification of LMO with nickel-iron oxide (NFO) on the electrochemical performance. ***Chapter 3, Part B*** explores the effect of surface coating of LMO material with nickel aluminum oxide (NAO) on the electrochemical stability of LMO cathode material. ***Chapter 4*** deals with the regeneration cathode material from used LIB for the second life application upon restoration of its structure by recoupment of lost Li content and studies the electrochemical performance of the regenerated cathode material. ***Chapter 5*** presents the methodology for recovering and functionalizing spent Graphite anode from used LIBs into reduced graphene oxide for the secondary electrochemical application. ***Chapter 6*** sheds light on the reusability of the recovered polymeric separator from the spend LIB for its second life application in Li-ion cells. ***Chapter 7*** summarizes the present thesis's overall work and recommends the research scope for their applications in energy storage and conversion.

List of Publication(s) in SCI Journal(s) Emanating from the Thesis Work

1. **BP Shivamurthy**, M Thripuranthaka, MV Shelke, **GP Nayaka***, Formation of the Secondary Phase Domain by Multi-Cation Substitution for the Superior Electrochemical Performance of Spinel Cathodes for High-Voltage Li-Ion Batteries, **ACS Applied Energy Materials** 5 (12), 15345-15355, 2022.
2. **BP Shivamurthy**, **GP Nayaka***, G Santhosh Performance Analysis of Regenerated rGO Electrodes from Spent Li-ion Battery Anodes for Secondary Energy Device Applications, **Energy & Fuels**, 37 (4), 3188–3195, 2023.
3. **BP Shivamurthy**, M Thripuranthaka, MV Shelke, **GP Nayaka*,** Influence of crystal plane orientation in enhancing the electrochemical performance of tri-cation substituted cathode for Li-ion batteries, **Energy Fuels**, 2024, 38, 5, 4653–4665.
4. **BP Shivamurthy**, Purnima Rawat, MV Shelke, Zhongren Zhou, **GP Nayaka*,** Recycling and direct regeneration of cathode material from spent Li-ion batteries towards re-claim second life. **ACS Sustainable Resour. Manage.** 2025, XXXX, XXX, XXX-XXX, https://doi.org/10.1021/acssusresmgt.4c00533

Published Patent

1. **BP Shivamurthy, GP Nayaka,** COBALT FREE $LiMn_{2-x-y-z}Ni_xFe_yAl_zO_4$ SPINEL AS CATHODE MATERIAL FOR Li-ION BATTERIES WO Patent **WO2023095155A1.**

Research Articles under Communication for Publication Emanating from the Thesis Work

1. **BP Shivamurthy**, MV Shelke, **GP Nayaka*,** Impact of surface modification with Nickel ferrite in reducing the Mn dissolution to enhanced cycle stability of $LiMn_2O_4$ cathode material for Li-ion batteries.
2. **BP Shivamurthy**, MV Shelke, **GP Nayaka*,** Electrochemical performance enhancement of $LiMn_2O_4$ cathode materials for Li-ion batteries through nickel aluminate surface modification
3. **BP Shivamurthy**, **GP Nayaka*,** Regeneration and reuse of polymeric separators from waste Li-ion batteries for second-life applications.

List of Papers with abstract presented (oral/poster) at national/international conferences/seminars.

1. *International Conference on Emerging Materials for Sustainable Development (EMSD 2022)* during October 10-11, **2022**, at CSIR-CSIO Chandigarh (Presented poster titled "Disorder structured multi-cation doped spinel cathode material for the high-voltage Li-ion batteries).
2. NCL-RF Annual Student Conference at CSIR-NCL Pune, November **2022** (Presented poster titled "Effect of crystal plane orientation on electrochemical performance of tri-cation substituted spinel cathode material for high-voltage Li-ion batteries").
3. Science Day Celebration
   i. CSIR-NCL, **2023** (Presented poster titled "Disorder structured multi-cation doped spinel cathode material for the high-voltage Li-ion batteries").
   ii. CSIR-NCL, **2023** Presented poster titled " प्रयुक्त Li-ion बैटरी एनोड से पुनर्जीवित rGO इलेक्ट्रोड का विद्युत रसायनिक प्रदर्शन विशलेषण : सर्कुलर इकोनॉमी की ओर अध्ययन").

ACS APPLIED ENERGY MATERIALS

www.acsaem.org Article

Formation of the Secondary Phase Domain by Multi-Cation Substitution for the Superior Electrochemical Performance of Spinel Cathodes for High-Voltage Li-Ion Batteries

Bogalera Papaiah Shivamurthy, Marulasiddappa Thripuranthaka, Manjusha V. Shelke, and Girish Praveen Nayaka*

Cite This: *ACS Appl. Energy Mater.* 2022, 5, 15345−15355 Read Online

ACCESS | Metrics & More | Article Recommendations | Supporting Information

ABSTRACT: Disorder-structured spinel oxides are opening frontiers for high-capacity/high-voltage cathodes to meet the challenges of independence on cobalt-containing cathodes toward cheap and sustainable energy storage sources in Li-ion batteries (LIBs). In the present work, a series of Co-free materials: $LiMn_{2-x-y-z}Ni_xFe_yAl_zO_4$ (x = 0.8−0.5, y = 0.1−0.25, and z = 0.1−0.25) with spinel/rock salt disordered structures are reported. The refinement studies confirmed that the materials synthesized are of mixed phase, and the I_{311}/I_{400} peaks ratio confirms that the synthesized materials are stable enough for electrochemical applications. This article addresses the influence of the secondary phase on the electrochemical activity and the reduction of the Mn^{3+} ratio to alleviate the Mn dissolution issue for bettered stability. The optimized $LiMnNi_{0.7}Fe_{0.1}Al_{0.2}O_4$ is appraised as a cathode material in the voltage range between 3.5 and 5 V (vs. Li^+/Li) with an initial discharge capacity of 148.7 mA h g^{-1} at a rate of 1 C. This material showed very good cycling stability with a capacity retention of 79.5% after 1000 cycles. The cyclic voltammetry studies showed that the material can be a potential candidate for 5 V applications.

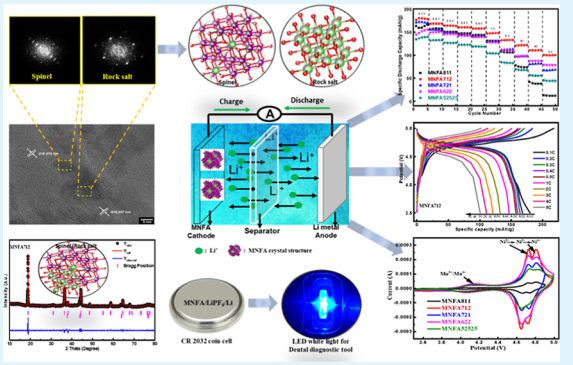

KEYWORDS: *cobalt-free cathode, cation-doped spinel cathode material, disorder structured spinel cathode material, li-ion batteries, $LiMn_2O_4$, $LiMn_{1.5}Ni_{0.5}O_4$, high-voltage cathode*

Downloaded via NATL CHEMICAL LABORATORY on March 21, 2023 at 12:19:48 (UTC).
See https://pubs.acs.org/sharingguidelines for options on how to legitimately share published articles.

1. INTRODUCTION

The large-scale consumption of fossil fuels worldwide deteriorates the environment day by day and causes ecological imbalance. Developing robust energy storage systems to hoard renewable energy and electrification of transport systems are necessary to reduce the dependence on fossil fuels.[1,2] Hybrid electric vehicles (HEVs) and electric vehicles (EVs) are considered sound alternative transport systems. Therefore, it is necessary to develop high-performing, environmentally safe, and economically feasible energy storage devices for the electrification of the transport system.[3,4] Li-ion batteries (LIBs) are the first choice among secondary batteries because of their high energy density, low memory effect, longer cyclability, and safety features.[3] The cathode material is a crucial part of the energy storage cells. Three cathode chemistries, layered, spinel, and olivine-type materials, have occupied the space.[5] In cathode chemistries, Co plays a vital role; there is an urgent need to develop Co-free cathode material owing to its scarcity, environmental compatibility, and significant fluctuation in their prices.[6−8] In current years, the price of Co has varied expansively from $ 30,000 to $90,000 per metric ton as EVs have developed rapidly around the globe; additionally, the global development of LIBs production size is projected to increase from ≈290 to ≈1700 GWh by 2028.[9] This global dependence on Co might affect the competition for raw materials and the subsequent conflicts, and this has encouraged scientists to look for Co-free energy storage technology.[10]

The $LiMn_2O_4$ (LMO) spinel cathode is economically and environmentally friendly among the existing cathode materials. It has attracted many researchers since its first report of lithiation and de-lithiation by Thackeray et al. in 1983 and 1984.[11−13] Mn-based cathode materials are the cost-effective alternative for automotive applications because of their high energy density and high voltage.[14] In recent years, $LiMn_{1.5}Ni_{0.5}O_4$ has been the focus of many researchers[15] because of its high capacity, less environmental impact, low

Received: September 14, 2022
Accepted: November 4, 2022
Published: November 16, 2022

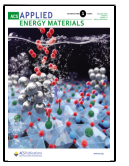

© 2022 American Chemical Society

https://doi.org/10.1021/acsaem.2c02667
ACS Appl. Energy Mater. 2022, 5, 15345−15355

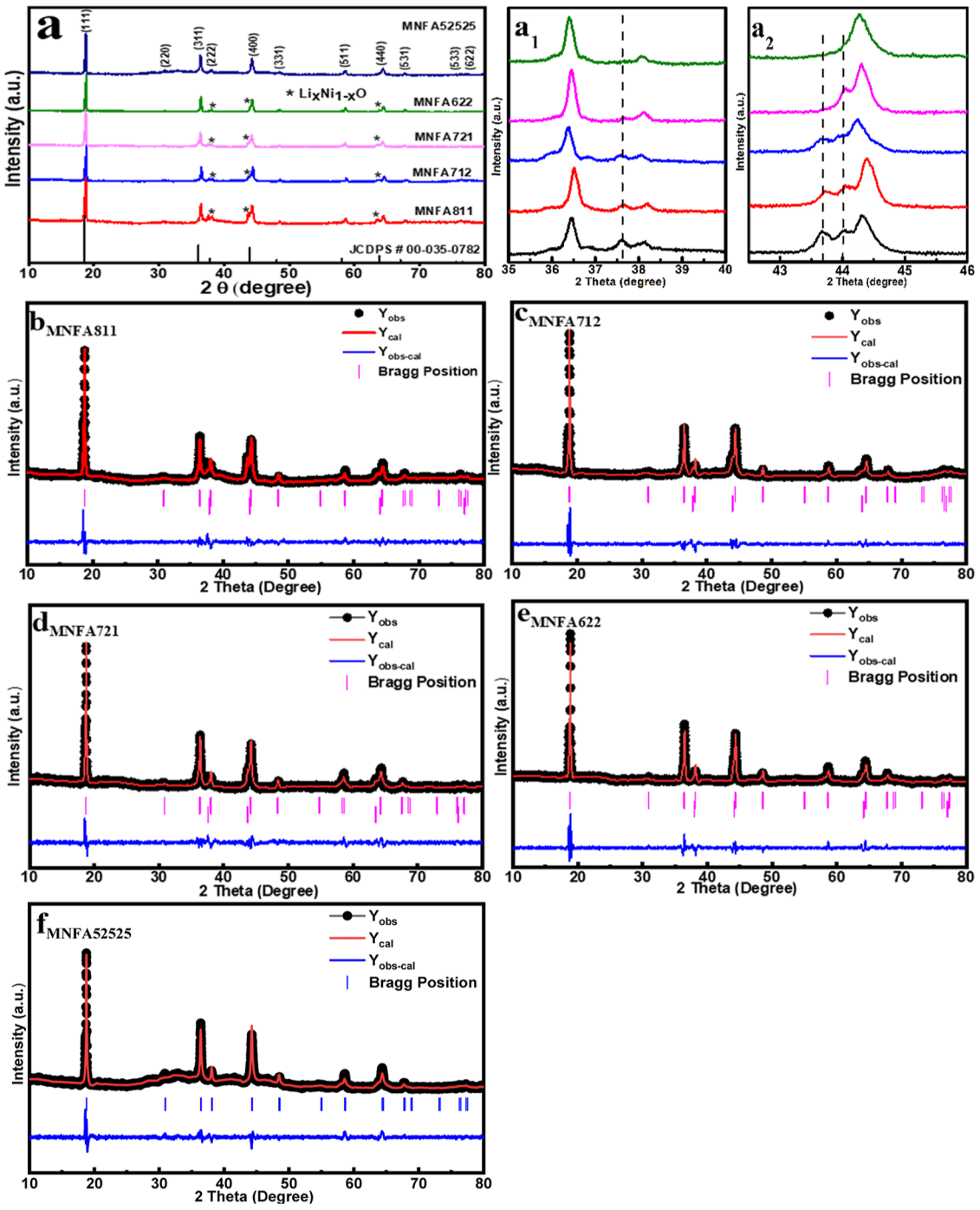

Figure 1. (**a**) XRD patterns and (**b**–**f**). Rietveld refinement results of $LiMn_{2-x-y-z}Ni_xFe_yAl_zO_4$. (a1–a2) Magnified parts of (**a**).

production cost, and high operating voltage of 4.7 V.[2] However, the practical capacity of materials with a spinel framework is less. It faces a capacity fading issue over the cycles, which pulls back this material in effective commercialization. This capacity fading over the cycling is mainly due to two factors: (i) the disproportionation reaction and (ii) Jahn–Teller distortion. The cycling performance of these spinel materials was affected by an irreversible phase transition in the crystal structure over the cycling[16,17] and oxygen loss. Another main issue with this spinel material is the dissolution of the Mn ion into the electrolyte, leading to passive layer deposition on the anode surface. This layer on the anode deteriorates the solid electrolyte interface (SEI) layer and leads to capacity decay.[18,19]

Researchers have made several approaches to date to accomplish better cyclability by suppressing the problems associated with LMO cathodes. They mainly include doping with transition metal ions[20−24] and surface coating with a conductive compound and inert materials.[25−27] Among them, doping with transition metal ions was found to be the efficient route to improve or enhance the system's structural stability and electrochemical properties. In this direction, many metal ions have been used as a dopant, namely, Ti,[20] Sc,[21] Cr,[23] Ni,[22] Fe,[24] Co,[22,28] Cu,[24,29] Zn,[30] Al,[29] and so on. Among the most reported substituent elements, Ni-, Fe-, and Al-doped materials

https://doi.org/10.1021/acsaem.2c02667
ACS Appl. Energy Mater. 2022, 5, 15345−15355

Table 1. Lattice Parameters of $LiMn_{2-x-y-z}Ni_xFe_yAl_zO_4$ (x = 0.8−0.5 and y and z = 0.1−0.25)

sample	space group	lattice constant (Å)	cell volume	R_{bragg}	R_F^2	$\chi 2$	phase fraction (%)
$LiMnNi_{0.8}Fe_{0.1}Al_{0.1}O_4$	$Fd\bar{3}m$	8.18	548.41	5.32	3.36	2.95	85.32
(**MNFA811**)	$Fm\bar{3}m$	4.14	70.99	2.63	1.64		14.68
$LiMnNi_{0.7}Fe_{0.1}Al_{0.2}O_4$	$Fd\bar{3}m$	8.2217	546.25	6.79	4.49	3.75	69.48
(**MNFA712**)	$Fm\bar{3}m$	4.13	70.68	2.34	3.48		30.52
$LiMnNi_{0.7}Fe_{0.2}Al_{0.1}O_4$	$Fd\bar{3}m$	8.20	552.34	5.33	3.11	2.56	70.29
(**MNFA721**)	$Fm\bar{3}m$	4.14	71.11	7.82	6.16		29.71
$LiMnNi_{0.6}Fe_{0.2}Al_{0.2}O_4$	$Fd\bar{3}m$	8.18	548.96	9.02	7.12	3.24	76.98
(**MNFA622**)	$Fm\bar{3}m$	4.11	69.48	3.29	3.15		23.02
$LiMnNi_{0.5}Fe_{0.25}Al_{0.25}O_4$ (**MNFA52525**) (pure spinel)	$Fd\bar{3}m$	8.17	546.82	8.33	8.74	2.46	100

showed improved performance. Ni doping enhances the capacity and energy density,[24,31−33] Fe doping enhances the electronic conductivity and Li^+ ion diffusion kinetics,[24,32,34] and Al doping enhances the structural stability and electrochemical performance.[31,35−37] To utilize the maximum contribution of Ni to achieve more capacity than that of the well-known $LiMn_{1.5}Ni_{0.5}O_4$ spinel cathode material, we have increased the Ni proportion with the support of other substituents, Al and Fe.

Herein, we developed multi-cation doped high-energy LMO cathodes. The effect of partial substitution of redox-active Ni^{+3} and redox inactive Al^{3+}, Fe^{3+}, and metal ions for Mn^{3+} in $LiMn_2O_4$ has been studied. The structural, morphological, and electrochemical characterization of a series of materials $LiMn_{2-x-y-z}Ni_xFe_yAl_zO_4$ (x = 0.8-0.5, y = 0.1−0.25, and z = 0.1−0.25) is reported in this work. An accelerating discussion regarding this series of materials is termed MNFA811, MNFA712, MNFA721, MNFA622, and MNFA52525. The structural and morphological characterization shows the effective formation of a disordered spinel at 750 °C. The electrochemical studies showed an excellent behavior toward high specific capacity and longer cyclability. As per our knowledge, this combination of elements as dopants forming disordered spinel structures for better performance has not been reported elsewhere.

2. EXPERIMENTAL SECTION

2.1. Preparation of $LiMn_{2-x-y-z}Ni_xFe_yAl_zO_4$ (x = 0.8−0.5, y = 0.1−0.25, and z = 0.1−0.25). Multi-cation doped $LiMn_2O_4$ spinel material is successfully synthesized by a simple sol−gel method. Stoichiometric amounts of lithium acetate dihydrate ($CH_3COOLi\cdot 2H_2O$) (Thomas Baker 99%) (5% excess taken to recompense the loss of Li at high temperature during calcination), manganese (II) acetate tetrahydrate [$(CH_3COO)_2Mn\ 4H_2O$] (Sigma-Aldrich >99%), nickel (II) acetate tetrahydrate [$(CH_3COO)_2Ni\ 4H_2O$] (Sigma-Aldrich >98%), iron oxalate dihydrate ($FeC_2O_4\ 2H_2O$) (Sigma-Aldrich >99%), and aluminum nitrate nonahydrate [$Al(NO_3)_3\ 9H_2O$] (Sigma-Aldrich >98%) were taken in a solution of 1:1 citric acid monohydrate ($C_6H_8O_7\ H_2O$) (Sigma-Aldrich >99%). The dissolved solution was kept for stirring and heating at 60 °C to get the viscous gel. The viscous gel obtained was dried in a hot air oven at 100 °C for 2 h and then ground for a few minutes. The obtained precursor was heat-treated at 400 °C for 4 h to get the intermediate compound. The powder was further ground, calcined at 750 °C for 10 h in air, cooled to room temperature, and then ground into a fine powder of $LiMn_{2-x-y-z}Ni_xFe_yAl_zO_4$ (x = 0.8−0.5, y = 0.1−0.25, and z = 0.1−0.25).

2.2. Material Characterization. Crystalline structure analysis of the prepared material was accomplished by X-ray diffraction (XRD) with Cu-Kα radiation (k = 1.54 Å) (Panalytical Xpert Pro). The microscopic images were obtained using a field emission scanning electron microscope (FEI-NOVA NANOSEM 450). Compositional analysis was performed by energy-dispersive spectroscopy (EDS), crystalline nanostructures were observed by high-resolution transmission electron microscopy (HR-TEM) (JEOL JEM F-200), and elemental mapping was performed by scanning transmission electron microscopy high-angle annular dark field (STEM-HAADF). X-ray photoelectron spectroscopy (XPS) was performed using a Thermo scientific Model K-alpha XPS instrument with monochromatic Al-Kα as the X-ray source. Raman spectra were acquired in the spectral region 100−1200 cm^{-1} using a HORIBA-J-Y Lab RAM HR 800 Raman spectrometer instrument with an NIR He−Ne laser (wavelength 632.88 nm). The elemental quantification has performed by using X-ray fluorescence (XRF) spectrometry by employing the Panalytical Epsilon3^{XLE}, energy-dispersive X-ray fluorescence spectrometer (EDXRF) with a Rh50 tube anode and a Ag100 filter.

2.3. Fabrication of the Electrode and Electrochemical Measurements. The electrical and electrochemical studies were performed by assembling CR-2032-coin cells in an argon-filled glovebox with oxygen and H_2O levels of ≤0.1 ppm. The as-prepared cathode active powder (80 wt %), super C-65 (10 wt %), and polyvinylidene fluoride (10 wt %) were mixed with a few drops of the *N*-methyl pyrrolidone solvent to obtain a homogeneous slurry. This slurry was then coated on the carbon-coated Al foil by the doctor blade method, dried at 80 °C in a vacuum oven, and cut into circular discs of 14 mm. Li foil was used and considered as both the reference and negative electrodes. Celgard2325 was used as a separator, and 1M $LiPF_6$ in ethylene carbonate−dimethyl carbonate−ethyl methyl carbonate (EC/DMC/EMC 1:1:1) solution was used as the electrolyte.

Cyclic voltammetry (CV) studies have been carried out at a scan rate of 0.1 mVs^{-1} in the voltage window of 3.50−4.99 V versus Li, and electrochemical impedance spectroscopy (EIS) was studied at a frequency range from 1 to 100 mHz with an amplitude of 50 mV in a Metrohm Auotolab multi-channel electrochemical work station (Multiautolab M204). Galvanostatic charge−discharge studies were carried out in a voltage window of 3.5 to 5 V at different current densities using a Neware battery testing system (BTS4000).

3. RESULTS AND DISCUSSION

3.1. Structural Characterization. Figure 1a. shows the XRD patterns of the $LiMn_{2-x-y-z}Ni_xFe_yAl_zO_4$ powders, and the obtained peak patterns are well-matched with standard JCPDS no. 00-035-0782. The obtained diffraction pattern describes the prominent peaks related to the cubic spinel phase with space group $Fd\bar{3}m$. The pattern also showed the presence of minor peaks related to the secondary phase in the material with space group $Fm\bar{3}m$ (JCPDS no. 01-075-0543). This secondary phase is due to the loss of oxygen during the calcination at higher temperatures,[24] leading the spinel material to decompose and form another phase $Li_xNi_{1-x}O$.[38−43]

To obtain more information about the mixed phase formed here, we have performed Rietveld refinement using Fullprof

https://doi.org/10.1021/acsaem.2c02667
ACS Appl. Energy Mater. 2022, 5, 15345−15355

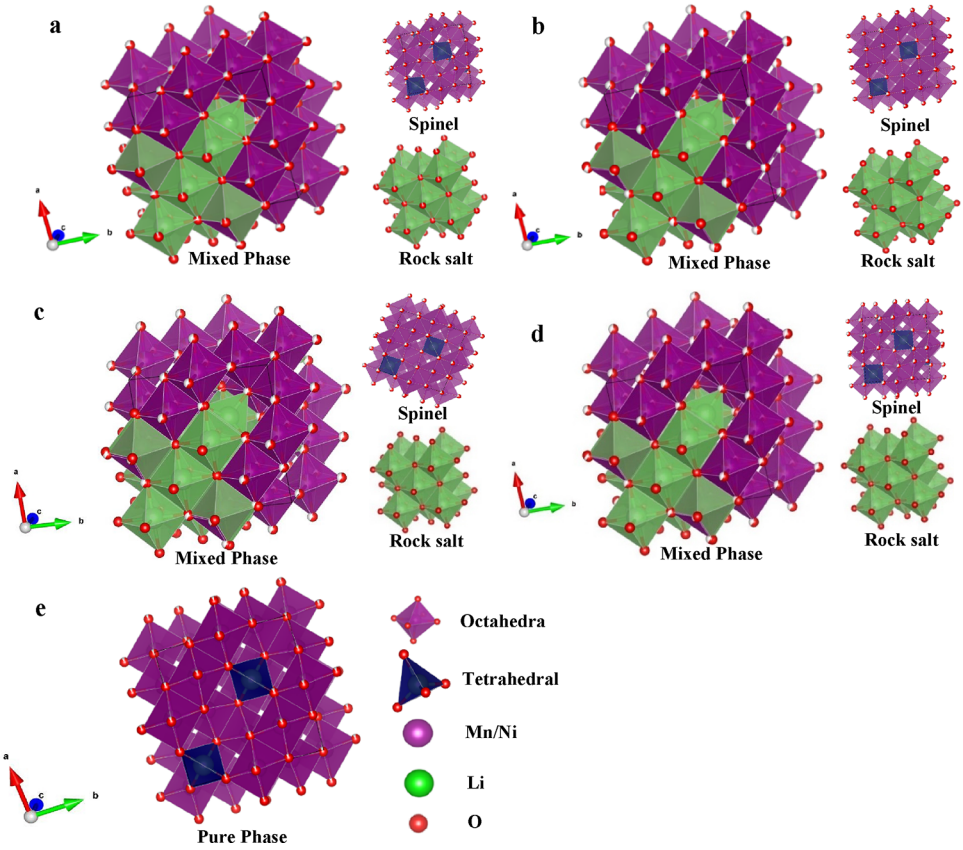

Figure 2. Structural illustrations of (a) MNFA811, (b) MNFA712, (c) MNFA721, (d) MNFA622, and (e) MNFA52525.

software, as shown in Figure 1b–f. The lattice parameters of the materials obtained after Rietveld refinement are given in Table 1. The refinement studies confirmed that the materials synthesized are of mixed phase, that is, cubic spinel, and cubic rock salt structures. More details on structural parameters from Rietveld refinement are given in Supporting Information Tables S1 and S2. Here, the Ni content played a major role in forming the secondary phase, that is, $Li_xNi_{1-x}O$. The crystal structure parameters reveal that the secondary phase fractions reduce as the Ni content reduces and the material forms a pure spinel structure (MNFA52525). The structural illustration of all materials demonstrates the presence of a secondary phase in all the materials except MNFA52525, as shown in Figure 2. The structural illustrations of MNFA811, MNFA712, MNFA721, and MNFA622 look the same as there is not much difference in the cell volume as well in the oxygen centers. The oxygen deficiency is different in all the materials, and the phase quantification is also different.

The structural stability of our synthesized materials was also predicted by evaluating the ratio of the relative integrated intensities of 311 and 400 reflections related to the degree of tetragonal distortion (M_2O_4) in spinel materials.[44] This I_{311}/I_{400} peaks ratio lies between 0.96 and 1.10 for all the multication doped materials [i.e., 1.05 for (MNFA811), 1.0 for (MNFA712), 1.08 for (MNFA721), 1.09 for (MNFA622), and 1.09 for (MNFA52525)], confirming that the synthesized materials are stable enough for electrochemical applications.[45,46]

The Raman spectra of $LiMn_{2-x-y-z}Ni_xFe_yAl_zO_4$ are shown in Supporting Information Figure S1, which confirm the successful incorporation of metal ions into their constituent sites. Figure 3a–e shows the XPS survey and expected elemental composition of MNFA811, MNFA712, MNFA721, MNFA622, and, MNFA52525. The XPS analysis was performed for all the materials to understand their elemental composition and valence states. XPSPEAK41 software is used to deconvolute the XPS spectra with a Shirley baseline and Lorentzian–Gaussian fitting. The deconvoluted spectra of Mn2p consist of $Mn2p_{1/2}$ and Mn $2p_{3/2}$ core levels and are shown in Figure $3a_1$–e_1. The deconvoluted peak Mn $2p_{3/2}$ core, shows Mn^{4+} and Mn^{3+} states with binding energies of 642.66, 643.89, 643.17, 643.6, and 646.44 and 641.89 eV, 642.56, 642.29, 642.58, and 642.14 eV, respectively, for MNFA811, MNFA712, MNFA721, MNFA622, and MNFA52525. The deconvoluted peak $Mn2p_{1/2}$ core shows only the Mn^{4+} state for all the materials in the series with binding energies of 653.98, 654.78, 654.56, 654.71, and 654.45 eV for MNFA811, MNFA712, MNFA721, MNFA622, and MNFA52525, respectively. These values are close to the reported values of Dang et al., Peng et al., and Xu et al.,[47−49] which clarifies the reason for the appearance of a tiny peak for Mn^{3+}/Mn^{4+} redox behavior at the ∼4 V range in the cyclic voltammograms, which is evident for the minimal existence of Mn^{3+} in the material. The peak intensity and peak area of Mn^{4+} are more than those of Mn^{3+} in the deconvoluted $Mn2p_{3/2}$ spectrum of all the materials, which gives a clear representation of substituent elements, and Ni, Fe, and Al significantly reduced the Mn^{3+} ratio in all materials. The reduced Mn^{3+} content ensures the structural stability to minimize the Jahn–Teller distortion and Mn^{3+}dissolution into the electrolyte, leading to better electrochemical performance.[24]

https://doi.org/10.1021/acsaem.2c02667
ACS Appl. Energy Mater. 2022, 5, 15345−15355

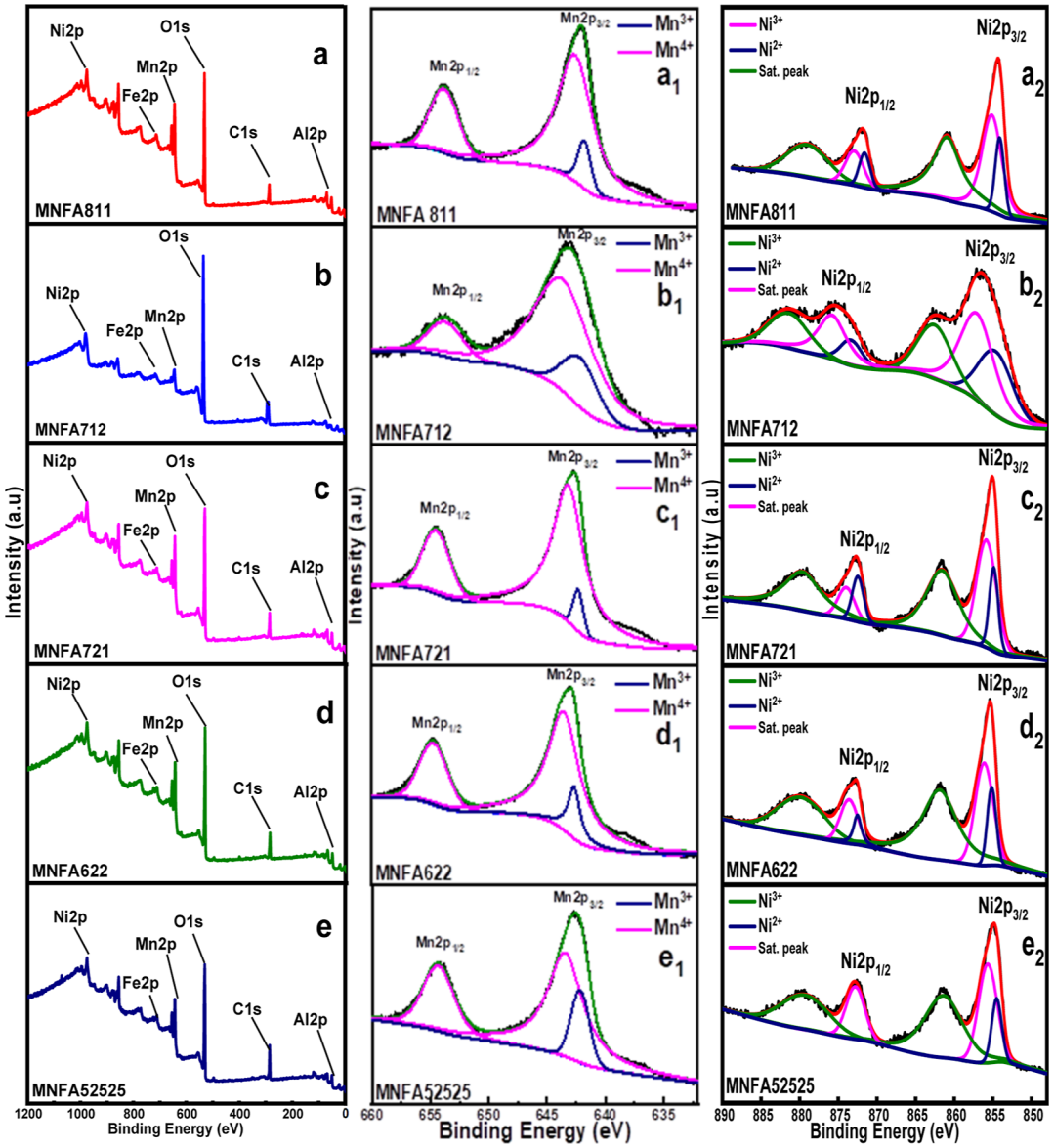

Figure 3. XPS survey spectra of (**a**) MNFA811, (**b**) MNFA712, (**c**) MNFA721, (**d**) MNFA622, and (**e**) MNFA52525. High-resolution XPS spectra of (a_1–e_1) Mn 2p and (a_2–e_2) Ni 2p for all samples.

The deconvoluted spectra of Ni 2p consist of Ni $2p_{3/2}$ and Ni $2p_{1/2}$ core levels situated at around 854–855 eV and 871–872 eV, respectively, for all the materials, as shown in Figure 3a_2–e_2. The deconvoluted peak Ni$2p_{3/2}$ core shows Ni^{2+} and Ni^{3+} states with binding energies of 854.12, 854.8, 854.68, 855.13, and 854.45 and 855.13 eV, 855.92, 855.83, 856.04, and 855.59 eV, respectively, for MNFA811, MNFA712, MNFA721, MNFA622, and MNFA52525. These values are in close agreement with the reported values.[49−51] The oxidation states of these can be correlated with the redox behavior seen in CV and galvanostatic charge/discharge profiles as Mn and Ni are redox elements present in the cathode active materials and the existence of redox inactive Fe^{3+} and Al^{3+} are acting as electrochemical stabilizers. As such, the charge/discharge behavior resembles that of the well-known cathode material $LiMn_{1.5}Ni_{0.5}O_4$. Deconvoluted spectra of the other substituent elements Fe and Al are given in Supporting Information Figure S2. The binding energies of Fe and Al confirm that all the substituents were properly doped to the Mn^{3+}site, which forms a well-aligned stable structure.

The morphology of multi-cation doped disorder structured spinel materials was studied by scanning electron microscopy (SEM) and transmission electron microscopy (TEM). Figure 4a shows the field emission SEM (FE-SEM) image of MNFA712. The particles obtained are agglomerated with good crystallinity and polydisperse in nature. The particles' grain size is in the range of ∼100–600 nm, with an average particle size of ∼236 nm for the selected FE-SEM image. The particle size distribution histogram of MNFA712 is given in Supporting Information Figure S3. The agglomeration of particles might be due to the use of citric acid as a complexing agent during the synthesis via the sol–gel method.[52]

Figure 4b shows the HR-TEM image of MNFA712, wherein the lattice fringes are marked with the *d* spacings of 0.210 and 0.247 nm at different areas, which correspond to crystal planes of (222) and (400), respectively. The inset of Figure 4b shows the fast Fourier transform (FFT) images for selected areas

https://doi.org/10.1021/acsaem.2c02667
ACS Appl. Energy Mater. 2022, 5, 15345−15355

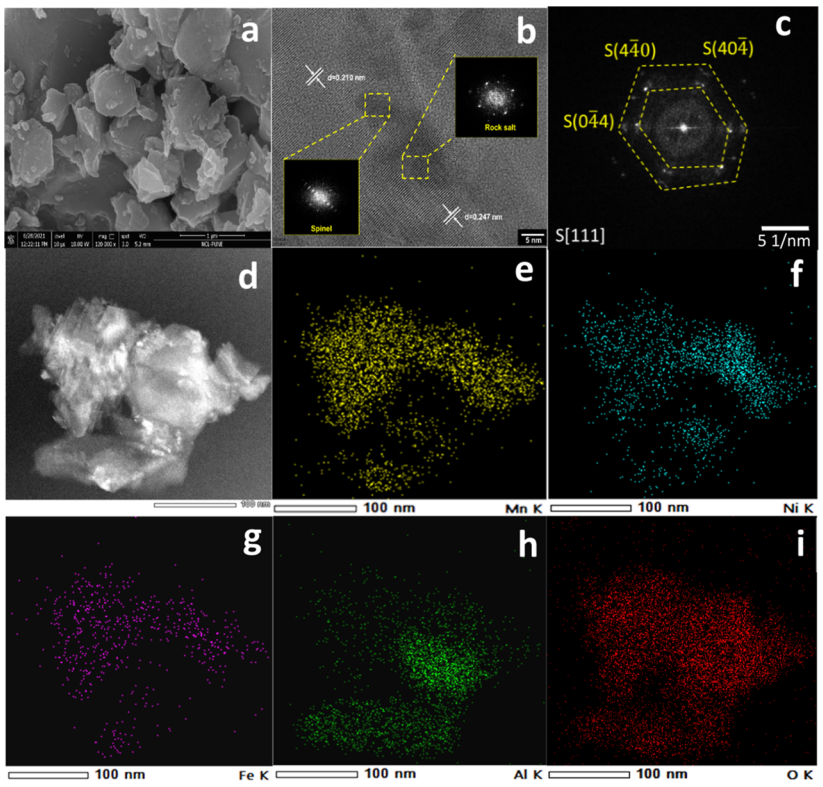

Figure 4. (a) FE-SEM image, (b) HR-TEM image, (c) SAED pattern, (d) STEM-HAADF image, and EDS elemental mapping of [(e) Mn, (f) Ni, (g) Fe, (h) Al, and (i) O] MNFA712 particles.

Table 2. Molar Percentage Composition of Metal Ions Obtained from XRF Spectrometry

Mn		Ni		Fe		Al	
theoretical	experimental	theoretical	experimental	theoretical	experimental	theoretical	experimental
49.98	54.8	42.72	37.8	5.08	5.5	2.45	1.7
51.34	53.4	38.39	36.6	5.21	5.3	5.04	4.5
49.99	51.2	37.39	36.3	10.16	10.5	2.45	1.7
51.48	51.3	33.01	32.8	10.46	10.3	5.05	5.4
52.33	53.9	27.95	27.5	13.29	13.8	6.42	4.6

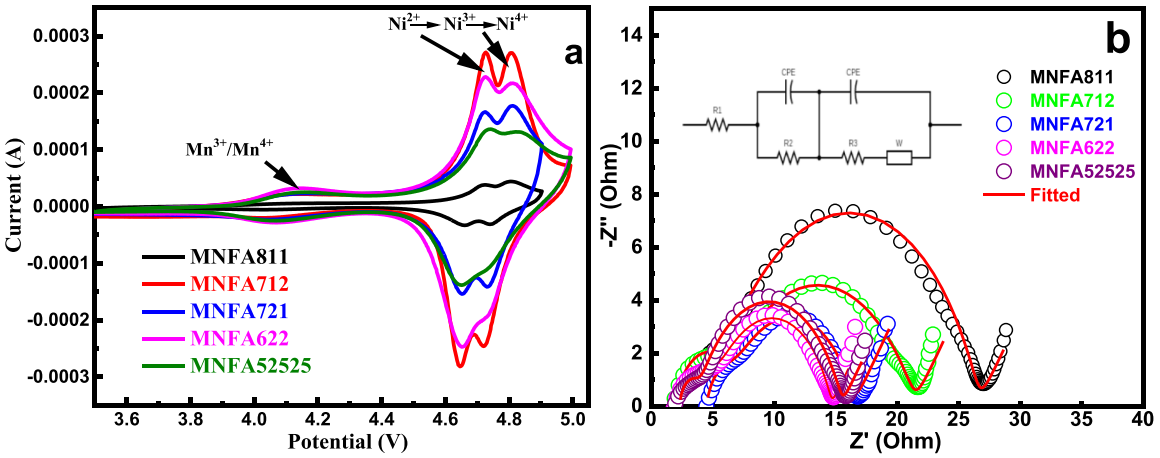

Figure 5. (a) Cyclic voltammograms at a scan rate of 0.1 $mVs^{-1}$and (b) Nyquist plots of MNFA811, MNFA712, MNFA721, MNFA622, and MNFA52525.

marked with rectangles that depict the presence of both spinel and rock salt phase structures.[53] The corresponding selected area electron diffraction (SAED) pattern is shown in Figure 4c, which confirms the presence of the mixed phase in the synthesized materials.[54] Furthermore, the materials composition has been evaluated by STEM-HAADF elemental mapping, as shown in Figure 4d–i. The mapping results reveal the proper infusion of all the dopants into the crystal structure.

https://doi.org/10.1021/acsaem.2c02667
ACS Appl. Energy Mater. 2022, 5, 15345−15355

The detailed information and electron microscopic images for all other materials are given in Supporting Information (Supporting Information-Figures S4−S7). The mapping results confirm the presence of Mn, Ni, Al, Fe, and O in the synthesized material.

XRF spectrometric studies were carried out to identify the elemental composition of all the samples. The mole percentage of metal ions present in the active materials (except Li as XRF spectrometry cannot detect Li) is given in Table 2. The outlook of this composition ratio of cations shows that the composition of Al is comparatively less because Al is a lighter element as compared to other heavier elements such as Mn, Ni, and Fe present in our materials. Because the XRF spectrometry is quite less sensitive for lighter elements, the overall ratio of the metals, which are matching with the composition, varied in all the materials.

3.2. Electrochemical Characterization. CV studies were carried out to understand the redox behaviors of synthesized materials. Figure 5a shows cyclic voltammograms of fabricated 2032-coin cells with MNFA811, MNFA712, MNFA721, MNFA622, and MNFA52525 as cathode materials at room temperature with a scan rate of 0·1 mV s^{-1}. It is clear from the CV curves that the peak positions of all materials are the same, but the intensity of the peaks is varying, which specifies that the lithiation/de-lithiation process is not the same for all materials.[55] As shown in Figure 5a, three pairs of redox peaks are observed at ∼ 4.08/4.03, ∼ 4.72/4.63, and ∼4.81/4.73 V, indicating three-step intercalation/deintercalation of Li^+ during the oxidation/reduction reaction. The first weak redox peak observed at 4.08/4.03 V corresponds to the Mn^{4+}/Mn^{3+} redox couple. This feeble peak is due to most of Mn being in the Mn^{4+} state, indicating the minimized content of Mn^{3+}in the material,[30] which minimizes the John−Teller distortion. The second and third high intense redox peaks observed at 4.72/4.63 and 4.81/4.73 V, respectively, correspond to Ni^{2+}/Ni^{4+}, which indicates the predominant electrochemical activity of Ni in the active material. These redox peaks of lithiation/de-lithiation at higher voltage indicate that more driving force is necessary to urge the Li ions from the cathode to the anode.

There is no peak observed in the CV curve for Fe because Fe is redox inactive and acts as an electrochemical stabilizer.[56] Also, there is no peak observed for Al because Al is a redox inactive dopant in this material, and therefore, it is not influencing the CV behavior. Though, the presence of Al in the structure helps in stability rather than improving the discharge capacity.[31,36,37,57]

EIS studies were performed with two-electrode system for the fresh cells to know the interface resistance and kinetics of the Li^+ insertion/exertion mechanism. The obtained data have been fitted with the equivalent circuit, which is provided in the inset of Figure 5b, where R1 represents the Ohmic resistance due to the electrochemical system (R_s), R_2 represents the resistance of the SEI (R_{SEI}), R_3 represents the chargetransfer resistance (R_{ct}), CPE represents the constant phase element (Q), and W is the Warburg diffusion impedance (W). The fitted results of the equivalent circuit for all materials are given in Table 3. The Nyquist plots (Figure 5b) of all materials show a depressed semicircle in the high-frequency region and a straight line in the low-frequency region. A depressed semicircle in the high-frequency region is the procreation of two semicircles related to the resistance of the SEI (R_{SEI}) and charge transfer resistance (R_{ct}), which indicates the insertion of Li ions into the electrode/electrolyte interface, and a straight line in the low-frequency region indicates the interface resistance. The sloping line in the low-frequency region corresponds to Warburg impedance (W), and the upright straight line indicates faster diffusion of Li^+ ions through the electrolyte toward the anode. These values of these circuit elements help to understand the kinetics of surface film formation between electrode−electrolyte, charge transfer, and Li-ion diffusion mechanisms.

Table 3. EIS Fitted Data of MNFA811, MNFA712, MNFA721, MNFA622, and MNFA52525

material	R_1 (Ω) R_s	R_2 (Ω) R_{SEI}	R_3 (Ω) R_{ct}	Chi-squared
MNFA811	1.7640	4.5927	20.2161	0.5360
MNFA712	1.9597	3.9529	15.2912	0.2879
MNFA721	4.5203	1.9434	9.98781	1.3802
MNFA622	1.8858	3.5832	9.15935	0.4385
MNFA52525	2.3364	1.3813	11.7527	0.3652

Figure 6a shows the rate capability of all materials at different current densities from 0.1 C to 5 C with a voltage window of 3.5 to 5.0 V. As shown in Figure 6a, the specific discharge capacities of all the materials show a gradual decrease as the applied current density is increased. Here, the reduced rate performance of all the materials at higher current rates might be due to the reformation of the layer on the surface of the electrode and phase transition of active material over cycling, which hinders the free movement of Li^+ ions.[58]

The galvanostatic charge/discharge studies were performed between 3.5 and 5 V at a constant current density of 1C over 1000 cycles, as shown in Figure 6b. It can be seen that the initial discharge capacities are 123.1 $mAhg^{-1}$ (MNFA811), 148.7 $mAhg^{-1}$ (MNFA712), 131.2 $mAhg^{-1}$ (MNFA721), 126.4 $mAhg^{-1}$ (MNFA622), and 101.2 $mAhg^{-1}$ (MNFA52525), while at the end of 1000 cycles, the discharge capacities were decreased to 104.5 $mAhg^{-1}$ (MNFA811), 118.3 $mAhg^{-1}$ (MNFA712), 108.7 $mAhg^{-1}$ (MNFA721), 112.4 $mAhg^{-1}$ (MNFA622), and 81.5 $mAhg^{-1}$ (MNFA52525) with almost 100% Coulombic efficiency. All the materials showed a very good capacity retention of 82.4.9% (MNFA811), 79.5% (MNFA712), 82.8% (MNFA721), 88.9% (MNFA622), and 80.5% (MNFA52525) over 1000 cycles. Compared to all other materials, MNFA712 showed much better electrochemical performance with high capacity and stability. The presence of redox-inactive Fe^{3+} and Al^{3+} helps to improve the stability, and it has been proved in our case as the stability of all the materials is excellent. In MNFA622, the capacity retention of the material is about 88.9%, which is more than that of all the materials and is due to the increased concentration of Al^{3+} as well as of Fe^{3+}. This proves that Al^{3+} and Fe^{3+} play a critical role in the stability of the material. MNFA52525 has the least capacity among all materials due to decreasing Ni content and increasing Fe and Al content, and this indicates that the increase in substitution of Fe and Al atoms to a certain level improves the capacity of materials and excess doping leads to capacity decay. The report of Peng Li et al. has shown that doping of Al^{3+} to a certain limit can reduce the capacity and increase the stability,[29] and the reports of C.Peng et al. and Xu et al. have shown that the capacity decays if the Al^{3+} ratio increases.[36,37] The same behavior is observed in our materials.

Figure 6c shows the specific capacity v/s voltage curves of MNFA712 cycled at different current densities, illustrating capacity degradation at higher current. In Figure 6d, the

https://doi.org/10.1021/acsaem.2c02667
ACS Appl. Energy Mater. 2022, 5, 15345−15355

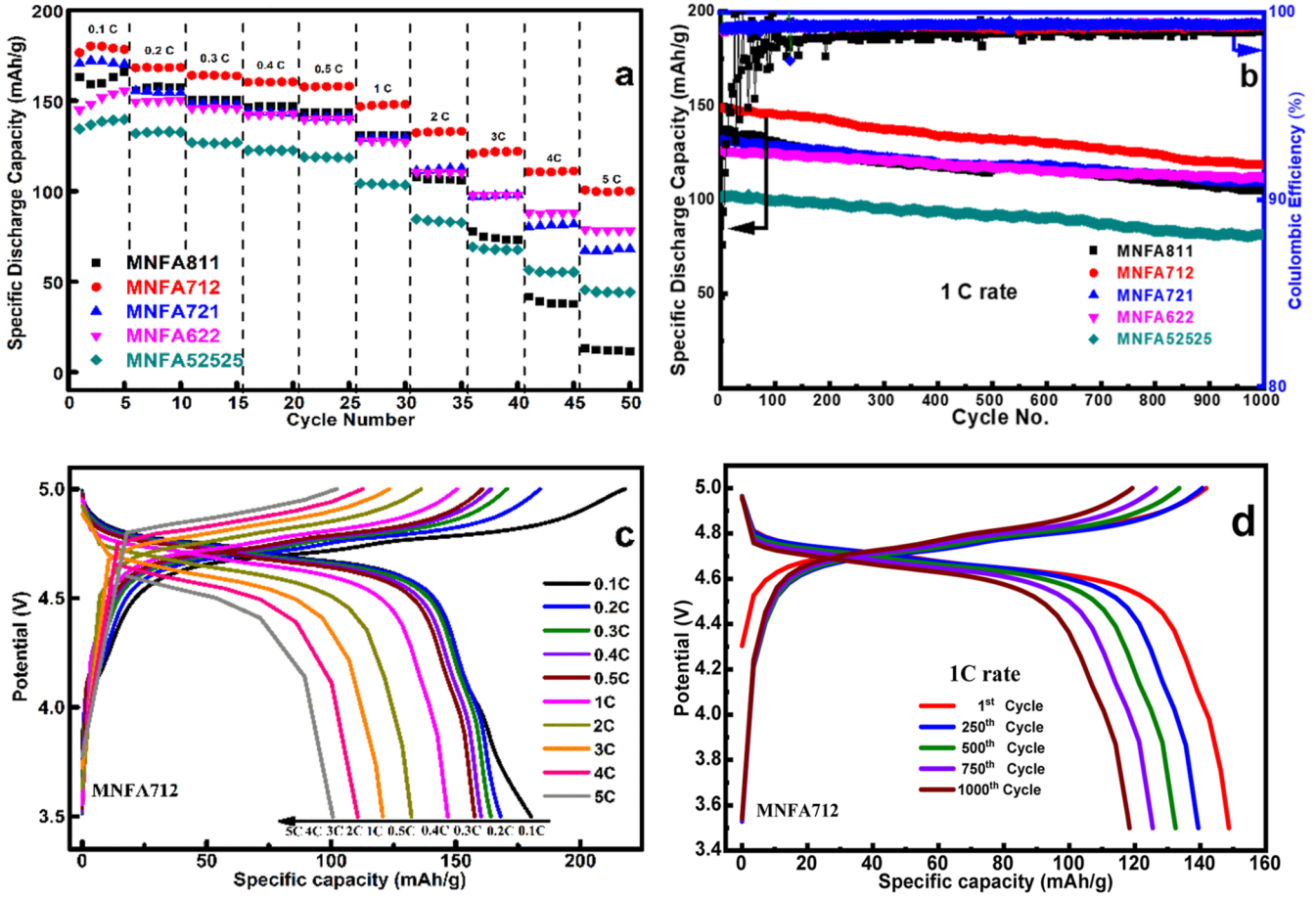

Figure 6. (**a**) Rate capability at different C rates, (**b**) cyclability plot at a 1C rate, (**c**) specific capacity ($mAhg^{-1}$) v/s potential (V) at different C rates, and (**d**) specific capacity ($mAhg^{-1}$) v/s potential (V) plot at a 1C rate.

capacity retention of MNFA712 is exhibited by specific capacity v/s voltage curves of different galvanostatic charge−discharge cycles of different intervals at a 1C rate. Initially, it showed 148.7 $mAhg^{-1}$ with a Coulombic efficiency of 98.8% at a 1C rate, while at the end of 1000 continuous galvanostatic charge−discharge cycles, the specific capacity has decreased to 118.3 mAg^{-1} with a Coulombic efficiency of 99.2%, which implies that the capacity retention of MNFA712 is 79.5%. This behavior of MNFA712, which is well-supported by various characterizations, can strongly imply that this material can be used for 5 V applications in LIBs.

It has been proved from the literature that disordered spinel-type cathode materials have shown a significant improvement in capacity compared to that of pure spinel material. The existence of the secondary phase in the spinel will enhance the energy density of the cathode materials.[7,59−61] According to the study of Patoux et al., the ordered spinel material exhibits rapid capacity fading at high C rates compared to the disordered spinel material.[62] This has been proved in our case also, where the disordered samples have shown better electrochemical performance than the ordered phase.

4. EFFECT OF THE CATION DISORDERED ROCK SALT STRUCTURE IN THE SPINEL STRUCTURE

The structural characterizations such as XRD, TEM, and Raman studies confirm the co-substitution of multiple cations, which can contribute to the formation of the cation disordered rock salt structure in the bulk spinel structure. In the efforts toward the reduction of the John-Teller distortion process, triple cations such as Ni, Fe, and Al were co-substituted into half of the Mn ions in the spinel structure. Particularly, Ni is the predominant substituent, which is the main candidate while forming the cation-disordered rock salt phase (i.e., $Li_xNi_{1-x}O$), which is due to the oxygen loss in the spinel structure at high temperature during the calcination. As a consequence of this second phase, the larger ionic radius of Ni^{2+} (0.72 Å) in the rock salt phase as than that of Mn^{3+} (0.65 Å) could expand the Li^+ ion diffusion channels,[63] while Fe^{3+} and Al^{3+} ions possibly accommodate in the stacks elicited due to the co-substitution of Ni ions. The synergistic effects of multi-cation substitution are attributed to the formation rock salt phase, which leads to attaining superior capacity at different C rates. The rock salt structure is considered to be favorable for capacity enhancement due to its minimal isotopic changes during the charge−discharge cycling. The proper ratio of the rock salt phase can improve the capacity by expanding the Li^+ ion diffusion channels and rapid Li^+ ion insertion and extraction, but the excess quantity of the rock salt phase can lead to high capacity as well as degradation.[59,62] In our case, MNFA712 has shown more capacity and stability than all other materials, which indicates that the proper amount of the rock salt phase can achieve superior capacity. Thus, the spinel cathode with appropriate rock salt proportions results in outstanding reversible cycling performance and rate capability.

https://doi.org/10.1021/acsaem.2c02667
ACS Appl. Energy Mater. 2022, 5, 15345−15355

5. CONCLUSIONS

This study equipped a Ni, Fe, and Al co-doped $LiMn_2O_4$ cathode material to improve rate performance and cyclability. $LiMn_{2-x-y-z}Ni_xFe_yAl_zO_4$ (x = 0.8−0.5, y = 0.1−0.25, and z = 0.1−0.25) with a disordered structure has been studied successfully, synthesized via the simple sol−gel method followed by calcination at 750 °C. XRD and TEM confirm the formation of mixed/disordered spinel. The multiple metal cation doping makes the structure stable by reducing the Jahn−Teller effect. XPS results suggest that all the substituents were properly doped to the Mn^{3+}site, which forms a well-aligned stable structure. Electrochemical studies of MNFA712 with a disordered spinel/rock salt structure have shown the possibility of an efficient cathode material for the next generations of LIBs for 5 V applications.

■ ASSOCIATED CONTENT

Supporting Information

The Supporting Information is available free of charge at https://pubs.acs.org/doi/10.1021/acsaem.2c02667.

Crystallographic data of cubic spinel and rock salt structures, Raman spectra and deconvoluted spectra for Al 2p and Fe 2p core levels of $LiMn_{2-x-y-z}Ni_xFe_yAl_zO_4$ (x = 0.8−0.5, y = 0.1−0.25, and$z$ = 0.1−0.25); FESEM image, HR-TEM image with d-spacing, SAED patterns, and all the EDS elemental mapping images of MNFA811, MNFA721, MNFA622, and MNFA52525; particle size distribution histogram of FESEM images, and post-test XRD analysis of the electrodes (a) before cycling (after coating on Al foil) (b) after cycling (PDF)

■ AUTHOR INFORMATION

Corresponding Author

Girish Praveen Nayaka − *Physical and Materials Chemistry Division, CSIR-National Chemical Laboratory, Pune 411008 Maharashtra, India; Academy of Scientific and Innovative Research (AcSIR), Ghaziabad 201002 U P, India;* orcid.org/0000-0001-8166-1465; Email: gp.nayaka@ncl.res.in

Authors

Bogalera Papaiah Shivamurthy − *Physical and Materials Chemistry Division, CSIR-National Chemical Laboratory, Pune 411008 Maharashtra, India; Academy of Scientific and Innovative Research (AcSIR), Ghaziabad 201002 U P, India;* orcid.org/0000-0003-4126-9885

Marulasiddappa Thripuranthaka − *Physical and Materials Chemistry Division, CSIR-National Chemical Laboratory, Pune 411008 Maharashtra, India; Academy of Scientific and Innovative Research (AcSIR), Ghaziabad 201002 U P, India;* orcid.org/0000-0002-5018-3939

Manjusha V. Shelke − *Physical and Materials Chemistry Division, CSIR-National Chemical Laboratory, Pune 411008 Maharashtra, India; Academy of Scientific and Innovative Research (AcSIR), Ghaziabad 201002 U P, India;* orcid.org/0000-0001-8323-2234

Complete contact information is available at: https://pubs.acs.org/10.1021/acsaem.2c02667

Author Contributions

S.B.P: methodology, carrying out experiments, formal analysis, and writing−original draft; M.T.: resource; M.V.S.: resource; and N.G.P: supervision, conceptualization, writing and editing the final draft, and funding acquisition.

Notes

The authors declare no competing financial interest.

■ ACKNOWLEDGMENTS

Shivamurthy B P thanks CSIR, New Delhi [31/011(1129)/2019-EMR-I] for providing a research fellowship. Dr. G P Nayaka thanks CSIR-NCL for providing the start-up fund (MLP036126) and all the facilities.

■ REFERENCES

(1) Scrosati, B.; Garche, J. Lithium Batteries: Status, Prospects and Future. *J. Power Sources* **2010**, *195*, 2419−2430.

(2) Nitta, N.; Wu, F.; Lee, J. T.; Yushin, G. Li-Ion Battery Materials: Present and Future. *Mater. Today* **2015**, *18*, 252−264.

(3) Manthiram, A. An Outlook on Lithium Ion Battery Technology. *ACS Cent. Sci.* **2017**, *3*, 1063−1069.

(4) Kim, T.; Song, W.; Son, D.-Y.; Ono, L. K.; Qi, Y. Lithium-Ion Batteries: Outlook on Present, Future, and Hybridized Technologies. *J. Mater. Chem. A* **2019**, *7*, 2942−2964.

(5) Mohamed, N.; Allam, N. K. Recent Advances in the Design of Cathode Materials for Li-Ion Batteries. *RSC Adv.* **2020**, *10*, 21662−21685.

(6) Li, W.; Cho, Y.-G.; Yao, W.; Li, Y.; Cronk, A.; Shimizu, R.; Schroeder, M. A.; Fu, Y.; Zou, F.; Battaglia, V.; Manthiram, A.; Zhang, M.; Meng, Y. S. Enabling High Areal Capacity for Co-Free High Voltage Spinel Materials in next-Generation Li-Ion Batteries. *J. Power Sources* **2020**, *473*, 228579.

(7) Muralidharan, N.; Self, E. C.; Dixit, M.; Du, Z.; Essehli, R.; Amin, R.; Nanda, J.; Belharouak, I.; Muralidharan, N.; Dixit, M.; Du, Z.; Essehli, R.; Amin, R.; Belharouak, I.; Self, E. C.; Nanda, J. Next-Generation Cobalt-Free Cathodes - A Prospective Solution to the Battery Industry's Cobalt Problem *Adv. Energy Mater.*, **2022**, *12*. DOI: 10.1002/aenm.202103050.

(8) Zhang, J.; Wang, P. F.; Bai, P.; Wan, H.; Liu, S.; Hou, S.; Pu, X.; Xia, J.; Zhang, W.; Wang, Z.; Nan, B.; Zhang, X.; Xu, J.; Wang, C. Interfacial Design for a 4.6 V High-Voltage Single-Crystalline LiCoO2 Cathoder. *Adv. Mater.* **2022**, *34*(). DOI: 10.1002/adma.202108353.

(9) Gourley, S. W. D.; Or, T.; Chen, Z. Breaking Free from Cobalt Reliance in Lithium-Ion Batteries. *iScience* **2020**, *23*. DOI: 10.1016/j.isci.2020.101505.

(10) Overland, I. The Geopolitics of Renewable Energy: Debunking Four Emerging Myths. *Energy Research and Social Science* **2019**, *49*. DOI: 10.1016/j.erss.2018.10.018.

(11) Thackeray, M. M.; David, W. I. F.; Bruce, P. G.; Goodenough, J. B. Lithium Insertion into Manganese Spinels. *Mater. Res. Bull.* **1983**, *18*(). DOI: 10.1016/0025-5408(83)90138-1.

(12) Thackeray, M. M.; Johnson, P. J.; de Picciotto, L. A.; Bruce, P. G.; Goodenough, J. B. Electrochemical Extraction of Lithium from LiMn2O4. *Mater. Res. Bull.* **1984**, *19*, 179−187.

(13) Huang, Y.; Dong, Y.; Li, S.; Lee, J.; Wang, C.; Zhu, Z.; Xue, W.; Li, Y.; Li, J. Lithium Manganese Spinel Cathodes for Lithium-Ion Batteries. *Adv. Energy Mater.* **2021**, *11*, 2000997.

(14) Hosono, E.; Kudo, T.; Honma, I.; Matsuda, H.; Zhou, H. Synthesis of Single Crystalline Spinel LiMn 2 O 4 Nanowires for a Lithium Ion Battery with High Power Density. *Nano Lett.* **2009**, *9*, 1045−1051.

(15) Xu, G.; Pang, C.; Chen, B.; Ma, J.; Wang, X.; Chai, J.; Wang, Q.; An, W.; Zhou, X.; Cui, G.; Chen, L. Prescribing Functional Additives for Treating the Poor Performances of High-Voltage (5 V-Class) LiNi 0.5 Mn 1.5 O 4 /MCMB Li-Ion Batteries. *Adv. Energy Mater.* **2018**, *8*, 1701398.

(16) Xie, Y.; Jin, Y.; Xiang, L. Tuning the Nanoarea Interfacial Properties for the Improved Performance of Li-Rich Polycrystalline Li-Mn-O Spinel. *ACS Appl. Mater. Interfaces* **2019**, *11*, 14796−14802.

(17) Liao, B.; Li, H.; Wang, X.; Xu, M.; Xing, L.; Liao, Y.; Liu, X.; Li, W. Significantly Improved Cyclability of Lithium Manganese Oxide, Simultaneously Inhibiting Electrochemical and Thermal Decomposition of the Electrolyte by the Use of an Additive. *RSC Adv.* **2017**, *7*, 46594−46603.
(18) Diederichsen, K. M.; McShane, E. J.; McCloskey, B. D. Promising Routes to a High Li + Transference Number Electrolyte for Lithium Ion Batteries. *ACS Energy Lett* **2017**, *2*, 2563−2575.
(19) Xu, J. Critical Review on Cathode−Electrolyte Interphase Toward High-Voltage Cathodes for Li-Ion Batteries. *Nano-Micro Lett.* **2022**, *14*, 166.
(20) Xue, J. Enhanced Electrochemical Properties of Titanium Doped Lithium Manganese Oxide with Nanorod-like Morphology. *Int. J. Electrochem. Sci.* **2020**, *15*, 8732−8742.
(21) Bhuvaneswari, S.; Varadaraju, U. V.; Gopalan, R.; Prakash, R. Structural Stability and Superior Electrochemical Performance of Sc-Doped LiMn 2 O 4 Spinel as Cathode for Lithium Ion Batteries. *Electrochim. Acta* **2019**, *301*, 342−351.
(22) Li, W.; Deng, H.; Jiang, J. Improved Electrochemical Performance of LiMn 2 O 4 via Ni and Co Gradient Doping. *Sci. Adv. Mater.* **2018**, *10*, 1823−1829.
(23) Iqbal, A.; Iqbal, Y.; Khan, A. M.; Ahmed, S. Effect of Bicatiorn (Cu-Cr) Substitution on the Structure and Electrochemical Performance of LiMn2O4 Spinel Cathodes at Low and High Current Ratesr. *J. Saudi Chem. Soc.* **2018**, *22*, 449−458.
(24) Sharma, P.; Das, C.; Indris, S.; Bergfeldt, T.; Mereacre, L.; Knapp, M.; Geckle, U.; Ehrenberg, H.; Darma, M. S. D. Synthesis and Characterization of a Mrultication Doped Mn Spinel, LiNi 0.3 Cu 0.1 Fe 0.2 Mn 1.4 O 4 , as 5 V Positive Electrode Material. *ACrS Omega* **2020**, *5*, 22861−22873.
(25) Wang, C. M.; Jin, F. M.; Shi, T.; Chen, L. The Effect of LaMnO3 with High Electronic Conductivity on the High Rate Charge-Discharge Performance of LiMn2O4. *J. Electroanal. Chem.* **2016**, *775*, 306−310.
(26) Park, K.; Park, J.-H.; Hong, S.-G.; Yoon, J.; Park, S.; Kim, J.-H.; Yoon, D.; Kim, H.; Son, Y.-H.; Park, J.-H.; Kwon, S. Induced AlF3 Segregation for the Generation of Reciprocal Al2O3 and LiF Coating Layer on Self-Generated LiMn2O4 Surface of over-Lithiated Oxide Based Li-Ion Battery. *Electrochim. Acta* **2016**, *222*, 830−837.
(27) Zhang, Z.-J.; Chou, S.-L.; Gu, Q.-F.; Liu, H.-K.; Li, H.-J.; Ozawa, K.; Wang, J.-Z. Enhancing the High Rate Capability and Cycling Stability of LiMn 2 rO 4 by Coating of Solid-State Electrolyte LiNbO 3r. *ACS Appl. Mater. Interfaces* **2014**, *6*, 22155−22165.
(28) Yi, Z. Rheological Phase Reaction Synthesis of Co-Doped LiMn2O4 Octahedral Particles. *J. Mater. Sci. Mater. Electron.* **2016**, *27*, 10347−10352.
(29) Li, S.; Wei, Y.; Wang, P.; Feng, Y.; Liang, W.; Ding, H.; Cui, X. Synergism of Cu and Al Co-Doping on Improvements of Structural Integrity and Electrochemical Performance for LiNi0.5Mn1.5O4. *J. Alloys Compd.* **2020**, *820*, 153140.
(30) Piao, J.-Y.; Duan, S.-Y.; Lin, X.-J.; Tao, X.-S.; Xu, Y.-S.; Cao, A.-M.; Wan, L.-J. Surface Zn Doped LiMn 2 O 4 for an Improved High Temperature Performance. *Chem. Commun.* **2018**, *54*, 5326−5329.
(31) Wang, S.; Xiang, M.; Lu, Y.; Guo, J.; Su, C.; Bai, H.; Liu, X. Facile Solid-State Combustion Synthesis of Al−Ni Dual-Doped LiMn2O4 Cathode Materials. *J. Mater. Sci. Mater. Electron.* **2020**, *31*, 6036−6044.
(32) Zhong, G. B.; Wang, Y. Y.; Yu, Y. Q.; Chen, C. H. Electrochemical Investigations of the LiNi0.45M0.10Mn1.45O4 (M=Fe, Co, Cr) 5V Cathode Materials for Lithium Ion Batteries. *J. Power Sources* **2012**, *205*, 385−393.
(33) Liu, H.; Li, M.; Xiang, M.; Guo, J.; Bai, H.; Bai, W.; Liu, X. Effects of Crystal Structure and Plane Orientation on Lithium and Nickel Co-Doped Spinel Lithium Manganese Oxide for Long Cycle Life Lithium-Ion Batteries. *J. Colloid Interface Sci.* **2021**, *585*, 729.
(34) Liu, J.; Manthiram, A. Understanding the Improved Electrochemical Performances of Fe-Substituted 5 V Spinel Cathode LiMn1.5Ni0.5O4. *J. Phys. Chem. C* **2009**, *113*, 15073−15079.
(35) Chen, M.; Wu, R.; Ju, S.; Zhang, X.; Xue, F.; Xing, W. Improved Performance of Al-Doped LiMn2O4 Ion-Sieves for Li+ Adsorption. *Microporous Mesoporous Mater.* **2018**, *261*, 29−34.
(36) Peng, C.; Huang, J.; Guo, Y.; Li, Q.; Bai, H.; He, Y.; Su, C.; Guo, J. Electrochemical Performance of Spinel LiAlxMn2-XO4 Prepared Rapidly by Glucose-Assisted Solid-State Combustion Synthesisr. *Vacuum* **2015**, *120*. DOI: 10.1016/j.vacuum.2015.07.001.
(37) Xu, W.; Zheng, Y.; Cheng, Y.; Qi, R.; Peng, H.; Lin, H.; Huang, R. Urnderstanding the Effect of Al Doping on the Electrochemical Performance Improvement of the LiMn 2 O 4 Cathode Material. *ACS Appl. Mater. Interfaces* **2021**, *13*, 45446−45454.
(38) Amdouni, N.; Zaghib, K.; Gendron, F.; Mauger, A.; Julien, C. M. Structure and Insertion Properties of Disordered and Ordered LiNi0.5Mn1.5O4 Spinels Prepared by Wet Chemistry. *Ionics (Kiel).* **2006**, *12*, 117−126.
(39) Kim, D.; Shiiba, H.; Zettsu, N.; Yamada, T.; Kimijima, T.; Sánchez-Santolino, G.; Ishikawa, R.; Ikuhara, Y.; Teshima, K. Full Picture Discovery for Mixed-Fluorine Anion Effects on High-Voltage Spinel Lithium Nickel Manganese Oxide Cathodes. *NPG Asia Mater.* **2017**, *9*, No. e398.
(40) Wang, L.; Li, H.; Huang, X.; Baudrin, E. A Comparative Study of Fd-3m and P4332 "LiNi0.5Mn1.5O4. *Solid State Ionics* **2011**, *193*, 32−38.
(41) Idemoto, Y.; Narai, H.; Koura, N. Crystal Structure and Cathode Performance Dependence on Oxygen Content of LiMn1.5Ni0.5O4 as a Cathode Material for Secondary Lithium Batteries. *J. Power Sources* **2003**, *119-121*, 125−129.
(42) Xue, Y.; Wang, Z.; Zheng, L.; Yu, F.; Liu, B.; Zhang, Y.; Ke, K. Investigation on Preparation and Performance of Spinel LiNi0.5Mn1.5O4 with Different Microstructures for Lithium-Ion Batteries. *Sci. Rep.* **2015**, *5*, 13299.
(43) Bianchini, M.; Fauth, F.; Suard, E.; Leriche, J.-B.; Masquelier, C.; Croguennec, L. Spinel Materials for Li-Ion Batteries: New Insights Obtained by Operando Neutron and Synchrotron X-Ray Diffractionr. *Acta Crystallogr. Sect. B Struct. Sci. Cryst. Eng. Mater.* **2015**, *71*, 688−701.
(44) Liu, J.; Li, G.; Yu, Y.; Bai, H.; Shao, M.; Guo, J.; Su, C.; Liu, X.; Bai, W. Synthesis and Electrochemical Performance Evaluations of Polyhedra Spinel LiAlxMn2-XO4 (X≤0.20) Cathode Materials Prepared by a Solution Combustion Technique. *J. Alloys Compd.* **2017**, *728*. DOI: 10.1016/j.jallcom.2017.09.098.
(45) Zhao, H.; Li, F.; Liu, X.; Cheng, C.; Zhang, Z.; Wu, Y.; Xiong, W.; Chen, B. Effects of Equimolar Mg (II) and Si (IV) Co-Doping on the Electrochemical Properties of Spinel LiMn2-2xMgxSixO4 Prepared by Citric Acid Assisted Sol-Gel Method. *Electrochim. Acta* **2015**, *151*. DOI: 10.1016/j.electacta.2014.11.095.
(46) Feng, X. Y.; Shen, C.; Xiang, H. F.; Liu, H. K.; Wu, Y. C.; Chen, C. H. High Rate Capability of 5 V LiNi0.5Mn1.5O4 Cathode Material Synthesized via a Microwave Assist Method. *J. Alloys Compd.* **2017**, *695*, 227−232.
(47) Dang, R.; Qu, Y.; Ma, Z.; Yu, L.; Duan, L.; Lü, W. The Effect of Elemental Doping on Nickel-Rich NCM Cathode Materials of Lithium Ion Batteries. *J. Phys. Chem. C* **2022**, *126*, 151−159.
(48) Peng, Z.; Mu, K.; Cao, Y.; Xu, L.; Du, K.; Hu, G. Enhanced Electrochemical Performance of Layered Li-Rich Cathode Materials for Lithium Ion Batteries via Aluminum and Boron Dual-Doping. *Ceram. Int.* **2019**, *45*(). DOI: 10.1016/j.ceramint.2018.11.087.
(49) Xu, W.; Zheng, Y.; Cheng, Y.; Qi, R.; Peng, H.; Lin, H.; Huang, R. Understanding the Effect of Al Doping on the Electrochemical Performance Improvement of the LiMn2O4Cathode Material. *ACS Appl. Mater. Interfaces* **2021**, *13*(). DOI: 10.1021/acsami.1c11315.
(50) Abebe, E. B.; Yang, C.-C.; Wu, S.-H.; Chien, W.-C.; Li, Y.-J. J. Effect of Li Excess on Electrochemical Performance of Ni-Rich LiNi 0.9 Co 0.05 Mn 0.05 O 2 Cathode Materials for Li-Ion Batteries. *ACS Appl. Energy Mater.* **2021**, *4*(). DOI: 10.1021/acsaem.1c03004.
(51) Meng, Y.; Wang, M.; Zhu, Z.; Jiang, T.; Liu, Z.; Chen, N.; Shen, C.; Peng, Q.; Chen, W. Multifunctional Nickel-Cobalt Phosphates for High-Performance Hydrogen Gas Batteries and Self-Powered Water

Splitting. *ACS Appl. Energy Mater.* **2021**, *4*(). DOI: 10.1021/acsaem.1c02582.
(52) Seyedahmadian, M.; Houshyarazar, S.; Amirshaghaghi, A. Synthesis and Characterization of Nanosized of Spinel LiMn 2O4 via Sol-Gel and Freeze Drying Methods. *Bull. Korean Chem. Soc.* **2013**, *34*(). DOI: 10.5012/bkcs.2013.34.2.657., DOI: 10.5012/bkcs.2013.34.2.622
(53) Nguyen, T. X.; Patra, J.; Chang, J. K.; Ting, J. M. High Entropy Spinel Oxide Nanoparticles for Superior Lithiation-Delithiation Performance. *J. Mater. Chem. A* **2020**, *8*(). DOI: 10.1039/d0ta04844e.
(54) Zhang, H.; Karki, K.; Huang, Y.; Whittingham, M. S.; Stach, E. A.; Zhou, G. Atomic Insight into the Layered/Spinel Phase Transformation in Charged LiNi0.80Co0.15Al0.05O2 Cathode Particles. *J. Phys. Chem. C* **2017**, *121*(). DOI: 10.1021/acs.jpcc.6b10220.
(55) Jerliu, B.; Hüger, E.; Dörrer, L.; Seidlhofer, B. K.; Steitz, R.; Horisberger, M.; Schmidt, H. Lithium Insertion into Silicon Electrodes Studied by Cyclic Voltammetry and: Operando Neutron Reflectometry. *Phys. Chem. Chem. Phys.* **2018**, *20*(). DOI: 10.1039/c8cp03540g.
(56) Callegari, D.; Coduri, M.; Fracchia, M.; Ghigna, P.; Braglia, L.; Anselmi Tamburini, U.; Quartarone, eliana. Lithium Intercalation Mechanisms and Critical Role of Multi-Doping in LiFexMn2-x-YTiyO4 as High-Capacity Cathode Material for Lithium-Ion Batteries. *J. Mater. Chem. C* **2022**, *10*. DOI: 10.1039/D2TC00573E.
(57) Cai, Z.; Ma, Y.; Huang, X.; Yan, X.; Yu, Z.; Zhang, S.; Song, G.; Xu, Y.; Wen, C.; Yang, W. High Electrochemical Stability Al-Doped Spinel LiMn2O4 Cathode Material for Li-Ion Batteries. *J. Energy Storage* **2020**, *27*. DOI: 10.1016/j.est.2019.101036.
(58) Edge, J. S.; O'Kane, S.; Prosser, R.; Kirkaldy, N. D.; Patel, A. N.; Hales, A.; Ghosh, A.; Ai, W.; Chen, J.; Yang, J.; Li, S.; Pang, M. C.; Bravo Diaz, L.; Tomaszewska, A.; Marzook, M. W.; Radhakrishnan, K. N.; Wang, H.; Patel, Y.; Wu, B.; Offer, G. J. Lithium Ion Battery Degradation: What You Need to Know. *Phys. Chem. Chem. Phys.* **2021**, *23*. DOI: 10.1039/d1cp00359c.
(59) Kwon, D. H.; Lee, J.; Artrith, N.; Kim, H.; Wu, L.; Lun, Z.; Tian, Y.; Zhu, Y.; Ceder, G. The Impact of Surface Structure Transformations on the Performance of Li-Excess Cation-Disordered Rocksalt Cathodes. *Cell Reports Phys. Sci.* **2020**, *1*(). DOI: 10.1016/j.xcrp.2020.100187.
(60) Lee, J.; Kitchaev, D. A.; Kwon, D. H.; Lee, C. W.; Papp, J. K.; Liu, Y. S.; Lun, Z.; Clément, R. J.; Shi, T.; McCloskey, B. D.; Guo, J.; Balasubramanian, M.; Ceder, G. Reversible Mn2+/Mn4+ Double Redox in Lithium-Excess Cathode Materials. *Nature* **2018**, *556*(). DOI: 10.1038/s41586-018-0015-4.
(61) Freire, M.; Kosova, N. V.; Jordy, C.; Chateigner, D.; Lebedev, O. I.; Maignan, A.; Pralong, V. A New Active Li-Mn-O Compound for High Energy Density Li-Ion Batteries. *Nat. Mater.* **2016**, *15*(). DOI: 10.1038/nmat4479.
(62) Patoux, S.; Daniel, L.; Bourbon, C.; Lignier, H.; Pagano, C.; Le Cras, F.; Jouanneau, S.; Martinet, S. High Voltage Spinel Oxides for Li-Ion Batteries: From the Material Research to the Application. *J. Power Sources* **2009**, *189*, 344−352.
(63) Xu, L.; Chen, S.; Li, N.; Li, Y.; Fang, Y.; Wei, C.; Chen, L.; Cao, D.; Lu, Y.; Wang, M.; Bao, L.; Su, Y. Formation of Rocksalt Domains by Dual Substitution to Boost Electrochemical Capability of Co-Free Li-Rich Layered Cathodes. *ACS Appl. Energy Mater.* **2022**, *5*. DOI: 10.1021/acsaem.2c01620.

Recommended by ACS

High-Entropy $Sn_{0.8}(Co_{0.2}Mg_{0.2}Mn_{0.2}Ni_{0.2}Zn_{0.2})_{2.2}O_4$ Conversion-Alloying Anode Material for Li-Ion Cells: Altered Lithium Storage Mechanism, Activation of Mg, a...

Maciej Moździerz, Andrzej Kulka, *et al.*
SEPTEMBER 12, 2022
ACS APPLIED MATERIALS & INTERFACES
READ

Formation of Rocksalt Domains by Dual Substitution to Boost Electrochemical Capability of Co-Free Li-Rich Layered Cathodes

Lifeng Xu, Yuefeng Su, *et al.*
AUGUST 07, 2022
ACS APPLIED ENERGY MATERIALS
READ

Surface-Phase Engineering via Lanthanum Doping Enables Enhanced Electrochemical Performance of Li-Rich Layered Cathode

Ziwei Liu, Yulin Ma, *et al.*
JULY 18, 2022
ACS APPLIED ENERGY MATERIALS
READ

Al-Doped Co-Free Layered-Spinel Mn/Ni Oxides as High-Capacity Cathode Materials for Advanced Li-Ion Batteries

Prasant Kumar Nayak, Doron Aurbach, *et al.*
APRIL 04, 2022
ACS APPLIED ENERGY MATERIALS
READ

Get More Suggestions >

energy&fuels

pubs.acs.org/EF

Article

Influence of the Crystal Plane Orientation in Enhancing the Electrochemical Performance of a Trication-Substituted Cathode for Li-Ion Batteries

Bogalera Papaiah Shivamurthy, Marulasiddappa Thripuranthaka, Manjusha V. Shelke, and Girish Praveen Nayaka*

Cite This: *Energy Fuels* 2024, 38, 4653−4665

Read Online

ACCESS | Metrics & More | Article Recommendations | Supporting Information

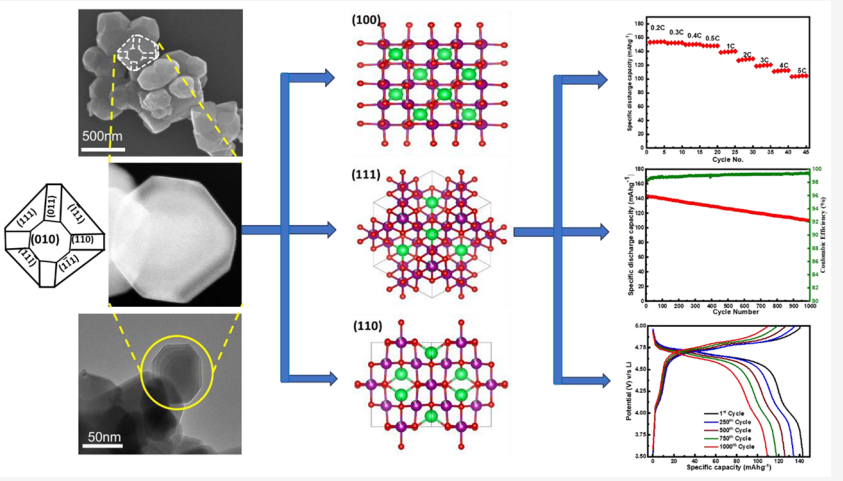

ABSTRACT: High-voltage spinel cathodes with low nickel are promising candidates for Li-ion batteries owing to their high energy and power density, thermal stability, and eco-friendliness. However, the high operating voltage (∼4.7 V) leads to the decomposition of electrolytes, structural disorder, and deterioration of the cathode−electrolyte interphase (CEI) as well as hinders practical capability. We have synthesized trication-substituted spinel cathode materials with exposed (111) crystal planes and truncated octahedral shapes. These materials have demonstrated high specific discharge capacity and high rate capability up to 1000 cycles with a voltage window of 3.5−5 V. The crystal plane orientation of these materials has been investigated using X-ray diffraction of electrodes and electron microscopic studies and correlated with the electrochemical performance of the surface plane of exposed cathode materials. Among the three synthesized materials, the LMNFA2 cathode has shown a specific discharge capacity of 109.29 mAh g^{-1} at 1 C after 1000 cycles with a capacity retention of 76.3%, which is nearly equal to the previously reported dual-phase material with the same metal compositions.

Downloaded via NATL CHEMICAL LABORATORY on March 19, 2024 at 11:17:37 (UTC).
See https://pubs.acs.org/sharingguidelines for options on how to legitimately share published articles.

1. INTRODUCTION

Cathode materials play a vital role in the determination of the energy density of Li-ion batteries (LIBs). The eagerness toward the invention and development of high-energy cathode materials comprises low-cost and earth-abundant elements that could reduce the production cost of batteries. Besides, the availability of high-voltage cathode materials with increased energy density is the present concern toward successful commercialization. The $LiMn_2O_4$ cathode materials belong to the spinel type of cathode materials, which are the priority choice for high-voltage applications because they can exhibit exceptional thermal stability. At the same time, it suffers from Mn dissolution issues in electrolytes. This forced the researchers to modify this spinel cathode material to reduce Mn dissolution. As a result, $LiMn_{1.5}Ni_{0.5}O_4$ spinel (LMNO) cathode materials emerged as promising candidates because of their high operational voltage of ∼4.7 V and their ability to perform at a high energy density and power density with a longer cycling performance.[1] However, the real-time applications of spinel-based cathode materials are still hindered by

Received: October 3, 2023
Revised: January 16, 2024
Accepted: January 18, 2024
Published: February 7, 2024

© 2024 American Chemical Society

https://doi.org/10.1021/acs.energyfuels.3c03794
Energy Fuels 2024, 38, 4653−4665

several drawbacks, such as (i) structural instability arising from the presence of Mn^{3+} ions (these Mn^{3+} ions have a $3d^4$ configuration, which undergoes a rapid disproportionation reaction to form Mn^{4+} and Mn^{2+} ions; this disproportionation reaction of Mn^{3+} ions tends to dissolve in the electrolyte solutions, which will shorten the cycle life of the battery[2]) and (ii) low interfacial stability between the electrode and electrolyte, which hinders the real-time application of the materials.[3]

The LMNO-based cathodes are the choice for high-voltage LIB applications; generally, this class of cathode materials has been reported with *P*4332 and $Fd\bar{3}m$ space groups. The *P*4332 space group is associated when the low-temperature synthesis conditions are employed, and the $Fd\bar{3}m$ space group is associated when the high-temperature synthesis conditions are employed.[4] This $Fd\bar{3}m$ space group is also accompanied by rock salt impurity, which we have reported previously.[5] In our case, the synthetic temperature is higher; therefore, the phase of the material belongs to the $Fd\bar{3}m$ space group through a cubic close-packed structure with the capability of intercalating one Li^+ ion into an anode per unit formula. The oxygen atoms form the cubic close packing, and the corresponding oxygen octahedra are associated with common edges. Li and Mn ions occupy 8a tetrahedral and 16d octahedral sites, respectively.[6] A three-dimensional network is present in the structure, which allows the Li ions to diffuse easily; this makes spinel materials more suitable for their use in giant power batteries. Nevertheless, still, spinel-based materials face several problems because their cycling stability and high-rate discharge capacity are not sufficient, particularly at elevated temperatures, which pull back this material for larger scale applications. The said problems are due to the dissolution of Mn ions into the electrolyte and the Jahn−Teller (J−T) distortion of Mn ions, which hinders the practical applicability of this material. To overcome the issues linked with these spinel materials, researchers have tried different approaches, viz., doping with stable cations (Ni,[7−9] Zn,[10] Cu,[7] Fe,[7] Co,[11] Al,[8,12] etc.), anions (F^-,[13] Cl^-,[14] etc.), and surface modifications with metal oxides (Al_2O_3,[15] AlF_3,[16] ZnO,[17] ZrO_2,[18] etc.). To uplift the capacity of this spinel cathode material, Mn^{3+} ions have been replaced by Ni ions.[7] Alongside, to achieve electrochemical stability and extend the cycle life of the cathode materials during charge/discharge processes, lithium manganese oxide (LMO) cathodes have been substituted by Fe^{3+} and Al^{3+} ions into Mn^{3+} sites.[7,12] Therefore, the combination of all of these metal ions in LMO cathodes will enhance the electrochemical performance by reducing the J−T effect and Mn^{3+} ion dissolutions. The influence of Fe^{3+} and Al^{3+} in the material is discussed in our previously published work, where we reported dual-phase material.[5] Therefore, our prime focus in the present work was to achieve pure phase material by substituting trications, and we have succeeded in synthesizing pure phase material. Further, the dissolution issue of Mn ions can also be resolved by tailored exposure of planes,[19] particularly the (111) plane, which is truncated into octahedron with partial proportions of other planes (100) and (110).[20,21] Herein, for the (111) plane, the atomic arrangement will be denser, and this will help to form solid−electrolyte interphase (SEI) layers, which mitigates Mn dissolution in the electrolyte,[22] whereas the other plane (100) and (110) arrangements will be less dense, which will help in the close interaction of Mn ions with the electrolyte, which assists in fast diffusion channels for Li ions.[20,21,23] Hence, this truncated structure demonstrates a stable and enhanced electrochemical performance. Nevertheless, developing materials with truncated octahedral geometry is a challenging task; it requires harsh synthetic conditions and template-based methods. However, here, in this case, we succeeded in synthesizing material with a truncated octahedral geometry with an exposed (111) plane via a sol−gel approach.

In the present work, we report the continued work of our previously published material with the same metal composition to achieve single-phase material. Here, we have synthesized pure/single-phase $LiMn_{2-x-y-z}Ni_xFe_yAl_zO_4$ (x = 0.4−0.5 and y and z = 0.05−0.1) cathode materials with substitution of multications, Ni, Al, and Fe, into the crystal.

2. MATERIALS AND METHODS

2.1. Materials. $LiMn_{2-x-y-z}Ni_xFe_yAl_zO_4$ (x = 0.4−0.5 and y and z = 0.05−0.1) cathode materials were synthesized using the sol−gel method. The stoichiometric amount of manganese(II) acetate tetrahydrate [$Mn(CH_3COO)_2{\cdot}4H_2O$, >99%, Sigma-Aldrich], nickel-(II) acetate tetrahydrate [$Ni(CH_3COO)_2{\cdot}4H_2O$, >98%, Sigma-Aldrich], iron oxalate dihydrate ($FeC_2O_4{\cdot}2H_2O$, >99%, Sigma-Aldrich), aluminum nitrate nonahydrate [$Al(NO_3)_3{\cdot}9H_2O$, >98%, Sigma-Aldrich], and lithium acetate dihydrate ($CH_3COOLi{\cdot}2H_2O$, 99%, Thomas Baker) (5% excess) were dissolved in an appropriate quantity of demineralized water, and these solutions were mixed with citric acid monohydrate ($C_6H_8O_7{\cdot}H_2O$, >99%, Sigma-Aldrich) (1:1 ratio). The mixed solution was kept for stirring at 80 °C to obtain homogeneous and viscous gel, which was further dried and ground to collect the precursor powder. The powder was then heat-treated at 400 °C for 4 h with a temperature ramp rate of 5 °C/min to reach 400 °C. Then, the obtained powder was ground and further calcined for 800 °C for 10 h with a ramp rate of 3 °C/min to reach 800 °C. After the heating process, it was allowed to cool naturally, and finally, the calcined material was ground into fine powder and collected.

2.2. Material Characterization. The crystal structure of the prepared materials was studied using X-ray diffraction (XRD, Panalytical X'Pert Pro) with Cu as an X-ray source at 40 kV and 30 mA with Ni as the Kβ filter. The obtained XRD patterns were refined using the Rietveld refinement technique with the help of FullProf suite software. The input parameters were gathered from the Powder Diffraction File (PDF) number 00-035-0782. Raman spectra of the samples were recorded between the spectral region of 100−1200 cm^{-1} using a Horiba Jobin-Yvon LabRam HR800 Raman spectrometer instrument with a near-infrared (NIR) He−Ne laser (wavelength of 632.88 nm). The Brunauer−Emmett−Teller (BET) surface area of the materials was measured by the nitrogen gas adsorption−desorption method on a Quantachrome Quadrasorb surface area measurement and pore size analyzer instrument. The surface structure and morphology of the materials were studied using field emission scanning electron microscopy (FE-SEM, FEI Nova NanoSEM 450) and high-resolution transmission electron microscopy (HR-TEM, JEOL JEM-F200) coupled with energy-dispersive spectroscopy (EDS). The valence states of the elements are studied by employing X-ray photoelectron spectroscopy (XPS), which was performed using the Thermo Scientific model Kα XPS instrument with monochromatic Al Kα as the X-ray source. For ease of discussion, the series of materials is termed LMNFA1 ($LiMn_{1.4}Ni_{0.4}Fe_{0.1}Al_{0.1}O_4$), LMNFA2 ($LiMn_{1.3}Ni_{0.5}Fe_{0.1}Al_{0.1}O_4$), and LMNFA3 ($LiMn_{1.5}Ni_{0.4}Fe_{0.05}Al_{0.05}O_4$).

2.3. Electrochemical Characterization. The as-prepared cathode materials were studied for their electrochemical behavior by fabricating 2032-type coin cells. The positive electrodes are comprised of 80 wt % of the active cathode material, 10 wt % polyvinylidene difluoride (PVDF) as the binder, and 10 wt % Super C-60 carbon black as the conducting material. All of these materials were mixed well by adding *N*-methyl pyrrolidone as the solvent to form a uniform slurry. The as-prepared slurry was cast onto a carbon-coated aluminum foil by the doctor blade method and dried at 100 °C for

https://doi.org/10.1021/acs.energyfuels.3c03794
Energy Fuels 2024, 38, 4653−4665

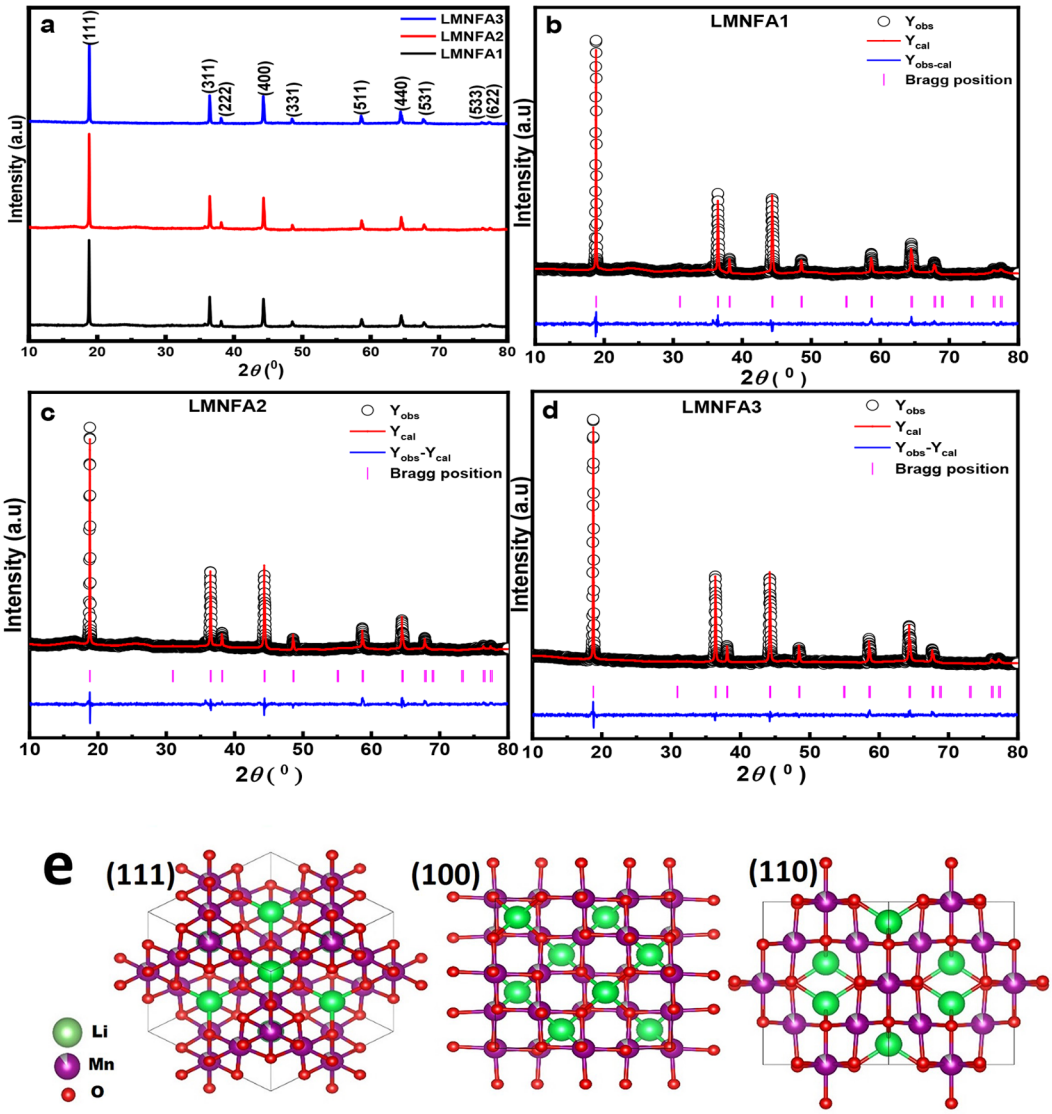

Figure 1. (a) XRD patterns of $LiMn_{2-x-y-z}Ni_xFe_yAl_zO_4$ (x = 0.4−0.5 and y and z = 0.05−0.1), Rietveld refinement plots of (b) LMNFA1, (c) LMNFA2, and (d) LMNFA3, and (e) crystal structures of LMNFA1 represented along the planes (111), (100), and (110).

12 h under vacuum. The foil was subjected to calendaring and punched into 14 mm circular discs. These circular cathode discs were used to fabricate the 2032-type coin cells, with Li metal disc as the anode, Celgard 2325 as the separator, and 1 M $LiPF_6$ in a 1:1:1 volume ratio of EC/DMC/EMC solvents as the electrolyte. The fabrication of coin cells was carried out in an argon-filled glovebox at ≤0.1 ppm of O_2 and H_2O levels. These fabricated coin cells were used to perform cyclic voltammetry (CV, voltage window of 3.5−4.9 V at a scan rate of 0.1 mV s^{-1}) and electrochemical impedance spectroscopy (EIS) using the Metrohm electrochemical workstation (Multi Autolab M204). The galvanostatic charge/discharge (GCD) studies were performed using the Neware battery testing system (CT4008). The theoretical capacity of all of the materials was calculated using eq 1

$$C_T = \frac{nF}{3.6MW} \quad (1)$$

where n is the number of electrons transferred, F is the Faraday constant value, the factor of 3.6 converts the theoretical specific capacity of C g^{-1} to mAh g^{-1}, and MW is the molecular weight of active material.

3. RESULTS AND DISCUSSION

3.1. Structural and Morphology Characterization. A set of cathode materials $LiMn_{2-x-y-z}Ni_xFe_yAl_zO_4$ (x = 0.4−0.5 and y and z = 0.05−0.1) were prepared by the sol−gel method and are characterized by XRD (Figure 1a) to know the structural details. XRD patterns show that all planes indexed the pure phase formation of the $LiMn_{2-x-y-z}Ni_xFe_yAl_zO_4$ (x = 0.4−0.5 and y and z = 0.05−0.1) spinel structure without any dopant-related impurities. The obtained XRD patterns are well-matched with standard PDF number 00-035-0782. To attain more information about the orientation, lattice parameter, and occupancy of the plane, Rietveld refinement studies were performed using FullProf software and are shown in panels b−d of Figure 1. The diffraction patterns of all three materials are indexed to a cubic spinel structure with $Fd\bar{3}m$ space group and good crystallinity. In the cubic spinel structure, Li^+ ions occupy 8a sites, and there are chances of entering the other cation into the 8a site when we dope multiple cations. The stability factor for spinel-type materials could be analyzed by the intensity ratio of diffraction peaks

https://doi.org/10.1021/acs.energyfuels.3c03794
Energy Fuels 2024, 38, 4653−4665

Table 1. Crystal Parameters Calculated from XRD Data

	intensity ratio		lattice constant (Å)	
sample	(111)/(400)	(111)/(440)	$1/d_{hkl}^2 = 1/a^2(h^2 + k^2 + l^2)$]	crystallite size (nm)
LMNFA1	2.58	4.82	8.168	39.73
LMNFA2	2.62	4.96	8.162	43.46
LMNFA3	2.51	4.56	8.170	38.29

Table 2. Rietveld Refinement Results of LMNFA1, LMNFA2, and LMNFA3 Materials

material	space group	lattice constant (Å)	cell volume	R_p	R_{wp}	R_{Bragg}	R_{F^2}	χ^2
LMNFA1	$Fd\bar{3}m$	8.169	545.27	3.55	3.48	3.55	3.4	2.1
LMNFA2	$Fd\bar{3}m$	8.168	545.12	3.06	4.19	5.08	6.1	3.1
LMNFA3	$Fd\bar{3}m$	8.186	548.55	2.61	3.37	2.77	2.6	1.6

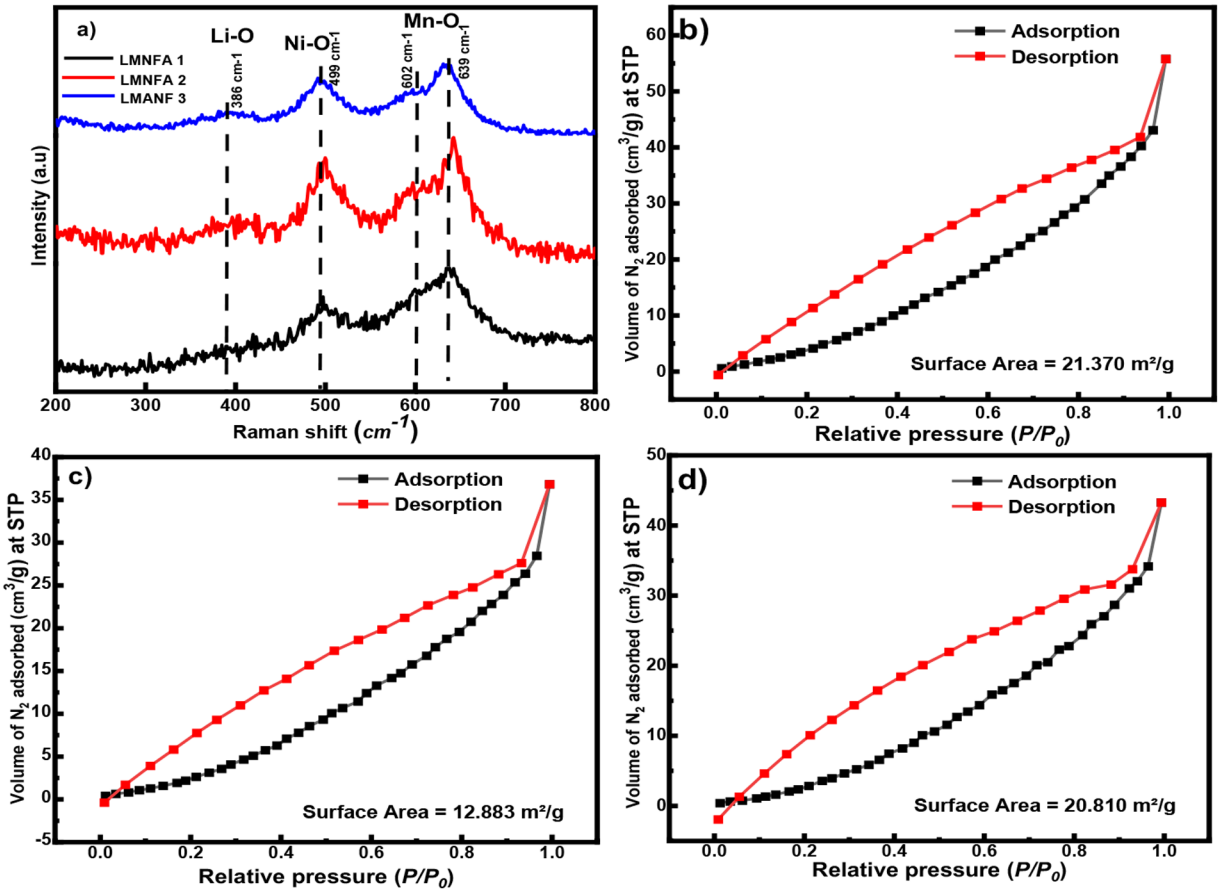

Figure 2. (a) Raman spectra of LMNFA cathode materials and (b–d) BET adsorption–desorption curves of LMNFA1, LMNFA2, and LMNFA3 cathode materials.

(400) and (311). The tetrahedral site occupancy of cations was further confirmed by calculating the integrated intensity ratios of (400) and (311) planes. The obtained intensity ratio values are lower than the reported value for $LiMn_2O_4$,[6,23] which indicates that the occupancy of cations is more in tetrahedral 8a Li lattice sites. To understand the influence of variable dopant composition on lattice parameters, the lattice parameter "a" of the materials is calculated for XRD results using the *d*-spacing value of the (400) plane and is given in Table 1 (obtained from XRD raw data) and Table 2 (obtained from Rietveld refinement of XRD data), which are in close agreement with each other for the spinel phase. Other refined parameters are given in Table S1 of the Supporting Information. The average crystallite size of the synthesized materials is calculated using a Scherrer relation by considering prominent (111) peak.[6] The extent of the surface orientation of the LMNFA cathode materials is determined by calculating the intensity ratio of the planes (111) and (400) (Table 1). From the table, it can be observed that the intensity ratio value of the (111)/(400) plane for LMNFA2 material is slightly more than that of LMNFA1 and LMNFA3, which is due to the dominance of the (111) plane in the crystal structure.[24] In addition, it also shows the dominant facets of the (111) plane, which corresponds to the truncated type.[9] The Mn^{3+} (0.64 Å) ions in $LiMn_2O_4$ are substituted by Fe^{3+} (0.65 Å) ions, which results in a low-angle shift according to Bragg's law. Variations in the Fe concentration in all of the materials influence (111)

https://doi.org/10.1021/acs.energyfuels.3c03794
Energy Fuels 2024, 38, 4653–4665

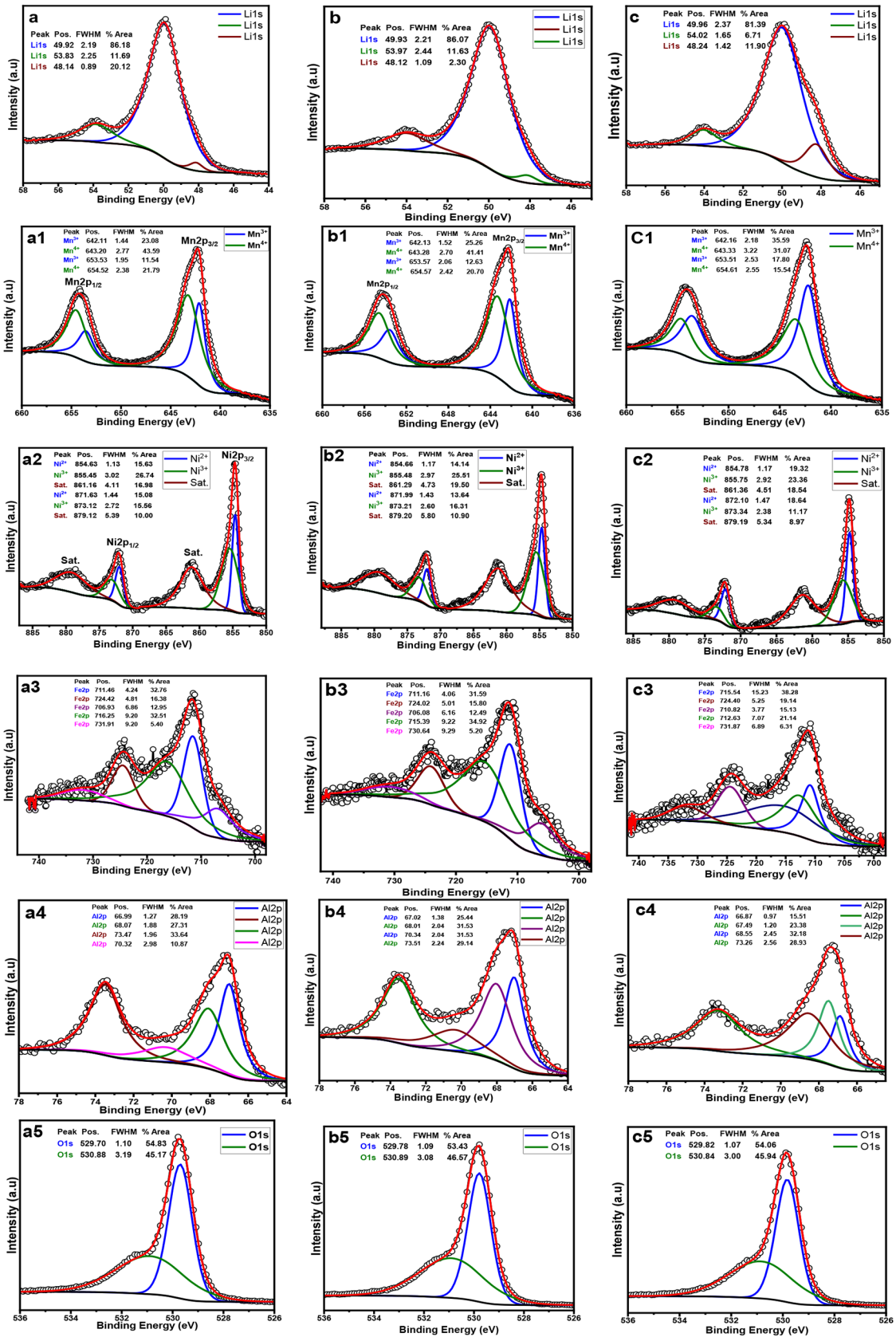

Figure 3. Deconvoluted XPS spectra of Mn 2p and Ni 2p of (a) LMNFA1, (b) LMNFA2, and (c) LMNFA3.

plane dominance in the crystal surface, which could affect the growth of the truncated octahedral shape.[24]

The {100} and {110} planes whose orientations are associated with Li diffusion channels are most susceptible to

https://doi.org/10.1021/acs.energyfuels.3c03794
Energy Fuels 2024, 38, 4653−4665

Mn dissolution, whereas the {111} facets, on which Mn atoms are utmost compactly packed, have the lowest surface energy and exhibit better stability.[25] The exposure of the dominant (111) plane forms the crystals with the lowest surface energy state than the (100) and (110) planes.[26] The dominant (111) planes are packed with dense atomic arrangements that are prone to stable SEI layers, which suppress the Mn dissolution into the electrolyte. Meanwhile, the (100) and (110) planes less densely packed with Mn ions could mitigate Mn dissolution and provide faster Li^+ diffusion channels to achieve superior performance.[27,28] This confirms that the dominant (111) plane influences the electrochemical capabilities of the materials.[27] The corresponding crystal structures [generated from VESTA software using a crystallographic information file (CIF) obtained from Rietveld refinement][29] of the atomic arrangement and Li^+ diffusion channels along the planes (111), (100), and (110) are shown in Figure 1e.

The Raman spectra of the synthesized LMNFA cathode materials are shown in Figure 2a, and the broad peak observed at 639 cm^{-1} indicates the presence of Mn−O stretching vibrations of the MnO_6 octahedral geometry through A_{1g} symmetry in O_h^7 spectroscopic space group. The blue shift observed in the A_{1g} symmetry level for the material LMNFA2 with an increased Ni ratio could cause a change in bond lengths. The A_{1g} mode comprises the mixed information on Mn−O and Ni−O bonds in $[Mn(Ni)O_6]$ octahedrons, because it is quite complex to resolve the Mn^{4+}−O, Mn^{3+}−O, and Ni−O bands.[30] The slight excess Ni content contributed to an increase in intensity and caused a slight shift in the main phonon mode at 623 cm^{-1}, which was attributed to the change in electronic states of Mn by Ni substitution. Because the material LMNFA has a slightly higher concentration of Ni, the Mn(Ni)−O bond in the doped material is responsible for the blue shift, which demonstrates the structural stability of the cathode material.[31] A feeble peak observed at 602 cm^{-1} indicates the existence of F_{2g}(I) symmetry, which corresponds to the Mn average electronic state in the spinel-structured cathode materials.[32,33] The peak at 499 cm^{-1} indicates the presence of Ni−O stretching vibration of NiO_6 octahedral geometry through F_{2g}(II) symmetry.[34,35] This confirms the doping of Ni into the octahedral Mn sites in the spinel structure, which helps in achieving structural stability of the active material during electrochemical studies.[33] The low intense peak observed at 390 cm^{-1} indicates the presence of the Li−O stretching vibration of the LiO_4 tetrahedral geometry.[36] The analysis of the obtained Raman results confirms the successful incorporation of metal ions into their constituent sites.

The BET specific surface area measurements of the synthesized LMNFA series cathode materials were carried out to understand the effect of the surface area on the electrochemical performances. As per the literature, a higher specific surface area of the material leads to extending the contact region between the electrode and electrolyte. As a result, Mn ions in cathode materials could suffer from the dissolution in electrolytic solution.[37] Therefore, the materials with lower specific surface area will help in extending the cycle life and providing better rate capability. This has been proven in our material, as the LMNFA2 (12.88 m^2/g) cathode material has a less specific surface area compared to LMNFA1 (21.370 m^2/g) and LMNFA3 (20.810 m^2/g) materials. LMNFA2 has shown better capacity and stability. The report by Ryu et al.[38] has shown that the larger surface area of the cathode materials would lead to more interfacial contact between the electrode and electrolyte, which could demonstrate a higher discharge capacity, but, simultaneously, undergoes a large extent of metal ion dissolution results in the reduced cycle life.[38,39] In correlation with our synthesized cathode materials, LMNFA1 and LMNFA3 have shown higher discharge capacities but lower cycle stability compared to the LMNFA2 cathode material.

The electronic valence states and elemental composition of the synthesized cathode materials were characterized by XPS. Figure 3 shows the XPS peak signals of LMNFA1, LMNFA2, and LMNFA3; the peak signals observed for Li 1s, Mn 2p, Ni 2p, Fe 2p, and Al 2p confirm the well-matched composition, as expected. The deconvoluted spectra of Li 1s core levels of all of the materials are shown in panels a−c of Figure 3, and the binding energy of prominent peak Li 1s core levels is 49.92 eV (LMNFA1), 49.93 eV (LMNFA2), and 49.96 eV (LMNFA3), confirming the chemical and electronic states.[40] The deconvoluted spectra of the Mn 2p (panels a1−c1 of Figure 3) core level exhibits two components Mn $2p_{3/2}$ and Mn $2p_{1/2}$ as a result of spin−orbit coupling.[12,41] The binding energies of Mn $2p_{3/2}$ and Mn $2p_{1/2}$ core levels are 642.2 eV (LMNFA1), 642.3 eV (LMNFA2), and 642.2 eV (LMNFA3) and 654.0 eV (LMNFA1), 654.2 eV (LMNFA2), and 654.0 eV (LMNFA3), respectively. The obtained binding energy values for Mn^{4+} and Mn^{3+} in Mn 2p core levels are in close agreement with the values reported by Nesbitt et al.[42] The binding energy values provided the information on Mn^{4+} and Mn^{3+} states, which gives evidence of the existence of both of the states, which supplements the Raman results. The deconvoluted spectra of the Ni 2p (panels a2−c2 of Figure 3) core level also have two components Ni $2p_{3/2}$ and Ni $2p_{1/2}$ as a result of spin−orbit coupling. The binding energies of Ni $2p_{3/2}$ and Ni $2p_{1/2}$ core levels are 854.7 eV (LMNFA1), 854.8 eV (LMNFA2), and 854.6 eV (LMNFA3) and 872.2 eV (LMNFA1), 872.2 eV (LMNFA2), and 872.0 eV (LMNFA3), respectively. These electronic states of Ni are complemented with the Raman signals for Ni−O in NiO_6 and $[Mn(Ni)O_6]$ octahedrons. The deconvoluted peaks of Fe 2p core levels exhibit two components Fe $2p_{3/2}$ and Fe $2p_{1/2}$ displayed in panels a3−c3 of Figure 3. The binding energies of Fe $2p_{3/2}$ and Fe $2p_{1/2}$ core levels are 711.46 eV (LMNFA1), 711.16 eV (LMNFA2), and 715.54 eV (LMNFA3) and 724.42 eV (LMNFA1), 724.02 eV (LMNFA2), and 724.40 eV (LMNFA3), respectively, which confirms the successful substitution of the Fe^{3+} ion into the lattice.[43,44] The deconvoluted peaks of Al 2p levels are also given in panels a4−c4 of Figure 3, along with the resolved peak area proportion. The binding energies of Al $2p_{1/2}$ and Al $2p_{3/2}$ core levels are 73.47 eV (LMNFA1), 70.34 eV (LMNFA2), and 68.55 eV (LMNFA3) and 68.07 eV (LMNFA1), 68.01 eV (LMNFA2), and 67.49 eV (LMNFA3), respectively, which confirms the incorporation of Al^{3+} into the lattice.[12,45] The deconvoluted peaks of the O 1s core level are observed at 529.7 eV (LMNFA1), 529.78 eV (LMNFA2), and 529.82 eV (LMNFA1). The obtained binding energies indicate a M−O (M = Mn and Ni) relation with full width at half maximum (fwhm) values of ∼1.1, which indicates the oxide lattice structure. Peak fitting of all of the elemental core levels is performed using CasaXPS software (peak-fitted parameters are given in the respective plots).

Scanning electron microscopy (SEM) and transmission electron microscopy (TEM) studies were performed to know the structural morphology of the synthesized materials. Panels

https://doi.org/10.1021/acs.energyfuels.3c03794
Energy Fuels 2024, 38, 4653−4665

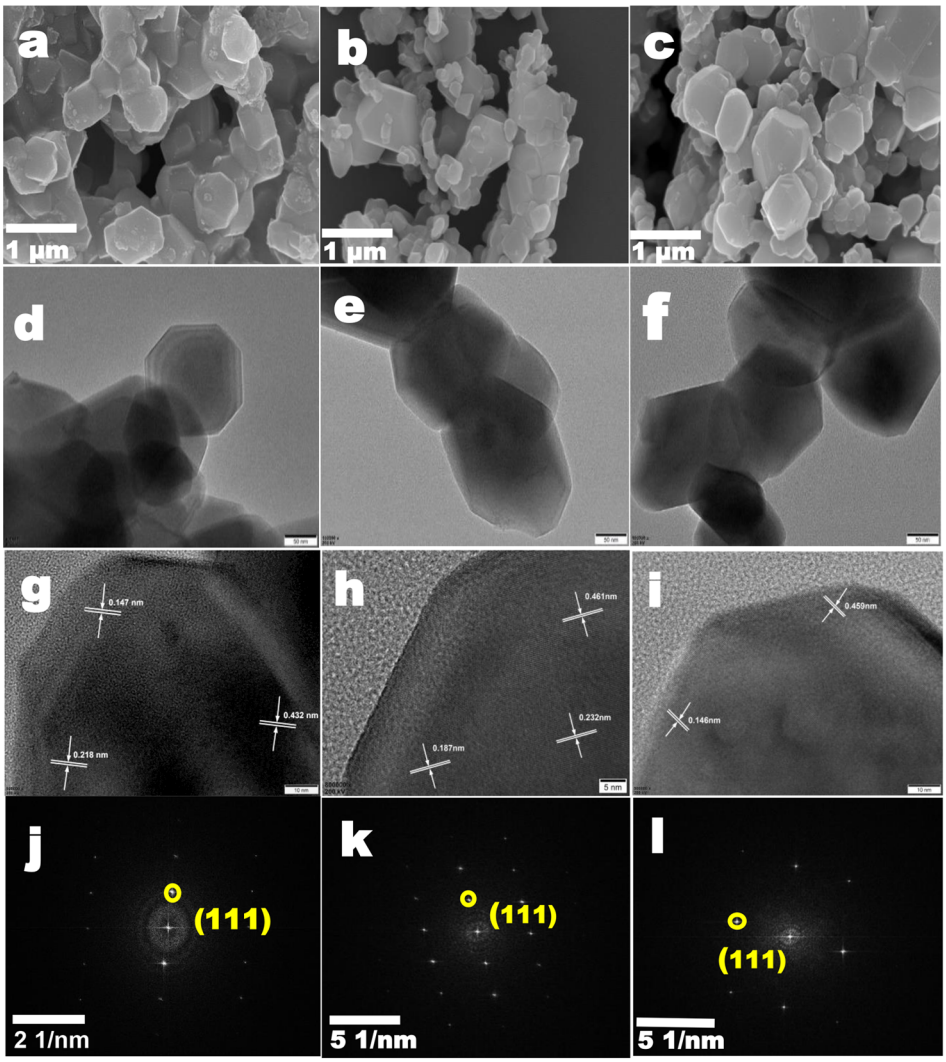

Figure 4. FE-SEM images of (a) LMNFA1, (b) LMNFA2, and (c) LMNFA3, TEM images of (d) LMNFA1, (e) LMNFA2, and (f) LMNFA3, HR-TEM images of (g) LMNFA1, (h) LMNFA2, and (i) LMNFA3 indexed with lattice spacing values, and SAED patterns of (j) LMNFA1, (k) LMNFA2, and (l) LMNFA3 with the (111) plane indexed.

a–c of Figure 4 show FE-SEM images that visualize the truncated octahedral shape of the particles. From the SEM images, it is understood that the extent of morphological orientation is not the same in all three materials, and they are slightly different from one another. This difference in morphology gives an idea about the influence of the crystal plane orientation on the electrochemical performance of the materials. The truncated octahedral shapes are formed more effectively in the case of LMNFA2 compared to the other two materials. Also, the average particle size of truncated octahedral-shaped LMNFA2 is smaller than that of LMNFA1 and LMNFA3, as per histogram results, shown in panels a–c of Figure S1 of the Supporting Information. The TEM images given in panels d–f of Figure 4 confirm the truncated octahedral-shaped particles, which visualize the soft edges of octahedral morphology. Panels g–i of Figure 4 show the HRTEM images of LMNFA1, LMNFA2, and LMNFA3 samples, where one edge portion of the truncated octahedron structure has been magnified to view the lattice fringes, which were used to calculate the *d*-spacing values. The lattice-spacing values for the (111) planes of all three materials identified in HRTEM images and compared are around ~0.471 nm. The *d*-spacing values obtained are related to (111) crystal planes from the XRD and are depicted in the respective images. The obtained *d*-spacing values are well-matched with the interplanar spacing values obtained from XRD data. Panels j–l of Figure 4 show the selected area electron diffraction (SAED) pattern, which shows the well-defined diffraction spots, which are marked to corresponding planes (111), (311), and (022).[9] The distribution of all of the elements in the synthesized materials is confirmed by scanning transmission electron microscopy–energy-dispersive spectroscopy (STEM–EDS) elemental mapping, which confirms the incorporation of all of the elements into the cathode structure, and the results for all of the materials are provided in panels a–h of Figure S2 of the Supporting Information.

3.2. Electrochemical Performance Analysis. To evaluate the electrochemical performance of the electrodes prepared from the trication-substituted LMO active materials, coin cells were fabricated. These fabricated coin cells were subjected to CV (panels a and b of Figure 5) to understand the redox behavior at a voltage window of 3.5–4.9 V versus Li. All three materials have shown three pairs of well-defined anodic and cathodic characteristic peaks, which indicates a three-step

https://doi.org/10.1021/acs.energyfuels.3c03794
Energy Fuels 2024, 38, 4653–4665

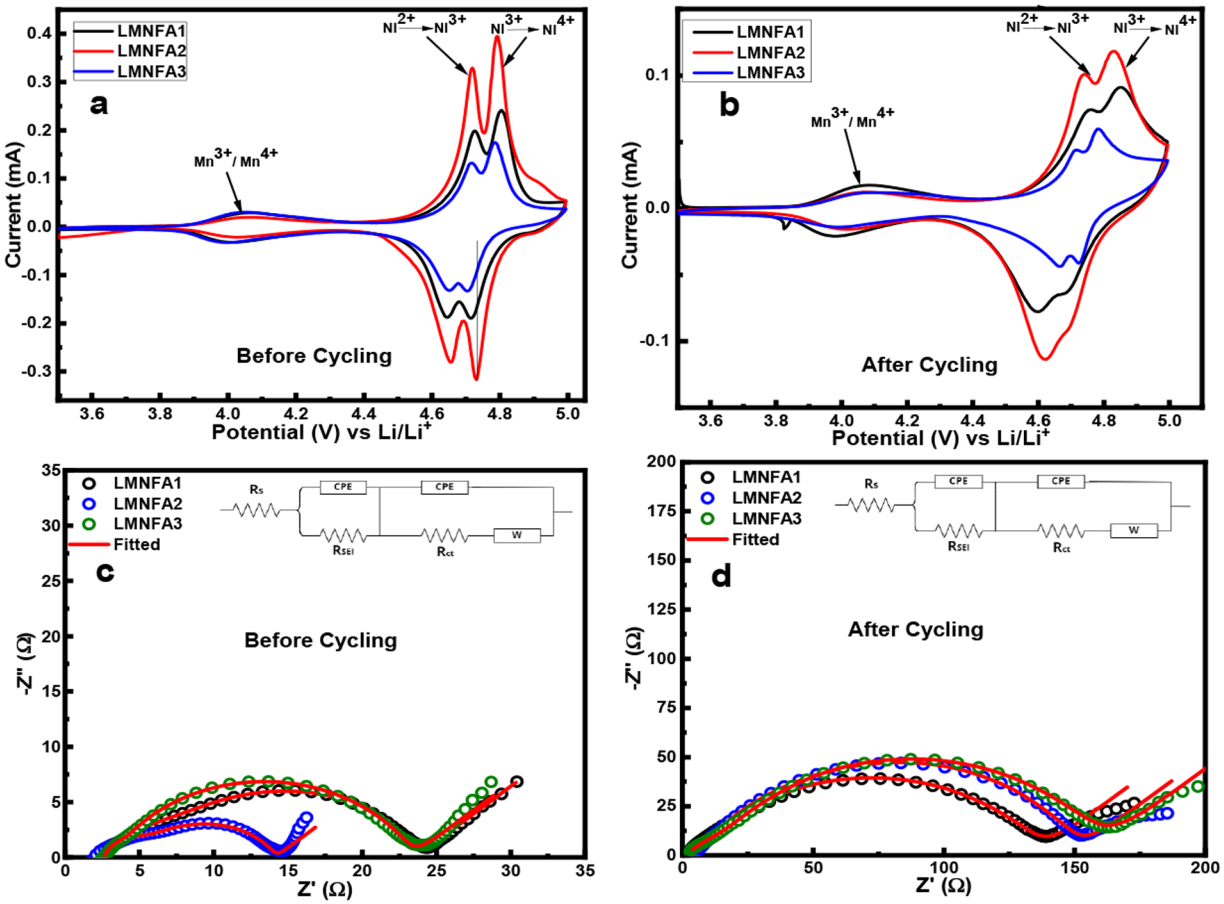

Figure 5. CV (a) before and (b) after cycling and Nyquist plots (c) before and (d) after cycling.

Table 3. Resistance Values Were Obtained from the EIS Fitting Data

	material					
	LMNFA1		LMNFA2		LMNFA3	
parameter	before cycling	after cycling	before cycling	after cycling	before cycling	after cycling
R_s (Ω)	2.443	1.379	1.138	1.209	2.617	1.230
R_{SEI} (Ω)	5.585	8.889	3.800	17.430	1.255	17.987
R_{ct} (Ω)	15.576	126.142	9.280	132.009	19.46	138.577
χ^2	0.301	0.417	0.624	0.528	0.492	0.225

lithiation and delithiation process. Here, the dopants Fe and Al are redox-inactive[8,46] and are not involved in charge compensation in the redox reactions. Mn and Ni ions are responsible for redox reactions.

As shown in panels a and b of Figure 5, the characteristic weak redox peaks for Mn^{3+}/Mn^{4+} are observed at ∼4.06/4.01 V (before cycling, Figure 5a) and ∼4.08/3.98 V (after cycling, Figure 5b), which indicates the minimized content of Mn^{3+} in the cathode active material. This minimized content of Mn^{3+} in the spinel improves the stability of the material by reducing the J−T effect and results in better electrochemical performance.[7] The second pair of redox peaks observed at ∼4.71/4.65 and 4.79/4.72 V (before cycling, Figure 5a) and 4.74/4.61 and 4.83/4.68 V (after cycling, Figure 5b) corresponds to the redox behavior of Ni^{2+}/Ni^{3+} and Ni^{3+}/Ni^{4+}, respectively. From the CV curves, we can observe that the peak current is not the same for all of the materials, even though the scan rate is maintained the same. The peak current is varied concerning cathode materials, which is influenced by the varied concentration of the redox active species in the cathode active materials.[47,47] The material LMNFA2 showed an increased peak current and sharp redox peaks, and these behaviors might be due to the faster diffusion of Li^+ ions. As already discussed above in the XRD section, the dominant (111) plane influences the electrochemical capabilities of the materials because it is densely packed with Mn ions, which mitigates the dissolution of Mn and provides faster Li^+ diffusion channels. These observed redox peaks are dominating the overall redox behavior of the materials, which influences the high voltage operational capabilities of the cathode active materials. In CV, Fe and Al have not shown any redox activity because these two are redox-inactive but act as an electrochemical stabilizer to improve stability.[12,46]

The Li^+ ion diffusion kinetic studies were performed through EIS, and the Nyquist plots for all of the sets of materials before and after GCD studies are given in panels c and d of Figure 5. The inset of panels c and d of Figure 5 shows the equivalent circuit used to fit the data, where CPE denotes constant phase

https://doi.org/10.1021/acs.energyfuels.3c03794
Energy Fuels 2024, 38, 4653−4665

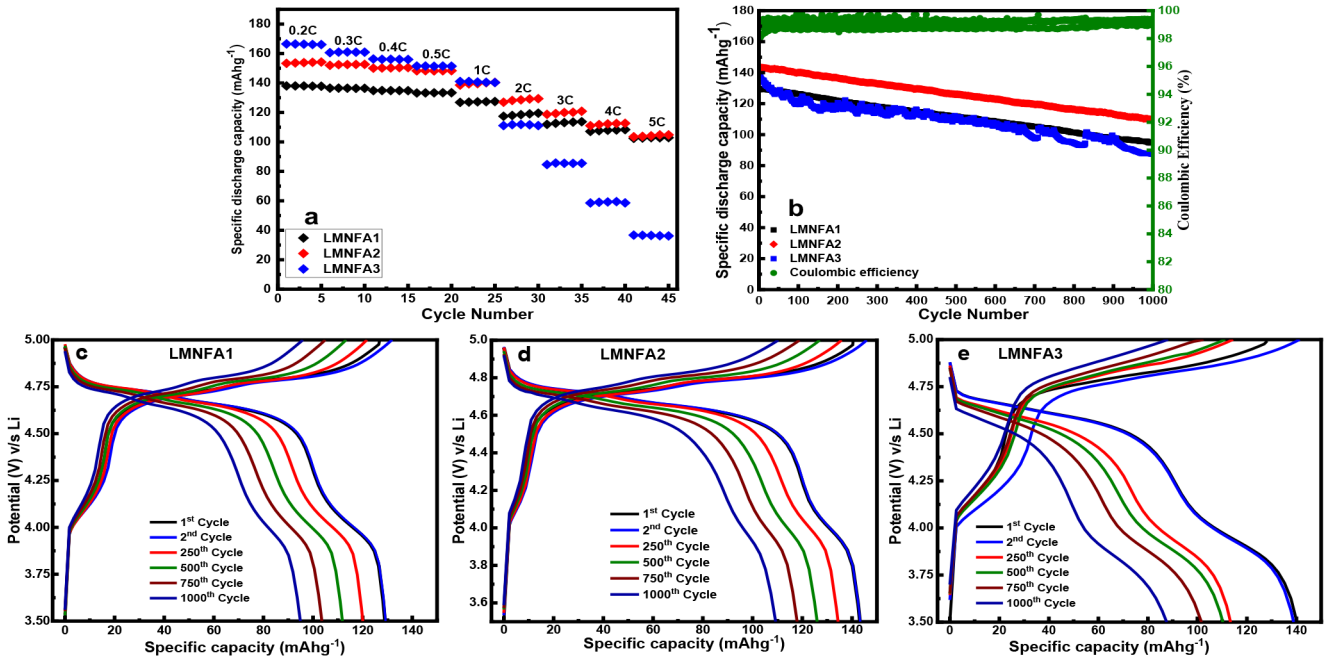

Figure 6. (a) Rate capability, (b) cycle stability (at 1 C), and (c−e) specific capacity versus potential (V) curves of LMNFA1, LMNFA2, and LMNFA3.

element, R_s denotes ohmic resistance, R_{SEI} denotes resistance of the SEI, R_{ct} denotes charge transfer resistance, and W denotes Warburg diffusion impedance. In Figure 5c, all materials showed a semicircle in the high-frequency region as a result of charge transfer resistance (R_{ct}) and SEI resistance (R_{SEI}); this semicircle in the high-frequency region indicates the Li^+ ion insertion into the electrode/electrolyte interface. Also, we can observe that a straight line in the low-frequency region indicates the interfacial resistance and corresponds to Warburg impedance (W). Figure 5d. shows the Nyquist plots for the same materials but after cycling, which exhibits a large difference in the impedance. After 1000 repeated charge/discharge cycles, the resistance of the materials is increased, which leads to the capacity fade. The fitted values of the equivalent circuit are given in Table 3.

Figure 6a depicts the rate capabilities of LMNFA1, LMNFA2, and LMNFA3 electrodes at 0.2−5 current densities (C rate) with a 3.5−5.0 V voltage window. Here, the performance of LMNFA2 at different current densities is better than that of LMNFA1 and LMNFA3 materials. The three substituents for Mn in LMO are Ni^{3+}, Al^{3+}, and Fe^{3+} and contributed differently to the performance of the cathode materials. This variation is due to the largely exposed facet of the plane (111) in the truncated octahedral crystals.[25] Correspondingly, the replacement of Ni^{3+}/Ni^{2+} ions for Mn^{3+} ions is responsible for the increase in the specific capacity of the material. Al^{3+} and Fe^{3+} ion substitution could enhance the conductivity and stability of the cathode material during the prolonged cycling process because they are not redox-active in the potential window. The Ni composition plays an important role in the capacity enhancement at higher currents, and the Al and Fe compositions act as stabilizers. Here, in Figure 6a, we can observe that the practical capacity at a lower C rate is higher than that of theoretical capacity, and this may be due to the reversible redox reaction of Li ions of the electrolyte and Li anode. Figure 6b shows a specific discharge capacity versus voltage curve at 1 C current density between 3.5 and 5 V over 1000 cycles. It can be observed that LMNFA2 has shown better specific discharge capacity and stable cyclability than the other two materials. This is due to a slightly higher ratio of Ni in LMNFA2 compared to LMNFA1 and LMNFA3. The materials LMNFA1, LMNFA2, and LMNFA3 show initial specific capacities of 129.01, 143.18, and 140.22 $mAhg^{-1}$, respectively. At the end of 1000 continuous charge/discharge cycles, the gradual decrease in capacity is observed up to 94.86, 109.29, and 87.59 $mAhg^{-1}$ with a capacity retention of 73.52, 76.33, and 62.47%, respectively. The capacity retention of LMNFA2 is more than that of LMNFA1 and LMNFA3 as a result of more Ni concentration and lesser capacity retention of LMNFA1 and LMNFA3 as a result of lesser proportions of Ni, Fe, and Al. Here, Ni acts as a capacity enhancer, and Fe and Al act as electrochemical stabilizers. In addition, the other reason might be the crystal plane orientation of the truncated octahedral geometry. The XRD result values (Table 2) supported the statement. The GCD profiles are shown graphically (panels c−e of Figure 6) to visualize the decrease in specific discharge capacities of the electrodes. The initial discharge capacities of LMNFA1, LMNFA2, and LMNFA3 are 129.01, 143.18, and 140.22 $mAhg^{-1}$ at a 1 C rate, while at the end of 1000 continuous GCD cycles, the specific capacity has decreased to 94.86, 109.29, and 87.59 $mAhg^{-1}$ with a coulombic efficiency of 98, 99, and 99%, respectively. The discharge capacity of LMNFA1, LMNFA2, and LMNFA3 in the first cycle at 1 C rate is slightly higher than that of charge capacities (panels c and d of Figure 6). This difference in charge and discharge capacity is because the cells were tested from 0.2 to 5 C rate and then immediately 1 C rate without resting time. This sudden change in current from 5 to 1 C rate may lead to structural interferences and transportation of irregular amounts of Li^+ ions. As a result, a smaller number of Li^+ ions may be intercalated during the charging and more Li^+ ions are

https://doi.org/10.1021/acs.energyfuels.3c03794
Energy Fuels 2024, 38, 4653−4665

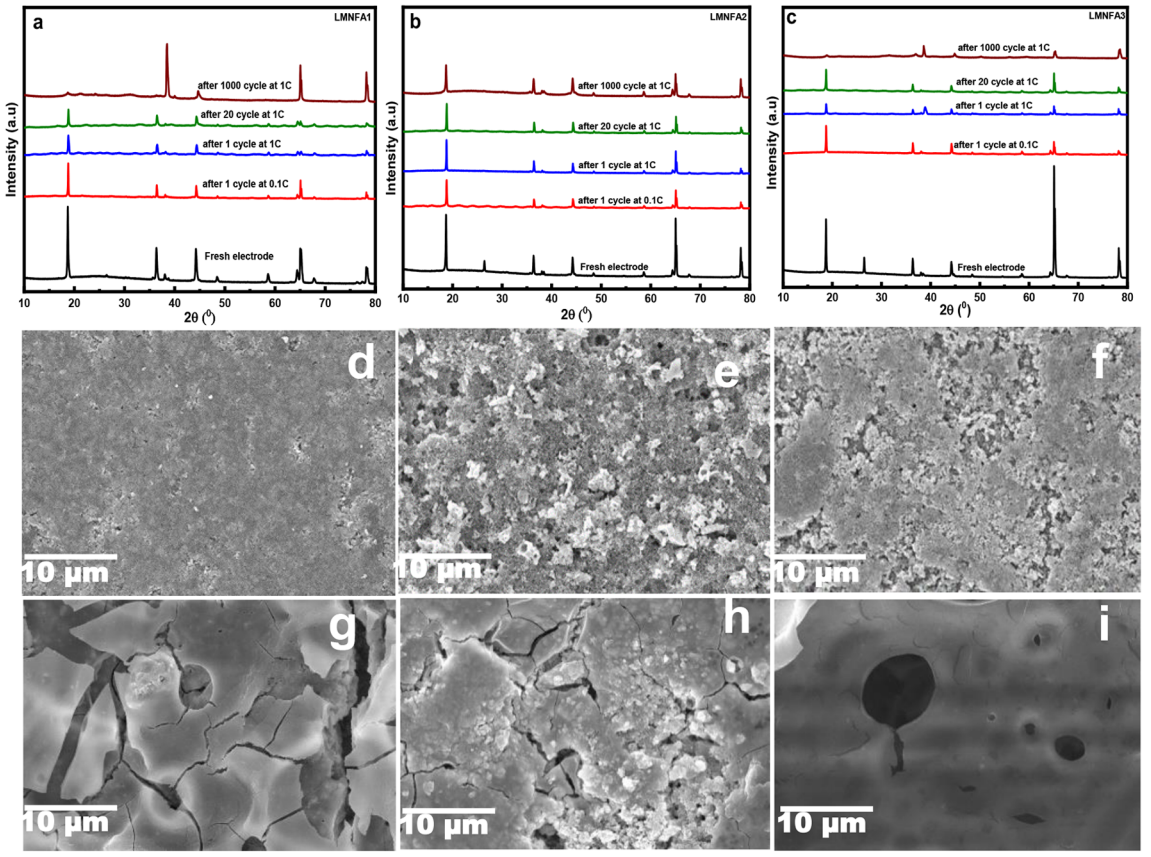

Figure 7. XRD patterns of the electrodes at different GCD cycle intervals of (a) LMNFA1 (b) LMNFA2, and (c) LMNFA1 and FE-SEM images of the electrodes (d) LMNFA1, (e) LMNFA2, and (f) LMNFA1 before and (g) LMNFA1, (h) LMNFA2, and (i) LMNFA1 after electrochemical testing.

deintercalated during the discharge process at 1 C. The normal charge−discharge behavior was observed from the second cycle onward. The above results are compared to the published results of spinel cathode material $LiMn_{1.5}Ni_{0.5}O_4$ with similar morphological features,[48−50] which enlightens the present cathode materials with the appropriate ratio of cation substitution improving the cell performance.

4. IMPACT OF PLANE ORIENTATION ON THE ELECTROCHEMICAL PERFORMANCE

The cation migration and conforming surface chemical evolution are always making an impact on the electrochemical performance, especially when it is operated within the wider range of the voltage window. The kind of uncontrolled reactions can occur through unexpected reactions, resulting from the complicated cation migration phenomena by the structural instability over the electrochemical cycling process, which implies their cyclic performance. Reports of Liu et al.[48] have shown that the material with fully exposed (111) planes has not shown better performance. However, the materials along with truncated geometry and more exposed (111) planes and less exposed (100) and (110) planes have shown better performance. This is due to (100) and (110) planes being well-aligned to wider Li^+ ion diffusion channels, which are in favor of stable interfacial contact establishment between the cathode and electrolyte.[48,51] This type of plane exposure will help to control the side reaction such as dissolution of active material, decomposition and passivation of the binder, as well as conductive carbon.[52] The prevention of such unwanted side reactions makes the crystal structure stable and avoids the structural evolution, which causes deterioration of the cathode structure. The Ni- and Fe-substituted LMO spinel cathode material with an exposed (111) plane with truncated octahedral geometry has shown enhancement in cycling stability and rate capability. The exposed (111) plane in LMNFA cathode materials provides channels for Li^+ ions and lowers the dissolution of Mn ions with extra stable surface orientation than other crystal facets of the cathode.[27,28] The highest specific discharge capacity and better capacity retention delivered by the LMNFA2 cathode demonstrates that the exposed (111) plane orientation in the crystal structure is more stable and could meritoriously reduce the dissolution of Mn ions. This more stable and exposed plane will delay the structure rearrangements during cycling and lead to better capacity retention.[53] In the crystal structure, the dominant (111) plane surfaces were densely packed with Mn ions and were less exposed to the dissolution compared to the (100) and (110) plane surfaces, which are less densely packed with Mn ions.[7] These less densely packed Mn ions are more liable to interact with electrolytes and accelerate the Mn dissolution. Here, the minimized Mn dissolution leads to the superior cycle life and enhanced discharge capacity with the support of Ni, Fe, and Al as dopants.[20] From the literature, there are some theoretical studies that suggest that the majority of Mn ions will be at the surface in a trivalent state.[45,46] These trivalent Mn ions will disproportionate into tetravalent and divalent Mn ions, and the tetravalent Mn ions will be retained in a solid state, whereas the divalent Mn ions will be dissolved into an

https://doi.org/10.1021/acs.energyfuels.3c03794
Energy Fuels 2024, 38, 4653−4665

electrolyte solution, which leads to degradation of the cathode.[54] Reports of Sun et al. showed that the density functional theory (DFT)-based calculations on dissolution energies of surface orientations of Mn at (100), (110), and (111) planes are 13.8, 8.6, and 5.3 eV respectively. The plane (111) surface has shown maximum positive dissolution energy, which has more competence to avoid Mn dissolution compared to the other two plane surfaces (100) and (110) and is more susceptible to Mn dissolution, which leads to capacity loss and reduced cycle life.[55] Our materials also showed the same behavior and correlate with the experimental studies, and the material with a more exposed (111) plane surface has shown superior performance. As discussed earlier in the XRD studies, the LMNFA2 cathode material has a crystal structure with extensively exposed (111) plane and has shown superior capacity as well as retention compared to LMNFA1 and LMNFA3. Although the LMNFA3 material showed higher discharge capacity initially, later, it decayed faster than the other two materials over continuous cycling. This might be due to the substituent concentration effects because it has a higher Mn content in the structure. LMNFA2 is shown to become an efficient cathode material for extended electrochemical applications in LIBs.

5. POST-ELECTROCHEMICAL TEST ANALYSIS OF ELECTRODES

Generally, the oxide-based cathode materials exhibit structural changes during the charge−discharge cycles. We have attempted to track the changes by conducting the XRD studies for the electrodes at different cycled conditions at current densities of 0.1 C for the activation cycle and 1 C for the prolonged cycles. To know the structural and morphology changes of active-material-coated electrodes before and after electrochemical studies, XRD and FE-SEM studies were conducted. Panels a−c of Figure 7 show the XRD results of the fresh and used electrodes. Initially, at 0.1 C rate, there is no large difference between the diffraction patterns from the fresh electrodes and the electrode after one cycle at a low current density of 0.1 C rate. Later, slight changes in diffraction patterns can be observed in the peak intensity at 2θ of ∼18.5, which corresponds to the (111) plane, and finally, the results clearly show that after 1000 continuous charge−discharge cycles, there is not much change in the peak position of LMNFA2 material compared to XRD results of fresh electrodes. This indicates that there is not much structural change in the cathode even after 1000 cycles. However, in the other two materials, LMNFA1 and LMNFA3, the peak positions are not maintained in comparison to fresh electrodes, which is due to material degradation over the repeated cycling. The material LMNFA2 with a more exposed (111) plane has shown better electrochemical performance. This indicates that the crystal orientation of the material plays a major role in the enhancement of the electrochemical performance of the material. The FE-SEM images of the electrode surface before and after electrochemical studies are given in Figure 7, which shows that the fresh electrodes (panels d−f of Figure 7) do not show any kind of cracks on the surface, whereas used electrodes (panels g−i of Figure 7) have developed cracks and holes, which provide an idea about the cause for the electrochemical performance degradation. The extent of cracks is not the same in all of the cases. As mentioned above in XRD studies, the materials with a more exposed (111) plane are less prone to electrode degradation, which can be visualized with the given images.

6. CONCLUSION

In summary, a set of trication-substituted LMO spinel cathode materials was synthesized with truncated octahedral geometry via the simple sol−gel method. XRD and Rietveld refinement results show that the spinel materials are formed with a pure phase $Fd\bar{3}m$ space group. The trication-substituted LMNFA cathode materials with the appropriate ratio of substituents exhibit a well-defined crystal structure with a desired orientation of exposed (111) planes to minimize Mn dissolution along with (110) plane orientations to support the Li^+ diffusion. As a result of the advantageous crystal plane orientation, the trisubstituted cathode material manifests superior rate capability as well as cycle life with a high specific capacity. Furthermore, the modified spinel cathode material LMNFA2 exhibited 76.3% of capacity retention after 1000 prolonged cycles, and the specific capacity is 109.29 mAh g^{-1} with ∼99% coulombic efficiency at 1 C. The aforementioned results displayed that the crystal plane orientation plays an important role in the minimization of transition metal dissolution into the electrolyte to boost the performance of the cathode material. This combination of elements and the approach in designing the cathode materials show great potential toward the development of high-energy-density spinel cathode materials along with high rate capability and cycle stability.

■ ASSOCIATED CONTENT

Supporting Information

The Supporting Information is available free of charge at https://pubs.acs.org/doi/10.1021/acs.energyfuels.3c03794.

Crystallographic data of the cubic spinel structure, particle size distribution histogram of FE-SEM images, and EDS elemental mapping images of LMNFA1, LMNFA2, and LMNFA3 (PDF)

■ AUTHOR INFORMATION

Corresponding Author

Girish Praveen Nayaka − *Physical and Materials Chemistry Division, Council of Scientific and Industrial Research (CSIR)−National Chemical Laboratory (NCL), Pune, Maharashtra 411008, India; Academy of Scientific and Innovative Research (AcSIR), Ghaziabad, Uttar Pradesh 201002, India;* orcid.org/0000-0001-8166-1465; Email: gp.nayaka@ncl.res.in

Authors

Bogalera Papaiah Shivamurthy − *Physical and Materials Chemistry Division, Council of Scientific and Industrial Research (CSIR)−National Chemical Laboratory (NCL), Pune, Maharashtra 411008, India; Academy of Scientific and Innovative Research (AcSIR), Ghaziabad, Uttar Pradesh 201002, India;* orcid.org/0000-0003-4126-9885

Marulasiddappa Thripuranthaka − *Physical and Materials Chemistry Division, Council of Scientific and Industrial Research (CSIR)−National Chemical Laboratory (NCL), Pune, Maharashtra 411008, India; Academy of Scientific and Innovative Research (AcSIR), Ghaziabad, Uttar Pradesh 201002, India;* orcid.org/0000-0002-5018-3939

https://doi.org/10.1021/acs.energyfuels.3c03794
Energy Fuels 2024, 38, 4653−4665

Manjusha V. Shelke − *Physical and Materials Chemistry Division, Council of Scientific and Industrial Research (CSIR)−National Chemical Laboratory (NCL), Pune, Maharashtra 411008, India; Academy of Scientific and Innovative Research (AcSIR), Ghaziabad, Uttar Pradesh 201002, India;* orcid.org/0000-0001-8323-2234

Complete contact information is available at: https://pubs.acs.org/10.1021/acs.energyfuels.3c03794

Notes

The authors declare no competing financial interest.

■ ACKNOWLEDGMENTS

Bogalera Papaiah Shivamurthy thanks CSIR, New Delhi, India [31/011(1129)/2019-EMR-I] for providing a research fellowship. Girish Praveen Nayaka thanks CSIR−NCL for providing the start-up fund (MLP036126) and all of the facilities.

■ REFERENCES

(1) Zhu, Z.; Zhang, D.; Yan, H.; Li, W.; Qilu. Precise Preparation of High Performance Spherical Hierarchical $LiNi_{0.5}Mn_{1.5}O_4$ for 5 V Lithium Ion Secondary Batteries. *J. Mater. Chem. A* **2013**, *1* (18), 5492.

(2) Talyosef, Y.; Markovsky, B.; Salitra, G.; Aurbach, D.; Kim, H.-J.; Choi, S. The Study of $LiNi_{0.5}Mn_{1.5}O_4$ 5-V Cathodes for Li-Ion Batteries. *J. Power Sources* **2005**, *146* (1−2), 664−669.

(3) Mereacre, V.; Stüble, P.; Ghamlouche, A.; Binder, J. R. Enhancing the Stability of $LiNi_{0.5}Mn_{1.5}O_4$ by Coating with Linbo3 Solid-State Electrolyte: Novel Chemically Activated Coating Process versus Sol-Gel Method. *Nanomaterials* **2021**, *11* (2), 548.

(4) Wang, L.; Li, H.; Huang, X.; Baudrin, E. A Comparative Study of Fd-3m and P4332 "$LiNi_{0.5}Mn_{1.5}O_4$. *Solid State Ionics* **2011**, *193* (1), 32−38.

(5) Shivamurthy, B. P.; Thripuranthaka, M.; Shelke, M. V.; Nayaka, G. P. Formation of the Secondary Phase Domain by Multi-Cation Substitution for the Superior Electrochemical Performance of Spinel Cathodes for High-Voltage Li-Ion Batteries. *ACS Appl. Energy Mater.* **2022**, *5* (12), 15345−15355.

(6) Taddesse, P.; Tsona, C.; Murali, N.; Babu, K. V. Effect of Ni and Fe Substitution on the Thermal, Structural, Vibrational Spectroscopic and Electrochemical Properties of $LiMn_2O_4$ Cathode Material. *Sci. Afr.* **2021**, *14*, No. e00975.

(7) Sharma, P.; Das, C.; Indris, S.; Bergfeldt, T.; Mereacre, L.; Knapp, M.; Geckle, U.; Ehrenberg, H.; Darma, M. S. D. Synthesis and Characterization of a Multication Doped Mn Spinel, $Li-Ni_{0.3}Cu_{0.1}Fe_{0.2}Mn_{1.4}O_4$, as 5 V Positive Electrode Material. *ACS Omega* **2020**, *5* (36), 22861−22873.

(8) Wang, S.; Xiang, M.; Lu, Y.; Guo, J.; Su, C.; Bai, H.; Liu, X. Facile Solid-State Combustion Synthesis of Al−Ni Dual-Doped $LiMn_2O_4$ Cathode Materials. *J. Mater. Sci. Mater. Electron.* **2020**, *31* (8), 6036−6044.

(9) Liu, H.; Li, M.; Xiang, M.; Guo, J.; Bai, H.; Bai, W.; Liu, X. Effects of Crystal Structure and Plane Orientation on Lithium and Nickel Co-doped Spinel Lithium Manganese Oxide for Long Cycle Life Lithium-Ion Batteries. *J. Colloid Interface Sci.* **2021**, *585*, 729−739.

(10) Piao, J.-Y.; Duan, S.-Y.; Lin, X.-J.; Tao, X.-S.; Xu, Y.-S.; Cao, A.-M.; Wan, L.-J. Surface Zn Doped $LiMn_2O_4$ for an Improved High Temperature Performance. *Chem. Commun.* **2018**, *54* (42), 5326−5329.

(11) Garhi, G.; Aklalouch, M.; Favotto, C.; Mansori, M.; Saadoune, I. Coprecipitation Synthesis of Co-Doped $LiMn_{1.5}Ni_{0.5}O_4$ Material as 5 V Cathode of Li-Ion Batteries with Huge Rate Capability for High Power Applications. *J. Electroanal. Chem.* **2020**, *873*, No. 114413.

(12) Xu, W.; Zheng, Y.; Cheng, Y.; Qi, R.; Peng, H.; Lin, H.; Huang, R. Understanding the Effect of Al Doping on the Electrochemical Performance Improvement of the $LiMn_2O_4$Cathode Material. *ACS Appl. Mater. Interfaces* **2021**, *13* (38), 45446−45454.

(13) Bao, S. J.; Liang, Y. Y.; Zhou, W. J.; He, B. L.; Li, H. L. Enhancement of the Electrochemical Properties of $LiMn_2O_4$ through Al^{3+} and F^- Co-substitution. *J. Colloid Interface Sci.* **2005**, *291* (2), 433−437.

(14) Han, D.-W.; Ryu, W.-H.; Kim, W.-K.; Eom, J.-Y.; Kwon, H.-S. Effects of Li and Cl Codoping on the Electrochemical Performance and Structural Stability of $LiMn_2O_4$ Cathode Materials for Hybrid Electric Vehicle Applications. *J. Phys. Chem. C* **2013**, *117* (10), 4913−4919.

(15) Liu, H.; Yang, F.; Guo, J.; Xiang, M.; Bai, H.; Wang, R.; Su, C. Facile Combustion Synthesis of Amorphous Al_2O_3-Coated $LiMn_2O_4$ cathode Materials for High-Performance Li-Ion Batteries. *New J. Chem.* **2021**, *45* (23), 10534−10540.

(16) Shapira, A.; Tiurin, O.; Solomatin, N.; Auinat, M.; Meitav, A.; Ein-Eli, Y. Robust AlF3 Atomic Layer Deposition Protective Coating on $LiMn_{1.5}Ni_{0.5}O_4$ Particles: An Advanced Li-Ion Battery Cathode Material Powder. *ACS Appl. Energy Mater.* **2018**, *1* (12), 6809−6823.

(17) Li, Q. L.; Xu, W. Q.; Bai, H. L.; Guo, J. M.; Su, C. W. ZnO-Coated $LiMn_2O_4$ Cathode Material for Lithium-Ion Batteries Synthesized by a Combustion Method. *Ionics* **2016**, *22* (8), 1343−1351.

(18) Zhao, J.; Wang, Y. Atomic Layer Deposition of Epitaxial ZrO_2 Coating on $LiMn_2O_4$ Nanoparticles for High-Rate Lithium Ion Batteries at Elevated Temperature. *Nano Energy* **2013**, *2* (5), 882−889.

(19) Fu, S.; Zhang, Y.; Bian, Y.; Xu, J.; Wang, L.; Liang, G. Effect of Fe^{3+} and/or PO_4^{3-} Doping on the Electrochemical Performance of $LiNi_{0.5}Mn_{1.5}O_4$ Cathode Material for Li-Ion Batteries. *Ind. Eng. Chem. Res.* **2023**, *62* (2), 1016−1028.

(20) Kim, J. S.; Kim, K.; Cho, W.; Shin, W. H.; Kanno, R.; Choi, J. W. A Truncated Manganese Spinel Cathode for Excellent Power and Lifetime in Lithium-Ion Batteries. *Nano Lett.* **2012**, *12* (12), 6358−6365.

(21) Jiang, C.; Tang, Z.; Wang, S.; Zhang, Z. A Truncated Octahedral Spinel $LiMn_2O_4$ as High-Performance Cathode Material for Ultrafast and Long-Life Lithium-Ion Batteries. *J. Power Sources* **2017**, *357*, 144−148.

(22) Karunawan, J.; Suryadi, P. N.; Mahfudh, L.; Santosa, S. P.; Sumboja, A.; Iskandar, F. Truncated Octahedral Shape of Spinel $LiNi_{0.5}Mn_{1.5}O_4$ via a Solid-State Method for Li-Ion Batteries. *Energy Fuels* **2023**, *37* (1), 754−762.

(23) Hashem, A. M.; Abbas, S. M.; Hou, X.; Eid, A. E.; Abdel-Ghany, A. E. Facile One Step Synthesis Method of Spinel $LiMn_2O_4$ Cathode Material for Lithium Batteries. *Heliyon* **2019**, *5* (7), No. e02027.

(24) Lee, S.-N.; Park, D.; Kim, J.; Moon, S.-H.; Jang, J.-S.; Kim, S.-B.; Shin, J.-H.; Park, Y.; Park, K.-W. Enhanced Cycling Performance of Fe-doped $LiMn_2O_4$ Truncated Octahedral Cathodes for Li-Ion Batteries. *ChemElectroChem* **2022**, *9* (11), No. e202200385.

(25) Huang, S.; Wu, H.; Chen, P.; Guo, Y.; Nie, B.; Chen, B.; Liu, H.; Zhang, Y. Facile PH-Mediated Synthesis of Morphology-Tunable $MnCO_3$ and Their Transformation to Truncated Octahedral Spinel $LiMn_2O_4$ Cathode Materials for Superior Lithium Storage. *J. Mater. Chem. A* **2015**, *3* (7), 3633−3640.

(26) Hendriks, R.; Cunha, D. M.; Singh, D. P.; Huijben, M. Enhanced Lithium Transport by Control of Crystal Orientation in Spinel $LiMn_2O_4$ Thin Film Cathodes. *ACS Appl. Energy Mater.* **2018**, *1* (12), 7046−7051.

(27) Yang, C.; Deng, Y.; Gao, M.; Yang, X.; Qin, X.; Chen, G. High-Rate and Long-Life Performance of a Truncated Spinel Cathode Material with off-Stoichiometric Composition at Elevated Temperature. *Electrochim. Acta* **2017**, *225*, 198−206.

(28) Luo, X.; Xiang, M.; Li, Y.; Guo, J.; Liu, X.; Bai, H.; Bai, W.; Su, C. Surface-Orientation for Boosting the High-Rate and Cyclability of Spinel $LiNi_{0.02}Mn_{1.98}O_4$ Cathode Material. *Vacuum* **2020**, *179*, No. 109505.

(29) Momma, K.; Izumi, F. VESTA 3 for Three-Dimensional Visualization of Crystal, Volumetric and Morphology Data. *J. Appl. Crystallogr.* **2011**, *44* (6), 1272−1276.
(30) Tabassam, L.; Nazir, T.; Manzoor, U.; Mehmood, S.; Hassan, M. U.; Bhatti, A. S. Raman Spectroscopy of Nominally Ni-Doped $LiMn_{2-x}Ni_xO_4$ ($0 \leq x \leq 0.20$). *Mater. Res. Express* **2019**, *6* (11), 115550.
(31) Dos Santos Junior, G. A.; Fortunato, V. D. S.; Bastos, G. A. A.; Silva, G. G.; Ortega, P. F. R.; Lavall, R. L. High-Performance Lithium-Ion Hybrid Supercapacitors Based on Lithium Salt/Imidazolium Ionic Liquid Electrolytes and Ni-Doped $LiMn_2O_4$ Cathode Materials. *ACS Appl. Energy Mater.* **2020**, *3* (9), 9028−9039.
(32) Samarasingha, P. B.; Andersen, N. H.; Sørby, M. H.; Kumar, S.; Nilsen, O.; Fjellvåg, H. Neutron Diffraction and Raman Analysis of $LiMn_{1.5}Ni_{0.5}O_4$ Spinel Type Oxides for Use as Lithium Ion Battery Cathode and Their Capacity Enhancements. *Solid State Ionics* **2016**, *284*, 28−36.
(33) Nageswara Rao, B.; Narsimulu, D.; Srinadhu, E. S.; Satyanarayana, N. Structural, Electrical, and Dielectric Properties of Nickel-Doped Spinel $LiMn_2O_4$ Nanorods. *Ionics* **2019**, *25* (3), 981−990.
(34) Bhatia, A.; Dridi Zrelli, Y.; Pereira-Ramos, J. P.; Baddour-Hadjean, R. Detailed Redox Mechanism and Self-Discharge Diagnostic of 4.9 V $LiMn_{1.5}Ni_{0.5}O_4$ spinel Cathode Revealed by Raman Spectroscopy. *J. Mater. Chem. A* **2021**, *9* (23), 13496−13505.
(35) Boulet-Roblin, L.; Villevieille, C.; Borel, P.; Tessier, C.; Novák, P.; Ben Yahia, M. Versatile Approach Combining Theoretical and Experimental Aspects of Raman Spectroscopy to Investigate Battery Materials: The Case of the $LiNi_{0.5}Mn_{1.5}O_4$ Spinel. *J. Phys. Chem. C* **2016**, *120* (30), 16377−16382.
(36) Vijayan, S.; Kirubasankar, B.; Pazhamalai, P.; Solarajan, A. K.; Angaiah, S. Electrospun Nd^{3+}-Doped $LiMn_2O_4$ Nanofibers as High-Performance Cathode Material for Li-Ion Capacitors. *ChemElectroChem* **2017**, *4* (8), 2059−2067.
(37) Bakierska, M.; Świętoslawski, M.; Gajewska, M.; Kowalczyk, A.; Piwowarska, Z.; Chmielarz, L.; Dziembaj, R.; Molenda, M. Enhancement of Electrochemical Performance of $LiMn_2O_4$ Spinel Cathode Material by Synergetic Substitution with Ni and S. *Materials* **2016**, *9* (5), 366.
(38) Ryu, J. H.; Park, B. G.; Kim, S. B.; Park, Y. J. Effects of Surface Area on Electrochemical Performance of $Li[Ni_{0.2}Li_{0.2}Mn_{0.6}]O_2$ Cathode Material. *J. Appl. Electrochem.* **2009**, *39* (7), 1059−1066.
(39) Wang, F. X.; Xiao, S. Y.; Gao, X. W.; Zhu, Y. S.; Zhang, H. P.; Wu, Y. P.; Holze, R. Nanoporous $LiMn_2O_4$ Spinel Prepared at Low Temperature as Cathode Material for Aqueous Supercapacitors. *J. Power Sources* **2013**, *242*, 560−565.
(40) Zhao, H.; Li, D.; Wang, Y.; Li, F.; Wang, G.; Wu, T.; Wang, Z.; Li, Y.; Su, J. Sol-Gel Synthesis of Silicon-Doped Lithium Manganese Oxide with Enhanced Reversible Capacity and Cycling Stability. *Materials* **2018**, *11* (8), 1455.
(41) Gieu, J. B.; Winkler, V.; Courrèges, C.; El Ouatani, L.; Tessier, C.; Martinez, H. New Insights into the Characterization of the Electrode/Electrolyte Interfaces within $LiMn_2O_4/Li_4Ti_5O_{12}$ Cells, by X-Ray Photoelectron Spectroscopy, Scanning Auger Microscopy and Time-of-Flight Secondary Ion Mass Spectrometry. *J. Mater. Chem. A* **2017**, *5* (29), 15315−15325.
(42) Nesbitt, H. W.; Banerjee, D. Interpretation of XPS Mn(2p) Spectra of Mn Oxyhydroxides and Constraints on the Mechanism of MnO_2 Precipitation. *Am. Mineral.* **1998**, *83* (3−4), 305−315.
(43) Ji, Y.; Liu, H.; Guo, Y.; Guo, J.; Xiang, M.; Bai, W.; Liu, X.; Bai, H. Improved Capacity Retention and Ultralong Cycle Performance of Ni-Fe Co-doped $LiMn_2O_4$ Cathode Material at High Current Densities. *Colloids Surf., A* **2022**, *648*, 129259.
(44) Medvedeva, A.; Makhonina, E.; Pechen, L.; Politov, Y.; Rumyantsev, A.; Koshtyal, Y.; Goloveshkin, A.; Maslakov, K.; Eremenko, I. Effect of Al and Fe Doping on the Electrochemical Behavior of $Li_{1.2}Ni_{0.133}Mn_{0.534}Co_{0.133}O_2$ Li-Rich Cathode Material. *Materials* **2022**, *15* (22), 8225.
(45) Li, F.; Zhang, G.; Zhang, Z.; Yang, J.; Liu, F.; Jia, M.; Jiang, L. Regeneration of Al-Doped $LiNi_{0.5}Co_{0.2}Mn_{0.3}O_2$ Cathode Material by Simulated Hydrometallurgy Leachate of Spent Lithium-Ion Batteries. *Trans. Nonferrous Met. Soc. China* **2022**, *32* (2), 593−603.
(46) Callegari, D.; Coduri, M.; Fracchia, M.; Ghigna, P.; Braglia, L.; Anselmi Tamburini, U.; Quartarone, E. Lithium Intercalation Mechanisms and Critical Role of Multi-Doping in $LiFe_xMn_{2-x-y}Ti_yO_4$ as High-Capacity Cathode Material for Lithium-Ion Batteries. *J. Mater. Chem. C* **2022**, *10* (23), 8994−9008.
(47) Kim, T.; Choi, W.; Shin, H. C.; Choi, J. Y.; Kim, J. M.; Park, M. S.; Yoon, W. S. Applications of Voltammetry in Lithium Ion Battery Research. *J. Electrochem. Sci. Technol.* **2020**, *11*, 14−25.
(48) Liu, H.; Wang, J.; Zhang, X.; Zhou, D.; Qi, X.; Qiu, B.; Fang, J.; Kloepsch, R.; Schumacher, G.; Liu, Z.; Li, J. Morphological Evolution of High-Voltage Spinel $LiNi_{0.5}Mn_{1.5}O_4$ Cathode Materials for Lithium-Ion Batteries: The Critical Effects of Surface Orientations and Particle Size. *ACS Appl. Mater. Interfaces* **2016**, *8* (7), 4661−4675.
(49) Wang, P.; Li, H.; Wei, Y.; Zhao, D.; Mao, L.; Cui, X.; Zhang, H.; Zhou, X.; Li, S. Truncated Octahedral $LiNi_{0.5}Mn_{1.5}O_4$ with Excellent Electrochemical Properties for Lithium-Ion Batteries Prepared by a Graphite Assisted Calcination Method. *New J. Chem.* **2019**, *43* (38), 15396−15404.
(50) Nasrinpour, H.; Masoudpanah, S. M.; Soltanieh, M. Oxalate-Assisted Solvothermal Synthesis of Octahedral $LiMn_{1.5}Ni_{0.5}O_4$ Particles for Lithium-Ion Batteries. *J. Mater. Res. Technol.* **2021**, *13*, 61−69.
(51) Kong, F.; Zhang, G.; Wu, D.; Sun, F.; Tao, S.; Chu, S.; Qian, B.; Chu, W.; Song, L. Insight into the Cation Migration and Surface Structural Evolution of Spinel $LiNi_{0.5}Mn_{1.5}O_4$ Cathode Material for Lithium-Ion Batteries. *Chem. Eng. J.* **2023**, *451*, No. 138708.
(52) Kim, J.; Cha, H.; Lee, H.; Oh, P.; Cho, J. Surface and Interfacial Chemistry in the Nickel-Rich Cathode Materials. *Batteries Supercaps* **2020**, *3*, 309−322.
(53) Xu, C.; Li, J.; Feng, X.; Zhao, J.; Tang, C.; Ji, B.; Hu, J.; Cao, C.; Zhu, Y.; Butt, F. K. The Improved Performance of Spinel $LiMn_2O_4$ Cathode with Micro-Nanostructured Sphere-Interconnected-Tube Morphology and Surface Orientation at Extreme Conditions for Lithium-Ion Batteries. *Electrochim. Acta* **2020**, *358*, No. 136901.
(54) Manthiram, A. A Reflection on Lithium-Ion Battery Cathode Chemistry. *Nat. Commun.* **2020**, *11* (1), 1550.
(55) Sun, W.; Li, Y.; Xie, K.; Luo, S.; Bai, G.; Tan, X.; Zheng, C. Constructing Hierarchical Urchin-like $LiNi_{0.5}Mn_{1.5}O_4$ Hollow Spheres with Exposed {111} Facets as Advanced Cathode Material for Lithium-Ion Batteries. *Nano Energy* **2018**, *54*, 175−183.

https://doi.org/10.1021/acs.energyfuels.3c03794
Energy Fuels 2024, 38, 4653−4665

energy&fuels

pubs.acs.org/EF

Article

Performance Analysis of Regenerated rGO Electrodes from Spent Li-ion Battery Anodes for Secondary Energy Device Applications

Bogalera Papaiah Shivamurthy, Girish Praveen Nayaka,* and Girish Santhosh

Cite This: *Energy Fuels* 2023, 37, 3188−3195

Read Online

ACCESS | Metrics & More | Article Recommendations

ABSTRACT: At the end of their life, disposal of Li-ion batteries is a severe issue. Therefore, this study aims to recycle graphite from the spent anode material and synthesize reduced graphene oxide (rGO) in an eco-friendly approach. rGO was prepared from graphene oxide (GO), which is obtained from the spent graphite (G) by the modified Hummer's method. The graphene powder was reduced by ascorbic acid at 60 °C through a chemical reduction process using GO. The structural morphology of G, GO, and rGO was characterized by X-ray diffraction (XRD), Fourier transform infrared (FTIR) spectroscopy, ultraviolet−visible (UV−vis) spectroscopy, X-ray photoelectron spectroscopy (XPS), Raman spectroscopy, field-emission scanning electron microscopy (FE-SEM), and high-resolution transmission electron microscopy (HR-TEM). The Brunauer−Emmett−Teller (BET) surface area and porous behavior of rGO are studied and checked for their capacity in supercapacitor applications. The cyclic voltammogram of rGO (between 0.0−1.0 V) showed a pair of redox peaks corresponding to the electrical double-layer capacitance. The galvanostatic charge/discharge studies for rGO showed a discharge capacity of 278.5 F/g after 200 cycles (coated on a glassy carbon electrode) and 207.9 F/g after 2000 cycles (coated on a Toray carbon electrode) at a 1 A/g current density.

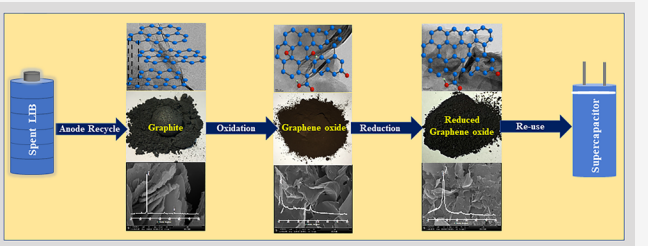

Downloaded via NATL CHEMICAL LABORATORY on March 21, 2023 at 12:19:43 (UTC).
See https://pubs.acs.org/sharingguidelines for options on how to legitimately share published articles.

1. INTRODUCTION

Li-ion batteries (LIBs) are the key components for the energy sources in the present era owing to their uniqueness like lightweight, long cycle life, high energy density, and small memory effect.[1] A study by Natarajan et al.[2] has reported that the consumption of spent LIBs between 2017 and 2030 is estimated to be 11 million tons or more. Ultimately, this huge amount of spent LIBs will cause major environmental issues if not handled properly because these spent LIBs contain heavy metals, hazardous gases, and flammable elements.[3] Therefore, disposal of these spent LIBs into a landfill is impossible, as this will cause danger to the health and environment by contaminating soil and water.[4] As a result, recycling these spent LIBs is the most favored way to conquer the problem connected with it.

We are in urgent need of scalable, effective, environmentally friendly, and economical recycling methods to recover metals from spent LIBs. The majority of the recycling technologies are not cost-effective and could not recover the critical components. Throughout the recycling of these spent LIBs, more extra attentiveness has been given to cathode materials recycling than the anode materials. This may be due to the presence of transition metals in oxide materials as they take part in several applications.[5] During the recycling of cathode materials, LIBs' external metal cases and anodes were neglected. The anode materials contain graphite in a larger percentage, which can also be recycled easily and used to synthesize graphene. Due to its excellent electrical properties, graphene has been used in a variety of applications like supercapacitors, fuel cells, batteries, solar cells, and many more.[6−10]

Till today, many methods have been developed to synthesize reduced graphene oxide (rGO), viz., chemical vapor deposition,[11] thermal reduction,[12] arc discharge,[13] epitaxial growth,[14] and solution-based methods.[15] Among the mentioned methods, the solution-based method is the best method to synthesize rGO in bulk at a low cost.[15] To synthesize rGO, graphene oxide (GO) is reduced chemically using various reducing agents like sodium borohydrate,[16] hydrazine monohydrate,[17] hydroquinone,[18] and alkali.[19] All of these methods need expensive and ecologically hazardous chemicals in sophisticated environments. By keeping this in mind, in this study, we have used ascorbic acid to reduce GO. Ascorbic acid is an environmentally friendly mild reducing agent that has a non-toxic property and has also been used as a primary

Received: November 17, 2022
Revised: January 16, 2023
Published: January 26, 2023

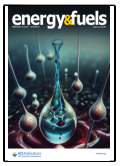

ACS Publications

© 2023 American Chemical Society

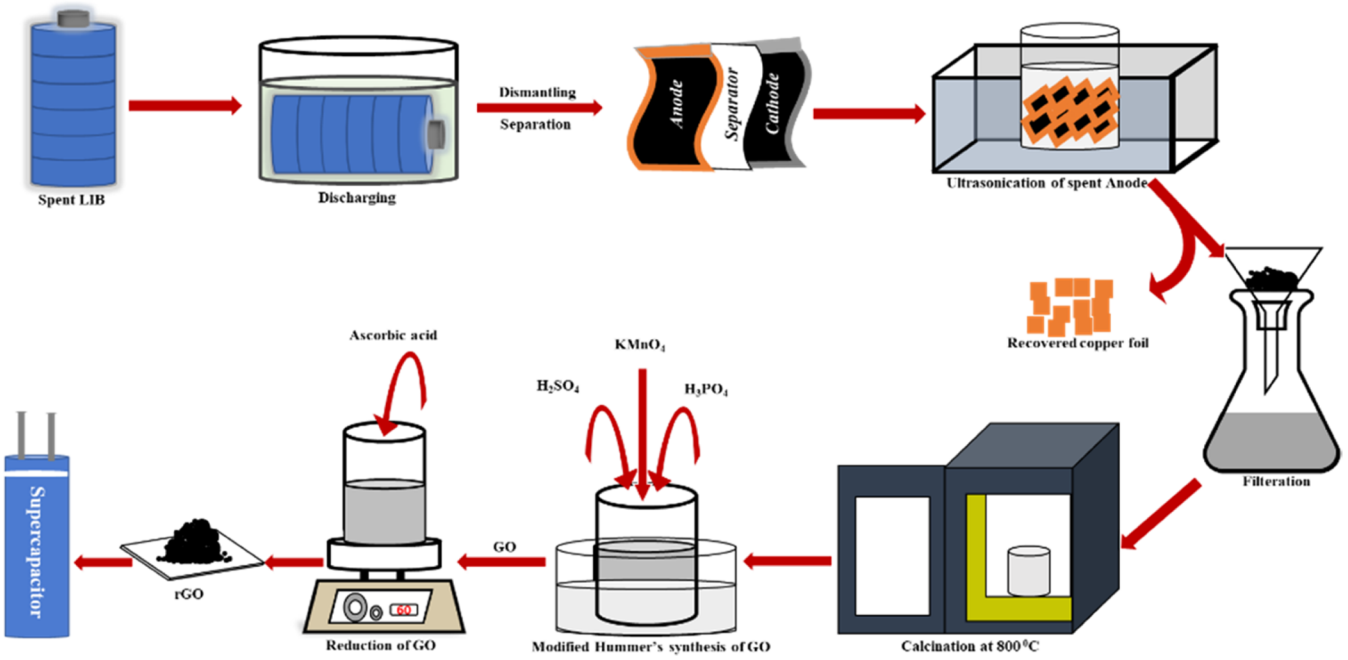

Figure 1. Flow chart for the complete recycling process.

reductant in laboratories. It is naturally employed as a reducing agent in living organisms.[20,21]

In this study, GO was successfully prepared from graphite (G) powder recovered from the spent LIB anode through the modified Hummer's method. The prepared GO was reduced by a reducing agent, ascorbic acid, at 60 °C for about 30 min. The flow chart for the complete process is depicted in Figure 1. The as-synthesized samples were characterized by X-ray diffraction (XRD), Fourier transform infrared (FTIR) spectroscopy, ultraviolet−visible (UV−vis) spectroscopy, X-ray photoelectron spectroscopy (XPS), Raman, Brunauer−Emmett−Teller (BET) surface area, field-emission scanning electron microscopy (FE-SEM), and high-resolution transmission electron microscopy (HR-TEM). Electrochemical studies were carried out to know cyclic voltammetry, impedance, and charge−discharge behaviors. In the present study, we propose an easy waste-to-wealth approach for synthesizing rGO from spent LIBs.

2. EXPERIMENTAL SECTION

2.1. Materials and Reagents. Chemicals and reagents used in this study are of analytical grade. The graphite powder used here was taken from spent Li-ion polymer batteries (iPhone) and dismantled to obtain the anode material. To avoid explosion and hampering, the spent LIBs were discharged fully in a salt solution and dissembled to take apart the anode and cathode materials layered on coiled Al foil and Cu foil, correspondingly. The Cu foil was uncoiled and cut into small pieces of 1 × 1 cm^2 and then immersed in deionized water followed by sonication. After the complete removal of the active anode material from Cu foil, it was filtered and calcined at 800 °C for 2 h under air atmosphere to burn out the binder and other organic materials.

2.2. Synthesis of Graphene Oxide from Graphite of the Spent LIB Anode. GO was prepared through a modified Hummer's method using spent graphite powder recovered from spent LIBs.[22] H_3PO_4 and H_2SO_4 with a volume ratio of 1:9 was taken in a beaker and stirred for 30 min in an ice bath. To this, 1 g of recovered graphite powder was added, followed by the slow addition of 6 g of $KMnO_4$, and stirred for 30 min till the color of the mixture turns dark brown, and then 100 mL of deionized water was added slowly, which led to an exothermic reaction. Finally, to stop the $KMnO_4$ reaction, a mixture of H_2O_2 and deionized water was added. After keeping this mixture overnight, the supernatant liquid was separated from the powder and neutralized to convert it into water-soluble nitrogen, phosphorus, and potassium plant fertilizer (also known as NPK fertilizers) to balance the soil pH level, and the separated powder sample was washed with a mixture of HCL and water ratio of 1:10. Finally, the obtained GO was dried in a hot air oven at 60 °C. This was ground in an agate mortar for the use of the next step.

2.3. Reduction of GO Using Ascorbic Acid. The obtained GO (0.5 g) was dispersed in a beaker containing 100 mL of deionized water. Then, 5 g of ascorbic acid was added into the beaker and kept on a hot plate with a stirrer at 60 °C for 1 h. Finally, the mixture was centrifuged, washed, and dried at 60 °C for 24 h to get rGO.

2.4. Material Characterization. The recovered and synthesized powder samples were characterized by X-ray diffraction (XRD) with Cu Kα radiation (k = 1.54 Å) (PANalyticalX'pert pro). The Raman spectra were obtained using a HORIBA-J-Y Lab RAM HR 800 Raman spectrometer instrument. Fourier transform infrared (FTIR) analyses were carried out from the samples prepared in potassium bromide pellets using a PerkinElmer Spectrum Two spectrometer. XPS studies were done on a Thermo Fisher Scientific Instrument (K-α^+) with monochromatic Al-Kα as the X-ray source. The BET surface area and porosity of the material were assessed by a Quantasorb instrument. UV−vis studies were performed using a VARIAN (Cary 300) instrument by dispersing the samples in deionized water. The morphology of the samples was observed using a Quanta 200 3D, field-emission scanning electron microscope (FE-SEM), and transmission electron microscope (JEOL JEM F-200).

Cyclic voltammetry and charge−discharge (galvanostatic) analyses were carried out in three electrodes with a potentiostat−galvanostat (Autolab) system (Ag/AgCl as the reference electrode, rGO modified electrode as the working electrode, and platinum wire as the counter electrode). The working electrodes were prepared with active material (80 wt %), super P carbon black (15 wt %), and polyvinylidene fluoride (5 wt %). These were ground with a drop of N-methyl pyrrolidone solvent to form a slurry. This slurry was drop-cast onto a glassy carbon electrode and also coated on a Toray carbon paper and dried at 60 °C for a few hours. A 1 M H_2SO_4 solution was used as an electrolyte for this study.

https://doi.org/10.1021/acs.energyfuels.2c03888
Energy Fuels 2023, 37, 3188−3195

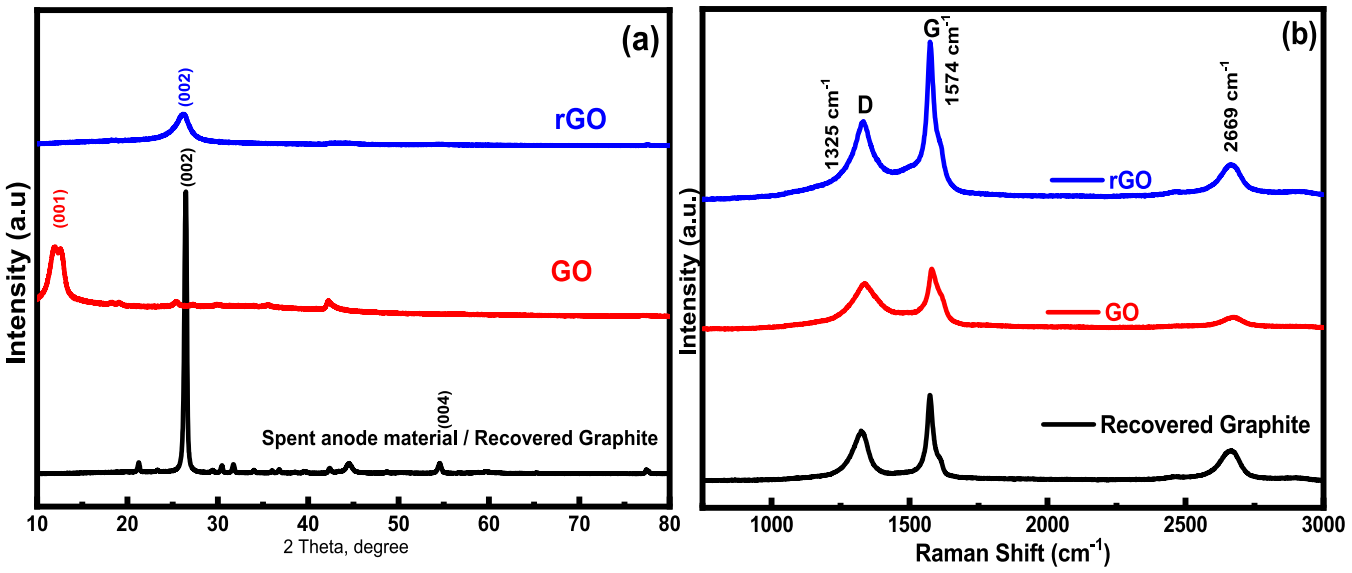

Figure 2. (a) XRD patterns. (b) Raman spectra of G, GO, and rGO.

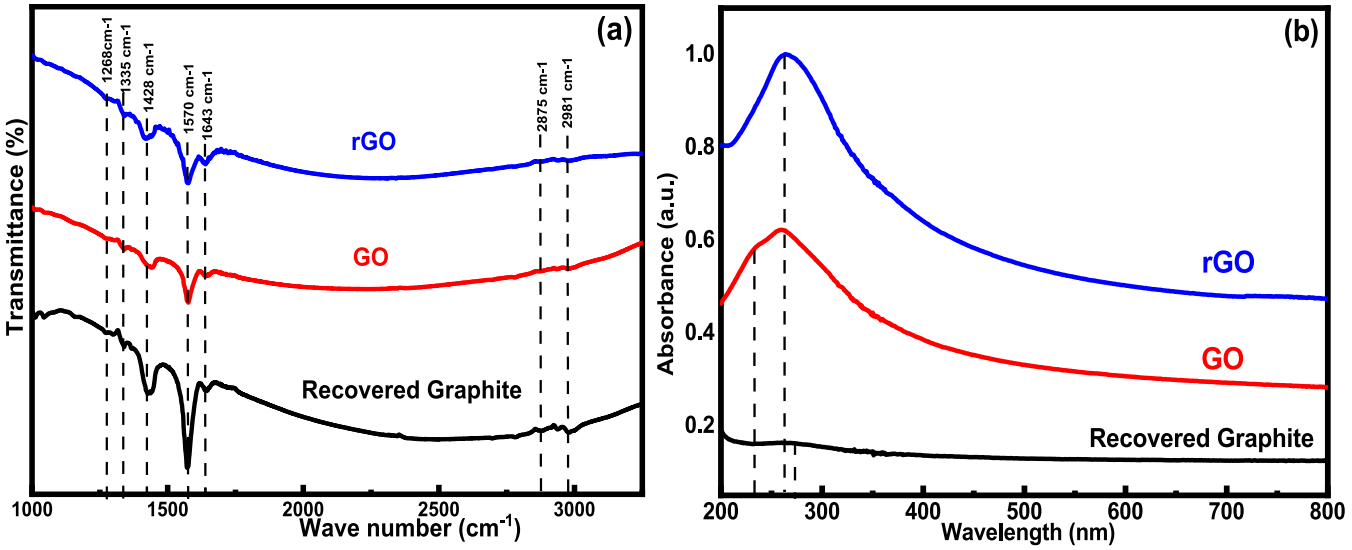

Figure 3. (a). FTIR spectra and (b) UV−vis spectra of G, GO, and rGO.

3. RESULTS AND DISCUSSION

3.1. Structural Studies. The XRD is used to determine the transformation of graphite (G) to graphene oxide (GO) and GO to reduced graphene oxide (rGO). Figure 2a depicts the XRD patterns of recovered G, GO, and rGO. The high-intensity diffraction peak for the recovered anode is observed at 26.4 and 54.5°, which correspond to the (002) and (004) planes, respectively, which indicates the high crystallinity of graphite. Upon oxidation, a fresh diffraction peak appears at 12° corresponding to the (001) plane and is a characteristic of carbon. The appearance of this peak confirms the successful formation of GO. Upon chemical reduction of GO with ascorbic acid, the diffraction peak at 12° disappears, and a broad peak (002) appears at 26°. This confirms the reduction of GO and refurbishment of sp^2 conjugation.

Raman study is the most powerful technique to analyze the defects and structural changes of carbon-based materials. Along with this, allotropes of carbon can also be well-defined.[23] Figure 2b depicts the Raman spectra of recovered G, GO, and rGO samples. The D band corresponds to the breathing mode of the *k* point phonon of A_{1g} symmetry, related to the defects and disorder in structure. The G band corresponds to the scattering of first-order E_{2g} phonons by sp^2 hybrid atoms.[10,24] G, GO, and rGO show a strong G band and weak D band at 1574 and 1325 cm^{-1}, correspondingly, and a 2D band also appeared at 2669 cm^{-1} is due to the eradication of oxygenase groups and configuration of new conjugated carbon atoms.[24] After reducing GO by ascorbic acid, rGO showed a slight shift owing to the distortion of sp^2 nature and configuration of defects. In comparison, G, GO, and rGO spectra showed a slight shift in D and G bands by 5−10 cm^{-1}, which agrees with the previous reports.[24,25]

To further know the conversion of G to GO and GO to rGO, an FTIR study was done and shown in Figure 3a. Graphite has shown a distinctive signal at 2981 cm^{-1} corresponding to symmetric and 2875 cm^{-1} corresponding to asymmetric C−H stretching vibrations, which exists in a hexagonal backbone structure of graphite. Also, it has shown a weak signal at 1643 cm^{-1} and a strong signal at 1570 cm^{-1}

https://doi.org/10.1021/acs.energyfuels.2c03888
Energy Fuels 2023, 37, 3188−3195

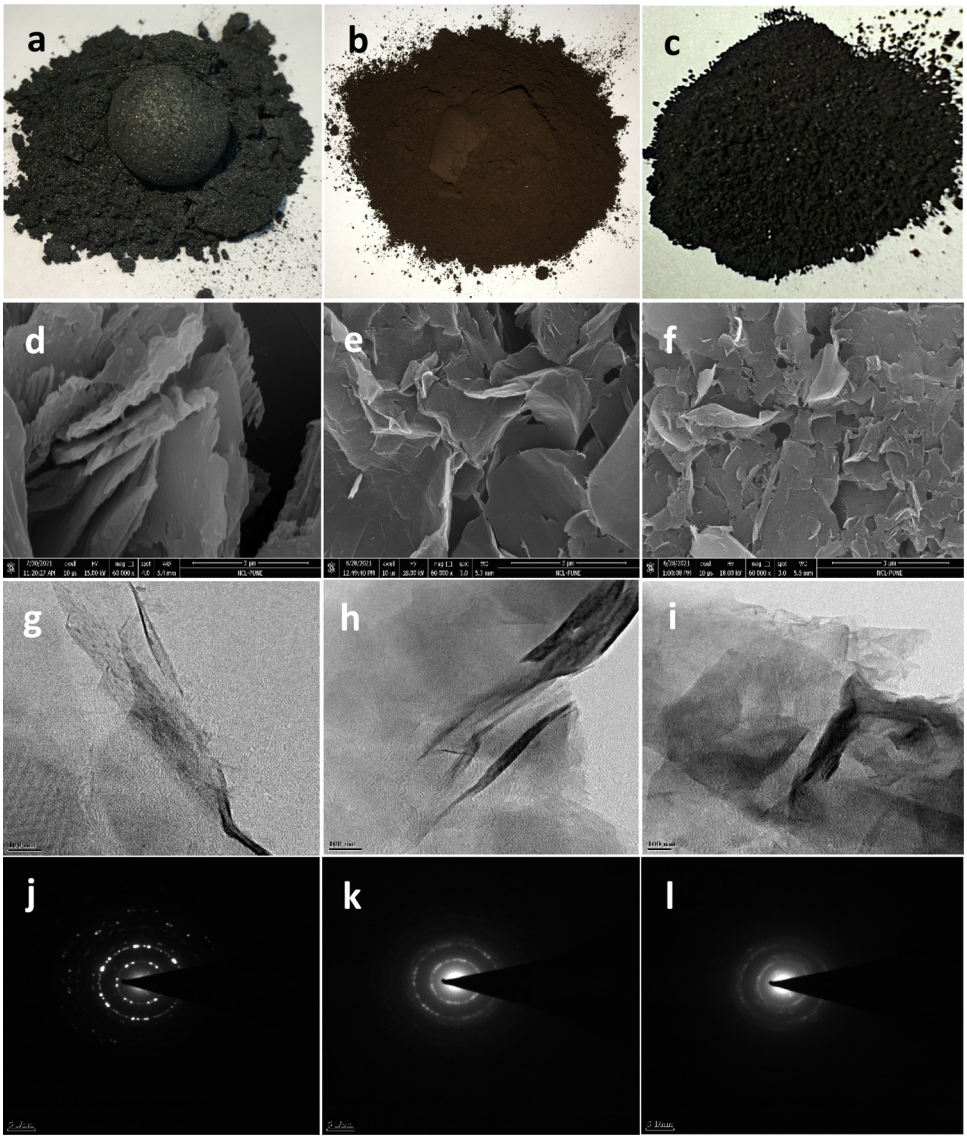

Figure 4. (a–c) Powder images, (d–f) FE-SEM images, (g–i) HR-TEM images, and (j–l) SAED patterns of G, GO, and rGO, respectively.

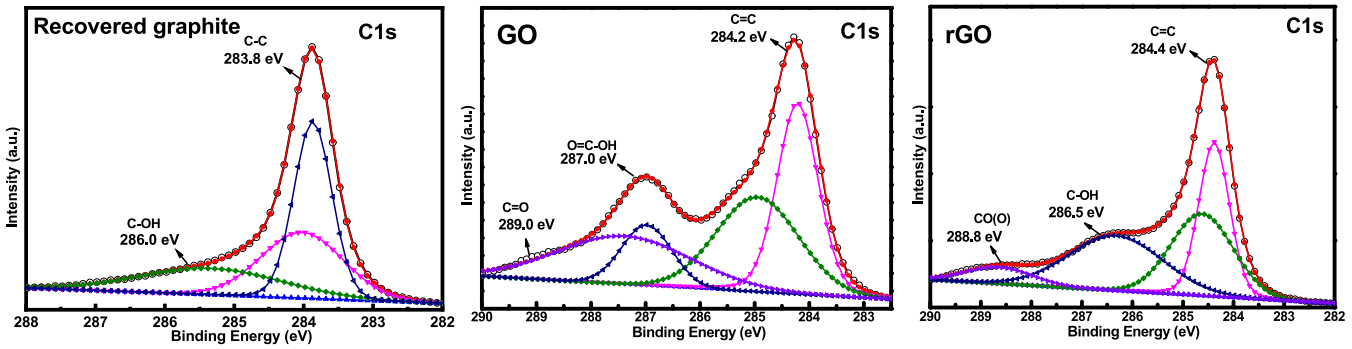

Figure 5. C 1s XPS spectra of G, GO, and rGO.

corresponding to the C═C stretching vibrations.[26] Other prominent peak signals at 1428, 1335, and 1268 cm^{-1} correspond to the O−H deformation, the C−O stretching vibration (epoxy), and the C−O stretching vibration (alkoxy), respectively. These stretching vibrations of G and GO have been weakened in the rGO's spectrum, and these weakened stretching vibrations of epoxy, alkoxy, and carbonyl groups indicate the effective conversion of graphite to GO and reduction of GO to rGO.[27]

Figure 3b depicts the UV−vis spectra of G, GO, and rGO. The absorption spectra were observed at 272 nm for G, 235 nm and 260 nm for GO, and 264 nm for rGO. GO shows that two absorption peaks are attributed to the $\pi-\pi^*$(C−C) and $n-\pi$ (C═O) transition. Here, the peak observed for GO is

https://doi.org/10.1021/acs.energyfuels.2c03888
Energy Fuels 2023, 37, 3188−3195

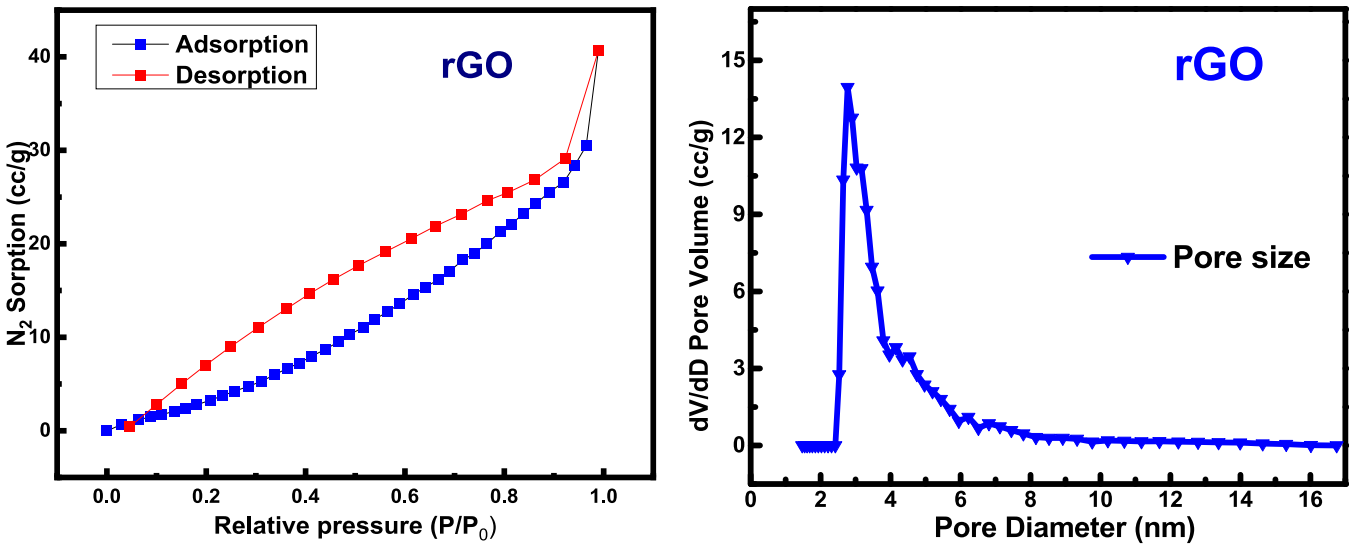

Figure 6. BET Surface area analysis of rGO.

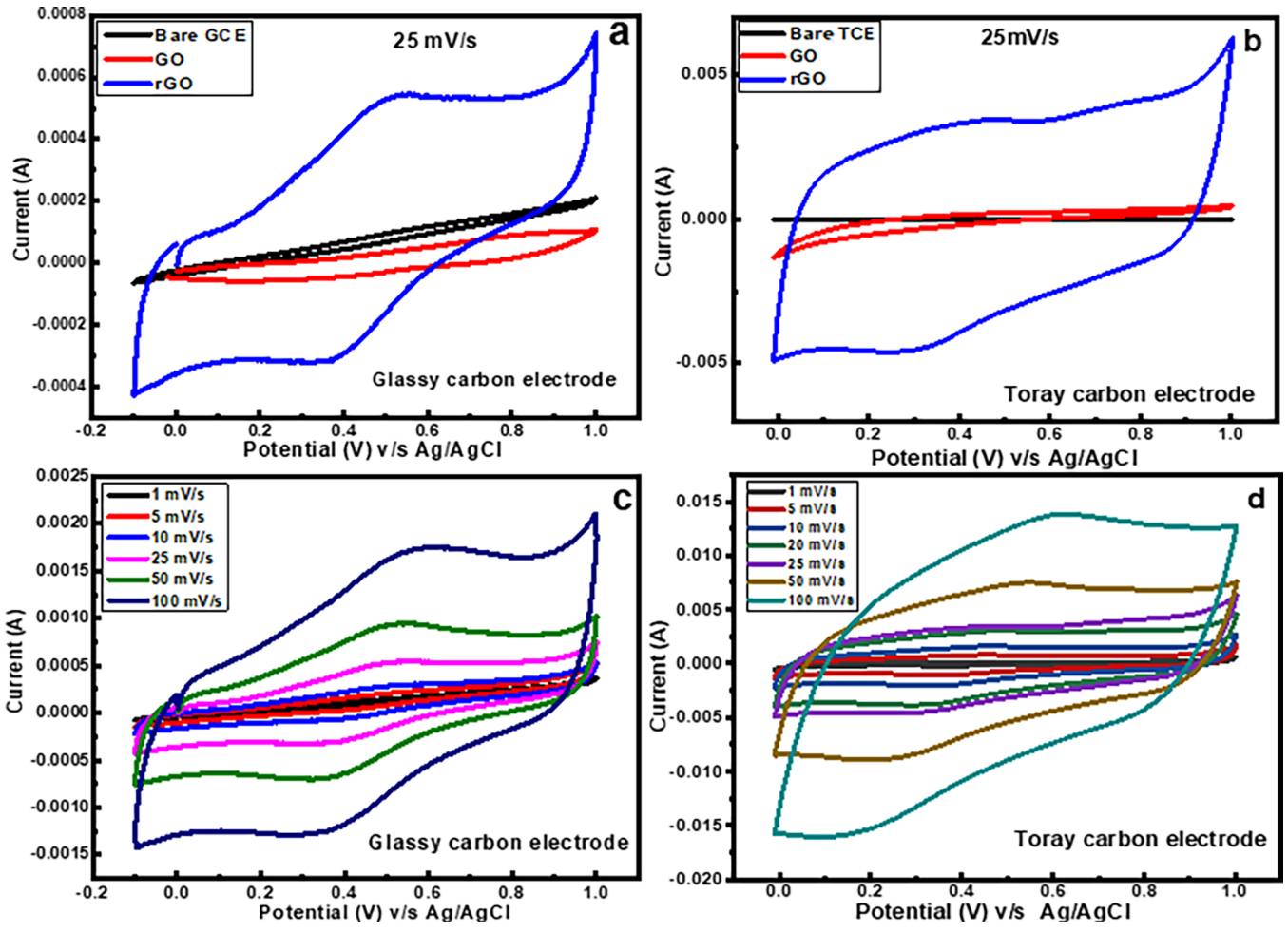

Figure 7. Cyclic voltammogram of (a) bare GCE, GO-coated GCE, and rGO-coated GCE, (b) bare TCE, GO-coated TCE, and rGO-coated TCE at 25 mV/s in 1.0 M H_2SO_4, (c) rGO on the GCE, (d) rGO on the TCE at different scan rates.

slightly red-shifted in rGO, which indicates the elimination of oxygen-containing functional groups. This result well matches with the literature reports.[9,10]

The structure and morphology of the obtained samples were observed by FE-SEM, HR-TEM, and selected area electron diffraction (SAED) patterns shown in Figure 4. The obtained powder images of G, GO, and rGO are shown in Figure 4a–c. The FE-SEM image in Figure 4d–f shows a flake-like structure of G, GO, and rGO, which encloses the distinct and interlinked three-dimensional sheets. The images show the existence of

https://doi.org/10.1021/acs.energyfuels.2c03888
Energy Fuels 2023, 37, 3188−3195

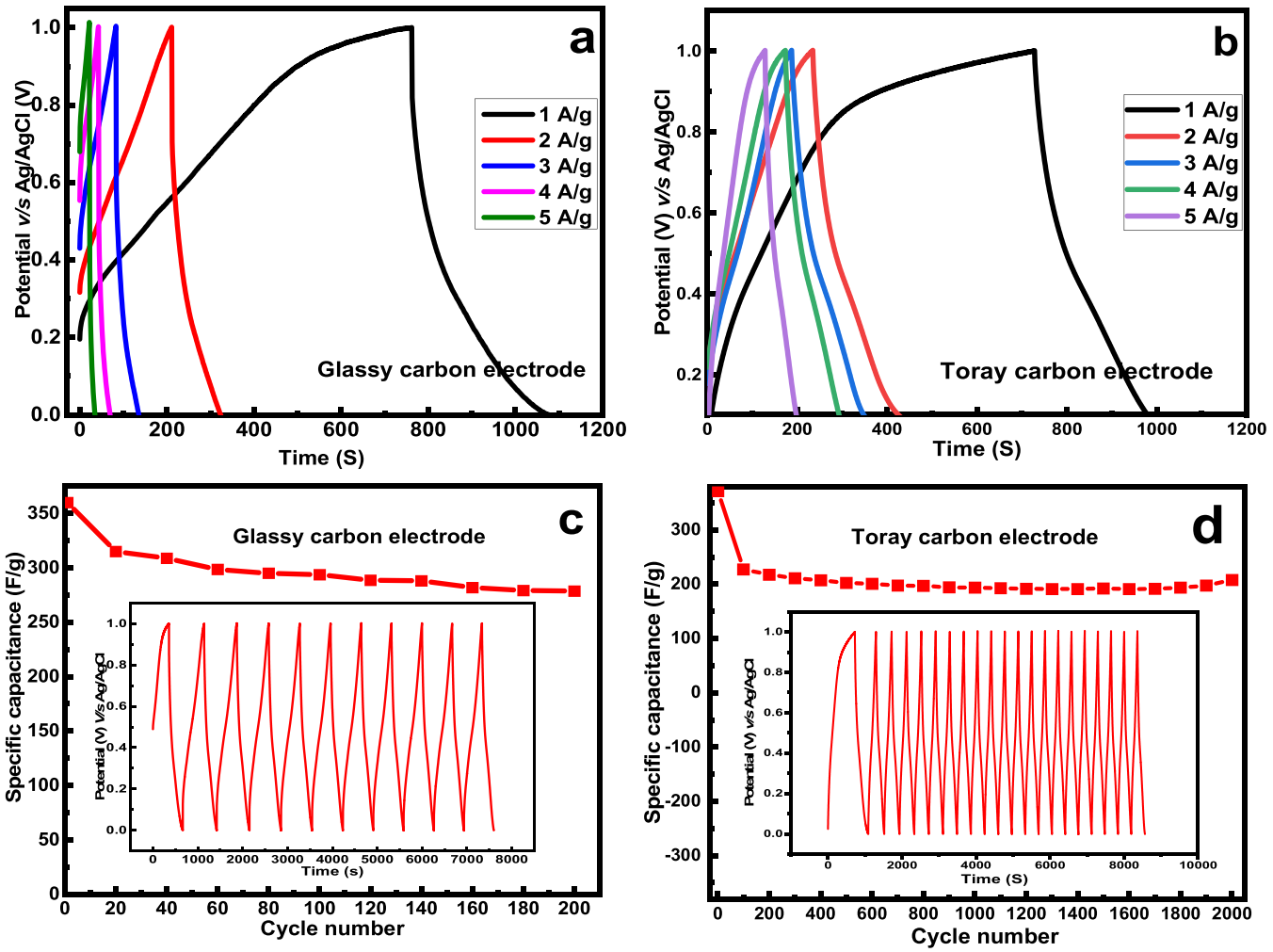

Figure 8. Galvanostatic charge−discharge (GCD) curves of (a) rGO/glassy carbon electrode and (b) rGO/Toray carbon electrode at different current densities. Specific capacitance of (c) rGO/glassy carbon electrode and (d) rGO/Toray carbon electrode for different cycles at 1 A/g.

sharp edges, which are advantageous for field emission. Figure 4g−i shows the HR-TEM images, which indicate that there is no agglomeration on the surface of the sheets, which suggests that we have successfully recovered graphite and synthesized pure rGO. The thickness of the sample is very thin, and folds can also be observed in some areas due to the overlapping of sheets. Figure 4j−l shows SAED patterns of G, GO, and rGO, indicating that there are no bright visible spots in the diffraction rings except that G is due to oxidation/reduction.[23]

3.2. XPS Studies. To study the reduction behavior of GO, XPS analysis is carried out. Figure 5 shows the C 1s spectra of G, GO, and rGO. The C 1s spectra of G show a prominent peak at ≈283.8 eV, which corresponds to C−C, and a small peak at ≈286 eV, which corresponds to C−OH. In GO, the C 1s spectrum consists of three peaks centered at 284.2, 287.0, and 289.0 eV, which corresponds to C═C/C−C (aromatic), O═C−OH (hydroxyl), and C═O (carbonyl) groups. The C═C/C−C and O═C−OH peaks indicate the oxidation of G.[12] The peak intensities of oxygen-containing groups were lower after the reduction by ascorbic acid, which indicates that the oxygen functional group is converted. This demonstrates that the carbon atom is partly transformed from SP^3 to SP^2 hybridization.[12] The C 1s spectrum of rGO also consists of three peaks, centered at 284.4, 286.5, and 288.8 eV, corresponding to graphitic carbon,[28] C−OH (epoxy/hydroxyl), and C═O (carbonyl) groups, respectively.

Figure 6 shows the N_2 adsorption−desorption isotherm and corresponding pore size distribution curves of rGO. BET isotherm follows type IV isotherms with a hysteresis loop, indicating the presence of mesopores, according to IUPAC classification.[29,30] Pore size distribution has been assessed by assuming slit pore shapes through hybrid nonlocal density functional theory (NLDFT) revealed that the pore diameter is in the range 2−17 nm, confirming the mesoporous structure of rGO.[24,31,32]

3.3. Electrical and Electrochemical Studies. Figure 7a,b shows the cyclic voltammogram (CV) profiles with the glassy carbon electrode (GCE) and Toray carbon electrode (TCE) with a scan rate of 0.25 mV/s within the voltage range of 0−1 V in 1.0 M H_2SO_4. The CV behavior of rGO coated on the GCE and TCE is different from the bare GCE and GO-coated GCE (Figure 7a) and bare TCE and GO-coated TCE (Figure 7b). The CV behavior of rGO on the GCE and TCE is almost rectangular in shape compared to GO-coated and bare electrodes, which indicates the reductive and resistive behavior of GO-coated and bare electrodes. respectively. The rectangular shaped behavior is due to electrical double-layer capacitance (EDLC).[31] The redox behavior of rGO was observed around 0.5/0.3 V (Figure 7a) and 0.5/0.25 V (Figure

https://doi.org/10.1021/acs.energyfuels.2c03888
Energy Fuels 2023, 37, 3188−3195

7b). This behavior of rGO is due to carbon−oxygen (C-O) functionalities and EDLC.[24,28] The cyclic voltammetry of rGO at varied scan rates is shown in Figure 7c,d. The change in shape and shift of redox peaks was observed in Figure 7c,d as the scan rate increased from 1 to 100 mV/s. This shift is due to ohmic resistance and polarization, resulting from irreversible kinetics in the redox process. The peak current increases as the scan rate increases and is evidence for better rate capability and better electrochemical performances.

Figure 8a,b shows the galvanostatic charge−discharge curves recorded using rGO on the GCE and TCE at varied current densities. From the figure, it is clear that rGO shows good reversible charge−discharge characteristics for supercapacitor applications. The specific capacitance of rGO on the GCE is 359 F/g (1 A/g), 318 F/g (2 A/g), 268 F/g (3 A/g), 220 F/g (4 A/g), and 158 F/g (5 A/g) (Figure 8a) and the specific capacitance of rGO on the TCE is 371.47 F/g (1 A/g), 201.01 F/g (2 A/g), 211.90 F/g (3 A/g), 157.44 F/g (4 A/g), and 104.78 F/g (5 A/g) (Figure 8b), which are calculated using the below equation by taking the slope of the discharge curve.[26]

$$C_{sp} = \frac{I\,dt}{m\,dV}$$

where C_{sp} is the specific capacitance of the electrode (F), I is the current (A) applied, dt is the discharge time (s), m is the mass of active material on the electrode, and dV is the voltage difference of discharge curve (V). The specific capacitance of rGO is decreased as the current density increases. This decrease in specific capacitance is due to lesser ionic diffusion into the surface of the electrode at higher currents. To know the stability of rGO, charge−discharge cycles were performed at a current density of 1 A/g.

Figure 8c,d, shows the cycling performance of the rGO-coated GCE (200 cycles) and TCE (2000 cycles) between 0 and 1 V at a current density of 1 A/g. It can be seen that the initial discharge capacities were 359 and 371.47 F/g for GCE and TCE, respectively. At the end of 200 cycles (for GCE) and 2000 cycles (for TCE), the discharge capacities were decreased to 278.5 F/g (77.5% capacity retention) and 207.9 F/g (55.9% capacity retention) for the GCE and TCE, respectively. The inset in Figure 8c,d, shows the symmetric charge−discharge behavior of the electrode, which maintains good symmetry even after long cycles, which verifies its good electrochemical durability. More studies are needed to enhance capacity retention over a large number of cycles.

4. RESIDUAL SECONDARY ACIDIC WASTE TREATMENT AND REUSE

The acidic waste left out after the Hummer's method process contains H_2SO_4, $KMnO_4$ in major proportion, and H_3PO_4 in minor proportion. To treat this secondary acidic waste, we have neutralized it by adding NH_4OH solution and the byproducts of it can be a useful plant fertilizer. Below are the possible reactions that can occur, which are given in eqs 1−3. The major byproducts of these reactions are ammonium sulfate, ammonium phosphate, potassium sulfate, and little amount of $MnSO_4$. It is well known that nitrogen-, phosphorus-, and potassium-based fertilizers (known as NPK fertilizers) provide essential nutrients to plants,[33,34] so the byproducts obtained from the secondary acidic waste treatment are water-soluble compounds, which can be used as plant fertilizers.

$$2NH_4OH + H_2SO_4 \xrightarrow{\text{yields}} (NH_4)_2SO_4 + 2H_2O \quad (1)$$

$$3NH_4OH + H_3PO_4 \xrightarrow{\text{yields}} (NH_4)_3PO_4 + 3H_2O \quad (2)$$

$$2NH_4OH + 2KMnO_4 + 3H_2SO_4 \xrightarrow{\text{yields}} K_2SO_4 + 2MnSO_4 + 8H_2O + N_2\uparrow \quad (3)$$

The byproduct obtained is a source of nitrogen and sulfur (see eq 1) and helps to balance the soil pH. Another byproduct, which is an effective fertilizer for years, is rich in nitrogen and phosphorous (see eq 2). Further, one more byproduct obtained is an excellent source of potash and sulfur (see eq 3), which provides nutrition and is useful in protein synthesis in plants. Additionally, a small amount of $MnSO_4$ is the other byproduct, which can also be used for foliar spray and the fertigation of plants and is an essential nutrient.[35]

5. CONCLUSIONS

Successful recovery of graphite from the active anode material of spent LIBs in an eco-friendly approach is reported here. rGO was synthesized by reducing GO using ascorbic acid as a reductant. Structural characterizations confirmed the reduction of GO. The FE-SEM analysis shows the flake-like structure. HR-TEM images indicate no agglomeration on the surface of the sheets, which suggests that we have successfully recovered graphite and synthesized pure rGO. Electrochemical studies of rGO show its potential to operate in supercapacitor applications, with a specific capacity of 207.9 F/g at the end of 2000 cycles at a current density of 1 A/g. Thus, this is a simple and easy method to recover graphite from spent LIBs.

AUTHOR INFORMATION

Corresponding Author

Girish Praveen Nayaka − *Physical and Materials Chemistry Division, CSIR-National Chemical Laboratory, Pune 411008 Maharashtra, India; Academy of Scientific and Innovative Research (AcSIR), Ghaziabad 201002 Uttar Pradesh, India;* orcid.org/0000-0001-8166-1465; Email: gp.nayaka@ncl.res.in

Authors

Bogalera Papaiah Shivamurthy − *Physical and Materials Chemistry Division, CSIR-National Chemical Laboratory, Pune 411008 Maharashtra, India; Academy of Scientific and Innovative Research (AcSIR), Ghaziabad 201002 Uttar Pradesh, India;* orcid.org/0000-0003-4126-9885

Girish Santhosh − *Department of Mechanical Engineering, NMAM Institute of Technology, Nitte (Deemed to be University), Nitte 574110, India;* orcid.org/0000-0003-0579-923X

Complete contact information is available at: https://pubs.acs.org/10.1021/acs.energyfuels.2c03888

Notes

The authors declare no competing financial interest.

ACKNOWLEDGMENTS

Shivamurthy B. P. thanks CSIR, New Delhi (31/011(1129)/2019-EMR-I), for providing a research fellowship. Dr. G. P. Nayaka thanks CSIR-NCL for providing the start-up fund (MLP036126) and all of the facilities.

REFERENCES

(1) Yang, L.; Yang, L.; Xu, G.; Feng, Q.; Li, Y.; Zhao, E.; Ma, J.; Fan, S.; Li, X. Separation and Recovery of Carbon Powder in Anodes from Spent Lithium-Ion Batteries to Synthesize Graphene. *Sci. Rep.* **2019**, *9*, No. 9823.

(2) Natarajan, S.; Aravindan, V. Recycling Strategies for Spent Li-Ion Battery Mixed Cathodes. *ACS Energy Lett.* **2018**, *3*, 2101−2103.

(3) Zheng, X.; Zhu, Z.; Lin, X.; Zhang, Y.; He, Y.; Cao, H.; Sun, Z. A Mini-Review on Metal Recycling from Spent Lithium Ion Batteries. *Engineering* **2018**, *4*, 361−370.

(4) He, L.-P.; Sun, S.-Y.; Yu, J.-G. Performance of LiNi1/3Co1/3Mn1/3O2 Prepared from Spent Lithium-Ion Batteries by a Carbonate Co-Precipitation Method. *Ceram. Int.* **2018**, *44*, 351−357.

(5) Meshram, P.; Pandey, B. D.; Mankhand, T. R. Hydrometallurgical Processing of Spent Lithium Ion Batteries (LIBs) in the Presence of a Reducing Agent with Emphasis on Kinetics of Leaching. *Chem. Eng. J.* **2015**, *281*, 418−427.

(6) Guo, P.; Song, H.; Chen, X. Electrochemical Performance of Graphene Nanosheets as Anode Material for Lithium-Ion Batteries. *Electrochem. Commun.* **2009**, *11*, 1320−1324.

(7) Stoller, M. D.; Park, S.; Zhu, Y.; An, J.; Ruoff, R. S. Graphene-Based Ultracapacitors. *Nano Lett.* **2008**, *8*, 3498−3502.

(8) Yoo, E.; Okata, T.; Akita, T.; Kohyama, M.; Nakamura, J.; Honma, I. Enhanced Electrocatalytic Activity of Pt Subnanoclusters on Graphene Nanosheet Surface. *Nano Lett.* **2009**, *9*, 2255−2259.

(9) Chen, J.; Yao, B.; Li, C.; Shi, G. An Improved Hummers Method for Eco-Friendly Synthesis of Graphene Oxide. *Carbon* **2013**, *64*, 225−229.

(10) Roy, I.; Sarkar, G.; Mondal, S.; Rana, D.; Bhattacharyya, A.; Saha, N. R.; Adhikari, A.; Khastgir, D.; Chattopadhyay, S.; Chattopadhyay, D. Synthesis and Characterization of Graphene from Waste Dry Cell Battery for Electronic Applications. *RSC Adv.* **2016**, *6*, 10557−10564.

(11) Miller, J. R.; Outlaw, R. A.; Holloway, B. C. Graphene Double-Layer Capacitor with Ac Line-Filtering Performance. *Science* **2010**, *329*, 1637−1639.

(12) Ramadoss, A.; Saravanakumar, B.; Kim, S. J. Thermally Reduced Graphene Oxide-Coated Fabrics for Flexible Supercapacitors and Self-Powered Systems. *Nano Energy* **2015**, *15*, 587−597.

(13) Shen, B.; Ding, J.; Yan, X.; Feng, W.; Li, J.; Xue, Q. Influence of Different Buffer Gases on Synthesis of Few-Layered Graphene by Arc Discharge Method. *Appl. Surf. Sci.* **2012**, *258*, 4523−4531.

(14) Huang, Q.; Kim, J. J.; Ali, G.; Cho, S. O. Width-Tunable Graphene Nanoribbons on a SiC Substrate with a Controlled Step Height. *Adv. Mater.* **2013**, *25*, 1144−1148.

(15) Rajagopalan, B.; Chung, J. S. Reduced Chemically Modified Graphene Oxide for Supercapacitor Electrode. *Nanoscale Res. Lett.* **2014**, *9*, No. 535.

(16) Shen, J.; Hu, Y.; Shi, M.; Lu, X.; Qin, C.; Li, C.; Ye, M. Fast and Facile Preparation of Graphene Oxide and Reduced Graphene Oxide Nanoplatelets. *Chem. Mater.* **2009**, *21*, 3514−3520.

(17) Li, D.; Müller, M. B.; Gilje, S.; Kaner, R. B.; Wallace, G. G. Processable Aqueous Dispersions of Graphene Nanosheets. *Nat. Nanotechnol.* **2008**, *3*, 101−105.

(18) Wang, G.; Yang, J.; Park, J.; Gou, X.; Wang, B.; Liu, H.; Yao, J. Facile Synthesis and Characterization of Graphene Nanosheets. *J. Phys. Chem. C* **2008**, *112*, 8192−8195.

(19) Fan, X.; Peng, W.; Li, Y.; Li, X.; Wang, S.; Zhang, G.; Zhang, F. Deoxygenation of Exfoliated Graphite Oxide under Alkaline Conditions: A Green Route to Graphene Preparation. *Adv. Mater.* **2008**, *20*, 4490−4493.

(20) Nayaka, G. P.; Manjanna, J.; Pai, K. V.; Vadavi, R.; Keny, S. J.; Tripathi, V. S. Recovery of Valuable Metal Ions from the Spent Lithium-Ion Battery Using Aqueous Mixture of Mild Organic Acids as Alternative to Mineral Acids. *Hydrometallurgy* **2015**, *151*, 73−77.

(21) Zhang, J.; Yang, H.; Shen, G.; Cheng, P.; Zhang, J.; Guo, S. Reduction of Graphene Oxide via <scp>l</Scp> -Ascorbic Acid. *Chem. Commun.* **2010**, *46*, 1112−1114.

(22) Marcano, D. C.; Kosynkin, D. V.; Berlin, J. M.; Sinitskii, A.; Sun, Z.; Slesarev, A.; Alemany, L. B.; Lu, W.; Tour, J. M. Improved Synthesis of Graphene Oxide. *ACS Nano* **2010**, *4*, 4806−4814.

(23) Paranthaman, V.; Sundaramoorthy, K.; Chandra, B.; Muthu, S. P.; Alagarsamy, P.; Perumalsamy, R. Investigation on the Performance of Reduced Graphene Oxide as Counter Electrode in Dye Sensitized Solar Cell Applications. *Phys. Status Solidi* **2018**, *215*, No. 1800298.

(24) Natarajan, S.; Rao Ede, S.; Bajaj, H. C.; Kundu, S. Environmental Benign Synthesis of Reduced Graphene Oxide (RGO) from Spent Lithium-Ion Batteries (LIBs) Graphite and Its Application in Supercapacitor. *Colloids Surf., A* **2018**, *543*, 98−108.

(25) Zhang, W.; Liu, Z.; Xia, J.; Li, F.; He, W.; Li, G.; Huang, J. Preparing Graphene from Anode Graphite of Spent Lithium-Ion Batteries. *Front. Environ. Sci. Eng.* **2017**, *11*, No. 6.

(26) Johra, F. T.; Jung, W.-G. Hydrothermally Reduced Graphene Oxide as a Supercapacitor. *Appl. Surf. Sci.* **2015**, *357*, 1911−1914.

(27) Thareja, S.; Kumar, A. One-Pot In Situ Synthesis of Mn3O4/N-RGO Nanohybrids for the Fabrication of High Cell Voltage Aqueous Symmetric Supercapacitors: An Analysis of Redox Activity of Mn3O4 toward Stabilizing the High Potential Window in Salt-in-Water and Water-in-Salt Electrolytes. *Energy Fuels* **2022**, *36*, 15177−15187.

(28) Gardner, S. D.; Singamsetty, C. S. K.; Booth, G. L.; He, G.-R.; Pittman, C. U. Surface Characterization of Carbon Fibers Using Angle-Resolved XPS and ISS. *Carbon* **1995**, *33*, 587−595.

(29) Sawangphruk, M.; Srimuk, P.; Chiochan, P.; Krittayavathananon, A.; Luanwuthi, S.; Limtrakul, J. High-Performance Supercapacitor of Manganese Oxide/Reduced Graphene Oxide Nanocomposite Coated on Flexible Carbon Fiber Paper. *Carbon* **2013**, *60*, 109−116.

(30) Alazmi, A.; El Tall, O.; Rasul, S.; Hedhili, M. N.; Patole, S. P.; Costa, P. M. F. J. A Process to Enhance the Specific Surface Area and Capacitance of Hydrothermally Reduced Graphene Oxide. *Nanoscale* **2016**, *8*, 17782−17787.

(31) Vermisoglou, E. C.; Giannakopoulou, T.; Romanos, G.; Giannouri, M.; Boukos, N.; Lei, C.; Lekakou, C.; Trapalis, C. Effect of Hydrothermal Reaction Time and Alkaline Conditions on the Electrochemical Properties of Reduced Graphene Oxide. *Appl. Surf. Sci.* **2015**, *358*, 100−109.

(32) Vadivel, S.; Tejangkura, W.; Sawangphruk, M. Graphite/Graphene Composites from the Recovered Spent Zn/Carbon Primary Cell for the High-Performance Anode of Lithium-Ion Batteries. *ACS Omega* **2020**, *5*, 15240−15246.

(33) Guha, T.; Gopal, G.; Kundu, R.; Mukherjee, A. Nanocomposites for Delivering Agrochemicals: A Comprehensive Review. *J. Agric. Food Chem.* **2020**, *68*, 3691−3702.

(34) Gawali, J.; Dhamak, A.; Zade, S. Effect of Water Soluble Fertilizers through Fertigation on Soil Available N, P, K and Yield of Bt Cotton. *Int. J. Curr. Microbiol. Appl. Sci.* **2020**, *9*, 512−516.

(35) Guo, Y.; Zhang, M.; Liu, Z.; Zhao, C.; Lu, H.; Zheng, L.; Li, Y. C. Applying and Optimizing Water-Soluble, Slow-Release Nitrogen Fertilizers for Water-Saving Agriculture. *ACS Omega* **2020**, *5*, 11342−11351.

https://doi.org/10.1021/acs.energyfuels.2c03888
Energy Fuels 2023, 37, 3188−3195

ACS Sustainable Resource Management

pubs.acs.org/acssrm

Article

Restoration of Degraded Spinel Structure from Spent Li-Ion Battery Cathodes towards Reclaiming for Second Life

Bogalera Papaiah Shivamurthy, Purnima Rawat, Manjusha V. Shelke, Zhongren Zhou, and Girish Praveen Nayaka*

Cite This: https://doi.org/10.1021/acssusresmgt.4c00533

Read Online

ACCESS | Metrics & More | Article Recommendations | Supporting Information

ABSTRACT: As the volume of discarded Li-ion batteries grows, the need for effective recycling solutions has become crucial for economic and environmental preservation. The direct regeneration of electrode materials from used Li-ion batteries has gained significant attention and is interesting due to its streamlined approach, lower energy consumption, and high cost-efficiency. Typically, the regeneration of depleted cathodes requires a source of lithium to address the lithium loss. The precise management of Li^+ ion concentrations in the resulting lithium-rich solution can be employed directly to reintroduce lithium into depleted cathodes. This study involves the restoration of lost Li^+ ions in depleted Ni, Co dual substituted $LiMn_2O_4$ cathode through aqueous lithiation. The relithiated/regenerated Ni, Co substituted $LiMn_2O_4$ cathode demonstrates an initial specific capacity of 125.2 $mAhg^{-1}$ and 105.5 $mAhg^{-1}$ after 500 cycles at a current density of 100 mA with a capacity retention of 84.2%.

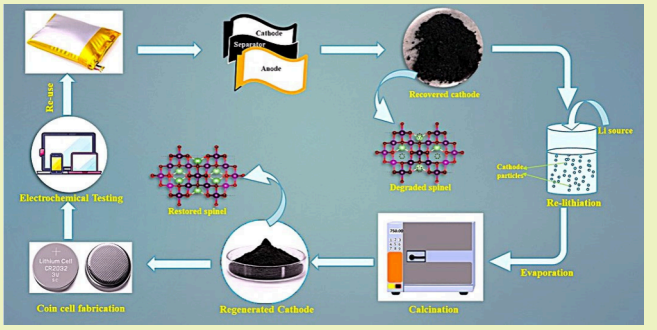

KEYWORDS: *recycling, regeneration, cathode materials, Li-ion batteries, e-waste, circular economy*

INTRODUCTION

Lithium-ion batteries (LIBs) have been widely used in various electric and electronic devices such as smartphones, laptops, and electric automobiles due to their high energy density and extended lifespan.[1,2] Expediting the shift towards electric vehicles (EVs) is crucial for the automotive sector to reduce our reliance on fossil fuels and mitigate energy and environmental concerns.[3,4] However, the flourishing production of LIBs results in the inevitable generation of large quantities of spent batteries containing hazardous metal elements and flammable electrolytes, posing environmental risks and potential threats to human health.[5] By 2030, it is estimated that the quantity of end-of-life (EoL) LIBs will hit 2 million metric tons.[6] The metals in spent LIBs, such as Li, Co, and Ni, hold precious/semiprecious status with considerable value and are recoverable. Developing efficient recycling methods to recover these valuable metals is essential in the present scenario, and better recycling strategies could relieve the mineral shortage issues. The existing methods for recycling EoL batteries encompass pyrometallurgical, hydrometallurgical, and direct regeneration.[7]

Typically, the pyrometallurgical approach involves high-temperature conditions for smelting and significant energy consumption to generate a metal alloy.[8,9] On the other hand, the hydrometallurgical method relies on strong acid or alkali reagents and entails multiple stages to acquire a high-purity precursor.[10,11] Furthermore, by considering the energy consumption and greenhouse gas emissions involved in the process, it is necessary to look into a feasible, easier method for the revival of the cathode material. In this regard, the direct regeneration of the electrode materials is an effective approach focused on rejuvenating the composition and structure of deteriorated cathode material back to its initial form, thereby maximizing the sustainability of used LIBs.[12] To rejuvenate the cathode material to its original state, it is crucial to understand the failure mechanism of the electrode materials, particularly concerning the restoration of the cathode materials. Primarily, the predominant cause of capacity decay upon prolonged charge−discharge cycles is the loss of Li ions. This happens due to a substantial amount of active Li ions utilized from the cathode, particularly during the initial cycles, alongside electrolyte decomposition. This process could form a shielding passivation layer on the anode (solid electrolyte interphase, SEI) and the cathode (cathode electrolyte interphase, CEI).[3,13] It has to be considered that this interphase layer could protect the electrode material from additional corrosion; however, the instability of the SEI layer due to the substantial volume

Received: December 27, 2024
Revised: February 13, 2025
Accepted: February 14, 2025

Downloaded via 152.58.31.219 on March 4, 2025 at 17:54:34 (UTC).
See https://pubs.acs.org/sharingguidelines for options on how to legitimately share published articles.

ACS Publications © XXXX American Chemical Society

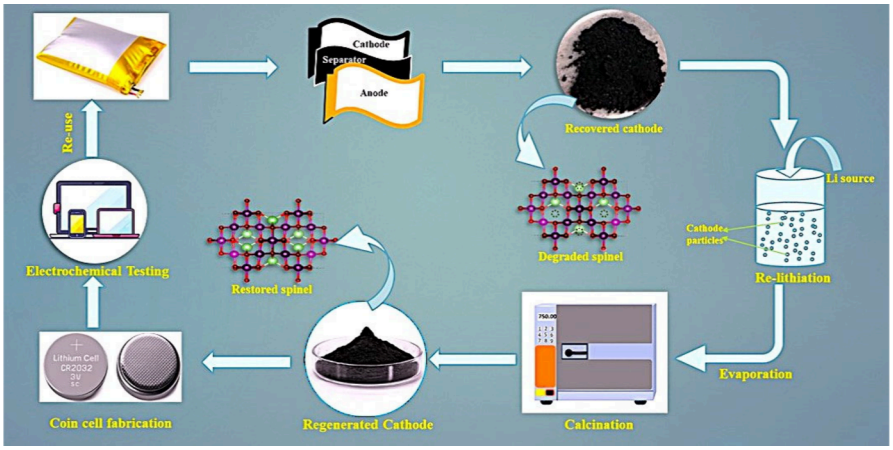

Figure 1. Schematic representation of regeneration of cathode material.

expansion in the anode, which accelerates the dendritic growth of Li on the electrode surface leads to the further irreversible loss of Li.[14] This could bring down the reversible capacity of the battery because of the significant loss of active Li^+ ion within the cathode.[15]

The kinetics of charge transfer between Li^+ ion and cathode at the electrode−electrolyte interface significantly influences the stability and efficiency of the batteries.[16−18] A key factor hindering optimal Li^+ ion charge transfer kinetics is the generation of an unstable cathode−electrolyte interphase (CEI) layer during the charging and discharging cycles.[16] Typically, a CEI layer comprises various organic and inorganic substances resulting from electrolyte and electrode breakdown. These components include LiF, Li_2CO_3, MnO_x, MnF_x, CoO_x, NiO, ROLi, and $ROCO_2Li$, where R represents an alkyl group.[16,19] These chemical substances can hinder the migration of Li^+ ions at the interface between the electrode and electrolyte.[19] Nevertheless, this process leads to oxidative breakdown of the electrolyte, resulting in the production of gases and undesirable side products. In the highly delithiated state, the cathode surface's crystal structure becomes distorted, causing electrolyte oxidation and the formation of a nonuniform cathode−electrolyte interphase (CEI).[20] During charge−discharge cycles, mixing cations in cathode materials leads to irreversible changes in the crystal structure and the release of transition metal ions into the electrolytes. These liberated transition metal ions initiate undesired reactions at the interface with the electrolyte through catalytic and complexation mechanisms, leading to unstable cathode electrolyte interphase (CEI) growth.[21] The dynamic instability of the CEI fails to effectively shield against interfacial reactions and degradation, consequently resulting in significant performance deterioration.[22] For the regeneration of cathode material, it is crucial to eliminate the undesired Li-based compounds that form on the cathode materials surface due to the unstable cathode−electrolyte interface (CEI). The oxidative leaching process must remove these compounds without impacting the cathode material's transition metals. Ammonium persulfate is an effective oxidizing agent that selectively leaches out Li and facilitates the removal of the unwanted layer on the cathode surface. The potential reaction mechanism of ammonium persulfate is presented in eq 1. The depleted Li ions are likewise replenished through chemical relithiation processes. Hence, to regenerate the recycled cathode materials from EoL LIBs, the relithiation of the cathode is essential to make it a potential candidate for their second life, which makes these batteries more sustainable.

$$LiMO_4 + xSO_2O_8^{2-} \rightarrow Li_{1-x}MO_2 + xSO_4^{2-} + xLi^+ \quad (1)$$

In this work, we report on the facile method of regenerating cathode materials from spent LIBs. The recovered cathode materials were investigated to estimate the loss of Li ions and their impact on the performance of the cathode material. The recovered material is identified as Ni, Co co-doped $LiMn_2O_4$-based cathode material, and detailed structural and compositional analyses are discussed in subsequent article sections. A simple lithiation strategy was employed to rejuvenate the cathode materials, and the varied concentrations of relithiation of cathode materials and their electrochemical performances were studied. The performance of the recovered cathode materials was significantly improved after the relithiation. The schematic of the regeneration process is given in Figure 1

EXPERIMENTAL METHODS

Recovery of Cathode Material from Spent Batteries. The spent LIBs were collected from the electronics service centers in Pune. The spent batteries are subjected to chemical discharge to remove the residual potential in the cells. After chemical discharge, the cells dry sufficiently and are dismantled to separate the cell components such as the cathode, anode, separator, and outer cell cases. The separated cathodes were cut into 5 cm × 5 cm slices and immersed in DI water. Ammonium persulfate is added into the beaker containing cathode slices for the oxidative separation of cathode material from the Al current collector. The beaker containing cathode slices is subjected to ultrasonication for 10 min to completely remove the cathode material from the Al current collector. The Al current collector foils were separated, and the cathode materials were filtered off and dried at 80 °C for 12 h. The recovered cathode material is divided into two portions. One is defined as RECAT, and the other is heated at 600 °C for 4 h in the air, defined as RECAT600. Heating is done to remove the possible impurities from the binder and conductive agents.

Relithiation of Recovered Cathode Material. The relithiation of RECAT materials was done using the sol-gel method by introducing 5%, 10%, and 15% of Li_2CO_3. The calculated quantity of Li_2CO_3 was dispersed in 50 mL of deionized water and stirred to get the uniform dispersion mixture of partially dissolved Li_2CO_3/water sol. Then, the requisite quantity of the heat-treated cathode material obtained from the previous step is added and kept for constant stirring for 1 h. The excess water was evaporated at 80 °C completely to obtain Li_2CO_3 encapsulated cathode materials. Then, the cathode materials were calcinated at 750 °C for 10 h to get lithiated cathode materials. For ease of discussion, the lithiated

https://doi.org/10.1021/acssusresmgt.4c00533
ACS Sustainable Resour. Manage. XXXX, XXX, XXX−XXX

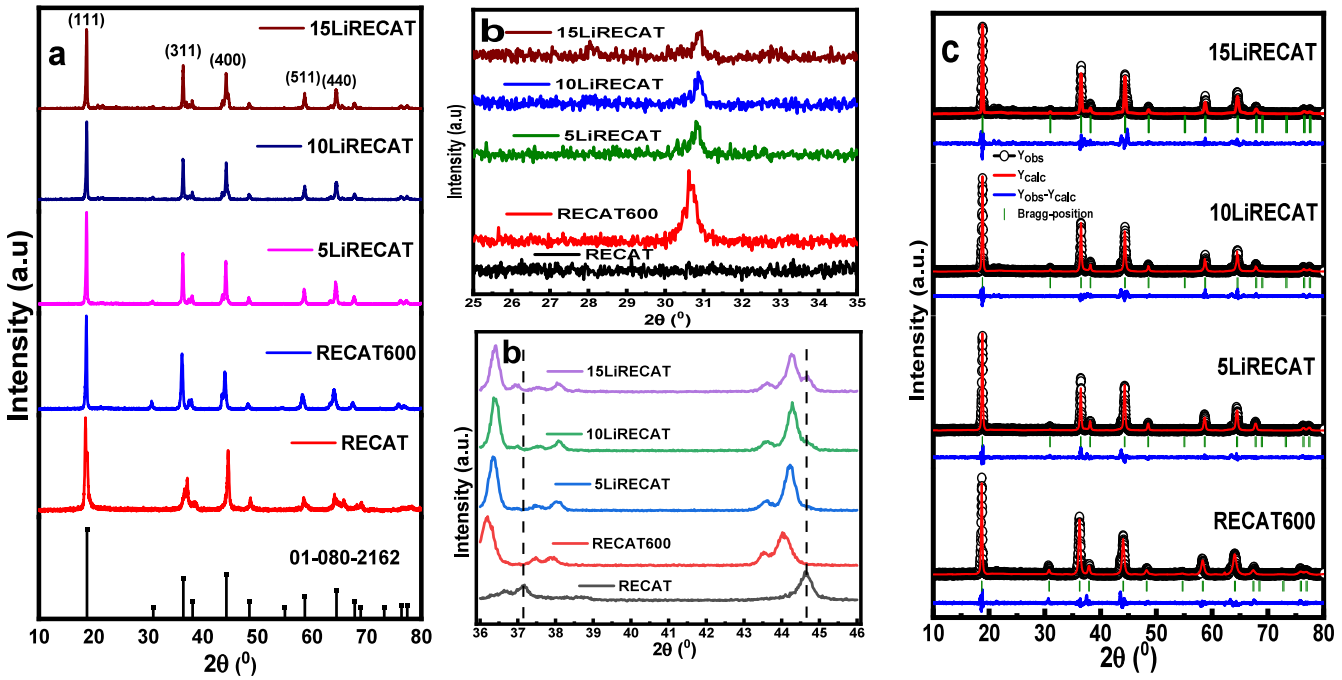

Figure 2. (a) X-ray diffraction patterns of RECAT, RECAT600, 5LiRECAT, 10LiRECAT, and 15LiRECAT materials, respectively. (b) Magnified part of 2θ value range from 25 to 35 and 36 to 46 degrees of X-ray diffraction patterns of image (a). (c) Rietveld refinement plots of RECAT600, 5LiRECAT, 10LiRECAT, and 15LiRECAT materials, respectively.

materials were labeled as 5LiRECAT, 10LiRECAT, and 15LiRECAT based on the ratio of lithium source used.

Material Characterization. *Analytical Methods.* The crystal structure of the recovered and regenerated cathode materials was studied using powder X-ray diffraction (PXRD) (Rigaku Smartlab) with Cu as an X-ray source at 40 kV and 30 mA with Ni as the kβ filter. The obtained XRD patterns were refined using the Rietveld refinement technique with the help of the Fullprof suite software. The surface structure and morphology were analyzed by using a field emission scanning electron microscope (FE-SEM) (FEI-NOVA NANOSEM 450) and a high-resolution transmission electron microscope (HR-TEM) (JEOL JEM F-200) coupled with an energy dispersive spectrometer (EDS). The electronic states of the elements are studied by using X-ray photoelectron spectroscopy (XPS), performed by the Thermo Scientific Model K-alpha XPS instrument with monochromatic Al Kα as the X-ray source.

Electrochemical Methods. The electrochemical analyses of the recovered and regenerated cathode materials were conducted in 2032-type coin cells. Cell fabrication uses directly recovered, heat-treated, and regenerated materials as the cathodes. All these positive electrodes comprise 80:10:10 weight% of the active cathode material, poly(vinylidene difluoride) (PVDF) as the binder, and Super C-60 carbon black as the conducting material. All of these materials were mixed well by adding an appropriate *N*-methyl pyrrolidone as the solvent to form a uniform slurry. The slurry was coated onto a conductive carbon-coated aluminum foil by doctor blade method and dried at 100 °C for 12 h under vacuum. The foil was subjected to calendaring and punched into 14 mm circular discs. These circular cathode disks were used to fabricate the 2032-type coin cells. A circular Li metal disc is used as an anode, Celgard-2325 as the separator, and 1M $LiPF_6$ in a 1:1:1 volume ratio of EC/DMC/EMC solvents as the electrolyte. The coin cells were prepared in an argon-filled glove box at $\leq$0.1 ppm of O_2 and H_2O levels. The coin cells were tested by performing cyclic voltammetry and electrochemical impedance analysis (EIS) using a Metrohm electrochemical workstation (Multiautolab M204). The galvanostatic charge/discharge measurements were carried out with a Neware battery testing system (CT4008).

RESULTS AND DISCUSSION

Structural and Elemental Characterization. The cathode material from the spent LIB was subjected to ICP-OES and XRF to determine the elemental composition of all of the metals in the recovered cathode (RECAT) materials. The ICP-OES ((0.23 ppm of Li), (4.47 ppm of Mn), (1.43 ppm of Ni) (0.54 ppm of Co)), and XRF ((61.3% Mn), (24.7% Ni), and (11.3% Co)) results reveal that the recovered cathode material contains Mn metal predominantly followed by Ni and Co. Considering the ICP-OES and XRF results, the recovered cathode material can be identified as $LiMn_{1.5}Ni_{0.5}O_4$ cathode material with Co doping.

The recovered and relithiated cathode materials are subjected to X-ray diffraction analysis to understand the crystallographic information on the cathode materials. The X-ray diffraction patterns are given in Figure 2a, which were well-matched with the diffraction peaks of PDF reference number 01-080-2162 of $LiMn_{1.5}Ni_{0.5}O_4$ (LMNO) material. The X-ray diffraction planes are indexed as per the reference PDF file. The X-ray diffraction patterns reveal that there was no peak observed at 2θ around 31° for the recovered cathode material, but in the case of heat-treated material, a small peak appeared at 2θ around 31° and remained after the lithiation of cathode materials (see Figure 2b). This indicates the reconstruction/reformation of the crystal lattice of the recovered cathode material by removing passive surface and inactive compounds over the surface of the cathode material. The small diffraction peak is identified as the (220) plane in the X-ray diffraction pattern of the cathode material.

During prolonged charge−discharge cycles, the loss of Li ions occurs, and this loss of Li ions leads to the distortion or dilation of the cathode active material.[23] Li et al.'s[24] report suggests that the collapse in the crystal lattice of the cathode material depends entirely on utilizing Li content irrespective of the transition metals; the loss of Li ions from cathode materials

https://doi.org/10.1021/acssusresmgt.4c00533
ACS Sustainable Resour. Manage. XXXX, XXX, XXX−XXX

distorts the cathode structure. The irreversible structural changes happen due to cation mixing during the lithiation, and the delithiation mechanism of cathode active material could lead to Li loss, which leads to structural collapse due to the change in the oxidation states of the metals.[25] Further, the X-ray diffraction pattern analysis reveals that the diffraction peaks indexed as (311) and (400) are compared between the recovered and regenerated cathode materials. It is observed that the peaks are shifted toward lower 2θ, and also, it could be observed that the splits in the peaks are due to the expansion of the lattice parameters and crystal lattice. The contracted crystal lattice of the used cathode material regained its stable structure after heat treatment and relithiation. The literature report advocates that the contraction of crystal structure occurs due to delithiation.[25,26] The shift of diffraction peaks towards lower 2θ indicates increased lattice parameters and expanded volume.[26] The diffraction peaks shift toward higher 2θ indicates the contraction of the crystal lattice due to stress and nonstoichiometric phase reasons. In our case, the recovered cathode material showed a shift in the critical diffraction peaks toward higher 2θ due to the loss of Li after continuous charge−discharge cycles in their first life, causing the formation of nonstoichiometric phases that led to the contraction of the crystal lattice. After the removal of inactive compounds over the surface of the cathode active material upon heating, the cathode materials regained the crystal structure. They caused expansion of the crystal lattice, which could be confirmed by identifying the shift in the diffraction peaks toward lower 2θ due to the expansion of the crystal lattice. The shift in the 2θ values for the peaks indexed as (311) and (400) is shown in Figure 2b; in the exact figure, it can be observed that the appearance of small peaks upon an increase in the lithiation percentage, which indicates the formation of Li-rich phases. In the X-ray diffraction patterns, the peak labeled as (311) is considerably small; it might be due to structural changes during the charge−discharge mechanism of their first life. The change in the X-ray diffraction pattern is identified as the transformed material crystal structure, which was converted into a low Li manganese oxide, which also belongs to the cubic crystal with space group $Fd\bar{3}m$. This phase material was possibly formed due to the reaction between the byproducts of the unstable CEI layer and the dissolved Mn ions in the electrolyte. The comparison of the X-ray diffraction pattern of RECAT with corresponding reference datasets is given in SI Figure 1 of Supporting information. Several reports say the spinel phase favors faster Li-ion diffusion kinetics and better battery performance.[27,28] However, during long charge−discharge cycles and loss of Li ions, the cathode structure undergoes phase changes, which cause failure of the battery. The (311) peaks of regenerated cathode materials eventually grew upon lithiation and reconstructed the spinel phase. Rietveld refinement studies for the X-ray diffraction patterns of the RECAT600, 5LiRECAT, 10LiRECAT, and 15LiRECAT were performed using Fullprof software and are shown in Figure 2c. The diffraction patterns of all the materials are indexed to a cubic spinel structure with the $Fd\bar{3}m$ space group (Table 1).

Figure 3a shows Raman spectra of the recovered, heat-treated, and regenerated cathode materials. It is observed that the vibrational peaks for the recovered and heat-treated cathodes are slightly broader compared to the relithiated cathode materials, which is due to the loss of long-range translational symmetry and reciprocal lattice/crystal lattice

Table 1. Rietveld Refinement Data of the Cathode Materials

Sample	Lattice constant (a=b=c)	Cell volume	Reliability factors		
			Rwp (%)	Bragg Rf	χ^2
RECAT600	8.22	555.95	17.2	6.6	2.06
5LiRECAT	8.18	547.18	17.3	8.2	2.6
10LiRECAT	8.17	545.24	18.0	9.2	2.54
15LiRECAT	8.16	544.39	19.2	9.8	3.1

distortion,[29] which correlates well with X-ray diffraction results. The broadening of the peaks in Raman spectra indicates the distorted entities[30] in the used cathode material, which is also slightly present even after heat treatment. The peak broadening is reduced in relithiated cathode materials, resulting in sharp peaks comparatively. The prominent peak appeared at around 627.3 and 602.4 cm^{-1} for RECAT and RECAT600 materials. The redshift in RECAT and RECAT600 material spectra indicates the distorted structure of used cathode materials as the vibrational peak at this range is related to the Mn−O bonding of MnO_6 Oh symmetry. The blueshift in the spectra 607.4 cm^{-1} for 5LiRECAT, 614.6 cm^{-1} for 10LiRECAT, and 615.4 cm^{-1} for 15LiRECAT materials indicate the lithiation and formation of a stable structure. The other peaks indicate the vibrational behavior of Ni−O bonding of NiO_6 octahedral groups at Raman shift around 498.2, 478.7, 485.7, 495.5, and 495.5 cm^{-1} for RECAT, RECAT600, 5LiRECAT, 10LiRECAT, and 15LiRECAT, respectively. This also follows a similar trend as in the case of the Mn−O vibrational peak, as it shifts toward the left (redshift) initially and toward the right (blueshift) side of the spectra. The small broad peak in the range at around 390 cm^{-1} can be observed only in the case of the relithiated material. Such a peak is significantly weak or not clearly observed for recovered and heat-treated cathode material and is related to the Li−O stretching vibrations of LiO_4 tetrahedral groups.

Field emission scanning electron microscopy (FESEM) images of RECAT, RECAT600, 5LiRECAT, 10LiRECAT, and 15LiRECAT materials are displayed in Figure 3(b−f). Recovered cathode material (Figure 3b) (before heating) shows the bulk structure, which has a mixture of metal oxide cathode material and carbon structure that can be seen as small fibrous structures over the surface of the cathode particles. The carbon content and the cathode material are present due to the usage of carbon conductive agents during the electrode fabrication process. After heat treatment of the recovered cathode material, such carbonaceous structures were burned away, and the cubical morphology of the particles formed, which can be observed in Figure 3c. The lithiated cathode materials also formed cubic structures with sharp edges, as seen in the Figure 3(d−f).

Figure 3(g−k) shows the high-resolution transmission electron microscopic (HR-TEM) images of the recovered and regenerated cathode materials. The inset figures are magnified areas of the particular region marked with a square with a white outline generated by fast Fourier transform (FFT) and inverse FFT given to ease of visualization of the lattice fringe widths. The inset of Figure 3g displays the composite behavior identified by measuring the lattice fringe widths from the HRTEM image and the fringe width of 0.45 nm, which is comparable to the d-spacing of the value of (111) plane of the X-ray diffraction pattern of the cathode material; the same image has shown the lattice fringe width of 0.23 nm which is

https://doi.org/10.1021/acssusresmgt.4c00533
ACS Sustainable Resour. Manage. XXXX, XXX, XXX−XXX

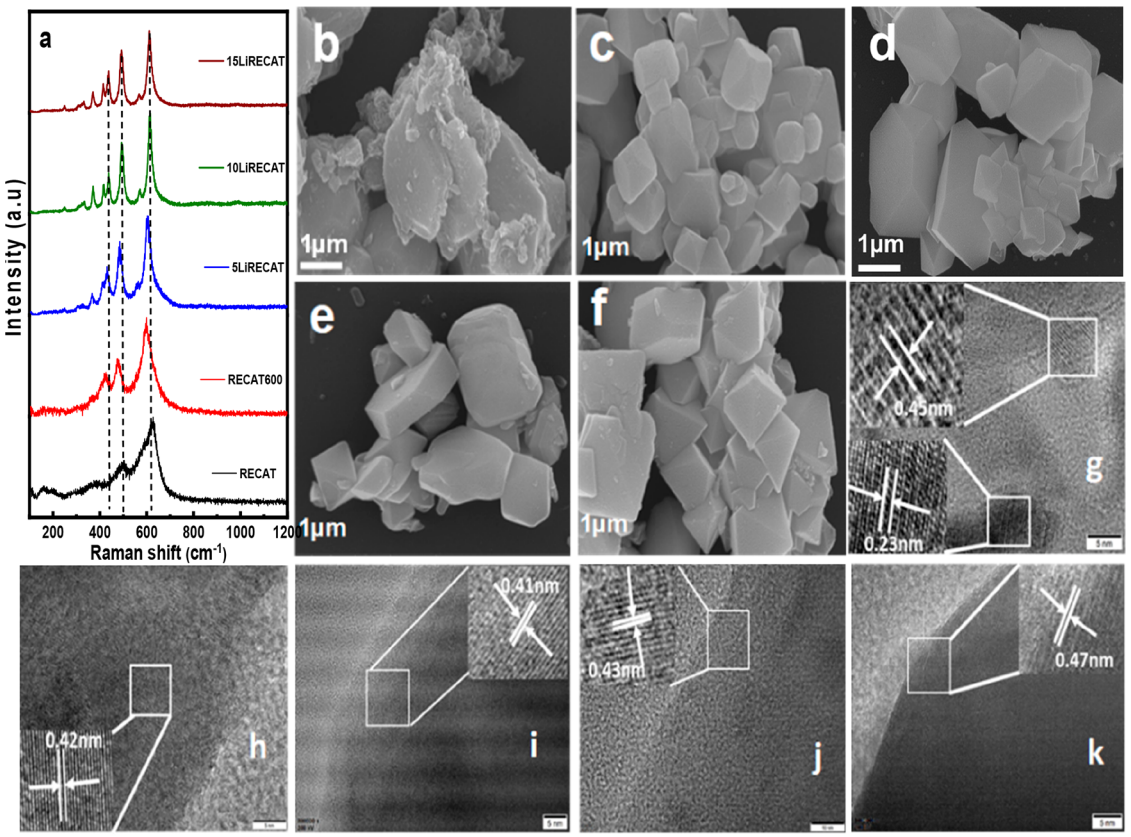

Figure 3. (a) Raman spectra (b–f) FESEM image and (g–k) HR-TEM image of RECAT, RECAT600, 5LiRECAT, 10LiRECAT, and 15LiRECAT materials, respectively (inset images are the marked fast Fourier transform (FFT) region).

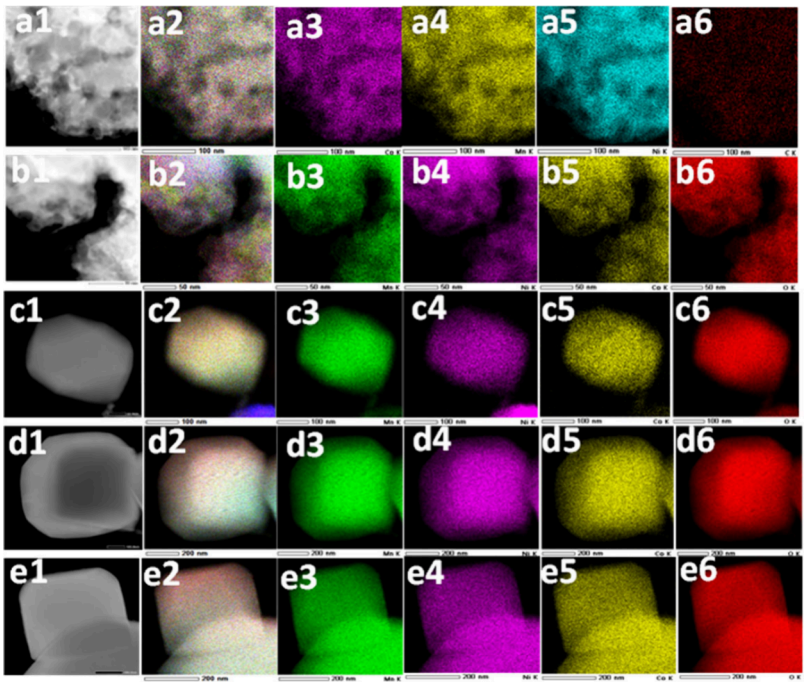

Figure 4. (a1–e1) Scanning tunneling electron microscopic (STEM) images, (a2–e2) EDS elemental mapping overlay of all the elements, and remaining images (a3–e6) are of mapping of individual elements C, Mn, Ni, Co (a3–a6) for RECAT; Mn, Ni, Co, O (b3–b6) RECAT600; (c3–c6) 5LiRECAT; (d3–d6) 10LiRECAT; and (e3–e6) 15LiRECAT.

related to the (100) plane of the X-ray diffraction of pattern of carbonaceous material. Figure 3(h–k) shows the HRTEM images of the RECAT600, 5LiRECAT, 10LiRECAT, and 15LiRECAT materials, and the inset images show the lattice fringe widths of 0.42, 0.41, 0.43, and 0.47 nm, respectively; all

https://doi.org/10.1021/acssusresmgt.4c00533
ACS Sustainable Resour. Manage. XXXX, XXX, XXX–XXX

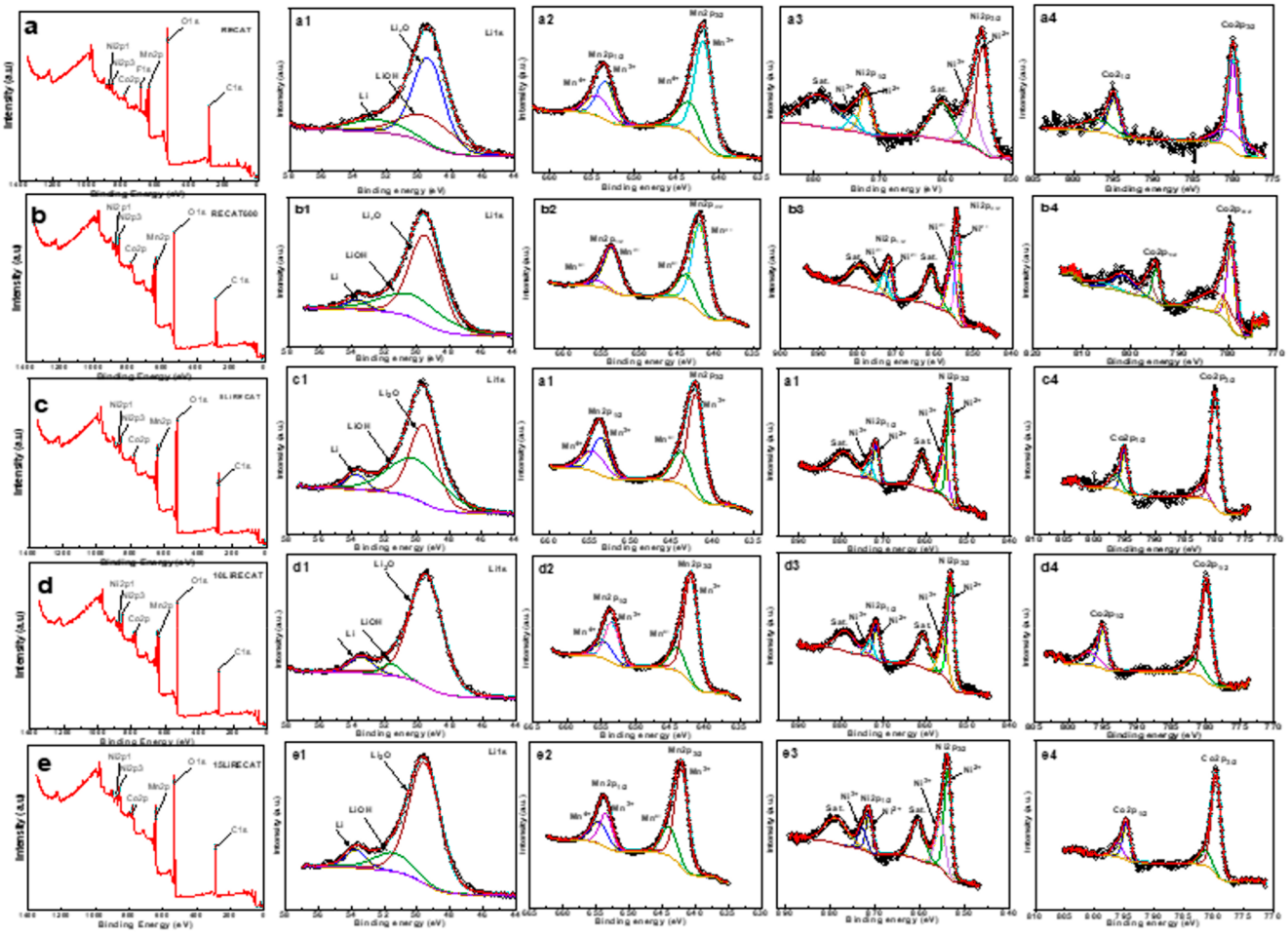

Figure 5. (a−e) XPS survey spectra: (a1−a4) Deconvoluted peaks of XPS core levels of Li 1s, Mn 2p, Ni 2p, Co 2p for RECAT; RECAT600 (b1−b4; 5LiRECAT (c1−c4); 10LiRECAT (d1−d4); and 15LiRECAT (e1−e4).

these values are analogous to the lattice spacing of the (111) plane of the LMNO-based cathode materials.

The STEM images and the EDS elemental mapping of the recovered and regenerated cathode materials are shown in Figure 4(a1−e1) and (a2−e2). The STEM images and elemental mapping of the respective area of the spread particles confirm the morphological changes from the recovered cathode and the regenerated cathode materials upon heating. The careful observation of the images in Figure 4(a1−e1) could reveal the evolution of particle morphology changing from bulk structure to a particular cubical shape. The elemental mapping confirms the uniform distribution of all of the elements throughout the material structures. It can be observed that carbon content is present in the recovered cathode material RECAT. However, in the case of heated and lithiated materials, there is no carbon content, which appears and indicates the removal of carbon upon heating. The mapping results confirm the presence of all the elements Mn, Ni, Co, and O, distributed thoroughly in the cathode structures, which indicates that the transition element composition was not affected in the first life of the cathode materials in the used cells. As a result, the cathode material was revived successfully after lithiation.

The XPS analysis was employed to understand the valence states and elemental composition of the recovered, regenerated, and relithiated cathode materials. All of the peaks were deconvoluted and resolved using CasaXPS software. Figure 5 shows the XPS survey spectra (Figure 5a−e) and deconvoluted signals of Li 1s, Mn 2p, Ni 2p, Co 2p, and O 1s core levels for the RECAT, RECAT600, 5LiRECAT, 10LiRECAT, and 15LiRECAT materials. The deconvoluted spectra of the Li 1s core level are shown in Figure 5a1−e1. The prominent peak of the Li 1s core level has the binding energy 49.4 eV for the RECAT material confirms the chemical and electronic state, and the binding energy values for the Li 1s level for heat-treated and relithiated materials are around 49.6 eV. However, the intensity of the prominent peak of the Li 1s core level for recovered material is less than that of other materials, such as heat-treated and relithiated cathode materials. RECAT material has F 1s signals; the deconvoluted spectra of the F 1s core level are given in SI Figure 2. The F 1s signal is due to the formation of LiF over the surface of the used cathode material, which is also contributed by the PVDF binder or other carbon fluorides formed by the side reactions during the charge−discharge reactions. The F 1s XPS signal has not been observed in the case of other electrode materials such as RECAT600, 5LiRECAT, 10LiRECAT, and 15LiRECAT, which can be seen in survey spectra (Figure 5a−e), and this indicates that upon heat treatment and lithiation thermal treatment vanishes the LiF and other unwanted impurities. The 15LiRECAT materials have shown more intensity for the Li 1s core level, confirming the Li ions' loss in the used

https://doi.org/10.1021/acssusresmgt.4c00533
ACS Sustainable Resour. Manage. XXXX, XXX, XXX−XXX

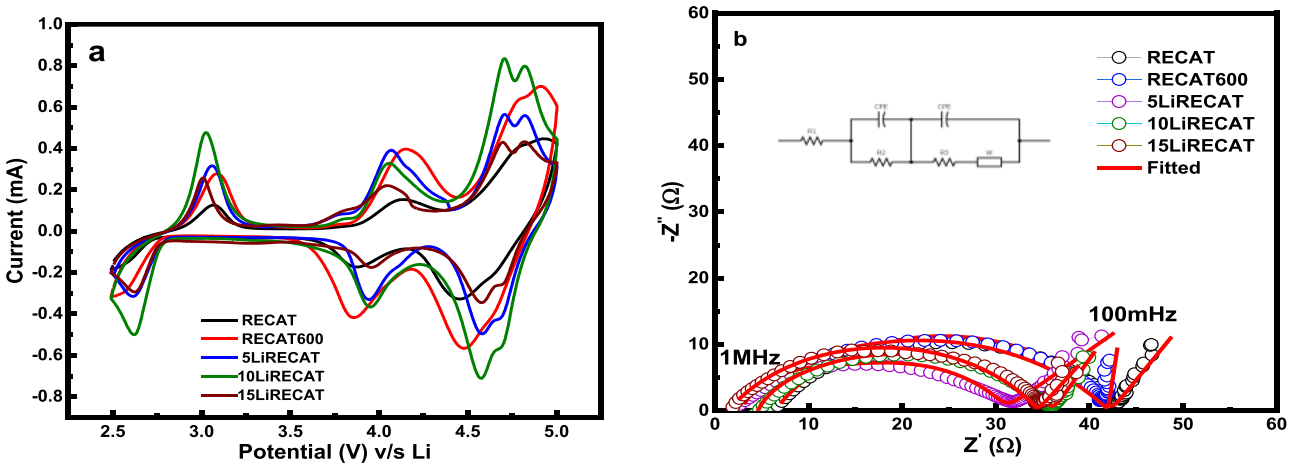

Figure 6. (a) Cyclic voltammograms and (b) Nyquist plots of RECAT, RECAT600, 5LiRECAT, 10LiRECAT, and 15LiRECAT materials.

Table 2. Resistance Values Were Obtained from EIS Fitting Data

	Material				
Parameter	RECAT	RECAT600	5LiRECAT	10LiRECAT	15LiRECAT
R_s (Ω)	5.45	2.48	2.17	4.71	2.32
R_{SEI} (Ω)	3.65	3.82	4.86	3.51	3.43
R_{ct} (Ω)	32.53	35.52	24.59	27.86	28.91

cathode material and the increased Li ions after relithiation. It can be concluded that the relithiation could revive the cathode structure effectively. The deconvoluted spectra for Mn 2p core levels of RECAT, RECAT600, 5LiRECAT, 10LiRECAT, and 15LiRECAT materials are displayed in Figure 5(a2−e2); the Mn 2p core level exhibits two components, Mn $2p_{3/2}$ and Mn $2p_{1/2}$, due to spin-orbit coupling.[31] Mn 2p core levels are composed of Mn $2p_{3/2}$ levels with binding energy 641.9 eV (RECAT), 642.05 eV (RECAT600), 642.3 eV (5LiRECAT), 642.2 eV (10LiRECAT), and 642.2 eV (15LiRECAT), and Mn $2p_{1/2}$ levels with binding energy 653.7 eV (RECAT), 653.8 eV (RECAT600), 653.9 eV (5LiRECAT), 653.8 eV (10LiRECAT), and 653.8 eV (15LiRECAT). The obtained values of binding energies for Mn 2p core levels are in close agreement with the values for Mn^{3+} and Mn^{4+}, as reported by Nesbitt et al.[32] The spin-orbit coupling occurs at the Ni 2p core level as well; the deconvoluted spectra of the Ni 2p core level also have two components, Ni $2p_{3/2}$ and Ni $2p_{1/2}$ (Figure 5(a3−e3)). Ni 2p core levels comprise Ni $2p_{3/2}$ levels with binding energy 854.7 eV (RECAT), 854.8 (RECAT600), 854.6 (5LiRECAT), 854.6 (10LiRECAT), and 854.6 (15LiRECAT) and Ni $2p_{1/2}$ levels with binding energy 872.2 eV (RECAT), 872.2 (RECAT600), 872.0 eV (15LiRECAT), 871.9 eV (10LiRECAT), and 871.7eV (15LiRECAT). The Co 2p core level also has two sublevels, Co $2p_{3/2}$ and Co $2p_{1/2}$ (Figure 5(a4−e4)); the deconvoluted spectra of the Co 2p core have Co $2p_{3/2}$ levels at binding energy values 779.9 eV (RECAT), 779.6 eV (RECAT600), 780.2 eV (5LiRECAT), 779.9 eV (10LiRECAT), and 779.7 eV (15LiRECAT). $Co_2p_{1/2}$ levels with binding energies of 795.11 eV (RECAT), 795.03 eV (RECAT600), 795.22 eV (5LiRECAT), 795.13 eV (10LiRECAT), and 794.8 eV (15LiRECAT).

Electrochemical Performance of Recovered and Regenerated Cathode Materials. Cyclic voltammetry and electrochemical impedance spectroscopic studies were employed to assess the electrochemical redox characteristics and ionic transport capabilities of recovered (RECAT), heat-treated (RECAT600), and regenerated (5LiRECAT, 10LiRECAT, and 15LiRECAT) cathode materials. Figure 6a shows the cyclic voltammograms carried out in a potential window of 2.5 and 5 V under the sweep rate 100 mVS^{-1} conditions. It can be observed that there are four pairs of reversible redox peaks at three different potential regions, which are characteristic of different redox-active metals present in the cathode-active materials. The first pair of redox peaks appeared at around 2.6 V/3.0 V, a characteristic behavior of the transition of Mn^{2+}/Mn^{3+} states.[33] The other prominent redox peaks at around 4.0-4.2 V in all of the materials correspond to the redox couples Mn^{3+}/Mn^{4+}. The other charge peak appeared at ∼3.2 V, and its redox pair peak appeared on the discharge curve at 2.75 V. The redox pair corresponds to the Li^+ extraction of the cathode and insertion into the cathode active material. The third and fourth redox peaks with predominant intensity were observed at higher potential ranges of 4.72/4.63 and 4.81/4.73 V, respectively, corresponding to Ni^{2+}/Ni^{4+}, which indicates the electrochemical activity of Ni in the active material.[34] These redox peaks of lithiation/delithiation at higher voltage indicate that more driving force is necessary to urge the Li ions from the cathode to the anode. It is observed that after careful comparison and analysis of the redox peaks in the cyclic voltammograms of the recovered cathode material, heat-treated cathode, and relithiated cathode materials, the redox peaks of RECAT material are less intense and much sharper as compared to the regenerated/relithiated cathode materials which indicate the destitute nature of the cathode structure to be an efficient cathode active material. The recovered cathode material has been subjected to reprocessing steps such as heat treatment and relithiation, which has supported the regain of its cathode active capabilities and efficient performance.

Electrochemical impedance spectroscopy (EIS) was employed to investigate the kinetics of the Li-ion insertion and exertion processes. The Nyquist plots for all cathode materials

https://doi.org/10.1021/acssusresmgt.4c00533
ACS Sustainable Resour. Manage. XXXX, XXX, XXX−XXX

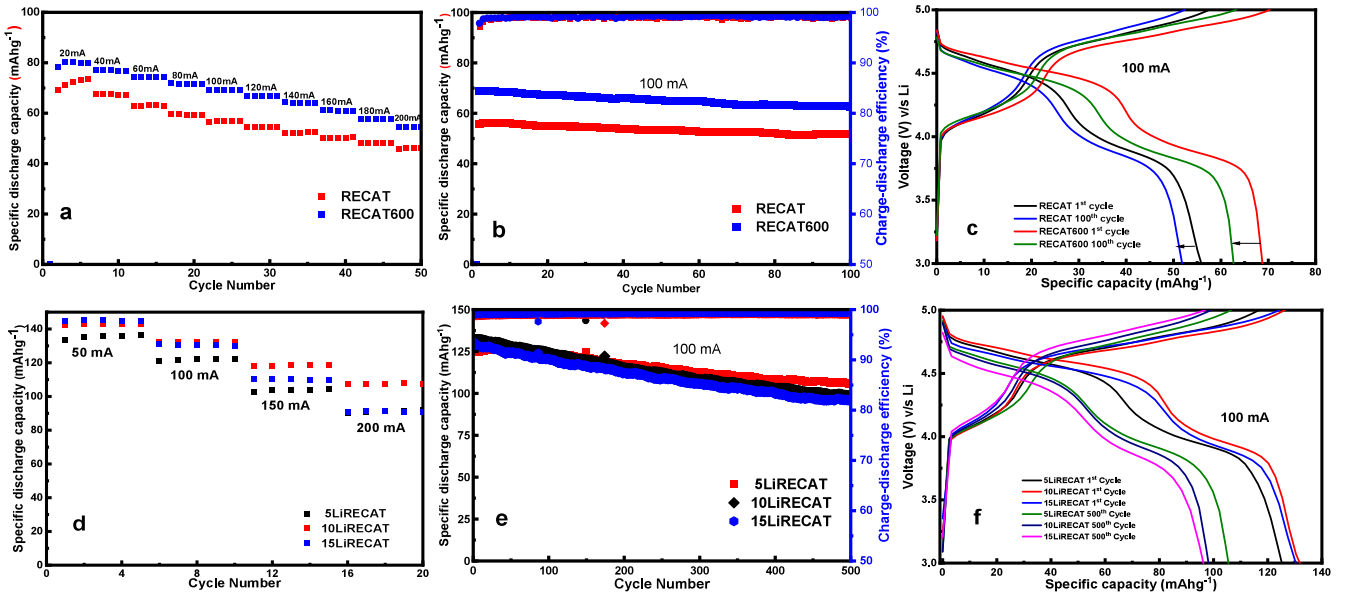

Figure 7. (a) Rate capability, (b) cycle stability, and (c) potential vs specific capacity curves of RECAT and RECAT600 cathode materials. (d) Rate capability, (e) cycle stability, and (f) potential v/s specific capacity curves of 5LiRECAT, 10LiRECAT, and 15LiRECAT cathode materials.

are displayed in Figure 6b, with the inset showing the equivalent circuit to fit the experimental data. This circuit comprises several resistance components: R_s represents the system resistance, R_{SEI} denotes the solid-electrolyte interface resistance, and R_{ct} stands for the charge transfer resistance. Additionally, the circuit includes a constant phase element (CPE) and Warburg impedance (W). The equivalent circuit is depicted in the figure inset; 6b was used to fit the Nyquist plots. The fitting values for the equivalent circuit are given in Table 2. In the high-frequency region, all materials exhibit an overlapping semicircle, attributed to both the SEI resistance (R_{SEI}) and the charge transfer resistance (R_{ct}), indicating the insertion of Li ions at the interface between the electrode and electrolyte. A more detailed examination reveals two distinct semicircles: a smaller one in the higher frequency range and a larger one in the mid-frequency range. The smaller semicircle at higher frequencies is associated with the cathode-electrode resistance (R_{SEI}), while the larger semicircle in the mid-frequency region corresponds to the charge transfer resistance (R_{ct}). The 5LiRECAT has shown the least charge transfer resistance among all of the cathode materials. Conversely, the recycled cathode material exhibited higher charge transfer resistance than other materials. This indicates that the recovered cathode materials are degraded during their initial use, losing their ability to efficiently transport electrochemically active ions and resulting in reduced specific capacities during charge−discharge tests. By relithiating the recovered cathode materials, their capacity for rapid ion transfer, crucial in Li-ion batteries, has been restored. A linear segment in the low-frequency range signifies the interface resistance and enhanced diffusion of Li^+ ions from the electrolyte to the anode.

The recovered cathode material has more resistance than the regenerated cathode materials. However, the RECAT600 electrode has shown more charge transfer resistance than the RECAT electrode due to the lower availability of Li^+ ions in the cathode material. The relithiated cathode materials have shown comparatively lower resistance values, which indicates the cathode materials are well restored to their Li^+ ions insertion−deinsertion properties, which is essential for the faster Li^+ ion diffusion kinetics, which is a critical requirement for a good cathode material.[35]

Figure 7 displays the galvanostatic charge−discharge studies of the recovered, heat-treated, and regenerated cathode materials. Initially, the recovered cathode materials from the spent LIBs were used directly, after heating and lithiation, to fabricate fresh coin cells and electrochemically tested to understand the charge−discharge behavior and efficiency of the spent cathode material. The rate capability tests were conducted in the range of current densities, starting from 20 to 200 mA. The recovered cathode material subjected to the heat treatment and lithiation was also tested similarly.

As shown in Figure 7a, the recovered cathode material (RECAT) has shown a low initial specific discharge capacity of 69.18 $mAhg^{-1}$ at a 20 mA current density. In contrast, the heat-treated cathode material (RECAT600) exhibited an initial specific discharge capacity of 78.37 $mAhg^{-1}$. The specific discharge capacity slightly increases after heat treatment because the unwanted impurity surface over the spent cathode material is burned off, which can enhance the activity of the cathode materials. In both recovered and heat-treated cathode materials, the charge−discharge efficiency is lower at initial cycles, which is increased gradually; it might be due to the cathode surface slowly getting activated by forming a cathode−electrolyte interface (CEI). The spent cathode materials have shown low discharge capacities due to the loss of Li^+ ions during their first life.[3,12,36] The spent cathode materials were rejuvenated by retrieving lost Li^+ ions from the cathode structures by relithiation with different ratios of lithium source. The relithiated spent cathode materials were also subjected to the electrochemical examination to understand the effect of relithiation on the performance of regenerated cathode materials. The heat-treated cathode materials were relithiated with 5% (5LiRECAT), 10% (10LiRECAT), and 15% (15LiRECAT) Li sources of the total cathode mass used for the relithiation. The rejuvenated cathode materials were used as the cathode materials for the fabrication of coin cells. The as-prepared coin cells are imperiled to the galvanostatic charge−discharge tests for a better understanding of their

https://doi.org/10.1021/acssusresmgt.4c00533
ACS Sustainable Resour. Manage. XXXX, XXX, XXX−XXX

rate capability at different current densities, which is displayed in Figure 7a and b, and long cycle stability tests at 100 mA current density, which are shown in Figure 7c and d. The 5LiRECAT, 10LiRECAT, and 15LiRECAT materials have shown an initial specific discharge capacity of 125.2, 131.8, and 130.3 $mAhg^{-1}$, and at the end of 500 cycles, they showed 105.5, 100.2, and 96.2 $mAhg^{-1}$ with a capacity retention of 84.2%, 76.1%, and 73.8%, respectively. These charge−discharge results indicate that lithiation could revive the electrochemical activity of the used cathode materials by lithiation. Excessive lithiation causes a relatively lower capacity compared to controlled lithiation, which might be because excess lithiation may form nonfavorable sedimentation over the surface of the cathode materials. The excess Li can reorder the cathode materials, which may cause structural instabilities, which lead to lower capacity retention. The 5% lithiated cathode materials have shown more capacity retention but lower discharge capacity compared to 10% and 15% lithiated cathode materials. The excess lithiated cathode materials have shown more discharge capacities, as they behave as lithium-rich cathode active materials. The controlled lithiation could revive the activity of the cathode material. Figure 7c and d shows the specific capacity v/s voltage curves of recovered, heat-treated, and lithiated cathode materials cycled at 100 mA current density, illustrating capacity degradation at different cycles. Therefore, this study supplements the drastic improvement in the capacity of the material after lithiation. Also, the obtained capacity retention with long cycle stability of electrochemical studies displays the potential of the recovered cathode material for the second life.

CONCLUSION

This study has demonstrated an effective method of regenerating cathode active materials from spent LIBs via an aqueous method for chemical lithiation to directly regenerate the Ni and Co ion-doped LMO-based spinel class of cathode materials. The elements in the used cathode material Li, Mn, Ni, Co, and O are identified and evaluated in their crystal structure. The lithiation proportions are controlled by increasing the Li^+ concentration in the solution. The initial specific discharge capacity of the electrode made of the relithiation strategy could demonstrate 125.2, 131.8, and 130.3 $mAhg^{-1}$ at 100 mA current density for 5LiRECAT, 10LiRECAT, and 15LiRECAT, respectively. The electrode materials' specific discharge capacities reached 105.5, 100.2, and 96.2 $mAhg^{-1}$ after 500 continuous cycles for 5LiRECAT, 10LiRECAT, and 15LiRECAT, respectively. Among these electrodes, the 5% lithiated cathode material (5LiRECAT) has shown a capacity retention of 84.2%, which is more than other variants of the regenerated cathode materials. Overall, the simple aqueous-based strategy to relithiate the diminished cathode material could provide a second life for the used cathode materials from the waste LIBs.

ASSOCIATED CONTENT

Supporting Information

The Supporting Information is available free of charge at https://pubs.acs.org/doi/10.1021/acssusresmgt.4c00533.

X-ray diffraction data of recovered cathode material and deconvoluted XPS spectra of F 1s level (PDF)

AUTHOR INFORMATION

Corresponding Author

Girish Praveen Nayaka − *Physical and Materials Chemistry Division, CSIR-National Chemical Laboratory, Pune 411008 Maharashtra, India; Academy of Scientific and Innovative Research (AcSIR), Ghaziabad 201002 UP, India;* orcid.org/0000-0001-8166-1465; Email: gp.nayaka@ncl.res.in

Authors

Bogalera Papaiah Shivamurthy − *Physical and Materials Chemistry Division, CSIR-National Chemical Laboratory, Pune 411008 Maharashtra, India; Academy of Scientific and Innovative Research (AcSIR), Ghaziabad 201002 UP, India;* orcid.org/0000-0003-4126-9885

Purnima Rawat − *Physical and Materials Chemistry Division, CSIR-National Chemical Laboratory, Pune 411008 Maharashtra, India; Academy of Scientific and Innovative Research (AcSIR), Ghaziabad 201002 UP, India*

Manjusha V. Shelke − *Physical and Materials Chemistry Division, CSIR-National Chemical Laboratory, Pune 411008 Maharashtra, India; Academy of Scientific and Innovative Research (AcSIR), Ghaziabad 201002 UP, India;* orcid.org/0000-0001-8323-2234

Zhongren Zhou − *Faculty of Metallurgical and Energy Engineering, Kunming University of Science and Technology, Kunming 650093, China; National and Local Joint Engineering Laboratory for Lithium-ion Batteries and Materials Preparation Technology, Key Laboratory of Advanced Battery Materials of Yunnan Province, Kunming University of Science and Technology, Kunming 650093, China*

Complete contact information is available at: https://pubs.acs.org/10.1021/acssusresmgt.4c00533

Notes

The authors declare no competing financial interest.

ACKNOWLEDGMENTS

B. P. Shivamurthy thanks CSIR, New Delhi (31/011(1129)/2019-EMR-I), for providing a research fellowship. G. P. Nayaka thanks CAF (Central Analytical Facility) and CSIR-NCL for providing facilities.

DEDICATION

This paper is dedicated to the Platinum Jubilee Foundation Day Celebration of CSIR-National Chemical Laboratory, India.

REFERENCES

(1) Zhao, Y.; Yuan, X.; Jiang, L.; Wen, J.; Wang, H.; Guan, R.; Zhang, J.; Zeng, G. Regeneration and Reutilization of Cathode Materials from Spent Lithium-Ion Batteries. *Chemical Engineering Journal.* **2020**, *383*, 123089.

(2) Zhang, X.; Li, L.; Fan, E.; Xue, Q.; Bian, Y.; Wu, F.; Chen, R. Toward Sustainable and Systematic Recycling of Spent Rechargeable Batteries. *Chemical Society Reviews.* **2018**, *47*, 7239.

(3) Zhang, B.; Xu, Y.; Silvester, D. S.; Banks, C. E.; Deng, W.; Zou, G.; Hou, H.; Ji, X. Direct Regeneration of Cathode Materials in Spent Lithium-Ion Batteries toward Closed-Loop Recycling and Sustainability. *J. Power Sources* **2024**, *589*, 233728.

(4) Fan, E.; Li, L.; Wang, Z.; Lin, J.; Huang, Y.; Yao, Y.; Chen, R.; Wu, F. Sustainable Recycling Technology for Li-Ion Batteries and

Beyond: Challenges and Future Prospects. *Chemical Reviews.* **2020**, *120*, 7020.
(5) Nayaka, G. P.; Manjanna, J.; Pai, K. V.; Vadavi, R.; Keny, S. J.; Tripathi, V. S. Recovery of Valuable Metal Ions from the Spent Lithium-Ion Battery Using Aqueous Mixture of Mild Organic Acids as Alternative to Mineral Acids. *Hydrometallurgy* **2015**, *151*, 73−77.
(6) Wang, T.; Luo, H.; Bai, Y.; Belharouak, I.; Jayanthi, K.; Paranthaman, M. P.; Manard, B. T.; Wang, E. T. H.; Dogan, F.; Son, S. B.; Ingram, B. J.; Dai, Q.; Dai, S. Direct Recycling of Spent Nickel-Rich Cathodes in Reciprocal Ternary Molten Salts. *J. Power Sources* **2024**, *593*, 233798.
(7) Baum, Z. J.; Bird, R. E.; Yu, X.; Ma, J. Lithium-Ion Battery Recycling—Overview of Techniques and Trends. *ACS Energy Lett.* **2022**, *7* (2), 712.
(8) Makuza, B.; Tian, Q.; Guo, X.; Chattopadhyay, K.; Yu, D. Pyrometallurgical Options for Recycling Spent Lithium-Ion Batteries: A Comprehensive Review. *Journal of Power Sources.* **2021**, *491*, 229622.
(9) Reinhart, L.; Vrucak, D.; Woeste, R.; Lucas, H.; Rombach, E.; Friedrich, B.; Letmathe, P. Pyrometallurgical Recycling of Different Lithium-Ion Battery Cell Systems: Economic and Technical Analysis. *J. Clean. Prod.* **2023**, *416*, 137834.
(10) Jung, J. C. Y.; Sui, P. C.; Zhang, J. A Review of Recycling Spent Lithium-Ion Battery Cathode Materials Using Hydrometallurgical Treatments. *Journal of Energy Storage.* **2021**, *35*, 102217.
(11) Yao, Y.; Zhu, M.; Zhao, Z.; Tong, B.; Fan, Y.; Hua, Z. Hydrometallurgical Processes for Recycling Spent Lithium-Ion Batteries: A Critical Review. *ACS Sustainable Chemistry and Engineering.* **2018**, *6*, 13611.
(12) Ji, G.; Wang, J.; Liang, Z.; Jia, K.; Ma, J.; Zhuang, Z.; Zhou, G.; Cheng, H. M. Direct Regeneration of Degraded Lithium-Ion Battery Cathodes with a Multifunctional Organic Lithium Salt. *Nat. Commun.* **2023**, *14* (1), 584.
(13) Hausbrand, R.; Cherkashinin, G.; Ehrenberg, H.; Gröting, M.; Albe, K.; Hess, C.; Jaegermann, W. Fundamental Degradation Mechanisms of Layered Oxide Li-Ion Battery Cathode Materials: Methodology, Insights and Novel Approaches. *Materials Science and Engineering: B* **2015**, *192*, 3.
(14) Pastor-Fernández, C.; Yu, T. F.; Widanage, W. D.; Marco, J. Critical Review of Non-Invasive Diagnosis Techniques for Quantification of Degradation Modes in Lithium-Ion Batteries. *Renewable and Sustainable Energy Reviews.* **2019**, *109*, 138.
(15) Mao, N.; Zhang, T.; Wang, Z.; Cai, Q. A Systematic Investigation of Internal Physical and Chemical Changes of Lithium-Ion Batteries during Overcharge. *J. Power Sources* **2022**, *518*, 230767.
(16) Kim, T.; Ono, L. K.; Qi, Y. Understanding the Active Formation of a Cathode-Electrolyte Interphase (CEI) Layer with Energy Level Band Bending for Lithium-Ion Batteries. *J. Mater. Chem. A* **2022**, *11* (1), 221−231.
(17) Li, W.; Dolocan, A.; Oh, P.; Celio, H.; Park, S.; Cho, J.; Manthiram, A. Dynamic Behaviour of Interphases and Its Implication on High-Energy-Density Cathode Materials in Lithium-Ion Batteries. *Nat. Commun.* **2017**, *8* (1), 14589.
(18) Cherkashinin, G.; Motzko, M.; Schulz, N.; Späth, T.; Jaegermann, W. Electron Spectroscopy Study of Li[Ni,Co,Mn]O $_2$ /Electrolyte Interface: Electronic Structure, Interface Composition, and Device Implications. *Chem. Mater.* **2015**, *27* (8), 2875−2887.
(19) Takahashi, I.; Kiuchi, H.; Ohma, A.; Fukunaga, T.; Matsubara, E. Cathode Electrolyte Interphase Formation and Electrolyte Oxidation Mechanism for Ni-Rich Cathode Materials. *J. Phys. Chem. C* **2020**, *124* (17), 9243−9248.
(20) Li, J.; Manthiram, A. A Comprehensive Analysis of the Interphasial and Structural Evolution over Long-Term Cycling of Ultrahigh-Nickel Cathodes in Lithium-Ion Batteries. *Adv. Energy Mater.* **2019**, *9* (45), 1902731.
(21) Zhang, J.; Wang, P.-F.; Bai, P.; Wan, H.; Liu, S.; Hou, S.; Pu, X.; Xia, J.; Zhang, W.; Wang, Z.; Nan, B.; Zhang, X.; Xu, J.; Wang, C. Interfacial Design for a 4.6 V High-Voltage Single-Crystalline LiCoO2 Cathode. *Adv. Mater. Deerfield Beach Fla* **2022**, *34* (8), No. e2108353.
(22) Zhang, Z.; Qin, C.; Wang, K.; Han, X.; Li, J.; Sui, M.; Yan, P. Deciphering the Critical Effect of Cathode-Electrolyte Interphase by Revealing Its Dynamic Evolution. *J. Energy Chem.* **2023**, *81*, 192−199.
(23) Stallard, J. C.; Wheatcroft, L.; Booth, S. G.; Boston, R.; Corr, S. A.; De Volder, M. F. L.; Inkson, B. J.; Fleck, N. A. Mechanical Properties of Cathode Materials for Lithium-Ion Batteries. *Joule* **2022**, *6* (5), 984−1007.
(24) Li, W.; Asl, H. Y.; Xie, Q.; Manthiram, A. Collapse of $LiNi_{1-x-y}Co_xMn_yO_2$ Lattice at Deep Charge Irrespective of Nickel Content in Lithium-Ion Batteries. *J. Am. Chem. Soc.* **2019**, *141* (13), 5097−5101.
(25) Pender, J. P.; Jha, G.; Youn, D. H.; Ziegler, J. M.; Andoni, I.; Choi, E. J.; Heller, A.; Dunn, B. S.; Weiss, P. S.; Penner, R. M.; Mullins, C. B. Electrode Degradation in Lithium-Ion Batteries. *ACS Nano* **2020**, *14* (2), 1243−1295.
(26) Zhu, J.; Yoo, K.; Denduluri, A.; Hou, W.; Guo, J.; Kisailus, D. Crystal Structure and Size Effects on the Performance of Li-$[Ni_{1/3}Co_{1/3}Mn_{1/3}]O_2$ Cathodes. *J. Mater. Res.* **2015**, *30* (2), 286−294.
(27) Zhu, X.; Huang, A.; Martens, I.; Vostrov, N.; Sun, Y.; Richard, M.; Schülli, T. U.; Wang, L. High-Voltage Spinel Cathode Materials: Navigating the Structural Evolution for Lithium-Ion Batteries. *Adv. Mater.* **2024**, *36* (30), 2403482.
(28) Zhu, W.; Su, H.; Bai, P.; Li, Z.; Zhang, J.; Zhang, J.; Li, M.; Chen, Y.; Xu, Y. A Layered/Spinel Heterostructured Cathode for Li-Ion Batteries Prepared by Ultrafast Joule Heating. *Chem. Eng. J.* **2024**, *480*, 148045.
(29) Gouadec, G.; Colomban, P. Raman Spectroscopy of Nanomaterials: How Spectra Relate to Disorder, Particle Size and Mechanical Properties. *Prog. Cryst. Growth Charact. Mater.* **2007**, *53* (1), 1−56.
(30) Gao, Y.; Yin, P. Origin of Asymmetric Broadening of Raman Peak Profiles in Si Nanocrystals. *Sci. Rep.* **2017**, *7* (1), 43602.
(31) Gieu, J. B.; Winkler, V.; Courrèges, C.; El Ouatani, L.; Tessier, C.; Martinez, H. New Insights into the Characterization of the Electrode/Electrolyte Interfaces within LiMn2O4/Li4Ti5O12 Cells, by X-Ray Photoelectron Spectroscopy, Scanning Auger Microscopy and Time-of-Flight Secondary Ion Mass Spectrometry. *J. Mater. Chem. A* **2017**, *5* (29), 15315−15325.
(32) Nesbitt, H. W.; Banerjee, D. Interpretation of XPS Mn(2p) Spectra of Mn Oxyhydroxides and Constraints on the Mechanism of MnO2 Precipitation. *Am. Mineral.* **1998**, *83* (3-4), 305−315.
(33) De Taeye, L. L.; Vereecken, P. M. Chemo-Mechanical Effect of Chlorine Modified TiO $_2$ Coatings on LMO. *J. Mater. Chem. A* **2022**, *10* (45), 24398−24409.
(34) Bencherifi, Y.; Larhrib, B.; Sayegh, A.; Nikiforidis, G.; Anouti, M. Phosphonium Ionic Liquid-Based Electrolyte for High Voltage Li-Ion Batteries: Effect of Ionic Liquid Ratio. *J. Appl. Electrochem.* **2021**, *51* (12), 1651−1664.
(35) Gaberšček, M. Understanding Li-Based Battery Materials via Electrochemical Impedance Spectroscopy. *Nat. Commun.* **2021**, *12* (1), 6513.
(36) Liu, Y.; Jiao, B.; Guo, X.; Li, S.; Lou, X.; Jiang, F.; Weng, X.; Cao, M.; Chen, J.; Zhang, Q.; Wang, G.; Di, J.; Xu, P. Retrieving Lost Li in LIBs for Co-Regeneration of Spent Anode and Cathode Materials. *Energy Storage Mater.* **2024**, *72*, 103684.

https://doi.org/10.1021/acssusresmgt.4c00533
ACS Sustainable Resour. Manage. XXXX, XXX, XXX−XXX